

Department of Mechanical and Aerospace Engineering

**Investigation of the thermo-elastic effect on
the satellite panels identified by an industrial problem
of de-pointing**

Author: **Olga Ganilova**

Supervisor: **Prof Matthew Cartmell**

A thesis submitted in partial fulfilment for the requirement of degree in

Doctor of Philosophy

2022

Declaration of Authenticity and Author's Rights

This thesis is the result of the author's original research. It has been composed by the author and has not been previously submitted for examination which has led to the award of a degree.

The copyright of this thesis belongs to the author under the terms of the United Kingdom Copyright Acts as qualified by University of Strathclyde Regulation 3.50. Due acknowledgement must always be made of the use of any material contained in, or derived from, this thesis.

Signed: *Olga Ganilova*

Date: 26/09/22

Abstract

Satellite system design in most circumstances demands “distortion free” behaviour or a quantifiable and budgeted system approach with respect to structural distortion for on-station pointing performance. Due to variation in material properties through the spacecraft structure and payload and temperature gradients the structure will deform under such conditions, hence this will affect pointing vectors or the Line of Sight of critical payloads. As has been discovered, industrial practice at Airbus DS in particular approaches this problem using finite element techniques established by years of experience and practical tests. However this approach does not provide an accurate enough tool for the prediction of coupling effects between the mechanical deformation and the thermal loading, which would guarantee high accuracy of the thermo-elastic model. The finite element approach as well as experimental tests were both unable to simulate the deformation effect within the honeycomb core, noting that has a nonlinear nature of deformation and could contribute to the inaccuracy of the model output. Therefore in this thesis a partially-coupled analytical thermo-mechanical model has been developed to provide Airbus DS with a tool for the prediction of the displacement within a typical honeycomb panel, taking into account the coupling between the mechanical and thermal effects. The model predicts the displacement of the panel taking into account dynamic mechanical and thermal loadings and is capable of predicting the heat distribution along the thickness of the panel core. The work concludes with a guide for use of the analytical model and also with a discussion and suggestions for how Airbus DS could investigate other phenomena caused by parasitic vibration which could potentially contribute to the problem of de-pointing.

Acknowledgement

The author would like to gratefully acknowledge financial and confidential data support provided by Airbus DS.

The author would like to thank her supervisor, Prof Cartmell, for enormous support and expertise in the field.

The author would also like to thank her family for endless love and support during the time of working and writing up of this thesis.

Table of Contents

Introduction	9
1. Background of the thermo-elastic problem in the industrial Airbus DS context.	14
1.1 Main approach to thermo-elastic analysis	14
1.2. Thermo-elastic analysis – Finite element techniques	24
1.2.1. <i>Finite element techniques used within established practice at Airbus DS</i>	24
1.2.2. <i>Key thermoelastic outputs and conclusions from previous Airbus DS experiments</i>	29
1.2.3. <i>Composite Plate Theory versus the Finite Element Method</i>	36
1.2.4. <i>Comparison of the DSM (based on FSDT) with the FEM (based on Nastran results)</i>	41
1.2.5. <i>Accuracy and applicability to the cases, as previously considered by Airbus DS.</i>	47
1.2.6. <i>Software available for elastic and thermal effects in industrial practice</i>	49
1.3. Thermo-elastic analysis – Analytical coupled thermo-mechanical models	51
1.3.1. <i>Thermoelasticity</i>	51
1.3.2. <i>Functionally Graded Materials and modelling techniques used</i>	60
1.3.2.1. <i>Modelling the material properties of FGMs</i>	60
1.3.2.2. <i>Temperature Dependent Properties.</i>	62
1.3.3. <i>Partially coupled thermo-mechanical analysis</i>	63
1.3.3.1. <i>Temperature distribution along the thickness.</i>	64
1.3.3.2. <i>Thermo-mechanical model, governing equations of motion</i>	67
1.3.4. <i>Carrera’s Unified Formulation (CUF)</i>	73
1.3.5. <i>A Third order theory with Thermomechanical Coupling (TTC).</i>	76

1.4. Environmental conditions and structure of the satellite panel under investigation..	81
1.4.1. <i>Key strategies learnt from laboratory simulation of the thermal environment</i>	87
1.4.2. <i>Thermal cycles in Low Earth Orbit (LEO)</i>	90
1.4.3. <i>Honeycomb panels in space applications</i>	92
1.5. Conclusions	99
2. Development of the coupled analytical model for thermo-mechanical analysis	
.....	102
2.1. A model for the mechanical behaviour of the panel	105
2.2. A model for the thermal behaviour of the panel.	109
2.3. Application of the derived model for a panel in the free heat exchange conditions.	
.....	117
2.3.1 <i>The case of thermal loading</i>	119
2.3.2 <i>The case of thermo-mechanical loading at constant temperature</i>	128
2.3.3 <i>The case of thermo-mechanical loading with time variable thermal loading</i> ...	134
2.4. <i>Application of the derived model for a panel subjected to the heat flux</i>	136
2.5. Conclusions	143
3. Experimental study of the thermo-elastic behaviour of the honeycomb panel.	146
3.1. Experimental set-up	150
3.2. Results analysis and discussion	159
3.2.1. <i>The effect of retention or loss of heat due to dynamic mechanical loading in extreme thermal environments, and the implications of this for modelling.</i>	159
3.2.2. <i>Effect of the dynamic loading and extreme environmental temperature on the temperature distribution along the surfaces and through the thickness of the panel</i> ...	168
3.2.3. <i>Effect of extreme environmental temperature on the panel deflection response under the imposed dynamic mechanical loading</i>	172
3.2.4 <i>Effect of deflection on the temperature distribution along the surface and through the thickness of the panel in extreme environmental temperatures.</i>	175

3.3. Effect of simultaneous mechanical loading and extreme environmental temperatures on the heating-up and cooling-down processes within the panel.....	181
3.4. Conclusions.	183
4. Correlation of the results from the analytical model with the experimental data.	187
4.1 Displacement distribution in response to the dynamic mechanical loading and variable environmental temperature	189
4.2 Temperature distribution along the thickness of the panel in response to the dynamic mechanical loading and variable environmental temperature.	197
4.3. Conclusions.	201
5. Discussion of the results from a Thermomechanical Finite Element Model for a Honeycomb Sandwich Panel.....	203
5.1 FE Models developed in [Appendix H].	204
5.2. Simulation Results for three FE models.	208
5.2.1. <i>Output for 3D Geometrically Accurate Model</i>	208
5.2.2 <i>Simulation results for the 3D Continuum Model</i>	211
5.2.3 <i>Simulation results for the 2D Continuum Model.</i>	214
5.3 Conclusions.	214
6. Application of the method of multiple scales for the derivation of an approximate analytical solution for thermo-mechanical model developed	216
6.1. Multiple Scales Perturbation Analysis.	223
6.1.1. <i>Governing equation of motion and multiple time scaling.</i>	223
6.1.2 <i>Perturbation equations.</i>	225
6.1.3. <i>Identification of secular terms and resonance conditions</i>	227
6.1.4. <i>Slow-time modulation equations and solvability conditions</i>	229
6.1.5. <i>Particular solution</i>	232
6.2. Solution procedure.	239
6.3. Numerical example.	240

6.4 Conclusions.	244
7. Guidance for the use of the code developed for obtaining the deflection results and heat distribution along the thickness of the panel.	245
7.1 A guide for the use of the annotated code for obtaining the deflection results and heat distribution along the thickness of the panel under free heat exchange conditions.	245
7.2 Guid for the use of the annotated code for obtaining the deflection results and the heat distribution along the thickness of the panel under heat flux conditions.	256
7.3 Conclusions	263
Conclusions.	264
References.	276
Appendix A. <i>Mathematica</i> code for derivation of the mechanical and thermal equations for the coupled system.....	294
Appendix B. Output from the <i>Mathematica</i> coded solution (Appendix B) presented in an annotated format	299
Appendix C. Open Data for the paper ‘Experimental investigation of the thermoelastic performance of an aerospace aluminium honeycomb composite panel’ by Olga A. Ganilova, Matthew P. Cartmell, and Andrew Kiley.....	300
Appendix D. Experimental tests procedure log.....	301
Appendix E. Communication on properties for the panels supplied.....	302
Appendix F. Temperature distribution along the thickness for other environments..	303
Appendix G. Published papers as a result of work performed for this thesis.....	308
Appendix H. Draft of the paper for publication ‘Development of a Simplified Thermomechanical Finite Element Model of a Honeycomb Sandwich Panel for Satellites in Orbit’, Eoin Reilly, Aaron Weidmann, Jon Richardson, Matthew Dougan, Neil Gordon, Olga Ganilova	360

Introduction

Satellite system design in most circumstances demands “distortion free” behaviour or a quantifiable and budgeted system approach with respect to structural distortion for on-station pointing performance. Due to variation in material properties through the spacecraft structure and payload and temperature gradients the structure will deform under such conditions hence this will affect pointing vectors or Line of Sight of critical payloads. Mission pointing needs demands on payloads to vary from several arc-seconds to sub-arc seconds of angular shift of pointing vectors, dependent upon the mission and science needs.

Therefore such anomalies of distortion have to be taken into account and accommodated within the system design. However in reality it is generally not possible or not practical to implement all mission thermal loading scenarios, or not possible to implement the true environment and gradients that will be detected in the form of a preliminary test. Hence thermo-elastic behaviour prediction is normally conducted through analysis in the form of model development and appropriate budgeting of pointing.

As will be demonstrated in this work, the research based evidence confirms that historically in Airbus DS practice, de-pointing is budgeted for *analytically* through a multi-disciplinary approach involving:

- Thermal control /analysis specialists able to predict structural thermal distributions both of a static and transient nature. The thermal mathematical models (TMMs) are subject to correlation and validation relatively late in the spacecraft development life cycle via thermal balance tests conducted in specialist vacuum chamber facilities.
- Structural specialists responsible for architectural management and finite element method (FEM) analysis take the thermal ‘maps’ from the thermal specialists, and predict thermal distortion and payload (angular) changes from nominal states. Often numerous thermal cases (mappings) are applied to the FE model to establish worst case scenarios for de-point. Key outputs from the FE model are normally angular shifts in pointing vectors at discrete payload locations or from discrete payload features. Calculated angular changes are then provided typically to

mission system engineers, for further data processing or as direct input into system budget allocation.

- Mission specialists for supporting definition of the mission scenario and usually the final de-point budget management.

It is also known that typically the process of mapping is quite complex and requires an experienced engineer. Different methods exist or have been developed in house to perform the correspondence between mechanical and thermal nodes. In most cases the geometry of the thermal model is much simpler than the FEM geometry and the number of thermal nodes is much smaller than used for the FEM elements. The correspondence method should be adapted to these constraints. Correspondence methods are often nodal methods: temperatures are applied on FEM nodes. These methods should take into account the geometry differences between the mechanical and thermal models.

Airbus DS follows a post-processing procedure with in-house tools to provide both performance results and data for physical understanding by providing the following information:

- Thermal contributors, through a mapping in the thermal model of the temperature variations with respect to particular events (*Systema* tool is used),
- Mechanical contributors from the macro-node analyses by providing a synthesis table or a mapping of the FEM representing the influence of the defined macro-nodes. This is achieved due to a sequence of Nastran, Matlab and FEMAP tools.
- Thermo-elastic performance results in the form of distortion temporal evolution.
- Deformed shape animation of the complete scenario using a separate graphical representation software.

Until recently, the thermo-elastic analyses have been restricted to running the FEM with specific thermal maps in order to check that the end-to-end predictions satisfy the thermo-elastic requirement allocation. This was acceptable as long as the stability requirements were not too demanding.

It was also found that modelling of spacecraft structure (panels, cleats, tubes) is dependent on the assessment of the temperature gradients through the thickness. For 2D modelling the temperature should be homogenous through the panel. The main risk with 2D modelling here is a non-representative bending by not taking into account the gradient in

the thickness of the panel. In case of an asymmetrical panel, 2D modelling is not representative. This modelling introduces an error in the computed distortions calculated, in comparison with the 3D modelling, for example. Modelling of equipment is normally performed after sensitivity analyses, which shows a significance of the thermo-elastic contribution of a specific piece of equipment to the stability. In this case a refinement to be representative of the equipment stiffness and thermal expansion can be performed. Modelling of interfaces (glued and bolted) is dependent of the modelling assumptions.

Thermo-elastic stability predictions include a large number of hypotheses which need to be listed and evaluated to assess the reliability of the predictions associated with a level of confidence:

- Thermal modelling,
- Structural modelling,
- Mission requirements definition (margins & uncertainties),
- Correspondence of thermal and structural models,
- Test measurement accuracy.

Thermal uncertainties impacting on the thermo-elastic computation are not systematically assessed, whereas the temporal thermal variations on certain areas of the spacecraft are major contributors for thermo-elastic analyses.

For mechanical uncertainties the analysis of the main mechanical contributors is essential during the design phase in order to optimise the design and to understand the mechanical behaviour. Once the main contributors are known, the uncertainty analysis can be performed to determine the impact of mechanical parameters and mechanical modelling choice. Therefore mechanical contributors can be impacted by:

- Modelling parameters,
- Uncertainty in material,
- Uncertainty in orientation of orthotropic material,
- Uncertainty in cleat modelling (spring stiffness),
- Uncertainty in geometrical dimension (thickness).

Since 2000, a number of initiatives have been run separately in different programs in order to improve the thermo-elastic process: to get better correspondence between the

mechanical and thermal models, evaluation of the main structural and thermal contributors, post-processing of the results by combining temperatures variations, and temporally deformed shape analyses.

In the same way a number of technologies have been used for testing several devices and satellites: videogrammetry, holography and interferometry but without a consolidation of the findings for use on future programs. All these initiatives are available and quite a few of them were evaluated, based on confidential material supplied by Airbus DS, in order to propose a consolidated and reliable thermo-elastic methodology to be used on future demanding mission programs.

It should also be pointed out that the thermal control system in the spacecraft aims at keeping all the equipment in a favourable thermal environment during all mission phases. The impact of major thermal contributors is usually not, or only partially, studied. Thermal analyses of the contributors give useful information on thermal uncertainties to be taken into account in the thermo-elastic analyses. This analysis should be realised by heat flux in these zones. These analyses will allow the determination of the thermal parameters impacting on the thermo-elastic analyses in order to consider the associated thermal uncertainties. The dissipation of the equipment is not constant during the spacecraft mission. Dissipation varies according to the mission phases of the spacecraft. The maximum thermal flux variations are found for electrical loads, specifically data reception, amplification, and signal transmission.

Therefore considering the uncertainties in dynamic and thermal analysis, as well current practice in Airbus DS, there is a strong need for further research into an increase of the accuracy of prediction in existing multistage techniques or an alternative modelling approach to the existing mapping approach. Since it has been evidenced that modelling of a spacecraft structure is dependent on the ability of the model to predict or take into account the temperature gradients through the thickness, the alternative approach should include not only a resolution of the mapping approach but the influence of the thermal distribution through the thickness as well.

Therefore in this thesis a study has been performed into the analysis of existing approaches in Airbus DS practice, based on the confidential reports provided (Chapter 1), which shaped up the problem as driven by the industrial partner, Airbus DS. Once the current approaches were clear a study of environmental conditions of the spacecraft or satellite has been performed, based on the open literature (Chapter 1), to understand the thermal and mechanical loading conditions as well as the environmental conditions. In Chapter 1 an extensive analysis of modelling techniques has been performed to identify the most appropriate approach which could benefit the Airbus DS with an alternative higher accuracy model reducing the number of uncertainties, eliminating the need for use of two models and their subsequent mapping, as well as to provide an ability to incorporate the effect of the thermal gradient along the thickness of the satellite panel. This intention also resulted in deeper research into the phenomena of thermo-elasticity which indicated the need for a coupled or partially coupled model to address the scope of the alternative modelling approach (Chapter 1). Therefore in Chapter 2 a partially coupled thermo-mechanical analytical model was developed and applied to the case of a typical panel used in Airbus DS practice. A set of experimental tests have been performed and discussed in Chapter 3 where samples provided by Airbus DS were tested under a variety of thermal and mechanical loading conditions. Chapter 4 then presents the process of correlation of results from the analytical model developed and experimental work performed. Some finite element work was performed in Chapter 5 as part of a final year group student project to identify the ability of the FEM package to make a prediction similar to the one obtained using the developed analytical model. Since the solution for the analytical model was obtained using integration techniques in *Mathematica*, it was decided to explore the possibility of obtaining a closed form solution using the method of multiple scales in Chapter 6. Since the problem considered was defined by the industrial partner, Airbus DS, Chapter 7 is dedicated to the development of the annotated code and guidance for code use for engineers at Airbus DS. The conclusions section finalises the thesis, critically reflecting on the whole study, the analytical model developed, its applicability and use, its advantages and limitations, as well benefits for Airbus DS practice.

Appendix G provides a copy of the published papers as a result of the work performed in the thesis. Appendix H consists of a draft of the paper prepared by the author of this thesis and students working on the final year project dedicated to the development of the FEM for a satellite panel.

1. Background of the thermo-elastic problem in the industrial Airbus DS context

Composite materials are increasingly being used in structural design in the practices of Airbus DS and other industrial partners, particularly in the aerospace industry. This is mainly due to their high strength and specific directional properties. This allows the design of structures with minimum weight and maximum strength to achieve desirable aeroelastic and dynamic properties. To understand the material properties their static and dynamic behaviour is studied, for example as free vibration analyses of representative composite structures. The results from free vibration analysis are generally used to characterise aeroelastic behaviour, dynamic response, acoustic performance, and to avoid possible resonance [1]. This method is commonly used for aeroelastic analysis of aircraft structures.

It has been pointed out in the introduction that the problem for the this project came from evidence gathered up by Airbus DS based on practical tests and general observation of satellite behaviour, as well as from modelling outputs. Therefore a series of confidential reports provided by Airbus DS [2-108] were analysed as the main basis for the resolution of the practically observed problem.

1.1 Main approach to thermo-elastic analysis

After analysis of confidential reports provided Airbus DS it was concluded that thermoelastic analyses at Airbus DS is performed mainly to investigate a spacecraft's stability on orbit (i.e. its relative position or pointing accuracy) and structural strength [109]. This analysis may focus on units, instruments or satellites. The main aim of the analysis in this case is to take into account thermo-elastic phenomena either by accurate modelling or at least by knowing the boundaries of accuracy.

To investigate the aspects of stability in pointing the process normally involves three steps [109]:

1. Thermal control /analysis. This involves the development of the thermal mathematical models (TMMs) based on thermal finite difference analysis, subjected to correlation and validation later in the spacecraft development life cycle via thermal balance tests in vacuum chamber facilities.

2. Structural analyses. Development of finite element models (FEM) to predict mechanical distortion due to thermal effects. As a rule, specialists responsible for architectural management and FE analysis take the thermal ‘maps’ from the thermal specialists, and predict thermal distortion and payload (angular) changes from nominal states. This is performed to establish worst case scenarios for de-point. Key outputs from the FE model are normally angular shifts in pointing vectors at discrete payload locations or from discrete payload features. Calculated angular changes are then provided, typically to mission system engineers for further data processing.

3. The last stage is application of the model output to the mission scenario. This is undertaken by Mission specialists for supporting their definition of the mission scenario and usually the final de-point budget management.

Until recently, Thermo-Elastic Deformation (TED) analyses have been restricted to running the FEM with specific thermal maps [109,110], as described above. This has been done in order to check that the end-to-end predictions satisfy the TED requirement allocation. This was acceptable as long as the stability requirements were not too demanding.

Usually the satellite thermo-elastic stability performance predictions imply a large number of parameters:

- mission scenario (duration, attitude variations, internal / external thermal flux variations),
- mechanical and thermal model representativeness with respect to the ‘as designed’ and ‘as-built’ forms,
- mechanical and thermal model correspondences and completeness.

However with increasing instrument resolutions and more demanding missions (longer imaging periods with significant Sun aspect angle variations), thermo-elastic stability becomes a key contributor for future mission pointing performance [110]. Thus there is a strong need to improve the thermo-elastic analysis accuracy, to develop new verification techniques and to define an overall thermo-elastic engineering methodology to be applied in future projects in order to guarantee higher accuracy of the prediction, and therefore the expected stability. In parallel three in-orbit anomalies on an Earth observation satellite have confirmed that thermo-elastic predictions do not always consider all the major

stability contributors, and that high accuracy in the whole thermo-elastic engineering process is required. Precision in specification to prediction and up to testing is necessary to guarantee the expected stability performance of future demanding projects.

Since 2000 a number of initiatives have been run separately in different programmes in order to improve the thermo-elastic process: to get better correspondence between the mechanical and thermal models, evaluation of the main structural and thermal contributors, post-processing of the results by combining temperatures variations, and temporally deformed shape analyses [109]. During these initiatives a number of devices and satellites have been tested using photogrammetry [111,112] videogrammetry, holography and interferometry, when the displacement contours resulting from thermal loading were correlated with the system FEM deflections under test conditions [111]. However this has been done without a complete consolidation of the findings [112].

During these experimental procedures it has become obvious that recent image processing developments can lead to accurate measurements down to a few tens of microns resolution on large structures using videogrammetry [110]. Videogrammetry is also widely used because of the cost of testing in vacuum. The only possibility of affording a vacuum chamber test would be to have the measurement device fitted as a “passenger” on a thermal vacuum test on one representative spacecraft. But this would introduce the presence of active and passive thermal hardware, preventing a direct measurement of the structure’s external surface temperature. It is also difficult to guarantee a null effect of the test set-up on the thermal environment. Therefore the videogrammetry technology is applied to a small satellite (such as the Astrobus spacecraft) subjected to local conductive heating through test heaters. As a more advanced option videogrammetry could be used on a large satellite (for example, the Solar Orbiter STM in [94]) placed in a climatic chamber to perform the test on large size reflectors. This would provide results to validate the predictions for future programmes.

These programmes which concentrate on thermal issues are necessary because of the effect of the following thermal contributors during the mission [110]:

•Heaters

Electrical heaters are used to prevent excessive cooling of any part of the spacecraft and this cooling is defined as a specific dissipation according to the mission and the unit's temperature limit. Heaters are often the solution for limiting temperature variations of the unit. One of the solutions envisaged for limiting thermo-elastic distortions is to add thermal control onto the structure to limit thermo-elastic distortion.

•Solar flux

The solar flux constant changes from 1423 W/m^2 to 1321 W/m^2 during a low Earth orbit. The variation of solar flux absorbed by the spacecraft during its mission contributes to the temperature variation and distortion.

•Earth flux (or other planetary flux) and albedo

The Earth flux and albedo flux contribute to the spacecraft temperature change during the orbit and also contribute to the distortion.

•Infrared (IR) flux

These fluxes are due to the exchange flux between spacecraft sub-assemblies and the radiative coupling between the spacecraft and space. The variation between solar exposure and eclipse contributes to generate temperature variation with IR flux.

A knowledge of these fluxes is important since it defines the necessary extent of the thermo-elastic analyses through introducing the parameters of thermo-elastic distortions. In the design phase this information is crucial for thermo-elastic dimensioning and improvement of spacecraft stability [110]. The identification of the expected major thermo-elastic distortion contributors for the mechanical and the thermal sides (Bi-metallic areas, high temperature/gradient variations, instruments/sensors mechanical/thermal interfaces, etc) is the first stage of the design process. It defines the initial conditions for both the FEM and the TMM, the areas requiring detailed modelling to achieve [113]:

- accurate thermal gradients
- accurate structural distortions
- a direct interpolation between the mechanical and thermal models.

Most of the missions described above, targeted to improve the thermo-elastic analyses procedure, concentrated on early testing and verification in the most accurate and cost

effective way. There have been a few attempts to introduce additional tools to improve the process of interpolation/matching of the outputs from FEM and TMM. In this work the principal interest and motivation lies in the improvement of the modelling side. To understand how the process of modelling can be improved the current practice at Airbus DS has been carefully reviewed.

In the three-stage process defined above for the thermo-elastic stability predictions usually a large number of hypotheses are introduced due to uncertainties [110]:

- Thermal modelling:
 - Obtaining material characteristics,
 - Understanding the implications of simplified modelling (2D vs 3D, interfaces),
 - Recognising the differences with respect to the “as designed and “as built” forms.
- Structural FEM modelling:
 - Material characteristics,
 - Simplified modelling (2D vs 3D, interfaces),
 - Recognising the differences with respect to the “as designed and “as built” forms.
- Mission requirements definition (margins & uncertainties):
 - Time frame,
 - Satellite attitude,
 - Identification of the variations in dissipation.
- FEM / TMM correspondence,
- Test measurement accuracy
 - In deformation and temperature data

The uncertainty analysis aims to determine the impact of mechanical parameters and mechanical modelling choice on the main contributor coefficients. This analysis can begin only when the main contributors are known [110].

Mechanical contributors can be impacted by:

* **Modelling parameters:**

- Uncertainty in material (Young’s modulus - E, Coefficient of thermal expansion - CTE),

- Uncertainty in the orientation of orthotropic material,
- Uncertainty in cleat modelling (spring stiffness assumptions within cleat design),
- Uncertainty in geometrical dimensioning (thickness, for example),
- Uncertainty in Multi-Layer Insulation (MLI) (potential additional stiffness due to too much tightening of the MLI).

* **Modelling** choices:

- Use of gradient in thickness,
- Modelling of equipment,
- Modelling of interfaces,
- Meshing details of major contributors areas,

* **Differences between the “as-designed” and “as built” forms.**

The process of assessment of the various uncertainties can be summarised in Figure 1.1.

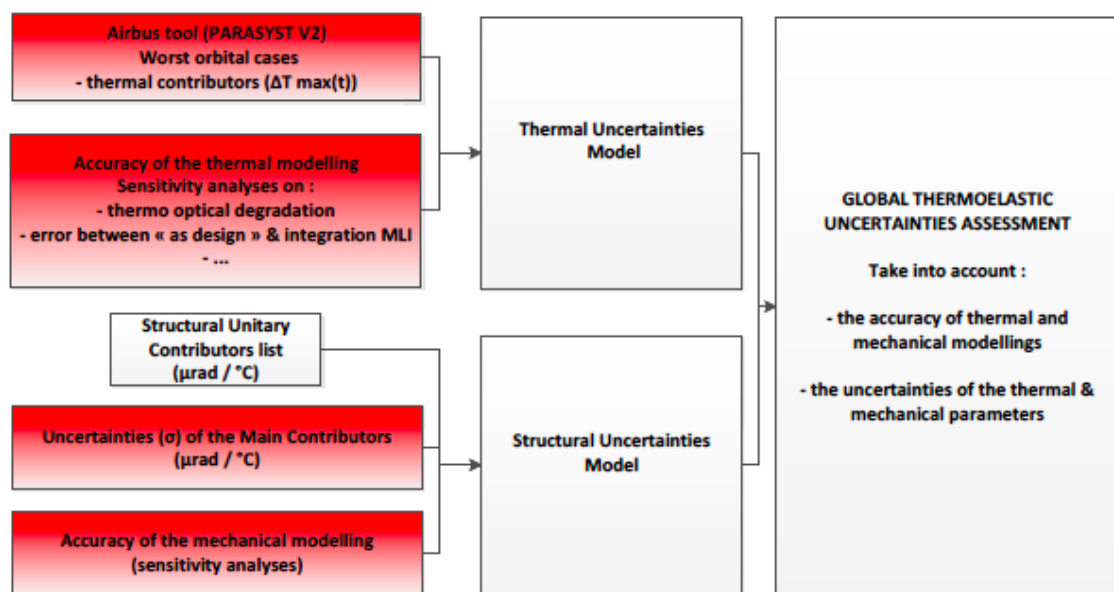


Figure 1.1. Thermo-elastic uncertainty assessment [110]

Once the uncertainty analysis is complete, and a number of hypothesis have been introduced, the modelling process can be started.

Modelling of the spacecraft structures [110] (panels, cleats, tubes) is dependent on the assessment of the temperature gradients through the thickness, whether it is linear or nonlinear. For 2D modelling the temperature should be homogenous through the panel.

However the main risk with 2D modelling is a non-representative bending since the variation of the thermal gradient along the thickness of the panel is not taken into account. This modelling introduces an error in the computed distortions, compared to results obtainable from 3D modelling.

Modelling of equipment is performed if sensitivity analyses show a significant thermo-elastic contribution from a specific piece of equipment to the vehicle's stability. In this case the structure would have to be assessed and modelled, taking fully into account the equipment stiffness and thermal expansion.

Modelling of interfaces (glued and bolted) is dependent on the general modelling assumptions that have been made, and can be included in the FEM if there is evidence of a significant thermal contribution.

For the modelling proposed Airbus DS uses well-developed in-house tools based on the Nastran, Matlab and FEMAP FEM packages and TMM based on *Systema* software, following the methodology shown in Figure 1.2.

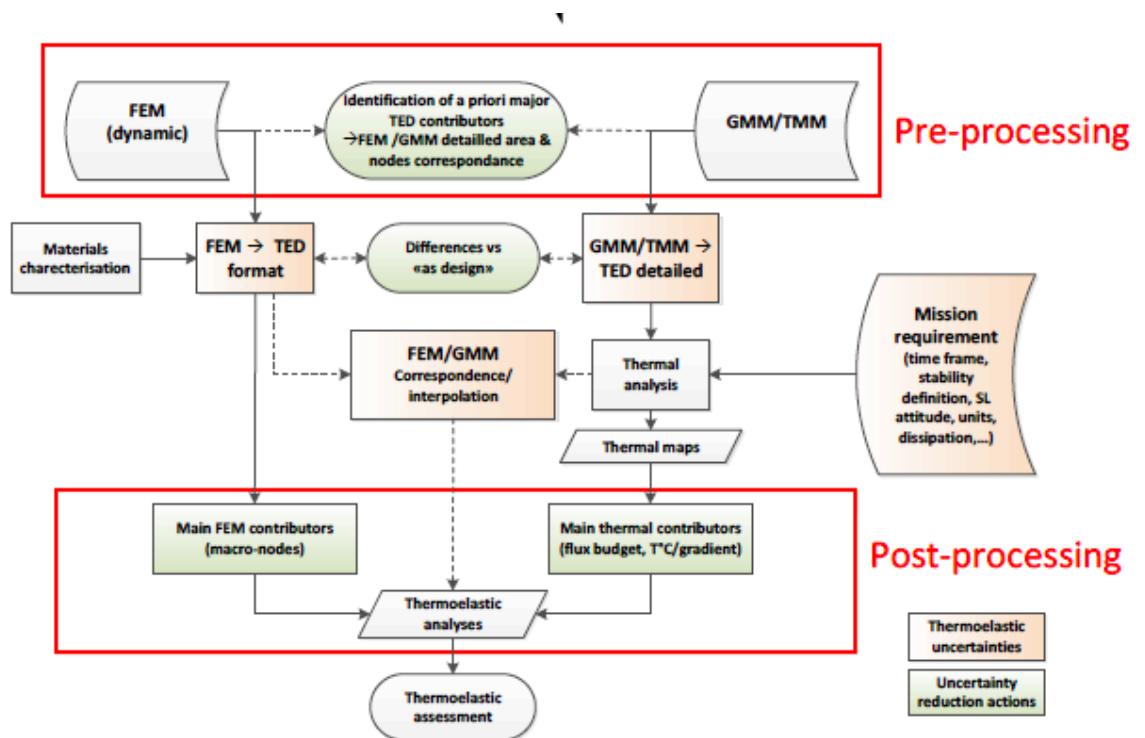


Figure 1.2. Modelling methodology for uniting FEM and TMM, as used by Airbus DS [110].

The aim of this complete modelling process is to provide both performance results and data for physical understanding by going through the following steps [110]:

- Thermal contributions are defined by mapping the temperature variations in the thermal model with respect to particular events (using the *Systema* tool),
- Mechanical contributions are obtained from the macro-nodal analyses by providing a synthesis table or a mapping of the FEM, representing the influence of the defined macro-nodes. This is achieved due to the sequential use of Nastran, Matlab and FEMAP tools. This macro-node discretisation is possible by combining detailed thermal node influences into significant physical areas.
- Thermo-elastic performance results are presented as temporal evolutions of distortion, clouds of complete line of sight (LOS) distortions, tables of results synthesis (minima, maxima, excursion, orbital, seasonal, and ageing effects).
- Deformed shape animation of the complete scenario. This can be completed by adding a visual comprehension of the thermal and mechanical contributions in order to understand the physical phenomena (thermal flux, coefficient of thermal expansion (CTE)) that generate the distortions.

This means that the proposed thermo-elastic prediction methodology can be summarised as:

- A direct correspondence between the mechanical (FEM) and thermal (TMM) models,
- Evaluation of the main structural and thermal contributors,
- Identification of the differences between the two models and the “as-designed” / “as-built” forms,
- Detailed post-processing by combining temperature variations and deformed shapes.

Thermal prediction is based on the thermal parameters presented in Fig. 1.3.

$$P_{INT} + P_{EXT} - \sum_{j=1}^n R_{ij} \sigma (T_i^4 - T_j^4) - \sum_{j=1}^n C_{ij} (T_i - T_j) - H_i (T_i - T_a)^\eta = M_i C_p \frac{dT_i}{dt}$$

↑
↑
↑
↑
↑

Power
Radiation
Conduction
Convection
Thermal inertia

<p>With:</p> <p>P_{int} : Internal dissipation power (W)</p> <p>P_{ext} : External absorbed power (Solar Flux, Albedo, and Earth) (W)</p> <p>$R_{i,j}$: Radiative coupling (m²)</p> <p>$C_{i,j}$: Conductive coupling (W/K)</p>	<p>Simplification in space environment:</p> <p>$P_{EXT} = \alpha S_r \Phi_S + \alpha S_r \Phi_A + \epsilon S_r \Phi_T$</p> <p>$\Phi_S =$ Solar Flux</p> <p>$\Phi_A = \alpha F_T C_s$ Albedo Flux (F_T view factor and C_s solar constant)</p> <p>$\Phi_T = F_T C_T$ Earth Flux and C_T Earth constant</p> <p>$H_i (T_i - T_a)^\eta = 0$ (No convection in space)</p>
--	--

Figure 1.3. Thermal parameters for thermal prediction [110]

At the spacecraft level, the potential thermal contributions to thermo-elastic prediction discrepancies in panels are:

- Temperature predictions in panels & cleats.
- General temperature mapping.
- The management of thermal gradients in panels (in-plane and/or through the thickness of the panel).

For the mechanical model based on Nastran finite element modelling, a thermal expansion coefficient $\alpha = 10^{-5}$ m/(m K) and a 20° C reference temperature are set to the model, and a 100° C temperature increase is applied [114]. If changes in FEM are needed only the thermoelastic properties of the material data input are modified in order to ensure that stiffness of the model is still the same.

To support the correlation process of the mechanical model and the thermal model certain Airbus DS in-house tools are available, including the commercially available Nastran suite of tools for static solution sequences and the ESATAN-TMS thermal software. The main aim of correlation is to obtain a valid FEM justified as ‘fit for purpose’, for use at system level.

A common workspace to perform the correspondence between thermal and mechanical models is within the I-DEAS tool [114]. In I-DEAS, only finite element models may be imported as mathematical models, so if a finite difference or finite volume model has been used for the thermal modelling it would then require to be transformed into a finite element model in order to be imported successfully.

The classical workspace for thermal analysis is *Systema*. This software allows thermal users to export their thermal model to an I-DEAS universal format (a “.unv” file), as shown in Fig.4. The principle of such an exporting process is to transform the thermal nodes into the equivalent shell elements. This means that a thermal node may in practice be transformed into one or several shell finite elements. It has to be pointed out that I-DEAS tool has now been replaced by another tool.

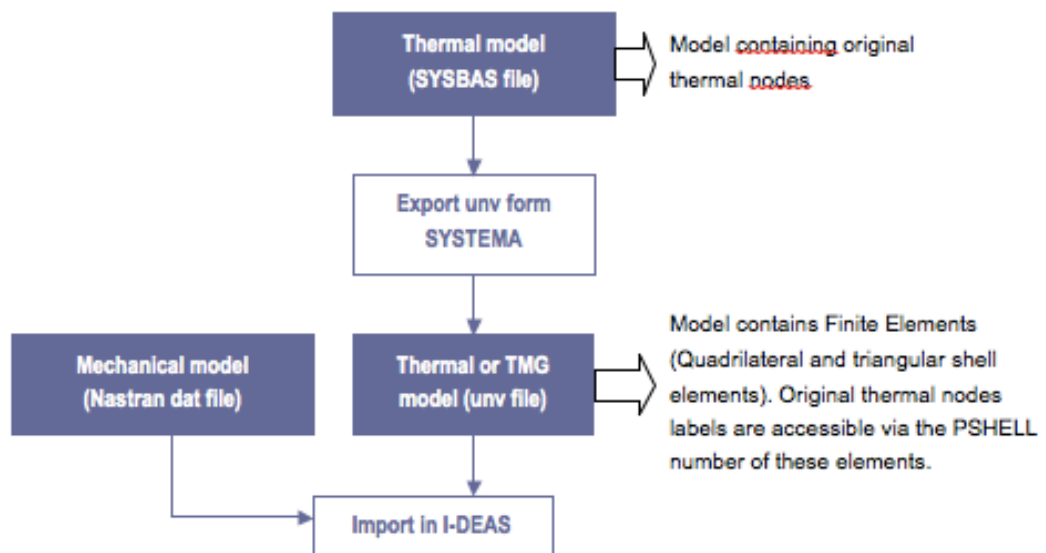


Figure 1.4. Export of Mechanical and thermal models into I-DEAS [114].

Before implementing the correspondence process it has to be verified that the thermal model fits correctly with the mechanical model. Based on the reports analysed it was evident that generally, the thermal and mechanical models do not have the same level of maturity, or are not coming from exactly the same CAD model. This could cause a potential longer term continuity problem when a design is continuously modified. Only the thermal analyst can, under this system, be responsible for choosing the correct thermal map to be applied to the mechanical FEM. This is to guarantee that correspondence is established to fit the best with the thermal model, and conductive interpolation is used only for model parts which are for some reason not included in the thermal model.

Conductive interpolation results necessarily have to be checked and validated by the thermal analyst as well.

1.2. Thermo-elastic analysis – Finite element techniques

1.2.1. Finite element techniques used within established practice at Airbus DS

Until recently TED analyses have been restricted to running the two detailed mechanical and thermal models in parallel, in order to get the required outputs into forms that can satisfactorily be compared to the corresponding requirements.

This includes the satellite dynamic FEM update to be compatible with thermo-elastic calculations by removing all rigid elements that will prevent a realistic thermal expansion, and by adding the relevant materials coefficient of thermal expansion (CTE). The injected thermal maps come from the detailed thermal model, without there necessarily being a full correspondence with the FEM. This requires the use of specific FEM-to-TMM interpolation hypotheses [110].

In the development of the FEM stage it is accepted that industrial practice requires that the full structural model is delivered using only linear elastic elements and properties [115]. The need for special FEM entities to suit specific analysis applications, such as accommodating nonlinearities, would have to be identified and specially agreed prior to delivery of the FEM.

In the second step, with the requirements having been defined in the first step, FEM, GMM and TMM modelling must be compared to the “as designed” representation in order to check the impact of the non-modelled elements (or perhaps the effects of simplified modelling) before application of thermal node temperature in the thermo-elastic FEM [110]. In order to get exact predictions of thermo-elastic distortions it is important to apply the correct temperature within the FEM, and to try to get a smooth and realistic temperature distribution.

Different methods exist, or have been developed in house, to perform the correspondence work between the mechanical and thermal nodes. In most cases the geometry of the thermal model is much simpler than the FEM geometry (Fig. 1.5) and the number of thermal nodes is much smaller than that of the FEM elements [110]. Correspondence methods are often nodal methods where temperatures are applied to the FEM nodes. These methods should really take into account the geometry difference between the mechanical and thermal models.

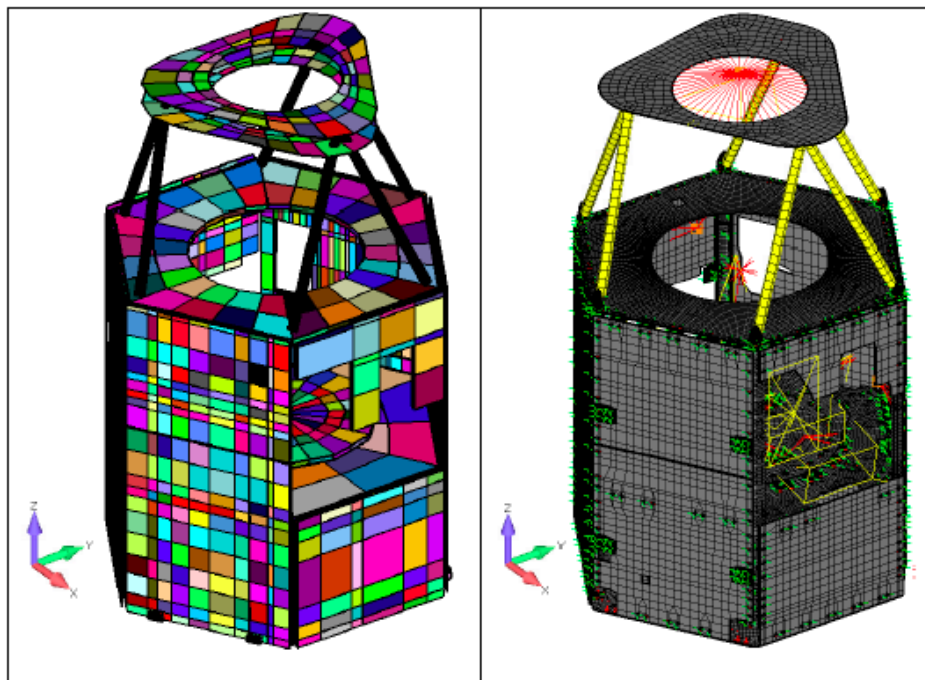


Figure 1.5. Example of thermal and mechanical models [110]

It should be noted that the major structural contributions are defined through application of the unitary method. This method works on the basis of increasing the temperature by 1°C on each thermal node in the thermo-elastic model so that it is possible to obtain the contribution of each area of the structure. During the design phase the thermal nodes are usually gathered into macro-nodes to define the major structural contributions [110].

The **FEM macro-nodal analysis** objective is to get a physical understanding of the local deformation and performance contribution under unitary temperature / gradient cases, which can then be easily ranked and multiplied by the expected temperature variations

for making quick checks [113]:

- One homogenous load case of 1°C on each part of the model
- Three gradient load cases of $1^{\circ}\text{C}/\text{m}$ for each part length, width and thickness.

The gradient is therefore a function of the macro-node size (0.5°C for a 0.5m long macro-node).

In order to get an accurate comparison of all the macro-nodes contributions to the vehicle's overall stability performance, they should all have an equivalent size in order not to under-estimate the contribution of very small macro-nodes compared to bigger ones.

Some mechanical nodes are not associated with TMM thermal nodes. The impact of such nodes has to be evaluated by using a unitary case with an increase of 1°C loading, compared with the impact of a 1°C increase on the entire mechanical model. For nodes with significant impact there are also some other options [113]:

- To give them a mean temperature by using the temperatures of neighbouring nodes (this can be done within Nastran by running an interpolation job).
- To use the temperature from a thermal node close to these mechanical nodes (a mapping process).
- To modify the thermal model by adding missing thermal nodes.

It should be emphasised that the interpolation with Nastran can only use temperature inputs from the thermal model. The Nastran software is not used here as a real thermal solver since the entire model uses an assumed (potentially incorrect) conductivity of 1 W/m/K . The interpolated temperatures are only an arithmetic mean of the near nodal temperatures, weighted by the volume of the adjacent element.

To consider an example of how the nodes are interpolated we can look at a commonly used 2 skin panel within a 2D FEM model [113]: On the panel there are often two thermal nodes associated with only one mechanical node (typically relating to the temperatures

on the upper and lower skins). To handle this type of correspondence the average of the two temperatures from the thermal nodes is applied in the 2D FEM. For the unitary method the panel mechanical nodes are associated with only one sensitivity coefficient. Thus this coefficient is divided by two, and the value is applied for the upper skin thermal node and for the lower skin thermal node. However if the gradient through the panel is very important a Nastran calculation has to be added to simulate the gradient through the 2D elements, and re-meshing then takes place for the **mechanical FEM** in 3D to have each side of the FEM associated with only one thermal node. **This example is of particular importance for the work performed in other Chapters 2-4.**

In some cases a detailed unitary thermoelastic analysis method [113] can be applied.

The detailed thermoelastic analysis is a unitary case within the full thermal model. It's similar to the macro-nodal method, but there are some differences:

- The number of thermal nodes can be most important (up to 4000 thermal nodes),
- Gradient load cases are not computed.

For each thermal node in the thermal model, a Nastran thermoelastic subcase is computed (with 1°C increase). The subcase analysis provides a sensitivity matrix, with distortions given per °C, for each restitution grid.

This detailed analysis come with its own advantage and disadvantages.

The advantages of a detailed analysis with the sensitivity matrix are:

- Only one computation of the sensitivity matrix is needed, leading to multiple reuse of this matrix for additional temperature load cases.
- Fast computation of different distortion loading cases.
- Deep analysis of the distortion behaviour, since the sensitivity matrix can be transformed into a macro-nodal analysis.

The drawbacks are:

- It's not possible to mix this method with the interpolation method (which uses Nastran

to compute the distortions).

- The unitary case method needs to define temperature everywhere in the FEM.

In summary the FEM unitary case method allows the fast computation of distortion loading cases, and can provide a good understanding of the distortion behaviour. However it requires a full thermal mapping, and interpolation is not possible.

Temperature dependency can be introduced into the model [113].

If temperature loading varies in a large range (from ambient down to very low temperatures) then the coefficients of thermal expansion (CTE) are made dependent on the temperature. For more accurate results a CTE table may be used, but this would lead to a nonlinear thermoelastic analysis. The Young's Modulus should then also be temperature dependent.

Coming back to the **example of a 2-skin panel**. For a composite material such as an aluminum honeycomb core and a (carbon fibre reinforced plastic) CFRP skin, the CTE to be used is generally that of the CFRP. A more accurate way to predict the panel CTE is to use the general laminate theory.

This evaluation can be performed within Nastran by transforming the composite properties into an equivalent shell property with a new CTE. The analysis of the panel is restricted to that required for linear structures, i.e. the material is assumed to be linear, the couplings are rigid to prevent interpenetration (no contact processing, no sliding), and the strains and displacements are small.

The validation process of the FEM through thermo-elastic measurements is *not* intended to replicate the mission environment in terms of the complexity of transients or stationary gradients [111]. The regime of loading is static and there are only two overall parameters to address with respect to validation of the deflection variables $\{x\}$, these are the loading $\{F\}$ and stiffness $[K]$:

$$\{F\} = [K] \{x\}$$

The loading, identified as $\{F\}$ is a function of:

- The thermal distribution, which is an output from the TMM (correlated separately).
- The thermo-mechanical properties defined in the FEM (with correct CTE definition).

Assuming the problem is linear the validation of the FEM stiffness matrix $[K]$ only needs to be fulfilled for single scalar temperature cases $K \neq f(T)$. For the thermo-static loading ‘ $\{F\}$ ’, only the thermo-mechanical properties need validating, and this is addressed by cross-checking the model properties within the correlation exercise. This test provides a correlation input for validation of the stiffness matrix $[K]$ definition in the model, along with confirmation of the thermal loading to be considered (which is simplified if isothermal and stable).

It has been shown in [111] that for isothermal loading the global distortion was found to be dispersed through the Solar Orbiter structure, and hence such isothermal loading can fulfil the thermo-elastic correlation requirement. With moderate thermal load the structural deflections are measurable and these should offer a good measured deflection-to-noise threshold. The advantage of starting the correlation from an isothermal basis is:

- The uncertainty in temperature distribution (“applied loading”) is negligible.
- There are no further uncertainties applying the stiffness contribution as a result of attempting to impart gradients.
- If the measurements are made under a stabilised state, transient deflections or strains do not exist.

1.2.2. Key thermoelastic outputs and conclusions from previous Airbus DS experiments

Some reports describing experimental studies of thermal effects and thermo-elastic deformation were describing the tests performed in climatic chambers. In [116] the testing of SOLO STM was conducted in the Rhino climatic chamber.

The objectives of the test was to measure a thermal cartographic image of the hardware

and to measure the thermo-elastic deformation caused by the thermal load with the purpose of verification of the FEM deflection outputs. During this test:

- a number of 1D displacement sensors were installed;
- a tension test was performed on a calibration panel;
- the IR temperature relative accuracy was of ± 1 °C for temperature [-20 to +100 °C];
- the software used for recording and post-processing was FLIR Research IR.
- the deflections due to the thermal load were measured by photogrammetry with a High Speed Videogrammetry System (HSVGS) using cameras in multiple locations. Videogrammetry absolute accuracy was < 50 ppm;
- the data obtained was used to correlate the 3D displacement vectors of the videogrammetry point clouds.

In this case thermo-elastic measurements may also involve deformation measurements using holographic camera, and temperature using thermocouples and a thermographic camera, as was done in [113].

The whole test set-up in [116] was built in the Rhino climatic chamber facility to perform the test within the temperature range of -20 to +40 °C. The chamber dimensions were approximately 4.8 x 3.6 x 4.0 metres. It should be pointed out that in the experiment performed in [117] the temperature range was extended to [-120°C to +30°C].

In [111] the mechanical static test (MS), the thermal sweep test (TS) and the thermal test (TH) were all performed on the calibration panel. During the MS test loadings of 25, 50, 100N were applied to the panel three times (0-Load-0) and recorded using an LVDT. If the panel deflections exceeded 2mm at 50N, the test was not conducted and a 40N load was applied instead.

The TS test was designed to identify the displacement data for a simply loaded calibration panel as well as the determination of dwell times to reach thermal stability at each test point. The thermal sequences were applied as described in Fig. 1.6. The data recorded was strain, displacement and temperature after reaching thermal stability.

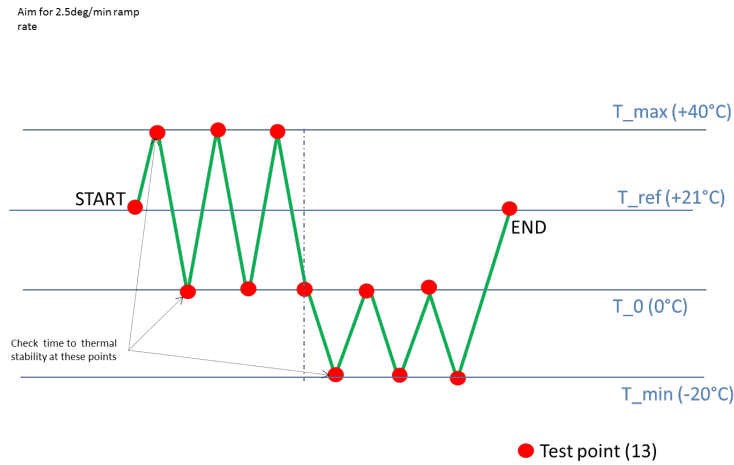


Figure 1.6. Calibration Panel thermal test sequence [111]

For the TH test, LVDTs, strain gauges and thermo-couples in multiple locations were used. Thermal imaging and photogrammetry were used in the climatic chamber after a period of stabilisation (around 30 mins). The key parameters of the test are presented in Table 1 and thermal loading was as described in Fig. 1.6.

Table 1.1. The chamber test conditions are described in [111]

1	Climatic chamber environment (atm)	Dry circulatory N ₂ atm
2	Climatic chamber environment (pressure)	Ambient pressure
3	Climatic chamber environment (stability)	-
4	Climatic chamber environment (temperature uniformity)	1.5 °C max. variation within chamber enclosed volume
5	Predicted relative deflection (magnitude) over measurement domain.	0.2 - 0.3mm

6	Max. absolute thermo-elastic deflection	$\leq \pm 1.5\text{mm}$
7	Relative deflection measurement accuracy	Determine during test. Target: $< 25 \mu\text{m}$
8	Relative deflection measurement resolution	Determine during test. Target: $< 12 \mu\text{m}$
9	Max. chamber HOT soak temperature	$+ 40^{\circ}\text{C}$
10	Min. chamber COLD soak temperature	$- 20^{\circ}\text{C}$
11	Max. image temperature	$+ 55^{\circ}\text{C}$ (TBC/TBD)
12	Min. imaging temperature	$- 30^{\circ}\text{C}$
13	Imaging temperature accuracy	$\pm 0.5^{\circ}\text{C}$
14	Temperature ramp rate	Not exceeding $5 \text{ (TBC)}^{\circ}\text{C} / \text{min}$
15	Measurement domain	-

It should be pointed out that the photogrammetry acquisition (scan domain) is defined by the boxed region which was approximately 2.4m x 2.0m.

In [118] the test was conducted in the Rhino thermal chamber as well, with a temperature interval from -20 to +40 degrees C, $\pm 0.5^{\circ}\text{C}$, relative humidity 65% maximum, ambient pressure 760 ± 25 mm of mercury. For the data acquisition, the LVDT, thermocouples and strain gauges were used. At the stabilised temperature, within the limits of the test point:

- the thermal images were captured using the thermal imaging camera;
- photogrammetry images of the structure were taken
- LVDT displacements were recorded all throughout the duration of the test.

Aluminium honeycomb panels have been tested in [113] for the dimensions presented in Fig. 1.7.

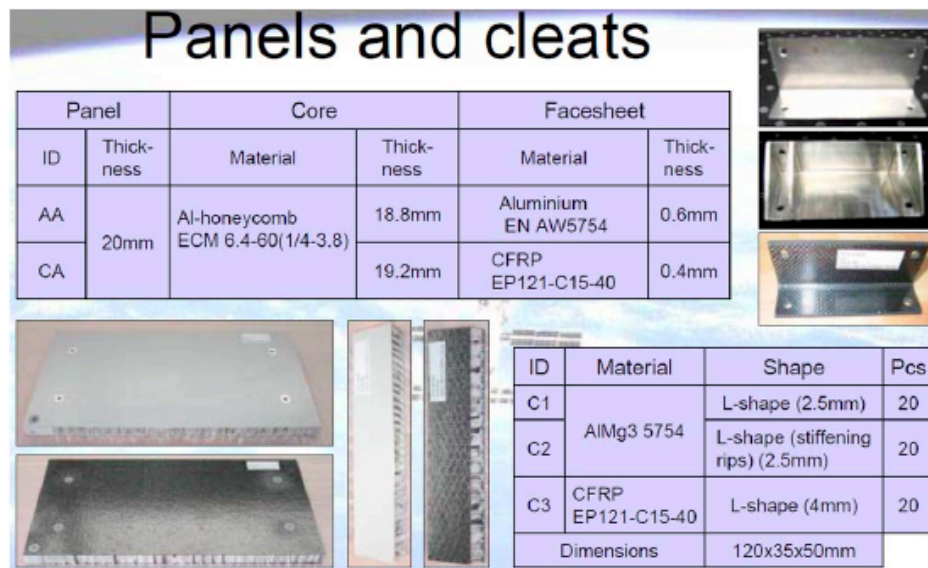


Figure 1.7. Panels and cleats tested in [113]

The panels and their assemblies (Fig. 1.8) were tested with specific goals as emphasised in Table 1.2.

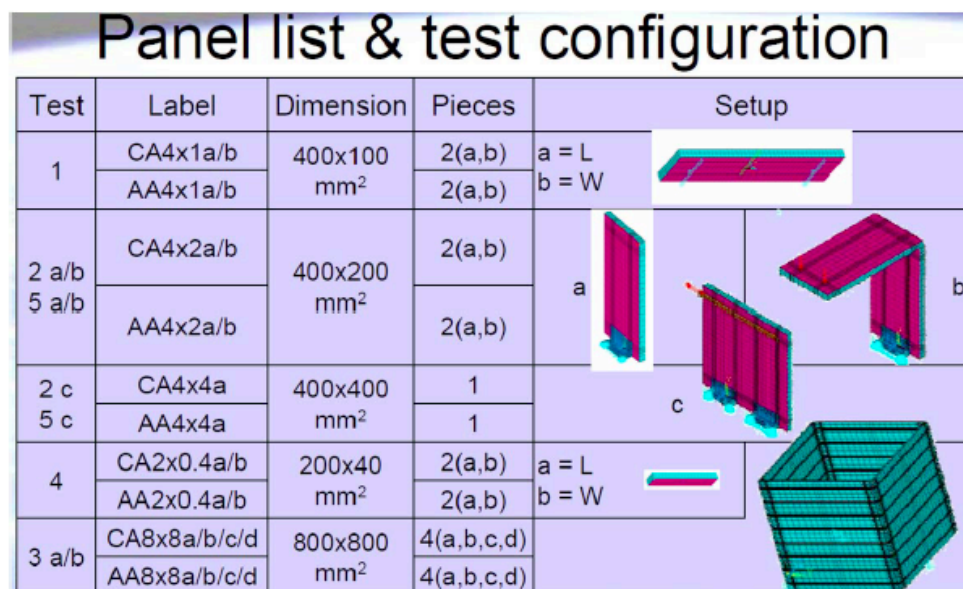

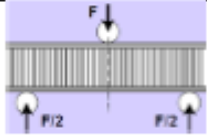
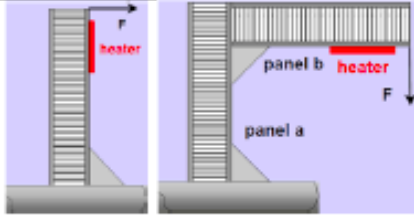

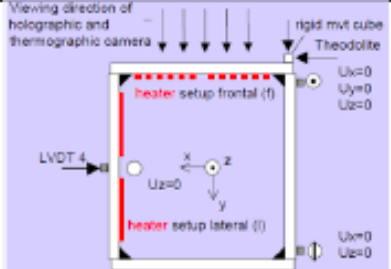


Figure 1.8. Geometry of the panels tested in [113]

Table 1.2. Panels tested in [113] and goals of the tests.

	Test	Goal
	Test n°4 CTE test with thermal load	CTE verification
	Test n°1 Bending Test	Correlation of the panel stiffness parameters (panel stiffness, shell model sandwich option)
	Test 2a/2b Static loading	Correlation of the cleat interface stiffness
	Test 5a/5b Thermal loading	Correlation with the thermal loading (temperature level of cleats, heater power...)
	Test 2c Static loading	Correlation of the cleat interface shear stiffness
	Test 5c Thermal loading	Correlation with the thermal loading
	Test n°3 Realistic thermo-mechanical test	Correlation on a realistic satellite structure with four panels and two thermal surfaces

For mechanical simulations 2D and 3D FEM models were used. A 3D fine model consisted of 3D elements (8 node structural finite elements) and was used for the mechanical load and for the thermoelastic load. A 2D coarse model used 2D elements (layered shell finite elements) for panels and cleats, and used the sandwich panel option for both the mechanical and thermoelastic loads.

For the test in [113] the holographic camera was used for non-contact displacement measurements and the thermographic camera was used for temperature measurements.

As can be seen in Table 3, it was found that the coarse 2D model was considered to be better than the fine 3D model for aluminium panels. For carbon skin panels, the results were mixed: 2D was better with cleats C1 and C2, 3D was better with cleat C3.

Table 1.3. Correlation of results for the panel and cleats test – out of plane displacement (μm) [113]

panel	cleat	configuration	Test (μm)	Pre-test simulation	Post-test correlated fine volume	Post-test correlated coarse shell
AA8x8	C1	a	14	60	31.2	27.0
AA8x8	C2	a	9	40	11	7.8
CA8x8	C1	a	13	19	8.1	14.3
CA8x8	C2	a	4	6	-6.3	-4.1
CA8x8	C3	a	10.5	22	9	3.5
CA8x8	C3	b	-10	-94	-27.3	-32.0

In this work it was also highlighted that in the 2D model of the panel the glue between the skins and the core are not taken into account and the temperature profiles as in Fig. 1.9 cannot be taken into account due to the thickness of the panels, testing set-ups and limitations of the FEM techniques.

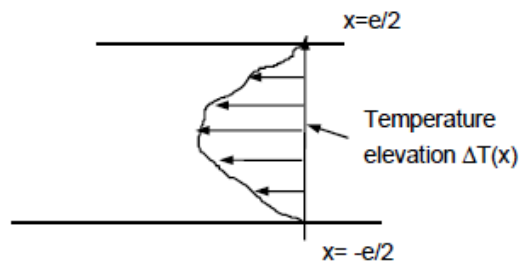


Figure 1.9. Temperature profile of the panel in [113]

In [110] the thermo-mechanical loading initial test was proposed to be performed within the range of stabilised temperature [-10 °C; +50 °C]. Such stabilised isothermal loading offers an ideal regime for thermo-elastic FEM correlation as a baseline to start the

correlation activity. The drawback of this type of testing is that this case alone is not sufficient to claim a fully correlated FEM. This is because in the stabilised state the same temperature occurs on both the internal volume and the exterior, and thus no through sandwich panel induced gradient may occur. To evaluate this more complex case a scheme to induce and measure such a gradient needs to be considered.

Specific tests to address key sensitivities of the sandwich panel and through thickness thermal gradient were suggested. To induce the thermal gradient (load through the skin and through the honeycomb) local heaters can be installed and activated within the hot stabilised environment. In [110] a proposal was made to repeat a stabilised soak and to impart thermal energy into one skin 'alone' of a selected payload sandwich panel. It was concluded that by heating and elevating locally the skin temperature, it is possible to avoid structural influences (unavoidable for cooling systems) and the heater attachment will not compromise stiffness.

1.2.3. Composite Plate Theory versus the Finite Element Method

Based on the analysis of the problem conducted in Chapter 1.1, it has become apparent that the main technique used in structural analysis by industry, particularly Airbus DS Ltd, is the Finite Element Method (FEM), particularly within the Nastran software package for prediction of the mechanical deformation of panels.

Therefore it is important to look into the open literature, in terms of analysis and the comparison of the various FEM approaches and analytical techniques that are available, and their accuracy and efficiency. It was found that there has been a comparison conducted for composite plates where the FEM results were compared with available analytical results or those based on the Dynamic Stiffness Method [1].

The problem can also be presented in the finite element form, as done in the case of the FGM beam in [119]. A four noded rectangular finite element was used to discretise the domain. The global finite element equation for evaluating the time dependent temperature across the transverse plane of the beam, when the beam is exposed to heat load on one surface and insulated on the other surface, has the following form:

$$\mathbf{K}_{cond}\mathbf{T} + \mathbf{C}_{cap}\mathbf{T} = \mathbf{F}_Q \quad (1.1)$$

\mathbf{K}_{cond} is a conduction matrix, \mathbf{C}_{cap} is a thermal capacitance matrix and \mathbf{F}_Q is a force vector due to the combined effects of internal heat generation, external heat flux such as step heat loading, shock heat loading, and moving and concentrated-line heat sources:

$$[\mathbf{K}_{ij}^e] = \int_{A^e} [\mathbf{B}]^T [\mathbf{D}] [\mathbf{B}] dA^e$$

$$[\mathbf{C}_{ij}^e] = \int_{A^e} \rho_{eff} c_{P_{eff}} [\mathbf{N}]^T [\mathbf{N}] dA^e$$

$$[\mathbf{F}_i^e] = \int_{A^e} \dot{q} [\mathbf{N}]^T dA^e$$

(1.2a,b,c)

where $i, j = 1, 2, 3, 4$; $dA^e = (dx dz)$ - the area of the e^{th} element, and $[\mathbf{N}]$ is the two-dimensional Lagrangian interpolation function, $[\mathbf{B}]$ is the derivative of the Lagrange shape function; $[\mathbf{D}] = \begin{bmatrix} k_{x_{eff}} & 0 \\ 0 & k_{z_{eff}} \end{bmatrix}$ is the thermal conductivity matrix, and ρ_{eff} is the density of the material which is considered to be independent of temperature, and $c_{P_{eff}}$ is the temperature dependent specific heat of the FGM beam. For solution the numerical time integration method of Crank-Nicolson was used.

It has been stated in [1] that apart from the Finite Element Method (FEM) a more accurate method is available, and this is known as the Dynamic Stiffness Method (DSM). The DSM is appealing in dynamic analysis because unlike the FEM it provides an exact solution of the equation of motion of a structure once the initial assumptions on the displacement field have been made (e.g. the Euler-Bernoulli, Timoshenko theories for beams, or Kirchhoff, Mindlin or higher order theories for plates). No further approximation is required in the analysis and any number of natural frequencies can be computed using the DSM, with just a single element which, of course, is impossible in the FEM. The DSM can be very effectively used to study the free vibration behaviour of complex structures because once the dynamic stiffness (DS) matrix of a structural element has been developed, it can be rotated, offset and assembled in a similar way to that of the

FEM, to build the global dynamic stiffness matrix of the final structure.

It is important to note that DS plate elements based on the classical plate theory (CPT) have been developed for simply supported boundary conditions, mainly due to research by Wittrick and Williams [120],[121] and implemented in a program called VIPASA [121], and then subsequently developed further into VICON [122], PASCO [123],[124], and VICONOPT [125],[126]. At the same time it is well recognised that for composite plates the effect of shear deformation can be significant even when the plate is thin because fibre reinforced composites in general have low shear moduli. Considering that the DS is based on CPT in [1] an attempt has also been made to include the effects of shear deformation and rotatory inertia, by using bespoke code written in a symbolic computation language (Mathematica). This has been achieved mathematically by introducing the displacement field for a plate based on the Mindlin formulation:

$$\begin{aligned} u(x, y, z, t) &= u^0(x, y, t) + z\phi_y(x, y, t), & v(x, y, z, t) &= v^0(x, y, t) - z\phi_x(x, y, t) \\ w(x, y, z, t) &= w^0(x, y, t) \end{aligned} \tag{1.3}$$

where u^0, v^0, w^0 are the membrane displacements along the x, y, z directions respectively and ϕ_x, ϕ_y are the bending rotations. Although a composite plate is made of many layers of different materials the displacement is usually assumed to be linear through the thickness, and the plate is considered to be an equivalent plate with equivalent properties (classical laminate theory [1],[127]).

Then Hamilton's principle is applied. The use of Hamilton's principle, as opposed to Newton's second law, has the added advantage of giving access to the natural boundary conditions. This is important because the connections between forces and displacements are essential when applying the dynamic stiffness method [1].

$$\delta \int_{t_1}^{t_2} (T - U) dt = 0 \tag{1.4}$$

where the kinetic energy T for the plate is given as

$$T = \frac{1}{2} \int_A \sum_{k=1}^{N_l} \int_{z_{k-1}}^{z_k} \rho_k \left(\left(\frac{\partial u}{\partial t} \right)^2 + \left(\frac{\partial v}{\partial t} \right)^2 + \left(\frac{\partial w}{\partial t} \right)^2 \right) dz dA \quad (1.5)$$

where ρ is the density, k is the layer reference, and N_l is the number of layers of the composite plate.

Similarly, the potential energy U can be written as:

$$U = \frac{1}{2} \int_A \sum_{k=1}^{N_l} \int_{z_{k-1}}^{z_k} \sigma_k^T \varepsilon_k dz dA \quad (1.6)$$

where

$$\sigma^T = [\sigma_{xx} \ \sigma_{yy} \ \sigma_{xy} \ \sigma_{yz} \ \sigma_{xz}] \quad \text{and} \quad \varepsilon^T = [\varepsilon_{xx} \ \varepsilon_{yy} \ \varepsilon_{xy} \ \varepsilon_{yz} \ \varepsilon_{xz}] \quad (1.7)$$

By substituting the geometric and constitutive equations into Eqs. (1.5) and (1.6) and applying Hamilton's principle the equations of motion in free vibration with the natural boundary conditions are obtained:

$$A_{11}u_{,xx}^0 + 2A_{16}u_{,xy}^0 + A_{66}u_{,yy}^0 + A_{16}v_{,xx}^0 + (A_{66} + A_{12})v_{,xy}^0 + A_{26}v_{,yy}^0 - B_{16}\phi_{x,xx} - (B_{66} + B_{12})\phi_{x,xy} - B_{26}\phi_{x,xy} + B_{11}\phi_{y,xx} + 2B_{16}\phi_{y,xy} + B_{66}\phi_{y,yy} = I_0\ddot{u}^0 + I_1\ddot{\phi}_y$$

$$A_{16}u_{,xx}^0 + (A_{66} + A_{12})u_{,xy}^0 + A_{26}u_{,yy}^0 + A_{66}v_{,xx}^0 + 2A_{26}v_{,xy}^0 + A_{22}v_{,yy}^0 - B_{66}\phi_{x,xx} - (B_{66} + B_{12})\phi_{y,xy} - 2B_{26}\phi_{x,xy} - B_{22}\phi_{x,yy} + B_{16}\phi_{y,xx} + B_{26}\phi_{y,yy} = I_0\ddot{u}^0 + I_1\ddot{\phi}_x$$

$$kA_{55}w_{,xx}^0 + 2kA_{45}w_{,xy}^0 + kA_{44}w_{,yy}^0 - kA_{45}\phi_{x,x} - kA_{44}\phi_{x,y} + kA_{55}\phi_{y,x} + kA_{45}\phi_{y,y} = I_0\ddot{w}^0$$

$$\begin{aligned}
& B_{11}u_{,xx}^0 + 2B_{16}u_{,xy}^0 + B_{66}u_{,yy}^0 + B_{16}v_{,xx}^0 + (B_{66} + B_{12})v_{,xy}^0 + B_{26}v_{,yy}^0 - D_{16}\phi_{,xx} - \\
& -(D_{66} + D_{12})\phi_{,xy} - D_{26}\phi_{,yy} + D_{11}\phi_{,xx} + 2D_{16}\phi_{,xy} + D_{66}\phi_{,yy} - kA_{55}w_{,x}^0 - \\
& -kA_{45}w_{,y}^0 + kA_{45}\phi_x - kA_{55}\phi_y = I_0\ddot{u}^0 + I_2\ddot{\phi}_y \\
& -B_{16}u_{,xx}^0 - (B_{66} + B_{12})u_{,xy}^0 - B_{26}u_{,yy}^0 - B_{66}v_{,xx}^0 - 2B_{26}v_{,xy}^0 - B_{22}v_{,yy}^0 + D_{66}\phi_{,xx} + \\
& +(D_{66} + D_{12})\phi_{,xy} + 2D_{26}\phi_{,xy} + D_{22}\phi_{,yy} - D_{16}\phi_{,xx} - D_{26}\phi_{,yy} + kA_{45}w_{,x}^0 + \\
& +kA_{44}w_{,y}^0 - kA_{44}\phi_x + kA_{45}\phi_y = -I_1\ddot{v}^0 + I_2\ddot{\phi}_x
\end{aligned} \tag{1.8a,b,c,d,e}$$

The equations of motion (Eqs.(1.8)), taking into account the general boundary conditions, can be solved as a system of differential equations in Navier's or Levi's form, where:

$$\begin{aligned}
w^0(x, y, t) &= \sum_{m=1}^{\infty} W_m(x)e^{i\omega t} \sin(\alpha_m y) \\
\phi_y(x, y, t) &= \sum_{m=1}^{\infty} \Phi_{y_m}(x)e^{i\omega t} \sin(\alpha_m y) \\
\phi_x(x, y, t) &= \sum_{m=1}^{\infty} \Phi_{x_m}(x)e^{i\omega t} \cos(\alpha_m y)
\end{aligned} \tag{1.9a,b,c}$$

and where ω is at this stage an arbitrary circular frequency, and $\alpha_m = m\pi/L$ and $m=1, 2, \dots, \infty$.

This (Eqs.(1.9)) is also called Levi's solution, which assumes that two opposite sides of the plate are simply supported (SS), i.e. $w = \phi_y = 0$ at $y = 0$ and $y = L$.

Particular boundary conditions can be applied to derive the frequency equation by eliminating the integration constants. This method, although extremely useful in studying a single plate, lacks generality and cannot be easily applied to complex structures that are often solved by approximate methods. *However if there is a way to apply DSM to a complex structure, for example by representing it as a composition of plates, the method*

would retain the exactness of the solution. Once the dynamic stiffness matrix of an element is obtained, it can be offset and/or rotated and finally assembled in a global DS matrix of a complex structure. This global DS matrix implicitly contains all the exact natural frequencies of the structure which can be computed by using the Wittrick-Williams algorithm [128]. The complete dynamic stiffness matrix of a single element composite plate was obtained in [1] based on first order shear deformation theory (FSDT). In [1] a strong advantage of the DSM over the FEM was pointed out such that *unlike in the FEM, DS plate elements do not have point nodes but instead they have line nodes for each strip, so no changes in geometry along the y-direction can be modelled and the two sides $y=0$ and $y=b$ must necessarily be simply supported*. The other two sides can have any boundary conditions (BCs). The BCs are applied to the global dynamic stiffness matrix using the penalty method. This consists of adding a large stiffness to the position on the leading diagonal term, which corresponds to the degree of freedom of the node, and which needs to be constrained.

Because of similarities between the FEM and DSM methods, DS element can be implemented in FEM code to increase the accuracy considerably, say for an accurate free vibration analysis of the structure. It should be emphasised that when analytical solutions are available the persistent use of numerical techniques can result in loss of accuracy and excessive computational costs [1].

1.2.4. Comparison of the DSM (based on FSDT) with the FEM (based on Nastran results)

In [129] the authors used the dynamic stiffness method for composite plate elements based on the first order shear deformation theory (FSDT), and implemented this approach in a program called DySAP, in order to compute the exact natural frequencies and mode shapes of composite structures, and to compare the results with solutions obtained in Nastran. For thick plates showing both bending and in-plane modes Carrera's Unified Formulation (CUF) was used for obtaining comparable analytical results.

As can be seen in Table 1.4, 1.5, 1.6, for a composite square plate, Nastran consistently produces conservative estimates of the natural frequencies, and the error increases for the

higher natural frequencies. This can be attributed to the fact that the FEM gives an approximate solution for the total elastic energy.

Table 1.4. First 6 dimensionless bending frequencies for a square composite plate with different boundary conditions (n/s – results not shown, NASTRAN mesh uses 50x50 CQUAD4 elements). Exact results are from [130,131] ([21,22] in the table respectively).

Mode	SSSS				SSSC			
	Exact [21] ω^*	DySAP m n	ω^*	FEM ω^* (error %)	Exact [21] ω^*	DySAP m n	ω^*	FEM ω^* (error %)
1	14.766	1 1	14.766	14.716 (-0.3)	17.175	1 1	17.175	17.059 (-0.7)
2	22.158	2 1	22.158	21.718 (-2.0)	23.677	2 1	23.676	23.241 (-1.8)
3	36.900	3 1	36.900	34.945 (-5.3)	37.720	3 1	37.720	35.814 (-5.1)
4	n/s	1 2	37.380	37.072 (-0.8)	n/s	1 2	38.326	37.976 (-0.9)
5	n/s	2 2	41.158	40.728 (-1.0)	n/s	2 2	41.942	41.495 (-1.1)
6	n/s	3 2	50.896	49.268 (-3.2)	n/s	3 2	51.461	49.853 (-3.1)
Mode	SCSC				SFSF			
	Exact [21] ω^*	DySAP m n	ω^*	FEM ω^* (error %)	Exact [22] ω^*	DySAP m n	ω^*	FEM ω^* (error %)
1	19.669	1 1	19.669	19.490 (-0.9)	4.343	1 1	4.343	4.302 (-0.9)
2	25.349	2 1	25.349	24.915 (-1.7)	missed	1 2	6.262	6.201 (-1.0)
3	38.650	3 1	38.650	36.795 (-4.8)	16.212	2 1	16.212	15.675 (-3.3)
4	n/s	1 2	39.082	38.700 (-1.0)	missed	2 2	18.175	17.619 (-3.1)
5	n/s	2 2	42.585	42.125 (-1.1)	missed	1 3	30.340	30.307 (-0.1)
6	n/s	3 2	51.938	50.347 (-3.1)	33.186	3 1	33.186	31.121 (-6.2)
Mode	SSSF				SFSC			
	Exact [22] ω^*	DySAP m n	ω^*	FEM ω^* (error %)	Exact [22] ω^*	DySAP m n	ω^*	FEM ω^* (error %)
1	4.914	1 1	4.914	4.869 (-0.9)	7.331	1 1	7.331	7.296 (-0.5)
2	16.742	2 1	16.742	16.200 (-3.2)	17.558	2 1	17.557	17.045 (-2.9)
3	missed	1 2	21.670	21.627 (-0.2)	missed	1 2	23.172	23.066 (-0.5)
4	missed	2 2	27.881	27.499 (-1.4)	missed	2 2	28.961	28.566 (-1.4)
5	33.644	3 1	33.644	31.579 (-6.1)	34.019	3 1	34.019	31.981 (-6.0)
6	n/s	3 2	41.057	39.220 (-4.5)	n/s	3 2	41.721	39.918 (-4.3)

Table 1.5. First dimensionless bending frequencies for a simply supported square composite plate with different Young’s modulus ratios. Exact results are from [132] in [129]. FEM results by NASTRAN use 50x50 CQUAD4 elements and the DySAP results are mesh independent.

E_1/E_2	Exact CPT	Exact FSDT	DySAP	FEM (error %)
10	10.65	8.2982	8.2981	8.350 (0.6)
20	13.948	9.5671	9.5671	9.526 (-0.4)
30	16.605	10.326	10.326	10.196 (-1.3)
40	18.891	10.854	10.854	10.641 (-2.0)

Table 1.6. First dimensionless bending frequencies for a simply supported square composite plate for different thickness ratios. Exact results are from [130],[133]. NASTRAN results are mesh 50x50 CQUAD4 elements and the DySAP results are mesh independent.

h/a	Exact CPT	Exact FSDT	DySAP	FEM (error %)
0.5	15.830	5.492	5.500	5.134 (-6.7)
0.25	17.907	9.369	9.395	9.117 (-3.0)
0.2	18.215	10.820	10.854	10.641 (-2.0)
0.1	18.652	15.083	15.143	15.086 (-0.4)
0.05	18.767	17.583	17.660	17.647 (-0.1)
0.04	18.780	17.991	18.071	18.061 (-0.1)

It was suggested in [129] that the anomaly could be explained by the fact that CQUAD4 finite elements in NASTRAN use reduced integration to compute the stiffness matrix of the element in order to avoid the shear locking problem which generally affects thin plates. Reduced integration is used to solve this problem by reducing the precision of the integration on the surface of the element which lead to a lower element stiffness. The user has no control over the type of integration used in CQUAD4 elements and this particular feature is not mentioned in NASTRAN's user guide. Nevertheless, the reduced integration is the most likely cause for FEM giving a lower frequency, i.e. a lower stiffness. Clearly, the FEM should overestimate the stiffness, and if the element is subjected to shear locking, the plate will then appear to be much stiffer than it actually is. This reduced stiffness is what really causes a lower frequency when compared with the exact one. This assertion is further strengthened by observing the fact that the error is much higher for thicker plates (Table 1.6). Thick plates are not generally subjected to shear locking problems, so the reduced integration merely leads to a less accurate stiffness matrix and thus to higher errors. Shear locking is basically a numerical problem which affects thin FE plates. DySAP and the DSM are, strictly speaking, not numerical methods since the equations of motions are solved in strong/closed form and thus the results are not affected by shear locking.

An example of a relatively thick square composite plate, simply supported on its four sides (S2-S2-S2-S2) was considered. Only the first natural frequency was found in the literature [130,131] and obtained by using the Navier exact approach. Thus, the DySAP

results were compared with those obtained by using the CUF and FEM obtained using NASTRAN (Table 1.7).

Table 1.7. First 21 dimensionless natural frequencies for a simply supported square plate. Classical solutions are from [130,131], CUF is Carrera’s Unified Formulation, p, b, m represent in-plane, bending and in-plane m=0 mode shapes respectively.

Mode	CS	CUF (a)		CUF (b)		DySAP			FEM, NASTRAN			
	ω^*	ω^*	ω^*	type	m	n	ω^*	type	m	n	ω^* (error %)	
1	8.30	8.30	8.30	b	1	1	8.30	b	1	1	8.35 (0.7)	
2	/	15.30	15.30	b	2	1	15.30	b	2	1	15.09 (-1.4)	
3	/	18.87	18.87	b	1	2	18.87	b	1	2	18.99 (0.6)	
4	/	23.13	23.13	b	2	2	23.13	b	2	2	23.09 (-0.2)	
5	/	25.32	25.32	b	3	1	25.32	b	3	1	24.34 (-3.8)	
6	/	30.02	30.02	b	1	3	30.02	b	3	2	30.06 (0.1)	
7	/	30.84	30.84	b	3	2	30.84	b	1	3	30.10 (-2.4)	
8	/	32.99	32.99	b	2	3	32.99	b	2	3	33.01 (0.1)	
9	/	36.10	36.10	p	1	1	36.10	b	4	1	34.17 (-5.4)	
10	/	36.25	36.25	b	4	1	36.25	p	/	/	36.10 (-0.4)	
11	/	/	/	p	1	2	36.95	p	/	/	36.95 (0.0)	
12	/	/	/	m	0	1	36.95	m	/	/	36.95 (0.0)	
13	/	38.84	38.84	b	3	3	38.84	b	3	3	38.24 (-1.6)	
14	/	40.37	40.37	b	4	2	40.37	b	4	2	38.46 (-4.7)	
15	/	41.06	41.06	b	1	6	41.06	b	1	6	41.06 (0.0)	
16	/	40.71	41.52	p	1	3	41.52	p	/	/	41.51 (0.0)	
17	/	43.35	43.35	b	2	4	43.35	b	2	4	43.36 (0.0)	
18	/	43.47	43.70	p	1	4	43.70	p	/	/	43.69 (0.0)	
19	/	43.48	43.70	p	2	1	43.70	p	/	/	43.69 (0.0)	
20	/	46.79	46.79	b	4	3	46.79	b	5	1	44.03 (-5.9)	
21	/	47.42	47.42	b	5	1	47.42	b	4	3	45.10 (-4.9)	

In this case NASTRAN is still showing inaccurate results at higher frequencies. The authors of [129] have also performed computational efficiency comparisons for the practical examples below and found some evidence of DySAP demonstrating a much smaller computational cost.

L stringer panel was considered in [129] as presented in Fig.1.10.

The exact results for this study were obtained by DySAP and these were compared with those obtained by the FEM (using NASTRAN) with 3250 square plate elements (CQUAD4) to investigate the first 20 natural frequencies (Table 1.8).

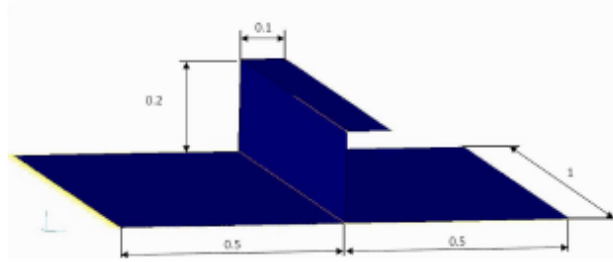


Figure 1.10. Geometry of an L stringer composite panel (in metres) [129].

Table 1.8. First 20 dimensionless natural frequencies for a simply supported composite plate reinforced by an L-shaped stringer.

Mode	$h/a = 0.001$		$h/a = 0.005$	
	DySAP	FEM	DySAP	FEM
	ω^*	ω^* (error %)	ω^*	ω^* (error %)
1	83.3	83.3 (0.0)	81.5	81.5 (0.0)
2	89.3	89.1 (-0.1)	88.6	88.5 (-0.1)
3	106.1	106.1 (0.0)	100.5	100.4 (0.0)
4	107.6	107.3 (-0.3)	107.1	106.8 (-0.3)
5	111.1	110.9 (-0.1)	109.3	109.1 (-0.1)
6	126.5	126.1 (-0.3)	125.2	124.9 (-0.3)
7	143.6	143.2 (-0.3)	143.1	142.5 (-0.4)
8	158.5	157.9 (-0.4)	157.4	156.8 (-0.4)
9	197.9	197.2 (-0.3)	197.0	196.1 (-0.5)
10	209.1	208.3 (-0.4)	199.1	198.6 (-0.2)
11	268.8	268.0 (-0.3)	207.9	206.8 (-0.5)
12	271.4	270.5 (-0.3)	253.6	252.7 (-0.3)
13	275.4	274.2 (-0.4)	267.4	266.0 (-0.5)
14	277.4	276.4 (-0.4)	270.8	269.5 (-0.5)
15	285.0	283.4 (-0.6)	275.7	274.1 (-0.6)
16	304.6	302.2 (-0.8)	281.3	279.6 (-0.6)
17	329.4	327.1 (-0.7)	290.0	288.9 (-0.4)
18	334.7	331.9 (-0.8)	301.1	298.6 (-0.8)
19	338.2	334.9 (-1.0)	314.4	312.8 (-0.5)
20	340.8	340.2 (-0.2)	327.7	326.4 (-0.4)

Computational time was also analysed and the main outputs are presented in Table 1.10.

Table 1.10. Comparison of the relative computational times using DySap (Dynamic Stiffness Method) and NASTRAN.

Method	Number of Elements	Degree of Freedom	Number of modes	Relative real time
DySAP	8	45	1	1.00
DySAP	8	45	25	2.45
FEM	3250	20196	1	15.09
FEM	3250	20196	25	19.69

An omega stringer panel was considered in Figure 1.11.

In Table 1.11 the first 30 dimensionless natural frequencies were computed by DySAP and NASTRAN, using a fine structured mesh composed of 31200 square elements (CQUAD4). The DySAP results are mesh independent and the number of elements used in the analysis is not important when computing the natural frequencies.

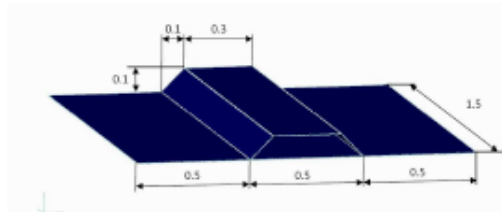


Figure 1.11. Geometry of the Omega stringer composite plate (in metres) [129].

Table 1.11. First 30 dimensionless natural frequencies for a simply supported composite plate reinforced by an omega-shaped stringer.

Mode	DySAP			FEM		Mode	DySAP			FEM	
	m	n	ω^*	ω^* (error %)	m		n	ω^*	ω^* (error %)		
1	1	1	204.4	204.6 (0.1)	16	6	2	342.5	347.5 (1.5)		
2	2	1	208.0	208.3 (0.2)	17	5	3	355.6	358.1 (0.7)		
3	1	2	215.9	216.2 (0.1)	18	6	3	401.6	405.9 (1.1)		
4	3	1	217.9	218.7 (0.4)	19	7	1	409.0	416.5 (1.8)		
5	2	2	220.4	220.7 (0.2)	20	7	2	416.0	423.4 (1.8)		
6	3	2	230.0	230.8 (0.3)	21	7	3	466.3	472.8 (1.4)		
7	4	1	239.7	241.4 (0.7)	22	8	1	501.6	511.7 (2.0)		
8	4	2	250.9	252.5 (0.7)	23	8	2	507.5	517.5 (2.0)		
9	5	1	277.7	280.8 (1.1)	24	8	3	549.8	558.9 (1.7)		
10	5	2	287.5	290.6 (1.1)	25	9	1	610.8	623.9 (2.1)		
11	1	3	294.3	294.6 (0.1)	26	9	2	615.7	628.7 (2.1)		
12	2	3	302.1	302.5 (0.1)	27	1	4	633.0	633.5 (0.1)		
13	3	3	310.0	310.7 (0.2)	28	9	3	651.4	663.6 (1.9)		
14	4	3	326.2	327.5 (0.4)	29	2	4	673.7	674.3 (0.1)		
15	6	1	334.1	339.2 (1.5)	30	1	5	678.4	679.0 (0.1)		

Table 1.12. Comparison of the relative computational time using DySAP and NASTRAN.

Method	Number of Elements	Degree of Freedom	Number of modes	Relative real time
DySAP	13	65	1	1.00
DySAP	13	65	25	2.72
FEM	31200	188448	1	35.07
FEM	31200	188448	25	49.54

It has been concluded in [129] that the Dynamic Stiffness Method is more accurate and computational efficient in free vibration analysis than the traditionally used finite element method. The advantage of computational time gained using DySAP would increase for more complex structures, which would require more finite elements for accurate modelling. Thus a DySAP analysis would be particularly useful in optimisation studies which are generally computationally intensive. However it should be remembered that DySAP should be used only when at least two sides of the structure are simply supported, and importantly when the structure can be modelled as an assembly of plates. Therefore it cannot universally replace the use of the finite element method. This has highlighted the need for multi-method software that would use the most accurate and efficient solution procedure which is appropriate for each particular problem, without resorting to the finite element method on all occasions.

1.2.5. Accuracy and applicability to the cases, as previously considered by Airbus DS

As has been demonstrated in Section 1.1 where a possible gap in the working practice at Airbus DS Ltd has been identified, there is a strong need for higher accuracy in the thermo-elastic assessment of structures with rapidly increasing complexity. It was emphasised that with the development of technology even simplified tests provide highly accurate measurements and can be performed at an early stage to eliminate any risks/doubts and to highlight the areas most sensitive to the effects of thermal expansion and heat conduction/energy dissipation. However testing facilities still require labour and equipment and involve prototype costs, not to mention the time needed. Testing procedure cannot necessarily be used on demand, and so an effective and highly accurate tool for prediction of the thermo-elastic deformation of the structural elements is required.

Furthermore, from the review of the testing procedures in Section 1.2.2 it has become evident that most programmes performing experimental measurements were only done for isothermal cases, and with the purpose of FEM model verification. At the same time the FEM model can reflect the influence of temperature because it can be combined with the TMM, but any dynamic effects of the temperature applied and body temperature variation due to the energy dissipation are ignored. This means that from the final FEM, in terms of thermo-elastic

deformation, we obtain only a ‘snap-shot’ of the thermo-elastic behaviour. Looking closer behind the FEM interface we can describe the process as:

1. From the TMM, which solves the heat conduction equation for the structural element, we obtain a single value of temperature for that particular moment of time, and for a particular area/structural element.
2. Then this single value, together with a static CTE, is included into the mechanical equation which calculates the displacement of the particular node.

So the question arises as to what happens when the energy is dissipated in the area, affecting the neighbouring area/structural element/node? What happens at the next ‘snap-shot’, when the structural element, which may, for example, be as sensitive as honeycomb, has been deformed, losing its symmetry so that it now has a completely different pattern of heat conduction? One has to ask if the boundary conditions will be changes for the next step, giving the initial temperature? Or will the material show changes from the orthotropic form to an anisotropic layout? These questions give a potential taste of where the premise of applying FEM modelling can lose relevance, especially when we wish to retain accuracy at the highest level.

Of course this is not to mention the fact that during the process of merging of two models based on TMM and FEM we lose accuracy, specifically during:

- the exporting of the TMM into the FEM package
- then the interpolation of the TMM in the FEM package nodes over the FEM model nodes, with some nodal values being averaged due to the availability of too few or too many nodal assignments.

Going further it has to be mentioned that a mechanical FEM model is normally based on linear classical theory, which means that it is based on the hypotheses of classical theory. This means that it is incapable of predicting any layer-wise effects within a structure as well as possibly missing the effects of shear, from which thermal effects might well arise in sensitive honeycomb-like structures.

As a final point on inaccuracy, it has to be mentioned that different FEM packages might give slightly different results, with better or worse accuracy than NASTRAN. This is due to the internal numerical models they use and the adopted methods of numerical integration. As shown in Section 1.2.4, for the case of the composite plate (without any thermal effects) the DSM method-based software was shown to out-perform the Nastran package, with strong evidence emerging that Nastran often underestimates the prediction. This is because the DSM, unlike the FEM, uses an exact solution of the equation of motion for a structure once the initial assumptions on the displacement field have been made (e.g. the use of Euler-Bernoulli or Timoshenko theories for beams, or Kirchhoff, Mindlin or higher order theories for plates). DSM also includes the effects of shear deformation, which are highly important for composite plates, and rotatory inertia, and crucial for the successful solution of dynamic problems. This has been achieved for plates by introducing the displacement field based on the Mindlin formulation, and not by using a simple linear term within the classical Kirchhoff theory.

All the inaccuracies pointed out are not case/structure specific. This means that an improvement within any of these will be an improvement to the general approach/methodology which can be applied to any structure, or to cases that might be considered by Airbus DS in their programmes described in Section 1.

1.2.6. Software available for elastic and thermal effects in industrial practice

There is a wide range of FEM software available with different add on tools and capabilities. As has become evident from the review in Section 1.1, Airbus DS has a preference for using Nastran for the main FEM calculations, and for their interpretation, or for necessary intermediate calculations, Matlab and FEMAP tools are used. It has been demonstrated that there are other options for the FEM type software, for example those based on the DSM method, which could provide additional accuracy in calculations. However the intention of this work is not to try to change established industrial practice but to provide an additional tool for verification to obtain predictions of higher accuracy.

Nastran is written in the Fortran language. At the same time it has become ‘fashionable’ now to present solution codes in open access form. This is probably due to the general

availability of basic representations of black-box operations and sequences which can be easily adjusted to suit the syntaxes of any solver written in codes such as Matlab, Mathematica, and Maple for example. Nastran is principally intended to be the processor of the FEM job in hand. It does not have a graphical interface for model composition or meshing. There is a whole range of programs that can be used to supplement Nastran in that way. After processing the job the data is presented in text files, and in coded columns. There are manuals and guiding notes which allow the user to interpret boundary conditions, stresses, displacements etc for each and every node of the model. At Airbus DS Ltd there are engineers and analysts who are used to dealing with the text-file data representation approach, and who find it the most comfortable way of dealing with the Nastran output.

Considering all these points it seems to be most appropriate to develop a tool which can provide **higher accuracy** in the thermo-elastic analysis, but by providing **text-file style or annotated output** data. Therefore to guarantee a verification process of higher accuracy, it is intended:

1. To develop a tool which has a completely different approach to the problem from its basic level. The model will consider the physics behind the thermo-elastic effect, as has been highlighted, and will not be separated into two parts, thermal and mechanical, and, unlike in current practice, it will be coupled. Only by coupling together the thermal effects and mechanical deformations will it be possible to take into account how the *thermal effects influence the deformation of the structure* and *how distortion of the structure influences the thermal energy dissipation*. In this way we can tackle the problem of inaccuracy by starting from a fundamental understanding and representation. Additionally we will not need to lose accuracy due to data export and the inefficient process of interpolation of nodes from different software packages.

2. To develop the annotated output text-file style output. Annotated data output has the strongest advantage of universality. If properly presented in coded tables it can be interpreted easily and efficiently by trained staff, or it can be exported without any loss into other software packages for graphical representation. This means that the development of the tool will target for a text-file style representation of results to make the code more accessible for trained staff at Airbus DS. This will guarantee the universality and accessibility of the code for further development. To develop the model and process the solutions *Mathematica software* was chosen. This has plain syntaxes which can easily be converted into Fortran style code. It is also easy to obtain the solution in a matrix/table format or to represent a function

as a set of data, which can be saved in an annotated output file.

1.3. Thermo-elastic analysis – Analytical Coupled thermo-mechanical models

As we have seen above the down side of the FEM approach adopted in industrial practice is in the separation of two phenomena, mechanical and thermal. Therefore the increase accuracy can be achieved if these two effects are coupled directly or indirectly and therefore the result of their dynamics is reflected in dynamics of the other one. Therefore in this section we will be considering existing analytical approaches to the problem of prediction of thermo-elastic behaviour with coupling of these two effects.

1.3.1. Thermoelasticity

A deformation of the body is connected to a change of heat inside it, and therefore with a change of the temperature distribution in the body. A deformation of the body leads to temperature changes, and conversely, as shown in Fig.1.12. The internal energy of the body depends on both the temperature and the deformation. The science which deals with the investigation of the above *coupled* processes is called thermoelasticity [134].

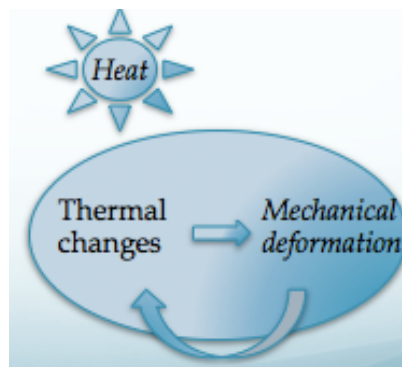


Figure 1.12. Coupled interpretation within the thermoelasticity problem

Thermoelasticity is a branch of applied mechanics that is concerned with the effects of heat on the deformation and stresses in solid/elastic bodies, and vice versa [135]. Thus it is a combination of isothermal elasticity effects caused by mechanical forces, and those caused by thermal processes.

Development of the field of thermoelasticity was preceded by extensive investigations in the theory of thermal stresses (TTS). It is often considered that the state of strain and stress in an elastic body due to a heating, can be expressed under the simplifying assumption that *the influence of the deformation on the temperature field may be neglected* [134].

In the TTS the classical heat conduction (HC) equation is usually used but this does not routinely contain the term representing the deformation of the body. Knowing the temperature distribution from the solution of the HC equation, the displacement equations of the theory of elasticity can be solved.

At the same time classical dynamic elasticity has been developed under the assumption that the heat exchange between different parts of the body due to the heat conduction occurs very slowly, and therefore the thermal motion may be regarded as adiabatic.

Thermoelasticity deals with a wide class of phenomena. It covers the general theory of heat conduction and the general theory of thermal stresses, and it describes the temperature distribution produced by deformation. Thermoelasticity also describes the phenomenon of thermoelastic dissipation. In addition it allows a deeper study of the mechanisms of deformation and the thermal processes occurring in an elastic body.

Despite the fact that many modelling approaches tend to separate the mechanical and thermal effects, thermoelastic processes are not generally reversible: the elastic part may be reversed (the deformations may be recoverable through cooling), but the thermal part may not be reversed due to the dissipation of energy during heat transfer [135]. Apart

from that, thermal changes in the body cause mechanical deformation in the body, which in return affects these thermal changes representing the process as a two-way feedback. This means that the modelling techniques and representations would have to couple the mechanical and thermal aspects of the problem to achieve an adequate accuracy for the results.

If we consider an elastic isotropic homogeneous body we assume that it is:

- elastic – i.e. it is in a state such that when the forces producing the deformation are removed, the body returns to its initial undeformed state;
- isotropic – therefore the elastic properties of the body are independent of direction;
- homogeneous – meaning that it is independent of the elastic properties of the position.

The constitutive equations must represent the relations between the *stress tensor and the entropy*, and *the stress tensor and the temperature*. It is assumed that T_0 is the constant temperature at the initially natural state of the body.

Due to the heating of the body surfaces it undergoes a deformation giving rise to the displacement u and the temperature undergoes a change $T = \mathcal{T} - T_0$, where \mathcal{T} is the absolute temperature. We assume that the temperature increase does not affect the material properties, and we consider a geometrically linear thermoelasticity (so the squares and higher products of ε_{ij} can be neglected):

$$\varepsilon_{ij} = \frac{1}{2}(u_{i,j} + u_{j,i}) \tag{1.10}$$

The components of strain must satisfy six compatibility relationships.

The basic problem consists of the stress tensor σ_{ij} , the entropy S , the components of the strain tensor ε_{ij} and the temperature \mathcal{T} .

At a certain instance of time the mechanical and thermal state of the medium can be completely described by the distribution of the deformation ε_{ij} and the temperature \mathcal{T} .

Thus in an isothermal case we have processes which are elastically and thermally reversible.

However if the temperature varies in time we deal with two coupled processes, the *reversible elastic process* and the *irreversible thermodynamic process* (due to a spontaneous, and hence irreversible process of heat transfer by means of heat conduction).

Thermoelastic changes cannot be described by means of the classical thermodynamics valid for equilibrium states, so we must use the relations of the **thermodynamics of irreversible processes**.

In this case we start the derivation from the first and second laws of thermodynamics. The first law, the law of energy conservation (the Energy balance equation) is stated as follows:

$$\frac{d}{dt}(\mathcal{U} + \mathcal{K}) = \mathcal{L} + \frac{dQ}{dt} \quad (1.11)$$

where \mathcal{U} is the internal energy, \mathcal{K} is the kinetic energy, \mathcal{L} is the power of the external forces and \dot{Q} is the increment in time of the quantity of heat absorbed by the body.

Following the approach of [134] and replacing the values in equation (11) this can be simplified to the form:

$$\dot{U} = \sigma_{ji}v_{i,j} - q_{i,i} + W \quad (1.12)$$

where \mathbf{v} ($\mathbf{v}=\mathbf{du}/dt$) is the vector of the displacement velocity, \mathbf{q} is the vector of the heat flux, W is the quantity of heat generated in unit time and unit volume.

If we consider rigid displacement and rotations, we can get local relations:

$$\dot{U} = \sigma_{ij}\dot{\epsilon}_{ij} - q_{i,i} + W \quad (1.13)$$

Now we consider the local entropy balance equation:

$$\mathcal{T}\dot{S} = -q_{i,i} + W \quad \text{or} \quad \frac{dS}{dt} = -\left(\frac{q_i}{\mathcal{T}}\right)_{,i} - \frac{q_i \mathcal{T}_{,i}}{\mathcal{T}^2} + \frac{W}{\mathcal{T}} \quad (1.14a,b)$$

where S is the entropy per unit volume and unit time. If we integrate over the volume of the body, the increment of the entropy in time will consist of two parts:

- the first part is described by the surface integral constituting the increase of the entropy due to the heat flux through the surface (the heat exchange with the surroundings)
- also there are the volume integrals leading to the entropy produced by the heat exchange, and the entropy produced by the action of the heat sources.

In Eq.(1.14b) the first term refers to the heat exchange with the surroundings while the two remaining ones describe the entropy production in an elementary volume of the body.

The local statement of the second law of thermodynamics of irreversible processes leads to the Clausius-Duhem inequality:

$$-\frac{q_i \mathcal{T}_{,i}}{\mathcal{T}^2} \geq 0 \quad \text{or} \quad \frac{dS}{dt} + \left(\frac{q_i}{\mathcal{T}}\right)_{,i} - \frac{W}{\mathcal{T}} \geq 0 \quad (1.15)$$

This will be satisfied if:

$$q_i = -\lambda_{ij} \mathcal{T}_{,i} \quad (1.16)$$

This is the Fourier law of heat conduction for an anisotropic body.

The inequality imposes an additional restriction on the symmetric tensor of heat conduction λ_{ij} .

For an *isotropic* body we have $q_i = -\lambda_0 \mathcal{T}_{,i}$, $\lambda_0 > 0$.

In a solid the heat transfer occurs by means of the heat conduction and this is generally understood as representing the heat transfer from places of higher temperature to places

of lower temperature. This process is spontaneous and irreversible, and connected with entropy production. The equation of heat conduction (HC) can be derived from the entropy balance Eq.(1.14a):

$$\mathcal{T}\dot{S} = -q_{i,i} + W \quad (1.17)$$

Now we introduce:

- the Fourier law of heat conduction Eq.(1.16):

$$q_i = -\lambda_0 \mathcal{T}_{,i} = -\lambda_0 T_{,i} \quad (1.18)$$

- and the conductivity relation for entropy (derived from the concept of Helmholtz free energy $F=U-S\mathcal{T}$)

$$S = \gamma \varepsilon_{kk} + \frac{c_\varepsilon}{T_0} T \quad (1.19)$$

where $\gamma = (3\lambda + 2\mu)\alpha_t$, λ and μ are the material Lamé constants, α_t is the coefficient of linear volume expansion; ε_{kk} is the scalar from tensor ε_{ij} and named the dilatation; c_ε is the quantity $\mathcal{T} \left(\frac{\partial S}{\partial \mathcal{T}} \right)_\varepsilon$, the measure of heat generated in a unit volume of the body during a change of the temperature at a constant strain, and called the specific heat at constant strain $c_\varepsilon = \rho c$, where c is the specific heat referred to the unit mass of the body.

Therefore Eq.(1.17) becomes:

$$\mathcal{T} \left(\gamma \dot{\varepsilon}_{kk} + \frac{c_\varepsilon}{T_0} \dot{T} \right) = \lambda_0 T_{,ii} + W \quad (1.20)$$

If we assume that in general a change of temperature $T = \mathcal{T} - T_0$ accompanying the deformation is small, it is then possible to linearise the Heat Conduction (HC) Eq.(1.20) by $\mathcal{T} = T_0$:

$$T_{,ii} - \frac{1}{\chi} \dot{T} - \eta \dot{\varepsilon}_{kk} = -\frac{W}{\lambda_0} \quad (1.21)$$

where $\chi = \frac{\lambda_0}{c_\varepsilon}$, $\eta = \frac{\gamma T_0}{\lambda_0}$.

Or it can be re-written in the form:

$$\left(\nabla^2 - \frac{1}{\chi} \frac{\partial}{\partial t} \right) T - \eta \dot{\varepsilon}_{kk} = -\frac{Q}{\chi} \quad (1.22)$$

where $Q = \chi W / \lambda_0$.

It has to be noted that comparing to the HC equation derived in [136], this extended HC equation contains the term $\eta \dot{\varepsilon}_{kk}$ coupling the temperature increase with the rate of dilatation of the body.

The HC equation must be complemented by the mechanical equation of motion for displacements:

$$\sigma_{ji,j} + X_i = \rho \ddot{u}_i \quad (1.23)$$

From the Duhamel-Neumann relations:

$$\sigma_{ii} = 2\mu \varepsilon_{ij} + (\lambda \varepsilon_{kk} - \gamma T) \delta_{ij} \quad (1.24)$$

and remembering that strain is:

$$\varepsilon_{ij} = \frac{1}{2} (u_{i,j} + u_{j,i}) \quad (1.25)$$

then the equation of motion (1.23) can be re-written as

$$\mu u_{i,jj} + (\lambda + \mu)u_{j,ji} + X_i = \gamma T_{,i} + \rho \ddot{u}_i \quad (1.26)$$

Eqs.(1.21) to (1.26) constitute a complete set of the differential equations of thermoelasticity. These equations are coupled. The equations of motion contain the temperature increase T besides the displacement u_i whereas the HC equation contains the temperature T and the rate of dilatation $\dot{\epsilon}_{kk}$.

A literature review of commonly used techniques for thermoeleastic problems is presented in [135]. It was pointed out in that review that there have been a few works looking at the problem of displacements and stresses in laminated structures under thermal bending. These have assumed a linear temperature profile through the thickness direction for both laminated plates and multilayered composite shells, as well as for circular plates and cylindrical shells. In these models the assumption has been made that the temperature profile through the thickness is of linear and constant nature. This assumption however would not be valid for anisotropic structures where the thickness temperature profile is never linear. Therefore even if the structural model is accurate, the final solution would be characterised by a large error due to the incorrectly assumed profile of the temperature distribution along the thickness.

In [137,138] it has been summarised that depending on how the displacement and/or stress field are presented in the normal direction, mathematical models for thermal analysis of composite laminates can be derived using the three dimensional theory of elasticity, Equivalent Single Layer Theories (ESL), Layer Wise Theories (LW) or zig-zag theories and more recently by means of Carrera's Unified Formulation (CUF). To reduce the computational cost of 3D theories and maintain acceptable accuracy, several solutions for the thermal problems in composites have been proposed using the equivalent single layer. These are the Classical Laminated Plate Theory (CLPT), First-order Shear Deformation Theory (FSDT) and Higher-order Shear Deformation Theory (HSDT).

In [135] it has been highlighted that so far in the open literature there is only a small

amount of work devoted to the coupled thermo-mechanical analysis of structures, in the form of both thermoelastic and thermoplastic analysis. There also have been a few works comparing coupled and uncoupled analysis, the accuracy and efficiency of the coupled theory [139], and extending a higher-order zig-zag plate theory [140] for prediction of the fully coupled mechanical, thermal, and electric behaviour.

Partially coupled models are commonly derived with neglect of the interactions of ‘temperature effects / mechanical deformations’, assuming *a priori* the distribution of temperature along the thickness, or obtaining it from the heat conduction equation and then solving the mechanical equations with known temperature gradient terms. In contrast, **fully coupled thermoelastic models** take into account the interaction of ‘temperature effects / mechanical deformations’ explicitly because of the presence of displacement and temperature variables in the thermal/mechanical equations.

There has also been some work published on the problem of thermal shock [141] representing the very rapid thermal processes caused by momentary ignition and combustion in rocket engine chambers [135]. This thermoelasticity problem requires an analysis of the coupled temperature and deformation since the temperature shock induces very rapid movements in the structural elements, thus causing the rise of very significant inertial forces, giving rise to vibration. Rapidly changeable contractions and the expansions in oscillatory movements generate temperature changes in the material which is susceptible to diffusion due to heat conduction [135,142]. This means that in the case of the exact solution a plate can behaves as if it is less rigid [142].

Adam and Ponthot [143] have described an updated Enhanced Assumed Strain (EAS) finite element formalism developed to model the thermo-mechanical behavior of metals submitted to large strains.

1.3.2. Functionally Graded Materials and modelling techniques used

Due to the thermo-elastic problems discussed in Section 1, a new generation of materials has begun to evolve. The main purpose of Functionally Graded Materials (FGMs) is to provide a resistance to the high temperatures that can be generated or accumulated in a structure due to environmental changes, for example in air vehicles, nuclear reactors and in the chemical laboratory. Therefore further development of thermo-elastic modelling techniques can be usefully targeted towards applications which apply FGMs.

Commonly FGMs are made of a mixture with arbitrary composition of two behaviourally different materials (such as ceramic and metal). The volume fraction of each constituent material changes continuously and gradually through the entire volume of the material. Ceramics have high resistance to forming in the temperature field but on the other hand metals have a ductility property that diminishes the fragility of the ceramics.

There has been a lot of development within recent years to develop both analytical and finite element techniques, which would provide sufficient accuracy for FGM modelling with minimal computational cost. At the same time the main complexity in modelling these materials is their thermoelastic nature due to their structural inhomogeneity.

In [144] the authors demonstrated a variety of theories and solution methods available for the analysis of stress, vibration and buckling in FGM plates subjected to thermal loads. It has been pointed out that FGMs can be separated into two groups due to the continuous or discontinuous gradation of the material (for example it could be stepwise and layered).

1.3.2.1. Modelling the material properties of FGMs

Due to the nature of the FGM structure and inhomogeneity the Power Law method is widely used [144,145]. It is based on the linear [144] or exponential [145] principle of mixture, and extensively used in studies of thermal residual stresses and stability analysis of FGM plates.

In this model the material properties are differentiated along the thickness of the plate due to the volume fraction, variable from the lower metal rich part, to the upper ceramic rich layer [144,146]:

$$E_z = E_m + (E_c - E_m)V_f^p$$

$$\alpha_z = \alpha_m + (\alpha_c - \alpha_m)V_f^p$$

$$k_z = k_m + (k_c - k_m)V_f^p$$

$$V_f = \left(\frac{z}{h} + \frac{1}{2}\right)$$

(1.27a,b,c,d)

where E , α , and k are the modulus of elasticity, thermal coefficients of expansion and thermal conductivity, respectively. V_f represents the volume fraction of the ceramic phase and p is a power law index or material property gradient index. The subscripts c and m represent the constituents of ceramic and metal respectively.

Dependent on the application, specific variations of these equations can be found in [144,146,147].

However if there is a material with inclusions under consideration then an approach known as the Mori-Tanaka scheme (MT) is more appropriate [144,148]. This method takes into account the effect of the elastic fields among neighbouring inclusions and its interactions with the constituent materials. The relationships between the effective bulk modulus K_z and shear modulus G_z are as follows:

$$\frac{K_z - K_m}{K_c - K_m} = \frac{V_f^p}{1 + (1 - V_f^p) \left(\frac{K_c - K_m}{K_m + \frac{4}{3}G_m} \right)}$$

$$\frac{G_z - G_m}{G_c - G_m} = \frac{V_f^p}{1 + (1 - V_f^p) \left(\frac{G_c - G_m}{G_m + f_m} \right)}$$

$$f_m = \frac{G_m(9K_m + 8G_m)}{6(K_m + 2G_m)} \quad (1.28a,b,c)$$

The effective values of Young's Modulus of elasticity E_z and Poisson's ratio ν are calculated based on the effective Bulk modulus K_z and the shear modulus G_z and are related as:

$$E_z = \frac{9K_z G_z}{3K_z + G_z}; \quad \nu = \frac{3K_z - 2G_z}{2(3K_z + G_z)} \quad (1.29a,b)$$

The effective heat conductivity k_z and the coefficient of thermal expansion α_z are determined using the following relation:

$$\frac{k_z - k_m}{k_c - k_m} = \frac{V_f^p}{1 + (1 - V_f^p) \left(\frac{k_c - k_m}{3k_m} \right)} \quad (1.30a)$$

1.3.2.2. Temperature Dependent Properties

Now if we consider the fact that FGMs are characterised by their thermoelastic behaviour within the high temperature environment then we would need to make the material properties temperature dependent. This effect is studied by evaluating the material properties (P) of ceramics and metals depending on the environment temperature (T) [144-146, 149, 150]:

$$P = P_0 \left(\frac{P_{-1}}{T} + 1 + P_1 T + P_2 T^2 + P_3 T^3 \right) \quad (1.31)$$

where P_{-1} , P_0 , P_1 , P_2 , and P_3 , are constants that are representative of the material property and temperature. It should be noted that this series is truncated after $O(T^3)$. The temperature dependent expression can be composed of the modulus of elasticity, the

thermal conductivity and the thermal coefficient of expansion. Thus the material properties can be represented as being position (z) and temperature (T) dependent for a mixture of materials (c - ceramics and m - metals), typically in the form of:

$$P_{eff}(z, T) = P_m(T) + [P_c(T) - P_m(T)]V_f \quad (1.32)$$

The effective property also shows an explicit dependence on the volume fraction V_f of one of the materials.

1.3.3. Partially coupled thermo-mechanical analysis

Partially coupled thermo-mechanical models are extensively employed in the analysis of typical aeronautical structures, such as one-layered isotropic and multilayered composite plates and shells, where the temperature variation is one of the most important factors affecting the stress fields that in turn can cause failure of the structures [135]. These structures are subject to severe thermal environments, such as high temperatures, and high gradients and cyclic changes in temperature. Therefore the effects of high temperature and mechanical loading have to be carefully considered. An accurate description of local stress fields in the layers becomes mandatory to prevent thermally loaded structures from failure.

Tanaka et al. [151] have proposed a new boundary element method for the analysis of quasi-static problems in coupled thermoelasticity. Through some mathematical manipulation of the Navier equation of elasticity, they showed that the heat conduction equation can be transformed into a simpler form, similar to the uncoupled-type equation with the modified thermal conductivity which in turn showed the coupling effects. This procedure made it possible to treat the coupled thermoelastic problem as one that is actually uncoupled.

Partially coupled thermo-mechanical analysis is characterised by the temperature considered as an external load. The temperature profile must be defined *a priori* either by

assuming its linear distribution through the thickness direction or by calculating it from a solution of the Fourier heat conduction equation.

1.3.3.1. Temperature Distribution along the thickness

Since the temperature gradient along the thickness of the structure is of particular importance in problems described in Section 1, and as FEM approaches cannot predict it, it is useful to look into different ways of representation of this parameter.

FGMs tend to have an uneven structure and when exposed to the high temperature environment the temperature within the material is variable as well. It is commonly assumed [144, 145] that the temperatures at the top (T_1) and bottom (T_0) surfaces are the same, while representing the distribution as linear within the thickness [137, 144, 145]:

$$T_z = T_0 + (T_1 - T_0) \left(\frac{z}{h} + \frac{1}{2} \right) \quad (1.33)$$

where T_z is the temperature at any point through the plate thickness (h) along the coordinate direction z .

If the temperature is distributed across the thickness following inverse hyperbolic shear theory, it can be expressed as [152]:

$$T(x, y, z) = T_1(x, y) + \frac{z}{h} T_2(x, y) + \frac{f(z)}{h} T_3(x, y) \quad (1.34)$$

where T_1, T_2 , and T_3 represents the constant, linearly varying and nonlinear varying two dimensional temperature fields respectively.

In [153] it also has been demonstrated that the temperature field in an FGM layer within a sandwich doubly curved shallow shell may vary in the thickness direction, in the following polynomial form:

$$T(z) = T_b + (T_t - T_b)\eta_c^k(z) \quad (1.35)$$

where T_t and T_b are the temperature on the top and bottom surfaces of the shell, respectively, and $\eta^k(z)$ is represented as a polynomial series of the 5th order.

The initial conditions are often assumed to be [119]:

$$T(x, z, t = 0) = T_\infty \quad (1.36)$$

where T_∞ is the free air stream temperature as defined in the model developed in [119].

If the temperature within the material is not linearly distributed or following a certain law **then** its function would need to be defined by solving the HC equation [136]:

$$k_x \frac{\partial^2 T}{\partial x^2} + k_y \frac{\partial^2 T}{\partial y^2} + \frac{\partial k_z}{\partial z} \frac{\partial T}{\partial z} + k_z \frac{\partial^2 T}{\partial z^2} + q = \frac{1}{\alpha} \frac{\partial T}{\partial t} \quad (1.37)$$

where q is the internal heat source or heat flux.

This can also be stated in polar coordinates, as in [148]:

$$\frac{\partial q_r}{\partial r} + \frac{1}{r} \frac{\partial q_\theta}{\partial \theta} + \frac{\partial q_z}{\partial z} + \frac{q_r}{r} = 0 \quad (1.38)$$

where q_r , q_z and q_θ are the components of the heat flux vector.

From Eq(1.37) the thermal equilibrium or steady state response (where the heat flux $q = 0$) can be obtained setting $\frac{\partial T}{\partial t} = 0$ which means that the time rate of change of temperature is zero. The exact form of the HC equation is dependent on the required accuracy of the approximation and the application, i.e. the nature and existence of a heat source within

the environment.

The HC equation can also be presented in the following simpler form [119]:

$$\left(k_{x_{eff}} \frac{\partial^2 T}{\partial x^2} + k_{z_{eff}} \frac{\partial^2 T}{\partial z^2} \right) + q = \rho_{eff} c_{p_{eff}} \frac{\partial T}{\partial t} \quad (1.39)$$

where $k_{x_{eff}}$ and $k_{z_{eff}}$ are the temperature dependent effective thermal conductivities in the x and z directions respectively, and q is the internal heat generation rate per unit volume.

It can be simplified even further in the case of FG laminated plates as given in [137, 154-156] and for the layer-wise approach stated in [157]:

$$-\frac{d}{dZ} \left[k \frac{dT}{dZ} \right] = 0 \quad (1.40)$$

where $k(z)$ is the thermal conductivity of a certain layer.

This can also be stated in polar coordinates [158]:

$$\frac{1}{r} \frac{\partial}{\partial r} \left(K_r(r) r \frac{\partial T}{\partial r} \right) = 0, \quad r_a \leq r \leq r_b \quad (1.41)$$

where a and b indicate the inner and outer radii and K_r is the thermal conductivity which is assumed to be a function of the radial direction of the cylinder.

In [144] a strong need has been highlighted for further development of 2D theories. This is due to the fact that the majority of 2D theoretical approaches assume the transverse deformation to be linear, which is not a universally valid assumption for thermal and thermoelastic analysis. Therefore 2D models must be developed which include higher order transverse displacement for higher accuracy, but ideally without a significant increase in computational cost.

1.3.3.2. Thermo-mechanical model, governing equations of motion

After the temperature is found following the partially coupled modelling technique, the governing equations of motion must be derived.

Of course the simplest approach is to follow the Classical (Kirchhoff) theory for the free vibration of an FG plate [122], which could be extended to the third order shear deformation [124]. In this case the thermal stresses can be presented as [145, 146, 150, 152, 155, 159, 160, 161, 162, 163]:

$$\begin{Bmatrix} \sigma_{xx}^T \\ \sigma_{yy}^T \\ \tau_{xy}^T \end{Bmatrix} = - \begin{pmatrix} Q_{11} & Q_{12} & 0 \\ Q_{21} & Q_{22} & 0 \\ 0 & 0 & Q_{66} \end{pmatrix} \begin{pmatrix} 1 & 0 \\ 0 & 1 \\ 0 & 0 \end{pmatrix} \begin{Bmatrix} \alpha(z, T) \\ \alpha(z, T) \end{Bmatrix} \Delta T(z) \quad (1.42)$$

where

$$Q_{11} = Q_{22} = \frac{E(z, T)}{1 - \nu^2(z, T)}, Q_{12} = Q_{21} = \frac{\nu(z, T)E(z, T)}{1 - \nu^2(z, T)}, Q_{66} = \frac{E(z, T)}{2[1 + \nu(z, T)]} \quad (1.43)$$

These would give us the strain energy from the thermal stresses:

$$U_T = \frac{1}{2} \int_V (\sigma_{xx}^T d_{xx} + \sigma_{yy}^T d_{yy} + \tau_{xy}^T d_{xy}) dV \quad (1.44)$$

where

$$\begin{aligned} d_{xx} &= z^2 \left\{ \left(\frac{\partial^2 w}{\partial x^2} \right)^2 + \left(\frac{\partial^2 w}{\partial x \partial y} \right)^2 \right\} + \left(\frac{\partial w}{\partial x} \right)^2 \\ d_{yy} &= z^2 \left\{ \left(\frac{\partial^2 w}{\partial y^2} \right)^2 + \left(\frac{\partial^2 w}{\partial x \partial y} \right)^2 \right\} + \left(\frac{\partial w}{\partial y} \right)^2 \\ d_{xy} &= z^2 \left(\frac{\partial^2 w}{\partial x^2} + \frac{\partial^2 w}{\partial y^2} \right) \frac{\partial^2 w}{\partial x \partial y} + \frac{\partial w}{\partial x} \frac{\partial w}{\partial y} \end{aligned} \quad (1.45)$$

To find the solution in the form of frequency in [145] the Rayleigh–Ritz method was used by equating the effective strain energy U_{eff} and the maximum kinetic energy (T_{max}).

In [155] the strain energy had a more extended form due to the addition of shear terms:

$$U = \frac{1}{2} \int_A \left[N_{xx} \varepsilon_{xx}^{(0)} + N_{yy} \varepsilon_{yy}^{(0)} + N_{xy} \gamma_{xy}^{(0)} + M_{xx} \varepsilon_{xx}^{(1)} + M_{xy} \gamma_{xy}^{(1)} + P_{xx} \varepsilon_{xx}^{(3)} + P_{yy} \varepsilon_{yy}^{(3)} + P_{xy} \gamma_{xy}^{(3)} + Q_x \gamma_{xz}^{(0)} + Q_y \gamma_{yz}^{(0)} + R_x \gamma_{xz}^{(2)} + R_y \gamma_{yz}^{(2)} \right] dA \quad (1.46)$$

where

$$\begin{aligned} \begin{Bmatrix} N_{xx} \\ N_{yy} \\ N_{xy} \end{Bmatrix} &= \int_{-\frac{h}{2}}^{\frac{h}{2}} \begin{Bmatrix} \sigma_{xx} \\ \sigma_{yy} \\ \tau_{xy} \end{Bmatrix} dz; \quad \begin{Bmatrix} M_{xx} \\ M_{yy} \\ M_{xy} \end{Bmatrix} = \int_{-\frac{h}{2}}^{\frac{h}{2}} z \begin{Bmatrix} \sigma_{xx} \\ \sigma_{yy} \\ \tau_{xy} \end{Bmatrix} dz; \quad \begin{Bmatrix} Q_x \\ Q_y \end{Bmatrix} = \int_{-\frac{h}{2}}^{\frac{h}{2}} \begin{Bmatrix} \tau_{xz} \\ \tau_{yz} \end{Bmatrix} dz; \\ \\ \{P\} = \begin{Bmatrix} P_{xx} \\ P_{yy} \\ P_{xy} \end{Bmatrix} &= \int_{-\frac{h}{2}}^{\frac{h}{2}} z^3 \begin{Bmatrix} \sigma_{xx} \\ \sigma_{yy} \\ \tau_{xy} \end{Bmatrix}; \quad \{R\} = \begin{Bmatrix} R_x \\ R_y \end{Bmatrix} = \int_{-\frac{h}{2}}^{\frac{h}{2}} z^2 \begin{Bmatrix} \tau_{xz} \\ \tau_{yz} \end{Bmatrix} dz \end{aligned} \quad (1.47)$$

By deriving the potential and kinetic expressions the problem was solved in [155] by using the energy method.

This approach can easily be extended to the problem of thermally conducting elastic plates of circular or polygonal cross-section, which requires a polar coordinate representation as in [164].

In [165] a unified method was considered that allows the investigation of the flutter problem for a moderately thick orthotropic coupled plate with general boundary conditions. The Mindlin plate theory and supersonic piston theory are employed to formulate the theoretical model. A two-dimensional Fourier series combined with auxiliary functions was used for the displacements of the coupled plate to find the

solution. In this work the temperature was uniformly distributed in the thickness direction, and the boundary conditions for two coupled plates were simulated in terms of three sets of translational distributed springs.

The model was derived by starting with an assumption of displacement in the form [166]:

$$\begin{aligned}
 U^i(x_i, y_i, z_i, t) &= u^i(x_i, y_i, t) + z_i \phi_x^i(x_i, y_i, t) \\
 V^i(x_i, y_i, z_i, t) &= v^i(x_i, y_i, t) + z_i \phi_y^i(x_i, y_i, t) \\
 W^i(x_i, y_i, z_i, t) &= w^i(x_i, y_i, t)
 \end{aligned}
 \tag{1.48}$$

where u^i, v^i and w^i denote the displacements on the middle surface of each plate in the x_i, y_i and z_i directions, and ϕ_x^i and ϕ_y^i denote the rotations of transverse normal with respect to the x_i and y_i axes respectively, and t is the time.

Based on the linear elastic theory the strains for each plate were [166]:

$$\begin{aligned}
 \varepsilon_x^i(x_i, y_i, z_i, t) &= \frac{\partial u^i(x_i, y_i, t)}{\partial x_i} + z_i \frac{\partial \phi_x^i(x_i, y_i, t)}{\partial x_i} \\
 \varepsilon_y^i(x_i, y_i, z_i, t) &= \frac{\partial v^i(x_i, y_i, t)}{\partial y_i} + z_i \frac{\partial \phi_y^i(x_i, y_i, t)}{\partial y_i} \\
 \gamma_{xy}^i(x_i, y_i, z_i, t) &= \frac{\partial u^i(x_i, y_i, t)}{\partial y_i} + \frac{\partial v^i(x_i, y_i, t)}{\partial x_i} + z_i \left(\frac{\partial \phi_x^i(x_i, y_i, t)}{\partial y_i} + \frac{\partial \phi_y^i(x_i, y_i, t)}{\partial x_i} \right) \\
 \gamma_{xz}^i(x_i, y_i, z_i, t) &= \phi_x^i(x_i, y_i, t) + \frac{\partial w^i(x_i, y_i, t)}{\partial x_i} \\
 \gamma_{yz}^i(x_i, y_i, z_i, t) &= \phi_y^i(x_i, y_i, t) + \frac{\partial w^i(x_i, y_i, t)}{\partial y_i}
 \end{aligned}
 \tag{1.49}$$

According to the Mindlin plate theory the thermo-elastic constitutive relations for each plate can be presented as [149, 152, 167, 136, 163, 168]:

$$\begin{Bmatrix} \sigma_x^i \\ \sigma_y^i \\ \tau_{yz}^i \\ \tau_{xz}^i \\ \tau_{xy}^i \end{Bmatrix} = \begin{Bmatrix} Q_{11}^i & Q_{12}^i & 0 & 0 & 0 \\ Q_{21}^i & Q_{22}^i & 0 & 0 & 0 \\ 0 & 0 & kQ_{44}^i & 0 & 0 \\ 0 & 0 & 0 & kQ_{55}^i & 0 \\ 0 & 0 & 0 & 0 & Q_{66}^i \end{Bmatrix} \begin{Bmatrix} \varepsilon_x^i - \alpha_1^i \Delta T \\ \varepsilon_y^i - \alpha_2^i \Delta T \\ \gamma_{yz}^i \\ \gamma_{xz}^i \\ \gamma_{xy}^i - \alpha_{12}^i \Delta T \end{Bmatrix} \quad (1.50)$$

where α_1^i , α_2^i and α_{12}^i denote the linear thermal expansion coefficients for the i th plate; ΔT is the temperature change and k represents the shear correction factor defined as 5/6. The elastic stiffness coefficients were assumed as in [166]:

$$Q_{11}^i = \frac{E_1^i}{1 - \nu_{12}^i \nu_{21}^i}; \quad Q_{12}^i = \frac{\nu_{21}^i E_1^i}{1 - \nu_{12}^i \nu_{21}^i}; \quad Q_{22}^i = \frac{E_2^i}{1 - \nu_{12}^i \nu_{21}^i}$$

$$Q_{44}^i = G_{23}^i, \quad Q_{55}^i = G_{13}^i, \quad Q_{66}^i = G_{12}^i, \quad (i = 1, 2) \quad (1.51)$$

where the Poisson's ratio and Young's modulus are related as $\nu_{12}^i/E_1^i = \nu_{21}^i/E_2^i$.

To define the strain energy from the thermal stresses, the thermal stresses and nonlinear strains caused by the temperature variation were expressed following [167], similar to [145, 149, 136]:

$$\begin{Bmatrix} \sigma_{Tx}^i \\ \sigma_{Ty}^i \\ \tau_{Txy}^i \end{Bmatrix} = - \begin{bmatrix} Q_{11}^i & Q_{12}^i & 0 \\ Q_{21}^i & Q_{22}^i & 0 \\ 0 & 0 & Q_{66}^i \end{bmatrix} \begin{Bmatrix} \alpha_1^i \Delta T \\ \alpha_2^i \Delta T \\ \alpha_{12}^i \Delta T \end{Bmatrix} \quad (1.52)$$

and

$$d_{xx}^i = \left(\frac{\partial u^i}{\partial x_i} \right)^2 + \left(\frac{\partial v^i}{\partial x_i} \right)^2 + \left(\frac{\partial w^i}{\partial x_i} \right)^2 + z_i^2 \left(\frac{\partial \varphi_x^i}{\partial x_i} \right)^2 + z_i^2 \left(\frac{\partial \varphi_y^i}{\partial x_i} \right)^2$$

$$d_{yy}^i = \left(\frac{\partial u^i}{\partial y_i} \right)^2 + \left(\frac{\partial v^i}{\partial y_i} \right)^2 + \left(\frac{\partial w^i}{\partial y_i} \right)^2 + z_i^2 \left(\frac{\partial \varphi_x^i}{\partial y_i} \right)^2 + z_i^2 \left(\frac{\partial \varphi_y^i}{\partial y_i} \right)^2$$

$$d_{xy}^i = \left(\frac{\partial u^i}{\partial x_i} \right) \left(\frac{\partial u^i}{\partial y_i} \right) + \left(\frac{\partial v^i}{\partial x_i} \right) \left(\frac{\partial v^i}{\partial y_i} \right) + \left(\frac{\partial w^i}{\partial x_i} \right) \left(\frac{\partial w^i}{\partial y_i} \right) + z_i^2 \left(\frac{\partial \varphi_x^i}{\partial x_i} \right) \left(\frac{\partial \varphi_x^i}{\partial y_i} \right) +$$

$$+z_i^2 \left(\frac{\partial \varphi_y^i}{\partial x_i} \right) \left(\frac{\partial \varphi_y^i}{\partial y_i} \right) \quad (1.53)$$

According to the linear theory of elasticity the strain energy of each plate was defined as well as the kinetic energy and the potential energy stored in the boundary springs. Then, just like in [149], these terms were all summed up in the use of Hamilton's principle. The solution was found by introducing displacement functions for the transverse and in-plane vibration in the form of a two-dimensional Fourier series combined with supplementary terms, the latter being employed to adapt to various boundary conditions.

In [119] the equations were derived for the FG beam following the von Karman theory to account for the nonlinear strain in the FG material. In this case the Euler-Lagrange equations of motion gave the temperature dependent stress and moment relations:

$$\begin{aligned} -\frac{\partial N_{xx}}{\partial x} + m \frac{\partial^2 u_0}{\partial t^2} - \tilde{I} \frac{\partial^3 w_0}{\partial t^2 \partial x} - f &= 0 \\ -\frac{\partial^2 M_{xx}}{\partial x^2} - \frac{\partial}{\partial x} \left(N_{xx} \frac{\partial w_0}{\partial x} \right) + m \frac{\partial^2 w_0}{\partial t^2} + \tilde{I} \frac{\partial^3 u_0}{\partial t^2 \partial x} - \hat{I} \frac{\partial^4 w_0}{\partial x^2 \partial t^2} - q &= 0 \end{aligned} \quad (1.54)$$

where f and q are the axial and transverse load respectively. The stress resultants N_{xx} and moment resultants M_{xx} of the beam element with thermal load are related to the mid-plane displacements (u_0, w_0) and are defined as follows:

$$\begin{aligned} N_{xx} &= A_{xx} \left[\frac{\partial u_0}{\partial x} + \frac{1}{2} \left(\frac{\partial w_0}{\partial x} \right)^2 \right] - B_{xx} \frac{\partial^2 w_0}{\partial x^2} - N_{xx}^T \\ M_{xx} &= B_{xx} \left[\frac{\partial u_0}{\partial x} + \frac{1}{2} \left(\frac{\partial w_0}{\partial x} \right)^2 \right] - D_{xx} \frac{\partial^2 w_0}{\partial x^2} - M_{xx}^T \end{aligned} \quad (1.55)$$

where A_{xx} , B_{xx} and D_{xx} are the extensional, extensional-bending, and bending stiffness coefficients of the beam element defined as

$$(A_{xx}, B_{xx}, D_{xx}) = \int_z \bar{Q}_{11}(1, z, z^2) b dz$$

$$\text{and } N_{xx}^T = \int_A \bar{Q}_{11} \alpha_{eff} \Delta T dA; \quad M_{xx}^T = \int_A \bar{Q}_{11} \alpha_{eff} \Delta T z dA$$

The stiffness coefficient \bar{Q}_{11} for the FGM layer is given as $\bar{Q}_{11} = \frac{E_{eff}(z)}{1-\nu_{eff}^2(z)}$

where E_{eff} is a temperature dependent effective Young's modulus and ν_{eff} is a temperature dependent effective Poisson's ratio for the FGM beam, and $dA=dydz$.

In [154,169] the authors chose to use the Reddy higher order shear deformation plate theory to develop the elastic part of the model, in which the transverse shear strains are assumed to be parabolically distributed across the plate thickness.

In [157] the authors used a layer-wise theory which led to the membrane stress resultant and the bending stress resultants represented for the i th layer in relation to the membrane strain $\varepsilon_p^{(i)}$ and bending strain $\varepsilon_b^{(i)}$:

$$N^{(i)} = \begin{Bmatrix} N_{xx}^{(i)} \\ N_{yy}^{(i)} \\ N_{xy}^{(i)} \end{Bmatrix} = D_m^{(i)} \varepsilon_p^{(i)} + D_c^{(i)} \varepsilon_b^{(i)} - N^T(i)$$

$$M^{(i)} = \begin{Bmatrix} M_{xx}^{(i)} \\ M_{yy}^{(i)} \\ M_{xy}^{(i)} \end{Bmatrix} = D_c^{(i)} \varepsilon_p^{(i)} + D_b^{(i)} \varepsilon_b^{(i)} - M^T(i)$$

(1.57)

The matrices $D_m^{(i)}$, $D_c^{(i)}$ and $D_b^{(i)}$ are the extensional bending-extensional coupling and bending stiffness coefficients, respectively for the i th layer

$$\left[D_m^{(i)}, D_c^{(i)}, D_b^{(i)} \right] = \int_{\lambda_{i-1}}^{\lambda_i} \left[\bar{Q}_{lm}^{(i)} \right] (1, z^{(i)}, z^{(i)2}) dz, \quad (l, m = 1, 2, 6)$$

(1.58)

The thermal stress resultant and moment for the i th layer can be given as:

$$\begin{aligned}
N^{T(i)} &= \begin{Bmatrix} N_x^{T(i)} \\ N_y^{T(i)} \\ N_{xy}^{T(i)} \end{Bmatrix} = \int_{\lambda_{i-1}}^{\lambda_i} [\bar{Q}_{lm}^{(i)}] \begin{Bmatrix} \alpha^{(i)} \\ \alpha^{(i)} \\ 0 \end{Bmatrix} T(z) dz \\
M^{T(i)} &= \begin{Bmatrix} M_x^{T(i)} \\ M_y^{T(i)} \\ M_{xy}^{T(i)} \end{Bmatrix} = \int_{\lambda_{i-1}}^{\lambda_i} [\bar{Q}_{lm}^{(i)}] \begin{Bmatrix} \alpha^{(i)} \\ \alpha^{(i)} \\ 0 \end{Bmatrix} T(z) z dz
\end{aligned}
\tag{1.59}$$

where $\alpha^{(i)}$ and $T(z)$ are the coefficient of thermal expansion and the temperature distribution along the z direction, respectively for the i th layer.

1.3.4. Carrera's Unified Formulation (CUF)

In [134] the authors have considered a fully coupled thermo-mechanical model of one-layered and multilayered isotropic and composite plates, focusing on the *temperature* and *displacement* as primary variables in order to evaluate them through the thickness direction using two-dimensional theories based on Carrera's Unified Formulation (CUF) [170, 171]. It was mentioned in [138] that CUF's zig-zag approach was first pointed out by Lekhnitskii (Lekhnitskii Multilayered Theory – LMT) and then Ambartsumian showed a similar method (AMT). In the case of multilayered plates, both equivalent single layer (ESL) and layer wise (LW) approaches have been developed. As explained in [135] Carrera's Unified Formulation is a technique which handles a large variety of plate theories in a unified manner [170, 171]. According to CUF, the governing equations are written in terms of a few fundamental nuclei, which do not formally depend on the order of expansion N used in the thickness direction or on the description of variables (equivalent single layer (ESL) or layer wise (LW)). The application of a two-dimensional method for plates permits the unknown variables to be expressed as a set of thickness functions that only depend on the thickness coordinate z and the correspondent variable which depends on the in-plane coordinates x and y . Therefore, the generic variable $f(x,y,z)$, which could be, for instance, a displacement, and its variation $\delta f(x,y,z)$ are written according to the following general expansions:

$$f(x, y, z) = F_\tau(z)f_\tau(x, y), \quad \delta f(x, y, z) = F_\tau(z)f\delta_s(x, y) \quad (1.60)$$

where $\tau, s = 1, \dots, N$, (x, y) are the in-plane coordinates and z the thickness coordinate. The summing convention, with repeated subscripts τ and s , is assumed. The order of expansion N goes from first to fourth-order, and depending on the thickness functions used, a model can be: ESL, when the variable is assumed for the whole multilayer and a Taylor expansion is employed as the thickness functions $F(z)$; LW, when the variable is considered to be independent in each layer and a combination of Legendre polynomials is used for the thickness functions $F(z)$. In the thermo-mechanical models as proposed in [135], displacements can be modelled in both ESL or LW forms, and the temperature is always considered in the LW form. Therefore, a two-dimensional thermo-mechanical model is defined as ESL or LW, depending on the choice made for the displacement vector.

In [135] the thermo-mechanical analysis has been separated into three branches:

- a **static** analysis with imposed **temperature on the external surfaces** (by imposing a temperature at the top and bottom of the plate, the static response is given in term of displacements, stresses and temperature field);
- a **static** analysis of structures **subjected to a mechanical load**, with the possibility of considering the temperature field effects (a mechanical load is applied and the temperature effect is not considered). The fully coupled thermomechanical analysis gives smaller displacement values than those obtained with the purely mechanical analysis.
- a **free vibration problem**, with the evaluation of the **temperature field effects** (in which the fully coupled thermo-mechanical analysis permits the effect of the temperature field to be evaluated: noting that higher natural frequencies are obtained with respect to the purely mechanical analysis.)

In the case of a **fully coupled thermo-mechanical model** the constitutive equation was derived using thermodynamical principles and Maxwell's relations to show the coupling of mechanical and thermal fields [135]. Firstly the Gibbs free-energy function G and the thermomechanical enthalpy density H were derived [135]:

$$\begin{aligned}
G(\epsilon_{ij}, \theta) &= \sigma_{ij}\epsilon_{ij} - \eta\theta \\
H(\epsilon_{ij}, \theta, \vartheta_i) &= G(\epsilon_{ij}, \theta) - F(\vartheta_i)
\end{aligned}
\tag{1.61}$$

where σ_{ij} and ϵ_{ij} are the stress and strain components, η is the variation of entropy per unit of volume, and θ is the temperature considered with respect to the reference temperature T_0 . The function $F(\vartheta_i)$ is the dissipation function and it depends on the temperature gradient ϑ_i :

$$F(\vartheta_i) = \frac{1}{2}k_{ij}\vartheta_i\vartheta_j - \tau_0\dot{h}_i
\tag{1.62}$$

where k_{ij} is the symmetric, positive semidefinite conductivity tensor. In the second term, τ_0 is a thermal relaxation parameter and \dot{h}_i is the temporal derivative of the heat flux h_i . The thermal relaxation parameter is omitted in this work.

Then the thermomechanical enthalpy density H was expanded to obtain a quadratic form for a linear interaction:

$$H(\epsilon_{ij}, \theta, \vartheta_i) = \frac{1}{2}Q_{ijkl}\epsilon_{ij}\epsilon_{kl} - \lambda_{ij}\epsilon_{ij}\theta - \frac{1}{2}\chi\theta^2 - \frac{1}{2}k_{ij}\vartheta_i\vartheta_j
\tag{1.63}$$

where Q_{ijkl} is the elastic coefficients tensor considered for an orthotropic material in the reference system of the problem [172], λ_{ij} are the thermo-mechanical coupling coefficients, $\chi = \rho C_v/T_0$ where ρ is the material density, C_v is the specific heat per unit mass and T_0 is the reference temperature [173].

In addition, the constitutive equations were obtained in the form:

$$\sigma_{ij} = \frac{\partial H}{\partial \epsilon_{ij}}, \quad \eta = -\frac{\partial H}{\partial \theta}, \quad h_i = -\frac{\partial H}{\partial \vartheta_i}
\tag{1.64}$$

which were expanded into constitutive equations for the thermo-mechanical problem:

$$\sigma_{ij} = Q_{ijkl}\epsilon_{kl} - \lambda_{ij}\theta, \quad \eta = \lambda_{ij}\epsilon_{ij} + \chi\theta, \quad h_i = k_{ij}\vartheta_j \quad (1.65)$$

where σ_{ij} and ϵ_{kl} are (6 x 1) vectors of stresses and strain; θ is the temperature, λ_{ij} is (6 x 1) array of thermo-mechanical coupling coefficients ($\lambda^k = Q^k\alpha^k$, elastic coefficients matrix in Hooke's law and thermal expansion coefficients), the entropy for unit volume η and χ are scalar variables in each layer, h_i is the (3 x 1) vector of heat flux, ϑ_j is the (3 x 1) vector of spatial gradient of temperature, and k_{ij} is the (3 x 3) matrix of conductivity coefficients.

1.3.5. A Third order theory with Thermomechanical Coupling (TTC)

In [174] a third order theory with Thermomechanical Coupling (TTC) was developed. This was an attempt to obtain as accurate results using a third order theory as could be obtained by using CUF, which is a fourth order expansion of the configuration variables.

A Third order theory of shear-deformable von Karman laminated plates with Thermomechanical Coupling (TTC) was developed via Tonti's modelling approach, encompassing the mechanical Reddy theory [175] and the classical equations of thermal nature [176]. Consistent with the assumed cubic variation of the displacement field along the thickness coordinate [153], a corresponding cubic variation is assumed also for the temperature field, parallel to what was previously accomplished in [177]. The work follows the unified scheme (Fig. 1.13) for the formulation of the thermomechanical problem of laminated plates, which was presented in [177]. It integrates mechanical and thermal aspects by identifying generalised 2D variables and governing equations also for the thermal aspects of the problem. The scheme virtually embeds a multitude of possible models, resulting from different assumptions about the plate mechanical and thermal assumptions [178]. The structure the model was derived for was a laminated rectangular plate with N layers, subjected to both mechanical lateral and thermal loadings, with the edges of the plate subjected to uniform stretching forces of magnitudes p_x and p_y in the x

and y directions, respectively.

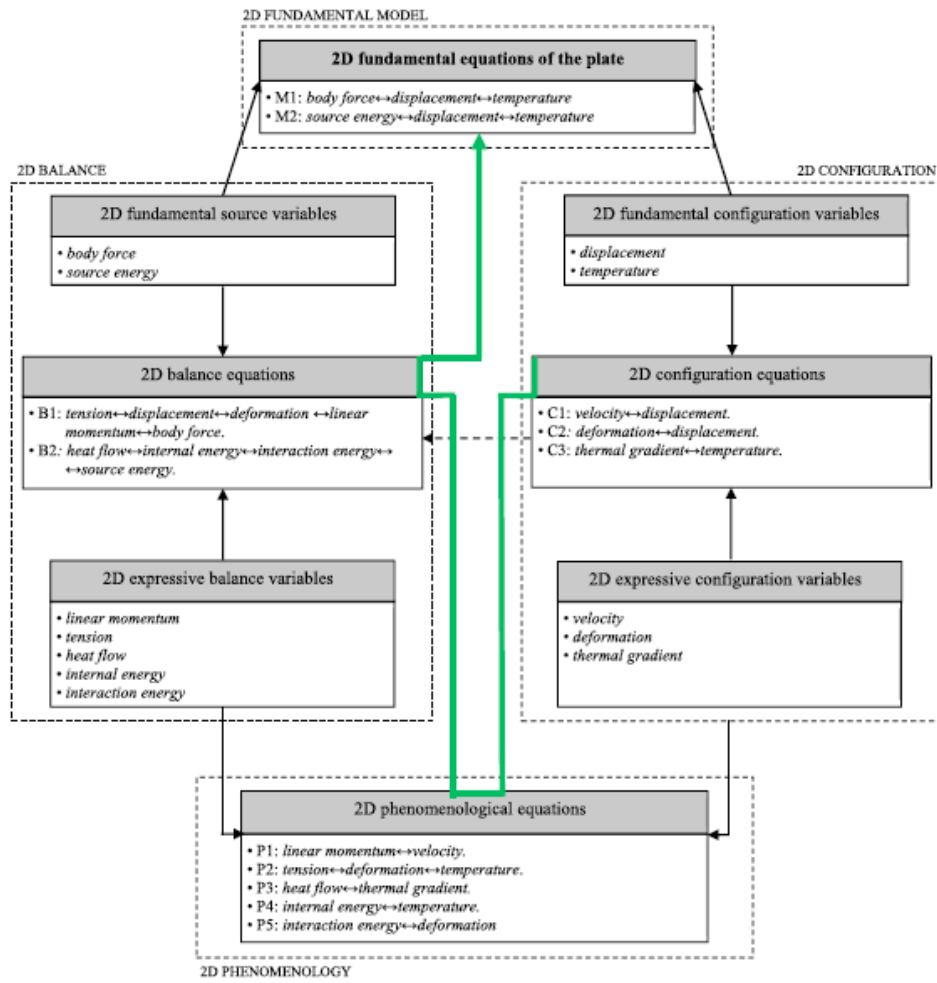


Fig.1.13. Unified formulation of the thermomechanical problem for a 2D nonlinear plate [174,177]

Following the unified scheme in Fig. 1.13, the problem of the thermoelastic plate was decomposed into:

$$\{\text{displacement 3D}\} = \{\text{shape}\} \times \{\text{displacement}\}$$

$$\{\text{temperature 3D}\} = \{\text{shape}\} \times \{\text{temperature}\}$$

(1.66)

In Eqs. (1.66) *displacement* and *temperature* variables depend only on the x and y coordinates of the reference plane and on time t , while the shapes govern the dependence on the thickness z coordinates.

For the TTC model, in Eqs.(1.66), has the following expression [175]:

$$u_1 = u + z\phi_1 - \frac{4}{3h^2}z^3(\phi_1 + w_{,x}), u_2 = v + z\phi_2 - \frac{4}{3h^2}z^3(\phi_2 + w_{,y}), u_3 = w \quad (1.67)$$

where $u_1(x, y, z, t)$, $u_2(x, y, z, t)$, and $u_3(x, y, z, t)$ are the components of the 3D displacement variable along the x, y and z directions, while $u(x, y, t)$, $v(x, y, t)$, $w(x, y, t)$ are the displacements of a point located on the mid-plane and $\phi_1(x, y, t)$, $\phi_2(x, y, t)$ are the rotations of a transverse normal about the y - and x -axes. The latter represent the unknown displacements of the 2D plate model (independent of z). Eq. (1.67) relaxes the classical assumption on the linearity and normality of the transverse normal after the deformation by expanding the 3D displacement components u_1 and u_2 as cubic functions of the thickness coordinate.

It was also assumed that the temperature varies according to a series truncated at the cubic order, consistent with assumptions (1.67):

$$T = T_0 + zT_1 + z^2T_2 + z^3T_3 \quad (1.68)$$

where $T(x, y, z, t)$ is the 3D temperature variable, while $T_0(x, y, t)$, $T_1(x, y, t)$,

$T_2(x, y, t)$, $T_3(x, y, t)$ are the unknown components of the temperature of the 2D model. The components T_2 and T_3 can be expressed in terms of T_0 and T_1 by imposing a variable combination of the following thermal boundary conditions on the upper and lower surfaces of the plate [175, 136]:

$$q_3|_{z=\pm h/2} = \pm H[T_\infty - (T)_{\pm h/2}] \quad \text{free heat exchange} \quad (1.69)$$

$$\frac{\partial T}{\partial z}|_{z=\pm h/2} = 0 \quad \text{thermal insulation} \quad (1.70)$$

$$T|_{z=\pm h/2} = T^*(x, y, t) \quad \text{temperature prescribed} \quad (1.71)$$

$$q_3|_{z=\pm h/2} = q_3^*(x, y, t) \quad \text{heat flow prescribed} \quad (1.72)$$

where q_3 is the heat flow in the z direction, H is the boundary conductance, T_∞ is the constant difference between the absolute temperature of the surrounding medium and the reference temperature, and T^* and q_3^* are the temperature and heat flow prescribed on the external surfaces, respectively.

$$T = f_a(z)T_0 + f_b(z)T_1 + f_c(z) \quad (1.73)$$

where

$$\begin{aligned} f_a(z) &= (r_1 + r_2z + r_3z^2 + r_4z^3) \\ f_b(z) &= (r_5 + r_6z + r_7z^2 + r_8z^3) \\ f_c(z) &= (r_9 + r_{10}z + r_{11}z^2 + r_{12}z^3) \end{aligned} \quad (1.74)$$

and where r_i is defined by the boundary conditions imposed.

The mechanical parameters of the model were the velocity with components defined as

$$u^v = u_{,t}; \quad v^v = v_{,t}; \quad w^v = w_{,t}; \quad \phi_1^v = \phi_{1,t}; \quad \phi_2^v = \phi_{2,t} \quad (1.75)$$

where the comma denotes the derivative with respect to the following independent variable, and the deformation with components defined as in [175]:

$$\begin{aligned} \varepsilon_{11}^{(0)} &= u_{,x} + \frac{1}{2}w_{,x}^2; \quad \varepsilon_{22}^{(0)} = v_{,y} + \frac{1}{2}w_{,y}^2 \\ \varepsilon_{12}^{(0)} &= u_{,y} + v_{,x} + w_{,x}w_{,y} \end{aligned} \quad (1.76)$$

$$\varepsilon_{11}^{(1)} = \phi_{1,x}; \quad \varepsilon_{22}^{(1)} = \phi_{2,y}; \quad \varepsilon_{12}^{(1)} = \phi_{1,y} + \phi_{2,x} \quad (1.77)$$

$$\begin{aligned} \varepsilon_{11}^{(3)} &= -C_1(\phi_{1,x} + w_{,xx}); \quad \varepsilon_{22}^{(3)} = -C_1(\phi_{2,y} + w_{,yy}) \\ \varepsilon_{12}^{(3)} &= -C_1(\phi_{1,y} + \phi_{2,x} + 2w_{,xy}) \end{aligned} \quad (1.78)$$

$$\gamma_2^{(0)} = \phi_2 + w_{,y}; \quad \gamma_1^{(0)} = \phi_1 + w_{,x}$$

$$\gamma_2^{(2)} = -C_2(\phi_2 + w_{,y}); \quad \gamma_1^{(2)} = -C_2(\phi_1 + w_{,x})$$

(1.79)

$$\text{where } C_2 = 3C_1; \quad C_1 = 4/(3h^2)$$

(1.80)

The latter are related to the 3D strains associated with Eq(1.67) as in [175]

$$\varepsilon_{11} = \varepsilon_{11}^{(0)} + z\varepsilon_{11}^{(1)} + z^3\varepsilon_{11}^{(3)}; \quad \varepsilon_{22} = \varepsilon_{22}^{(0)} + z\varepsilon_{22}^{(1)} + z^3\varepsilon_{22}^{(3)}; \quad \varepsilon_{12} = \varepsilon_{12}^{(0)} + z\varepsilon_{12}^{(1)} + z^3\varepsilon_{12}^{(3)}$$

(1.81)

$$\varepsilon_{23} = \gamma_2^{(0)} + z^2\gamma_2^{(2)}; \quad \varepsilon_{13} = \gamma_1^{(0)} + z^2\gamma_1^{(2)}$$

(1.82)

In Eq(1.81), $\varepsilon_{ij}^{(0)}$ are the von Karman nonlinear membrane strains, $\varepsilon_{ij}^{(1)}$ are the Kirchhoff linear bending strains (curvatures), $\varepsilon_{ij}^{(3)}$ are the Reddy higher order bending strains, $\gamma_i^{(0)}$ are the Mindlin linear transverse shearing strains [168], and $\gamma_i^{(2)}$ are the Reddy higher order transverse shearing strains.

For a laminated plate with arbitrarily oriented plies, the thermoelastic linear constitutive relations for the k th orthotropic lamina in the principal material coordinates of a lamina are:

$$\begin{Bmatrix} \sigma_{11} \\ \sigma_{22} \\ \sigma_{12} \end{Bmatrix} = \begin{bmatrix} Q_{11} & Q_{12} & Q_{16} \\ Q_{12} & Q_{22} & Q_{26} \\ Q_{16} & Q_{26} & Q_{66} \end{bmatrix}^{(k)} \begin{Bmatrix} \varepsilon_{11} \\ \varepsilon_{22} \\ \varepsilon_{12} \end{Bmatrix} - \begin{Bmatrix} \beta_{11} \\ \beta_{22} \\ \beta_{12} \end{Bmatrix}^{(k)} T$$

$$\begin{Bmatrix} \sigma_{23} \\ \sigma_{13} \end{Bmatrix}^{(k)} = \begin{bmatrix} Q_{44} & Q_{45} \\ Q_{45} & Q_{55} \end{bmatrix}^{(k)} \begin{Bmatrix} \varepsilon_{23} \\ \varepsilon_{13} \end{Bmatrix}$$

(1.83)

where $\bar{Q}_{ij}^{(k)}$ are the plane stress-reduced elastic stiffnesses, and

$\bar{\beta}_{11}^{(k)} = \bar{Q}_{11}^{(k)} \alpha_1 + \bar{Q}_{12}^{(k)} \alpha_2$ and $\bar{\beta}_{22}^{(k)} = \bar{Q}_{12}^{(k)} \alpha_1 + \bar{Q}_{22}^{(k)} \alpha_2$ are the thermoelastic stiffnesses, with α_1 and α_2 coefficients of thermal expansion along the x and y directions.

The model was tested through simplification of appropriate parameters to correspond to the problem considered. Results were compared with the CUF model and the TTC model showed values slightly higher due to the greater internal constraint.

1.4. Environmental conditions and structure of the satellite panel under investigation

To be able to develop an accurate model as well as perform experimental work with an appropriate experimental set up, a literature review has been conducted in order to study the main features and properties of the space environment.

It has become evident that extreme conditions in the International Space Station (ISS) environment include exposure to extreme heat and cold cycling, ultra-vacuum, atomic oxygen, and high energy radiation [179].

The materials used on the exterior of spacecraft are subjected to many environmental threats that can degrade materials and components. These include vacuum, solar ultraviolet (UV) radiation, charged particle (ionising) radiation, plasma, surface charging and arcing, temperature extremes, thermal cycling, impacts from micrometeoroids and orbital debris (MMOD), and environment-induced contamination. In terms of materials degradation in space, the low-Earth orbit (LEO) environment, defined as 200-1,000 km above the Earth's surface, is a particularly harsh environment for most non-metallic materials, because single-oxygen atoms (atomic oxygen [AO]) are present along with all other environmental components [179]. Space environmental threats to spacecraft components vary in their dependence on the component materials, thicknesses and stresses.

As the ISS moves in and out of sunlight during its orbit around Earth, the degree to which a material experiences thermal cycling temperature extremes depends on its thermo-optical properties (solar absorptance and thermal emittance), its view of the sun, its view of Earth, its view of other surfaces of the spacecraft, durations of time in sunlight and in shadow, its thermal mass and the influence of equipment or components that produce heat [179]. As a rule the cyclic temperature variation is $-120\text{ }^{\circ}\text{C}$ to $+120\text{ }^{\circ}\text{C}$, but high solar absorptance with low infrared emittance will contribute to greater temperature swings. Sixteen thermal cycles a day (the ISS orbits Earth approximately once every 92 minutes) may lead to cracking, peeling, spalling or formation of pinholes in the coating, which then allows AO to attack the underlying material [179].

Materials experiments are typically performed in different orientations, in the ram, wake, zenith and/or nadir directions. **Ram** refers to the velocity vector of the vehicle and is subject to the greatest influence of AO. **Zenith**, which points into space in the opposite direction of Earth, has the most solar illumination. **Wake** and **nadir** are the opposing faces of ram and zenith, respectively. The **wake** direction is good for studying UV effects with typically an order of magnitude less AO as the ram direction, and some experimenters may wish to fly duplicate samples (ram- and wake-facing) to differentiate between AO and UV effects. A nadir orientation is desired for Earth-viewing experiments.

The main forms of environmental heating on orbit are sunlight, sunlight reflected from Earth / a planet / the Moon (**Albedo**), and infrared (**IR**) energy emitted from Earth. During launch or in exceptionally low orbits, there is also a free molecular heating effect caused by friction in the rarified upper atmosphere [180].

Albedo is greater over continental regions and increases with latitude. Albedo heat flux reaching a spacecraft will also decrease as the spacecraft moves along its orbit and away from the subsolar point. It must be pointed out that the Albedo factor is a reflectivity, not a flux. The Albedo heat load on the spacecraft will approach 0 near the terminator (the dividing line between the sunlit and dark sides of a planet), even if the albedo value (reflectivity) is 1.0 [180].

The heat load is strongly dependent on the orbital location of the spacecraft. Orbital thermal environments may depend on the angle β (orbit angle) – Fig.1.14 [61].

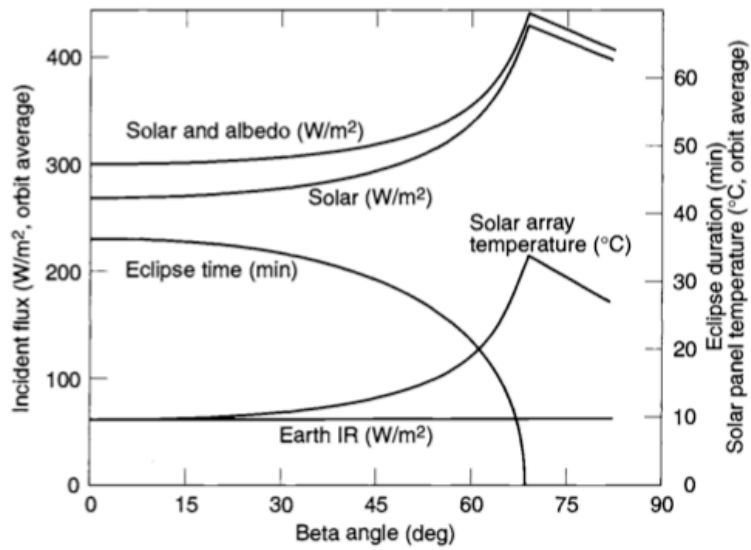


Figure 1.14. Incident flux against beta angle for a cylinder in low Earth orbit [180]

As orbit altitude increases, environmental loads from Earth (IR and albedo) decrease rapidly (Fig. 1.15) [180].

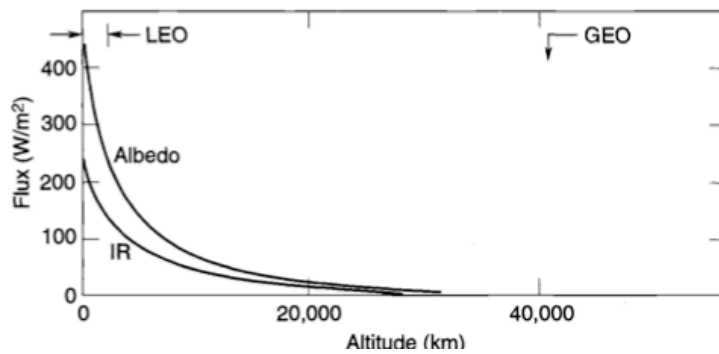


Figure 1.15. Earth heat load vs. altitude [180]

When a spacecraft reaches GEO the loads are insignificant for most thermal design problems.

The thermal environment in a 12-hour circular orbit is much like that in GEO (mainly used for GPS). Earth loads (IR and albedo) are not significant unless cryogenic systems are involved, leaving solar loads as the only environmental loads.

Molniya Orbits are unusual in that they have an extreme degree of eccentricity (very elliptical) and a high inclination (62°). The spacecraft in such an orbit goes through a wide swing in thermal environments. The spacecraft will spend most of a 12-hour orbit period at higher altitudes and relatively little time at low altitudes, where Earth loads are significant [180]. Fig. 1.16 shows the position of the spacecraft in a Molniya orbit at 1 hour intervals and a graph of Earth IR load vs time on a flat plate facing Earth [180].

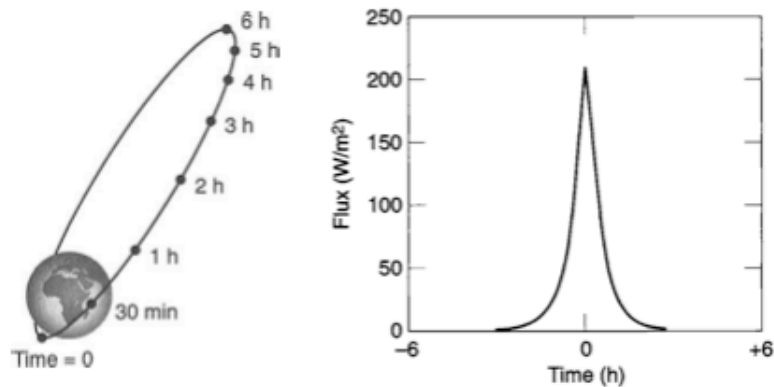


Figure 1.16. Earth IR heating in Molniya orbit for a flat black plate facing Earth [180]

The environment during Interplanetary Missions is characterised by a range of thermal environments much more severe than those encountered in Earth orbit. During most of these missions the only environmental heating which the spacecraft experiences is from direct sunlight. During a flyby, a spacecraft is exposed to IR and albedo loads from planets (Table 1.13). A spacecraft's distance from the sun determines the thermal environment at all times except during planetary flybys. Eq(1.84) and Fig.1.17 define solar flux as a function of distance from the sun in AU.

Table 1.13. Planetary size and orbit parameters [180]

Planet	Orbit Semimajor Axis (AU)	Perihelion Distance (AU)	Aphelion Distance (AU)	Equatorial Radius (km)
Mercury	0.3871	0.3075	0.4667	2425
Venus	0.7233	0.7184	0.7282	6070
Earth	1.000	0.9833	1.0167	6378
Moon	1.000	0.9833	1.0167	1738
Mars	1.524	1.381	1.666	3397
Jupiter	5.20	4.95	5.45	71,300
Saturn	9.54	9.01	10.07	60,100
Uranus	19.18	18.28	20.09	24,500
Neptune	30.06	29.80	30.32	25,100
Pluto/Charon	39.44	29.58	49.30	3,200 (Pluto)

$$Solar\ flux = \frac{1367.5\ W}{AU^2\ m^2} \tag{1.84}$$

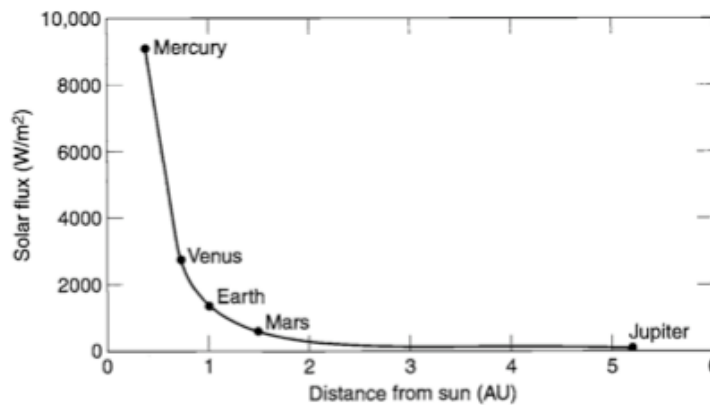


Figure 1.17. Solar flux as a function of distance from the sun [180]

As an example, Fig. 1.18 demonstrates the equilibrium temperature of an isothermal sphere (with absorptance and emittance of 1.0) as a function of the distance from the sun. At the Earth’s distance, the sphere’s temperature is 6°C, at the average orbital distance of Mercury, it is 174°C, and drops down to -229°C for the location of Pluto and Charon.

During planetary flybys, planetary IR and albedo loads are added to the solar load for a short period of time. On most spacecraft, the thermal mass of the vehicle largely damps out the temperature rise of most components during flybys. However lightweight components may be affected by the temperature change.

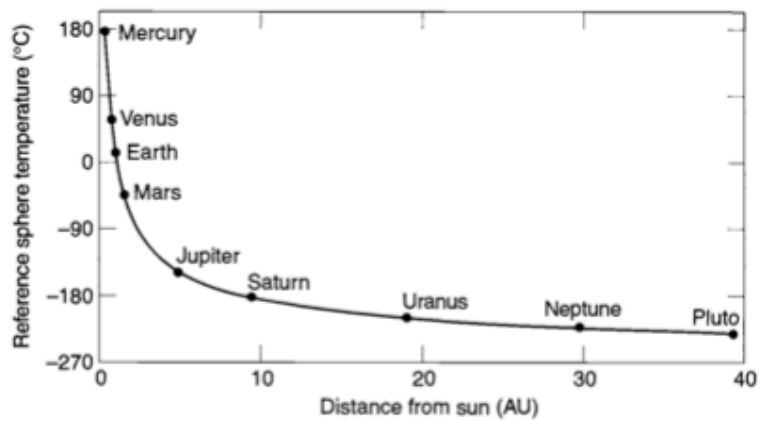


Figure 1.18. Temperature of an isothermal sphere as a function of distance from the sun

[180]

According to [179] the Materials and Processes Technical Information System (MAPTIS-<http://maptis.nasa.gov/>) has been created for registering all prospective experimenters to accumulate information for designers and materials engineers, particularly the Materials Selection Database. This is a useful reference to consult before building hardware so that safety, structural, pressure vessel and line, fracture-critical and contamination requirements are met. The database holds 50 years of analysed results of tests conducted on metallic and nonmetallic materials.

According to [113] the annual cycle in solar flux due to Earth's orbit is from 1293 W/m^2 to 1388 W/m^2 with a frequency spike at $0.0317 \mu\text{Hz}$. The quarterly cycle of solar illumination is dependent on the sunshield design (rectangular or circular wraparound, or full length extended flat shields). Examples of external heat flux on surfaces over a 90 day cycle on a wraparound shield are given in Fig. 1.19.

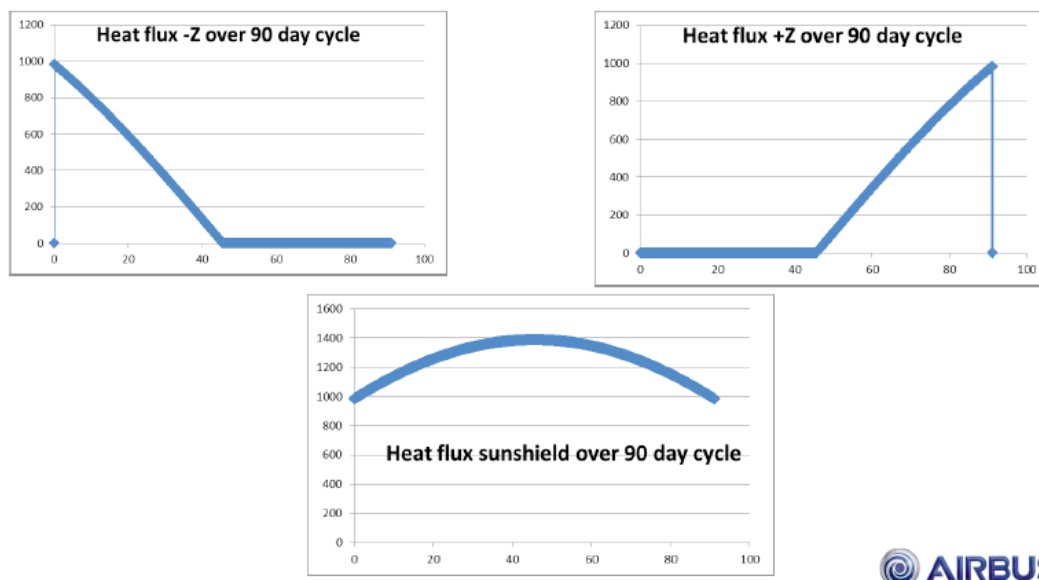


Figure 1.19. External heat flux on surfaces over 90 day cycle on wraparound shield [113]

It was pointed out in [113] that internal disturbances can introduce shifts in frequency around $12\mu\text{Hz}$ or even higher. There have been a few design principles suggested in [113] to minimise these frequency disturbances.

1.4.1. Key strategies learnt from laboratory simulation of the thermal environment

The experiment performed in [181] was one of the most comprehensive works found in the open literature with sufficient level of detail of the experimental set-up. It was intended to investigate thermal behaviour of a sandwich plate/panel deployable as an integral part of a satellite in a space environment using ground thermal-vacuum test.

Heat sink, solar radiation, infrared radiation of the Earth, heat conduction, surface radiation and cavity radiation all have influences on the temperature field (Fig.1.20). This poses a serious challenge to techniques used for thermal testing in laboratories of the simulated space environment.

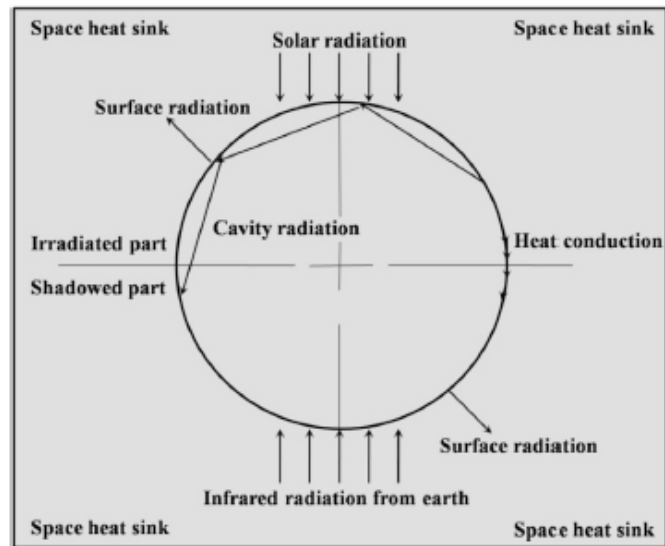


Figure 1.20. Heat transfer mechanism of thin-walled cavity structures in the space environment [181]

The heat sink of the space, solar radiation and infrared radiation from the Earth were considered as the main external heat sources. The heat sink temperature of space was 4 K with a solar constant of $I_0 = 1367 \text{ W/m}^2$.

In [181], as in Section 1.1, it was assumed that the solar radiation energy absorbed by the Earth is emitted from the Earth the form of infrared radiation. The heat flux of infrared radiation of the Earth decreases with the orbit altitude. The maximum heat flux of infrared radiation of the Earth was about 200 W/m^2 .

Typically thermal tests simulating a space environment included three key conditions:

- ultra-high level of vacuum (lower than 10^{-5} Pa),
- a heat sink (-180°C) that can be simulated using black panels with a liquid-nitrogen cooling system,
- a thermal loading that can be achieved through infrared lamps.

In [181] the thermal tests under seven typical heat fluxes were conducted to characterise

heat transfer mechanisms and to obtain temperature fields. The basic heat transfer methods were

- surface radiation,
- cavity radiation,
- heat conduction.

These led to significant temperature differences and gradients occurring on the irradiated and shadowed parts at nighttime and daytime.

It was shown that the maximum influence of heat sink temperature on infrared radiation was less than 8.38%, which was acceptable to simulate reasonably the space environment from the engineering perspective. Thirty temperature sensors were arranged in parallel on the top and bottom shells of the sample following five rows in the *Y* direction and three columns in the *X* direction.

The values of heat flux were selected from 200 W/m² to 1400 W/m², in seven steps. The heat flux was accurately controlled by changing the power of the infrared lamps. As the heat flux was loaded onto the specimen it was measured by heat flow meters and was captured as a feedback within the heat flux control system.

The whole cycle of activation can be described as follows:

Firstly vacuuming was carried out. The precooled system worked when the degree of vacuum was lower than 10⁻⁵ Pa. The infrared lamps were lit once the heat sink temperature was below 93.15 K (i.e. -180°C). The heat flux load increased from 200 W/m² to 1400 W/m² in seven increments of 200 W/m². There were seven heat flux conditions. The steady thermal equilibrium state of the specimen under a heat flux was kept for more than half an hour before recording the temperature data.

As a result the highest and lowest temperatures of the specimen under the heat flux of 200 W/m² corresponding to the thermal load at night were 217 K and 168.2 K; the highest

and lowest temperatures of the specimen under the heat flux of 1400 W/m^2 corresponding to the thermal load at daytime were 339.5 K and 221.6 K.

1.4.2. Thermal cycles in Low Earth Orbit (LEO)

Since the work in this thesis focuses on satellite panels suitable for the conditions of low Earth orbit, it was decided to conduct some further literature review into these conditions as well.

The study [182] considers the conditions of the International Space Station, analysing its survival in low Earth orbit and the damaging effects this region can have on spacecraft. Extensive background is given on many key aspects of low Earth orbit that can damage a spacecraft, such as the outgassing caused by the vacuum of space. Outgassing is the release of gas from a material that will then deposit on nearby surfaces – particularly cold surfaces – and contaminate them, affecting their optical properties. This is one of many reasons that aluminium and aluminium alloys are favoured for use in a vacuum as they tend to have low outgassing – along with the material's resistance to ultraviolet radiation. However, aluminium is eroded by atomic oxygen (AO) in LEO via oxidation, and this is at its densest between altitudes of 200 and 400 km [183]. AO degradation is considered to be one of the most damaging mechanisms of low Earth orbit, affecting the mechanical, thermal and optical properties of a material [184].

The main conditions of LEO that are highlighted are the temperature extremes and the thermal cycles experienced throughout the orbit with the spacecraft completing 11-16 thermal cycles daily with a temperature range of approximately -120°C to $+120^\circ\text{C}$. Thermo-optical properties of the spacecraft play a factor in the temperature that it reaches. For instance, a material with high solar absorptance and low thermal emittance will experience greater temperature swings. Thermal cycles will also result in thermal fatigue in the spacecraft body, due to expansion under heating and contraction under cooling, leading to plastic deformation and phase transformation with continued cycles.

In [185] thermal cycles in LEO environment were simulated to study the microhardness of aluminium alloys under thermal loading ranging from -140°C to $+110^\circ\text{C}$. This was introduced to simulate thermal fatigue and study the resulting stress state and mechanical

properties of the material. The testing resulted in cyclic plastic deformation, which was found to lead to crack initiation, identified using a transmission electron microscope (TEM). A total of 400 thermal cycles were carried out on the samples which showed an eventual decrease in hardness that, from 300-400 cycles, then increased with every cycle. Although rapid temperature changes are implied, the exact value of the rate of change of temperature was never stated in the study. The mechanical load was applied at intervals to test the microhardness of the material and was not applied in conjunction with the change in temperature. The study concluded that aluminium alloys exposed to extended thermal cycling (400 cycles) exhibited obvious softening behaviour, causing phase transformations that, if the cycles were to continue, would lead to crack initiation. It was summarised that the bulk of aerospace materials that undergo periodic heating and cooling are damaged to varying degrees, with thermal fatigue having a great impact on the mechanical properties of the materials used.

Although it is difficult to recreate truly the conditions of LEO on Earth, work has been carried out in the past in regards to this simulation in [186]. The study focused on subjecting graphite/epoxy composite materials to the conditions of LEO. Not only did the materials undergo thermal cycling similar to that experienced in LEO imposed on the samples, but the environment was also in a high vacuum state while the effect of ultraviolet radiation was applied during heating but not during cooling. A single thermal cycle was judged to be from -70°C to $+100^{\circ}\text{C}$ and back to -70°C again. This was with a temperature change rate of $3\text{-}5^{\circ}\text{C}$ per minute and a dwell-time at the temperature extremes of 15 minutes, giving an average cycle time of 100 minutes, typical of a low Earth orbital period. The results examined were for composites subjected to this environment for 8, 16, 40 and 80 thermal cycles in which the transverse flexural strength and transverse tensile strength showed the most severe reduction with thermal cycling, with losses of 34% and 21% respectively, after 80 thermal cycles. It was considered that mechanical properties suffered the greatest change due to high vacuum and thermal loading. Overall, the strength and stiffness of the graphite/epoxy composites was shown to decrease exponentially with increasing thermal cycles.

Further work into the synergistic effects of high vacuum and thermal cycling was implemented in [187], this time on carbon fibre/epoxy composites. The experiment took

place in a high vacuum state of 10^{-5} Torr where a single thermal cycle was judged to be from $+120^{\circ}\text{C}$ to -175°C and back to $+120^{\circ}\text{C}$ for which it had a duration of approximately 43 minutes. The experiment was run for 500, 1000, 1500 and 2000 cycles. Panels were then subjected to mechanical tests at an ambient temperature of 23°C to observe the mechanical properties of the samples. The results confirmed gradual damage with the progression of thermal cycles. This was coupled with the degradation of the fibre-matrix interface due to a weakened fibre-matrix bond which led to interfacial sliding.

Another paper [188] that measured distortion in a structure, cycled through a temperature range of -70°C to $+90^{\circ}\text{C}$, with a temperature change rate of $5^{\circ}\text{C}/\text{hour}$ and a dwell-time of 1 hour at the minimum and maximum. Distortion in the structure was recorded using laser interferometric measurement along with videogrammetry measurement for displacement of the external structure. Temperature sensors were installed throughout the structure to analyse the uniformity of the temperature distribution in the structure with the change in temperature. Once again, the results were corroborated against a finite element model of the structure. However, initially there was no load imposed on the structure, and different measurements were taken as well. The material was judged to remain stable after 20 thermal cycles, showing no measurable degradation in the compression modulus or compression strength, with equal stiffness behaviour on the top and bottom of the sandwich panel. Following the thermal cycle measurements, the panel was used in a 4-point bending test, in which compression failure occurred at the upper face sheet.

1.4.3. Honeycomb Panels in Space Applications

During orbit, satellite panels will experience three broad categories of loading: mechanical loads (such as installation stresses on the satellite or dynamic loading due to moving components), thermal loads (principally from solar flux, but also from internal components), and collisions from space debris, including meteoroids. Although loading during orbit is less intensive than during the launch, the extreme conditions - such as no shielding from UV radiation and large temperature variations, along with the long operational times in orbit - can have a serious degrading effect on panels [189].

While this is outside of the scope of this project it is worth mentioning that the mechanical loading of a satellite's life will be dominated by launch, where it experiences very large vibrational loads: loading due to acceleration, shocks due to stage separation, and so on. Therefore it is generally considered that a spacecraft that comfortably survives this stage is unlikely to struggle with the much smaller mechanical loads in orbit from the structural point of view.

While mechanical loads are typically small, and impacts are rare (if dangerous), thermal swings are both regular and significant. While precise temperatures are dependent on the precise design of a satellite and would have to be determined by a finite element model assessing the geometry, materials, orientation, internal components, and exposure time of the satellite, variations between -150°C and $+150^{\circ}\text{C}$ would not be unreasonable, with significant variations of temperature within a body at a given point in time [190]. As such, understanding the thermal behaviour of satellite components is crucial to ensuring the longevity of the structure.

Low-weight materials are crucial for space structures, due to high cost to deliver each unit mass into orbit. While solid metallic panels are sometimes used, sandwich panels are often preferred. These are constructions with thin metal faces and a lightweight core. Foam panels have a porous metallic foam at their core, which is brazed directly onto the face panels. Honeycomb panels are often preferred to foam panels as they are generally stronger per unit mass and are more effective when loaded in shear. It should be noted that honeycomb panels require inserted fasteners for installation which are typically added after construction, which can impact their performance. They are also sensitive to localised normal stresses, which can cause the thin-walled hexagons to buckle. This amplifies the danger posed by impacts from space debris [190]. Additionally, honeycomb panels are often vacuum-packed, so internal convection is minimal [191]. Typically in aerospace application heat dominates one side of the panel either due to internal components or external solar flux. This alongside the insulating properties of the epoxy, and internal heat transfer (driven by conduction) makes modelling heat flux through these panels a difficult task. However, it should be noted that widely the heat transfer considered to be broadly uniform, as discussed in [192].

The honeycomb sandwich panel is a highly innovative design employed in numerous high-tech, high load bearing applications across a wide range of industries including

aerospace, marine, rail and automotive. In recent years, honeycomb panels have become more and more popular in the aerospace industry due to their structural efficiency, demonstrating a high strength to weight ratio. For such applications it is usually desirable to produce components which are as light as possible, but which maintain sufficiently high stiffness, strength, and damage resistance. The development of honeycomb panel design to date has resulted in honeycomb structures exhibiting excellent mechanical performance with high strength to weight ratios as well as high stiffness/rigidity and superior energy absorption characteristics due to their unique geometrical construction. Honeycomb panels are comprised of 3 primary components: (a) the lightweight honeycomb core made up of regular and periodic arrays of hexagonal cells [193], which is ‘sandwiched’ between (b) two thin facing sheets using some form of (c) core-to-facing bonding adhesive/epoxy [193]. The outer face sheets are responsible for providing the flexural stiffness and panel strength, whilst the core is utilised to transmit the shearing action between the face sheets under external loading. The selected bonding adhesive must be suitable to allow the stresses from the facing sheets to be transferred to the core material to ensure that the mechanical properties of the configuration are fully utilised [193].

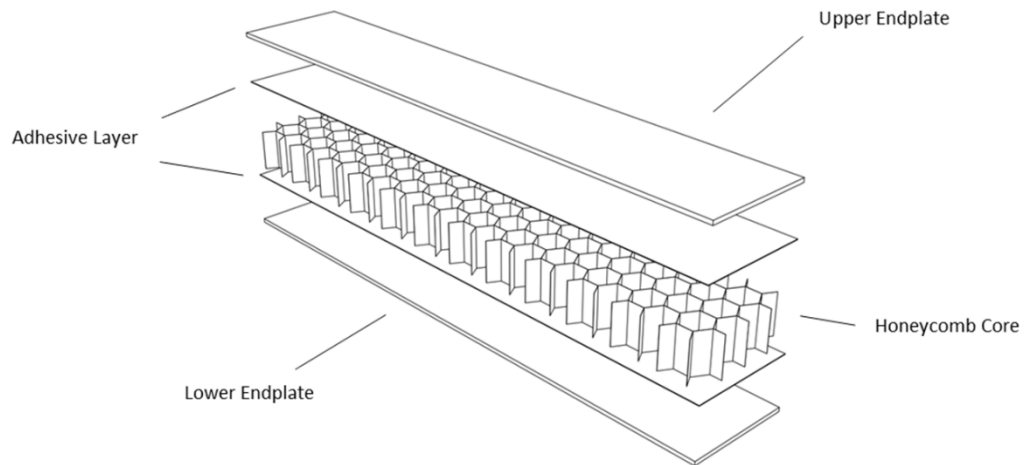


Figure 1.21. Honeycomb Sandwich Panel (HSP) exploded view [193]

The core can be composed of different types of material, but the most frequently used one is hexagonal honeycomb made from sheets of aluminium foil. There are two methods for the manufacturing of sandwich panels – brazing and adhesive bonding – that are favoured for production [194]. Brazing sheets or adhesive films are placed between the faces and the core material (Fig.1.22). The sandwich panel is then heated in a furnace to bond the

structure. These methods eliminate the need to weld stiffeners to the plates and also simplify the connections in the main support frame reducing the need for complicated welding. This, in turn, saves on manufacturing costs and reduces fatigue initiation points due to fewer weld seams, while demonstrating good energy absorption.

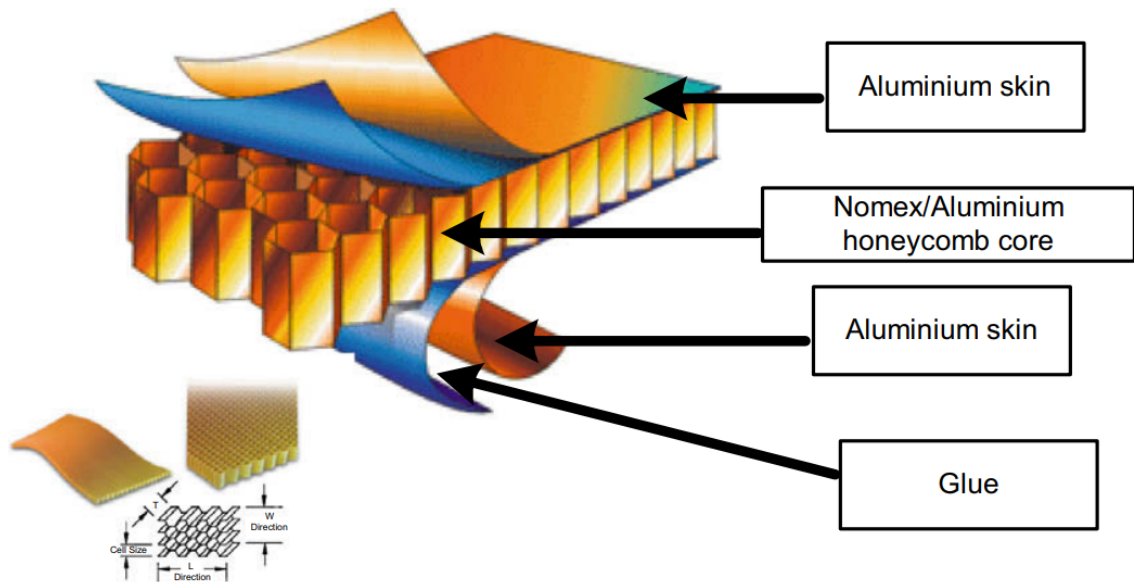


Figure 1.22. Layers of an Aluminium Hexagonal Honeycomb Panel [195]

Despite the numerous benefits and advantages of sandwich panels these structures do have limitations. They are known to have poor resistance to impact loads and – particularly under thermal loading – there is a risk of debonding between the sandwich core and the outer faces.

There are several failure modes that can occur in sandwich panels when used as strength members such as elasto-plastic deformation under bending, buckling in axial compression, core failure under lateral impact pressure, as well as delamination between the core and the face sheets.

It has also been found that there are studies concentrating on the mechanical characteristics of these panels with the initial focus on polymeric foam cores [196], but now more attention has been placed on aluminium centres – whether it is foam or a honeycomb design. A large proportion of research dedicated to sandwich honeycombs focuses on the strength under different loading conditions, such as three-point bending, four-point bending, axial compression and lateral crushing loads, along with mathematical models of these sandwich structures. These tests proved that a larger cell height, h_c , results in an increase in ultimate strength [197] (Fig.1.23).

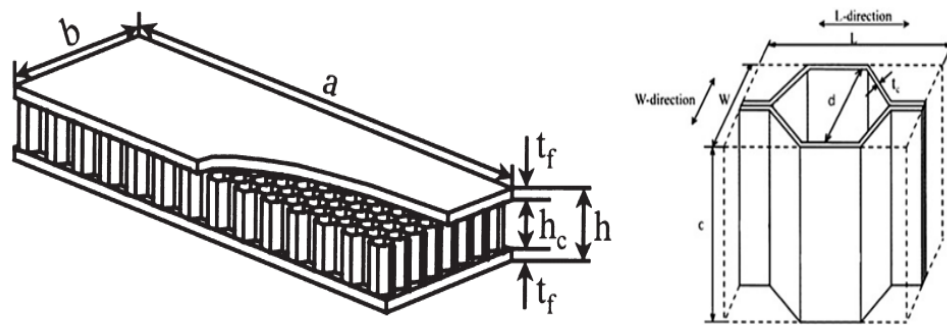


Figure 1.23. Schematic of Hexagonal Honeycomb Sandwich Panel [197]

A study of the strength characteristics of aluminium honeycomb panels was carried out in [197] both experimentally and theoretically. Three-point bending tests were carried out on sandwich panels to investigate the bending behaviour of the samples used. It was discovered that an increase in the honeycomb core thickness of the structure resulted in an increase in ultimate strength, which was evidenced by a delay in plastic deformation. The bending stiffness following the plastic buckling became more moderate with an increase in thickness of the honeycomb core cells, implying that effects of instability in a sandwich structure after collapse can be reduced with an increase in thickness of the core.

In [195] a physical experiment, a finite element analysis and an analytical model of honeycomb sandwich panels under a typical four-point bending test were considered, where the honeycomb core was modelled as one solid layer of equivalent material properties. Experiments were carried out for both aramid fibre and aluminium honeycomb core sandwich panels in which the aluminium cores had densities of 55 kg/m^3 and 82 kg/m^3 and the aramid fibre core had a density of 48 kg/m^3 . Based on the experimental results the study stated that an increase in the core density led to an increased stiffness of the sandwich structure and the aluminium-cored panels were more ductile than those with an aramid fibre core.

Another study based around the bending behaviour of sandwich panels under four-point bending tests was carried in [198] but instead focused on fatigue analysis, as opposed to the work [195] in which the experiment was designed to cause the test sample to rupture. Fatigue testing was carried out on two types of honeycomb sandwich panels – initially

undamaged samples and those damaged by partial debonding between the sandwich panel components. The sandwich panels had carbon fibre faces with aluminium honeycomb cores of density 50 kg/m³. Tests were administered at room temperature and showed two different modes of failure occurring in the undamaged and damaged samples. For the undamaged samples, buckling occurred at the face that was in compression, while failure occurred in the walls of the honeycomb core for the partially debonded samples. The initially undamaged samples that survived the fatigue testing were then subjected to a static bending test that established that the fatigue load had no effect on the residual strength and stiffness of the samples investigated.

More work into the analysis of aluminium honeycomb sandwich panels under static bending tests was undertaken in [196] to demonstrate that a change in honeycomb cell size as well as the distance between the supports would have an impact on the collapse mode for the experimental samples. A change in the distance between the supports can be shown to have an effect on whether the panel can be classified as a thin plate or thick plate, going by the ratio of the overall height of the panel over the length between supports, $\frac{h}{a}$, with a ratio greater than 0.1 being considered a thick plate and between 0.01 and 0.1 as a thin plate. The thin plate collapsed in the centre of the applied load, while the thicker plates experienced cell collapse and shearing in the core, causing the indentation of the applied load to be steeper on one side compared to the other.

A 2013 conference publication [199] focused on the use of the Finite Element Method to analyse the thermo-mechanical behaviour of a hexagonal honeycomb sandwich panel under cantilever bending. An equivalent honeycomb plate was employed to simplify the model and reduce the computing time in the solution process. The results gathered were considered to be accurate therefore proving a good example of cost and time reduction in the early stages of honeycomb sandwich panel design.

A study carried in [200] analysed the bending fatigue strengths of aluminium honeycomb sandwich panels with samples of varying core densities. The work was carried out both experimentally and using a finite element approach. Experimental results showed an increase in the bending fatigue strength with an increase in the relative density of the core

structure while the finite element analysis concluded that the failure mode under cyclic bending was debonding between the adhesive and the face sheet.

Another study [201] delved into the transverse mechanical shear behaviour and failure mechanism of aluminium hexagonal honeycomb cores made of Al-5056 using both experimental and finite element approaches. The results showed that shear deformation can be categorised into 4 stages: elastic deformation of cell walls, the plastic deformation of walls, followed by fractures in the cell walls and finally debonding of the core and the face sheets. In [202] a method to calculate the transverse shear modulus of honeycomb cores using the finite element method was presented and it was noted that the modulus decreased with an increase in the thickness of the core.

For a specified loading condition, the approach used to maximise the performance of the panel design is extremely important since different structures will perform in different ways depending on geometrical construction and the properties of the chosen material. In [203] the failure load/mode of glass fibre reinforced (GFRP)-Nomex manufactured panels under a 3-point bending configuration was investigated, concluding that the ratio of skin thickness to span length, as well as the honeycomb relative density, had the most significant influence on the experimental results for otherwise identical panels.

The choice of material for the panel construction is also crucial since it provides the necessary rigidity in the outer-plane direction that makes it suitable for its intended application. The most widely used materials for honeycomb panels include aluminium, polymer materials and composites such as Nomex. A key advantage of the honeycomb core design is that it can provide bidirectional support to the skins, whereas corrugated cores, for example, can provide only unidirectional support under loading. Factors including the core foil thickness, cell size and thickness of skin components all influence the compressive strength of the panel – a common loading condition in industrial applications.

1.5. Conclusions

In this chapter the key aspects of practice at Airbus DS in the treatment of the thermo-elastic problem have been discussed. It was shown that the Company gives preference to the Nastran FEM package and the Systema TMM tool in order to obtain results for mechanical/elastic and thermal parts of the problem separately, which later have to be merged through data export and interpolation techniques. Therefore this multistage process may potentially result in the reduction of accuracy of the thermo-elastic model and therefore in the quality of the final prediction of the dynamics of the system.

It was also shown that there are other software packages, which do not use FEM but use automated tools based on exact analytical solutions, and they provide more accurate results, when FEM software is found to underestimate the prediction. Arising from this discussion the problem of accuracy was discussed in Sections 1.2.4 and 1.2.5, with suggestions and ways of improvement proposed there. In Section 1.3 it was highlighted that a physics based coupling process of the two physical effects of temperature and deformation is the only real way forward to achieve a significant increase in accuracy of the results.

In this chapter, after a detailed review of the phenomenon of thermo-elasticity, it has also become clear that a deformation of the body is connected to a change of heat inside it and therefore with a change of the temperature distribution in the body. At the same time a deformation of the body leads to temperature changes, and conversely. The internal energy of the body depends on both the temperature and the deformation. The science of thermoelasticity deals with the investigation of these *coupled* processes. If we decide to develop a model under the simplifying assumption that the influence of the deformation on the temperature field may be neglected, then we are not operating within the field of thermoelasticity, but within the theory of thermal stress (TTS). It has become clear that in an **isothermal** case, which was considered by Airbus DS in their experimental programmes, we have processes which are elastically and thermally **reversible**. However if the temperature varies in time we deal with two coupled processes, the *reversible elastic process* and the *irreversible thermodynamic process* (due to a spontaneous and hence irreversible process of heat transfer by means of heat conduction).

As a result of the literature search with regard to the different theories and approaches to tackle the problem of thermo-elastic deformation, discussed in Section 1.1, it has become clear that modern development of the thermo-elastic modelling is mostly focused on application of multilayered FGM elements. This is an advantage, because considering structural elements such as plates, it is possible then to consider multilayered plates without constraints on the variation of material properties along the thickness, even the temperature dependent ones.

It also has been discussed that there are two main streams for the theoretical approaches, comprising partially coupled models and fully coupled models. From closer investigation it was clear that although within the partially coupled approach we still face a partial division of the models into the thermal part (defining the temperature or solving the HC equation) and the mechanical part (predicting the displacement based on the set or identified temperature) it can provide results as accurate as a fully coupled model at a reduced level of computational cost and complexity of the model.

This means that partially coupled approaches are the most appropriate candidates for our model development. To try to reduce the computational cost it was decided to develop the model following the TTC approach described in [174]. This approach is a third order theory with Thermomechanical Coupling and demonstrated in [174] giving results as accurate as by using CUF, which is a fully coupled approach using a fourth order expansion of the configuration variables. The theory is extensive and covers a wide range of approaches and cases, which means that we could introduce the necessary simplifications of the parameters and appropriate boundary and initial conditions.

Finally it was suggested that the newly developed coupled model must ideally be expressed in an annotated code for universality, accessibility, and further development. The output data could be presented graphically but the main output must be annotated and accompanied by a guidance for use to make the data representation easily accessible and usable for Airbus DS.

Since the problem defined by Airbus DS was concentrating on the thermo-elastic behaviour of the satellite the structural literature review in this chapter also provides a summary of the conditions the satellite panel would go through. Particular emphasis was given to the thermal environmental conditions, especially in LEO, which would be dominating as the structure undergoes extreme level of heat and cold while going through an orbital cycle. This thermal loading would obviously be combined with the vibration of the system due to equipment installed, and representing mechanical loading on the satellite panels. The case of impact, for example due to a collision with debris, is out of the scope of this work.

Since the samples of satellite panels provided by Airbus DS were sandwich honeycomb panels the work was built around an investigation of their behaviour. Therefore the literature review also consists of an insight into structure, manufacturing peculiarities, as well as behavioural features of similar honeycomb panels which are identified in the open literature.

2. Development of the coupled analytical model for thermo-mechanical analysis

Despite the fact that finite element analysis is widely used for thermo-mechanical analysis, it has been identified that there is an industrial requirement for a modelling capability that avoids the need for any major re-definition of statically and dynamically correlated spacecraft system level models. The modelling should provide ‘communication’ between the mechanical and thermal aspects of the problem in order to predict the behaviour of the panel in time. Such a facility would provide further insight into areas such as the structural reliability of the system, the dynamic changes in the structural properties due to thermo-mechanical loadings, and potential resonances arising from thermal loading and structural changes within the panel.

It is also desirable that this new and more accurate model remains conceptually straightforward in use and is able to accommodate different mechanical and thermal boundary conditions as well as dynamic mechanical and thermal loading, in order to simulate properly the behaviour of different structural elements. Clearly, the middle core of the panel will generally behave differently from the top and bottom plies, both mechanically and thermally. It is hypothesised that the middle core will experience nonlinear non-uniform deformation due to the long-lasting heating effects that it experiences from the top and bottom layers. This means that the model needs to accommodate dynamically varying thermal properties.

Looking at the problem of a spacecraft panel undergoing *cyclic loading* from the perspective of modelling it is possible to find that the structure must combine the effects of thermal loading as well as mechanical disturbance. This is because from a physical point of view the deformation of a body is connected to a change of heat inside it, and therefore to a change in the temperature distribution in the body. So, *a deformation of the body leads to temperature changes, and vice versa*. The internal energy of the body depends on both the temperature and the deformation and so, in the case of a practical body, such as a spacecraft panel, this necessarily undergoes processes that are intrinsically coupled, and defined collectively as thermoelasticity [176]. In order to summarise, the Theory of Thermal Stresses (TTS) commonly applies a simplifying assumption that the influence of the deformation on the temperature field may be neglected [176]. In TTS the classical heat conduction (HC) equation is usually used but this does not routinely contain the term representing the deformation of the body. Knowing the temperature distribution

from the solution of the HC equation, the displacement equations of the theory of elasticity can be solved. At the same time classical dynamic elasticity has been developed under the assumption that the heat exchange between different parts of the body due to the heat conduction occurs very slowly, and therefore the thermal motion may be regarded as *adiabatic*.

However, thermoelasticity deals with a wide class of phenomena. It covers the general theory of heat conduction as well as the general theory of thermal stresses, and it describes the temperature distribution produced by deformation. Thermoelasticity also describes the phenomenon of thermoelastic dissipation. As mentioned above many modelling approaches tend to separate the mechanical and thermal effects, but thermoelastic processes are not generally reversible because although the elastic part may be reversed - the deformations may be recoverable through cooling - the thermal part may not be reversed, due to the dissipation of energy during heat transfer [135].

Apart from that, thermal changes in the body cause mechanical deformation in the body, which in return affects these thermal changes, representing the process as two-way feedback, and this mechanism is at the heart of the current work presented in this chapter. To do this properly requires that the modelling techniques and representations really do have to couple the mechanical and thermal aspects of the problem to achieve results of meaningful accuracy. A literature review of commonly used techniques for thermoelastic problems is presented in [135]. It was pointed out there that some works have looked at the problem of displacements and stresses in laminated structures under thermal bending. These have assumed a linear temperature profile through the thickness direction for both laminated plates and multilayered composite shells, as well as for circular plates and cylindrical shells. In these models the assumption has been that the temperature profile through the thickness is linear and constant in nature. This assumption cannot be valid for anisotropic structures where the thickness temperature profile is never linear. Therefore, even if the structural model is accurate, the final solution could be in error due to the incorrectly assumed profile of the temperature distribution along the thickness. In [137, 204] it has been shown that dependent on how the displacement and/or stress field are presented in the normal direction, mathematical models for thermal analysis of composite laminates can be derived using the three-dimensional theory of elasticity, Equivalent Single Layer theories (ESL), Layer Wise theories (LW) or zig-zag theories, and more recently Carrera's Unified Formulation (CUF) are all used. To reduce the computational cost of three-dimensional theories and also maintain acceptable accuracy, several

solutions for the thermal problems in composites have been proposed using the ESLs. These are the Classical Laminated Plate Theory (CLPT), First-order Shear Deformation Theory (FSDT) and Higher-order Shear Deformation Theory (HSDT). It has been highlighted in [135] that the literature so far only contains a relatively small amount of work devoted to the coupled thermo-mechanical analysis of structures, in the form of both thermoelastic and thermoplastic analyses. There also have been some works comparing coupled and uncoupled analysis, the accuracy and efficiency of the coupled theory [139], and the extension of a higher-order zig-zag plate theory [205] for prediction of the fully coupled mechanical, thermal, and electric behaviour. Partially coupled models are commonly derived that neglect the interactions between temperature effects and mechanical deformations, and instead assume *a priori* the distribution of temperature along the thickness, or obtain it from the heat conduction equation, and then they solve the mechanical equations with known temperature gradient terms. In contrast, fully coupled thermoelastic models take into account explicitly the interaction between temperature effects and mechanical deformations, because of the presence of coupling displacement and temperature terms in the thermal and mechanical equations, respectively. Furthermore, if the temperature varies in time we deal with two coupled processes, the *reversible elastic process* and the *irreversible thermodynamic process*, due to a spontaneous and hence irreversible process of heat transfer by means of heat conduction. This means that fully coupled approaches are the most appropriate for model development to investigate the influence of the thermal loading on the global thermomechanical behaviour of the structure.

From the foregoing discussion it can be seen that in order to consider thermoelasticity reasonably properly it is necessary to accept that deformation of a body leads to temperature changes, and conversely, and the internal energy of the body depends on both the temperature and the deformation. Therefore, for increased accuracy the problem has to be treated as a *coupled* process.

In this chapter, in order to try to reduce the computational cost, it was decided to implement the Third order theory with the Thermomechanical Coupling (TTC) approach described in [174]. This approach is a third order theory with thermomechanical coupling and is demonstrated in [174] to give results as accurate as those obtained from using CUF, which is a fully coupled approach using a fourth order expansion of the configuration variables. The underlying theory is extensive and covers a wide range of approaches and

cases, which means that we are able to introduce the necessary simplifications to incorporate appropriate boundary and initial conditions.

To keep the model as tractable as possible it has been decided to develop a partially coupled model, and although TTC in [174,177] is indeed a partially coupled model it still demonstrates very high accuracy when compared with the fully coupled model using CUF [135, 208]. The TTC model consists of comprehensively developed mechanical and thermal parts which are connected through additional coupling terms, these being temperature and time dependent in the mechanical part, and displacement and time dependent in the thermal part, respectively.

Therefore in this chapter the TTC approach described in [174] is adopted and developed further for application to the thermomechanical problem of the sandwich honeycomb panel. The model is then verified, emphasising optimal ways of finding the solution and performance of the model through a numerical experiment. After this the model has been used for simulation of a multiple scenarios of thermomechanical loading to investigate the effect of thermal and mechanical loading, as well as their coupling. Conclusions to the effects discovered are then drawn at the end of the chapter.

2.1. A model for the mechanical behaviour of the panel

The mechanical equations of motion are based on the Reddy plate theory [174] and an adaptation of this follows on directly, noting that it is assumed that deflection due to shear is negligible with respect to flexure between the layers, and so the basis for the model has been reduced to the interpretation given by [209]:

$$N_{11,x} + N_{12,y} = 0$$

$$N_{12,x} + N_{22,y} = 0$$

$$\begin{aligned} M_{11,xx} + 2M_{12,xy} + M_{22,yy} + N_{11}w_{,xx} + 2N_{12}w_{,xy} + N_{22}w_{,yy} + q(x, y, t) - p_x w_{,xx} \\ - p_y w_{,yy} \\ = \rho h w_{,tt} + \delta w_{,t} \end{aligned}$$

(2.1a,b,c)

where:

$$\begin{cases} N_{11} \\ N_{22} \\ N_{12} \end{cases} = \int_{-h/2}^{h/2} \begin{cases} \sigma_{11} \\ \sigma_{22} \\ \sigma_{12} \end{cases} dz ; \quad \begin{cases} M_{11} \\ M_{22} \\ M_{12} \end{cases} = \int_{-h/2}^{h/2} z \begin{cases} \sigma_{11} \\ \sigma_{22} \\ \sigma_{12} \end{cases} dz ;$$

(2.2a,b)

and where N_{ij} are membrane forces, M_{ij} are bending moments, p_x and p_y are forces applied along the x and y coordinate directions respectively, δ is a damping coefficient, $q(x,y,t)$ is a transversely distributed loading, and ρ and h are the density and thickness of the panel. By justifiably and systematically neglecting some of these parameters it is then possible to simplify the equations.

For a laminated plate with arbitrarily oriented plies, the thermoelastic linear constitutive relations for the k th orthotropic lamina in the principal material coordinates of the lamina are

$$\begin{cases} \sigma_{11} \\ \sigma_{22} \\ \sigma_{12} \end{cases} = \begin{bmatrix} Q_{11} & Q_{12} & 0 \\ Q_{12} & Q_{22} & 0 \\ 0 & 0 & Q_{66} \end{bmatrix}^{(k)} \begin{cases} \varepsilon_{11} \\ \varepsilon_{22} \\ \varepsilon_{12} \end{cases} - \begin{cases} \beta_{11} \\ \beta_{22} \\ 0 \end{cases}^{(k)} T$$

(2.3)

where $\bar{Q}_{ij}^{(k)}$ are the plane stress-reduced elastic stiffnesses, and

$\bar{\beta}_{11}^{(k)} = \bar{Q}_{11}^{(k)}\alpha_1 + \bar{Q}_{12}^{(k)}\alpha_2$ and $\bar{\beta}_{22}^{(k)} = \bar{Q}_{12}^{(k)}\alpha_1 + \bar{Q}_{22}^{(k)}\alpha_2$ are the thermoelastic stiffnesses, with α_1 and α_2 being the coefficients of thermal expansion in the x and y directions.

The relationships between strains and displacements are given by the following [174]

$$\begin{aligned} \varepsilon_{11}^{(0)} &= u_{,x} + \frac{1}{2}w_{,x}^2; & \varepsilon_{22}^{(0)} &= v_{,y} + \frac{1}{2}w_{,y}^2 \\ \varepsilon_{12}^{(0)} &= u_{,y} + v_{,x} + w_{,x}w_{,y} \end{aligned}$$

(2.4)

$$\begin{aligned}\varepsilon_{11}^{(3)} &= -C_1(w_{,xx}); \quad \varepsilon_{22}^{(3)} = -C_1(w_{,yy}) \\ \varepsilon_{12}^{(3)} &= -C_1(2w_{,xy})\end{aligned}$$

where
$$C_1 = 4/(3h^2) \tag{2.5}$$

and $u(x,y,t)$, $v(x,y,t)$, $w(x,y,t)$ are the displacements of a point located on the mid-plane, where the comma in Eqs.(2.4) is used in the conventional way to denote the derivative with respect to the associated independent variables.

The strains in Eq. (2.4) are related to the three dimensional strains in Eq. (2.6), as in [174], neglecting the rotations of the transverse normal around the x - and y - axes

$$\varepsilon_{11} = \varepsilon_{11}^{(0)} + z^3 \varepsilon_{11}^{(3)}; \quad \varepsilon_{22} = \varepsilon_{22}^{(0)} + z^3 \varepsilon_{22}^{(3)}; \quad \varepsilon_{12} = \varepsilon_{12}^{(0)} + z^3 \varepsilon_{12}^{(3)} \tag{2.6}$$

In Eqs. (2.5)-(2.6), $\varepsilon_{ij}^{(0)}$ are the von Karman nonlinear membrane strains, and $\varepsilon_{ij}^{(3)}$ are the Reddy higher order bending strains. The transverse shearing strains are neglected.

Following [174] we also assume that the temperature varies according to a cubic law, consistent with assumptions stated in Eq. (2.6)

$$T = T_0 + zT_1 + z^2T_2 + z^3T_3 \tag{2.7}$$

where $T(x,y,z,t)$ is the three dimensional temperature variable, while $T_0(x,y,t)$, $T_1(x,y,t)$, $T_2(x,y,t)$, $T_3(x,y,t)$ are the hitherto unknown components of the temperature of the two dimensional model, and cover the full profile up to a cubic distribution, as shown in Fig. 2.1.

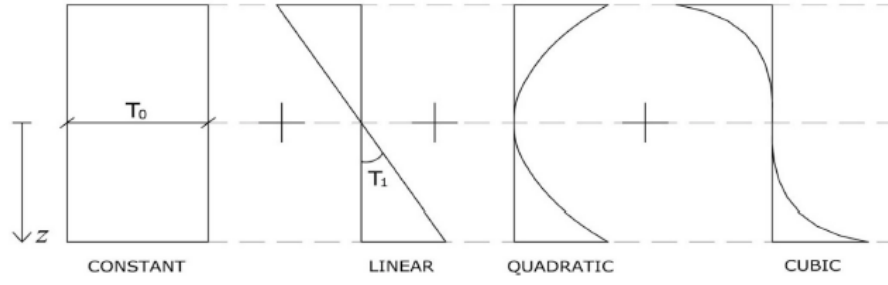


Figure 2.1. Contribution to the overall cubic temperature profile [174]

The components T_2 and T_3 can be expressed in terms of T_0 and T_1 by imposing a variable combination of the following thermal boundary condition, in this case a +/- distribution of the free heat exchange on the upper and lower surfaces of the plate [208, 210],

$$q_3|_{z=\pm h/2} = \pm H[T_\infty - (T)_{\pm h/2}] \quad (\text{for free heat exchange})$$

$$q_3|_{z=\pm h/2} = q_3^*(x, y, t) \quad (\text{for prescribed heat flow}) \quad (2.8)$$

where q_3 is the heat flow in the z direction, H is the boundary conductance, and T_∞ is a constant difference between the absolute temperature of the surrounding medium and the reference temperature

$$T = f_a(z)T_0 + f_b(z)T_1 + f_c(z) \quad (2.9)$$

where

$$\begin{aligned} f_a(z) &= (r_1 + r_2z + r_3z^2 + r_4z^3) \\ f_b(z) &= (r_5 + r_6z + r_7z^2 + r_8z^3) \\ f_c(z) &= (r_9 + r_{10}z + r_{11}z^2 + r_{12}z^3) \end{aligned} \quad (2.10)$$

and where the r_i are defined by the imposed boundary conditions.

For a free heat exchange thermal boundary condition the r_i are introduced as applied in [174, 210]

$$r_1 = r_6 = 1; \quad r_3 = -\frac{4H}{h(hH + 4\lambda_{33}^{(1)})}; \quad r_8 = -\frac{4(hH + 2\lambda_{33}^{(1)})}{h^2(hH + 6\lambda_{33}^{(1)})}$$

$$r_{11} = \frac{4HT_\infty}{h(hH + 4\lambda_{33}^{(1)})}; \quad r_2 = r_4 = r_5 = r_7 = r_9 = r_{10} = r_{12} = 0$$

It should be pointed out that for a symmetric cross-ply laminate with heat flow $q^*(x, y, t)$ prescribed on the upper surface and free heat exchange on the lower surface, the r_i are defined as [174, 210]:

$$r_1 = r_6 = 1; \quad r_3 = -\frac{12H}{h(5hH + 24\lambda_{33}^{(1)})}; \quad r_4 = -\frac{16H}{h^2(5hH + 24\lambda_{33}^{(1)})};$$

$$r_7 = -\frac{4H}{5hH + 24\lambda_{33}^{(1)}}$$

$$r_8 = -\frac{4(3hH + 8\lambda_{33}^{(1)})}{h^2(5hH + 24\lambda_{33}^{(1)})}; \quad r_{11} = -\frac{2(hHq^*(x, y, t) + 6\lambda_{33}^{(1)}(q^*(x, y, t) - HT_\infty))}{h\lambda_{33}^{(1)}(5hH + 24\lambda_{33}^{(1)})};$$

$$r_{12} = \frac{4hHq^*(x, y, t) + 4\lambda_{33}^{(1)}(q^*(x, y, t) - HT_\infty)}{h^2\lambda_{33}^{(1)}(5hH + 24\lambda_{33}^{(1)})}; \quad r_2 = r_5 = r_9 = r_{10} = 0$$

2.2. A model for the thermal behaviour of the panel

The thermal balance equations are introduced for the case of non-stationary conduction and thermoelastic coupling, as in [174]

$$q_{1,x} + q_{2,y} + q_{3,z} - b_{,t} - a_{,t} + E = 0 \tag{2.11}$$

where the $q_i(x, y, z, t)$ represents the three-dimensional heat flow along the x, y, z directions, $b(x, y, z, t)$ is the three dimensional internal energy due to non-stationary conduction, $a(x, y, z, t)$ is the three dimensional interaction energy due to the thermoelastic coupling,

and $E(x,y,z,t)$ is the three dimensional source energy. The two-dimensional balance consists of two equations obtained from Eq. (2.11), [174, 177]

$$\begin{aligned} q_{1,x}^{(0)} + q_{2,y}^{(0)} - b_{,t}^{(0)} - a_{,t}^{(0)} + Q^{(0)} &= 0 \\ q_{1,x}^{(1)} + q_{2,y}^{(1)} - b_{,t}^{(1)} - a_{,t}^{(1)} + Q^{(1)} &= 0 \end{aligned} \tag{2.12}$$

where the following two-dimensional quantities are defined as

$$\begin{aligned} \begin{Bmatrix} q_1^{(0)} \\ q_2^{(0)} \end{Bmatrix} &= \int_{-h/2}^{h/2} \begin{Bmatrix} q_1 \\ q_2 \end{Bmatrix} dz ; \quad b^{(0)} = \int_{-h/2}^{h/2} b dz ; \quad a^{(0)} = \int_{-h/2}^{h/2} a dz \\ \begin{Bmatrix} q_1^{(1)} \\ q_2^{(1)} \end{Bmatrix} &= \int_{-h/2}^{h/2} z \begin{Bmatrix} q_1 \\ q_2 \end{Bmatrix} dz ; \quad b^{(1)} = \int_{-h/2}^{h/2} bz dz ; \quad a^{(1)} = \int_{-h/2}^{h/2} az dz \\ Q^{(0)} &= \int_{-h/2}^{h/2} q_{3,z} dz ; \quad Q^{(1)} = \int_{-h/2}^{h/2} q_{3,z} z dz \end{aligned} \tag{2.13}$$

The source energy $E(x,y,z,t)$ is neglected due to the absence of chemical reactions, nuclear fission effects or inputs due to electric currents. The heat flow definition is based on the Fourier law for the k th orthotropic lamina and expressed in the principal material coordinates of a lamina as follows

$$\begin{aligned} \begin{Bmatrix} q_1^{(0)} \\ q_2^{(0)} \end{Bmatrix} &= \sum_{k=1}^N \int_{z_k}^{z_{k+1}} \begin{bmatrix} \lambda_{11}^{(k)} & \lambda_{12}^{(k)} \\ \lambda_{12}^{(k)} & \lambda_{22}^{(k)} \end{bmatrix} \left(\begin{bmatrix} f_a(z) & 0 \\ 0 & f_a(z) \end{bmatrix} \begin{Bmatrix} g_1^{(0)} \\ g_2^{(0)} \end{Bmatrix} + \right. \\ &\quad \left. + \begin{bmatrix} f_b(z) & 0 \\ 0 & f_b(z) \end{bmatrix} \begin{Bmatrix} g_1^{(1)} \\ g_2^{(1)} \end{Bmatrix} \right) dz \\ \begin{Bmatrix} q_1^{(1)} \\ q_2^{(1)} \end{Bmatrix} &= \sum_{k=1}^N \int_{z_k}^{z_{k+1}} \begin{bmatrix} \lambda_{11}^{(k)} & \lambda_{12}^{(k)} \\ \lambda_{12}^{(k)} & \lambda_{22}^{(k)} \end{bmatrix} \left(\begin{bmatrix} f_a(z) & 0 \\ 0 & f_a(z) \end{bmatrix} \begin{Bmatrix} g_1^{(0)} \\ g_2^{(0)} \end{Bmatrix} + \right. \\ &\quad \left. + \begin{bmatrix} f_b(z) & 0 \\ 0 & f_b(z) \end{bmatrix} \begin{Bmatrix} g_1^{(1)} \\ g_2^{(1)} \end{Bmatrix} \right) z dz \end{aligned} \tag{2.14}$$

where the $\lambda_{ij}^{(k)}$ are the thermal conductivities of the k th laminate, and $g_1^{(0)} = T_{0,x}$, $g_1^{(1)} = T_{1,x}$, $g_2^{(0)} = T_{0,y}$, $g_2^{(1)} = T_{1,y}$.

The internal energy for the k th lamina is defined in terms of temperature

$$b^{(k)} = C^{(k)}T = \rho^{(k)}c_v^{(k)} \quad (2.15)$$

where $C^{(k)}$ is the thermal capacity of a lamina, the function of mass density is $\rho^{(k)}$ and the specific heat at constant strain is given by $c_v^{(k)}$.

The components of internal energy can then be re-written, taking into account Eqs. (2.9)-(2.10), (2.15), as

$$b^{(0)} = \int_{-h/2}^{h/2} b dz = \sum_{k=1}^N \int_{z_k}^{z_{k+1}} b^{(k)} dz = \sum_{k=1}^N \int_{z_k}^{z_{k+1}} C^{(k)} [f_a(z)T_0 + f_b(z)T_1 + f_c(z)] dz \quad (2.16)$$

$$b^{(1)} = \int_{-h/2}^{h/2} b dz = \sum_{k=1}^N \int_{z_k}^{z_{k+1}} b^{(k)} dz = \sum_{k=1}^N \int_{z_k}^{z_{k+1}} C^{(k)} [f_a(z)T_0 + f_b(z)T_1 + f_c(z)] z dz \quad (2.17)$$

The interaction energy for the k th orthotropic lamina is expressed in terms of strain within the three dimensional thermoelastic theory, with the assumption that $\varepsilon_{zz} = \varepsilon_{33} = 0$

$$\begin{aligned} a^{(0)} &= \int_{-h/2}^{h/2} a dz = \sum_{k=1}^N \int_{z_k}^{z_{k+1}} a^{(k)} dz = \\ &= T_{ref} \sum_{k=1}^N \int_{z_k}^{z_{k+1}} \left[\beta_{11}^{(k)} \left(\varepsilon_{11}^{(0)} + z\varepsilon_{11}^{(1)} + z^3\varepsilon_{11}^{(3)} \right) + \beta_{22}^{(k)} \left(\varepsilon_{22}^{(0)} + z\varepsilon_{22}^{(1)} + z^3\varepsilon_{22}^{(3)} \right) + \right. \\ &\quad \left. + \beta_{12}^{(k)} \left(\varepsilon_{12}^{(0)} + z\varepsilon_{12}^{(1)} + z^3\varepsilon_{12}^{(3)} \right) \right] dz \end{aligned}$$

$$\begin{aligned}
a^{(1)} &= \int_{-h/2}^{h/2} az \, dz = \sum_{k=1}^N \int_{z_k}^{z_{k+1}} a^{(k)} z \, dz = \\
&= T_{ref} \sum_{k=1}^N \int_{z_k}^{z_{k+1}} \left[\beta_{11}^{(k)} \left(\varepsilon_{11}^{(0)} + z \varepsilon_{11}^{(1)} + z^3 \varepsilon_{11}^{(3)} \right) + \beta_{22}^{(k)} \left(\varepsilon_{22}^{(0)} + z \varepsilon_{22}^{(1)} + z^3 \varepsilon_{22}^{(3)} \right) + \right. \\
&\quad \left. + \beta_{12}^{(k)} \left(\varepsilon_{12}^{(0)} + z \varepsilon_{12}^{(1)} + z^3 \varepsilon_{12}^{(3)} \right) \right] z \, dz
\end{aligned} \tag{2.18}$$

The energy exchange rates of the out-of-plane heat flow $Q^{(0)}$ and $Q^{(1)}$ due to the heat flow q_3 in the z direction are

$$\begin{aligned}
Q^{(0)} &= \int_{-h/2}^{h/2} q_{3,z} \, dz \\
&= \sum_{k=1}^N \int_{z_k}^{z_{k+1}} \lambda_{33}^{(k)} g_{3,z} \, dz \\
&= \sum_{k=1}^N \int_{z_k}^{z_{k+1}} \lambda_{33}^{(k)} [(f_a(z)T_0 + f_b(z)T_1 + f_c(z))_{,zz}] \, dz
\end{aligned}$$

$$\begin{aligned}
Q^{(1)} &= \int_{-h/2}^{h/2} q_{3,z} \, z \, dz \\
&= \sum_{k=1}^N \int_{z_k}^{z_{k+1}} \lambda_{33}^{(k)} g_{3,z} \, z \, dz \\
&= \sum_{k=1}^N \int_{z_k}^{z_{k+1}} \lambda_{33}^{(k)} [(f_a(z)T_0 + f_b(z)T_1 + f_c(z))_{,zz}] \, dz
\end{aligned}$$

(2.19)

A procedure for computing the solutions to the principal Eqs.(2.1) and (2.12), and invoking all the parameters that follow, defined with respect to specified boundary and initial conditions, has been specifically coded in the *Mathematica* programming language.

Having derived the necessary components of the thermal and mechanical equations it is then possible to obtain the system of equations, in the following form

$$\begin{aligned}
\bar{C}_1 T_0(t) + \bar{C}_2 u(t) + \bar{C}_3 v(t) &= 0 \\
\bar{C}_4 T_0(t) + \bar{C}_5 u(t) - \bar{C}_6 v(t) &= 0 \\
C_1 \ddot{W}(t) + C_2 \dot{W}(t) + [C_3 + C_7 T_\infty(t)]W(t) + C_8 W^3(t) + C_9 T_1(t) + Q(t) &= 0 \\
C_{10} \dot{T}_0(t) + C_{11} T_0(t) + C_{12} T_\infty(t) + C_{13} \dot{W}(t)W(t) - C_{14} \dot{u}(t) - C_{15} \dot{v}(t) + C &= 0. \\
C_{16} \dot{T}_1(t) + C_{17} T_1(t) + C_{18} T_\infty(t) + C_{19} \dot{W}(t) &= 0
\end{aligned} \tag{2.20}$$

Since we are interested in the temperature and displacement distributions in the z -direction for the structure when it is subjected to combined mechanical and thermal loading, the system can be reduced to the following three equations to find the membrane temperature $T_0(t)$ and bending temperature $T_1(t)$ as defined in [177, 178], then to identify $T(t)$ in Eq. (2.9):

$$\begin{aligned}
C_1 \ddot{W}(t) + C_2 \dot{W}(t) + [C_3 + C_4 P_x(t) + C_5 P_y(t) + C_6 T_0(t) + C_7 T_\infty(t)]W(t) + C_8 W^3(t) \\
+ C_9 T_1(t) + Q(t) &= 0 \\
C_{10} \dot{T}_0(t) + C_{11} T_0(t) + C_{12} T_\infty(t) + C_{13} \dot{W}(t)W(t) &= 0 \\
C_{16} \dot{T}_1(t) + C_{17} T_1(t) + C_{18} T_\infty(t) + C_{19} \dot{W}(t) &= 0
\end{aligned} \tag{2.21}$$

It has to be pointed out that in reference [174] this type of equation system was solved analytically obtaining a general solution using features within bespoke *Mathematica* code. However, this was done by eliminating the nonlinear terms, and for static values of the mechanical and thermal loading, thus

$$C_1 \ddot{W}(t) + C_3 W(t) + C_9 T_1(t) = 0$$

$$\begin{aligned}
C_{10}\dot{T}_0(t) + C_{11}T_0(t) &= 0 \\
C_{16}\dot{T}_1(t) + C_{17}T_1(t) + C_{19}\dot{W}(t) &= 0
\end{aligned}
\tag{2.22}$$

Here our overall aim has been to look for a solution for the system in its generalised form, as stated in full in Eq. (2.21).

Before starting to look for an analytical solution it was decided to investigate whether the presence of the nonlinear terms eliminated in [174] would have a pronounced effect on the behaviour of the panel under consideration. Therefore, an analytical closed form solution (using code applying the DSolve function in *Mathematica*) was found for the simplified system (2.22), as well as a comparable numerical solution (using code applying NDSolve function in *Mathematica*) for the full system with nonlinear terms in Eq. (2.21). As an initial numerical example it was assumed that the panel should be subjected to a small constant mechanical load, arbitrarily set to 1N, and a thermal load in the form of an environmental soak temperature of 70°C, and without any mechanical damping. On this basis, substituting in the appropriate numerical data, the system of Eq. (2.21) takes the following form

$$\begin{aligned}
-0.32\ddot{W}(t) + [-2.32 \cdot 10^8 + 5.82 \cdot 10^{-11} T_0(t)]W(t) - 8.23 \cdot 10^{12} W^3(t) \\
+ 13.43 T_1(t) + 0.01 &= 0 \\
-547.26 \dot{T}_0(t) - 34.51T_0(t) + 13.44 - 1.22 \cdot 10^7 \dot{W}(t)W(t) &= 0 \\
-0.0082 \dot{T}_1(t) - 0.012 T_1(t) - 73.89 \dot{W}(t) &= 0
\end{aligned}
\tag{2.23}$$

This system of equations was then solved numerically using code applying the *Mathematica* NDSolve numerical integrators.

In addition to this the simplified system of Eq. (2.22) can be solved analytically using DSolve within some suitable *Mathematica* code

$$\begin{aligned}
-0.32\ddot{W}(t) + [-2.32 * 10^8]W(t) + 13.43 T_1(t) + 0.01 &= 0 \\
-547.26 \dot{T}_0(t) - 34.51T_0(t) + 13.44 &= 0
\end{aligned}$$

$$-0.0082 \dot{T}_1(t) - 0.012 T_1(t) - 73.89 \dot{W}(t) = 0 \quad (2.24)$$

The purely numerical solution to Eq. (2.23) for $W(t)$ and the closed form analytical solution for $W(t)$ obtained for the reduced system of Eq. (2.24) are both plotted in the time domain in Fig. 2.2.

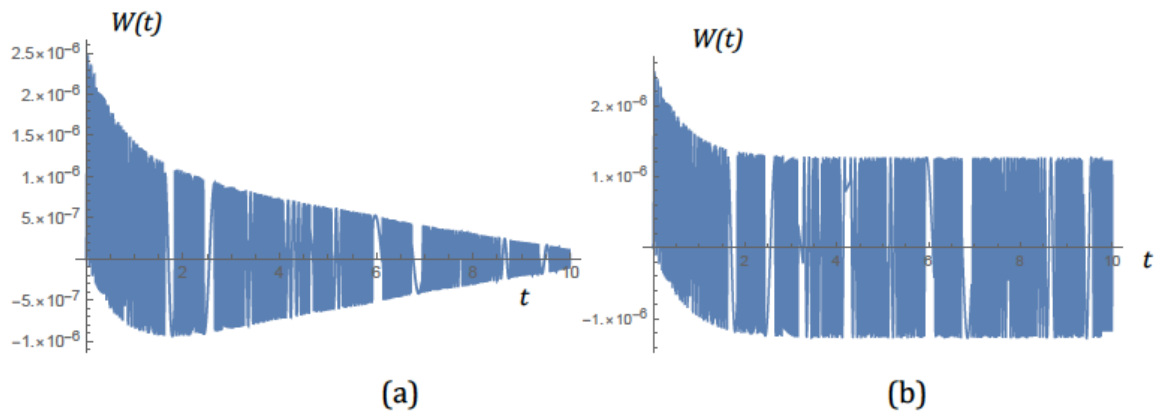


Figure 2.2. Deflection $W(t)$ in metres for the panel under $Q=1\text{N}$, $T=70^\circ\text{C}$ based on the following solutions: (a) – numerical solution of Eqs (2.23), (b)-closed form solution for Eqs (2.24). Time is in seconds.

The two time-domain plots of Fig. 2.2 suggest that for the data considered retaining the presence of the nonlinear and coupling terms provides a solution offering more detailed information about the behaviour of the panel, including an important internal energy transfer phenomenon arising from the interaction between the mechanical and thermal aspects of the problem, demonstrated in Fig. 2.2(a) as a transient decay in the displacement response. However, the numerical solution found for the full nonlinear system obviously doesn't offer any generic insight into the phenomenology of the problem and is restricted in use to specific data cases such as the one just discussed. Given that this particular numerical solution, and others too, confirm the transient nature of the displacement response with time, as one would fully expect, the next logical step in the investigation would be to obtain a proper closed form solution for the full nonlinear system. An immediate benefit of this would be the calculation of accurate and generalised responses, and greatly reduced calculation times for different geometries, loading conditions and different material properties for the panel.

Nevertheless, despite the limitations in the prediction of displacement of Eq. (2.24), it should be mentioned that the predicted profile of the temperature distribution along the thickness, as defined in Fig.2.3, is seen to be phenomenologically accurate for this solution and can be used without any loss of accuracy. This is shown as a comparison between the two solutions, for one numerical case, in Fig. 2.4.

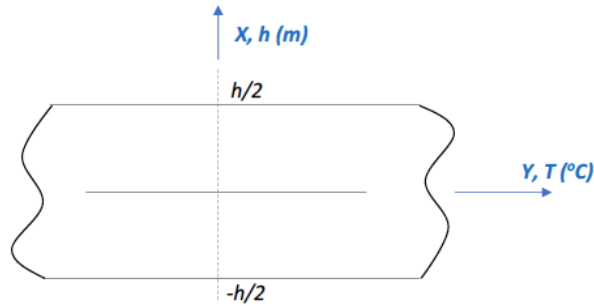


Figure 2.3. Representation of the panel for interpretation of temperature distribution across the thickness

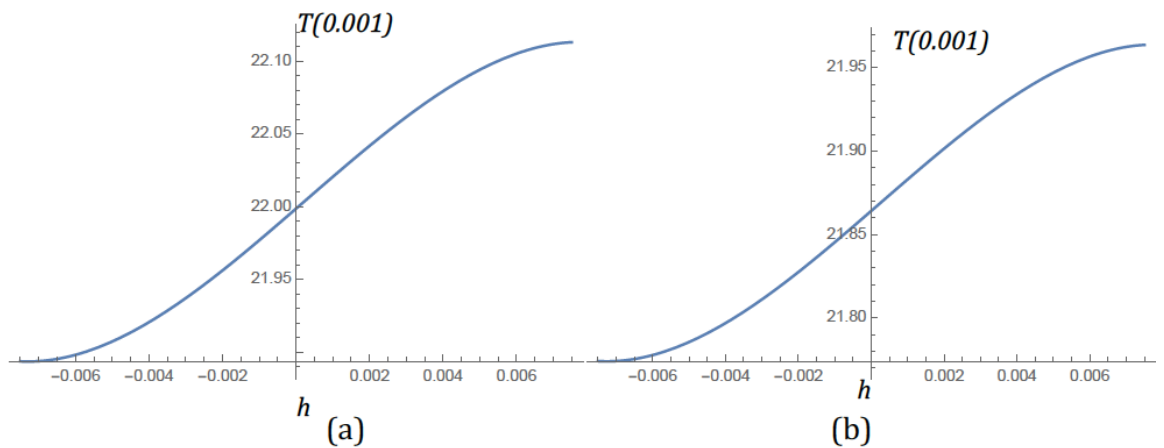


Figure 2.4. Distribution of the instantaneous thermal gradient along the thickness $T(t)$ (as given in Eq.(2.9)) for the panel under: $Q=1N$, $T=70^{\circ}C$, based on (a) – numerical solution of Eqs (2.23), (b)- closed form solutions for Eqs (2.24), both taken at $t=0.001s$. Temperatures in $^{\circ}C$, thickness h in metres.

From inspection of the system of Eq. (2.21) it is obvious that the main mathematical challenge in the solution of the whole system is found to be principally in the first equation, Eq.(2.21a), re-stated as Eq.(2.25)

$$\begin{aligned}
C_1\ddot{W}(t) + C_2\dot{W}(t) + \bar{C}(t)W(t) + C_8W^3(t) \\
+ C_9T_1(t) + Q(t) = 0
\end{aligned}
\tag{2.25}$$

where $\bar{C}(t) = C_3 + C_4P_x(t) + C_5P_y(t) + C_6T_0(t) + C_7T_\infty(t)$.

The difficulty arises due to the simultaneous presence of the time-variant coefficient $\bar{C}(t)$ in the term $W(t)$ and the nonlinear term $C_8W^3(t)$. For the sake of generality we can represent Eq. (2.25) as

$$C_1\ddot{W}(t) + C_2\dot{W}(t) + F_1(t)W(t) + C_5W^3(t) + F_2(t) = 0. \tag{2.26}$$

where the time variable coefficients are defined as $F_1(t) = \bar{C}(t) = C_3 + C_4P_x(t) + C_5P_y(t) + C_6T_0(t) + C_7T_\infty(t)$ and $F_2(t) = C_9T_1(t) + Q(t)$.

Eq.(2.26) can be readily solved to good approximation using the perturbation method of multiple scales, notwithstanding the fact that the principal parametric resonance condition emerges as a consequence of the treatment of secular terms required in order to guarantee the uniformity of the expansion for $W(t)$. It is also possible in principle to examine the non-resonant case for this solution, and both of these analyses will be discussed later in Chapter 6.

2.3. Application of the derived model for a panel in the free heat exchange conditions

The sandwich panel of $300 \cdot 10^{-3} \times 100 \cdot 10^{-3} \times 15 \cdot 10^{-3}$ m is composed of two types of aluminium alloy (Fig. 2.5). For the outer faces of thickness 0.004 m, an Al-2024 alloy is used, whilst an Al-5056 alloy foil is used to form the hexagonal honeycomb core. This core is of depth 14.24×10^{-3} m and comprises a foil of thickness 0.0254×10^{-3} m. The mechanical and thermal properties of these materials are summarised in Tables 2.1 and 2.2, noting that the data in Table 2.1 does not contain explicit information on the thin film

adhesive bonding of the core to the skin, and the structural coefficient of thermal expansion stated in Table 2.2 was extrapolated from the data made available for AL-5056 [23-57].

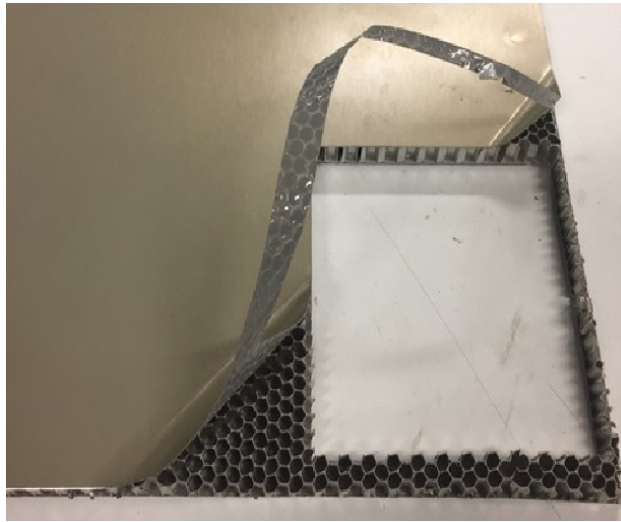


Figure 2.5. Honeycomb sandwich panel typically used in the aerospace industry

Table 2.1: Mechanical Properties of Sandwich Panel

	Al-2024	Al-5056 3/16 Honeycomb
Density, ρ (kg/m ³)	2780	50
Young's Modulus, E (Pa)	73.1×10^9	669×10^6
Shear Modulus, G (Pa)	27.5×10^9	310×10^6
Poisson's Ratio, ν	0.33	0.3
Foil thickness (m [in])		0.0254×10^{-3} [0.001]

Table 2.2: Thermal Properties of Sandwich Panel Materials

	Al-2024	Al-5056
Coefficient of Thermal Expansion ($^{\circ}\text{C}$)	2.47×10^{-5}	2.41×10^{-5}
Coefficient of Thermal Expansion for 3/16 honeycomb ($^{\circ}\text{C}$)		2.4×10^{-6}
Thermal Conductivity @ 25°C (W/mK)	149	149
Specific Heat (J/kg $^{\circ}\text{C}$)	875	904
Reference Temperature ($^{\circ}\text{C}$)	22	22

For the numerical study of the solutions obtained for the system (2.21) with full nonlinear coupling terms, and exploiting the powerful numerical functions within NDSolve, different forms of loading are considered: a constant thermal load only, a dynamic thermal load only, a constant mechanical load only, and a combined thermo-mechanical load consisting of a dynamic thermal component and a constant mechanical component. To verify the performance of the model, and to understand the extent of the results we can obtain from the model, results were also generated for a very thin and a very thick sample. This was achieved by varying the thickness of the honeycomb core layer.

The panel was considered to be simply supported and was analysed under three types of loading based on the thermal, mechanical, and thermo-mechanical conditions summarised above. The thermal loading was applied by means of imposing a difference between the reference temperature and the environmental temperature, in order to represent free heat exchange conditions. The mechanical loading was taken as a normal constant force applied centrally to the top-face sheet.

2.3.1 The case of thermal loading

When elevated temperature conditions apply at the outer faces of the sandwich panel, and thereby represent the free heat exchange condition, these faces will heat up first of all,

with the heat then distributing from the outer faces inwards towards the centre of the core. To understand the process of the displacement emerging due to this changing thermal equilibrium, as well as the characteristics of the thermal gradient along the thickness, a constant environmental surround temperature of 100°C was initially applied with the ambient reference (start) temperature set to 20°C , and a solution for the system of Eq. (2.21) was obtained using the NDSolve function in *Mathematica*TM (Fig. 2.6).

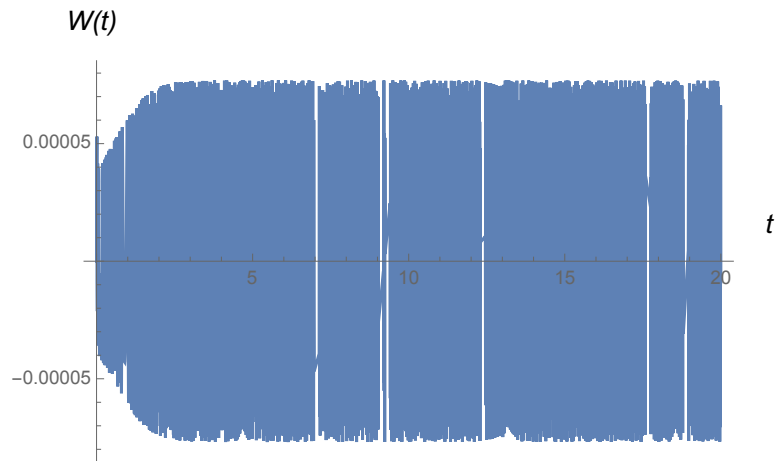


Figure 2.6. Displacement response in metres, shown in the time domain (t in seconds) when subjected solely to a thermal load defined by an environmental temperature of 100°C and with a core thickness of 0.01424m and total plate thickness of 0.015m .

The principal features of the displacement response is the transient over time and the largely symmetrical peak to peak amplitude over the time after the transient. This accords with practical expectations for a plate under this form of loading. In Fig. 2.7 discrete snapshots between 0.001 s through to 5 s are given for the time history of the thermal gradient *across the thickness of the panel*, in order to understand the thermal changes that the panel undergoes, and the conditions under which it stabilises for the specific times chosen.

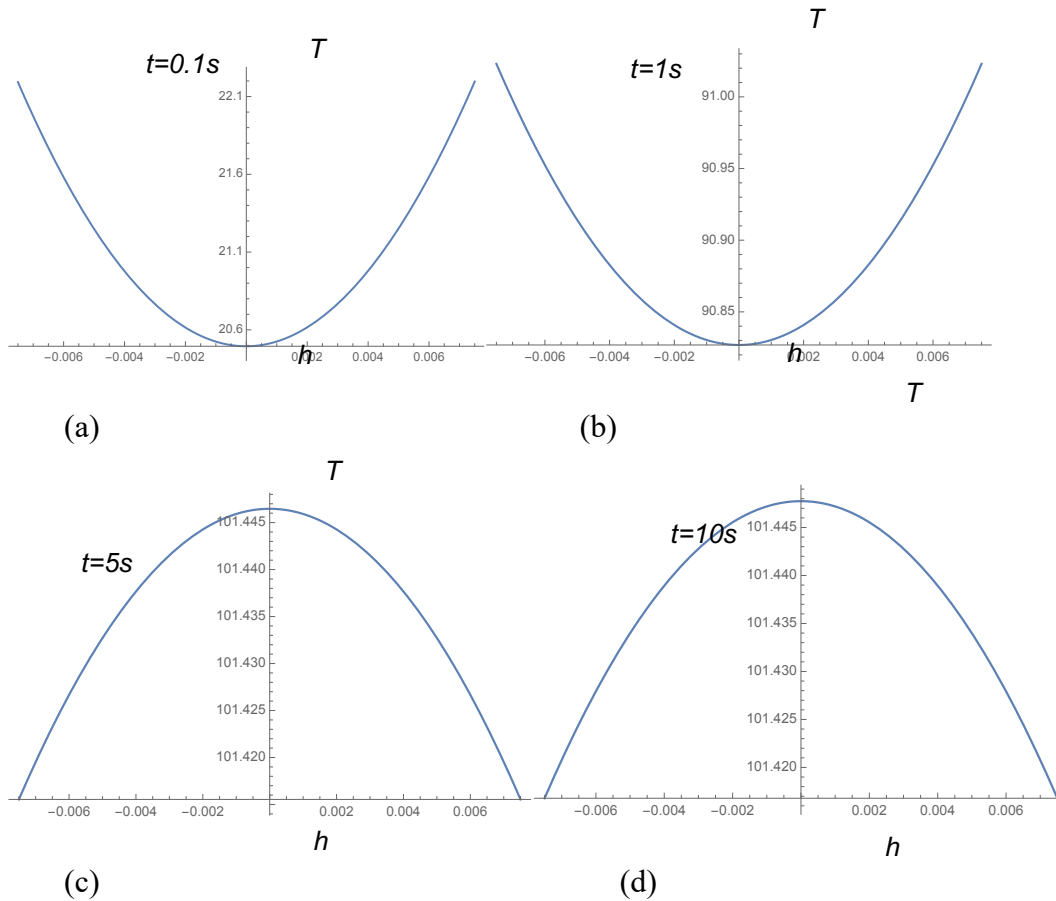


Figure 2.7. Time histories of the temperature distribution along the thickness of the panel under a thermal load due to an environmental soak temperature of 100°C .

Temperature in $^{\circ}\text{C}$, thickness h in metres.

By fixing the time steps and observing the progression of the temperature distribution through the plate we see the main stages of the temperature stabilisation process that are described in [174]. In brief this amounts to the following. By applying heat to the plate through an elevated environmental soak temperature the heat distributes through the thickness as shown in Fig. 2.7 (a-b) with the intermediate temperature of the honeycomb core being very close but lower than the top and bottom skins temperature. However, after 5s the small difference between the skin temperature and the honeycomb core flips and stabilises, with the core being slightly hotter by around 0.03°C . The process of the panel heating up in time is reflected in the behaviour of $T_o(t)$ in Fig. 2.8 where we can clearly see that after 5s the equilibrium temperature is reached around 101°C and the profile thereafter remains constant in time.

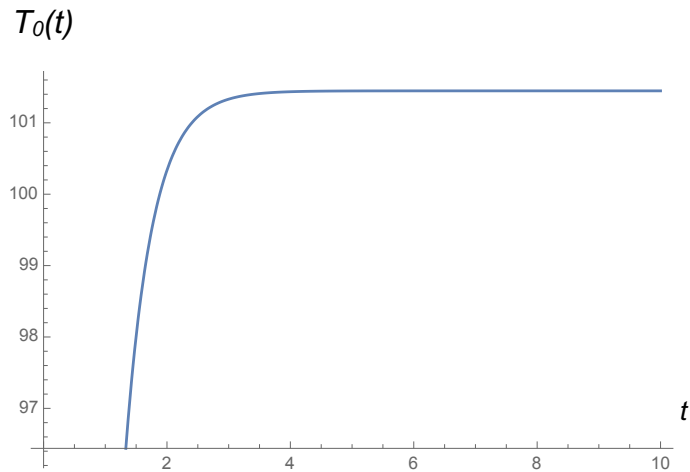


Figure 2.8. Time history of the distribution of the thermal component $T_0(t)$ for the panel under thermal load due to an environmental soak temperature of 100°C , with a core thickness of 0.01424m (for a total plate thickness 0.015m). Temperature in $^\circ\text{C}$, time in seconds.

It can be seen that the process of obtaining the solution for $T_0(t)$ can in itself be a useful tool for finding out if the temperature stabilises at a certain equilibrium, and what the temperature of that equilibrium might be, as well as to determine how long it takes for the panel to reach an equilibrium state.

To investigate the behaviour of the panel when the environmental temperature varies under the prescribed dynamic condition, Eqs.(2.21) are solved for $T(t) = 20 + 10t$ with the reference temperature set to 20°C , as in the previous case.

Initially a panel thickness of 0.015 m is considered, with the honeycomb core thickness of 0.01424m , and the results are given in Fig. 2.9.

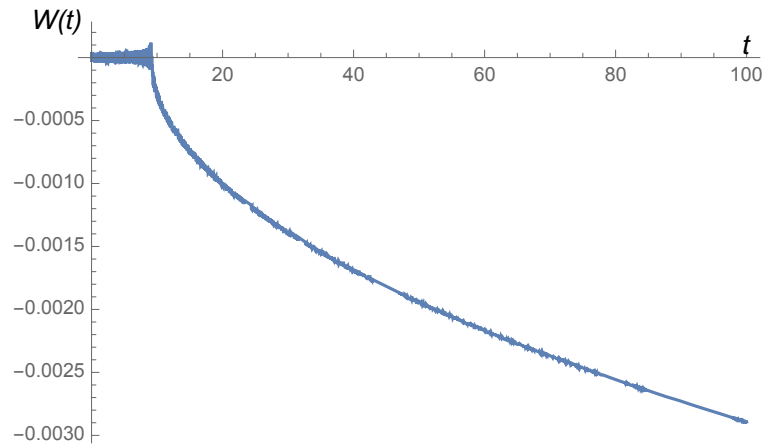


Figure 2.9. Displacement response (in metres) in the time domain (in seconds) when subjected only to thermal loading of $(20 + 10t)$ °C with core thickness 0.01424m and total plate thickness of 0.015m.

As can be seen in Fig. 2.9 due to the dramatic increase of the environmental temperature being transferred to the panel, the panel starts to accumulate thermal stresses, characterised by the transient response, and after around 10s it starts to buckle, exhibiting the displacement.

On analysing the history of the temperature distribution along the thickness of the panel over time it is evident that the sample is undergoing the same process of stabilisation in Figs. 2.10 (a,b) trying to reach the equilibrium state around $0.5s$. However, due to the linearly increasing nature of the thermal load $(20 + 10t)$ °C, the temperature in the sample starts rapidly increasing, as shown in Fig. 2.10 (c,d) in response to the thermal loading. This can be clearly observed from the distribution of the middle plane thermal component $T_0(t)$ in Figure 2.11. It should also be pointed out that in the time histories in Fig. 2.10 we do not observe the flip from the core being cooler than the skins to the skins being slightly cooler than the core which took place in Fig. 2.7. This confirms that the model reflects the fact that the core is constantly trying to catch up with the rapidly increasing temperature of the environment and the skins with the time-increasing temperature $(20 + 10t)$ °C, and cannot reach the point of stabilisation.

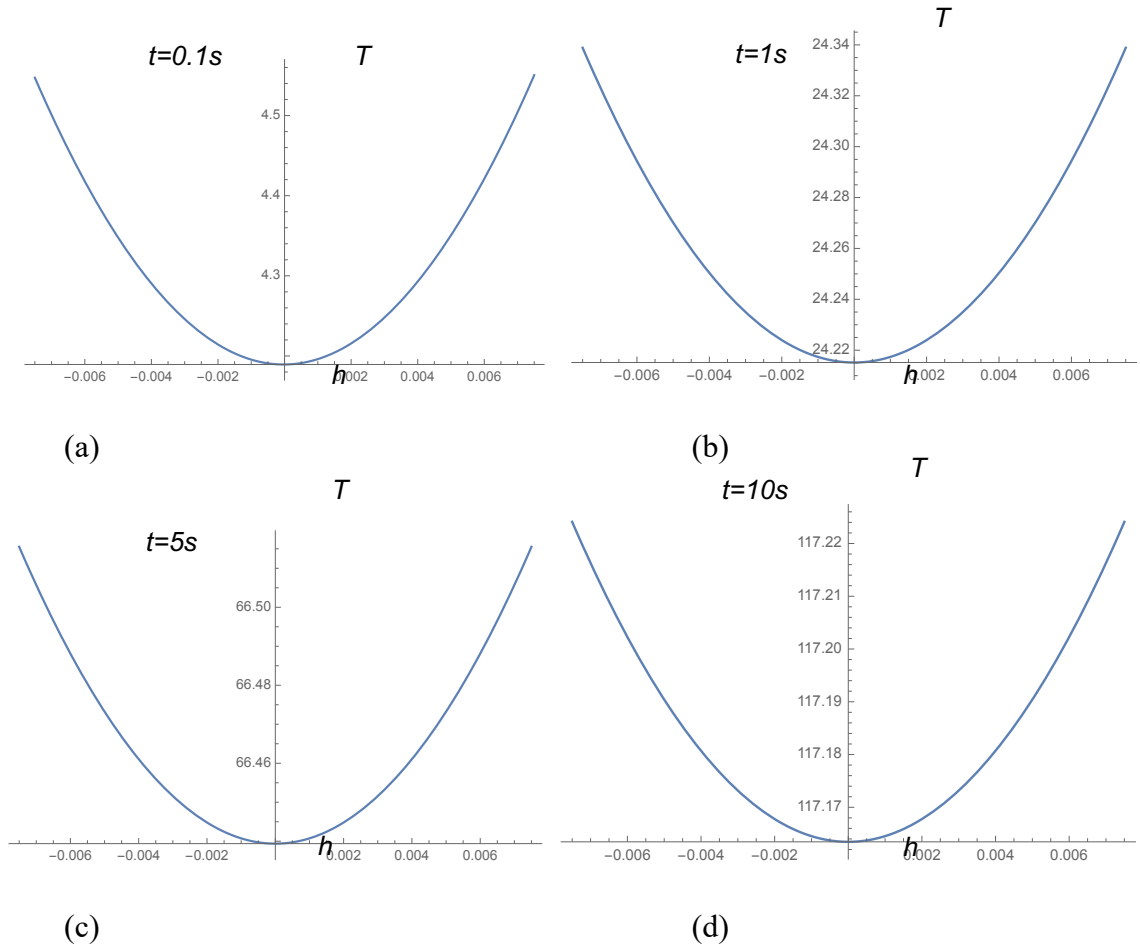


Figure 2.10. Time history of temperature (in °C) distribution along the thickness (in meters) of the panel under a thermal load of $(20 + 10t)$ °C with a core thickness of 0.01424m (for a total plate thickness of 0.015m).

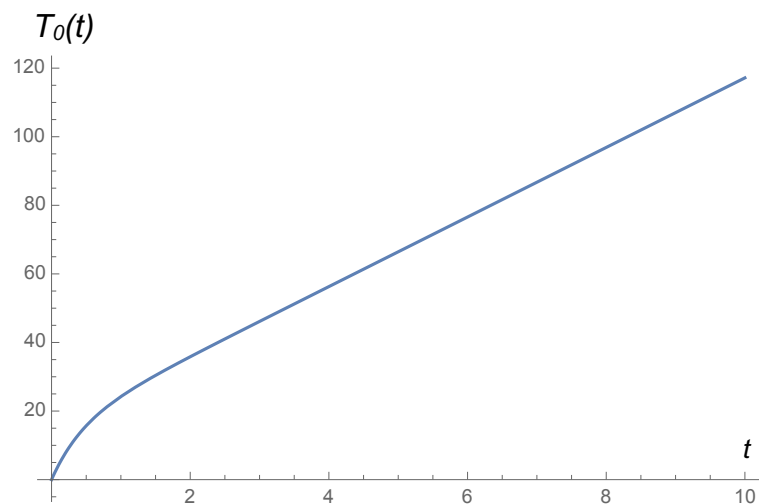


Figure 2.11. Time history of the thermal component $T_0(t)$ for the panel under a thermal load of $(20 + 10t)$ °C with a core thickness of 0.01424m, and for a total plate thickness of 0.015m. Temperature in °C, and time in seconds.

To investigate the effect of the dynamically increasing environmental temperature on panels of different thickness we also consider the case of a very thin and a very thick panel, by decreasing and increasing the thickness of the honeycomb core, and by leaving the skin thicknesses the same.

First we consider a very thin panel of thickness of 0.009m with the core thickness of 0.00824m and the skins' thickness remains the same.

Fig. 2.12 shows that a thinner panel is characterised by shorter period of transient behaviour (under 1s), and being thinner than the panel in Fig. 2.9 it starts buckling under dramatically increasing heat much earlier, reaching a higher level of displacement at 100s (Fig.2.12b).

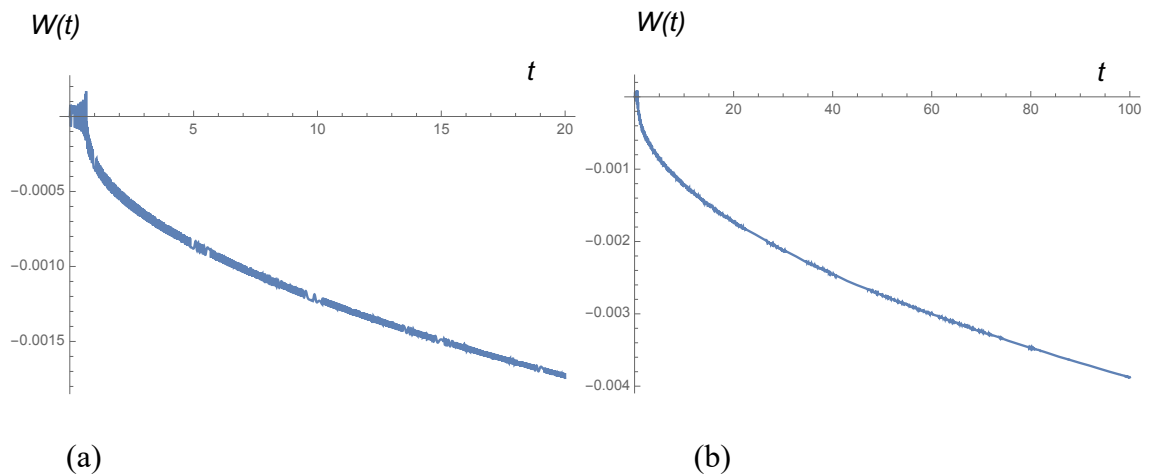


Figure 2.12. Displacement response in the time domain over 20s (a) and 100s (b) when subjected only to a thermal loading of $(20 + 10t)$ °C with core thickness 0.00824m and total plate thickness of 0.009m. Displacement in metres, time in seconds.

The time histories of the temperature distribution along the thickness of the panel for the thinner panel are presented in Fig. 2.13.

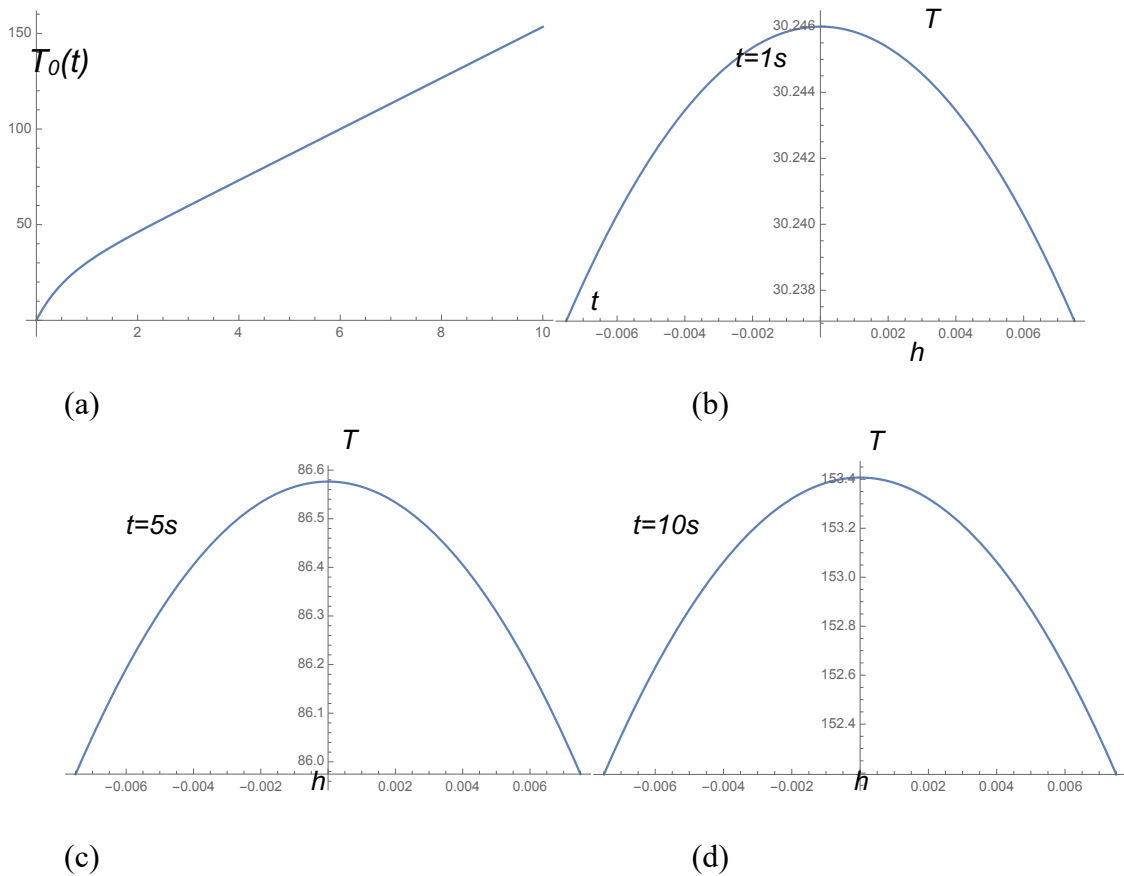


Figure 2.13. (a) Distribution of the thermal component $T_0(t)$ in the time domain, and (b) (c) (d) Time history of the temperature distribution $T(t)$ through the thickness, when $t=1s$, $t=5s$, $t=10s$, for the panel under a thermal load due to the linear environmental temperature $T(t) = 20 + 10t$, with a core thickness of 0.00824m (and for a total plate thickness of 0.009m). Temperature in °C, thickness h in metres.

The discrete time snapshots of Fig. 2.13 confirm that the temperature distribution through the thickness of the panel, just like the displacement, happen more rapidly due to the smaller thickness. It can also be observed that due to the small thickness of the panel the core heats up faster, being around 1°C warmer than the skins after 100s. The dynamically rapid heating up process reflects the linearly increasing thermal loading, as depicted by Fig.2.13a.

When considering a thicker panel we expect a lower displacement response due to the thermal instability created by the dynamic thermal load condition, and this is confirmed in the results of Fig. 2.14.

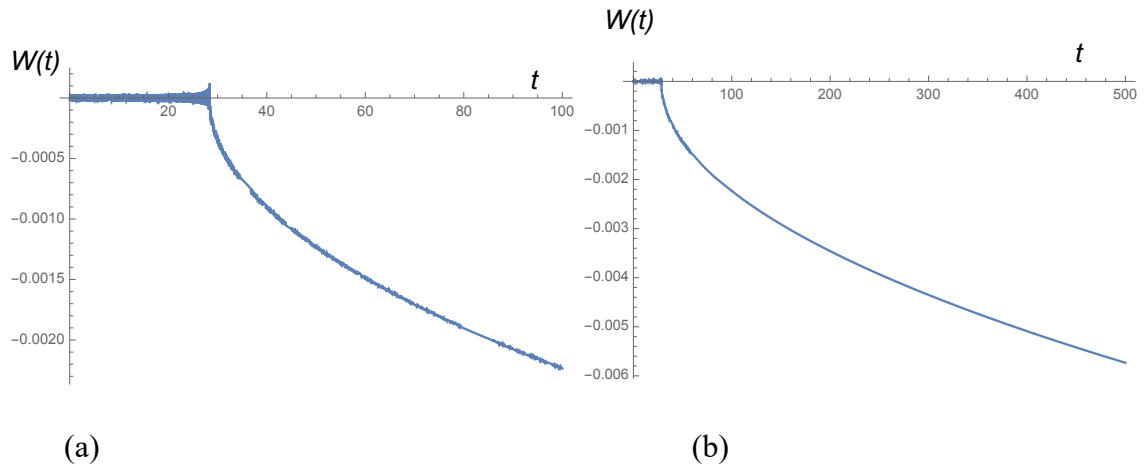
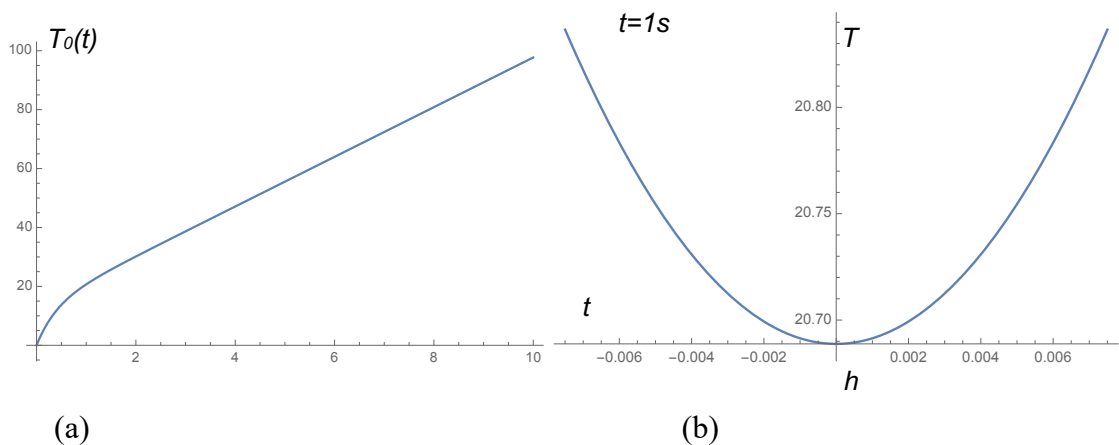


Figure 2.14. Displacement response in the time domain over 100s and 500s when subjected only to the thermal load due to the environmental temperature conditions given by $(20 + 10t)$ °C, and for a core thickness of 0.01924m and total plate thickness of 0.02m. Displacement in metres, time in seconds.

As can be seen in Fig.2.14 the transient behaviour is taking longer, well above 20s in fact, and therefore the buckling of the panel due to the dynamically increasing temperature occurs much later, reaching a lower value at 100s. This confirms that the disturbance caused by the thermal loading is more pronounced for a thinner panel than for thicker ones.

In Fig. 2.15 we are investigating the time history of the temperature distribution along the thickness of the panel as a time snapshot, as well as a general trend of the increasing temperature within the panel in response to the linearly increasing environmental temperature.



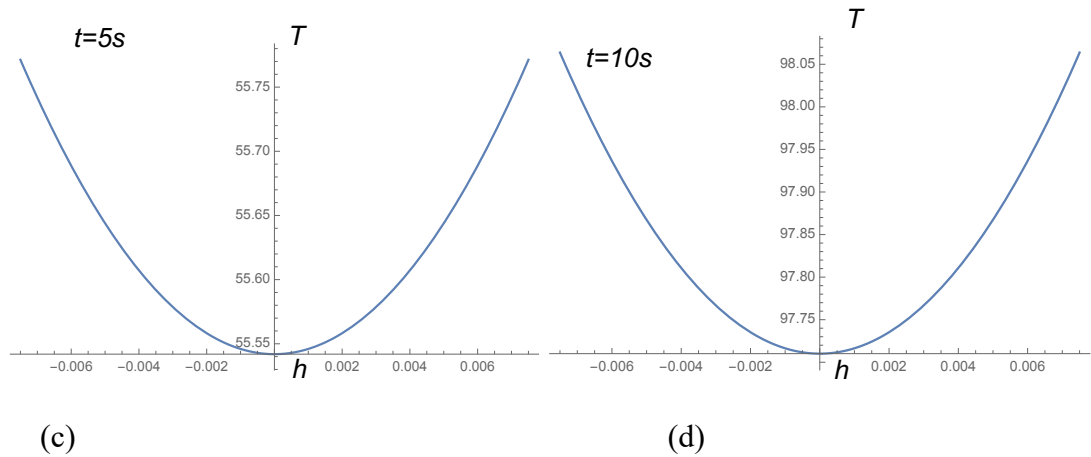


Figure 2.15. (a) Distribution of the thermal component $T_0(t)$ in the time domain, and (b) (c) (d) Time history of the temperature distribution $T(t)$ through the thickness, when $t = 1s$, $t = 5s$, $t = 10s$, for the panel under a thermal load due to the linear environmental temperature $T(t) = 20 + 10t$, with a core thickness of 0.01924m (and for a total plate thickness of 0.02m). Temperature in ° C, thickness h in metres.

The discrete snapshots in time shown in Fig. 2.15 comparing to the ones for the thinner panel (Fig.2.13) confirm that due to the larger thickness of the panel, the panel takes longer to heat up all the way through the core, and therefore the middle plane of the panel remains cooler than the skins, never managing to catch up with the rapidly increasing environmental and skin temperatures. Taking longer to heat up we can also see that the plate reaches a lower temperature along its thickness (Fig. 2.15d) comparing to the thinner panel (Fig.2.13d). The time history in Fig.2.15 (b-d), as well as the trend of the heating up process in time (Fig. 2.15a), reflects the linearly increasing temperature of the environment.

2.3.2 The case of thermo-mechanical loading at constant temperature

To study the case of thermo-mechanical loading of the panel a simple three-point bending test has been simulated to introduce the mechanical loading for the panel. In order to investigate the behaviour of the panel under the mechanical loading we first consider the panel subjected to 10N loading while the panel is being exposed to the thermal environment of 20°C. The analysis was carried out to investigate the displacement

distribution as well as the heating up process in time along the thickness of the panel (Fig. 2.16).

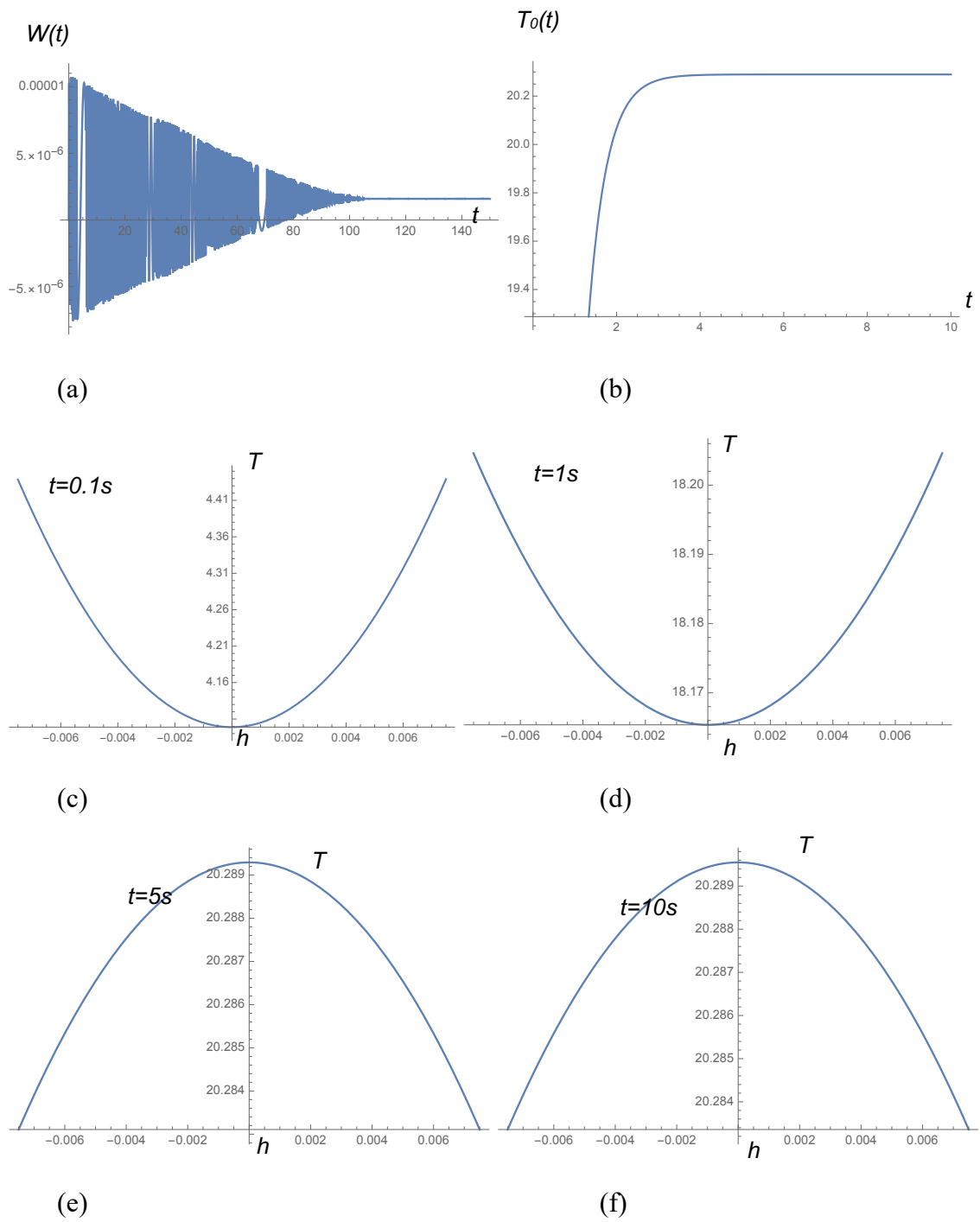
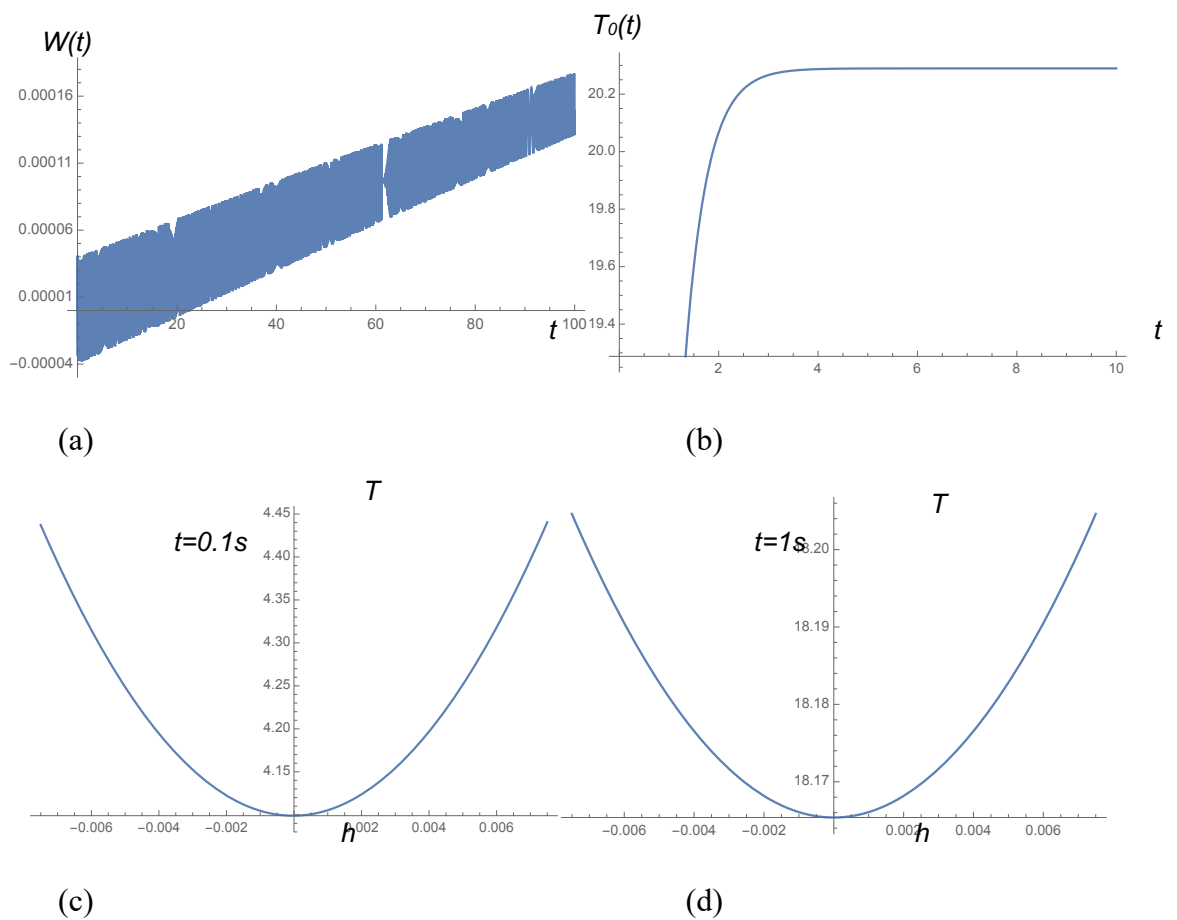


Figure 2.16. Displacement response in the time domain when subjected to the mechanical load of 10 N in 20°C environment, with core thickness of 0.01424m and total plate thickness of 0.015m. Displacement in metres, time in seconds.

As can be seen in Fig.16a the offset characterising the mechanical loading of 10N is clearly present in the displacement distribution. We also can see that the heating-up process through the time snapshots (Fig. 2.16c-f) is leading to stabilisation around 20°C, which is what is expected and reflected in Fig. 2.16b after around 2s.

As the next step of our investigation of the mechanical loading effect we introduce the dynamic mechanical loading of 10t within the same 20°C environment. The displacement response, as well as time history of the panel heating up process, are both presented in Fig.2.17.



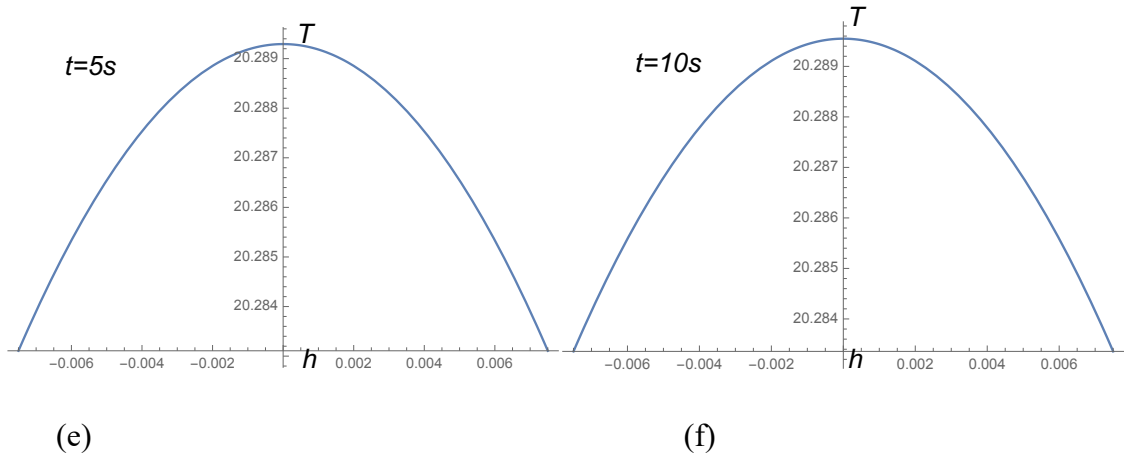
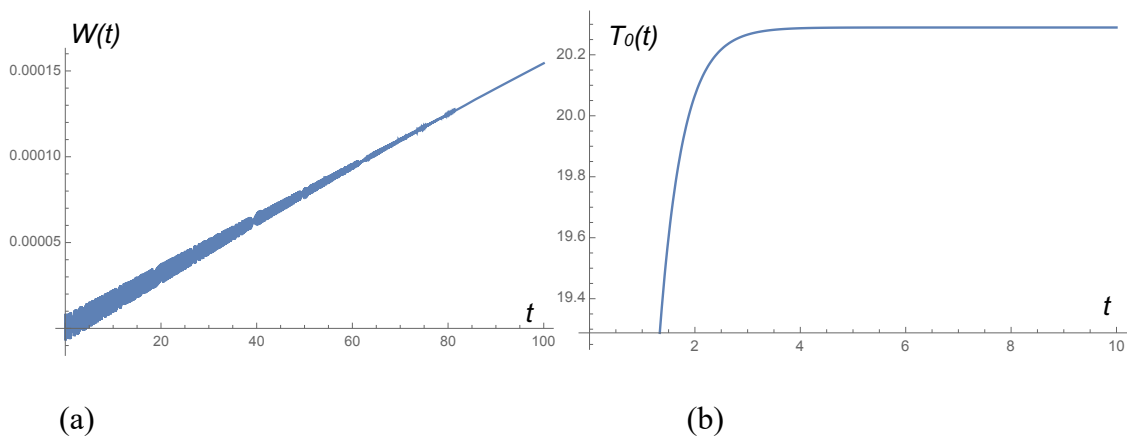


Figure 2.17. Displacement response in the time domain when subjected to the mechanical load of 10t in 20°C environment, with core thickness of 0.01424m and total plate thickness of 0.015m. Displacement in metres, time in seconds.

As can be seen in Fig. 2.17a, and contrary to Fig.2.16a, the displacement response is characterised by the linear increase which reflects the character of the mechanical loading 10t. The transient behaviour reflects the fact that we have two types of loading, thermal and mechanical, introducing a higher frequency disturbance within the panel. The time snapshots for the heating up process within the panel (Fig. 2.17c-f) reflect the increase of temperature within the panel, stabilising at around 20°C after 2s.

In a similar manner to what has gone before in Figs 2.18 and 2.19 we are now investigating the behaviour of the thinner and thicker panels by reducing or increasing the core thickness and analysing the effect of these geometrical changes on the displacement behaviour, as well as the heating-up process along the thickness of the panel. The mechanical loading is still kept at 10t and thermal loading is represented by 20°C.



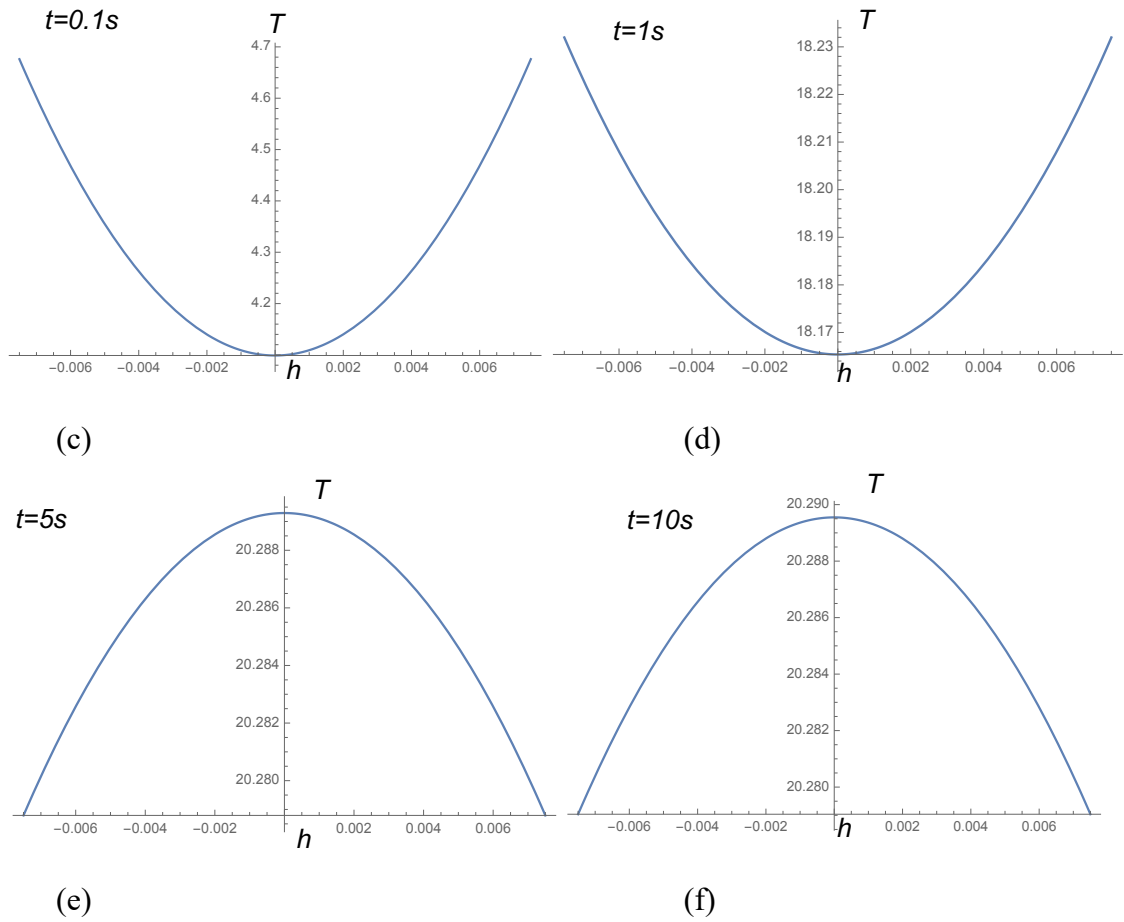
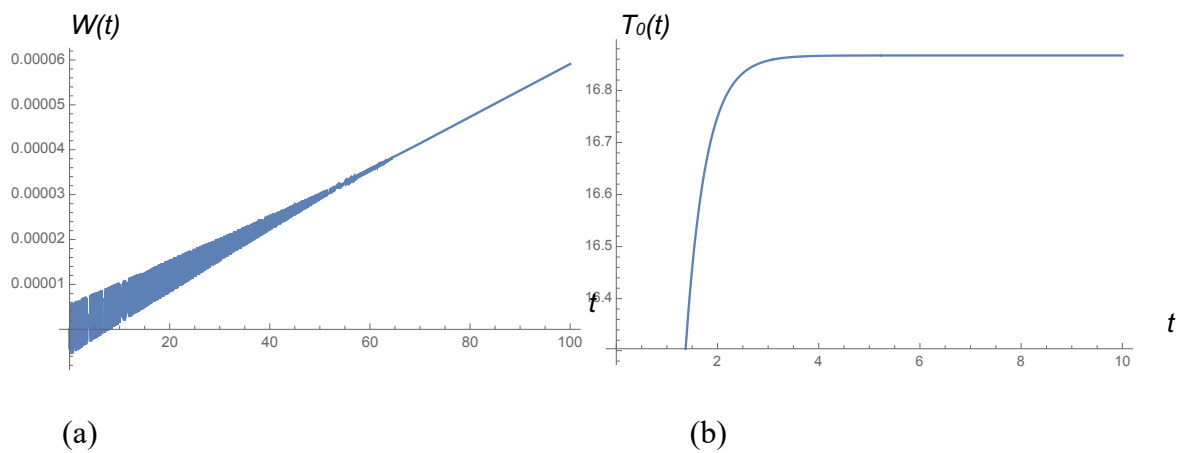


Figure 2.18. Displacement response in the time domain when subjected only to the mechanical load of 10t N at 20°C with core thickness of 0.00824m and total plate thickness of 0.009m – thinner plate. Displacement in metres and time in seconds.



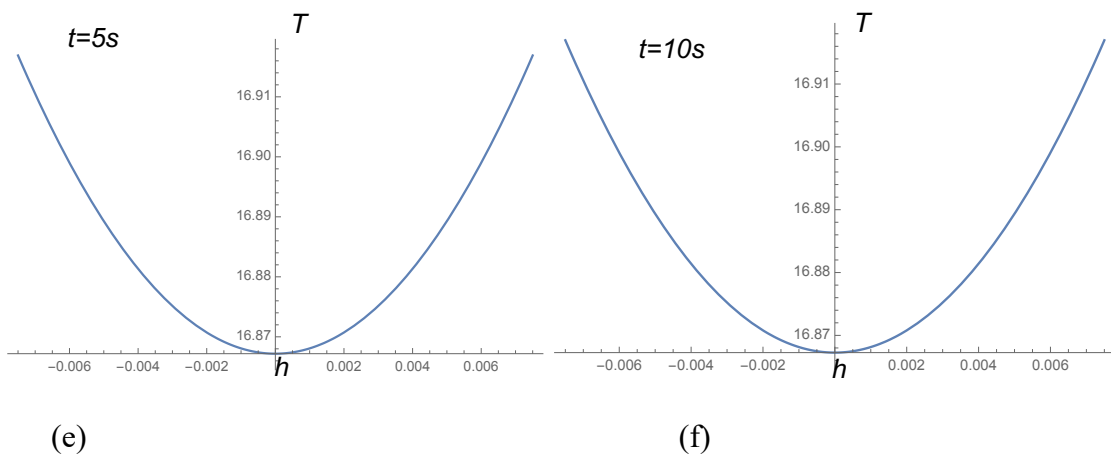
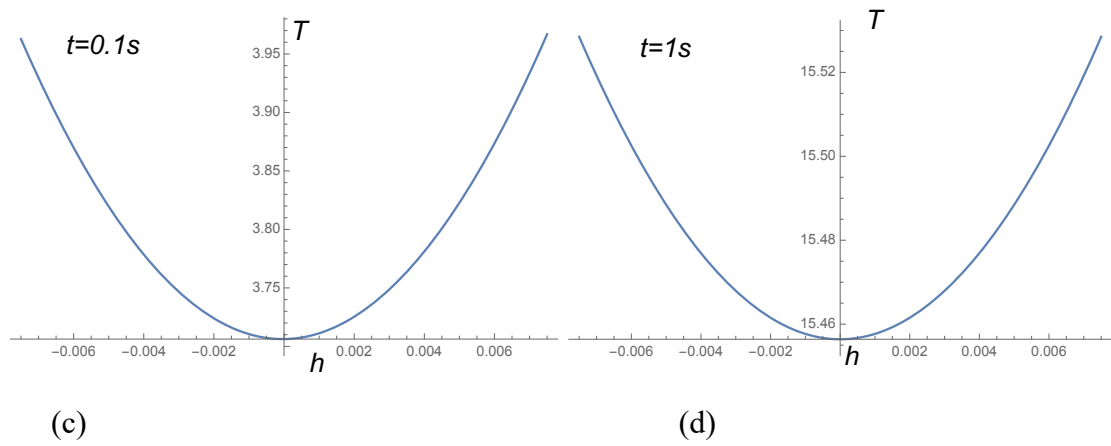


Figure 2.19. Displacement response in the time domain when subjected only to the mechanical load of $10t$ N at 20°C with core thickness 0.01924m and total plate thickness of 0.02m – thicker plate. Displacement in metres, time in seconds.

The results obtained for the thinner and thicker panels are in line with those observed for the panel subjected to thermal loading only in Section 2.3.1. The thinner panel is faster to respond to the dynamically increasing mechanical loading, reaching a higher displacement value at $100s$ than the thicker one (Fig.2.18a and Fig.2.19a). However, the transient behaviour introduced as a high frequency disturbance in the displacement output lasts longer in the thinner plate than the thicker one. Therefore, as in the previous case, the results in Figs. 2.18 and 2.19 confirm the effect of the change in the thickness of the panel on the deformation response, and show that it generally takes longer for a thinner panel to reach the equilibrium state than a thicker component.

Reflecting on the snapshots of the heating-up process, we are observing the same pattern as in Section 2.3.1 and the thicker panel (Fig.2.19c-f) takes longer to heat up than the

thinner (Fig.2.18c-f) one, and after 10s the thicker panel reaches around 17°C (Fig.2.19b,f) when the thinner one is at 20°C (Fig.2.18b,f).

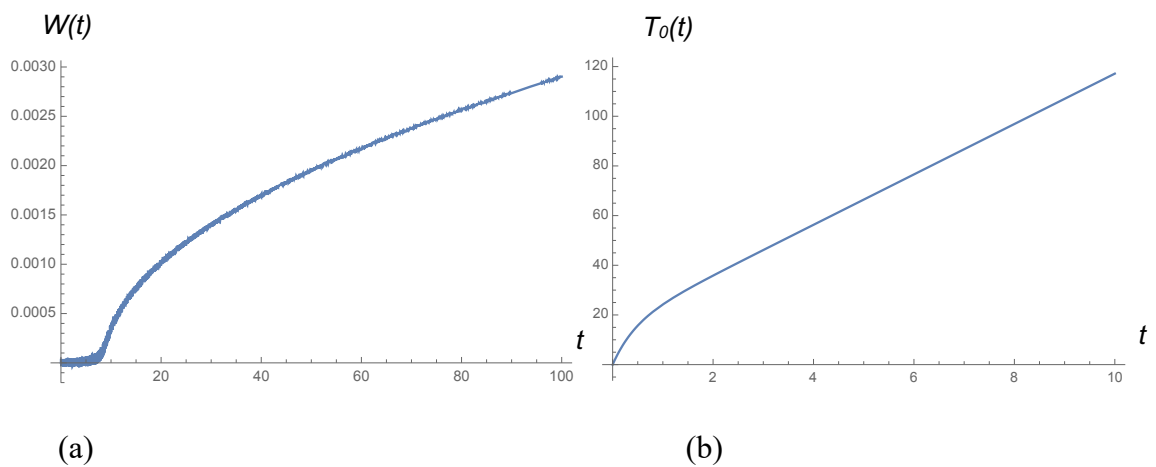
It can be noted that results are obtained for other thermal environment values, including extreme ones, for correlation with experimental results and these are presented in Chapter 4 and Appendix F.

2.3.3 The case of thermo-mechanical loading with time variable thermal loading

Continuing with the case of thermo-mechanical loading the physics of the separate dynamically-variable thermal and mechanical loading scenarios are combined into one, using the model discussed previously.

For consistency with the study performed earlier in Sections 2.3.1 and 2.3.1, the combined effect of a time-variant mechanical and thermal loading will be represented by $10t$ N, and a dynamic thermal load initiated by the environmental temperature which obeys the linear law given by $(20 + 10t)$ °C.

Following the line of investigation adopted in the previous sections we are looking into displacement distribution in Fig. 2.20a, the general trend of the heating-up process of the panel (Fig.2.20b) and the time history of the temperature distribution along the thickness of the panel (Fig.2.20c-f).



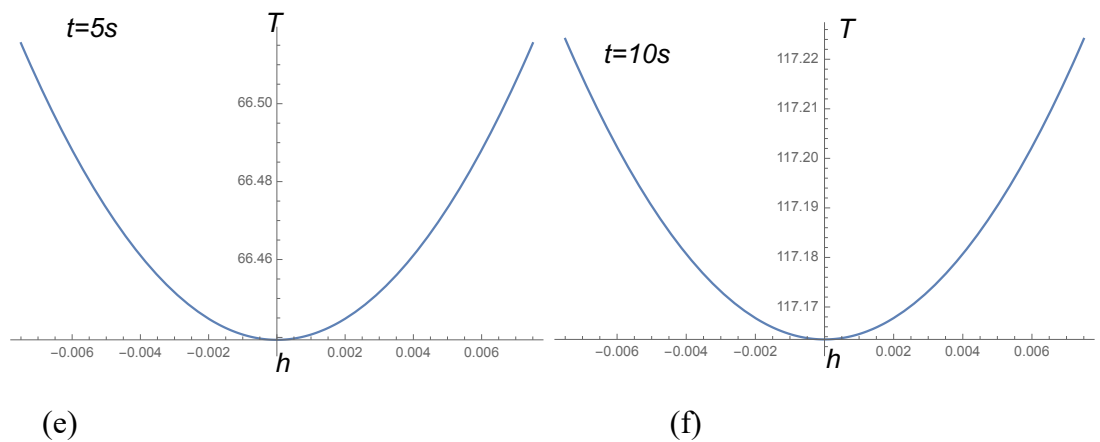
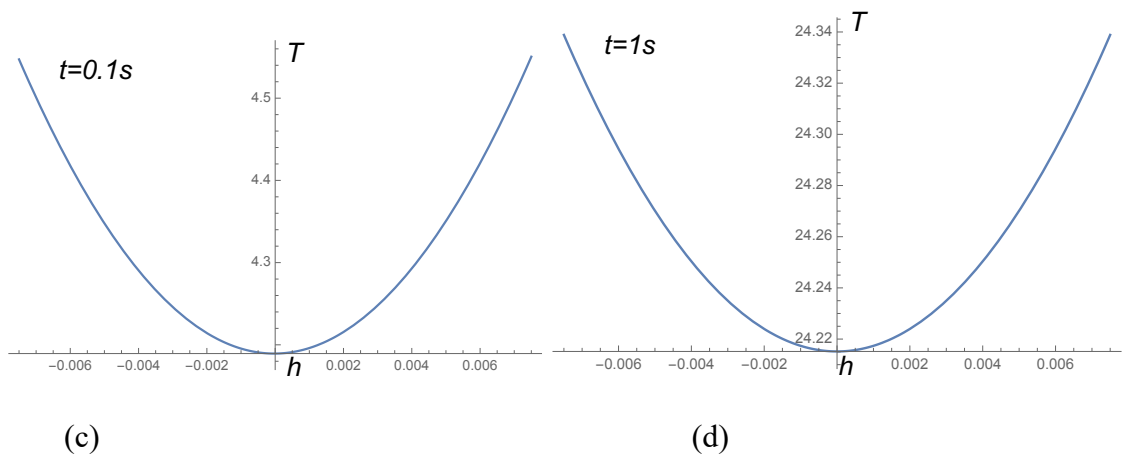


Figure 2.20. Displacement response in the time domain when subjected to the thermal load due to the environmental linear temperature law of $(20 + 10t)$ °C and a mechanical loading of $10t$ N with core thickness of 0.01424m and total plate thickness of 0.015m. Displacement in metres, time in seconds.

It can be noticed from Fig.2.20a that the main distinction in the displacement behaviour is the transient response within the first 5s. Since the rapid increase of the environmental temperature introduces the buckling effect, as evidenced in Section 2.3.1 (Fig. 2.9), and a linearly increased mechanical loading introduced the displacement (Fig.2.17a) there is a compensated response for around 5s until the mechanical loading dominates the response of the panel and introduces a clearer dynamically increasing displacement. The value of the displacement is thus increased due to the combined effects of the time-increasing mechanical and thermal loading.

The heating-up process within the panel corresponds to the previously observed response for a panel under the $(20 + 10t)$ °C thermal loading. Mechanical loading did not seem to have a significant impact on the heat distribution within the panel.

2.4. Application of the derived model for a panel subjected to the heat flux

In Section 2.3 a model was derived for the free heat exchange condition and in Sections 2.3.1-2.3.3 a variety of cases were considered for the panel being subjected to the environment of different temperatures, and thus exhibiting an appropriate response for both displacement and temperature distribution along the thickness. The study is also a crucial part of the correlation of the analytical model results with the experimental results presented later in chapter 4 for the panel tested in a climatic chamber in the free heat exchange setting.

However, coming back to the initial purpose of this work, simulation of the thermo-mechanical behaviour of a satellite and spacecraft panel while being exposed to the extreme environment, the free heat exchange condition is not the most accurate approximation of the undergoing scenario. Therefore, although the core model developed in Section 2.3 has been verified through experimental work presented in chapter 3, we are also producing a result for a more realistic scenario in a space application, when the panel is subjected to heat flux.

When introducing heat flux instead of free heat exchange conditions the model has to be adjusted through the change of thermal coefficients r_i in Eqs (2.10) which would affect Eq. (2.9) and thus all the equations representing the thermal part of the model discussed in Section 2.2.

The panel under consideration remains simply supported and was subjected to a combination of mechanical and thermal loading represented by the time-variant heat flux to represent a thermal cycle in LEO.

According to [174] the heat flow is typically represented as a dome-shaped distribution. Therefore the form of Eq. (2.8) defined for the heat flow prescribed will be defined as,

$$q_3^*(x, y, t) = q(t) \sin \frac{\pi x}{a} \sin \frac{\pi y}{b}$$

Dimensions and properties of the panel remain the same as discussed in Section 2.3.

The results of the simulation for the panel exposed to the heat flux are discussed in comparison to the free heat exchange conditions discussed earlier to be able to analyse and reflect on the critical difference of the simulation and confirm the validity of the results obtained.

In the first instance the panel is subjected to the heat flux represented by the law defined by $q_3^*(x, y, t) = 40t \sin \frac{\pi x}{a} \sin \frac{\pi y}{b}$ and the dynamically increasing mechanical loading $10t$ in a middle, environmental temperature of 40°C (Fig. 2.21a,b). For comparison the displacements for an environment at 40°C without heat flux but free heat exchange, and under a dynamic mechanical loading of $10t$, are also presented in Fig. 2.21c,d.

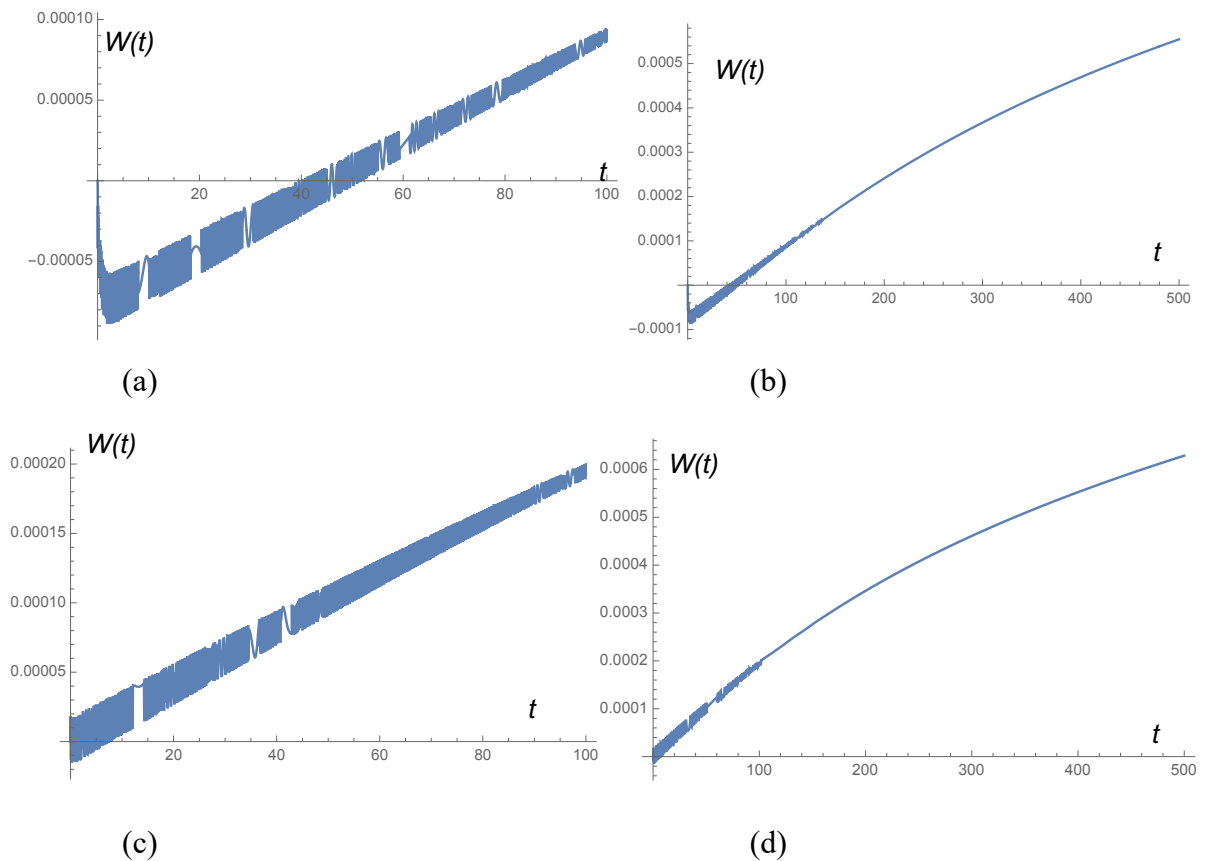


Figure 2.21. Displacement in time domain over 100s and 500s when subjected to heat flux $q_3^*(x, y, t) = 40t \sin \frac{\pi x}{a} \sin \frac{\pi y}{b}$ (a,b) and in the free heat exchange at 40°C (c,d) and a dynamically increasing mechanical loading $10t$. Displacement is in metres and time is in seconds.

As can be observed a stiffer response, characterised by a lower displacement value at 100s, was obtained for the panel subjected to the heat flux. This occurs due to the fact that the heat flux introduced a significant temperature increase on one side of the panel and hence a buckling effect which subsequently results in the snap-through after around 40s (Fig.2.21a) after the increasing mechanical loading is high enough to dominate the bending behaviour. It should be also pointed out that even in free heat exchange the disturbance introduced by the thermal loading encourages a trace of buckling behaviour (Fig.2.21c). Nevertheless, from Fig.2.21b,d, it can be seen that the deflection under heat flux still manages to ‘catch-up’ and has almost the same value at 500s, and is quite likely to stabilise to the same level as in the free heat exchange case.

The main distinction of the heat flux loading from the free heat exchange is that for heat flux loading one side of the panel is the exposed to intensive heat, and when in free heat exchange both sides of the panel are subjected to the environmental temperature.

Therefore, results were produced for the heat distribution through the thickness of the panel to confirm that this effect has taken place, and shown in Fig. 2.22.

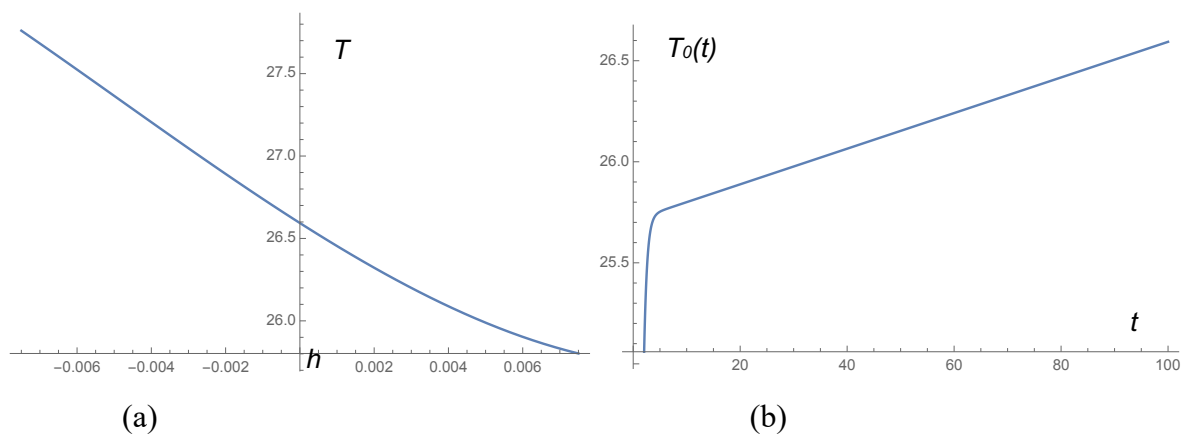


Figure 2.22. Temperature distribution along the thickness of the panel after 100s (a) and general trend of the temperature distribution representing the $T_0(t)$ (b) when subjected to heat flux $q_3^*(x, y, t) = 40t \sin \frac{\pi x}{a} \sin \frac{\pi y}{b}$. Thickness h is in metres, t is in seconds, and T is in °C.

As can be seen in Fig. 2.22 the trend of the heat distribution is not parabolic as was typical for free heat exchange in Section 2.3, where both skins were exposed to the same level of heat and thus had the same temperature readings. Under heat flux conditions we have one

skin exhibiting a higher temperature than the other one, and this is confirmed by the model in (Fig. 2.22a). We can clearly see how the heat distributes at the highest level on one side of the panel, then it is slightly lower in the middle plane and the lowest in the bottom skin (h). For easier visualisation refer to Figure 2.3 which demonstrates the thickness distribution along the x coordinate and the temperature level along the y coordinate. Since the heat flux $q_3^*(x, y, t) = 40t \sin \frac{\pi x}{a} \sin \frac{\pi y}{b}$ was chosen as a dynamically increasing function, the general trend of the temperature distribution representing the $T_o(t)$ demonstrates the linear increase of the heat after around 5s.

Since the free heat exchange analysis was performed in chapters 3 and 4 (dealing with the experiment and correlation, respectively) for a range of thermal environments including extreme cases, it was decided to consider results for 150°C (Fig. 2.23, 2.24) and -20°C (Fig.2.25, 2.26).

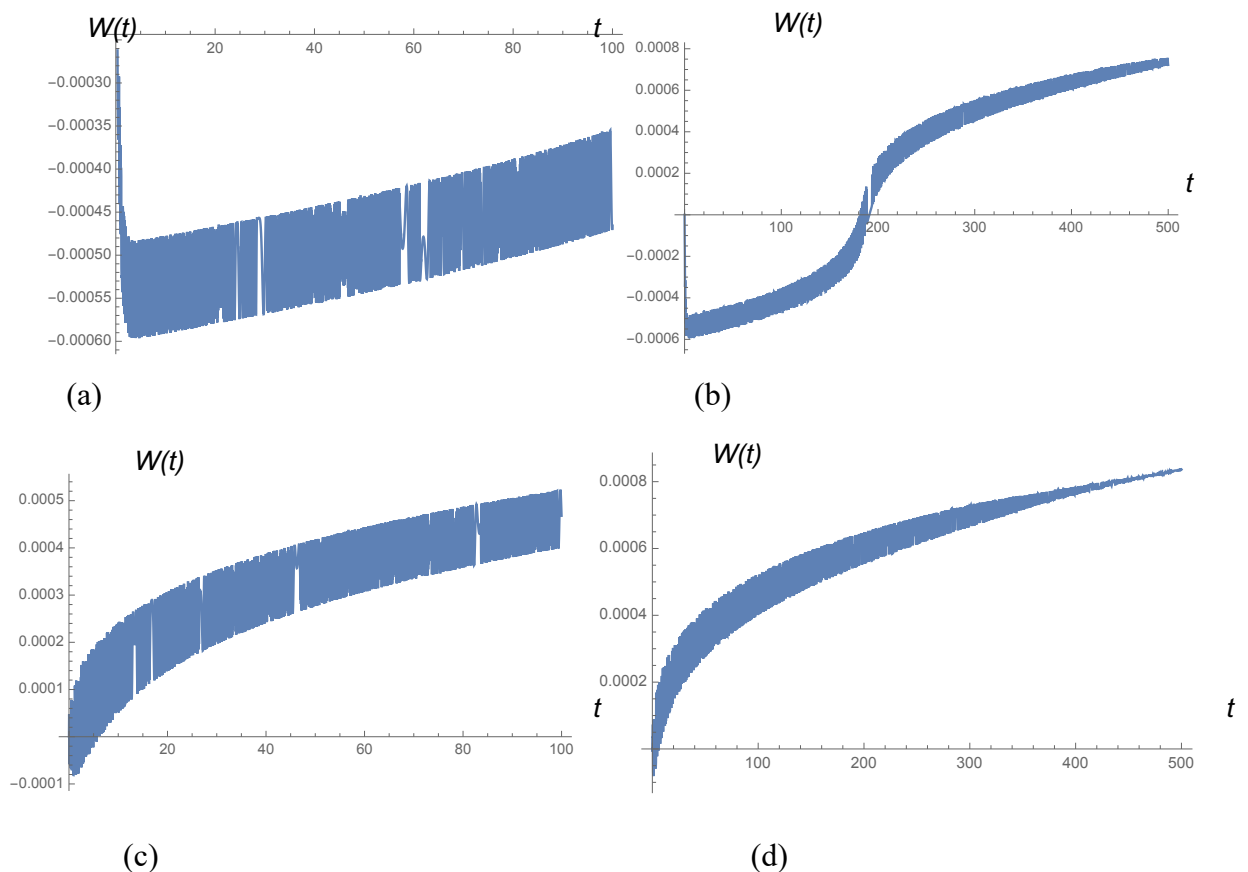


Figure 2.23. Displacement distribution in the time domain over 100s and 500s when subjected to heat flux $q_3^*(x, y, t) = 150t \sin \frac{\pi x}{a} \sin \frac{\pi y}{b}$ (a,b) and in the free heat exchange environment at 150°C (c,d), under dynamic mechanical loading of 10t.

Displacement $W(t)$ is in metres and t is in seconds.

It is shown in Fig. 2.23a that an extreme heat flux temperature has caused a more significant and long-lasting buckling effect, before the panel recovers the stiffness to respond to the time-dependent loading, than in Fig.2.21a and the snap-through effect has occurred at a later stage (Fig. 2.23b) than for 40°C (Fig. 2.21b). In terms of the level of deflection, we can see again a stiffer response at 100s in the heat flux case than in free heat exchange (Fig. 2.23 a,c) but the deflection in the heat flux case manages to ‘catch-up’ with the level in free heat exchange, and has the same value at 500s.

Considering the results for the heat distribution along the thickness of the panel for the case of heat flux $q_3^*(x, y, t) = 150t \sin \frac{\pi x}{a} \sin \frac{\pi y}{b}$ a similar trend to that of Fig. 2.22 has taken place, as shown in Fig. 2.24.

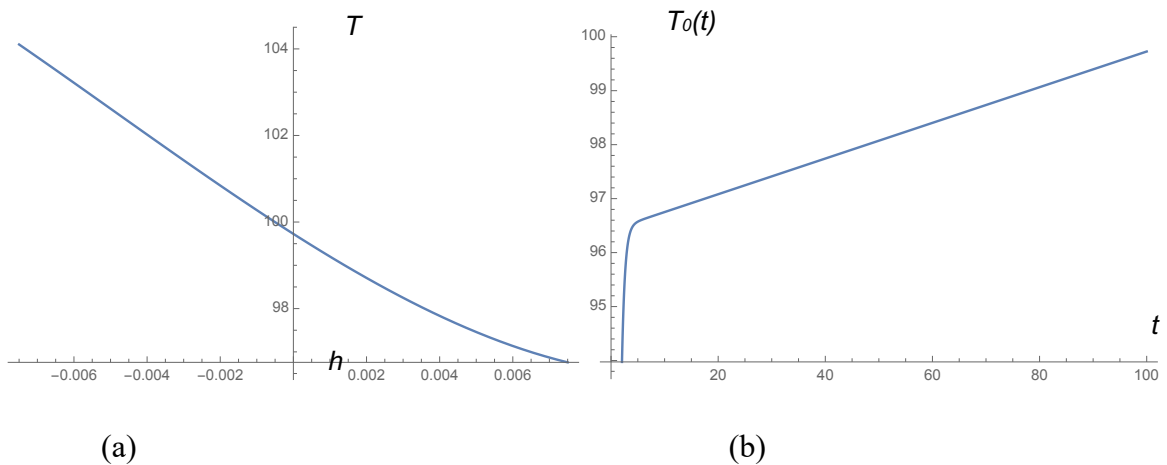


Figure 2.24. Temperature distribution along the thickness of the panel after 100s (a) and general trend of the temperature distribution representing the $T_0(t)$ (b) when subjected to dynamically increasing heat flux $q_3^*(x, y, t) = 150t \sin \frac{\pi x}{a} \sin \frac{\pi y}{b}$.

Thickness h is in metres, t is in seconds, and T is in °C

It can be seen in Fig. 2.24, that under heat flux conditions the top surface of the panel is demonstrating a higher temperature than the other one (Fig. 2.24a) and the general heat distribution within the panel corresponds to the dynamic increase of the temperature due to the time variant heat flux (Fig. 2.24b).

The last case to consider in line with the experimental study in chapter 3 is characterised by a negative temperature of -20°C (Fig. 2.25).

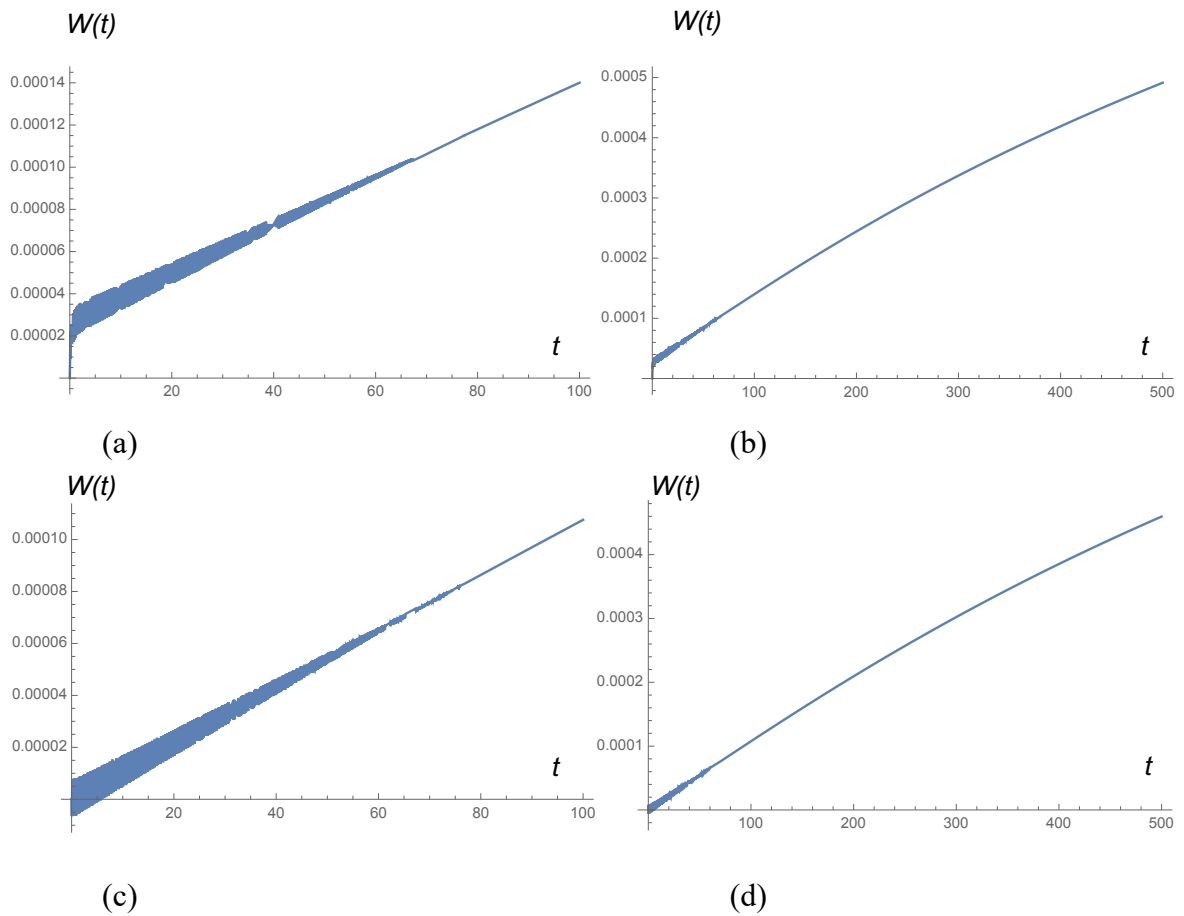


Figure 2.25. Displacement distribution in the time domain over 100s and 500s when subjected to heat flux $q_3^*(x, y, t) = -20t \sin \frac{\pi x}{a} \sin \frac{\pi y}{b}$ (a,b) and in the free heat exchange environment at -20°C (c,d), under a dynamic mechanical loading of $10t$. Displacement $W(t)$ is in metres and t is in seconds.

As noted in Fig. 2.25 a,c, in the case of negative heat flux a larger value of the displacement is obtained for the heat flux case (Fig. 2.25a), comparing to the free heat exchange case (Fig. 2.25c), as the cooling effect contributes to the deflection introduced by the mechanical loading. This effect becomes even more pronounced with time (Fig. 2.25b,d).

The temperature distribution pattern along the thickness of the panel due to the negative heat flux $q_3^*(x, y, t) = -20t \sin \frac{\pi x}{a} \sin \frac{\pi y}{b}$ and mechanical loading $10t$ is presented in Fig. 2.26a, and the general trend of the panel cooling down is described in Fig. 2.26b.

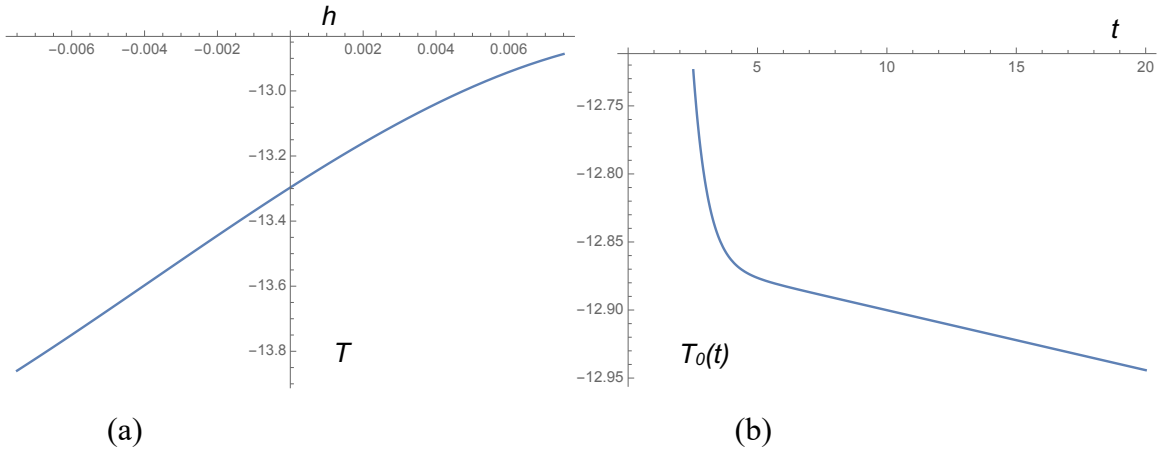


Figure 2.26. Temperature distribution along the thickness of the panel after 100s (a) and general trend of the temperature distribution representing the $T_0(t)$ (b) when subjected to dynamically increasing heat flux $q_3^*(x, y, t) = -20t \sin \frac{\pi x}{a} \sin \frac{\pi y}{b}$.

Thickness h is in metres, t is in seconds, and T is in °C

It is clarified in Fig. 2.26a that for the negative heat flux the same trend takes place with one side of the panel being cooler, and cooling distributes along the thickness. In the general trend of the temperature distribution we can see the temperature going down in response to the negative heat flux $q_3^*(x, y, t) = -20t \sin \frac{\pi x}{a} \sin \frac{\pi y}{b}$ (Fig.2.26b) but at a slower rate than in Fig. 2.24 due to the coefficient being ‘-20t’.

It can be noted that in chapter 5 a reflection on the FEM analysis of the honeycomb panels subjected to free heat exchange and heat flux is presented. The FEM work was performed under the supervision of the author of this thesis. This work confirms the outcomes found through using the analytical model. For the case of heat flux for a FEM model it was found that a positive heat flux resulted in a stiffer panel response. So, due to the thermally induced residual stress the bending opposed the direction of deformation, which was due to the preloading of the panel due to thermal strain opposing the point load. The nonlinearity due to possible snap-through behaviour was also detected (Fig. 2.27).

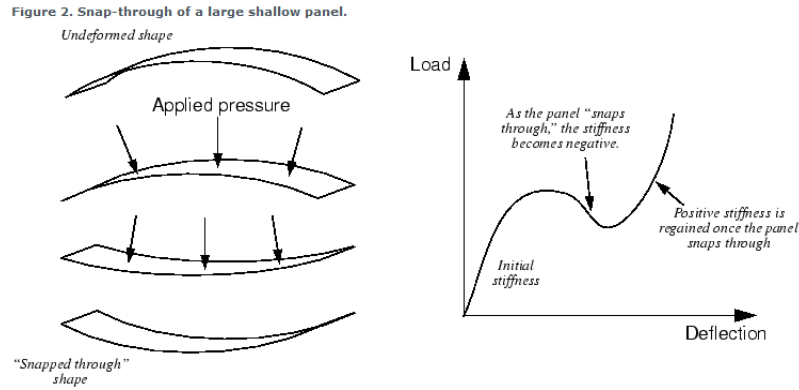


Figure 2.27. Snap-through effect [206]

The extent of the snap-through using FEM was small as the panel was not fixed at both ends, and it was likely to be due to the combined resistance of the two frictionless supports and equally opposing thermal strain effects. This behaviour was found for two different FEM models: the 3D continuum model and the Geometrically Accurate (GA) thermo-mechanical model with heat flux.

The outcomes for the case of free heat exchange are verified by the experimental work presented in chapter 3 for the panel tested in a climatic chamber under a variety of environmental temperatures.

2.5. Conclusions

1. A new modelling strategy for aluminium honeycomb composite panels has been suggested in this chapter, in which the physics of dynamic thermal and mechanical loadings are integrated into a conceptually straightforward partially-coupled modelling procedure coded in the *Mathematica*TM language, and which, in principle, can easily accommodate different boundary conditions and dynamically varying thermal properties.

2. The full nonlinear dynamic thermomechanical model comprises three coupled nonlinear ordinary differential equations has been derived. Previous work has shown that an analytical closed-form solution could only be obtained for the linearised equations and for static thermal and mechanical loads, and so a comparison has been undertaken here between this solution and a corresponding numerical solution for the full nonlinear model described here. The simplified analytical solution obtained in [174] has been found to be

useful for predicting the temperature profile through the thickness of panels with no appreciable loss of accuracy. However, for simulation of the displacement the system of coupled equations can be solved numerically quite quickly, and results are discussed. It is also suggested that an approximate closed-form analytical solution for this equation could be sought using a suitable asymptotic method, such as the perturbation method of multiple scales which is discussed in detail in chapter 6.

3. A full set of numerical results has been obtained for a simply supported aluminium honeycomb composite panel as commonly used within industry, undergoing thermal, mechanical, and thermo-mechanical loading conditions. The thermal load mechanism is underpinned by free heat exchange and the mechanical loading in all cases comprises a normal constant force exerted centrally on the top surface of the panel. The configuration can be readily altered in terms of panel aspect ratio, boundary conditions, and load location. When the panel is subjected solely to a thermal load, applied by means of a fixed environmental temperature, then the nonlinear numerical solution for the displacement of the panel shows a transient oscillation over time at a commensurately small amplitude. The temperature distribution along the thickness of the panel is also calculated based on the coupled system Eq.(2.21) using the numerical solution detailed from calculations carried out in bespoke code written in *Mathematica*, and thermal stabilisation emerges over time, as one would expect. For a linearly increasing thermal load temperature, due to a significant increase of the environmental temperature and its transfer to the panel, it was found that the panel showed signs of accumulating thermal stresses characterised by the transient response and subsequent buckling displacement. The temperature distribution along the thickness of the panel reflected the trend of the rising environmental temperature. Core thickness is seen to affect the results with the thinner panels displaying a more pronounced thermo-mechanical response than thicker components, through a higher level of displacement and faster heating up process along the thickness of the panel. It was also found that for a dynamically increasing thermal loading the core temperature in a thicker panel was always ‘catching-up’ with the surface temperature and never reached the level of being warmer than the panel surface. In the case of constant mechanical loading, at constant environmental temperature, a noticeable dc offset in the displacement was observed, as would be expected. The temperature profile in this case shows a thermal stabilisation around the environmental temperature. The effect of the core thickness was also investigated for the case of dynamic mechanical loading at the constant environmental temperature, confirming the conclusions drawn before for the

purely thermal loading. In the case of both dynamically increasing mechanical and thermal loading a transient response was observed for around 5s until the mechanical loading dominated the response of the panel and introduced a clearer dynamically-increasing displacement. In this case there was clear evidence of increased displacement due to the combined effects of the time-variant mechanical and thermal loading.

4. A more realistic case of heat flow for a space application was also considered. In this case the model had to be adjusted to introduce appropriate thermal coefficients, prescribed heat flow and thermal boundary conditions. Results were obtained for simulations of a number of dynamically increasing heat flows. The results of the simulations for the panel exposed to the heat flux were discussed, in comparison with the free heat exchange conditions, and the main differences in displacement outputs as well as heat distribution through the thickness of the panel were discussed. It was evident that the high level of heat introduced by the heat flux on one of the surfaces of the panel was initiating thermal stresses in the panel resulting in the buckling effect. This behaviour resulted in a stiffer deflection response for positive values of heat flux. Negative values of heat flux resulted in increased deflection of the panel. The profile of the temperature distribution along the thickness of the panel for the case of heat flux, confirmed the increased temperature on the top surface of the panel with reducing temperature values towards the bottom surface of the panel.

5. In this chapter the procedure for the composition of the principal Eqs.(2.1) and (2.12), and all the parameters, is defined with respect to the boundary and initial conditions, as well as the procedure for obtaining the solution coded in *Mathematica*. The process of composition of the mechanical equations of motion Eqs.(2.1)-(2.10) and equations describing thermal effects Eqs.(2.12)-(2.19) is fully automated in *Mathematica* code for an orthotropic type of material (Appendix A). The code is fully annotated to allow open access for any modifications, including when it is passed on to an industrial analyst. The code is generalised and not restricted to the values supplied, which means that the parameters described in the input section can be easily varied, and simulation can be performed for different type of materials. The code presented in Appendix B is the solution procedure for the equations derived in Appendix A as a coupled system of displacements in the x , y , z directions and temperature values T_0 and T_1 , allowing identification of the temperature distribution $T(x,y,z,t)$ along the thickness of the panel according to Eq (2.9).

3. Experimental study of the thermo-elastic behaviour of the honeycomb panel

The materials used on the exterior of spacecraft are subjected to many environmental threats that can degrade them quite quickly, including the vacuum of space itself, solar ultraviolet (UV) radiation, ionising charged particle radiation, plasma, surface charging and arcing, temperature extremes, thermal cycling, impacts from micrometeoroids and orbital debris (MMOD), and environment-induced contamination. In terms of material degradation in space, low-Earth orbit (LEO), defined as the region from 200 to 1000 km above the Earth's surface, is a particularly harsh environment because of the presence of atomic oxygen (AO) along with the other detrimental environmental components and effects [182]. The environmental threats of space to spacecraft components vary in their influence mainly due to the specific material properties of the component and its structural interconnections, its geometry, and the stresses that it undergoes during normal duty. All orbiting spacecraft move in and out of sunlight during their progress around Earth and the degree to which a material experiences thermal cycling temperature extremes depends on its thermo-optical properties (specifically solar absorptance and thermal emittance), its exposure to the sun, its view of Earth and other surfaces of the spacecraft, the duration of time in direct sunlight and shadow, its thermal mass, and the influence of equipment or components that produce heat [182]. As a rule, the cyclic temperature variation is from $-120\text{ }^{\circ}\text{C}$ to $+120\text{ }^{\circ}\text{C}$, but high solar absorptance with low infrared emittance can contribute to even greater temperature swings [182]. The ISS orbits Earth approximately once every 92 minutes and therefore experiences sixteen thermal cycles a day, and this can lead directly to cracking, peeling, spalling or the formation of pinholes in the coating, which then allows AO to attack the underlying material [182].

The main forms of environmental heating on orbit are sunlight, sunlight reflected from Earth, a planet, or the Moon, and infrared energy emitted directly from Earth. During launch or in exceptionally low orbits, there is also a free molecular heating effect caused by friction in the rarified upper atmosphere [180]. Therefore, the main conditions of LEO that may be highlighted are the severe temperature extremes and the thermal cycling experienced throughout the orbit, with an orbiting spacecraft typically completing from eleven to sixteen thermal cycles daily, all within a temperature range of approximately $-120\text{ }^{\circ}\text{C}$ to $+120\text{ }^{\circ}\text{C}$. The thermo-optical properties of the spacecraft itself can also play a

part in the temperature that it reaches. For instance, a material with high solar absorptance and low thermal emittance will experience greater temperature swings.

In [181] an experiment was performed to investigate the thermal behaviour of a sandwich panel which was to be deployed as an integral part of a satellite in the space environment, by means of a ground thermal-vacuum test. It was highlighted that the heat sink, solar radiation, infrared radiation of the Earth, heat conduction, surface radiation and cavity radiation would all influence the temperature field, and the conclusion was that these combined effects would present a serious challenge for realistic thermal testing in the laboratory of the simulated space environment. The experiment was relatively sophisticated and satisfied the general requirements for the inclusion of three key conditions: ultra-high level of vacuum (lower than 10^{-5} Pa), a heat sink (down to -180 °C) achieved in this case by using black panels with a liquid-nitrogen cooling system, and thermal loading achieved through infrared lamps. An interesting study carried out by [185] focused on the effect of thermal cycling in a simulated LEO environment on the microhardness of aluminium alloys, and subjected these alloys to cycles ranging from -140 °C to $+110$ °C. This was in order to induce thermal fatigue and to study the resulting stress state and mechanical properties of the material. The testing resulted in cyclic plastic deformation which was found to lead to crack initiation, identified using a transmission electron microscope (TEM). A test totalling 400 thermal cycles was carried out on the samples and these showed an eventual decrease in hardness, and then from 300-400 cycles the hardness started to increase with every cycle. Although rapid temperature changes were implied, the exact value of the rate of change of temperature was never stated in the study. The mechanical load was applied at intervals to test the microhardness of the material and was not applied simultaneously with the change in temperature. The study concluded that the bulk of aerospace materials that undergo periodic heating and cooling are damaged to varying degrees, with thermal fatigue having a significant impact on the mechanical properties of the materials used. Although it is difficult to recreate truly the conditions of LEO on Earth, such work has been attempted in the past by [186]. The study focused on subjecting graphite-epoxy composites to the conditions of LEO. Not only did the materials undergo thermal cycling similar to that experienced in LEO, but the environment was also in a high vacuum state while the effect of ultraviolet radiation was applied during heating but not during cooling. A single thermal cycle was judged to be from -70 °C to $+100$ °C and back to -70 °C again. This was with a rate of change of temperature of $3-5$ °C per minute and a dwell-time at the temperature extremes of 15

minutes, giving an average cycle time of 100 minutes, typical of a low Earth orbital period. The results examined were for composites subjected to this environment for 8, 16, 40 and 80 thermal cycles, in which the transverse flexural strength and transverse tensile strength showed the most severe reduction with thermal cycling, after 80 thermal cycles, with losses of 34 % and 21 % in each property respectively. It was considered that the matrix-dominated mechanical properties suffered the greatest loss, due to high vacuum and thermal cycling. Overall, the strength and stiffness of graphite epoxy composites was shown to decrease exponentially with increasing thermal cycles. Further work into the synergistic effects of high vacuum and thermal cycling was implemented by [187], this time on carbon fibre epoxy composites. The experiment took place in a high vacuum state of $133 \cdot 10^{-5}$ Pa, and a single thermal cycle was judged to be from +120 °C to -175 °C and back to +120 °C, with a duration of approximately 43 minutes. The experiment was run for 500, 1000, 1500 and 2000 cycles. Panels were then subjected to mechanical tests at an ambient temperature of 23 °C to observe the mechanical properties of the samples. The results confirmed the onset of gradual damage with increasing thermal cycles. This was coupled with the degradation of the fibre-matrix interface due to a weakened fibre-matrix bond, which led to interfacial sliding.

Some industrial experiments [2-4] involving the thermal loading of aluminium composite panels, but not using temperatures as extreme as those experienced in LEO, measured thermo-elastic deformation under thermal load with temperature steps from -20 °C to +40 °C and with static loads imposed on the panel between 0 and 78 N – in steps of 19.6 N. The experiment was carried out in a climatic chamber with the measurements being corroborated by a finite element model. Measurements for the deflection and sample temperature of the structural model were taken at set temperatures using photogrammetry and infrared cameras to map a thermal cartographic image of the structural model, where temperatures were assumed as for black body conditions. Looking at the problem of a spacecraft panel undergoing cyclic loading from the perspective of modelling it is possible to find that the structure must combine the effects of thermal loading as well as mechanical disturbance. This is because from a physical point of view the deformation of a body is connected to the change of heat inside it, and therefore to the change of the temperature distribution in the body. So, a deformation of the body leads to temperature changes, and vice versa. The internal energy of the body depends on both the temperature and the deformation and so, in the case of a practical body, such as a spacecraft panel,

this necessarily undergoes processes that are intrinsically coupled, defined collectively as thermoelasticity [176].

Apart from that, thermal changes in the body cause mechanical deformation in the body, which in return affects these thermal changes, involving two-way feedback. This means that the modelling techniques and representations really do have to couple the mechanical and thermal aspects of the problem to achieve results of adequate accuracy that describe the problem properly.

It should also be mentioned that in recent years honeycomb panels have become more and more widely used within the aerospace industry [185, 195, 197, 207] due to their structural efficiency, and because they demonstrate a generally high strength to weight ratio. This type of design consists of two thin parallel face sheets – usually coated – attached to a core material that separates them. The core can be composed of different types of material, but the most frequently used one is a hexagonal honeycomb made from sheets of aluminium foil, as shown in Figure 3.1.



Figure 3.1. A honeycomb sandwich panel as typically used in the aerospace industry

Despite their many benefits sandwich panels do have a number of structural limitations. They are known to have poor resistance to impact loads, particularly when combined with thermal loading, due to the risk of debonding between the sandwich core and the outer faces under these conditions.

It has been found in the literature that honeycombs with thicker core are characterised by higher strength [197] and an increase in the core density leads to an increased stiffness of the sandwich structure [195]. It was also shown experimentally in [211] that a change in

honeycomb cell size, as well as in the distance between the supports, has an impact on the collapse mode of the samples.

In [212] a thermal effect of the inserts in the honeycomb core was demonstrated. It was concluded that any electronic equipment (including batteries) that might be attached to the honeycomb would cause dissipation of possibly excessive heat through the inserts causing additional thermal loading within the panel.

Therefore, to the best of the author's knowledge, there has not yet been an experimental investigation on the behaviour of an aluminium sandwich panel undergoing simultaneous thermal and dynamic mechanical loading to investigate coupling between the two of them and the response of the panel to harsh thermal environments of up to +100°C and down to -150°C. Most authors consider the heat distribution within the material for mechanical testing performed after the thermal cycling has been completed. Thus, in this chapter we consider, for the first time, the thermoelastic response of a typical aluminium honeycomb sandwich panel when tested for load deflection characteristics within an environmentally controlled enclosure. It should be noted that this type of structural panel is routinely used within spacecraft structures.

3.1. Experimental set-up

In order to plan an appropriate experiment a literature review was undertaken in order to study the basic thermal properties of the space environment that would necessarily have to be emulated. It became evident that the International Space Station (ISS) environment would include exposure to extreme thermal cycling, ultra-vacuum, atomic oxygen, and high energy radiation [182]. As discussed previously when an orbiter such as the ISS moves in and out of sunlight during its orbit around Earth the degree to which the outer structural materials experience thermal cycling temperature extremes depends on their thermo-optical properties (solar absorptance and thermal emittance), exposure to the sun, their view of Earth and the other surfaces of the spacecraft, the duration of time spent in sunlight and shadow, the important thermal masses and the influences of nearby onboard equipment and components that produce heat [182]. As a rule, the cyclical temperature variation was taken to be -120 °C to +120 °C, acknowledging that high solar absorptance with low infrared emittance will contribute to greater temperature swings.

Therefore, the test was designed to simulate the extreme thermal environments experienced by the sandwich panel of the spacecraft due to the solar radiation. Based on the information in the open literature summarised at the beginning of this chapter, it was assumed that only solar radiation causes an extreme thermal impact on the spacecraft panel. Thus, the solar radiation was considered to vary, resulting in thermal loading from -150 °C up to 100 °C.

The test sandwich panel of $300 \cdot 10^{-3} \times 100 \cdot 10^{-3} \times 15 \cdot 10^{-3}$ m was composed of two types of aluminium alloy. For the outer skins of thickness $0.38 \cdot 10^{-3}$ m an Al-2024 alloy was used, whilst an Al-5056 alloy foil was used to form the hexagonal honeycomb core. This core was of cross-sectional thickness $14.24 \cdot 10^{-3}$ m and was made up from a foil of thickness $0.0254 \cdot 10^{-3}$ m. The mechanical and thermal properties of these materials are summarised in Tables 3.1 & 3.2, noting that the structural coefficient of thermal expansion stated in Table 3.2 was extrapolated from the data made available for AL-5056.

Table 3.3. Mechanical properties of the sandwich panel

	Al-2024	Al-5056 3/16 Honeycomb
Density, ρ (kg/m ³)	2780	50
Young's Modulus, E (Pa)	73.1×10^9	669×10^6
Shear Modulus, G (Pa)	27.5×10^9	310×10^6
Poisson's Ratio, ν	0.33	0.3
Foil thickness (m [in])		0.0254×10^{-3} [0.001]

Table 3.4. Thermal properties of the sandwich panel materials

	Al-2024	Al-5056
Coefficient of Thermal Expansion ($^{\circ}\text{C}$)	2.47×10^{-5}	2.41×10^{-5}
Coefficient of Thermal Expansion for 3/16 honeycomb ($^{\circ}\text{C}$)		2.4×10^{-6}
Thermal Conductivity @ 25°C (W/mK)	149	149
Specific Heat (J/kg $^{\circ}\text{C}$)	875	904
Reference Temperature ($^{\circ}\text{C}$)	22	22

It has to be pointed out that the selection of properties was not a straightforward task. Airbus DS provided the panels, however they did not have the description of the properties that were needed. After a series of communications (summarised in Appendix E) some mechanical properties were identified. The thermal properties were held by a different branch of the company and we did not manage to get a response with regard to those. Therefore, separate research was undertaken into the properties. Airbus DS recommended the data set [23-60] which was used to approximate some of the properties. Apart from that, in [216] some mechanical data was considered as it was based on an assessment of impact damage to the sandwich panels similar to those used in various types of satellites and spacecraft. The satellite types researched included scientific, polar-orbit meteorological and earth observation satellites as well as a cargo carrier vehicle that travelled to and from the International Space Station. Some commonly used materials within space structures, from aluminium alloys, metallic and non-metallic matrices and composite fillers, as well as commonly used honeycomb core materials and their properties were also discussed in [217]. However it should also be noted that thermal properties of materials are rarely stated in full and quite limited, with only approximate values available for the coefficients of thermal expansion and conduction for general metal groups. This limits its usefulness as an accurate source for thermo-mechanical properties. An investigation in [218] provides some insight into the mechanical properties of aluminium sandwich panels for a variety of materials. In [219] and [220] some

information on the thermal properties for Al-2024 and Al-3003, as well as HSPs of a vented Ti-6Al-4V composition was found. In summary the process of attaining reliable and detailed material properties from papers and other sources proves to be a difficult task. However, an attempt has been made to replicate approximations of properties that are as accurate as possible for the panel under investigation.

It was shown in [2-4] that typical models of the honeycomb panels do not take into account the fact that the temperature profiles within the thickness of the panel may vary, as in Figure 3.2.

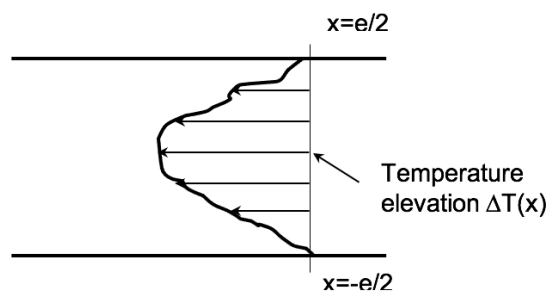


Figure 3.2. Temperature profile of a honeycomb panel [2-4]

This was considered to be a very important point so it was decided to take thermal measurements not only on the top and bottom skins but from within the honeycomb layer as well, to record any disparity in the temperature within the honeycomb and the skins.

The experiment was performed in an environmental testing chamber fitted to a computer driven Instron 8801 tensile and compressive testing machine of 100 kN capacity in the University of Strathclyde's Advanced Materials Research Lab (AMRL), as shown in Figure 3.3.

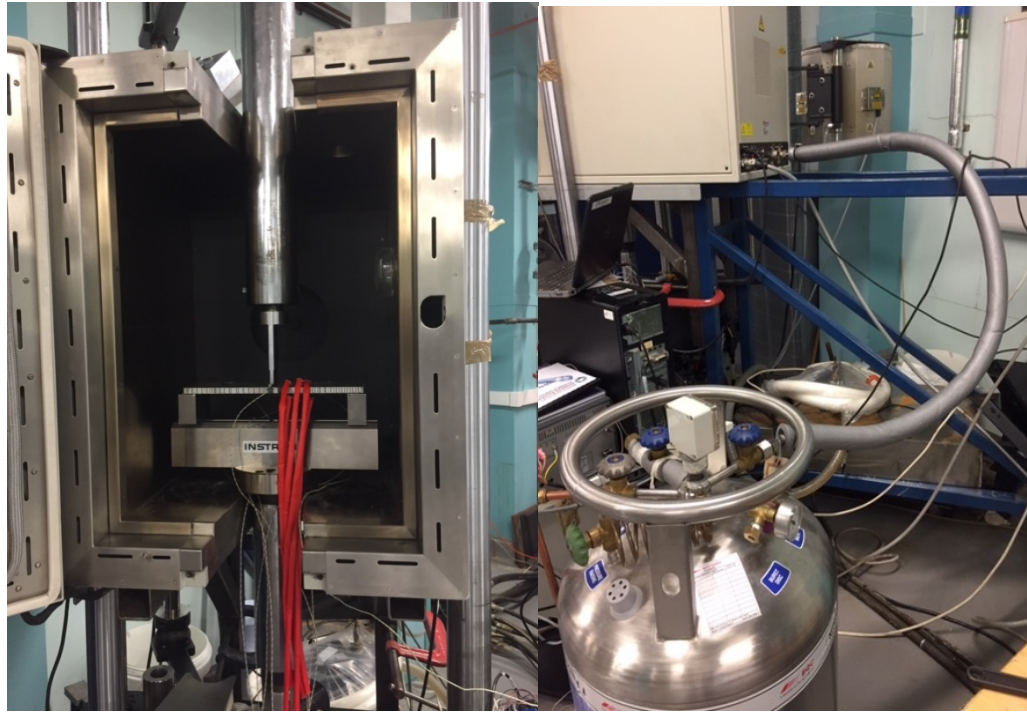


Figure 3.3. Panel sample fitted within the Instron test machine's heated environmental chamber, also showing the liquid nitrogen dewar required for cooling, and the nitrogen gas flow regulator system.

The environmental test chamber offered a precisely controlled temperature range of $-150\text{ }^{\circ}\text{C}$ to $+350\text{ }^{\circ}\text{C}$ (to within $\pm 1\text{ }^{\circ}\text{C}$) and used an internal heater and a liquid nitrogen cooling system, which were both operated automatically by the environmental control software to provide closed-loop control of the thermal environment of the test. When the chamber is sealed there is no internal visibility, therefore the use of externally located displacement imaging equipment wasn't possible and so strain gauges were used to register the displacement of the panel. High performance C series strain gauges from HBM UK (Fig. 3.4) were used, with an operating temperature range from -269 to $+250\text{ }^{\circ}\text{C}$, and a nominal terminal resistance of 120 Ohms.

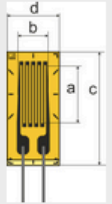
LC1 Linear strain gauges with 1 measuring grid and with leads								
	Ordering number	Nominal (rated) resistance [Ω]	Dimensions [mm/inch]				Solder terminals	Preferred types
			Measuring grid		Carrier			
			a	b	c	d		
1-LC11-3/120 Steel	120	3 0.118	3.3 0.13	8.5 0.335	5.5 0.217	LS5	1	
1-LC11-6/120 Steel	120	6 0.236	3.2 0.126	12 0.472	5.5 0.217	LS5	1	
1-LC1x-10/120	120	10 0.394	3.2 0.126	16 0.63	5.5 0.217	LS5	-	
1-LC1x-1.5/350	350	1.5 0.059	3.3 0.13	6.4 0.252	5.5 0.217	LS5	1	
1-LC1x-3/350	350	3 0.118	3.4 0.134	8.5 0.335	5.5 0.217	LS5	1	
1-LC1x-6/350	350	6 0.236	3.3 0.13	12 0.472	5.5 0.217	LS5	1	
1-LC1x-10/350	350	10 0.394	3.3 0.13	16 0.63	5.5 0.217	LS5	1	

Figure 3.4. Strain gauges selected for the experiment [221]

To extract as much information as possible from the experiment a rosette configuration was used on the top and bottom faces, adjacent in each case to the centralised load point, with uni-axial gauges elsewhere, as shown in Fig. 3.5.

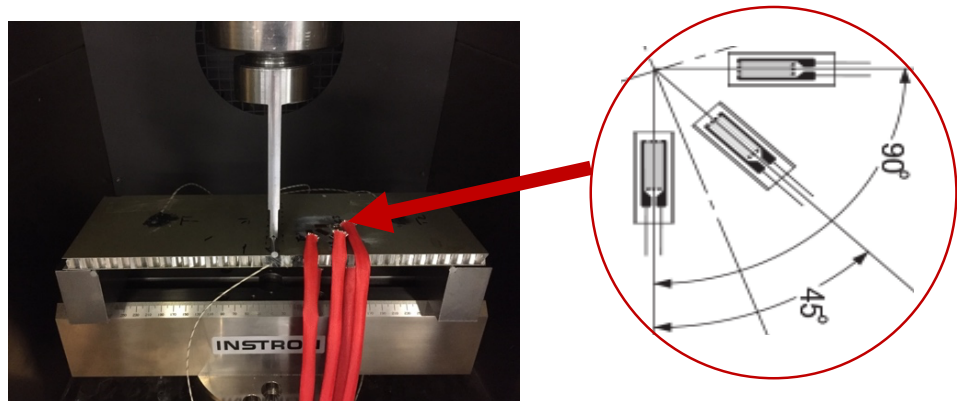


Figure 3.5. Strain gauge rosette configuration shown on the upper face of the sample, and thermocouples T₂, T₃, and T₄.

In order to record the temperature data on the panel sample within the chamber, as well as to validate the distribution of the heat flux within the panel, thermocouples of type T from RS Components Ltd were selected, with an operating range of -200 °C to +350 °C,

and shown in Fig. 3.6.

RS PRO Type T Thermocouple 0.3mm diameter, -200°C → +350°C

Specifications

Attribute	Value
Thermocouple Type	T
Probe Diameter	0.3mm
Maximum Temperature Sensed	+350°C
Termination Type	Cable
Cable Length	2m
Standards Met	RoHS Compliant
Response Time	0.7 s

Figure 3.6. RS Components Ltd Type T thermocouple specifications [222]

Six thermocouples were positioned on the top, bottom and middle layers of the panel to record the pattern of the temperature distribution in three dimensions, as shown in Fig. 3.7.

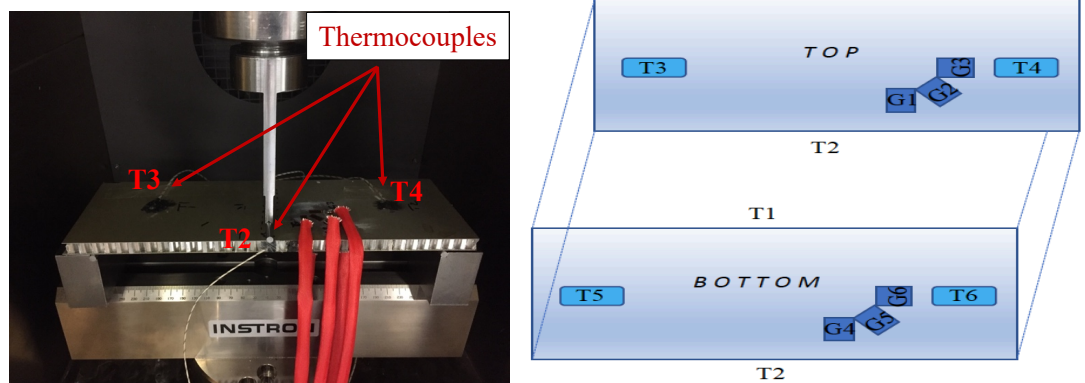


Figure 3.7. Thermocouple distribution on the test panel (a) on the top surface of the sample and (b) on the top and bottom surfaces, as a schematic. Note that gauges T1 and T2 are located halfway down the edge thickness of the panel.

For this experiment a three-point bending (TPB) test, as shown in Fig. 3.8, was selected. The TPB test is one of the most frequently used methods of mechanical bending testing

and in this case provided an assessment of the flexural behaviour of the panel when subjected to a transverse mechanical load at its midpoint. While this is the most representative loading scenario for the design of a satellite honeycomb panel, it is still a good representation of the forced excitation of vibration which can propagate in low-earth orbit satellites, without any undesirable residual stresses appearing in the simulation.

The main advantage is the ease of preparation of the specimen and the subsequent testing. Disadvantages include the fact that the results obtained are often sensitive to specimen and loading geometries, along with strain rate. The data extracted from this test is usually used for selecting materials or panels used for parts that need to support loads without significantly flexing.

Most experimental studies on honeycomb panels investigate the aspects of failure modes of material under high bending loading and /or in-panel compression [223].

Therefore since the TPB test is capable of providing us with all the necessary information about the deflection, the experiment comprised a TPB test, shown in Fig. 3.8, with the sample honeycomb panel simply supported in the thermal chamber, undergoing an incremental mechanical loading profile with line contact established between a 6 mm diameter circular loading bar and the upper surface of the plate, orientated such that the loading line was across the width of the plate, and centrally located along the length. The loading and unloading procedure was automated using the built-in control options embedded in the software of the Instron testing machine. The loading started from true calibrated zero and gradually increased up to 150 N, and then back to zero, and this was repeated at specific temperatures over the full range of environmental temperatures required, as follows: -150 °C, -100 °C, -60 °C, -40 °C, -20 °C, 20 °C (ambient), 40 °C, 60 °C, 80 °C, and 100 °C. It should be re-confirmed here that the process of cyclical loading and unloading, in the form of a dynamic mechanical load imposed over a range of different thermal environments, has not been reported in the literature to date, to the author's knowledge [213].

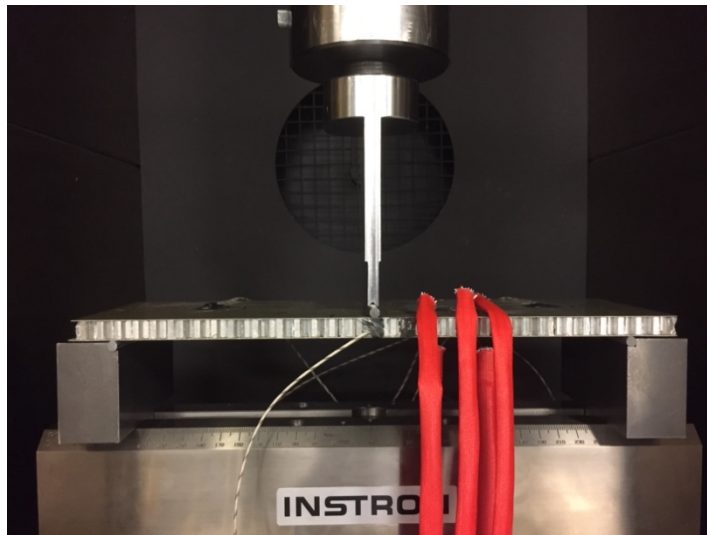


Figure 3.8. Three point bending test arrangement, looking end-on at the circular loading bar orientated across the width of the plate.

The overall aim of the experiment, and a fundamental novelty of this work, has been to evaluate the nature and significance of the coupling between the mechanical and the thermal effects within an aluminium composite plate. In order to accomplish this successfully, given prior expectations from the literature, and insights gained from the author's own modelling work in Chapter 2, the following research hypotheses were formulated, as a general basis for observation and interpretation:

H1. *Due to the different structural properties of the top, bottom, and middle plies of the sandwich panel, there may be a different distribution of temperature in the middle ply from that in the top and bottom layers.*

H2. *Within the environmental chamber the environmental temperature is stabilised, but there may still be a significant disparity between the temperature recorded on the top and bottom skins.*

H3. *The environmental temperature may have a significant quantitative effect on the bending performance as well as a generally qualitative effect on the deformation of the panel, and this may be due to possible thermoelastic coupling between the thermal and mechanical loading effects.*

H4. *The qualitative deformation characteristics of the panel at extreme environment temperatures may differ significantly from those observed at environmental temperatures that are closer to moderate ambient temperatures.*

In order to address these research questions systematically data was logged continuously for the applied load and the corresponding deflection at the load point, at the stabilised environmental temperature points, as well as local temperature data from the thermocouples located on the top and bottom skins and inside the honeycomb surface on the sides of the panel. This data set was then composed into suitable graphs for subsequent analysis. It should be noted that each set of deflection data was subject to a nonzero offset of magnitude 52.2707 mm, (stated here to four decimal places to replicate the setup accuracy for the Instron 8801 machine, running under the *Bluehill*TM control software) although the effects to be described are all based on relative displacements, so this offset only needed to be subtracted to give the absolute displacements.

The remaining sections of this chapter present the analysis and the findings that were deduced from this work, leading to conclusions formulated in the context of the defining research questions.

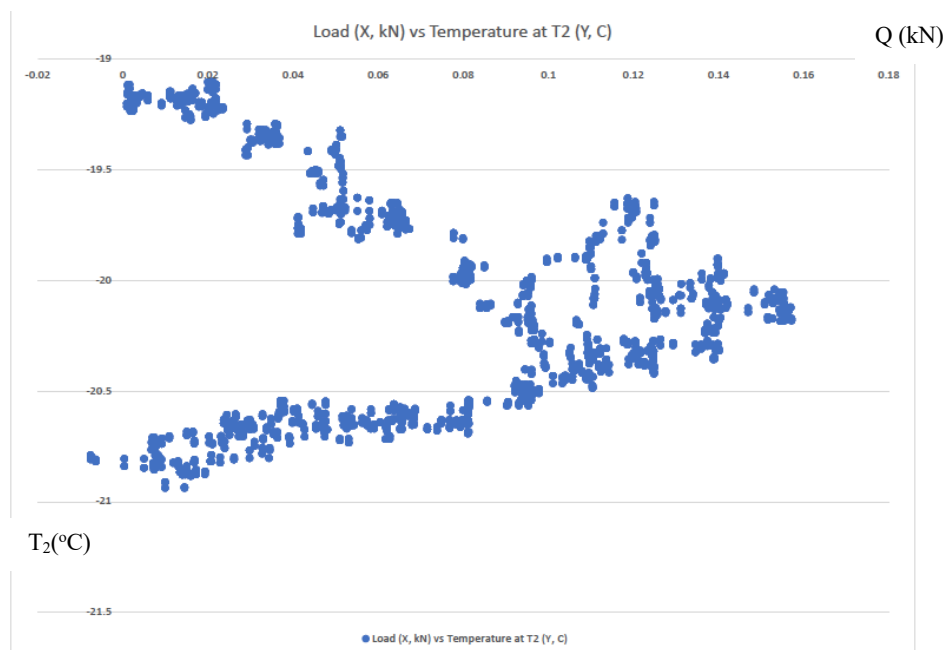
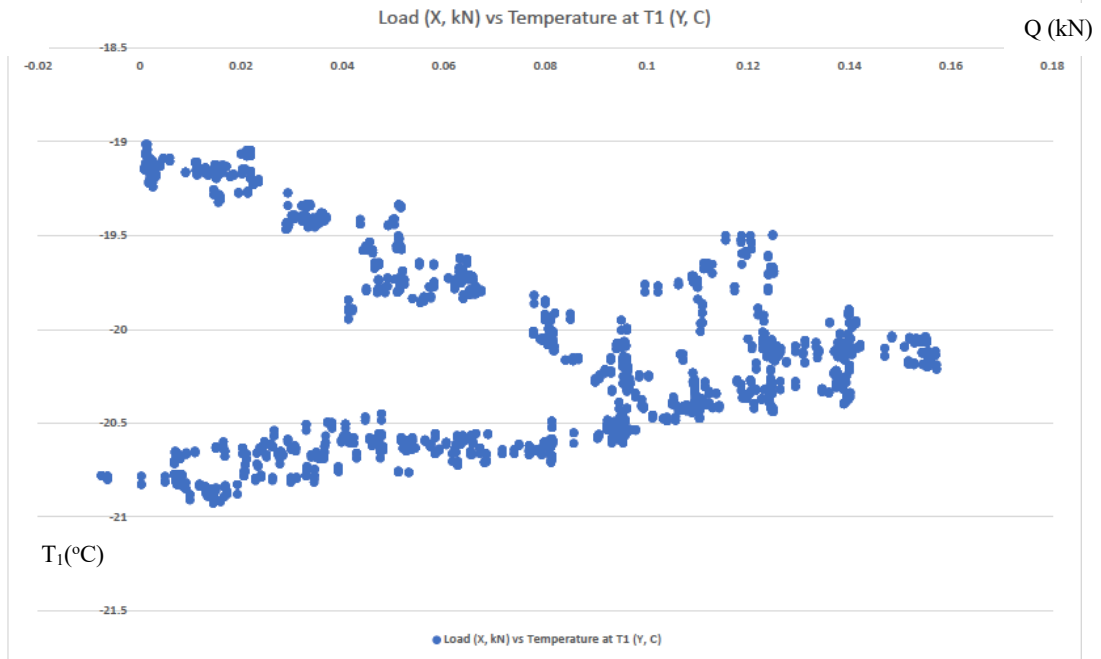
3.2. Results analysis and discussion

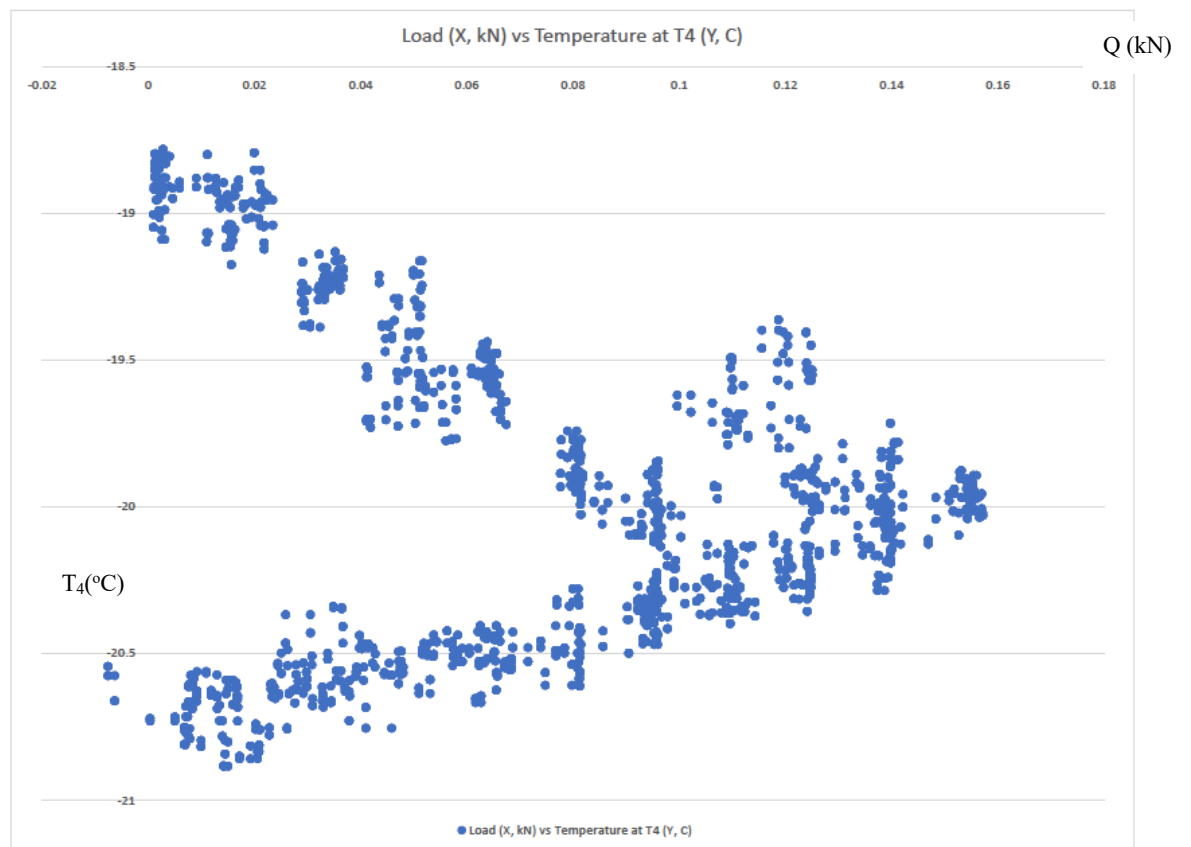
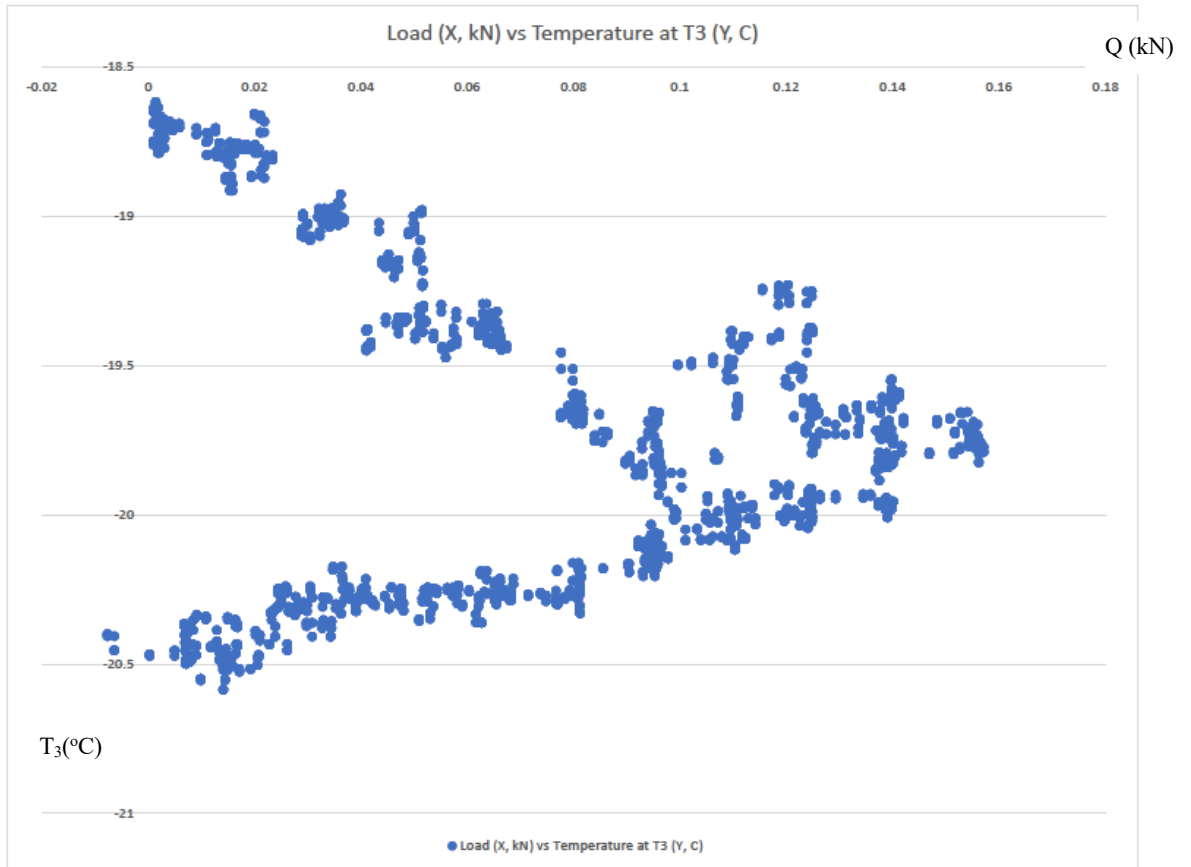
3.2.1. The effect of retention or loss of heat due to dynamic mechanical loading in extreme thermal environments, and the implications of this for modelling

The full data set was initially considered from all the thermocouples (T₁-T₆) and with respect to the mechanical loading. This first investigation of the data was undertaken in order to start to understand the effect of any possible cooperation between the mechanical loading and the thermal conditions of the environment, and also to ascertain the nature of the temperature distribution along the panel in different areas of the panel. Thus, the data was represented graphically as the temperature recorded by each thermocouple within the

environmental temperatures (T_{env}) of -150 °C, -100 °C, -60 °C, -40 °C, -20 °C, 20 °C, 40 °C, 60 °C, 80 °C, 100 °C against the mechanical load (Q) from 0 N up to 150 N.

Due to the constraints of space we present results from the 6 thermocouples only for two environmental temperatures of -20 °C and -150 °C , shown in Figures 3.9 and 3.10, together with summative findings from all data for all the environmental conditions considered. Graphical data for other environmental conditions are openly available from [213].





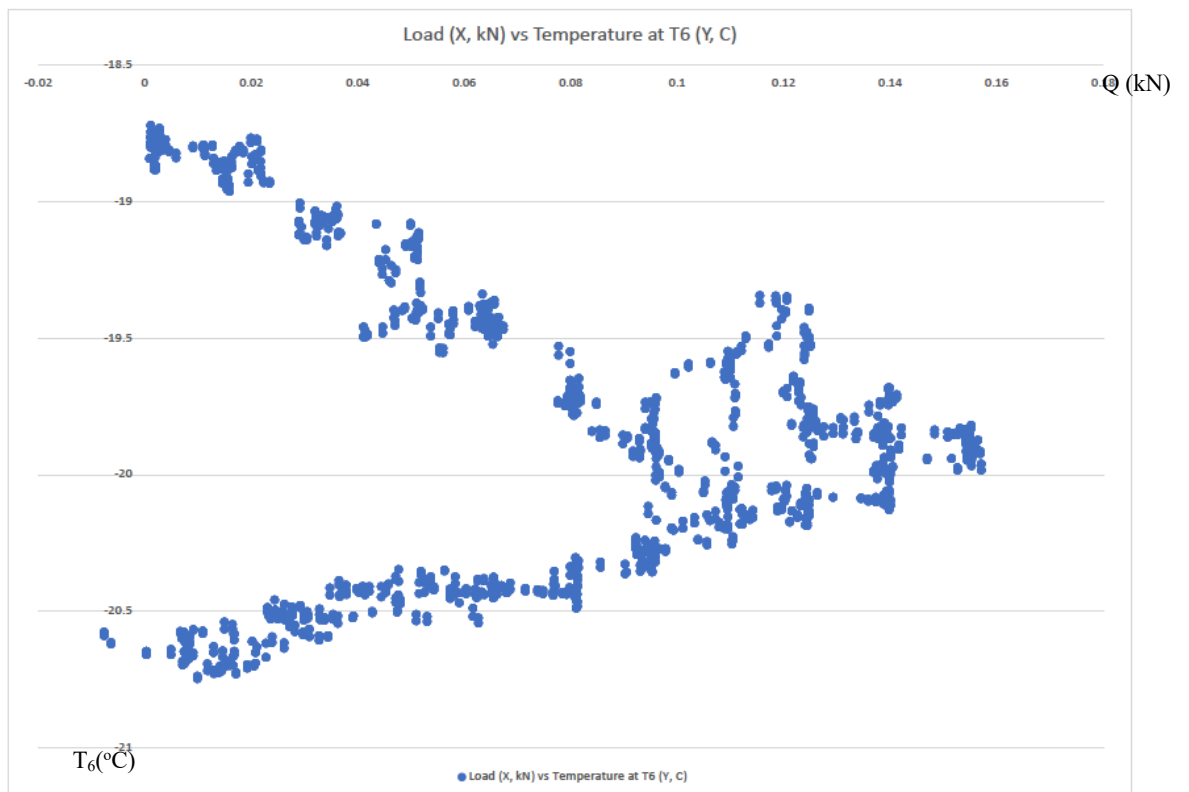
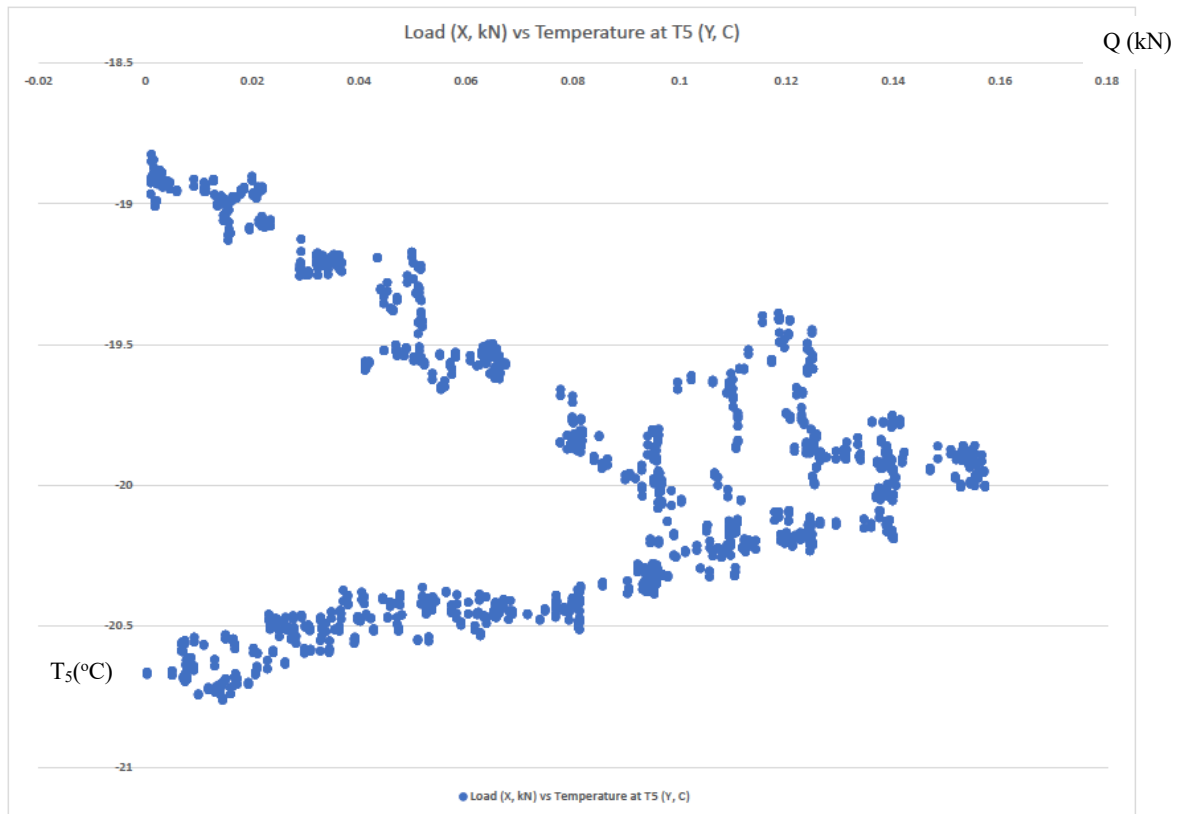
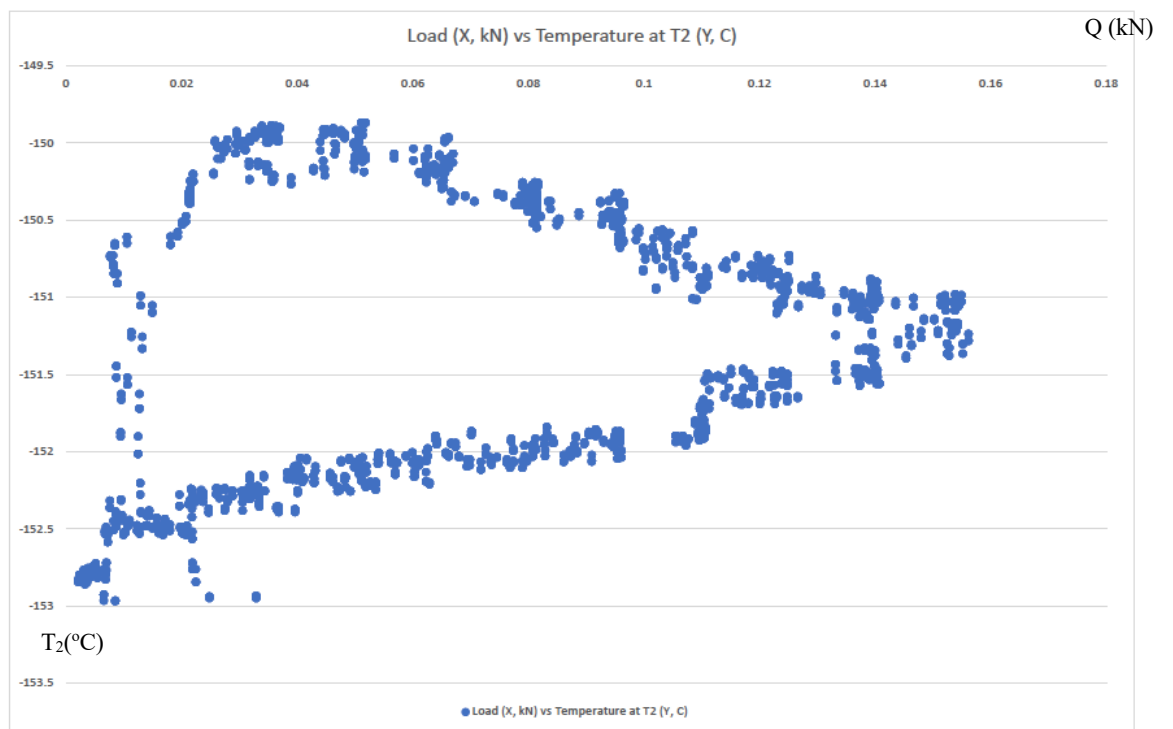
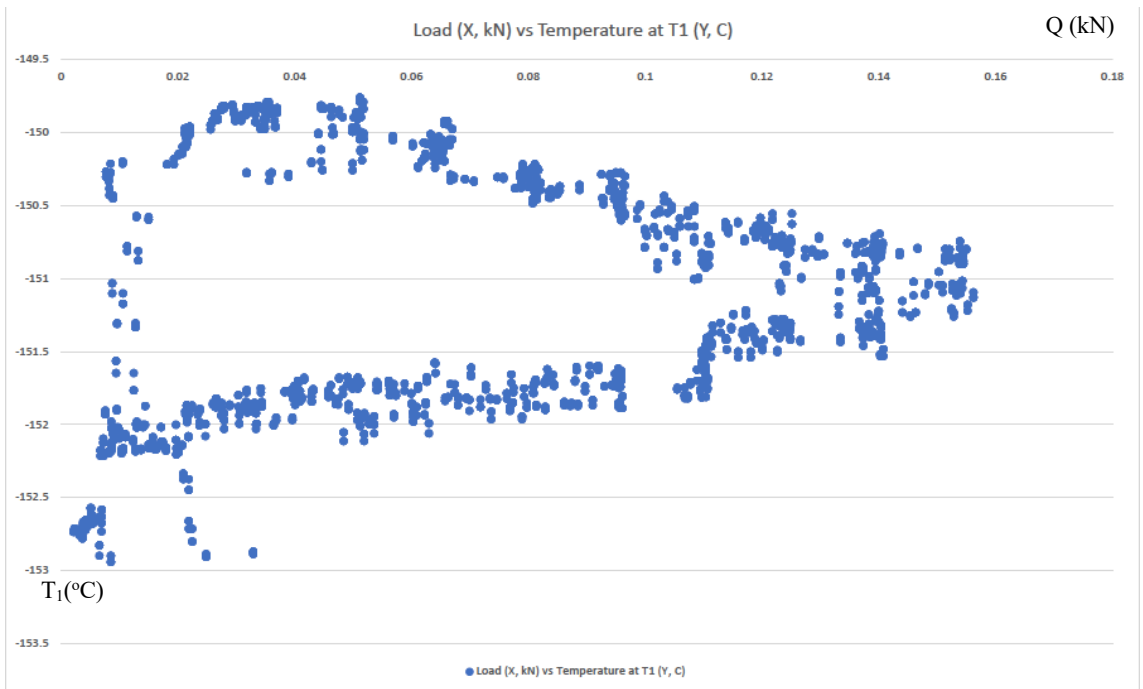
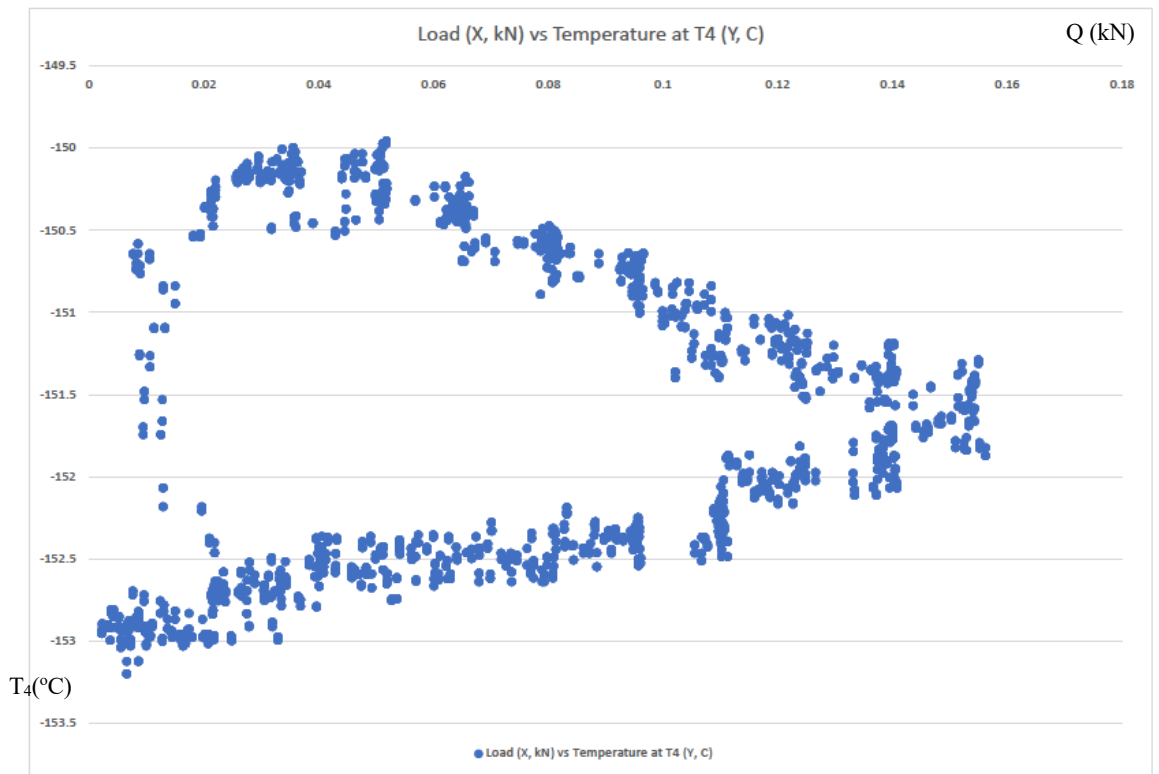
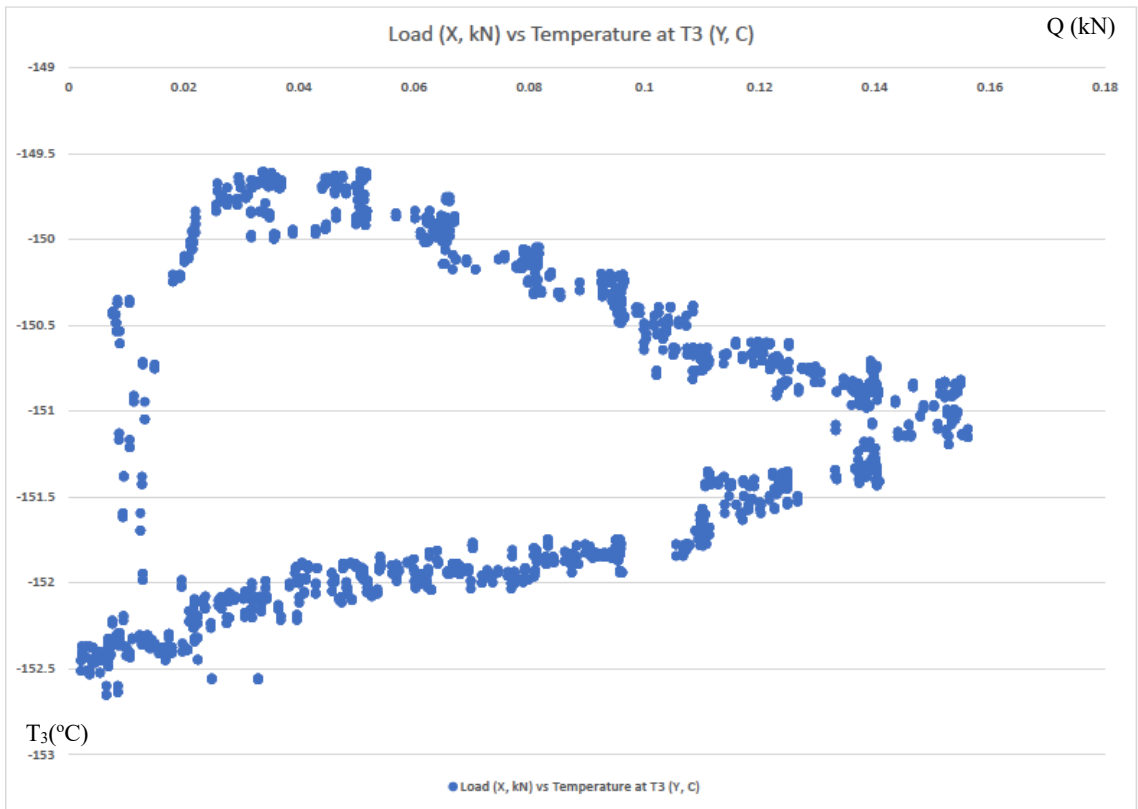


Figure 3.9. Temperature distribution from thermocouples T_1 - T_6 as a function of loading [0 N,150 N] at the environmental temperature of $T_{env} = - 20$ °C.





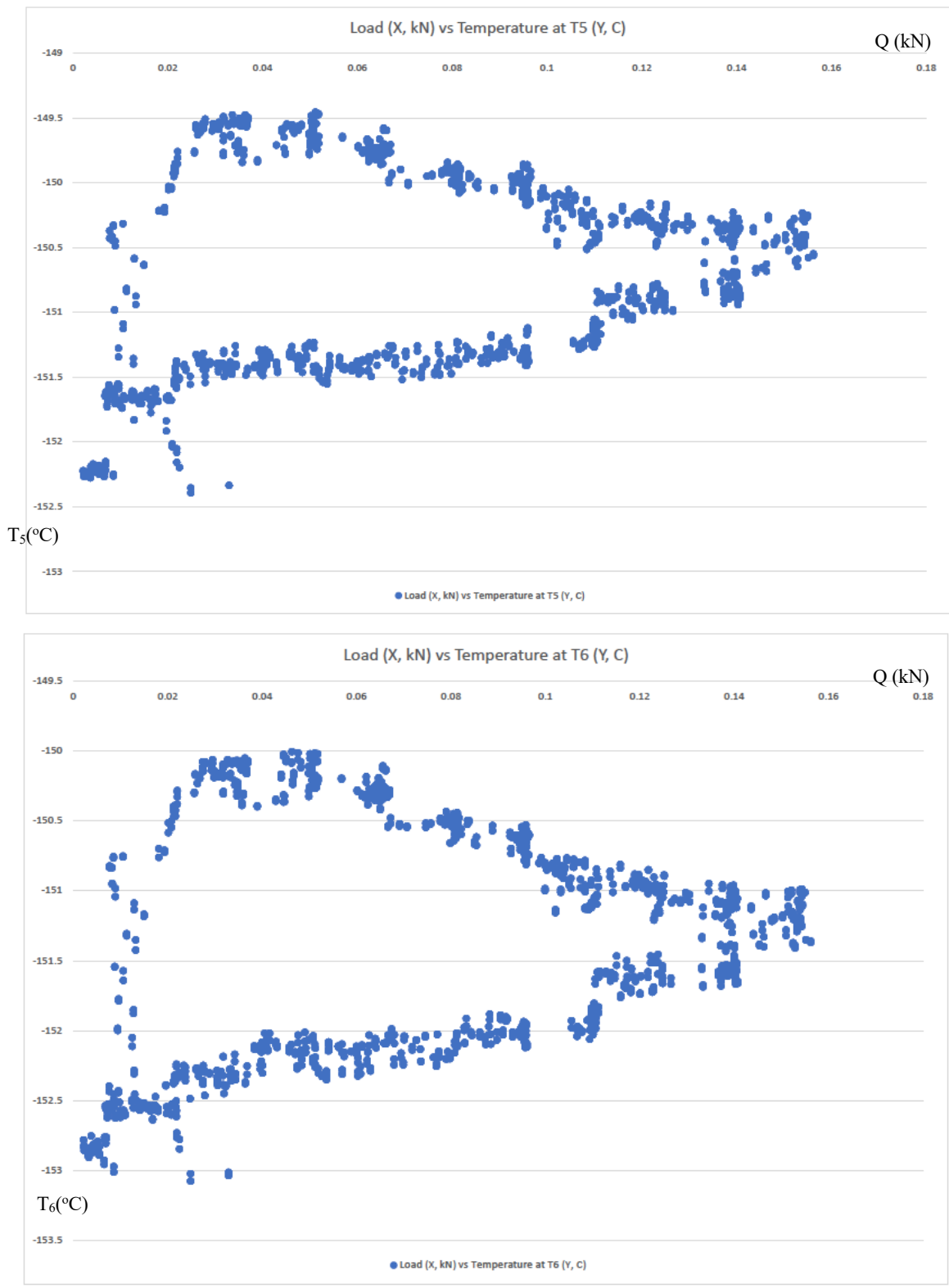


Figure 3.10. Temperature distribution from thermocouples T_1 - T_6 as a function of loading [0 N,150 N] at the environmental temperature of $T_{env} = - 150$ °C.

As a result of the data analysis it can be seen that the same qualitative form of hysteresis is evident in the temperature readings from all the thermocouples T_1 - T_6 for a specified environmental temperature T_{env} . An initial but very important conclusion from this is that all the thermocouples performed consistently and responded in the same manner to the local conditions in the material of the panel. It was also found that the hysteresis is represented by an open loop at the following environmental temperatures: - 20 °C, - 40 °C, ambient, and + 40 °C, see Figure 3.9 for the specific case of $T_{env} = - 20$ °C. It is also seen that when operating closer to the ambient temperature, and if the panel then undergoes a cycle of loading and unloading, shown counter-clockwise on the Figure 3.9, then after unloading it does not return to its initial thermal state. Instead, it retains some heat after unloading, resulting in a gain of 1-2 °C over the initial state, which is indicative of an irreversible process, as mentioned in [135].

The hysteresis is represented by a closed loop at the following environmental temperatures: - 150 °C, - 100 °C, + 60 °C, + 80 °C, + 100 °C, and Figure 3.10 can be referred to for the specific case of $T_{env} = - 150$ °C. This means that the panel appears not to retain residual heat when operating at the more extreme levels of environmental temperature, irrespective of whether or not this is positive or negative, and so after unloading at those temperatures it returns, reversibly, to the thermal condition from which it started. This is a novel finding detected only because of the cyclical dynamic loading and unloading regime that was specifically undertaken at extreme temperatures.

It must be mentioned that there is a distinctly unstructured response within the loop at the specific case of $T_{env} = - 60$ °C, noting that this phenomenon occurred only at this particular environmental temperature and that this is probably an artefact of the specific material we have been considering. It is also evident that this unstructured behaviour occurs as a transition from the open loop hysteretic behaviour, which is found closer to the ambient environmental temperature, to the closed loop response which occurred at the more extreme environmental temperatures. The fact that we do not see a clear hysteretic loop for the loading process at this environmental temperature means we do not see a clear temperature difference for the loading and unloading processes. This means that the thermal response of the panel changes during loading and unloading, and so there might be a retention of heat within the panel, but we cannot predict from this data how much hotter the sample would be during the unloading process. Therefore, we cannot predict in this specific case the extent of the thermo-mechanical coupling, i.e. how the deformation

that occurred resulted in a change of the thermal properties of the panel, and some further research around this phenomenon should be undertaken in the near future.

At the environmental temperature of $-100\text{ }^{\circ}\text{C}$ the behaviour is characterised by a bow-like double loop which becomes a more clearly defined single loop when the environment becomes colder still at $-150\text{ }^{\circ}\text{C}$. It seems obvious that the environmental temperatures of $-60\text{ }^{\circ}\text{C}$ and $-100\text{ }^{\circ}\text{C}$ are defining points at which there is a transition from an open hysteretic loop to one that is closed, and from an irreversible thermodynamic process to one that is reversible.

At the maximum load of 150 N it can be seen from Figure 3.9, 3.10 and in Appendix C that the loop ends at a single valued temperature for all the six thermocouples, and it was also noted that this is independent of the environmental temperature. This confirms the correctness of readings taken across the profile of thermocouples, and that the unloading phase starts from the point at which the maximum loading was reached.

Therefore, the experimental results offer strong evidence of progress from an open hysteresis loop (at $-40\text{ }^{\circ}\text{C}$, $-20\text{ }^{\circ}\text{C}$, and ambient temperature) towards a closed loop, and this progresses either in the positive or negative temperature directions starting from the ambient environmental temperature, down to the extreme value of $-150\text{ }^{\circ}\text{C}$ and up to $+100\text{ }^{\circ}\text{C}$. There is evidence that the hysteresis loop is structurally closed at the extreme environmental temperatures (very hot [$+100\text{ }^{\circ}\text{C}$] and very cold [$-150\text{ }^{\circ}\text{C}$]), showing thermodynamic reversibility, and also clearly open, and therefore thermodynamically irreversible, when the environmental temperature gets closer to $0\text{ }^{\circ}\text{C}$. This means we can conclude that the loading of the panel in the extreme temperature environment does not cause an accumulation of any residual heat after unloading. However, during the processes of loading and unloading there is evidence of thermo-mechanical coupling, which results in the presence of extra heat internally compared with the heat available from the environment. However, at an environmental temperature close to the ambient temperature (noticed specifically at $-40\text{ }^{\circ}\text{C}$, $-20\text{ }^{\circ}\text{C}$, and at ambient itself) the open hysteretic loop confirms an accumulation of residual heat within the panel which is still present to a large extent even at the point of complete unloading of the deformed sample. This means that a correction factor has to be introduced for the thermal initial condition of a panel when it is close to ambient environmental temperature and when it has undergone a mechanical deformation, even if the loading has been completely removed, due to the tendency to irreversible thermodynamics at those environmental temperatures.

Further research into the identification of this correction factor should be undertaken in the near future, as a priority.

It also has to be emphasised that the width of the hysteretic loop demonstrates the difference in the temperature of the sample at the position of loading and unloading, thus the extent of the heat that accumulates within the sample is due to the deformation, apart from that portion of heat that comes from the environment during the process of loading-unloading.

Table 3.3. Peak-to-peak (p-t-p) temperature range denoted by the width of the hysteresis loop

T _{env}	-20 °C	-40 °C	-60 °C	-100 °C	-150 °C	amb	+40 °C	+60 °C	+80 °C	+100 °C
p-t-p	2-3 °C	2-3 °C	1 °C	2-3 °C	2-3 °C	1 °C	1-2 °C	1 °C	1 °C	0.5 °C

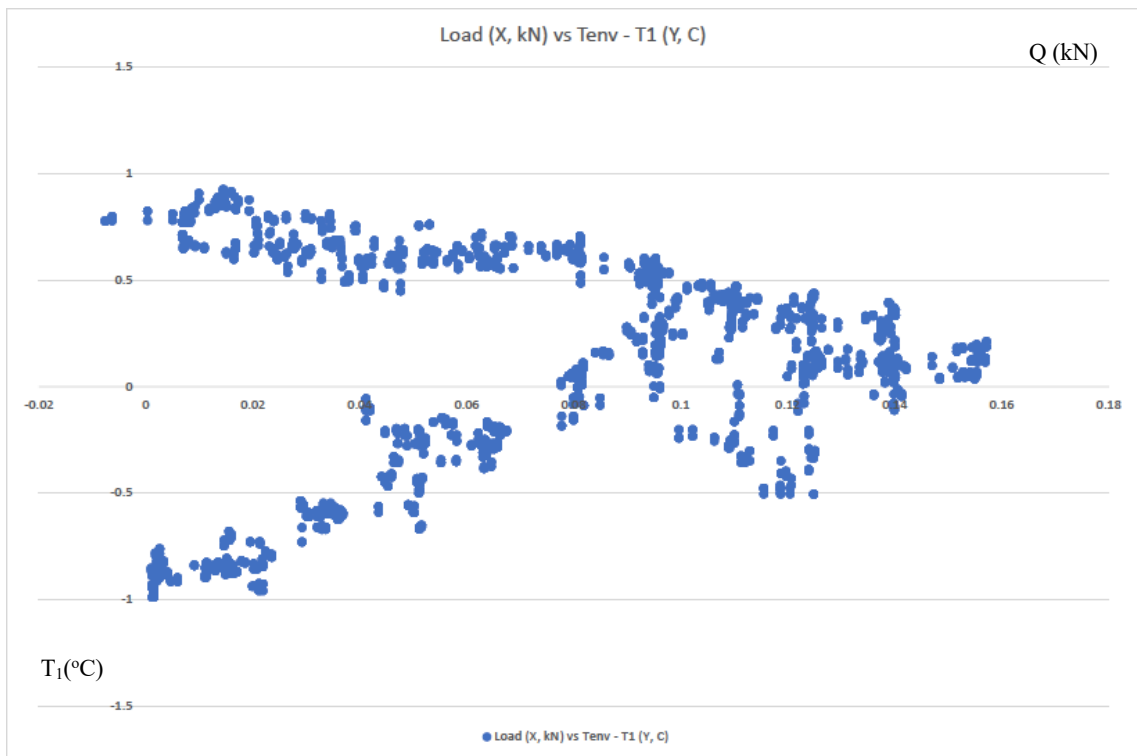
From Table 3.3 it is evident that the width of the temperature loop is the highest at an environmental temperature below 0 °C. This means that the loading and unloading process of a panel placed in an environment at a temperature below 0 °C will be accompanied by a temperature swing of up to 3 °C due to the thermo-mechanical coupling. Therefore, the thermal properties for such a panel cannot be assumed to be governed just by the temperature of the environment if a panel of this sort undergoes a form of dynamic mechanical loading, but would need to have a correction factor applied to cater for the thermo-mechanical coupling, thus guaranteeing a higher level of accuracy of the load-deflection prediction.

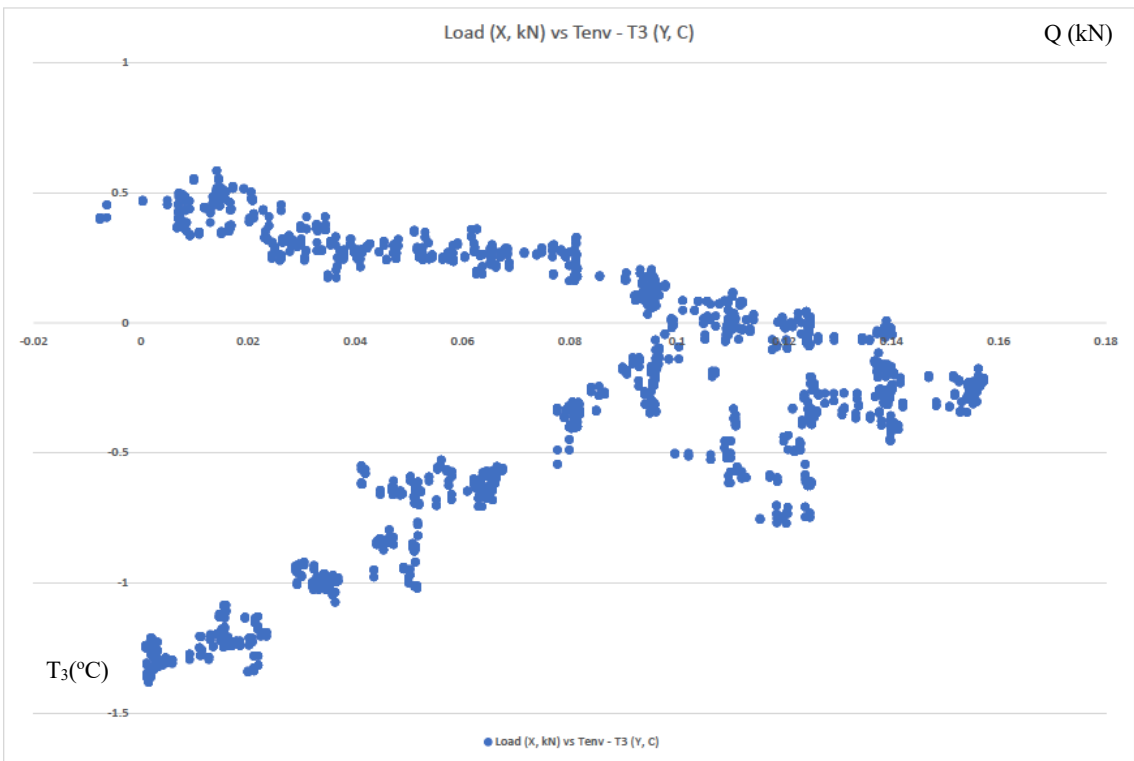
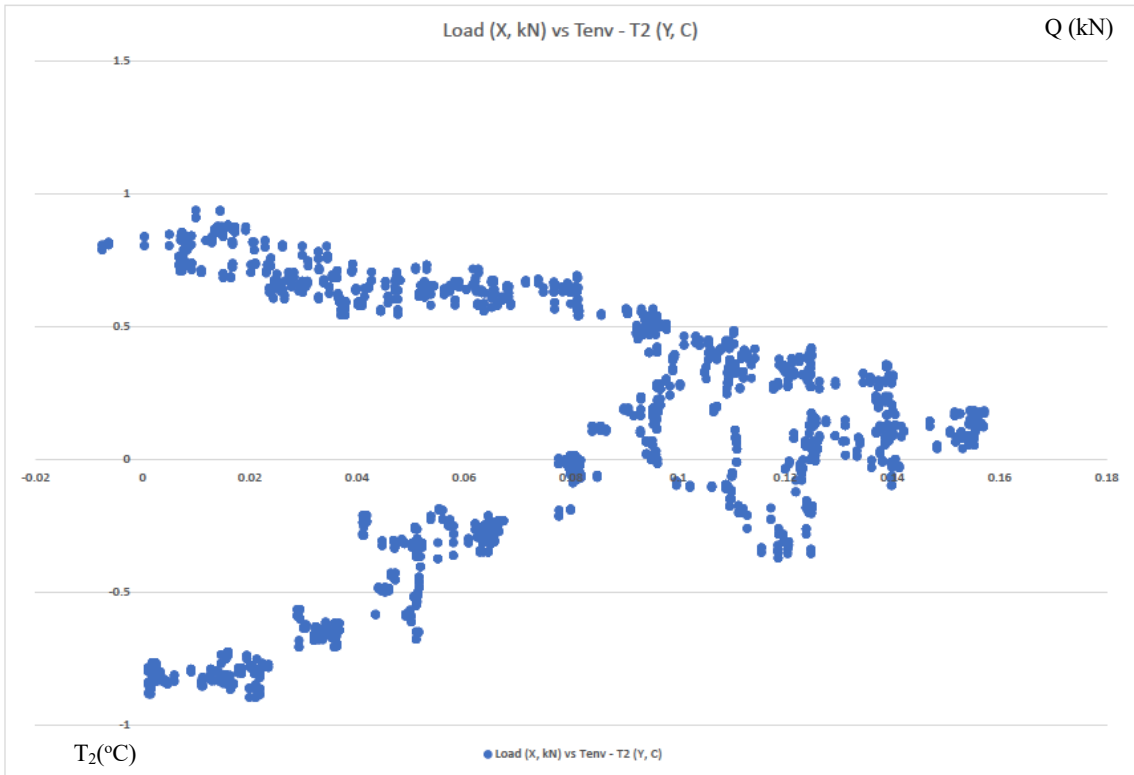
3.2.2. Effect of the dynamic loading and extreme environmental temperature on the temperature distribution along the surfaces and through the thickness of the panel

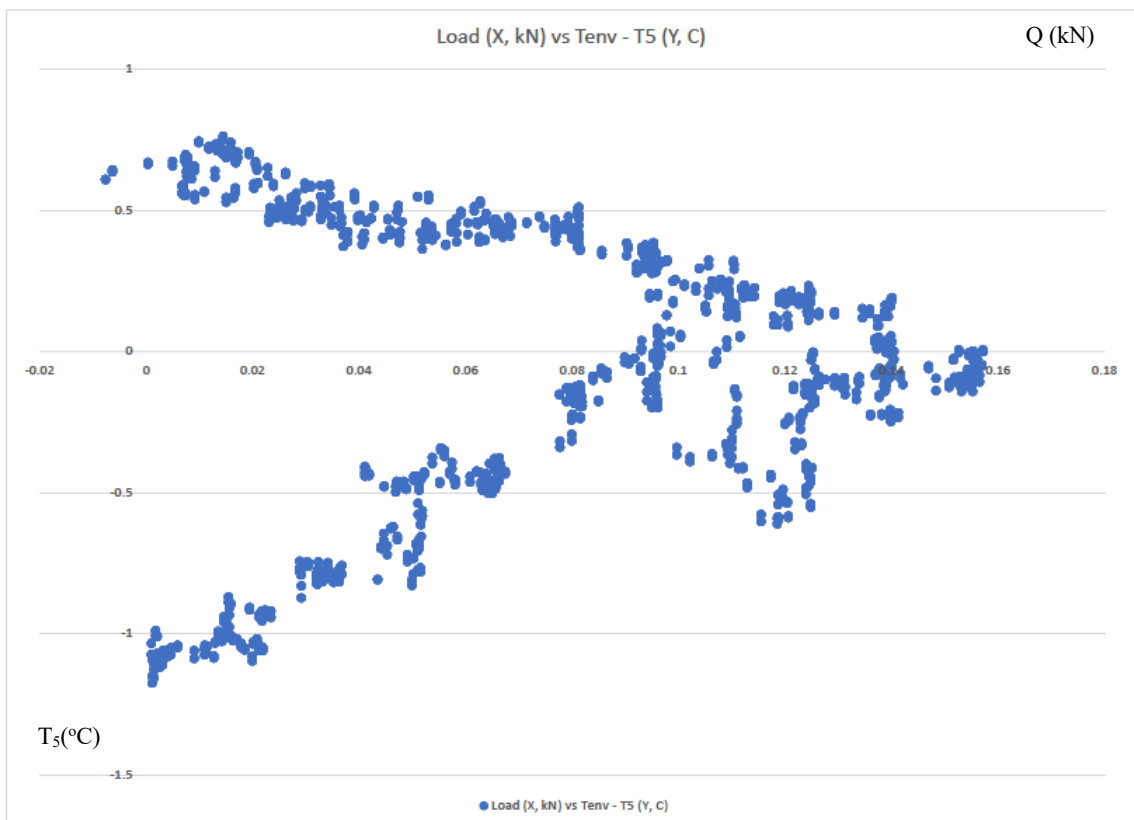
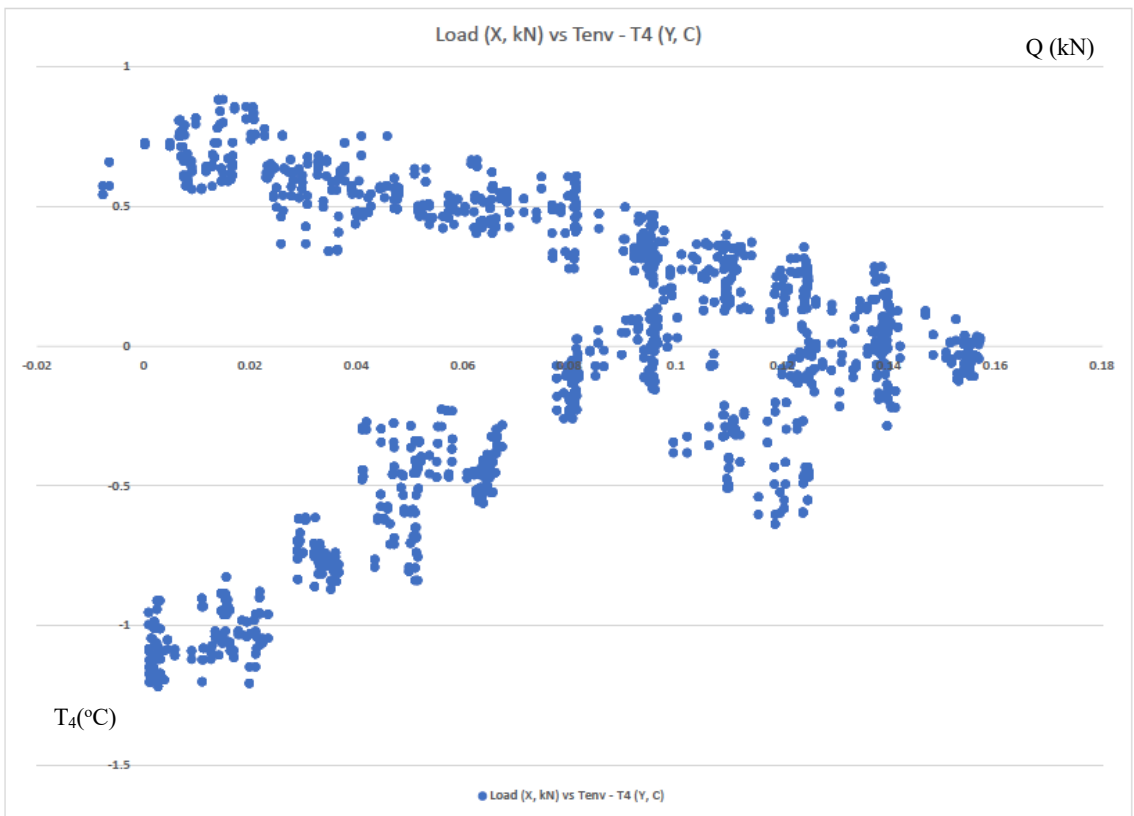
In order to analyse the temperature distribution at various locations of the panel it was decided to investigate how it differs from the temperature of the environment. Specific differences between the environmental temperature and the temperature feedback data from the individual thermocouples were evaluated. The intention was to see whether

certain areas of the panel would heat up faster in response to the environmental temperature. This difference was considered graphically with respect to the mechanical loading of up to 150 N and then unloading from there back to 0 N, for thermal environmental temperatures (T_{env}) of -150 °C, -100 °C, -60 °C, -40 °C, -20 °C, 20 °C, 40 °C, 60 °C, 80 °C, and 100 °C.

In Figure 3.11 the results for $T_{env} - T_i$ are presented for all 6 thermocouples, taken for the environmental temperature of -20 °C as an example, and this was calculated together with summative findings from all the data for all the environmental conditions mentioned. Graphical data for other environmental conditions are openly available from [213].







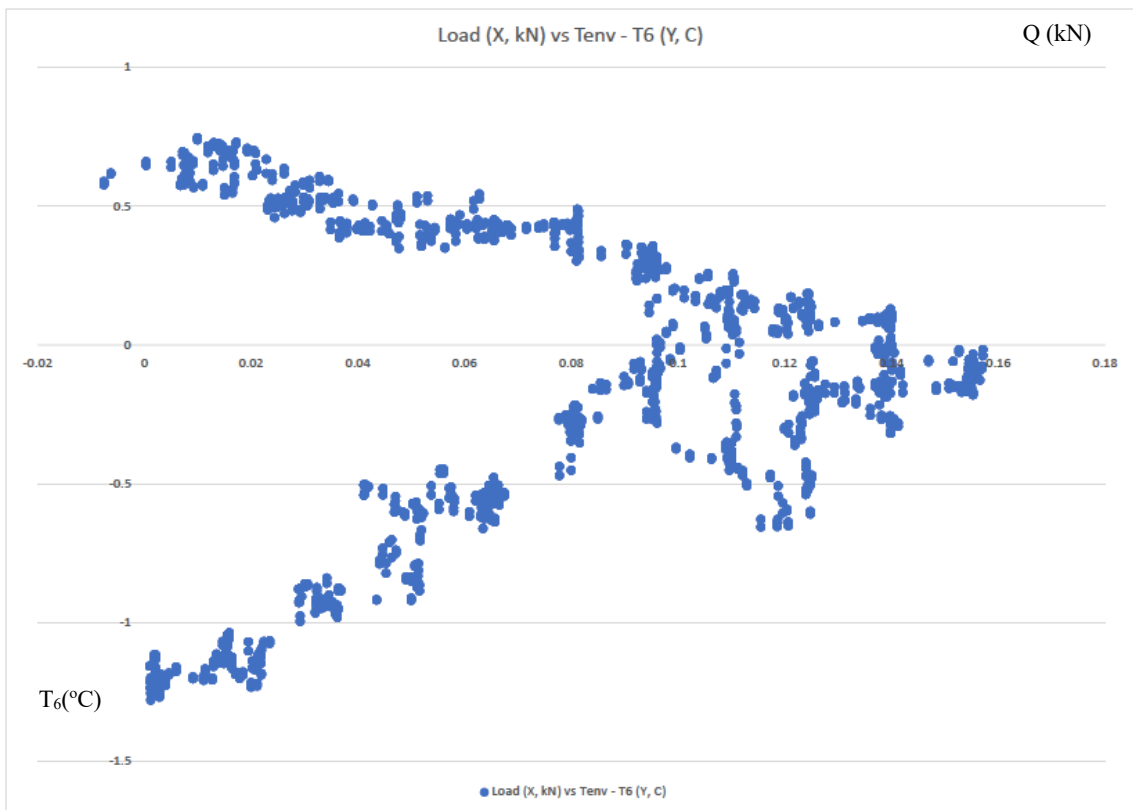


Figure 3.11. Distribution of the difference in temperature between the environmental temperature and the temperature recorded from the thermocouples ($T_{env} - T_i$) versus mechanical loading.

Referring again to Figure 3.7 we recall that thermocouples T_3 , T_4 are placed on the top skin surface, T_5 and T_6 are placed on the lower surface of the bottom skin, and T_1 and T_2 are fitted on both sides, directly onto the honeycomb material. Now from Figure 3.11 it is evident that when the environmental temperature is negative all the thermocouple data demonstrates the same hysteretic loop behaviour. From this we can conclude that the cooling of the sample at all six locations occurs in the same manner, at the same rate, and with the same level of thermo-mechanical effect during the loading and unloading processes. Conversely when the environmental temperature is positive the thermocouple data shows a difference in the feedback from all the thermocouples, especially when the environmental temperature is between $+20\text{ }^\circ\text{C}$ and $+80\text{ }^\circ\text{C}$. This confirms that the sample plate's heating-up process, during loading and unloading, can be faster at certain locations, especially when the environmental temperature is closer to ambient. Some distortion in the feedback from T_4 and T_6 is also evident, possibly because the strain gauges were attached to the skins very close to T_4 and T_6 which possibly resulted in a

slight increase in the width of the hysteretic loop. When the environmental temperature is going up to an extreme value, between +80 °C and +100 °C, all the thermocouples show results that demonstrate a generally flatter behaviour in the temperature loop output, with a peak-to-peak of around 0.5°C. This means that the difference between the environmental temperature and the thermocouple readings is smaller, implying that the temperature of the panel is closer to the environmental temperature, and has minimal thermal distortion due to the imposed mechanical loading and thus characterises a weaker thermo-mechanical coupling.

3.2.3. Effect of extreme environmental temperature on the panel deflection response under the imposed dynamic mechanical loading

This investigation shows how the extreme environmental temperature affects the panel deformation in response to gradual mechanical loading ramping up to 150 N and back down to 0 N. Data has been considered for the panel deflection (w) versus loading (Q) over the range of environmental temperatures, as follows, -150 °C, -100 °C, -60 °C, -40 °C, -20 °C, 20 °C, 40 °C, 60 °C, 80 °C, and 100 °C.

In this part of the study results are presented for an environmental temperature of -20 °C and also for the ambient temperature, as examples given in Figure 3.12, together with summative findings made available from the data for all the environmental temperatures under consideration. Graphical data for other environmental conditions are openly available from [213].

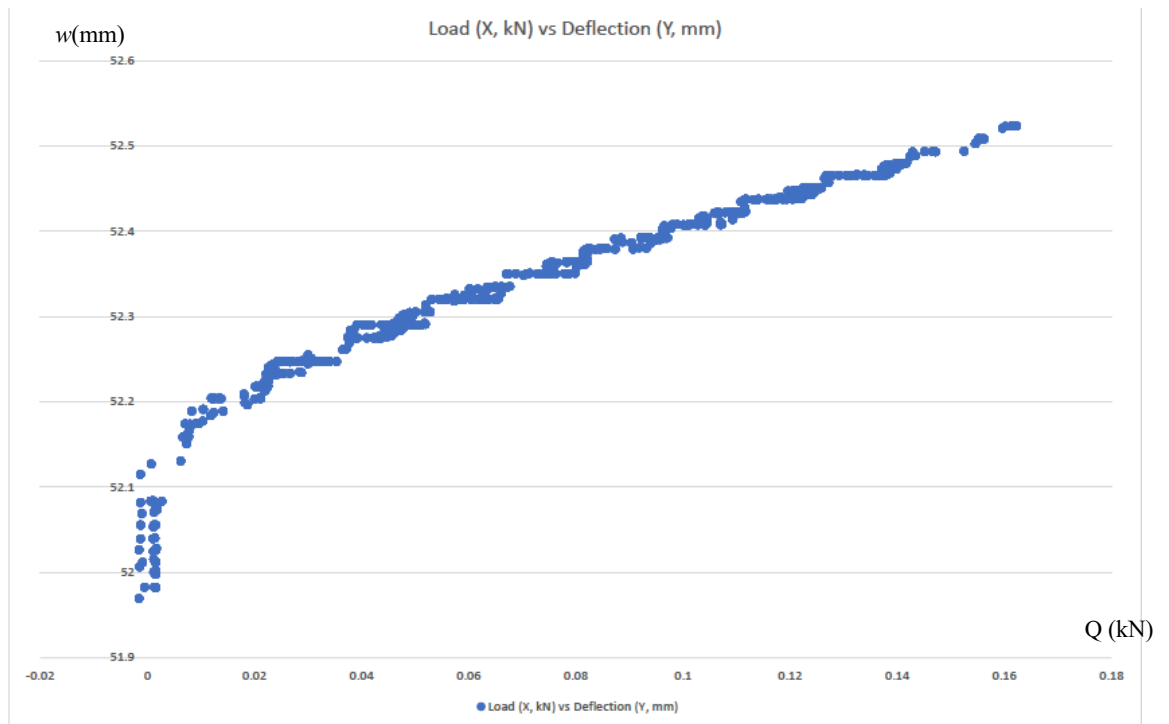
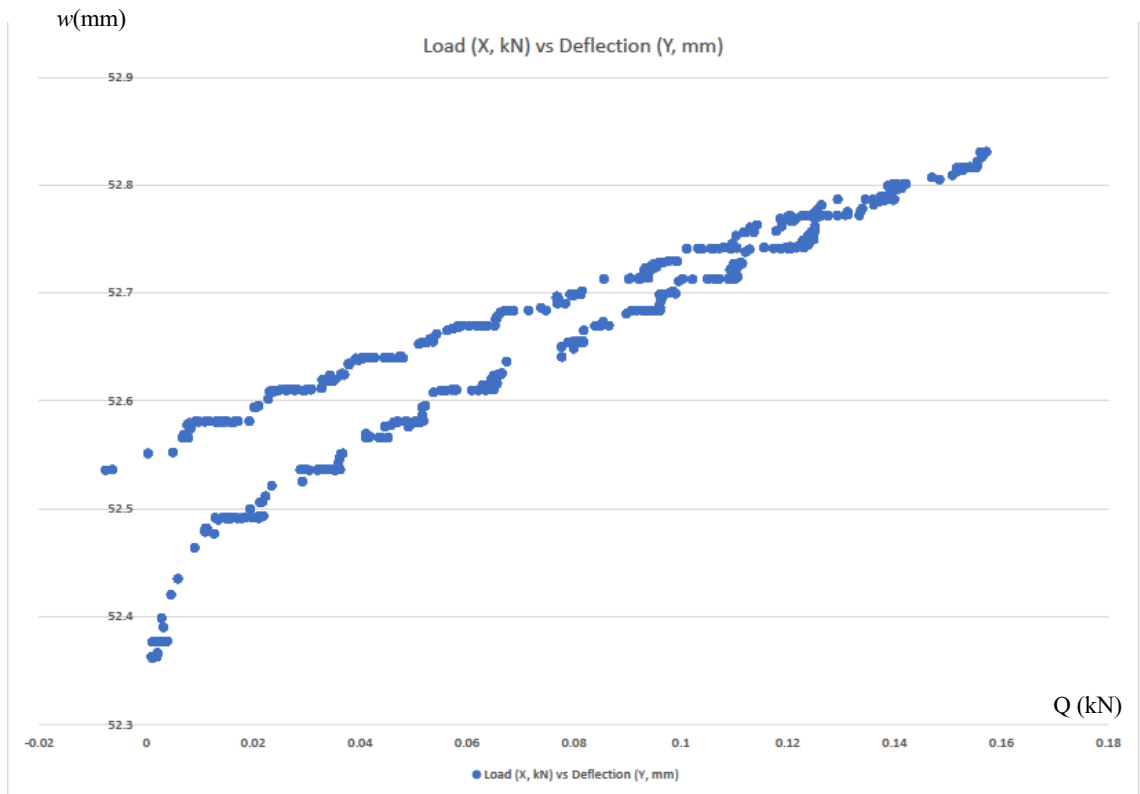


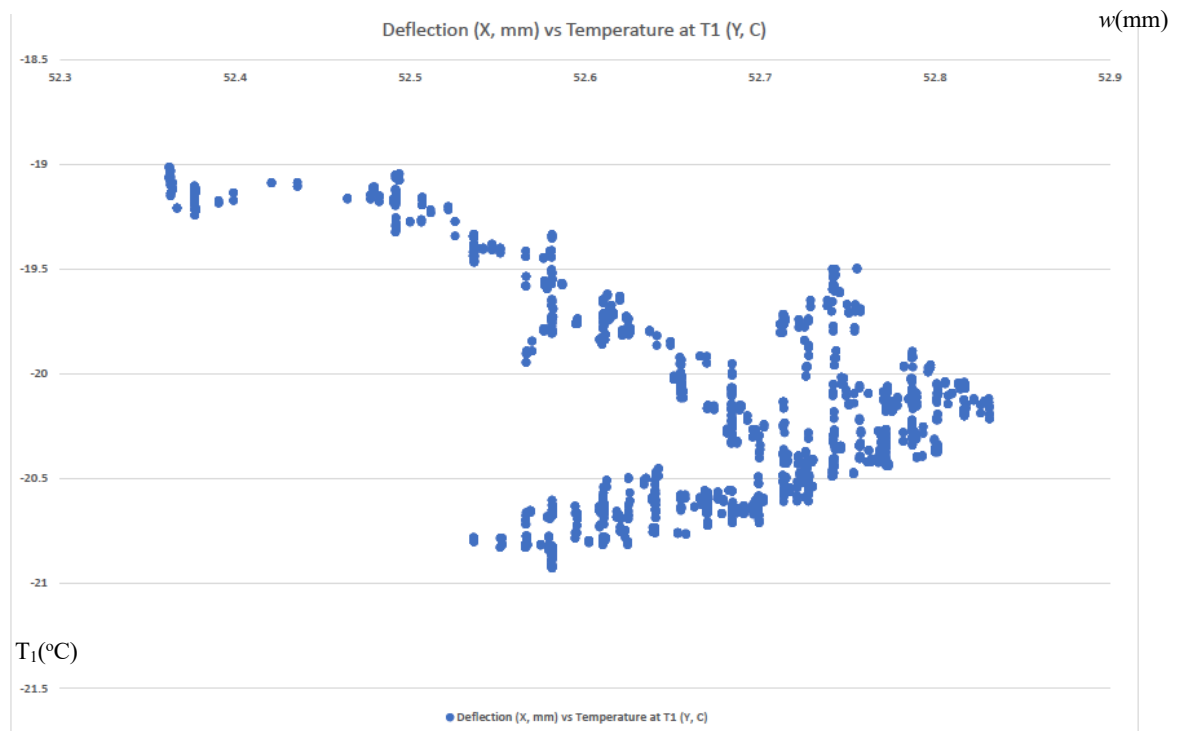
Figure 3.12. Deflection versus mechanical loading for two different thermal environments.

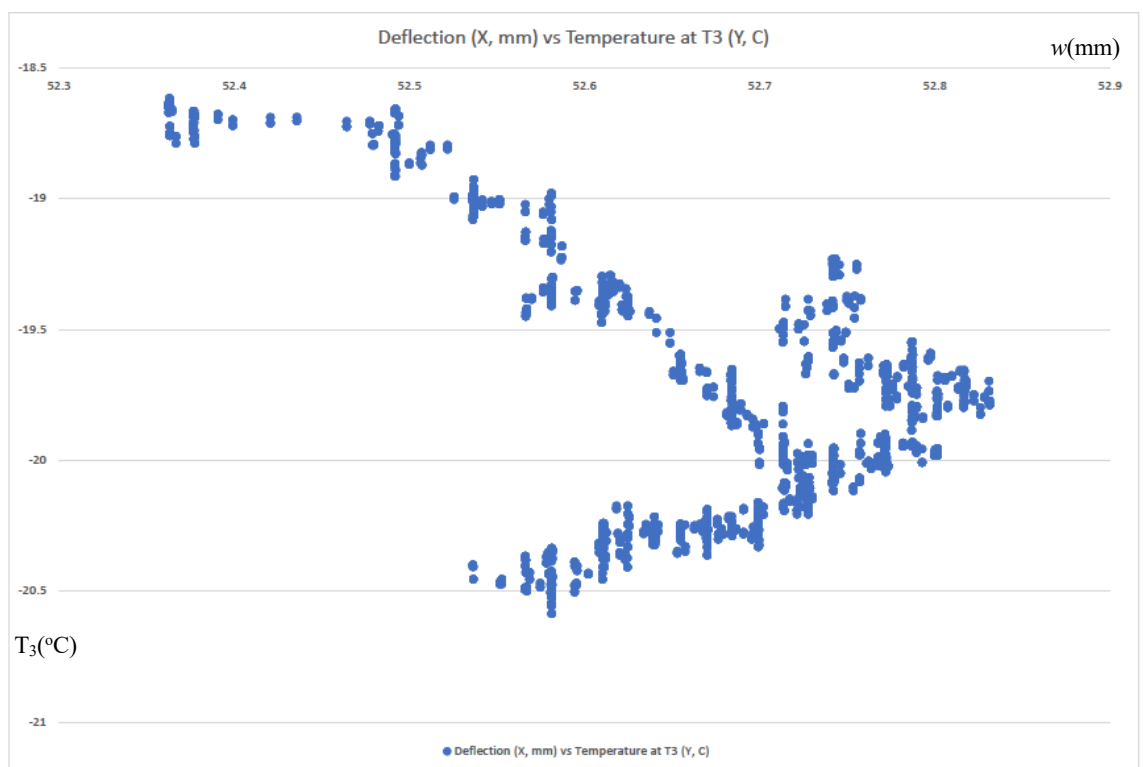
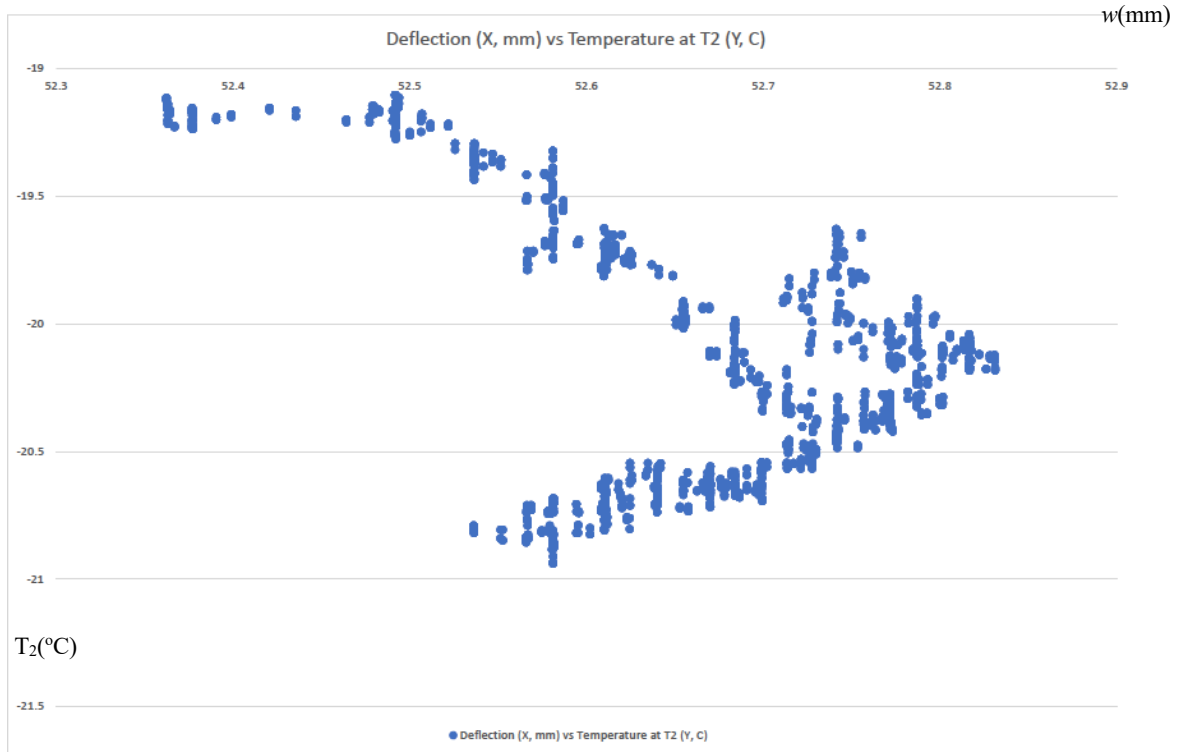
It can be seen in Figure 3.12 that the load - deflection characteristics are consistent for both positive and negative environmental temperatures, meaning that the progressive changes in the panel deformation, this being the deflection at the load line, in response to the external loading on the panel has the same general trend for both hot and cool environmental conditions. There is no hysteretic behaviour in the load-deflection curve at the ambient temperature, but this characteristic then progresses into a clearer open hysteretic loop form as the environment gets colder or hotter, and it can be noted that in the case of the colder environments the width (i.e. the peak-to-peak) of the loop is wider. The peak-to-peak of the hysteretic loading and unloading loop is generally bigger for negative environmental temperatures, at around 0.1 mm, than for the positive cases, but does build up again to approximately 0.1 mm at an environmental temperature of +100 °C. The fact that there is no hysteresis effect apparent at the ambient temperature environment means that the loading and unloading progression there is characterised by the same values of deflection. This is in line with findings from [181] where either an additional deflection took place, or a shift in vibration frequency [183] was evident, in response to the thermal changes, especially as the temperature was increased up to extreme values. This means that the deflection values for panels which have undergone some deformation do not come back to the initial values after removal of loading for hotter and especially for colder environments, and are characterised by some residual stress, and characterised thermodynamically by irreversibility. The extent of this residual stress is dependent on the environmental temperature to which the panel is exposed. Thus, another correction factor has to be introduced to account for the effect of the environmental temperature on the magnitude of the deformation of the panel. This further confirms the presence of thermo-mechanical coupling, especially for the colder environments. Therefore, in order to produce an accurate prediction of the deformation progression and regression during the loading and unloading processes, the environmental temperature should be the basis for introducing another correction factor for the deflection responses.

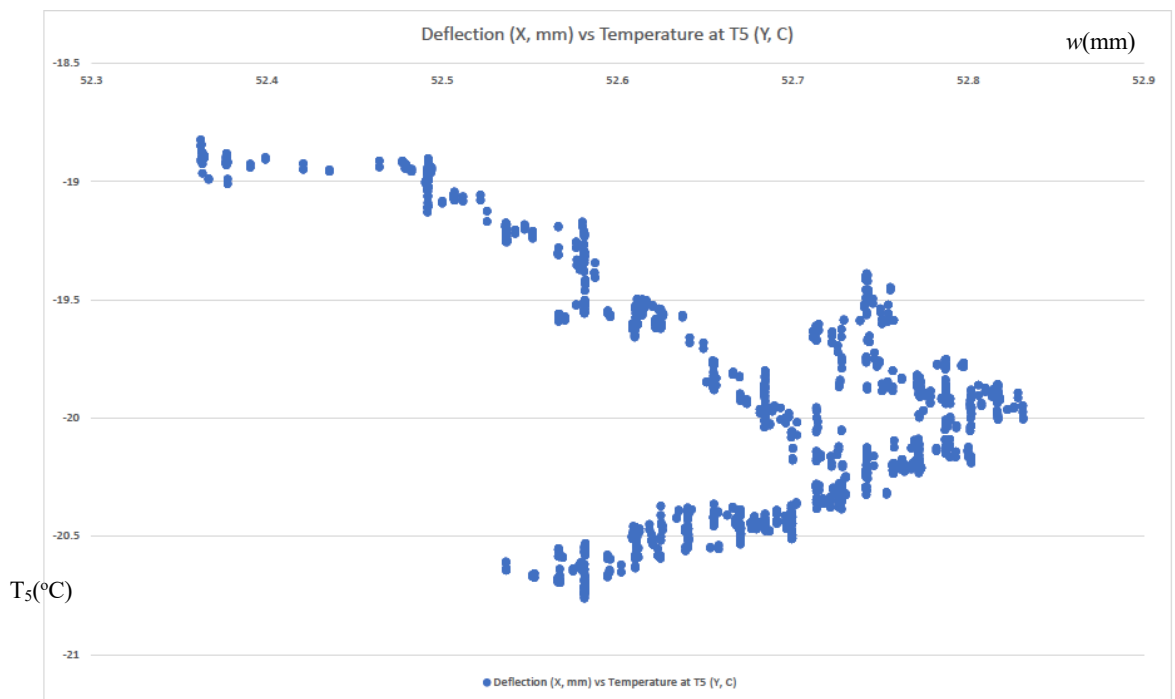
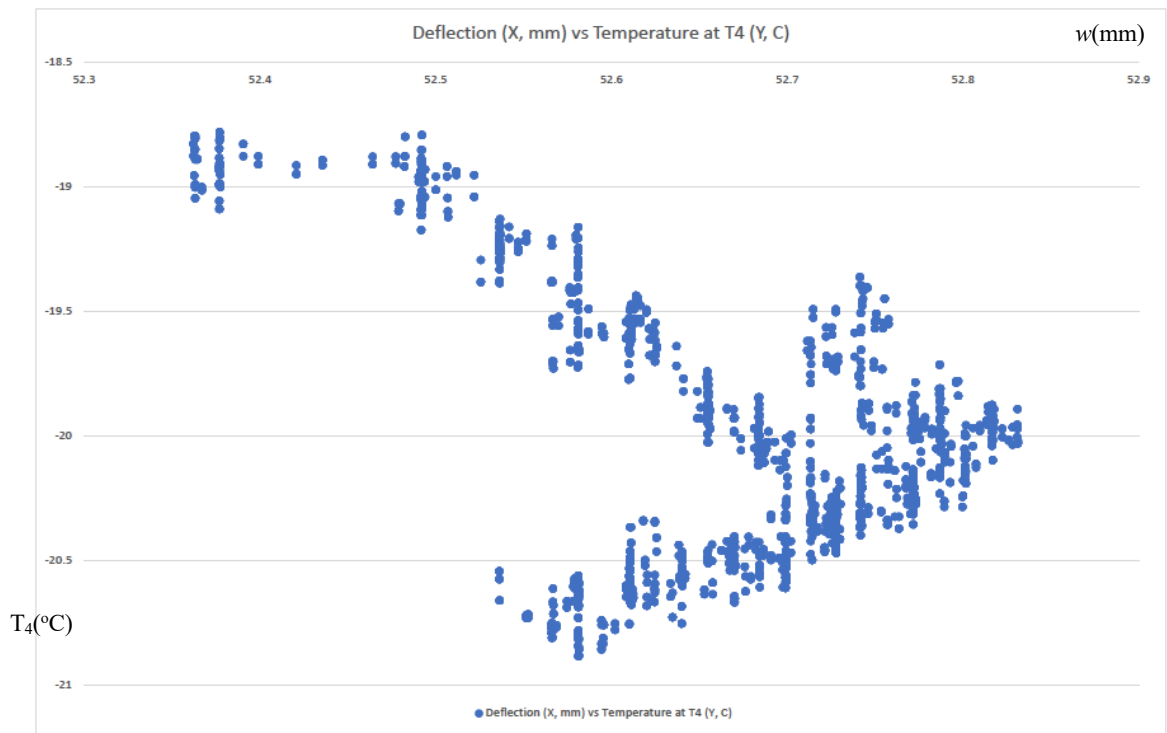
3.2.4 Effect of deflection on the temperature distribution along the surface and through the thickness of the panel in extreme environmental temperatures

This penultimate analysis was undertaken to find out if the environmental temperature affects not only the deflection of the panel but also if the deflection affects the temperature distribution along the panel. This potentially provides a novel perspective into the general problem, since the combination of dynamic mechanic loading within extreme thermal environments has not been investigated before, to the author's knowledge. To investigate this it was decided to consider how the temperature distribution in certain locations of the panel is affected by the induced deflection. Thus, the temperature feedback from thermocouples T_1 - T_6 at different locations of the panel has been considered against deflection within the discrete fixed thermal environmental temperatures of $-150\text{ }^\circ\text{C}$, $-100\text{ }^\circ\text{C}$, $-60\text{ }^\circ\text{C}$, $-40\text{ }^\circ\text{C}$, $-20\text{ }^\circ\text{C}$, $20\text{ }^\circ\text{C}$, $40\text{ }^\circ\text{C}$, $60\text{ }^\circ\text{C}$, $80\text{ }^\circ\text{C}$, and $100\text{ }^\circ\text{C}$.

Results are shown in Figure 3.13 for all 6 thermocouples at the environmental temperature of $-20\text{ }^\circ\text{C}$ as an example, again together with the summative findings made available from the data taken for all the environmental conditions. Graphical data for other environmental conditions are openly available from [213].







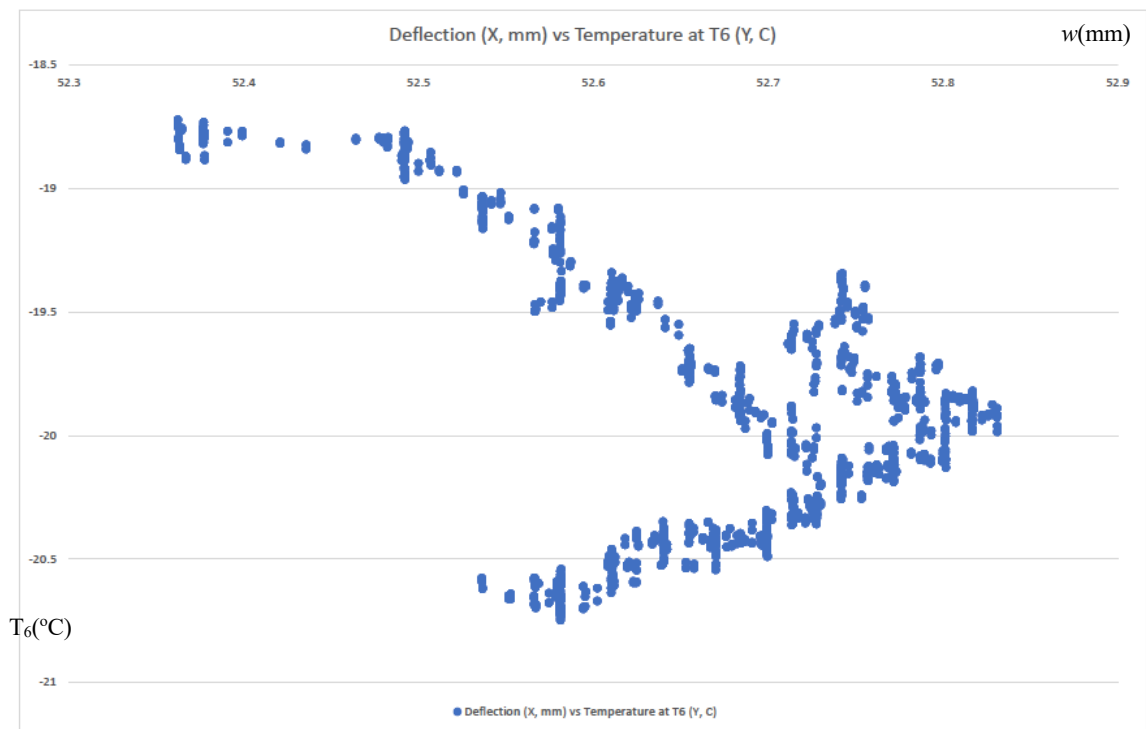
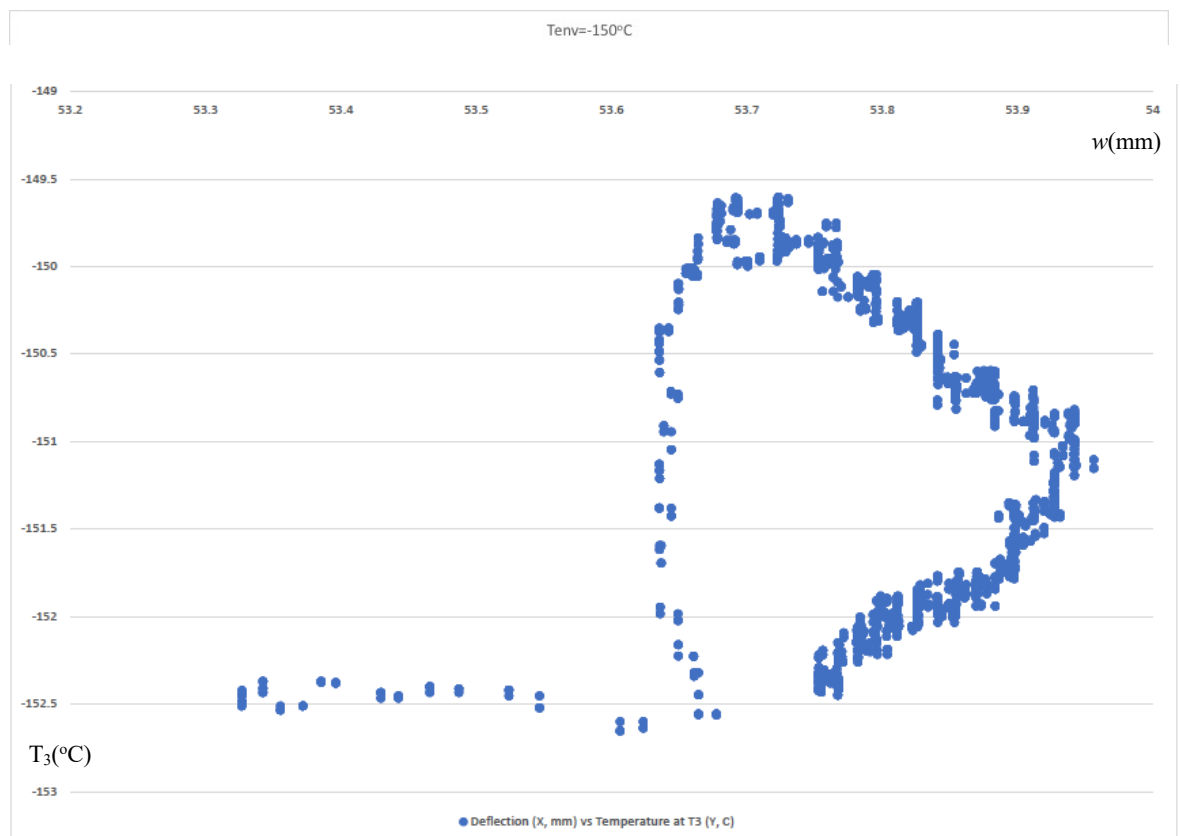


Figure 3.13. Fluctuation of the temperature feedback data from the thermocouples $T_1^{w(\text{mm})}$ T_6 with respect to the increasing deflection due to a loading ramped up to 150 N and then back to 0 N, subjected to an environmental temperature of $-20\text{ }^\circ\text{C}$.

As can be noted from Figure 3.13, the readings from all the thermocouples show the same trend with respect to the deflection within a certain environmental temperature T_{env} , except for the case of the ambient temperature for which T_5 shows a flatter hysteresis loop, and T_6 shows a wider loop for this thermocouple. This means that the deflection response from the surface of the panel appears to be the same, independent of the location of the thermocouples, except for the case of ambient environmental temperature. Although the thermal feedback is consistent for all thermocouples within a certain environment, there is evidence that the effect of the temperature of the environment T_{env} is significant and changes the trend of the deflection-temperature behaviour of the panel. For the environment characterised by a negative temperature the peak-to-peak temperature variation, with respect to the deflection is around $2.5\text{ }^\circ\text{C}$, and for the positive temperature environment the peak-to-peak decreases from $1.2\text{ }^\circ\text{C}$ down to $0.5\text{ }^\circ\text{C}$ at the hottest environment of $+100\text{ }^\circ\text{C}$. There is also a dramatic difference in the way the thermal changes occur in the panel due to the deformation for different extreme environmental temperatures. This means the connection between the thermal properties of the panel and its deformation, and how they affect each other as the deformation progresses, and

essentially what defines the thermo-mechanical coupling, is affected by the environmental temperature within which the panel is immersed. There is hysteresis to be found in the thermal response to the deformation, and this gets more significant in the colder environments, which was observed earlier on as well. The thermal properties of the panel demonstrate this through a swing in the temperature of the panel of 2.5 °C during the unloading process. The patterns of open and closed hysteresis loops are the same as for the loading-temperature feedback from the thermocouples in section 3.3.1, closing for the more extreme environmental temperatures above +60 °C and below -100 °C. As in section 3.3.1 the hysteresis loop is closed to a single value at the maximum value of deflection. This confirms that there is a direct connection between loading and deflection, and the readings are consistent with the data presented for loading versus temperature of the panel. This is a good control point for verifying that the results are consistent for deflection and loading.

It is interesting to note that when going into the extremely cold or hot environments the pattern of temperature feedback from the panel, with respect to the deflection, bifurcates as shown in Figure 3.14. This demonstrates how significantly the thermal changes in the environment can change the qualitative aspects of the coupling between the thermal properties and the mechanical deformation of the panel.



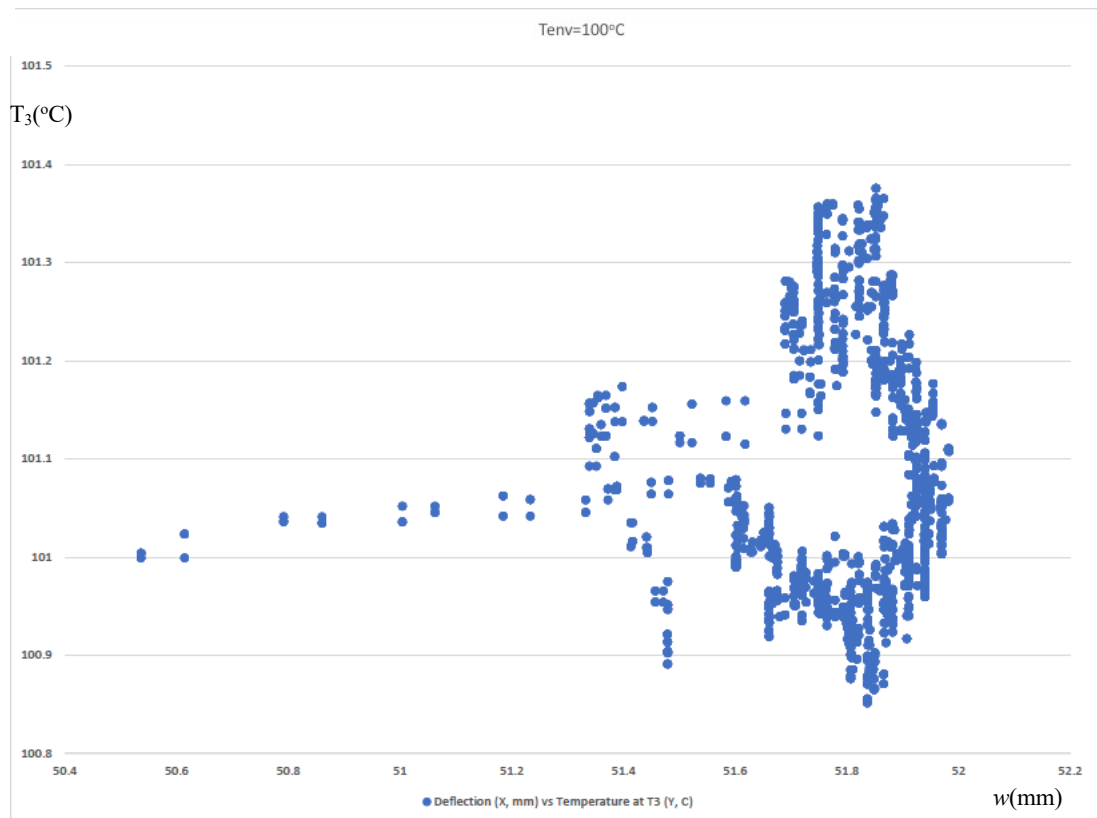
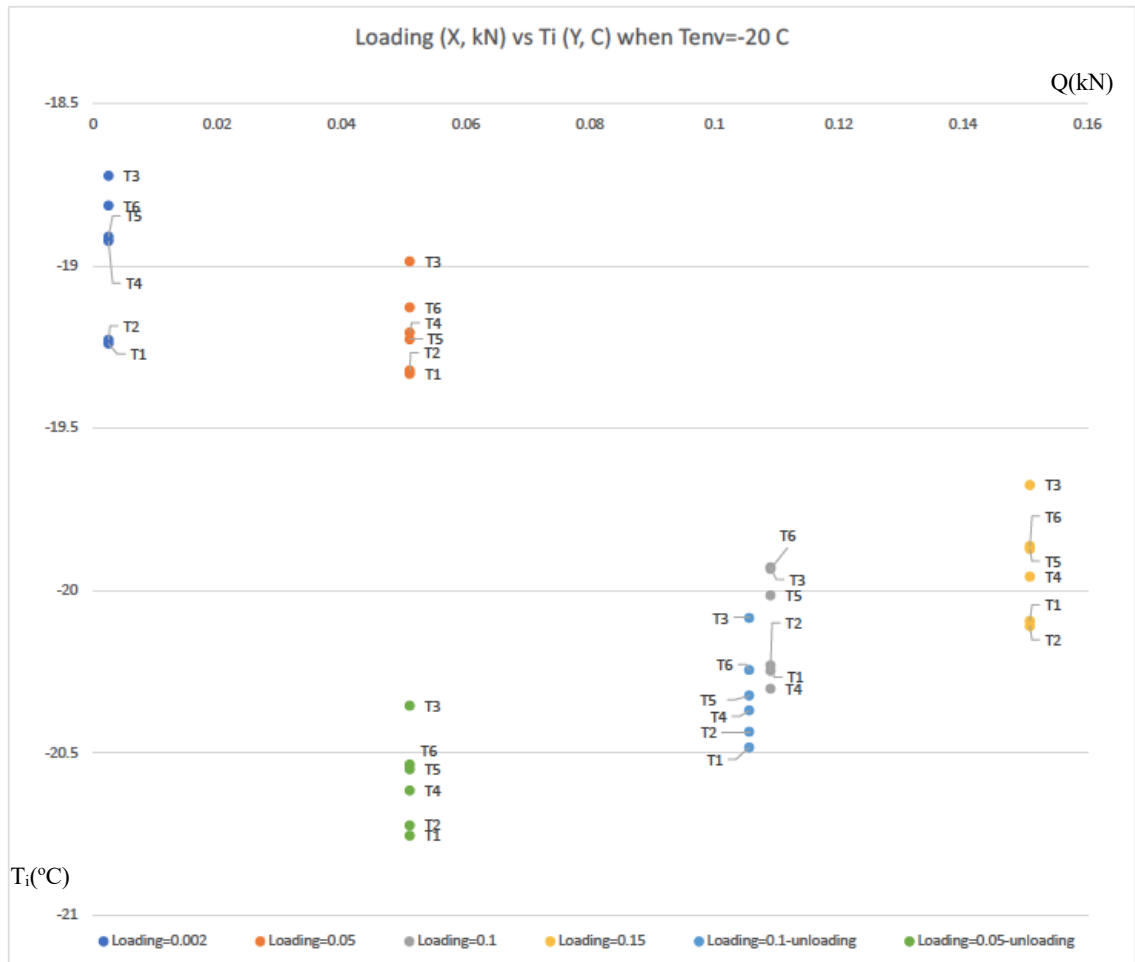


Figure 3.14. Fluctuation of the temperature feedback from the thermocouple T₃ with respect to the increasing deflection due to loading up to 150 N and back to 0 N, within the environments of (a) -150 °C and (b) 100 °C.

3.3. Effect of simultaneous mechanical loading and extreme environmental temperatures on the heating-up and cooling-down processes within the panel

Thermocouple data at fixed loading and unloading points can be used to understand in a clearer way how the temperature is distributed along the whole panel, and how thermal conditions of certain areas of the panel are affected by the mechanical loading as well as the extreme environmental temperature. For this part of the study the following specific loading values were taken, noting that a small amount of approximation was inevitable in extracting this particular data: 0 N, 50 N, 100 N, 150 N, 100 N [unloading], 50 N [unloading] within the environmental temperatures of -150 °C, -100 °C, -60 °C, -40 °C, -20 °C, 20 °C, 40 °C, 60 °C, 80 °C, and 100 °C.

Results are shown in Figure 3.15 for the environmental temperatures of -20 °C and -150 °C as examples, noting that summative findings are openly available for all the environmental conditions mentioned, from [213].



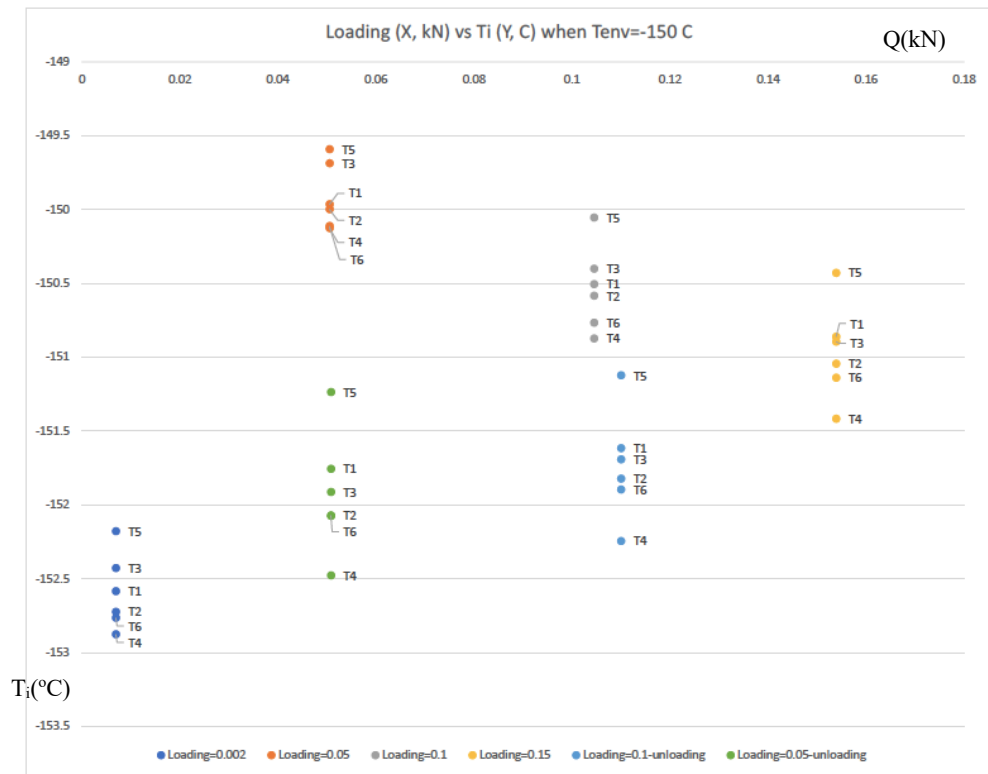


Figure 3.15. Temperature feedback from the thermocouples T₁-T₆ with respect to the loading ramping up to 150 N and back to 0 N within the environments of (a) -20 °C and (b) -150 °C.

From Figure 3.15(b) it can be noted that thermocouples T₃ and T₅ record the highest temperature readings for most cases, and for a variety of environmental temperatures, and T₄ and T₆ sense the lowest temperature readings. The exception to this seems to be at the environmental temperatures closest to 0 °C, i.e. +20 °C and -20 °C, for which T₁ and T₂ detect the lowest temperature and at +40 °C when the highest temperature is demonstrated by T₄ and the lowest by T₅. From this data it is evident that in the environment where the temperature is close to the ambient the skins do heat up faster than the honeycomb core, however this trend disappears as the temperature moves to higher or lower extremes. As mentioned in section 3.3.2, the proximity of the strain gauges to the T₄ and T₆ thermocouples seems to influence the response, and, as a result, those thermocouples sensed a lower panel skin temperature than thermocouples T₃ and T₅. It is possible to speculate from this that any reasonably significant geometrical imperfections, or extrusions, probably have to be accounted for when attempting to assimilate the thermal properties of the panel into the thermoelastic performance with full accuracy.

3.4. Conclusions

As a result of the analyses subsequently conducted on the data generated by this experiment it has been found that there is strong evidence of the thermo-mechanical coupling effect when the panel is immersed in an environment at an extreme temperature, and is loaded mechanically.

There are experimental precedents for the coupling of mechanical and thermal loading in certain structures, notably in NiTi-PU composites [184], and also for complex internal dissipation effects within aluminium structural elements constructed into the form of braced shear panels [184]. In addition, it is shown in [215] that hysteretic responses to mechanical loading are typically encountered in many different types of composite, in addition to plasticity effects due to isotropic strain hardening where post-yield hardening is observed. It is also pointed out in the conclusions to [215] that a mathematical model that properly represents the inherent hysteresis in a composite can potentially be used as a basis for thermo-mechanical simulations. It is interesting to note that the experimental results obtained in [184] explicitly confirm that for a given composition of the NiTi-PU composite the bending modulus and the area of the load-deflection hysteresis loops both decrease with increasing test temperature over the investigated range of 0 – 50 °C. It is the case that the phenomenology discussed in [184, 214, 215] is specific to those particular material compositions, and different in each study, and therefore not exactly the same as reported here. But it is important to note that there are parallels in terms of the stated thermo-mechanical dependencies with some of the key observations made in this chapter.

On the basis of the experimental work reported in this chapter, there is evidence that thermal loading caused by the extreme environment affects the deflection value and the level of residual stresses, and conversely the mechanical loading affects the heat accumulation and distribution within the panel. The following points may be made to elaborate a little further on this general finding.

- The extreme temperature environment does not cause an accumulation of any residual heat after unloading. However, during the processes of loading and unloading there is evidence of thermo-mechanical coupling which results in the presence of extra heat internally within the structure compared to the heat available from the environment, and

this can result in a temperature swing of up to 3 °C. If the environmental temperature is close to the ambient temperature (specifically noted for the cases at -40 °C, -20 °C, and ambient) then there is an accumulation of residual heat within the panel which is still present to a large extent even at the point of complete unloading of the deformed sample, indicating thermodynamic irreversibility for an environmental temperature close to the nominal ambient.

- It was found that the environmental temperature effect is significant and that it changes the trend of the deflection - temperature behaviour of the panel. The deflection of the panel affects the distribution of the heat within the panel resulting in a localised temperature swing in the material of around 2.5 °C if deformed in a cool environment and up to 1.2 °C in warmer environments;

- There was no evidence of residual stress accumulation only in the case of the panel operating in the ambient temperature environment. For negative environmental temperatures and the higher positive temperatures the deflection values for a panel which has already undergone some deformation did not come back to the initial values after the removal of the loading, and were characterised by the presence of some residual stress, and thermodynamic irreversibility. The extent of this residual stress is dependent on the environmental temperature within which the panel is immersed. For the sample considered here the deflection during unloading in a very cold environment could reach up 0.1mm lower than the corresponding value during loading. This confirms the damaging effect of thermal loading on the mechanical properties described in [185-187].

- Although there was no significant thermal swing initiated by deflection within the panel geometry at a certain fixed environmental temperature, there is a dramatic difference in the way the thermal changes occur in the panel due to the deformation for different hot or cold environments. This means that the connection between the thermal properties of the panel and deformation, and how they affect each other as the deformation progresses - constituting the thermo-mechanical coupling within the panel, is defined by the temperature of the environment in which the panel is immersed. There is hysteresis to be found in the thermal response to the deformation, which gets more significant for the colder environments, and the thermal properties of the panel demonstrate this through a swing in the temperature of the panel of 2.5°C during the unloading process.

Therefore, in order to produce an accurate prediction of the deformation progression and regression during the loading and unloading processes, as well as the heat distribution along the panel geometry, it is recommended to introduce corresponding correction factors to account for:

- the effect of the environmental temperature on the magnitudes of the deformation of the panel;
- the initial thermal conditions of a panel which has undergone a mechanical deformation, even if the loading has been completely removed. The thermal properties for such a panel cannot necessarily be assumed to be fully controlled by the value of the environmental temperature if the panel also undergoes mechanical loading.

This study has shown that the panel tends to cool down in a relatively uniform way in all three dimensions. However, the heating up process is not uniform and there is some localised heating resulting in certain hot-spot areas accumulating more heat than others. This is the case if the panel is in an environmental temperature between ambient and +80 °C. In the more extreme thermal environment the sample heats up more evenly and reflects the temperature of the environment linearly, even while being mechanically loaded. It can be noted that in [211] where an attached battery resulted in higher heat, there was also evidence of increased heat around the attached strain gauges, noting that these are passive devices that are conducting small currents due to their connection to the conditioning bridge electronics.

From the data obtained during this experimental work it is evident that in the environment with the temperature close to the ambient the skins do heat up faster than the honeycomb core, however this trend disappears as the environmental temperature moves to higher or lower extremes.

An interesting observation is that when going into the more extreme hot or cold environments the pattern of temperature feedback from the panel, with respect to the deflection, bifurcates, as shown in Figure 3.14, demonstrating how significant the thermal changes of the environment can be for the pattern of the coupling between the thermal properties and the mechanical deformation of the panel.

4. Correlation of the results from the analytical model with the experimental data

In this chapter an analytical-numerical coupled model has been derived to predict the effects of dynamic thermo-mechanical loading on aluminium composite panels specifically in the form of metallic skin sandwich structures, for the purposes of enhanced design of spacecraft structures where the environmental conditions comprise combined mechanical and thermal loading. The mechanical loading can arise as a consequence of localised structural dynamics, and the thermal loading is attributable principally to the effects of solar irradiation and eclipse during a satellite's orbit, and together they have the potential to influence de-point adversely, in particular. On this basis the importance of a combined physics model has been highlighted for dealing with the generalised thermoelastic problem. The research analysis presented in this chapter has considered the results from the refined model described in Chapter 2 and then developed for an aerospace application in the form of an analytical-numerical solution for the thermoelastic problem in aluminium composite panels. The results obtained were correlated with the data obtained from the experimental work presented in Chapter 3 to verify the accuracy of the analytical model. The model is explored for a panel under a range of centrally located static mechanical loads, in conjunction with thermal loading provided in the form of various controlled and elevated environmental temperature functions, all for prescribed physical boundary conditions to simulate the experimental tests performed in Chapter 3.

The sandwich panel considered is composed of two grades of aluminium alloy. For the outer faces of thickness 0.38×10^{-3} m, an Al-2024 alloy is used, whilst an Al-5056 alloy foil is used to form the hexagonal honeycomb core. This core is of depth 14.24×10^{-3} m and comprises a foil of thickness 0.0254×10^{-3} m. The mechanical and thermal properties of these materials, excluding the adhesive, are summarised in Tables 3.1 & 3.2, noting that the data in Table 3.1 does not contain explicit information on the thin film adhesive bonding of the core to the skin. It should be noted that the density of the Al-5056 core is much lower than that of the Al-2024 skins because it is an average figure covering the material itself and the volumetrically large voids within the honeycomb. This data is also consistent with the data used in previous chapters.

A numerical simulation of the analytical model is presented for the solutions obtained for the system (2.20) with full nonlinear coupling terms, and by exploiting the powerful numerical functions within NDSolve. The loading is considered as a combined thermo-mechanical load consisting of a constant thermal component and a dynamic mechanical component.

The plate-like panel under consideration is of the dimensions provided in Table 4.1. These properties, as well as loading conditions and boundary and initial conditions, are considered for verification of the performance of the model against the experimental results presented in Chapter 3.

Table 4.1: Dimensions of Sandwich Panel Sample

Length, a (x10 ⁻³ m)	Width, b (x10 ⁻³ m)	Face Thickness (x10 ⁻³ m)	Honeycomb layer thickness (x10 ⁻³ m)	Honeycomb Cell size (m)	Foil Thickness (m)
300	100	0.38	14.24	0.0048 (3/16 in)	2.54 x10 ⁻⁵ m (0.001 in)

The panel was considered to be simply supported and was analysed under dynamic mechanical loading increasing up to 160 N while being positioned within an environmental chamber exhibiting thermal loading in the form of a variety of thermal environments. Within the analytical model thermal loading was applied by means of imposing different environmental temperatures in order to represent free heat exchange conditions similar to those of the experiment in Chapter 3, and mechanical loading was taken as a dynamically increasing normal force governed by $Q=q(t)=10*t$ to simulate a ramped increase up to 160N after 16s had elapsed, and this is applied centrally to the top-face sheet.

It should be pointed out that in the experiment an initial displacement was introduced to more clearly portray the gradual displacement that emerged naturally within the experiment, therefore in order to calculate the actual displacement from the graphs presented in Appendix C the initial displacement has to be deducted (see example in Fig.4.1).

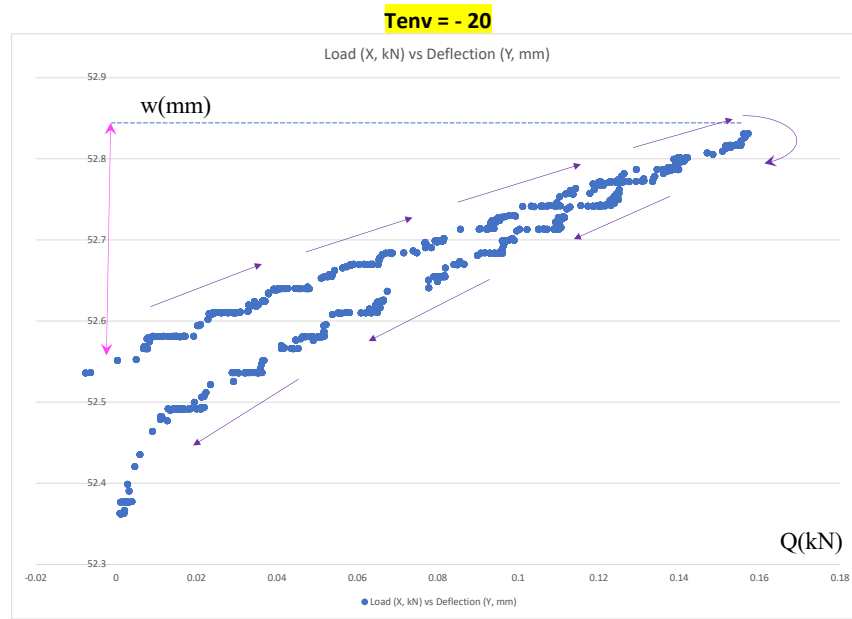


Figure 4.1. Subtraction of initial displacement from the raw experimental data.

Based on the results presented graphically in Appendix C the maximum value of the actual displacement is summarised in Table 4.2. These outputs from the experiment will be used for verification of the model discussed in this chapter.

Table 4.2: Maximum actual displacement presented in Appendix C at maximum mechanical loading of 160N

<i>Temperature of environment (°C)</i>										
	100	80	60	40	20	-20	-40	-60	-100	-150
<i>Maximum displacement ($\times 10^{-3} m$)</i>	0.7	0.5	0.45	0.45	0.4	0.3	0.3	0.25	0.25	0.2

4.1 Displacement distribution in response to the dynamic mechanical loading and variable environmental temperature

When elevated temperature conditions apply at the outer faces of the sandwich panel, representing the free heat exchange condition, these faces will heat up first of all, with the heat then distributing from the outer faces inwards towards the centre of the core. To understand the process of displacement due to the heating-up process, as well as the

characteristics of the thermal gradient along the thickness, constant value of the environmental surround temperature of 100°C , 80°C , 60°C , 40°C and ambient as 20°C were applied with the ambient reference temperature set to 20°C , and a solution for the system of Eq. (2.20) was obtained using the NDSolve function in *Mathematica* and presented in Fig 4.2-4.6, corresponding to the temperature of the environment.

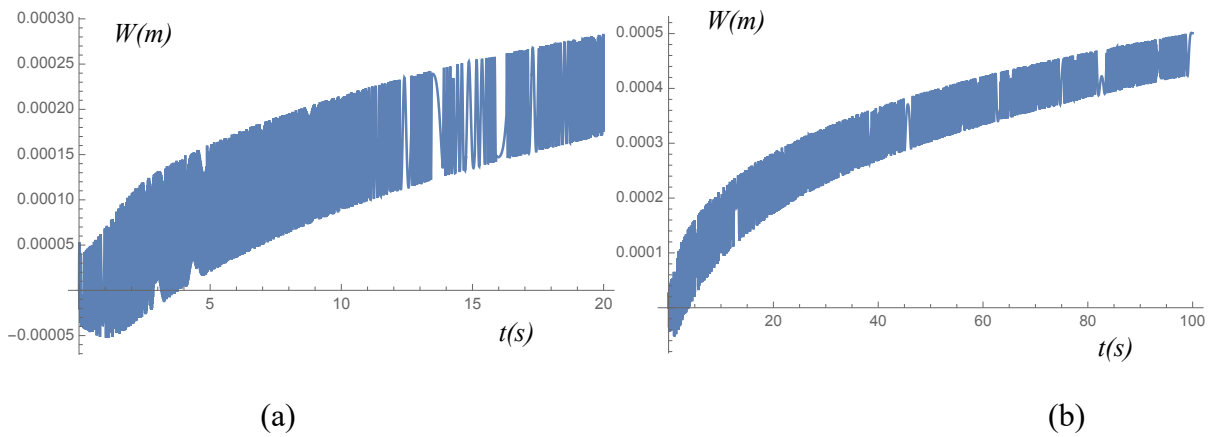


Figure 4.2. Displacement response in the time domain when subjected to increasing mechanical loading (a) up to 160 N at 16s and (b) – further loading in time, within an environmental temperature of 100°C .

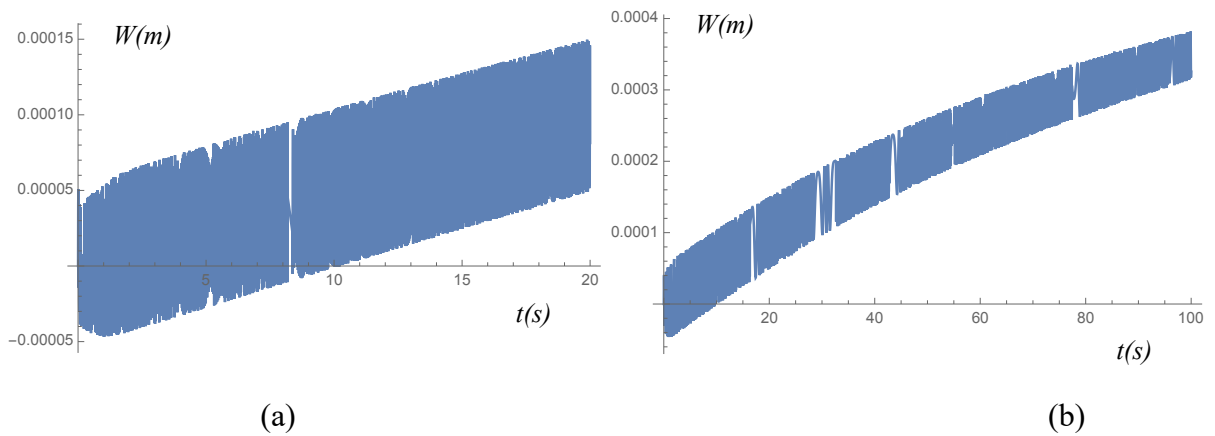


Figure 4.3. Displacement response in the time domain when subjected to increasing mechanical loading (a) up to 160 N at 16s and (b) – further loading in time, within an environmental temperature of 80°C .

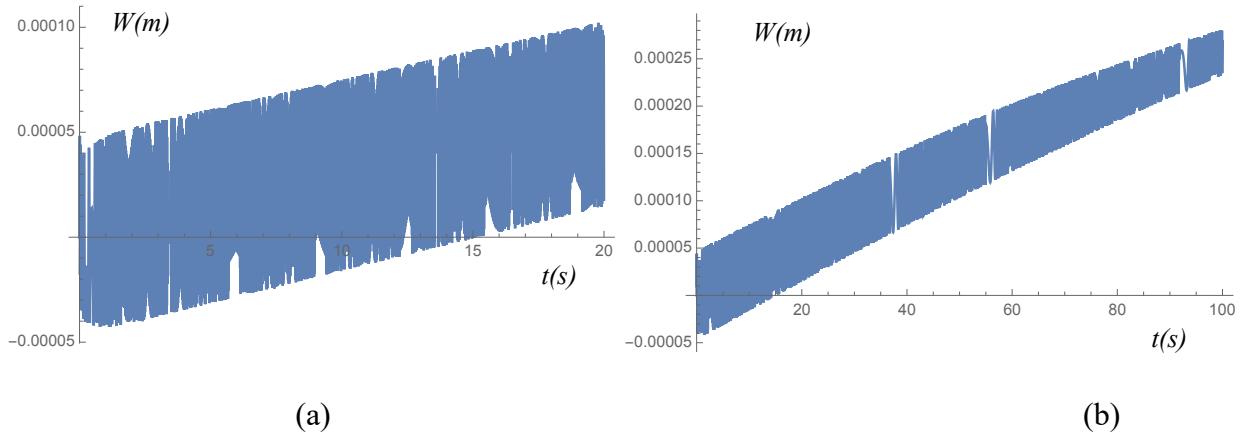


Figure 4.4. Displacement response in the time domain when subjected to increasing mechanical loading (a) up to 160 N at 16s and (b) – further loading in time, within an environmental temperature of $60^{\circ}C$.

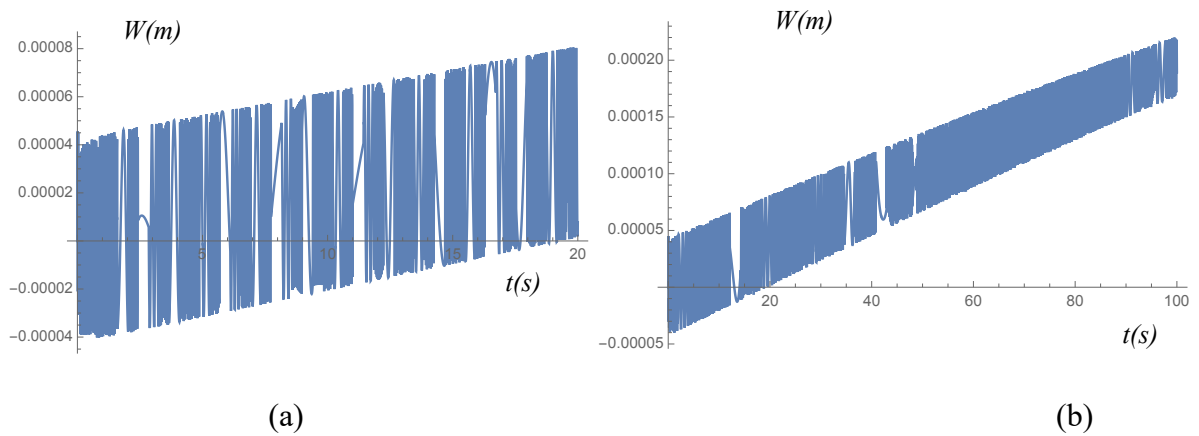


Figure 4.5. Displacement response in the time domain when subjected to increasing mechanical loading (a) up to 160 N at 16s and (b) – further loading in time, within an environmental temperature of $40^{\circ}C$.

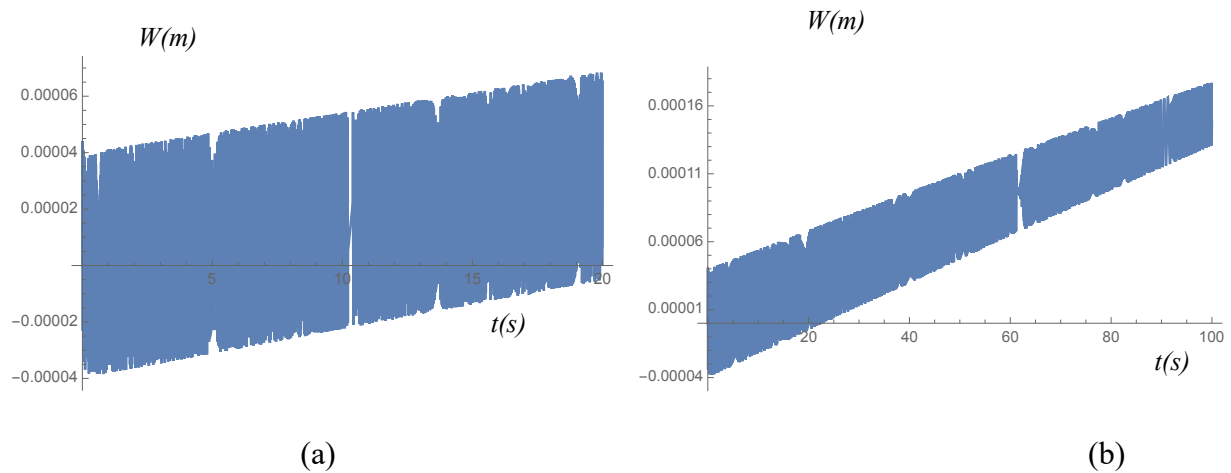


Figure 4.6. Displacement response in the time domain when subjected to increasing mechanical loading (a) up to 160 N at 16s and (b) – further loading in time, within an environment of ambient temperature.

Figures 4.2-4.6 (a) demonstrate the maximum value of the displacement after 16s when it has reached 160N according to the loading being represented by $q(t)=10*t$, as corresponding with the experimental study in [225]. As can be seen in Figs 4.2-4.6 (a) there is evidence of an increasing trend in the maximum displacement value, where it is seen to be increasing with the elevating temperature of the environment. This confirms the pattern of behaviour demonstrated in Chapter 3 and is summarised in Table 4.2. It can be justified by the presence of a softening effect of the material within hot environments. This trend becomes even more evident with time, as can be observed in Figs 4.2-4.6 (b).

In Figs. 4.2-4.6 we can also see clearly the reflection of the dynamically increasing mechanical loading in an almost linearly increasing behaviour of the displacement response. This accords with practical expectations for a plate under this form of loading, as well as with the results for loading up 160 N from the experiment in Chapter 3.

The principal features of the displacement responses are the transient over time and the largely symmetrical peak to peak amplitudes. It is also important to note that the peak-to-peak transient disturbance increases with the harshness of the environmental temperature, and this confirms the coupling between the environmental heat and the mechanical deformation, and the fact that harsh environments bring in a destabilising effect into the panel's response when undergoing mechanical loading.

To understand the process of the displacement distribution due to the cooler or even extreme environmental conditions constant environmental surround temperatures of -20°C , -40°C , -60°C , -100°C and -150°C were applied. A solution for the system of Eq. (2.20) was again obtained using the NDSolve function in *Mathematica* and presented in Fig 4.7-4.11 corresponding to the environmental temperature.

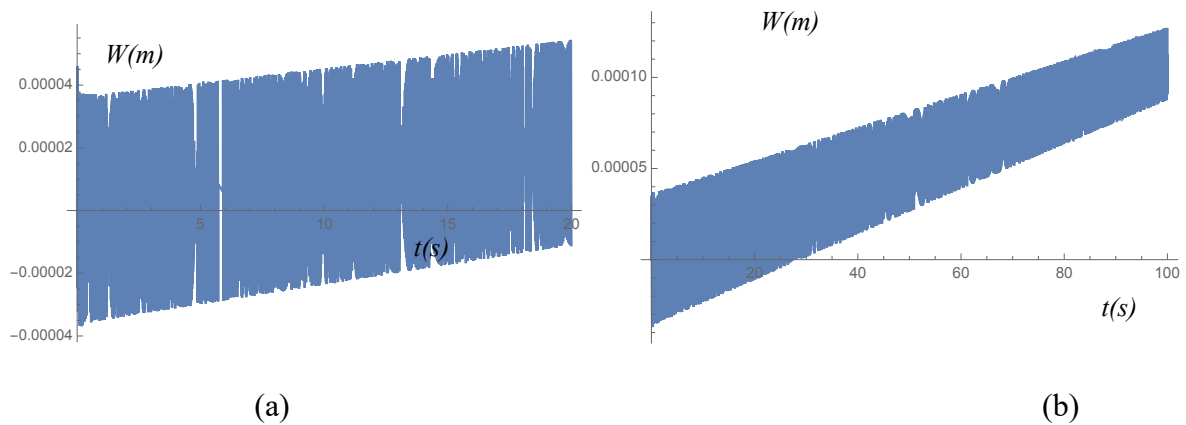


Figure 4.7. Displacement response in the time domain when subjected to increasing mechanical loading (a) up to 160 N at 16s and (b) – further loading in time, within an environmental temperature of -20°C .

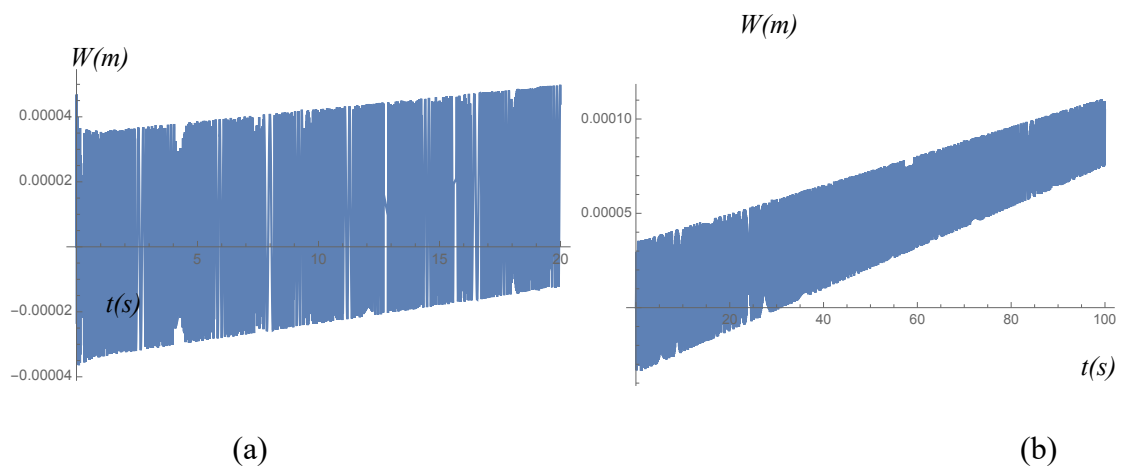


Figure 4.8. Displacement response in the time domain when subjected to increasing mechanical loading (a) up to 160 N at 16s and (b) – further loading in time, within an environmental temperature of -40°C .

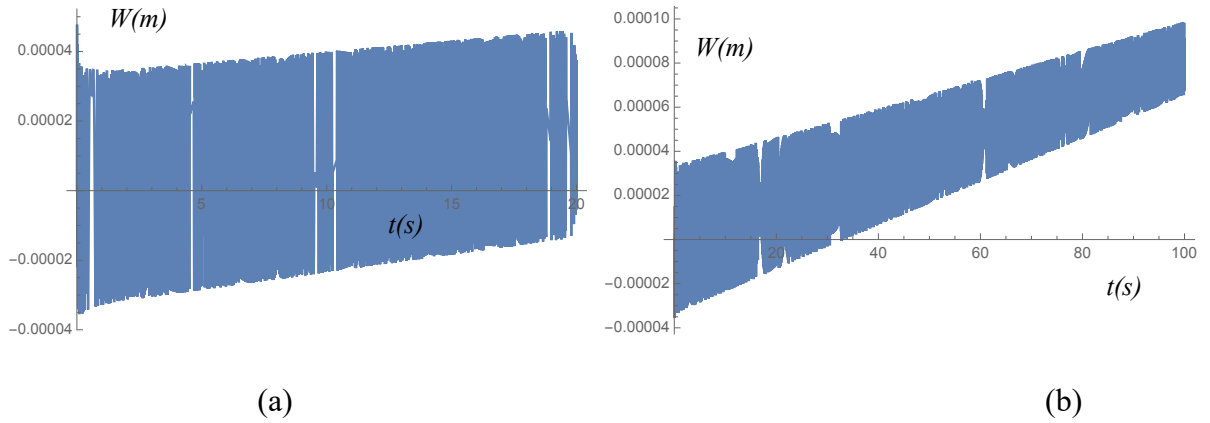


Figure 4.9. Displacement response in the time domain when subjected to increasing mechanical loading (a) up to 160 N at 16s and (b) – further loading in time, within an environmental temperature of -60°C .

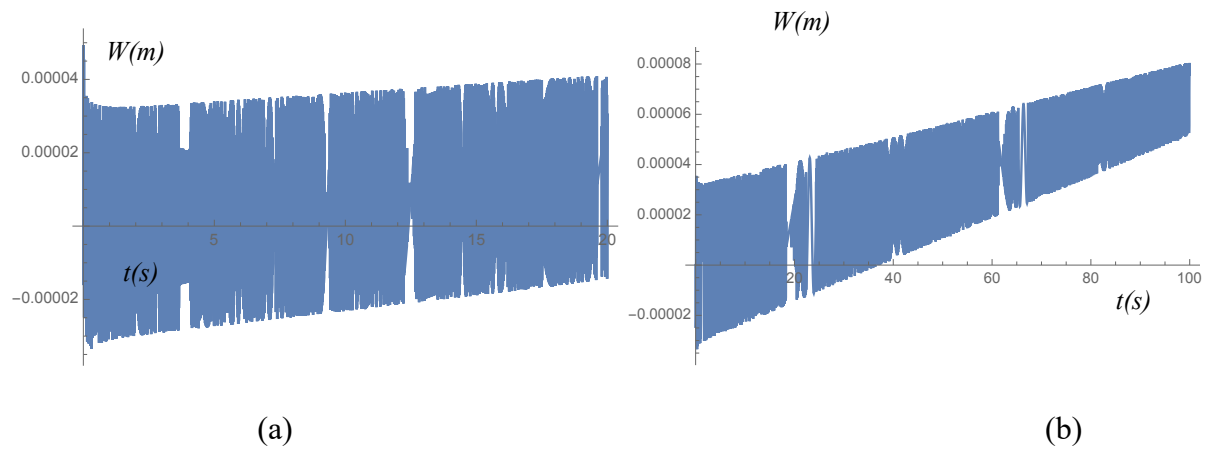


Figure 4.10. Displacement response in the time domain when subjected to increasing mechanical loading (a) up to 160 N at 16s and (b) – further loading in time, within an environmental temperature of -100°C .

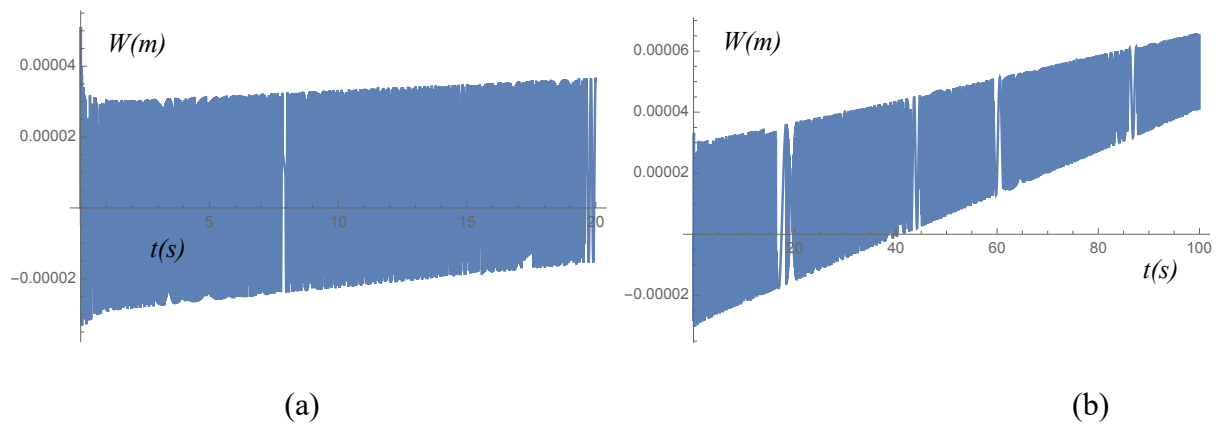


Figure 4.11. Displacement response in the time domain when subjected to increasing mechanical loading (a) up to 160 N at 16s and (b) – further loading in time, within an environmental temperature of -150°C .

An analysis of the response of the panel to the same increasing mechanical loading $q(t)=10*t$ but for a colder environment going down to the harsh extreme of -150°C (Figs 4.7-4.11), confirms the trend demonstrated in Chapter 3 which is summarised in Table 4.3. The maximum value of the displacement is reached at 16s and corresponds to 160N and is decreasing with decreasing environmental temperature (Figs 4.7-4.11 (a)) and this can again be justified by a hardening effect of the material within the colder environment. This trend becomes even more evident at times beyond 16s, as can be observed in Figs 4.7-4.11 (b). This hardening effect in a colder, harsher, environment also impacts on the transient response. The symmetrical peak to peak amplitude response of displacement clearly decreases, demonstrating stiffer structural properties. However, this ‘suppression’ of the amplitude might be characterised by a higher frequency response. This confirms the coupling between environmental temperature and mechanical deformation, and the fact that a colder environment is still characterised by a destabilising effect into the panel’s response when undergoing mechanical loading.

In Figs. 4.7-4.11 we can clearly see again the reflection of the dynamically increasing mechanical loading in an almost linearly increasing behaviour of the displacement response.

Table 4.3: Maximum actual displacement presented in [213] and obtained from analytical model at a maximum mechanical loading of 160 N

Temperature of environment (°C)										
	100	80	60	40	20	-20	-40	-60	-100	-150
Maximum displacement Experimental ($\times 10^{-3}$ m)	0.7	0.5	0.45	0.45	0.4	0.3	0.3	0.25	0.25	0.2
Maximum displacement Analytical ($\times 10^{-3}$ m)	0.3	0.15	0.1	0.08	0.06	0.053	0.05	0.045	0.04	0.03

It has to be pointed out that the disparity in the results from an experimental study and analytical model in in Table 4.3 occurs due to the possible inconsistency in material properties. Some properties required for the analytical model were not available for the sample tested in Chapter 3, therefore typical properties for Al-2024 and Al-5056 were assumed for some of the required material parameters.

In order to verify the response of the model the case of a larger plate of dimensions 0.8 x 0.8 m, otherwise with the same properties and under the same mechanical loading in an environment of 100°C, was considered with the results shown in Fig. 4.12.

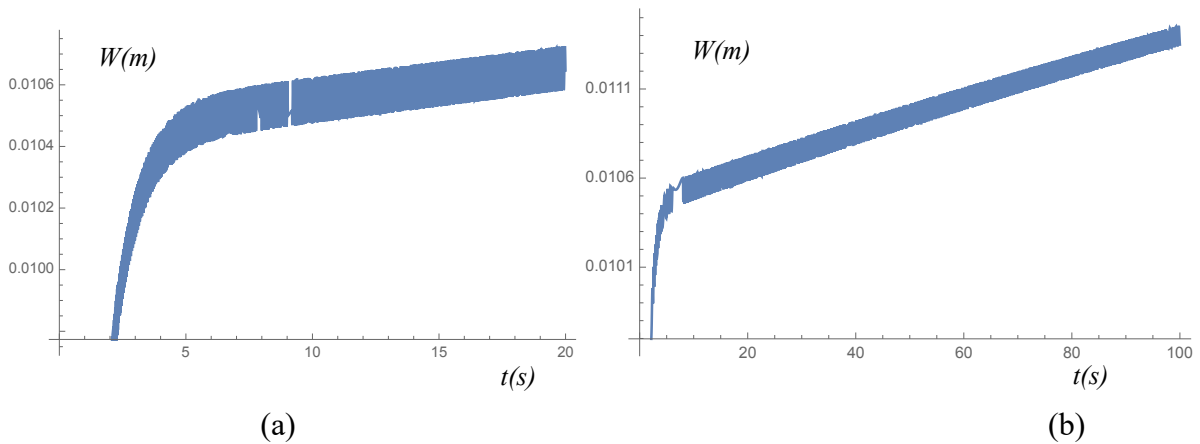


Figure 4.12. Displacement response for a larger panel 0.8x0.8 m when subjected to increasing mechanical loading up to 160 N within an environment of 100°C.

Comparing the response in Fig. 4.12 with the results presented in Fig. 4.2, the panel under consideration with the same thickness, but larger length and width dimensions, responds with a larger displacement, as expected for a large thin plate.

4.2 Temperature distribution along the thickness of the panel in response to the dynamic mechanical loading and variable environmental temperature

When elevated temperature conditions apply at the outer faces of the sandwich panel, representing the free heat exchange condition, these faces will heat up first of all, with the heat then distributing from the outer faces inwards towards the centre of the core. However, because of differences in the material of the skins and the honeycomb core, it is reasonable to predict a nonlinear temperature distribution along the thickness of the panel. This effect is very difficult to explore experimentally, especially if the panel is relatively thin. But the model applied in this paper allows us to predict the dynamic distribution of the heat along the thickness of the panel.

To understand the process of heating up or cooling down of the panel in response to the high or low environmental temperature, the following values for the constant environmental surround temperature were taken, 100°C, 80°C, 60°C, 40°C, ambient at 20°C and then down to -20°C, -40°C, -60°C, -100°C and -150°C in line with the investigation of the displacement response considered in Chapter 2 and 3. A solution for the system of Eq. (2.20) and Eq. (2.7) was obtained using the NDSolve function in *Mathematica*TM and presented in Fig 4.14-4.16 for environmental temperatures of 100°C, 20°C, -150°C and in Appendix F for 80°C, 60°C, 40°C and then -20°C, -40°C, -60°C, -100°C.

It should be noted that the thickness of the panel in Figs 4.14-4.16 is along the X coordinate and the temperature readings are along the Y coordinate, as shown schematically in Fig 4.13.

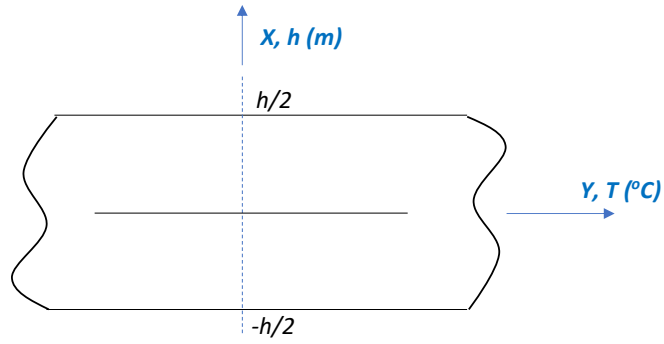


Figure 4.13. Representation of the panel for interpretation of temperature distribution across the thickness in Figs 4.14-4.16

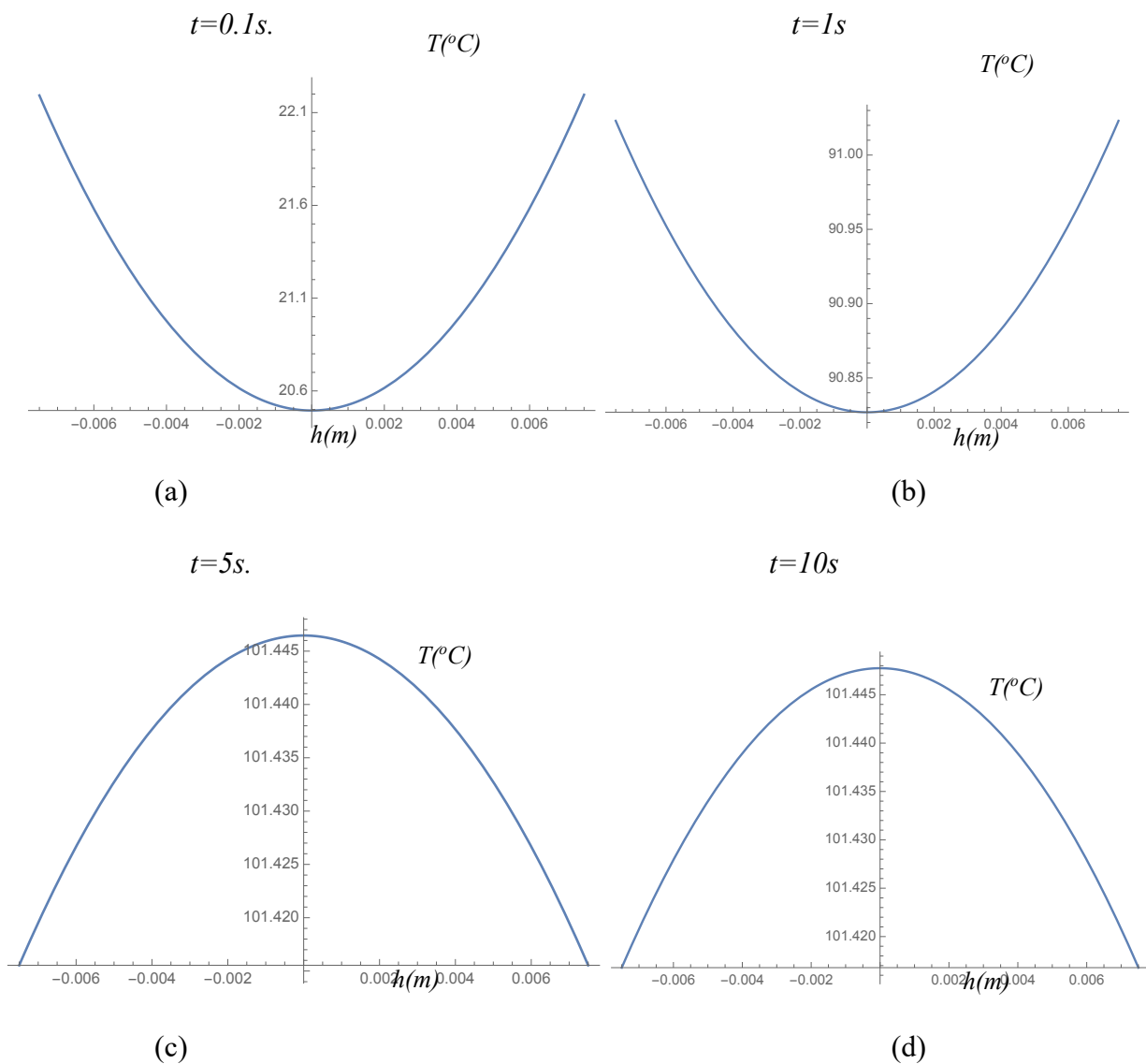


Figure 4.14. Temperature distribution across the thickness of the panel (x coordinate) when the panel is under dynamic mechanical loading and in an environmental soak temperature of 100 $^{\circ}$ C, presented for different instants in time.

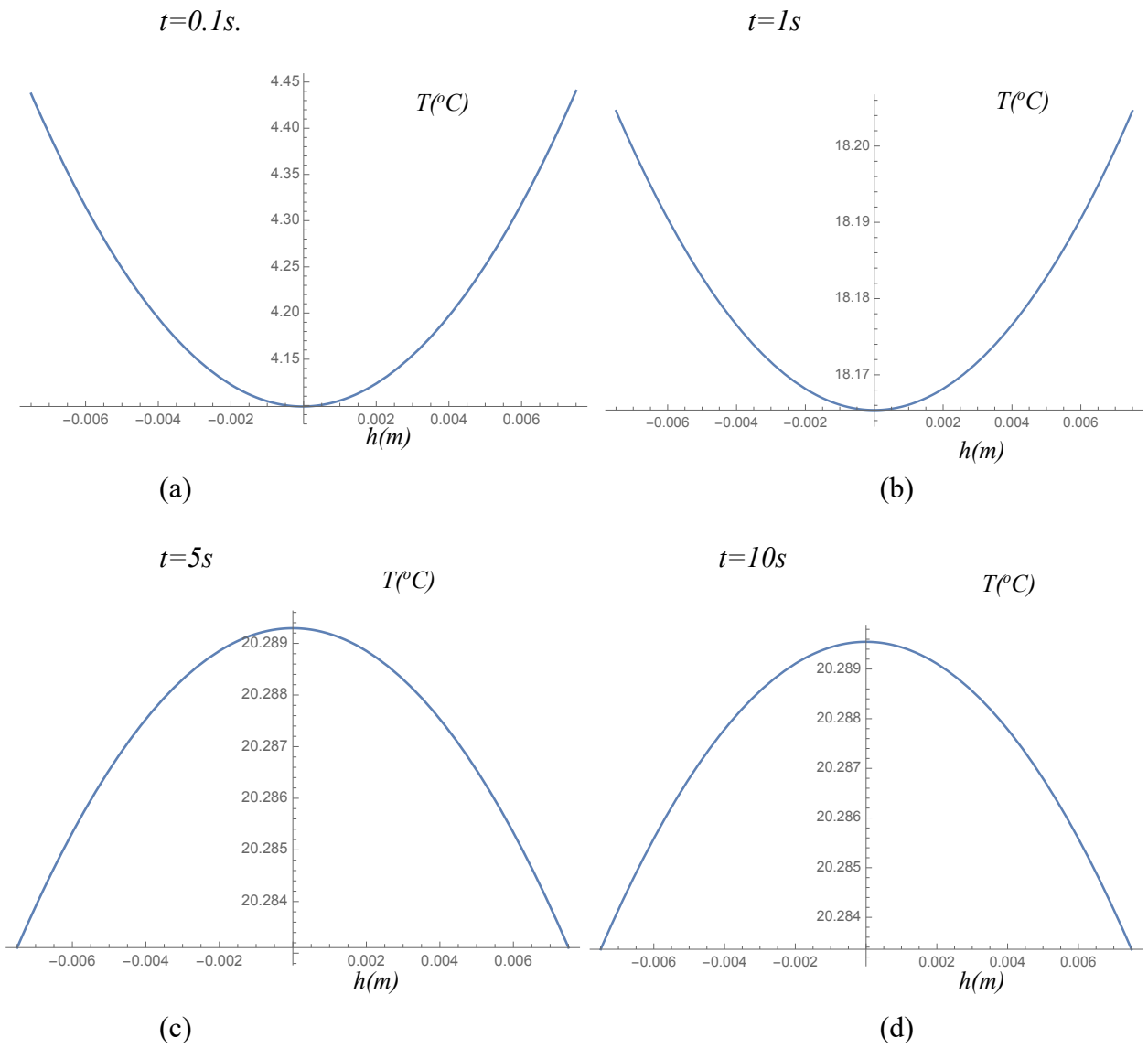
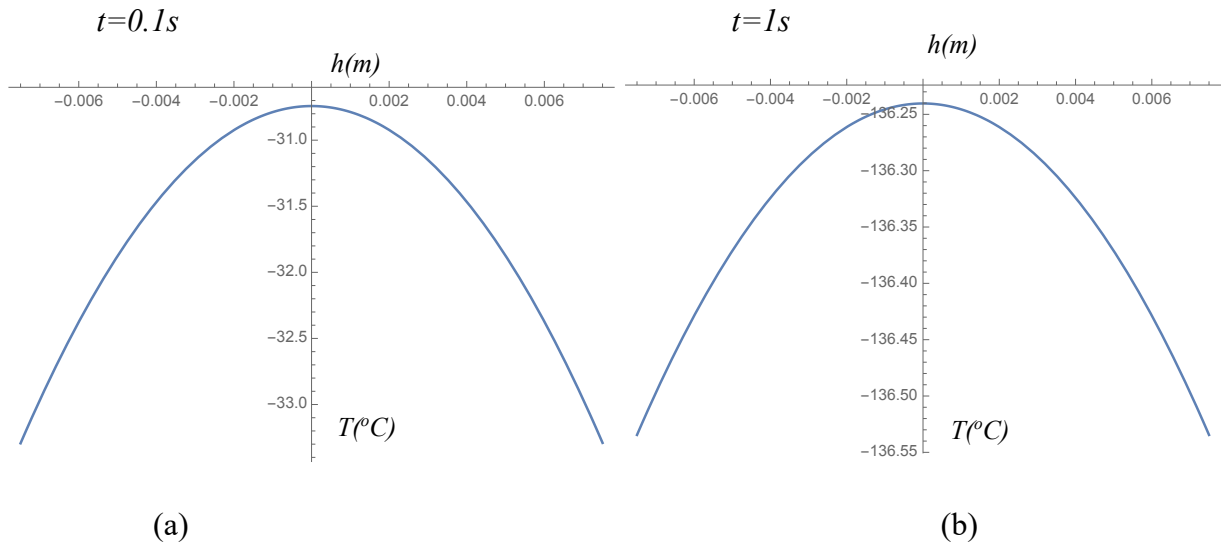


Figure 4.15. Temperature distribution across the thickness of the panel (x coordinate) when the panel is under dynamic mechanical loading and in an environmental soak temperature of $20^{\circ}C$, presented for different instants in time.



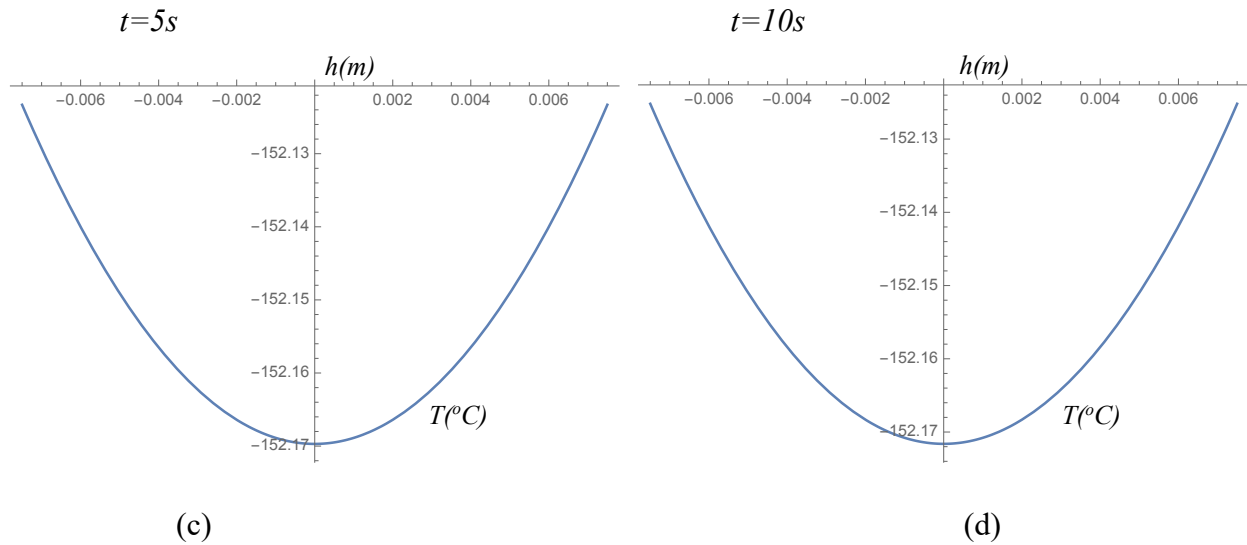


Figure 4.16. Temperature distribution across the thickness of the panel (x coordinate) when the panel is under dynamic mechanical loading and in an environmental soak temperature of $-150^{\circ}C$, presented for different instants in time.

By fixing the time steps and observing the progression of the temperature distribution through the plate we see the main stages of the temperature stabilisation process that are also described in [174]. In brief, this amounts to the following. By applying heat to the plate through an elevated environmental soak temperature the temperature distribution through the thickness is as shown in Fig. 4.14(a), with the temperature of the honeycomb core being close to the top skin temperature but slightly cooler by $1.8^{\circ}C$, and after 1s (Fig.4.14(b)) this stabilises and settles within a small difference of $0.2^{\circ}C$ between that of the skin temperature and the honeycomb core. The process of reaching the equilibrium temperature due to the plate heating-up progresses further with time, and after 5s an equilibrium temperature is reached and the profile thereafter remains constant in time exhibiting a small difference in temperature between the core and the skins of about $0.03^{\circ}C$ (Fig. 4.14(c-d)).

On analysing the history of the thermal outputs over time for other environments in Figs. 4.15, 4.16 and in Appendix F, it is evident that the plate is undergoing a similar process of stabilisation, and reaches the equilibrium state with a small residual disparity in temperature between the skins and core.

From the parabolic output in Figs. 4.14 it is also obvious that at the start of the heating-up process (time step $t = 0.1s$), when the heat is only just starting to distribute through the thickness of the panel, the temperature in the middle is lower than in the skins. However, as the heating-up process progresses, the core, made of thinner honeycomb aluminium, tends to heat up slightly further demonstrating a higher temperature reading around $0.03^{\circ}C$ than that of the skins. A similar flip in the behaviour can be observed for the cooling process shown in Figs.4.16, with around $0.04^{\circ}C$ difference between the skins and the core temperature. These internal transformations due to the heating-up or cooling-down process could be the key to an explanation for the transient response demonstrated in the displacement response which is clearly driven by the environmental temperature.

4.3. Conclusions

1. A new modelling strategy for aluminium honeycomb composite panels widely applied in aerospace structures, has been considered in this thesis. The physics of dynamic thermal and mechanical loadings have been integrated into a conceptually straightforward and partially coupled modelling procedure coded in the *Mathematica*TM language which can accommodate different boundary conditions, dynamically varying thermal properties, and dynamic forms of mechanical loading.
2. In this chapter the panel presented in the experimental set up in Chapter 3 has been considered to verify the analytical model through comparison of the maximum displacement of the panel, as well as the influence of the environmental temperature on the magnitude of displacement induced by a dynamic mechanical loading. The same trend of the higher displacement response in hotter environments and the lower displacement response in cooler environments was found, confirming the associated predictions of the analytical model developed in Chapter 2. It was also found that the displacement response was characterised by the transient behaviour, dependent on the environmental temperature, confirming the coupled effects of thermal and mechanical loading.
3. The model was also used to predict the dynamic thermal response of the material within the thickness of the panel, demonstrating a nonlinear temperature distribution profile within the thickness of the panel which is very difficult to perform experimentally. It was also found that during the heating up process the core remains at a lower temperature than the skins were at the beginning of the heating up process. However,

there was also evidence of heating up of the core beyond the skin temperature by a very small amount. Although the difference between the temperature of the core and the skins at the end of the transformation was very small, it still gave an indication of some nonlinear transformational phenomena occurring within the thickness of the panel when undergoing mechanical loading within the harsher environments. This of course might be more significant for larger or thicker panels and could be particularly significant for large aerospace structures exposed to harsh thermal cycles.

4. These internal transformations due to the heating-up or cooling-down processes could be the key to the explanation of the transient response demonstrated in the displacement response as driven by the environmental temperature. It is also hypothesised that the frequency of the transient response might be higher due to the amplitude ‘suppression’ in cooler environments due to the material stiffening effect, which could potentially introduce a parasitic resonance contributing to the problem of de-point of the parent satellite structure. This is still to be investigated in future research.

5. It also should be concluded that inclusion of the coupling effect between mechanical and thermal phenomena is essential in the process of modelling since there is strong evidence of their influence on the final dynamic behaviour of the system, which can also potentially be significant due to the effect of resonance.

5. Discussion of the results from a Thermomechanical Finite Element Model for a Honeycomb Sandwich Panel

This chapter reflects on the FEM work performed under the supervision of the author of this thesis. The full output of this work is presented in Appendix H as a journal paper being prepared for submission for publication. In this chapter the main outcomes from the paper which relate to this PhD project are discussed. Particular attention is paid to the simulation results for the heat flux thermal loading conditions, since the experimental work was performed for free heat exchange conditions only.

During space operation, mechanical loading on the panels is typically small and is restricted to vibrational loads from either the operation of machinery on the structure (such as adjustable solar panels) or impacts with space debris. Therefore, we are continuing to concentrate on the low-level vibration for a honeycomb sandwich panel (HSP). From the FEM approach the simplest approach to modelling HSP behaviour is a simulation using the FE method to obtain a detailed 3D model. Up until as recently as 2006 this approach would generally have been dismissed as unrealistic due to the computational demands but is now much more feasible [228]. Alternatively, a continuum model can be developed. This assumes that portions of the panel can be modelled as a homogenous solid with orthotropic material properties. This approach has been well researched and widely used due to its significant simplifications. However certain limitations of this approach mean that localised effects cannot be represented and the core does not even provide any support across the surface of the face sheet [229].

2D models have also been explored by several researchers notably in [230] and [229] who both considered a range of methods of interpreting the honeycomb core as a 2D model.

As is evident from Chapter 1, technology for space and aircraft applications involving honeycomb based structures has progressed, and a need for higher precision modelling has become noticeably more acute. Previously it has been emphasised that modelling of both the effects of heat and vibration had been separated in FE models to minimise the computational cost. However, there is more and more evidence of coupling and important mutual interactions between these two phenomena. Therefore, considering the advancement in modern FE techniques an attempt to include the coupling effect of the thermo-mechanical behaviour in the FE model was undertaken in Appendix H. It was

also important to investigate the accuracy of different FE approaches and their computational cost, in comparison to the analytical model developed in Chapter 2.

5.1 FE Models developed in [Appendix H]

Following the approach adopted in Chapters 2-4 to investigate the effect of coupling in the FE model a HSP was subjected to thermo-mechanical loading under three-point bending.

The methodology for the model was separated into mechanical loading (the mechanical model) and a combination of thermal and mechanical effects (the thermo-mechanical model). The mechanical model was used for verification purposes with the data presented in [232] and thermo-mechanical model produced novel results which are significant for the current work presented in this thesis.

The HSP geometry, F1.5-T0.07-H15-L4 was chosen, following the work by Sun *et al* in [232] (Fig.5.1).

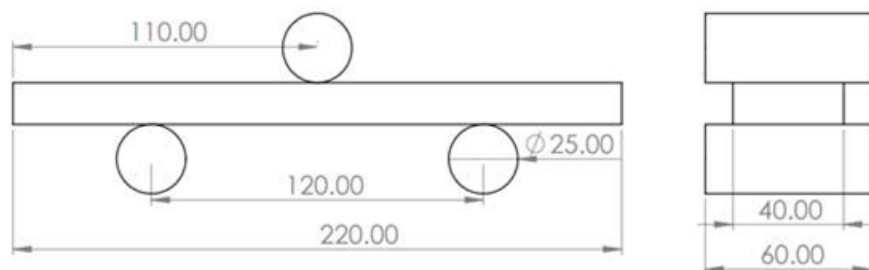


Figure 5.1. Three Point Bending Geometry

For this model the material properties from [232] were adopted for the geometry in ANSYS, the Young's modulus, the Poisson ratio, and the density for the A5052 skin alloy and the A3003 foil used for the honeycomb core, as summarised in Table 5.1. The choice of the material in this work was driven by the availability of the necessary material properties for a FEM simulation.

Table 5.1. Reference Material Properties from [232]

Material properties of skin panel (AA5052) and honeycomb core (AA3003).

Material	AA5052	AA3003
Young's modulus (GPa)	69	69
Yield strength (MPa)	138	94
Poisson's ratio	0.3	0.3
Density (kg/m ³)	2680	2680

In the Static Structural analysis the core was assigned as AA3003, the skin-plates as AA5052, and the supports were assigned as structural steel. Bonded contacts were used between the honeycomb and the skin, omitting the presence of a layer of adhesive, as can be seen in Figure 5.2.

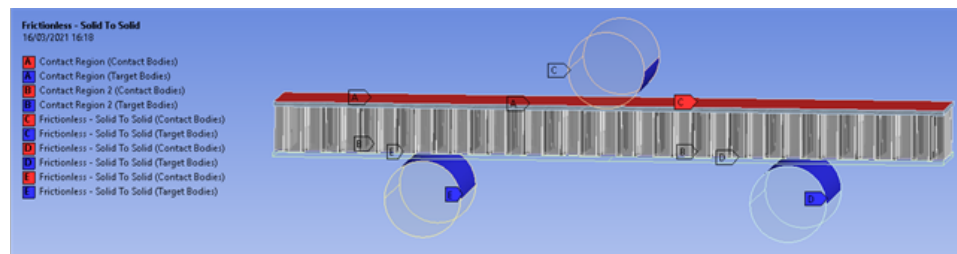


Figure 5.2. Geometrically Accurate Contact Modelling [Appendix H]

Frictionless contacts were used between the rods and the panel skins with the interface treatment set to “adjust to touch”. This allows the panel to slide against the supports during bending, simulating real world conditions.

The mesh size was controlled with body sizing, where both skin plates (hex elements) and core (tetrahedral elements) were sized at 2mm. The tetrahedral mesh (Figure 5.3) was a trade-off to minimise the computational cost and was kept the same for all analyses to ensure consistent behaviour.

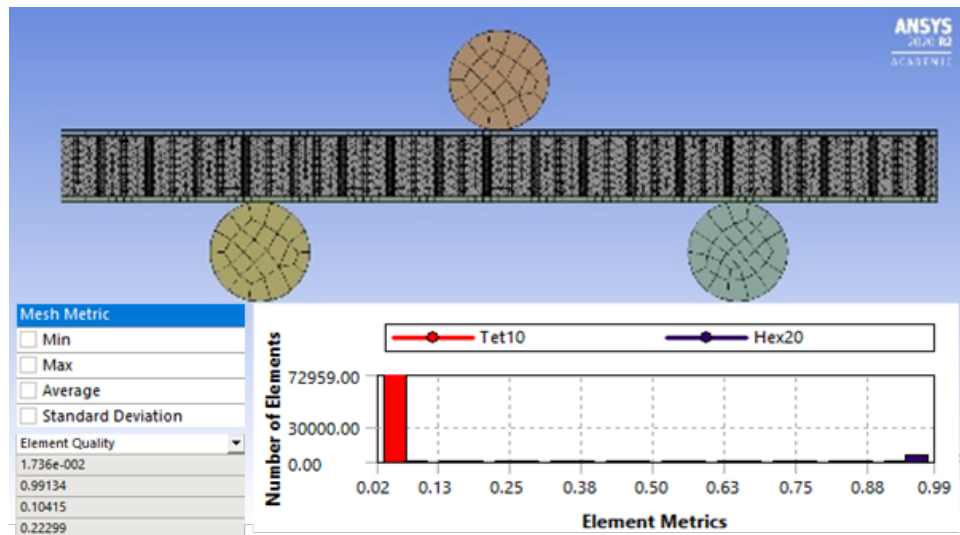


Figure 5.3. GA Tetrahedron Mesh Quality [Appendix H]

The two bottom rods were fixed in place, while the top rod was displaced in the negative y-direction by 1mm to create bending (Figure 5.4).

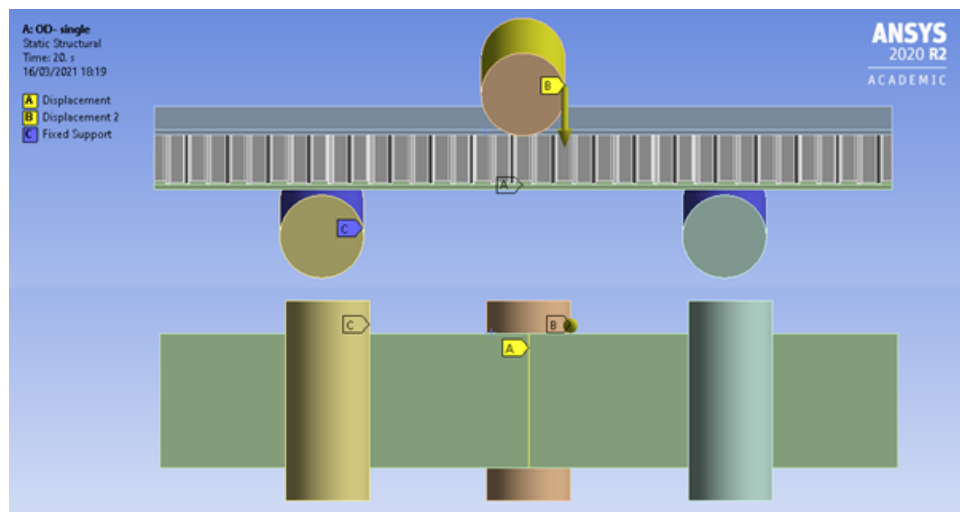


Figure 5.4. GA - Boundary Constraints [Appendix H]

The motion of the panel was constrained by creating a face split on the bottom face of the panel and applying a displacement constraint to that split. This constrained the centreline of the panel to move only in the y-direction. A force reaction probe was applied to the displaced rod to measure the load against the displacement, so that the model could be validated by the test data.

For temperature dependent analysis the data was sourced through the GRANTA *Edupack* material database considering the material with broadly the same chemical composition

and mechanical properties, the A3000/5000 series. The chosen materials are detailed in Table 5.2.

Table 4: Material Selection, Temperature Dependent Data

Edupack Material Data				
Material Properties	Paper AA5052	A5052H32	Paper AA3003	A3105 O
E (GPa)	69	70-73.6	69	69-72
Temperature dependent data?		yes		yes
Yield (MPa)	138	152-172	94	86-95
Temperature dependent data?	no	yes	no	no
Thermal Conductivity W/m°C	no	140-152	no	169-175
Specific Heat Capacity J/kg°C	no	963-1000	no	879-915
CTE (microstrains/°C)	no	23.7-24.9	no	23.4-24.6
Temperature dependent data?	no	Yes	no	yes

The free heat exchange conditions were simulated through varying the environmental temperature of a static structural analysis. This homogenous temperature distribution throughout the panel was a simplification of the actual temperature distribution, especially considering an application to space structures. However this was considered to be an acceptable simplification since the purposes of this analysis was to show general trends in mechanical response.

In the thermo-mechanical model with heat flux applied, a more complex varying temperature distribution was applied to the panel, in order to emulate more closely the conditions of a satellite in orbit. In the steady state thermal analysis (Figure 5.5), the desired temperature was set, and the convection at the opposing surfaces was adjusted such that the required temperature gradient was created within the panel. The supports were excluded from the static thermal analysis through the ‘element birth and death’ feature.

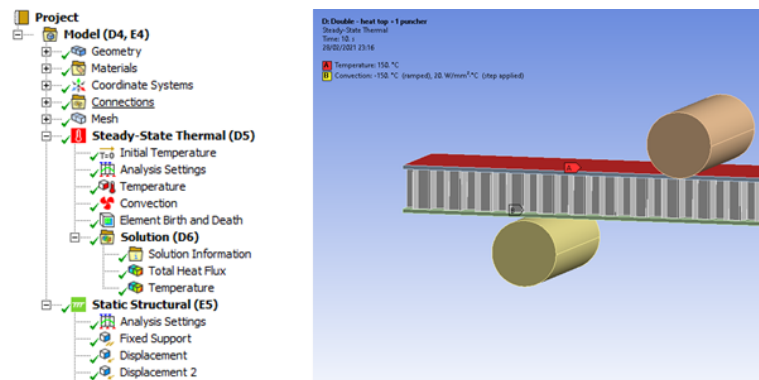


Figure 5.5. Steady State Thermal Boundary Conditions and Project Tree [Appendix H]

Multiple load case scenarios were created under extreme temperature gradients (22°C to 150°C as well as -150°C to 22°C) to observe correlation with results obtained from the application of an analytical model and also obtained experimentally in Chapters 2 and 3. Simulations for the panel were developed and analysed for scenarios with and without mechanical loading.

5.2. Simulation results for three FE models

To investigate the aspects of accuracy and computational cost, the panel was modelled by applying three different FE approaches: the 3D Geometrically Accurate Model, the 3D Continuum Model, and the 2D Continuum Model.

5.2.1. Output for 3D Geometrically Accurate Model

Considering the manufacturing techniques used for honeycomb cores it was concluded that the most common procedures were to introduce double wall thickness through the expansion method, and this was adopted for the 3D Geometrically Accurate Model (3D GAM). As can be seen in Fig. 5.6 the double thickness models demonstrated a more accurate prediction for the panel's behaviour.

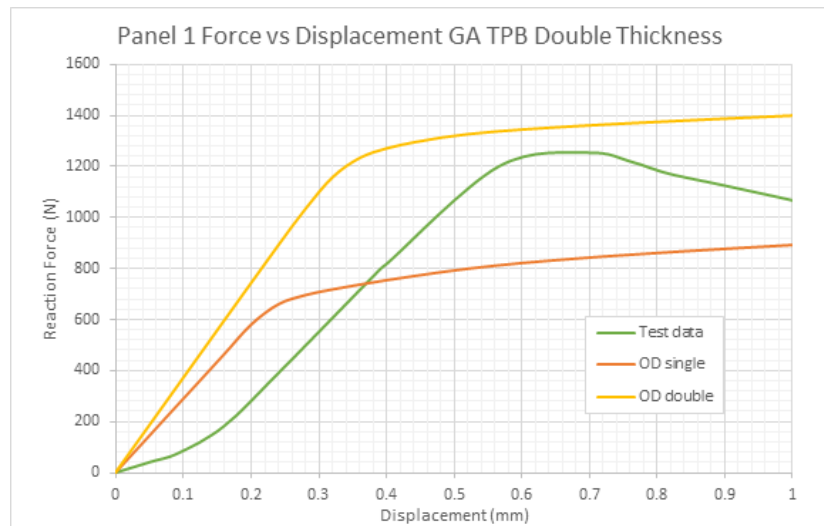


Figure 5.6. Validation of GA Double Thickness Model [Appendix H]

Thermo-mechanical behaviour for the 3D GAM was considered within the range of 200N, which typically occurs within the first 0.1mm of deflection.

The first simulation for the 3D GAM was run for the free heat exchange condition introduced by changing the environmental temperature within the static structural analysis. Results for a variation of thermal environmental conditions can be observed in Figure 5.7.

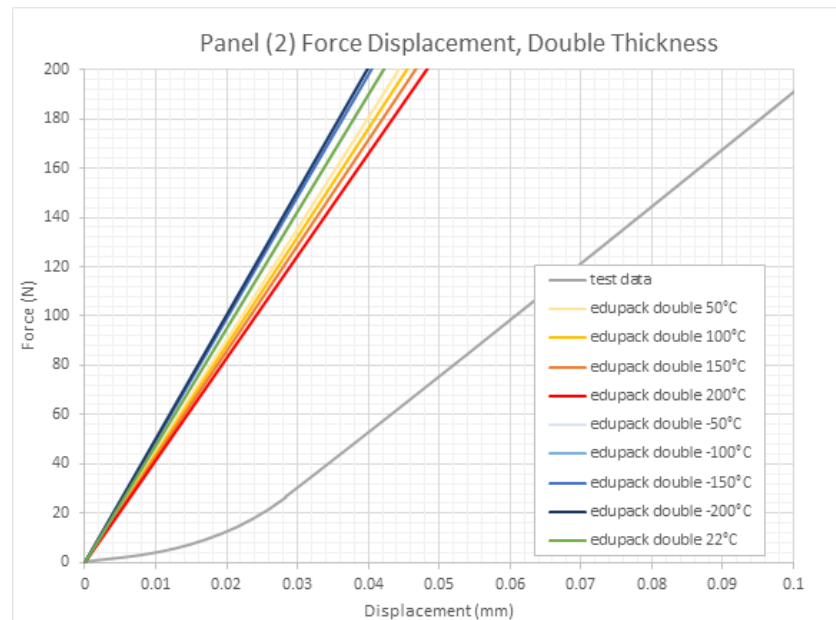


Figure 5.7. Thermomechanical Response of Varying Environmental Temperature (200N Range) [Appendix H]

As can be seen in Fig.5.7, a high temperature environment causes a decrease in the panel bending stiffness, whereas low temperatures increase the panel bending stiffness. The change in panel response at high temperatures is less varied than at lower temperatures (a 10°C difference in temperature will create a larger deviation in panel response at high temperatures than at a low temperature). From -50°C to 22°C there is hardly any change in behaviour, then a large jump from -100°C to -50°C, and again very little change from -200°C to -100°C. It is apparent that the impact of temperature is notable even at these low load and displacement conditions. This observation is directly related to the material model and has been similarly observed in the experimental Three Point Bending test of aluminium honeycomb sandwich panels under extreme temperature conditions [225]. Overall, smaller deflections occur in cold conditions and larger deflections occur in hotter conditions, and the extent of the deviation of deflection from room temperature increases at temperature extremes which is in line with the experimental results presented in Chapter 3 and summarised in Table 4.2, as well as the analytical model results in Chapter 4.

The thermo-mechanical model with heat flux allowed the creation of a more detailed FEM, capable of showing the mechanical response to thermal loading and combined thermo-mechanical loading. This was achieved by coupling a thermal analysis to a mechanical analysis in ANSYS. In this case it is hypothesised that the heat would cause an expansion of the panel, which may change the panel response which is quite often assumed to be negligible. The displacement of the panel due to the applied mechanical force, as well as the heat flux, can be seen in Figure 5.8.

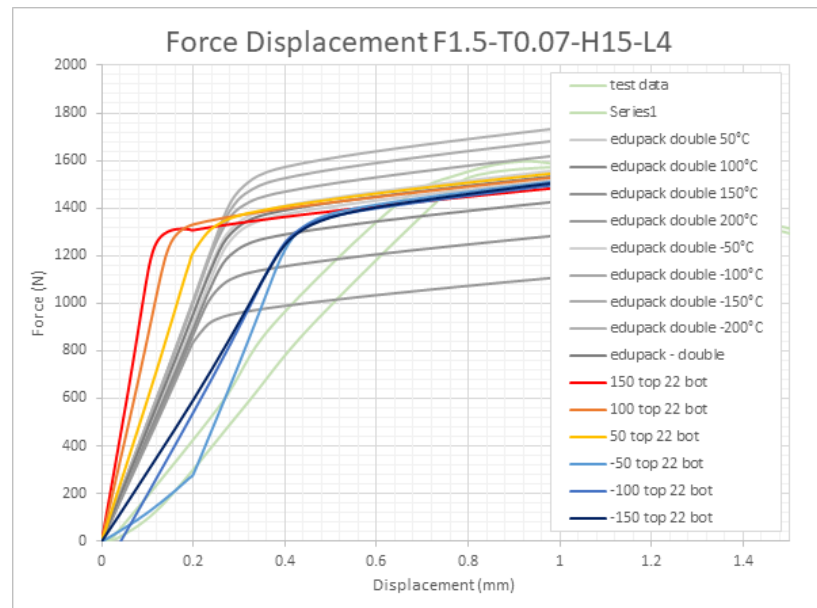


Figure 5.8. Force Displacement Response of GA Heat Flux Models [Appendix H]

As can be observed in Fig.5.8, the behaviour of the panel subjected to positive and negative heat flux appears to be different. The negative heat flux appears to be inconsistent in the initial displacement. It has to be noted that similar signs of initial buckling with follow on snap-through were also found in the analytical model for the heat flux condition (Section 2.4, Chapter 2). This could be due to the panel deforming from the thermal strain in the same direction that the puncher displaces the panel. Obviously this could be the case the other way round, for positive heat flux if the puncher was displacing the panel in an opposite direction. In Fig.5.8 the positive heat flux results in a stiffer panel response, which is due to the preloading of the panel due to thermal strain opposing the puncher, and this is in line with the results obtained for the analytical model in Chapter 2.

5.2.2 Simulation results for the 3D Continuum Model

The Continuum Modelling (CM) approach simplifies the GA Model by replacing the honeycomb core with an equivalent, homogenous, orthotropic material, in the form of a solid 3D element (Fig.5.9). In the development of this model an attempt was made to derive a model that would be just as accurate as the GA model, but with a much lower computational cost. The identification of equivalent material properties is the most important part of the development of the continuum model and this was discussed in detail

in [Appendix H]. A mesh convergence study was also conducted to identify the optimal mesh with the purpose of computational cost saving.

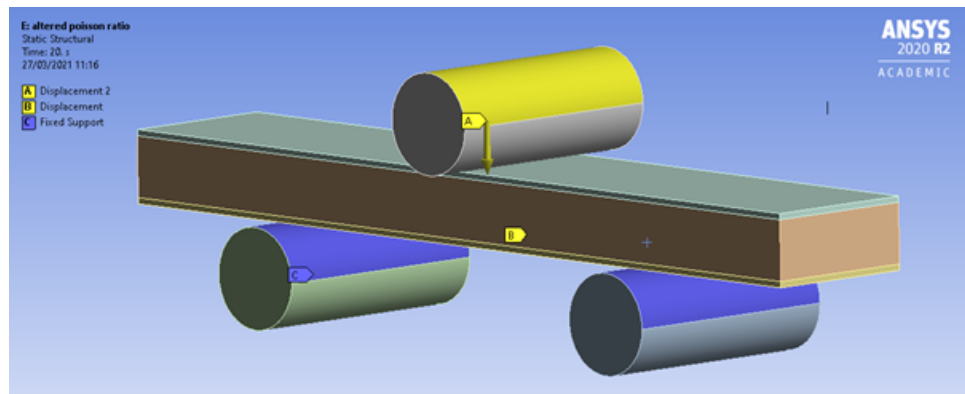


Figure 5.9. 3D Continuum Model Setup [Appendix H]

The model was considered for both heat exchange ranging from -150°C to 150°C and heat flux in the range of ± 150 - 22°C similar to the 3D GAM. Results for the 3D continuum mechanical model for the panel subjected to changes in environmental temperature and under mechanical loading are presented in Figure 5.10.

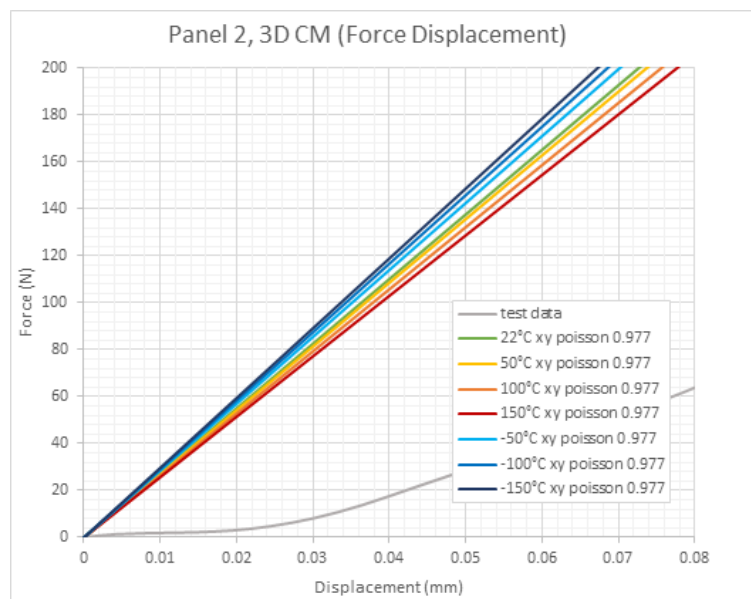


Figure 5.10. Force Displacement of CM at Varying Environmental Temperature 200N Range [Appendix H]

As can be noted in Fig.5.10 the temperature-dependent continuum model showed the same trends as the 3D GAM: higher temperature causes lower stiffness; lower temperature initiates higher stiffness, demonstrating a clear separation of panel behaviour

for changes in environmental temperature, over the 200N range. Therefore it was concluded that the 3D GAM results and the 3D continuum mechanical model results were found to be in good agreement.

Results of the simulation for the thermal effect introduced with heat flux were similar to the ones for the 3D GAM approach, and are presented in Figure 5.11.

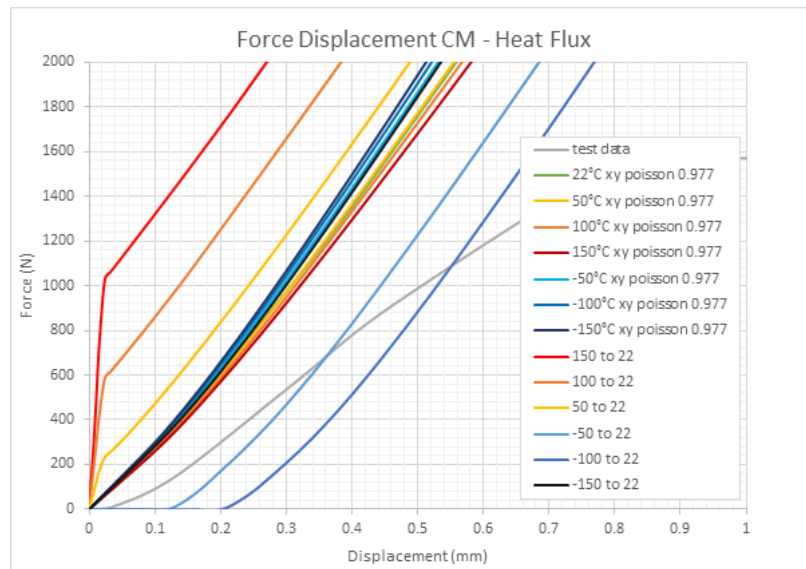


Figure 5.11. Force Displacement Response of the CM Panel at Varying Heat Flux
[Appendix H]

As can be noted in Fig. 5.11 for the positive heat flux, due to the thermally induced residual stress and bending opposing the direction of deformation the overall panel response is stiffer, which is once again in line with the results in Section 5.2.1, and the conclusions for the analytical model in Section 2.4, Chapter 2. For the negative temperature distributions the early response is similar to those of the 3D GAM approach. The positive heat flux models again showed the snap-through behaviour that was seen in the 3D GAM model, however here this behaviour was seen for all three positive heat flux scenarios, whereas the 3D GAM approach only showed this for the highest heat flux. This could be explained by the increased deformation along the length of the panel of the continuum model, whereas the 3D GAM model tends to show more localised deformations between the supports under purely mechanical loads. Therefore, it was concluded that for both implementations of the thermo-mechanical effects the continuum model is a valid simplification in terms of the prediction of general phenomena.

5.2.3 Simulation results for the 2D Continuum Model

To introduce further simplifications to the model and investigate its validity at even lower computational cost the 2D surfaces are used for the 2D continuum model in the ANSYS Design Modeller. It was demonstrated in Figure 5.12 that the 2D model showed some disparity with the 3D continuum model while performing the simulation over only a small fraction of the time. Therefore significant simplifications to the model can be performed but only for some limited cases where a compromise in accuracy is justified and considerations of more advanced coupling phenomena are not essential.

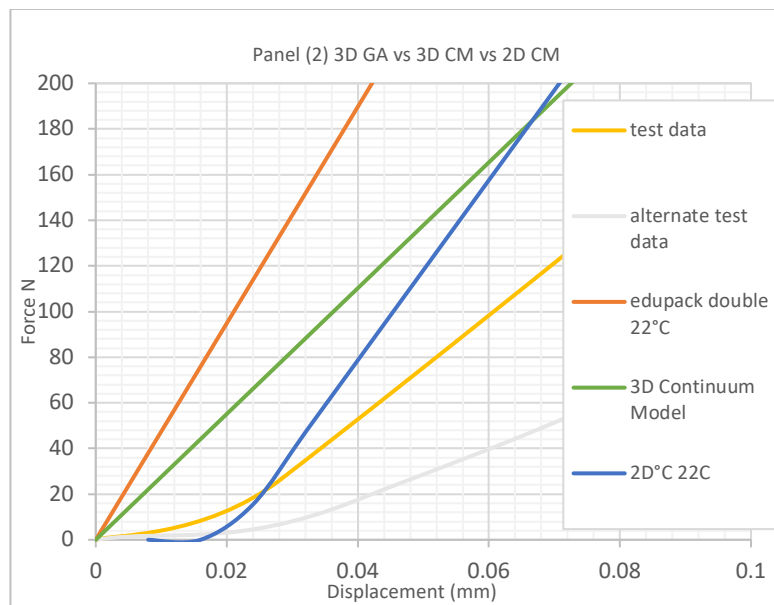


Figure 5.12. Force Displacement Response of 2D CM vs 3D CM vs 3D GA Model (Mechanical loading only) [Appendix H]

5.3 Conclusions

In this chapter a general reflection on modelling work related to the capability of the FEM simulation of the panel and coupling phenomena was presented. This work was performed under the supervision of the author of this thesis and resulted in a journal paper being prepared for publication (Appendix H). In this work three different FE models were developed to attempt to simulate a simplified thermo-mechanical FE model. Three models were analysed in terms of validity, accuracy, and computational cost. It was demonstrated that all three models were able to show a significant deviation of panel

response at the low load range typically associated with satellites, making them suitable for such analysis. The models also demonstrated clearly the effect of the thermal loading and interaction between mechanical and thermal loading in the form of larger deflection at higher thermal loading and stiffer response at lower temperatures, which was in line with the experimental results presented in Chapter 3 and Table 4.2. It was concluded that the 2D continuum model was the simplest model and delivered considerable computational savings at the cost of a lack of response under low-strain conditions, while the 3D continuum model offered good accuracy, generally with around 60% computational time saving comparing to the 3D Geometrically Accurate Model. The 3D models also demonstrated the effect of buckling with subsequent snap-through due to the initial high thermal loading because of the applied heat flux, which was consistent with results obtained for the analytical model in Section 2.4, Chapter 2. These are valuable results since the experimental work performed in Chapter 3 presented results for free heat exchange thermal loading only. In this way the analytical and FE models offer further, more detailed, predictions for the thermo-mechanical behaviour of the sandwich honeycomb panel. However it should be emphasised that the developed analytical model in Chapter 2 is still characterised by the additional capability of accurate prediction of nonlinear temperature distribution along the thickness of the panel, as well as prediction of the deflection response of the panel due to the two coupled phenomena while undergoing simultaneous mechanical and thermal loading.

6. Application of the method of multiple scales for derivation of an analytical solution for thermo-mechanical model developed

This Chapter represents further research into the model derived in Chapter 2. It particularly considers the system of Equations (2.20), describing the thermo-mechanical behaviour of the panel, and suggests an approach to finding a closed form solution for displacement identification. Therefore, we return to the model derived in Section 2.2, Chapter 2, for which all the necessary components can be found from the thermal and mechanical equations:

$$\begin{aligned}
 \bar{C}_1 T_0(t) + \bar{C}_2 u(t) + \bar{C}_3 v(t) &= 0 \\
 \bar{C}_4 T_0(t) + \bar{C}_5 u(t) - \bar{C}_6 v(t) &= 0 \\
 C_1 \ddot{W}(t) + C_2 \dot{W}(t) + [C_3 + C_7 T_\infty(t)]W(t) + C_8 W^3(t) + C_9 T_1(t) + Q(t) &= 0 \\
 C_{10} \dot{T}_0(t) + C_{11} T_0(t) + C_{12} T_\infty(t) + C_{13} \dot{W}(t)W(t) - C_{14} \dot{u}(t) - C_{15} \dot{v}(t) + C &= 0. \\
 C_{16} \dot{T}_1(t) + C_{17} T_1(t) + C_{18} T_\infty + C_{19} \dot{W}(t) &= 0
 \end{aligned}
 \tag{6.1}$$

As we are interested in the temperature and displacement distribution in the z -direction for the structure when it is subjected to combined mechanical and thermal loading, this system can be reduced to the following three equations to find the displacement $W(t)$, membrane temperature $T_0(t)$ and bending temperature $T_1(t)$ as defined in [177, 178], then to identify $T(t)$ in Eq. (2.9):

$$\begin{aligned}
 C_1 \ddot{W}(t) + C_2 \dot{W}(t) + [C_3 + C_4 P_x(t) + C_5 P_y(t) + C_6 T_0(t) + C_7 T_\infty]W(t) + C_8 W^3(t) \\
 + C_9 T_1(t) + Q(t) &= 0 \\
 C_{10} \dot{T}_0(t) + C_{11} T_0(t) + C_{12} T_\infty(t) + C_{13} \dot{W}(t)W(t) &= 0 \\
 C_{16} \dot{T}_1(t) + C_{17} T_1(t) + C_{18} T_\infty(t) + C_{19} \dot{W}(t) &= 0
 \end{aligned}
 \tag{6.2}$$

It has to be pointed out that in reference [174] this form of system of equations was solved analytically obtaining a general solution using features within the *Mathematica* code.

However, this was done by eliminating the nonlinear terms and for static values of the mechanical and thermal loading, thus,

$$\begin{aligned}
C_1 \ddot{W}(t) + C_3 W(t) + C_9 T_1(t) &= 0 \\
C_{10} \dot{T}_0(t) + C_{11} T_0(t) &= 0 \\
C_{16} \dot{T}_1(t) + C_{17} T_1(t) + C_{19} \dot{W}(t) &= 0
\end{aligned} \tag{6.3}$$

Here our overall aim has been to look for a solution for the system in its generalised form, as stated in full in Eq. (6.2) for which an analytical closed form solution cannot be obtained using the DSolve function in *Mathematica*.

The importance of retaining the presence of the nonlinear and coupling terms was emphasised in Section 2.2, Chapter 2, where solutions were represented graphically for both cases, with and without nonlinear terms.

From inspection of the system of Eq. (6.2) it is obvious that the main mathematical challenge in the solution of the whole system resides principally in the first equation, Eq (6.2a), re-stated here as Eq. (6.4),

$$C_1 \ddot{W}(t) + C_2 \dot{W}(t) + \bar{C}(t) W(t) + C_8 W^3(t) + C_9 T_1(t) + Q(t) = 0 \tag{6.4}$$

$$\text{where } \bar{C}(t) = C_3 + C_4 P_x(t) + C_5 P_y(t) + C_6 T_0(t) + C_7 T_\infty.$$

The difficulty arises due to the simultaneous presence of the time-variant coefficient $\bar{C}(t)$ in the term $W(t)$ and the nonlinear term $C_8 W^3(t)$. For the sake of generality we can represent Eq. (6.4) as,

$$C_1 \ddot{W}(t) + C_2 \dot{W}(t) + F_1(t) W(t) + C_8 W^3(t) + F_2(t) = 0. \tag{6.5}$$

where the time variant coefficients are defined as

$$F_1(t) = \bar{C}(t) = C_3 + C_4 P_x(t) + C_5 P_y(t) + C_6 T_0(t) + C_7 T_\infty \quad \text{and} \quad F_2(t) = C_9 T_1(t) + Q(t).$$

where, $P_x(t)$ and $P_y(t)$ are forces applied along the x and y coordinate directions respectively, $Q(t)$ is a time-dependent amplitude component of transversely distributed loading $q(x, y, t) = Q(t)\sin\frac{\pi x}{a}\sin\frac{\pi y}{b}$, T_∞ is a constant difference between the absolute temperature of the surrounding medium and the reference temperature.

Since $F_2(t)$ is the right-hand side term commonly dealt with by use of a particular integral then we have more flexibility in its function. At the same time functions inside $F_1(t)$ are of crucial importance and will eventually define if it is possible to solve the Eq.(6.5) using the multiple scales method.

If in-plane forces are present, then to represent a case of vibration the $P_x(t)$ and $P_y(t)$ in-plane loading functions are typically chosen as harmonic functions. Of course, if there is a case of simple tension or compression, then $P_x(t)$ and $P_y(t)$ can each be assumed to be either an appropriate constant or a linear function.

We will assume the most general case when $P_x(t)$ and $P_y(t)$ are harmonic functions representing vibration: $P_x(t) = \bar{A}\sin(\omega t)$ and $P_y(t) = \bar{B}\cos(\omega t)$. This means that $F_1(t)$ will be now re-written as,

$$F_1(t) = \bar{A}\sin(\omega t) + \bar{B}\cos(\omega t) + C_6T_0(t) + \bar{C}_7 \quad (6.6)$$

where $\bar{C}_7 = C_3 + C_7T_\infty$ is a constant.

In order to obtain a solution using the multiple scales method we need to know the type of general function for $F_1(t)$ and $F_2(t)$, and we also have two remaining functions to analyse, these being $T_1(t)$ and $T_0(t)$ in $F_1(t)$ and $F_2(t)$. Since we have now accumulated extensive knowledge of the behaviour of these two functions for the panel we can try to represent them as approximations dynamic functions based on the outputs from the model in Chapter 2.

In the model outputs discussed in Chapter 2 and it was found that $T_1(t)$ and $T_0(t)$ exhibit the following general behaviour (Figs. 6.1-6.2 - for free heat exchange and Fig. 6.3 - for heat flow).

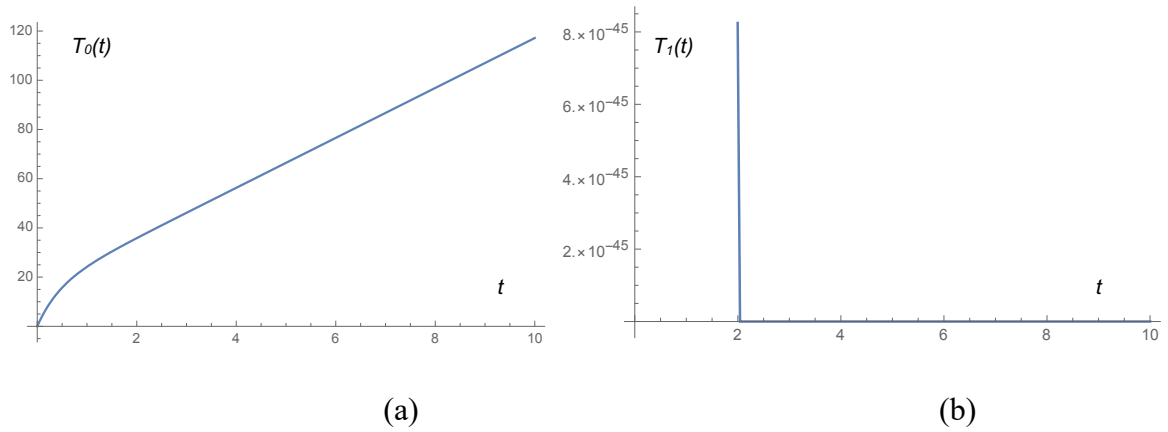


Figure 6.1. $T_0(t)$ – (a) and $T_1(t)$ – (b) responses in the time domain when subjected to the thermal load of $(20 + 10t)$ °C and a mechanical loading of $10t$ N with core thickness of 0.01424m and total plate thickness of 0.015m under free heat exchange conditions. Displacement in metres, time in seconds.

In this case it was possible to decouple the two equations to find closed form solutions for $T_0(t)$ and $T_1(t)$:

$$T_0(t) = 10.14e^{-2.26t}(-1.55 + 1.55e^{2.26t} + te^{2.26t})$$

$$T_1(t) = 100e^{-57.13t}$$

(6.7)

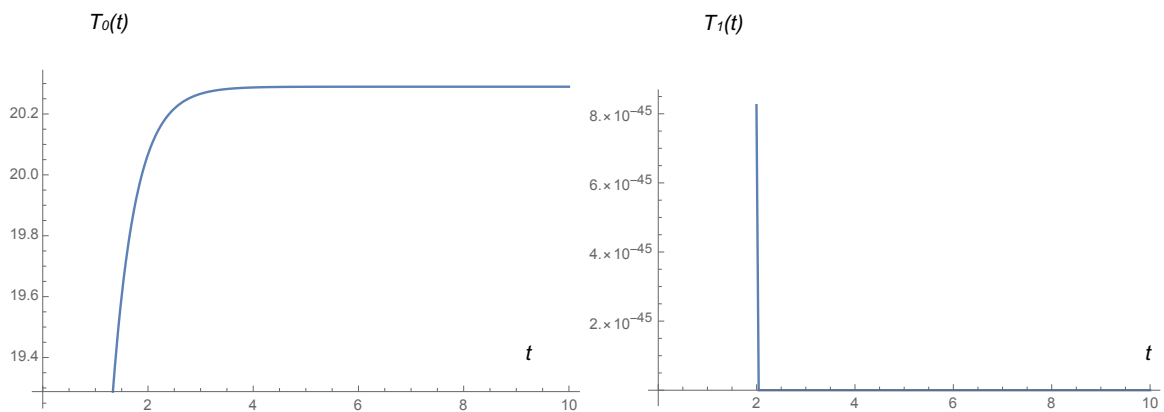


Figure 6.2. $T_0(t)$ response in the time domain when subjected to the mechanical load of $10t$ in 20°C environment, with core thickness of 0.01424m and total plate thickness of 0.015m under free heat exchange conditions. Displacement in metres, time in seconds.

Here it was also possible to decouple the two equations to find closed form solutions for $T_0(t)$ and $T_1(t)$:

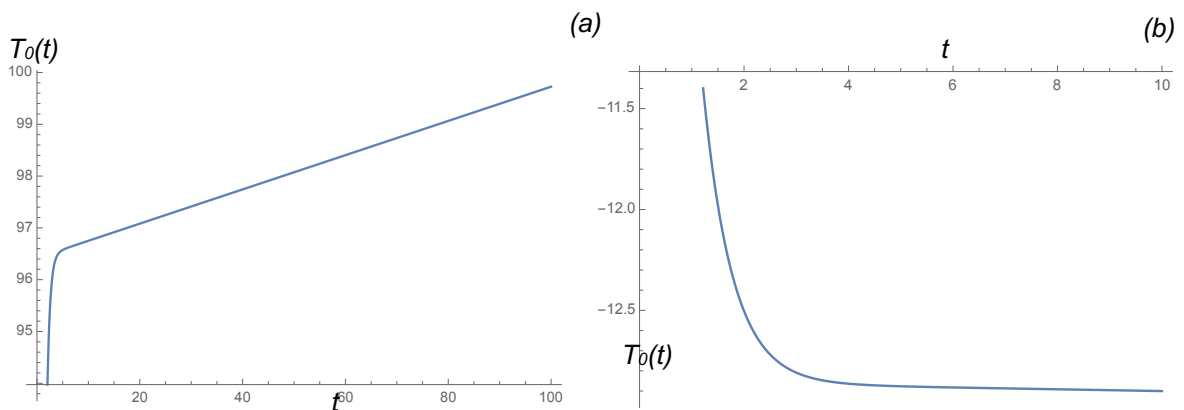
$$T_0(t) = 20.29e^{-2.26t}(-1 + e^{2.26t})$$

$$T_1(t) = 100e^{-57.13t}$$

(6.8)

As can be seen from Figures 6.1 and 6.2 $T_0(t)$ is directly dependent on the thermal loading applied to the panel and if this loading is set to be $(20 + 10t)^\circ\text{C}$ then the $T_0(t)$ will eventually settle down into this state after a short period of time and can therefore be approximated by $T_0(t)=(20 + 10t)^\circ\text{C}$. A similar scenario takes place for the 20°C environment and $T_0(t)$ eventually settles down into $T_0(t)=20$. This can also be justified if the exponents in the closed form solutions Eq.(6.7) and Eq.(6.8) are represented as Taylor series to the first approximation. The same approach can be applied to the solution for $T_1(t)$ representing the exponents to the first or second approximation of the Taylor series.

The $T_0(t)$ and $T_1(t)$ in the case of heat flux are presented in Figs.6.3.



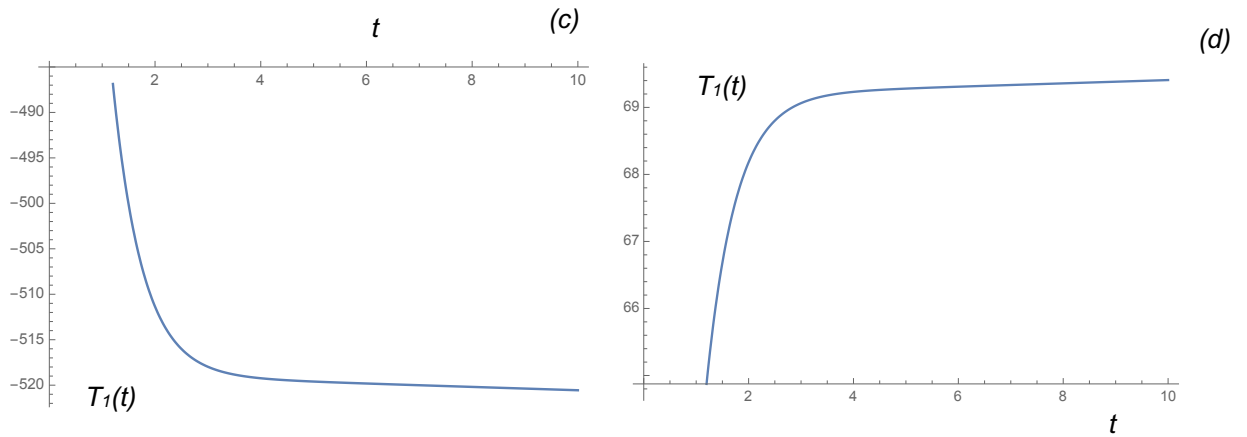


Figure 6.3. Thermal components $T_0(t)$ in (a, b) and $T_1(t)$ in (c, d) defined in Eq(2.21) for heat flux thermal loading 150°C in (a, c) and -20°C in (b,d)

In this case if we decouple the two equations to find the closed form solutions for $T_0(t)$ and $T_1(t)$ for the case of 150°C loading, the solution will be presented by a relatively complex function:

$$\begin{aligned}
 T_0(t) &= 0.033e^{-57.95t}(0.72e^{1.79t} - 2917.82e^{56.16t} + 2917.09e^{57.95t} - 5.25 \\
 &\quad \cdot 10^{-17}e^{112.328t} + te^{57.95t} - 2.56 \cdot 10^{-20}te^{112.33t}) \\
 T_1(t) &= e^{-57.95t}(393.8e^{1.79t} + 5.68 \cdot 10^{-14}e^{3.57t} + 274.92e^{56.16t} - 518.72 \cdot e^{57.95t} \\
 &\quad + 6.94 \cdot 10^{-18}e^{112.33t} + 1.39 \cdot 10^{-17}te^{3.57t} - 0.18 \cdot te^{57.95t} + 3.39 \\
 &\quad \cdot 10^{-21}te^{112.33t})
 \end{aligned}
 \tag{6.9}$$

Considering that the purpose of the analysis of the functions $T_0(t)$ and $T_1(t)$ is to identify cases when the equation can be solved using the multiple scales method to obtain the closed form solution, and the fact that Eq.(6.6) already has two harmonic functions, it was decided to assume that $T_0(t)=M_2$ – constant in the first approximation. This means that the case we will be considering will be applicable for a variety of mechanical loading but only for static thermal loading under free heat exchange as in Figure 6.2.

Since $F_2(t)$ is on the right hand side of the equation and we are less constrained in the choice of its functions, we will consider the most general case for $T_1(t) = N_1 + N_2t + M_1t^{-3}$. It should be pointed out that the term M_1t^{-3} was added not because of the Taylor series representation of the exponents involved in Eq(6.9) but due to the shape of the function in Figs 6.3, and in case it is possible simply to represent the function as M_1t^{-3} instead of using Eq.(6.9).

Since $Q(t)$ is a transversely distributed loading its often represented as a linear time-variant function $Q(t) = \bar{C}t$. This means that for the procedure of a multiple scales perturbation analysis it is reasonable to assume that,

$$F_2(t) = C_9T_1(t) + Q(t) = C_9M_1t^{-3} + C_9N_1 + (\bar{C} + N_2)t = \bar{C}_1 + \bar{C}_2t + \bar{C}_3t^{-3}$$

$$\text{where } \bar{C}_1 = C_9N_1, \bar{C}_2 = N_2 + \bar{C} \text{ and } \bar{C}_3 = C_9M_1$$

and

$$F_1(t) = \bar{A}\sin(\omega t) + \bar{B}\cos(\omega t) + C_{10}$$

where $C_{10} = C_3 + C_7T_\infty + C_6M_2$ is a constant.

Thus Eq.(6.5) can be re-written as

$$\begin{aligned} C_1\ddot{W}(t) + C_2\dot{W}(t) + (\bar{A}\sin(\omega t) + \bar{B}\cos(\omega t) + C_{10})W(t) + C_8W^3(t) \\ = \bar{C}_1 + \bar{C}_2t + \bar{C}_3t^{-3} \end{aligned} \tag{6.10}$$

Equation (6.10) is a particular case of the Mathieu-Hill equation and can be solved using the perturbation method of multiple scales, notwithstanding the fact that the principal parametric resonance condition will emerge as a consequence of the treatment of secular terms in order to guarantee the uniformity of the expansion for $W(t)$. It is also possible in principle to examine the non-resonant case for this solution.

6.1. Multiple Scales Perturbation Analysis

6.1.1. Governing equation of motion and multiple time scaling

An approximate analytical solution to the differential equation in $W(t)$ can be sought using the perturbation method of multiple scales [233, 234], on the basis that the coupling terms to the thermal degree of freedom can be represented by a constant and two time-variant quantities, and regarded as inhomogeneous terms resident on the right-hand side, all as shown in equation (6.11),

$$\ddot{W}(t) + 2\beta\dot{W}(t) + (\omega^2 + B \cos \Omega t + C \sin \Omega t)W(t) + DW^3(t) = E + Ft + Gt^{-3} \quad (6.11)$$

where $2\beta = C_2/C_1$; $\omega^2 = C_{10}/C_1$; $C = \bar{A}/C_1$; $B = \bar{B}/C_1$; $D = C_8/C_1$; $E = \bar{C}_1/C_1$; $F = \bar{C}_2/C_1$; $G = \bar{C}_3/C_1$.

This is clearly a special case of the Mathieu-Hill equation, where the modulating excitation term is split into two phased components of amplitudes B and C , and there is a cubic nonlinearity governed by constant D , together with the right-hand side function described above. The term ω^2 within the brackets multiplying $W(t)$ is a convenient way to introduce conventional notation representing the constant within of the bracketed terms so that the notion of resonance is more easily introduced later, when the secular terms are identified. Note that the symbol A is deliberately not used at this stage because it is reserved for the complex amplitude of the solution for $W(t)$, which appears later in equation (6.19).

The dependent variable $W(t)$ is expressed as a power series in terms of the perturbation parameter ϵ , as,

$$W(t) = W_0(T_0) + \epsilon W_1(T_1) + \epsilon^2 W_2(T_2) + \dots + \epsilon^n W_n(T_n). \quad (6.12)$$

In line with the method of multiple scales, where $T_n = \epsilon T_{n-1}$, each successive perturbation is expressed as a function of successively slower time-scales, implying that sufficient corrections will usually be available from a relatively small quantity of time-scales for a wide range of physical problems. In this case the aim is to cater for the three specific features of the differential equation (6.11): the two modulating excitation terms accommodating phase, the cubic nonlinearity, and the right-hand side function. The point at which the series in equation (6.12) is truncated depends on the decisions yet to be made on the ordering of terms. In systems of this sort, where the physicality of the problem is very important, the ordering is established from *a priori* knowledge of the quantities within the problem. In the case of the dissipation term governed by β there is some justification for considering this as reasonably light structural damping, so if we set $\beta \rightarrow \epsilon \bar{\beta}$ this means that damping will only appear to the first and all higher order perturbation corrections. This is in line with the concept of reasonably light structural damping. Modulating excitation amplitudes B and C and the magnitude of the cubic nonlinearity D are under our control and in order to conform with the traditional assumptions of reasonably low to medium level excitation amplitudes and weak system nonlinearities it is once again appropriate to order those terms by setting these quantities as follows, $B \rightarrow \epsilon \bar{B}$, $C \rightarrow \epsilon \bar{C}$, and $D \rightarrow \epsilon \bar{D}$. Similar arguments may be applied, in principle, to the constant coefficient quantities within the right-hand side function as well. However, it is important to note that the constant term E represents a DC offset, which could be accommodated at the lowest order perturbation, but the term that grows linearly with time, scaled by coefficient F , is necessarily always secular. A classical difficulty for perturbation arises here because this term cannot readily be included in the solution to the lowest order perturbation equation because it is unbounded with time, and would therefore rule out the necessary oscillating generating solution. The only way to make headway with this term is to include it at the first order perturbation level and then attempt later to place numerical bounds on its growth to reduce its secularity. The term proportional to t^{-3} decreases proportional to the cube of the evolving time, so this term although non-oscillatory, does not pose the same fundamental problem with secularity as does the linear term Ft . Noting that it is inevitable that the term Ft will eventually invalidate the uniformity of the power series at $\mathcal{O}(\epsilon^1)$ even for very small F , we cautiously proceed to order these terms so that they start to appear from the first order perturbations, $E \rightarrow \epsilon \bar{E}$, $F \rightarrow \epsilon \bar{F}$, and $G \rightarrow \epsilon \bar{G}$.

The method of multiple scales is also built on the premise that the (total) derivatives that operate in the governing equation of motion can also be expressed as power series which are themselves in terms of partial derivatives with respect to successively slower time-scales. It is algebraically convenient to use the D-operator notation for the partial derivatives, and so we can state the series for the first total time derivative as follows,

$$\frac{d}{dt} = D_0 + \epsilon D_1 + \epsilon^2 D_2 + \cdots + \epsilon^n D_n \quad (6.13)$$

On the basis of the informal ordering suggested above then the series expressed in equations (6.12) and (6.13) can be truncated after the first order corrections, and, after dropping the time arguments, we get,

$$W(t) = W_0(T_0) + \epsilon W_1(T_1) = W_0 + \epsilon W_1 \quad (6.14)$$

$$\frac{d}{dt} = D_0 + \epsilon D_1 \quad (6.15)$$

This means that the second total time derivative $\frac{d^2}{dt^2}$ is also truncated at the same point, for consistency, and by following D-operator algebra this is written as,

$$\frac{d^2}{dt^2} = D_0^2 + 2\epsilon D_0 D_1. \quad (6.16)$$

6.1.2 Perturbation equations

Equations (6.14)-(6.16) can now be substituted into equation (6.11) along with the ordered forms for the quantities β, A, B, C, D, E , and F . After retaining terms up to and including $\mathcal{O}(\epsilon)$ only, this leads to the following,

$$\epsilon^0: \quad D_0^2 W_0 + \omega^2 W_0 = 0 \quad (6.17)$$

$$\begin{aligned} \epsilon^1: \quad D_0^2 W_1 + \omega^2 W_1 = & -2D_0 D_1 W_0 - 2\bar{\beta} D_0 W_0 - \bar{B} W_0 \cos \Omega t - \\ & -\bar{C} W_0 \sin \Omega t - \bar{D} W_0^3 + \bar{E} + \bar{F} t + \bar{G} t^{-3}. \end{aligned} \quad (6.18)$$

The structural basis for this system of perturbation has depended on a simple physical scaling of the terms and leads to a homogeneous zeroth order perturbation equation (6.17) from which the oscillating generating solution for the remainder of the perturbation analysis can be directly written as,

$$W_0 = A e^{i\omega T_0} + \bar{A} e^{-i\omega T_0}. \quad (6.19)$$

Note that the overbar on A denotes its complex conjugate, *and is not representing an ordered quantity when it appears above A* . Complex exponentials are generally very useful in multiple scales perturbation schemes so it pays to re-state the modulating harmonic terms in the same way, as follows,

$$\cos \Omega t = \frac{1}{2} (e^{i\Omega T_0} + e^{-i\Omega T_0}) \quad \text{and} \quad \sin \Omega t = \frac{1}{i2} (e^{i\Omega T_0} - e^{-i\Omega T_0}). \quad (6.20, 6.21)$$

Substituting equations (6.19 – 6.21) into equation (6.18), the first order perturbation equation, leads to,

$$\begin{aligned} D_0^2 W_1 + \omega^2 W_1 = & -2D_0 D_1 [A e^{i\omega T_0} + \bar{A} e^{-i\omega T_0}] - 2\bar{\beta} D_0 [A e^{i\omega T_0} + \bar{A} e^{-i\omega T_0}] \\ & -\bar{B} [A e^{i\omega T_0} + \bar{A} e^{-i\omega T_0}] \frac{1}{2} (e^{i\Omega T_0} + e^{-i\Omega T_0}) - \bar{C} [A e^{i\omega T_0} + \\ & \bar{A} e^{-i\omega T_0}] \frac{1}{i2} (e^{i\Omega T_0} - e^{-i\Omega T_0}) - \bar{D} [A e^{i\omega T_0} + \bar{A} e^{-i\omega T_0}]^3 + \bar{E} + \bar{F} t + \\ & \bar{G} t^{-3}. \end{aligned} \quad (6.22)$$

Expanding equation (6.22) gives this,

$$\begin{aligned}
D_0^2 W_1 + \omega^2 W_1 &= -2D_1[i\omega A e^{i\omega T_0} - i\omega \bar{A} e^{-i\omega T_0}] - 2\bar{\beta}[i\omega A e^{i\omega T_0} - i\omega \bar{A} e^{-i\omega T_0}] \\
&\quad - \frac{\bar{B}}{2}[A e^{i(\omega+\Omega)T_0} + A e^{i(\omega-\Omega)T_0} + \bar{A} e^{i(-\omega+\Omega)T_0} + \bar{A} e^{-i(\omega+\Omega)T_0}] \\
&\quad - \frac{\bar{C}}{i2}[A e^{i(\omega+\Omega)T_0} - A e^{i(\omega-\Omega)T_0} + \bar{A} e^{i(-\omega+\Omega)T_0} - \bar{A} e^{-i(\omega+\Omega)T_0}] \\
&\quad - \bar{D}[A^3 e^{i3\omega T_0} + 3A^2 \bar{A} e^{i\omega T_0} + 3A \bar{A}^2 e^{-i\omega T_0} + \bar{A}^3 e^{-i3\omega T_0}] + \bar{E} + \bar{F}t \\
&\quad + \bar{G}t^{-3}.
\end{aligned} \tag{6.23}$$

6.1.3. Identification of secular terms and resonance conditions

The convention for the next stage is to extract a common factor of the resonant term from the right-hand side, and to express all the right-hand side terms in fully expanded form so that the process of identifying secular terms is as clear as possible. Following this procedure we get,

$$\begin{aligned}
D_0^2 W_1 + \omega^2 W_1 &= e^{i\omega T_0} \left\{ -i2\omega D_1 A + i2\omega D_1 \bar{A} e^{-i2\omega T_0} - i2\bar{\beta}\omega A + i2\bar{\beta}\omega \bar{A} e^{-i2\omega T_0} \right. \\
&\quad - \frac{\bar{B}}{2} A e^{i\Omega T_0} - \frac{\bar{B}}{2} A e^{-i\Omega T_0} - \frac{\bar{B}}{2} \bar{A} e^{i(-2\omega+\Omega)T_0} - \frac{\bar{B}}{2} \bar{A} e^{-i(2\omega+\Omega)T_0} \\
&\quad - \frac{\bar{C}}{i2} A e^{i\Omega T_0} + \frac{\bar{C}}{i2} A e^{-i\Omega T_0} - \frac{\bar{C}}{i2} \bar{A} e^{i(-2\omega+\Omega)T_0} + \frac{\bar{C}}{i2} \bar{A} e^{-i(2\omega+\Omega)T_0} \\
&\quad - \bar{D} A^3 e^{i2\omega T_0} - 3\bar{D} A^2 \bar{A} - 3\bar{D} A \bar{A}^2 e^{-i2\omega T_0} - \bar{D} \bar{A}^3 e^{-i4\omega T_0} + \bar{E} e^{-i\omega T_0} \\
&\quad \left. + \bar{F} t e^{-i\omega T_0} + \bar{G} t^{-3} e^{-i\omega T_0} \right\}.
\end{aligned} \tag{6.24}$$

We can identify secular terms from the right-hand side of equation (6.24), recalling that these terms are those which if left in would then invalidate the uniformity of the power series, so because of this possibility they have to be removed in order then to construct the particular integral solution for this level of perturbation. First of all, we consider terms which could be secular, in other words terms resonant at this level of perturbation. Clearly, we can immediately identify the following as unconditionally secular: $-i2\omega D_1 A - i2\bar{\beta}\omega A - 3\bar{D}A^2\bar{A}$, noting that they also have their complex conjugate counterparts. It's often the case that the complex conjugate secular terms do not add new information to the problem so the best procedure is to leave them for now and then, as necessary, extract them later for processing. Proceeding with the secular terms we see that there are other terms that are conditionally secular. The condition is that $\Omega \rightarrow 2\omega$, which can be expressed as $\Omega = 2\omega + \epsilon\eta$ where $\epsilon\eta$ is known as the detuning parameter and is definitionally small because of the presence of ϵ . This form of resonance condition is indicative of principal parametric resonance and is to be expected within a Mathieu-Hill type system, irrespective of whether it's linear or nonlinear. There are no other oscillating terms present in the right-hand side of equation (6.24) that are potentially secular, so we can proceed to analyse the single case identified, for principal parametric resonance. The identification of this resonance condition underlines the importance of using the natural frequency notation within the original differential equation (6.11). Extracting the secular terms for this resonance condition and setting them to zero, gives the following,

$$-i2\omega D_1 A - i2\bar{\beta}\omega A - 3\bar{D}A^2\bar{A} - \frac{\bar{B}}{2}\bar{A}e^{i(-2\omega+\Omega)T_0} - \frac{\bar{C}}{i2}\bar{A}e^{i(-2\omega+\Omega)T_0} = 0. \quad (6.25)$$

We note that since this stage of the analysis only involves secularity in the context of a resonance condition, the treatment of terms such as Ft and Gt^{-3} has to be deferred until the particular solution to $\mathcal{O}(\epsilon^1)$ is considered.

6.1.4. Slow-time modulation equations and solvability conditions

Equation (6.25) is the starting point for obtaining the slow-time modulation equations, which lead to the so-called solvability equations, and from which we can find numerical solutions to the amplitude of the response and the associated phase. After that we then return to equation (6.23) to find the particular integral solution to that level of perturbation, which can then be added to the zeroth order generating solution (Eq.(6.19)) to give the full solution for $W(t)$. Numerical solutions for $W(t)$ can be found because we can find the amplitude A and the associated phase from the processing done with equation (6.25) above.

Returning to equation (6.25) we introduce the amplitude and phase components of the complex amplitude A as follows. We note that $A = A(T_1)$ meaning that this is a slowly varying quantity,

$A(T_1) = \frac{p(T_1)}{2} e^{i\alpha(T_1)}$ and the complex conjugate is given by $\bar{A}(T_1) = \frac{p(T_1)}{2} e^{-i\alpha(T_1)}$. We do this so that p represents the actual amplitude and α its phase. In equation (6.25) we require to find $D_1 A$, and this evaluates as follows, noting that the prime denotes differentiation with respect to timescale T_1 and we drop the arguments for clarity,

$$D_1 A = \frac{p'}{2} e^{i\alpha} + \frac{p}{2} i\alpha' e^{i\alpha} \quad (6.26)$$

Substituting the forms for $A(T_1)$ and $\bar{A}(T_1)$ and equation (6.26) into (6.25) leads to this,

$$\begin{aligned} -i2\omega \left(\frac{p'}{2} e^{i\alpha} + \frac{p}{2} i\alpha' e^{i\alpha} \right) - i2\bar{\beta}\omega \frac{p}{2} e^{i\alpha} - 3\bar{D} \frac{p^2}{4} e^{i2\alpha} \frac{p}{2} e^{-i\alpha} - \frac{\bar{B} p}{2} e^{-i\alpha} e^{i(\Omega-2\omega)T_0} \\ - \frac{\bar{C} p}{i2} e^{-i\alpha} e^{i(\Omega-2\omega)T_0} = 0 \end{aligned} \quad (6.27)$$

Introducing the resonance condition $\Omega = 2\omega + \epsilon\eta$ and then multiplying through by $e^{-i\alpha}$ to tidy up gives,

$$-i\omega p' + \omega p \alpha' - i\bar{\beta}\omega p - \frac{3}{8}\bar{D}p^3 - \frac{\bar{B}}{4}pe^{i(\epsilon\eta T_0 - 2\alpha)} - \frac{\bar{C}}{i4}pe^{i(\epsilon\eta T_0 - 2\alpha)} = 0 \quad (6.28)$$

Then we multiply through by i to remove this from the denominator of the last term, getting,

$$\omega p' + i\omega p \alpha' + \bar{\beta}\omega p - \frac{i3}{8}\bar{D}p^3 - \frac{i\bar{B}}{4}pe^{i(\epsilon\eta T_0 - 2\alpha)} - \frac{\bar{C}}{4}pe^{i(\epsilon\eta T_0 - 2\alpha)} = 0 \quad (6.29)$$

In order to separate the terms from this equation out into real and imaginary parts it's convenient to revert back to trigonometrical forms,

$$\begin{aligned} \omega p' + i\omega p \alpha' + \bar{\beta}\omega p - \frac{i3}{8}\bar{D}p^3 - \frac{i\bar{B}}{4}p(\cos(\epsilon\eta T_0 - 2\alpha) + i \sin(\epsilon\eta T_0 - 2\alpha)) \\ - \frac{\bar{C}}{4}p(\cos(\epsilon\eta T_0 - 2\alpha) + i \sin(\epsilon\eta T_0 - 2\alpha)) = 0 \end{aligned} \quad (6.30)$$

Separating the terms,

$$Re: \quad \omega p' + \bar{\beta}\omega p + \frac{\bar{B}}{4}p \sin(\epsilon\eta T_0 - 2\alpha) - \frac{\bar{C}}{4}p \cos(\epsilon\eta T_0 - 2\alpha) = 0 \quad (6.31)$$

$$Im: \quad \omega p \alpha' - \frac{3}{8}\bar{D}p^3 - \frac{\bar{B}}{4}p \cos(\epsilon\eta T_0 - 2\alpha) - \frac{\bar{C}}{4}p \sin(\epsilon\eta T_0 - 2\alpha) = 0$$

We know that by definition the slow time scale T_1 is scaled such that $T_1 = \epsilon T_0$ so we can re-write the argument of the trigonometrical functions as follows in order to make the system of equations (6.31) autonomous,

$$\epsilon \eta T_0 - 2\alpha = \eta T_1 - 2\alpha = \Psi \quad (6.32)$$

It follows therefore that,

$$\eta - 2\alpha' = \Psi' \quad (6.33)$$

Therefore, the autonomous system phase is defined by Ψ and so because $p = p(T_1)$ and $\Psi = \Psi(T_1)$, and T_1 is a (very) slow time-scale, we can then say that $p' \sim 0$ and $\Psi' \sim 0$, which means that.

$$\alpha' = \frac{\eta}{2} \quad (6.34)$$

The slow-time first order differential equations (6.31) can now be re-stated in the form of transcendental equations,

$$\bar{\beta}\omega + \frac{\bar{B}}{4}\sin\Psi - \frac{\bar{C}}{4}\cos\Psi = 0 \quad (6.35)$$

$$\omega\frac{\eta}{2} - \frac{3}{8}\bar{D}p^2 - \frac{\bar{B}}{4}\cos\Psi - \frac{\bar{C}}{4}\sin\Psi = 0 \quad (6.36)$$

These equations can be solved analytically quite easily if $\bar{D} = 0$, but not if $\bar{D} \neq 0$. The complex conjugate secular terms do not give any new information here, and in fact return equations identical in structure to (6.36) and (6.37), so no further progress can be made to obtain analytical solutions to these equations for the case where $\bar{D} \neq 0$.

It makes practical sense to return to physical quantities in order to solve equations (6.35) and (6.36) numerically, and to do this we must multiple both equations by ϵ ,

$$\epsilon\bar{\beta}\omega + \frac{\epsilon\bar{B}}{4}\sin\Psi - \frac{\epsilon\bar{C}}{4}\cos\Psi = 0 \quad (6.37)$$

$$\omega\frac{\epsilon\eta}{2} - \frac{3}{8}\epsilon\bar{D}p^2 - \frac{\epsilon\bar{B}}{4}\cos\Psi - \frac{\epsilon\bar{C}}{4}\sin\Psi = 0 \quad (6.38)$$

Finally, re-stating these solvability equations now in terms of the original physical quantities, gives this,

$$\beta\omega + \frac{B}{4}\sin\Psi - \frac{C}{4}\cos\Psi = 0 \quad (6.39)$$

$$\omega\frac{(\Omega-2\omega)}{2} - \frac{3}{8}Dp^2 - \frac{B}{4}\cos\Psi - \frac{C}{4}\sin\Psi = 0 \quad (6.40)$$

This is a pair of nonlinear transcendental algebraic equations in p and Ψ , which are, respectively, the amplitude and phase of the autonomous system. We now proceed to obtain numerical solutions for equations (6.39) and (6.40) using the *Mathematica* NSolve function. The excitation enters through B and C , operating at frequency Ω . It should be noted that if the system is linearised then $\bar{D} = 0$ and there is no solution for the amplitude p . In fact, p will then be unbounded because the condition $\bar{D} = 0$ returns the governing differential equation (6.11) to a linear Mathieu-Hill equation for which there is no classical bounded solution. In that particular case the amplitude p is null when Ω is far from 2ω and unbounded when $\Omega \sim 2\omega$, which is when $\epsilon\eta$ is very small. In the nonlinear case here, where $\bar{D} \neq 0$, equations (6.39) and (6.40) have to be solved numerically in order to determine values for p and also for Ψ .

6.1.5. Particular solution

The second stage of this analysis is to find the particular solution for the first order perturbation equation (equation 6.24)). It is helpful to re-state that equation here,

highlighting in red the terms previously defined as secular and their complex conjugates in blue,

$$\begin{aligned}
D_0^2 W_1 + \omega^2 W_1 = e^{i\omega T_0} \left\{ -i2\omega D_1 A + i2\omega D_1 \bar{A} e^{-i2\omega T_0} - i2\bar{\beta}\omega A + i2\bar{\beta}\omega \bar{A} e^{-i2\omega T_0} - \right. \\
\left. \frac{\bar{B}}{2} A e^{i\Omega T_0} - \frac{\bar{B}}{2} \bar{A} e^{-i\Omega T_0} - \frac{\bar{B}}{2} \bar{A} e^{i(-2\omega+\Omega)T_0} - \frac{\bar{B}}{2} \bar{A} e^{-i(2\omega+\Omega)T_0} - \frac{\bar{C}}{i2} A e^{i\Omega T_0} + \frac{\bar{C}}{i2} \bar{A} e^{-i\Omega T_0} - \right. \\
\left. \frac{\bar{C}}{i2} \bar{A} e^{i(-2\omega+\Omega)T_0} + \frac{\bar{C}}{i2} \bar{A} e^{-i(2\omega+\Omega)T_0} - \bar{D} A^3 e^{i2\omega T_0} - 3\bar{D} A^2 \bar{A} - 3\bar{D} \bar{A} \bar{A}^2 e^{-i2\omega T_0} - \right. \\
\left. \bar{D} \bar{A}^3 e^{-i4\omega T_0} + \bar{E} e^{-i\omega T_0} + \bar{F} t e^{-i\omega T_0} + \bar{G} t^{-3} e^{-i\omega T_0} \right\}.
\end{aligned} \tag{6.41}$$

From here we can identify the remaining right-hand side terms from which a particular integral solution can now be obtained. This reduced form of equation (6.41) is as follows,

$$\begin{aligned}
& D_0^2 W_1 + \omega^2 W_1 \\
& = e^{i\omega T_0} \left\{ -\frac{\bar{B}}{2} A e^{i\Omega T_0} - \frac{\bar{B}}{2} \bar{A} e^{-i(2\omega+\Omega)T_0} - \frac{\bar{C}}{i2} A e^{i\Omega T_0} + \frac{\bar{C}}{i2} \bar{A} e^{-i(2\omega+\Omega)T_0} \right. \\
& \quad \left. - \bar{D} A^3 e^{i2\omega T_0} - \bar{D} \bar{A}^3 e^{-i4\omega T_0} + \bar{E} e^{-i\omega T_0} + \bar{F} t e^{-i\omega T_0} + \bar{G} t^{-3} e^{-i\omega T_0} \right\}.
\end{aligned} \tag{6.42}$$

We note the presence of $\bar{F} t e^{-i\omega T_0}$ and the fact that this troublesome term must be retained and included within the particular solution. It's convenient to re-absorb $e^{i\omega T_0}$ back into the right-hand side terms by multiplying out, to get,

$$\begin{aligned}
& D_0^2 W_1 + \omega^2 W_1 \\
& = \left\{ -\frac{\bar{B}}{2} A e^{i(\Omega+\omega)T_0} - \frac{\bar{B}}{2} \bar{A} e^{-i(\Omega+\omega)T_0} - \frac{\bar{C}}{i2} A e^{i(\Omega+\omega)T_0} + \frac{\bar{C}}{i2} \bar{A} e^{-i(\Omega+\omega)T_0} \right. \\
& \quad \left. - \bar{D} A^3 e^{i3\omega T_0} - \bar{D} \bar{A}^3 e^{-i3\omega T_0} + \bar{E} + \bar{F} t + \bar{G} t^{-3} \right\}.
\end{aligned} \tag{6.43}$$

The remaining tasks are to find the particular integral solution to equation (6.43), add that to the zeroth order perturbation solution via the perturbation series for $W(t)$ and then to compute numerical solutions from there.

Equation (6.43) requires substitution of the solution for A in terms of p and α , and this leads to,

$$D_0^2 W_1 + \omega^2 W_1 = \left\{ -\frac{\bar{B}p}{2} e^{i\alpha} e^{i(\Omega+\omega)T_0} - \frac{\bar{B}p}{2} e^{-i\alpha} e^{-i(\Omega+\omega)T_0} - \frac{\bar{C}p}{i2} e^{i\alpha} e^{i(\Omega+\omega)T_0} + \frac{\bar{C}p}{i2} e^{-i\alpha} e^{-i(\Omega+\omega)T_0} - \bar{D} \frac{p^3}{8} e^{i3\alpha} e^{i3\omega T_0} - \bar{D} \frac{p^3}{8} e^{-i3\alpha} e^{-i3\omega T_0} + \bar{E} + \bar{F}t + \bar{G}t^{-3} \right\}. \quad (6.44)$$

Finally, we get the fully expanded form,

$$D_0^2 W_1 + \omega^2 W_1 = \left\{ -\frac{\bar{B}}{4} p e^{i[(\Omega+\omega)T_0+\alpha]} - \frac{\bar{B}}{4} p e^{-i[(\Omega+\omega)T_0+\alpha]} - \frac{\bar{C}}{i4} p e^{i[(\Omega+\omega)T_0+\alpha]} + \frac{\bar{C}}{i4} p e^{-i[(\Omega+\omega)T_0+\alpha]} - \bar{D} \frac{p^3}{8} e^{i3[\omega T_0+\alpha]} - \bar{D} \frac{p^3}{8} e^{-i3[\omega T_0+\alpha]} + \bar{E} + \bar{F}t + \bar{G}t^{-3} \right\}. \quad (6.45)$$

In order to get the particular integral for W_1 we take a trial solution of the following form,

$$W_1 = Q_1 e^{i[(\Omega+\omega)T_0+\alpha]} + Q_2 e^{-i[(\Omega+\omega)T_0+\alpha]} + Q_3 e^{i3[\omega T_0+\alpha]} + Q_4 e^{-i3[\omega T_0+\alpha]} + Q_5 + Q_6 t + Q_7 t^{-3} \quad (6.46)$$

where the Q_i are functions to be determined.

The second time derivative, with respect to T_0 is needed. We start with the first derivative,

$$\begin{aligned} \frac{\partial W_1}{\partial T_0} = D_0 W_1 = & i(\Omega + \omega)Q_1 e^{i[(\Omega+\omega)T_0+\alpha]} - i(\Omega + \omega)Q_2 e^{-i[(\Omega+\omega)T_0+\alpha]} \\ & + i3\omega Q_3 e^{i3[\omega T_0+\alpha]} - i3\omega Q_4 e^{-i3[\omega T_0+\alpha]} + Q_6 - 3Q_7 t^{-4} \end{aligned}$$

Then, differentiating for a second time,

$$\begin{aligned} \frac{\partial^2 W_1}{\partial T_0^2} = D_0^2 W_1 = & -(\Omega + \omega)^2 Q_1 e^{i[(\Omega+\omega)T_0+\alpha]} - (\Omega + \omega)^2 Q_2 e^{-i[(\Omega+\omega)T_0+\alpha]} - \\ & 9\omega^2 Q_3 e^{i3[\omega T_0+\alpha]} - 9\omega^2 Q_4 e^{-i3[\omega T_0+\alpha]} + 12Q_7 t^{-5} \end{aligned} \quad (6.47)$$

We then substitute equations (6.46) and (6.47) into the left-hand side of (6.45). This generates the following equation, from which like terms can be extracted in order to construct the specific form of the particular integral.

$$\begin{aligned} & -(\Omega + \omega)^2 Q_1 e^{i[(\Omega+\omega)T_0+\alpha]} - (\Omega + \omega)^2 Q_2 e^{-i[(\Omega+\omega)T_0+\alpha]} - 9\omega^2 Q_3 e^{i3[\omega T_0+\alpha]} - \\ & 9\omega^2 Q_4 e^{-i3[\omega T_0+\alpha]} + 12Q_7 t^{-5} + \omega^2 [Q_1 e^{i[(\Omega+\omega)T_0+\alpha]} + Q_2 e^{-i[(\Omega+\omega)T_0+\alpha]} + \\ & Q_3 e^{i3[\omega T_0+\alpha]} + Q_4 e^{-i3[\omega T_0+\alpha]} + Q_5 + Q_6 t + Q_7 t^{-3}] = -\frac{\bar{B}}{4} p e^{i[(\Omega+\omega)T_0+\alpha]} - \\ & \frac{\bar{B}}{4} p e^{-i[(\Omega+\omega)T_0+\alpha]} - \frac{\bar{C}}{i4} p e^{i[(\Omega+\omega)T_0+\alpha]} + \frac{\bar{C}}{i4} p e^{-i[(\Omega+\omega)T_0+\alpha]} - \bar{D} \frac{p^3}{8} e^{i3[\omega T_0+\alpha]} - \\ & \bar{D} \frac{p^3}{8} e^{-i3[\omega T_0+\alpha]} + \bar{E} + \bar{F} t + \bar{G} t^{-3} \end{aligned} \quad (6.48)$$

In order to obtain forms for the Q_i it's necessary to identify like terms from both sides of equation (6.48) and extract them sequentially,

$$Q_1 = -\frac{\bar{B}p}{4[\omega^2 - (\Omega + \omega)^2]} - \frac{\bar{C}p}{i4[\omega^2 - (\Omega + \omega)^2]}$$

$$Q_2 = -\frac{\bar{B}p}{4[\omega^2 - (\Omega + \omega)^2]} + \frac{\bar{C}p}{i4[\omega^2 - (\Omega + \omega)^2]}$$

$$Q_3 = Q_4 = \frac{\bar{D}p^3}{64\omega^2}$$

We also have to consider the terms Q_5, Q_6 , and Q_7 , noting that for the first two this is trivial and from inspection they are merely $Q_5 = \bar{E}$, and $Q_6 = \bar{F}$. But in the case of Q_7 it can be seen that there is one left-hand term, proportional to t^{-5} which does not have a counterpart on the right-hand side. Given that for larger values of real time t any term proportional to t^{-5} will be very small, so we may well be justified in neglecting it simply for that reason. Making that assumption allows us to state $Q_7 = \bar{G}$. If this simplification is not acceptable then we will need to extend the series on the right-hand side of equation (6.11) to include a term Ht^{-5} . If we do that then the trial solution in equation (6.46) has to be extended, like this,

$$W_1 = Q_1 e^{i[(\Omega+\omega)T_0+\alpha]} + Q_2 e^{-i[(\Omega+\omega)T_0+\alpha]} + Q_3 e^{i3[\omega T_0+\alpha]} + Q_4 e^{-i3[\omega T_0+\alpha]} + Q_5 + Q_6 t + Q_7 t^{-3} + Q_8 t^{-5}.$$

(6.49)

The second total time derivative then becomes,

$$\frac{\partial^2 W_1}{\partial T_0^2} = D_0^2 W_1 = -(\Omega + \omega)^2 Q_1 e^{i[(\Omega+\omega)T_0+\alpha]} - (\Omega + \omega)^2 Q_2 e^{-i[(\Omega+\omega)T_0+\alpha]} - 9\omega^2 Q_3 e^{i3[\omega T_0+\alpha]} - 9\omega^2 Q_4 e^{-i3[\omega T_0+\alpha]} + 12Q_7 t^{-5} + 30Q_8 t^{-7}.$$

(6.50)

So now, equation (6.48) will also be similarly extended, and will include balancing terms proportional to t^{-5} . But, of course, we then have a new term proportional to t^{-7} . This is

clearly going to be extremely small so we can almost certainly neglect it without any serious problems. The difficulty with this approach is that the balancing of terms will now lead to an expression in which both Q_7 and Q_8 feature, and there is no additional equation relationship available with which to solve them simultaneously for independent calculation of Q_7 and Q_8 . This is shown in the next equation (6.51),

$$\begin{aligned}
& -(\Omega + \omega)^2 Q_1 e^{i[(\Omega+\omega)T_0+\alpha]} - (\Omega + \omega)^2 Q_2 e^{-i[(\Omega+\omega)T_0+\alpha]} - 9\omega^2 Q_3 e^{i3[\omega T_0+\alpha]} \\
& \quad - 9\omega^2 Q_4 e^{-i3[\omega T_0+\alpha]} + 12Q_7 t^{-5} + 30Q_8 t^{-7} \\
& \quad + \omega^2 [Q_1 e^{i[(\Omega+\omega)T_0+\alpha]} + Q_2 e^{-i[(\Omega+\omega)T_0+\alpha]} + Q_3 e^{i3[\omega T_0+\alpha]} \\
& \quad + Q_4 e^{-i3[\omega T_0+\alpha]} + Q_5 + Q_6 t + Q_7 t^{-3} + Q_8 t^{-5}] \\
& = -\frac{\bar{B}}{4} p e^{i[(\Omega+\omega)T_0+\alpha]} - \frac{\bar{B}}{4} p e^{-i[(\Omega+\omega)T_0+\alpha]} - \frac{\bar{C}}{i4} p e^{i[(\Omega+\omega)T_0+\alpha]} \\
& \quad + \frac{\bar{C}}{i4} p e^{-i[(\Omega+\omega)T_0+\alpha]} - \bar{D} \frac{p^3}{8} e^{i3[\omega T_0+\alpha]} - \bar{D} \frac{p^3}{8} e^{-i3[\omega T_0+\alpha]} + \bar{E} + \bar{F}t \\
& \quad + \bar{G}t^{-3} + Ht^{-5}
\end{aligned} \tag{6.51}$$

Taking terms proportional to t^{-5} gives this,

$$12Q_7 t^{-5} + \omega^2 Q_8 t^{-5} = Ht^{-5} \tag{6.52}$$

Whilst this is algebraically correct, the fact that Q_7 and Q_8 can't be recovered independently means that the earlier assumption must hold in which we neglected terms proportional to t^{-5} , and so $Q_7 = \bar{G}$.

If we go on to substitute the expressions we now have for Q_1 to Q_7 into equation (6.46) then we get the particular solution for the problem. After some intermediate algebra, and converting back from exponential to trigonometrical form, and multiplying through by ϵ , we get the particular solution for W_1 , using the fact that $T_0 \sim t$,

$$\epsilon W_1 = \frac{Bp}{2\Omega(\Omega+2\omega)} \cos[(\Omega + \omega)t + \alpha] + \frac{Cp}{2\Omega(\Omega+2\omega)} \sin[(\Omega + \omega)t + \alpha] + \frac{Dp}{32\omega^2} \cos[3(\omega t + \alpha)] + E + Ft + Gt^{-3}. \quad (6.53)$$

Note that the denominators of the coefficients of the three trigonometrical terms have been simplified by using $2[\omega^2 - (\Omega + \omega)^2] = -2\Omega(\Omega + 2\omega)$. We must also note the presence of Ft in this particular solution and the fact that this term will eventually dominate the solution to the first order perturbation, given enough time, and yet there was no clear alternative other than to order the system in this way. This highlights a difficulty with using a perturbation method to solve problems in which inherently secular terms such as Ft are found.

Returning to equation (6.19) to complete the full solution we now need to put this into a similarly useable form.

So, we get,

$$\begin{aligned} W_0 = Ae^{i\omega t} + \bar{A}e^{-i\omega t} &= \frac{p}{2} e^{i\alpha} e^{i\omega t} + \frac{p}{2} e^{-i\alpha} e^{i\omega t} = p \frac{1}{2} (e^{i(\omega t + \alpha)} + e^{-i(\omega t + \alpha)}) = \\ &= p \cos(\omega t + \alpha). \end{aligned} \quad (6.54)$$

Finally, the full solution to the problem, up to and including the first order perturbational correction, is given by,

$$\begin{aligned} W(t) = W_0 + \epsilon W_1 &= p \cos(\omega t + \alpha) + \frac{Bp}{2\Omega(\Omega+2\omega)} \cos[(\Omega + \omega)t + \alpha] + \\ &+ \frac{Cp}{2\Omega(\Omega+2\omega)} \sin[(\Omega + \omega)t + \alpha] + \frac{Dp}{32\omega^2} \cos[3(\omega t + \alpha)] + E + Ft + Gt^{-3} \end{aligned} \quad (6.55)$$

There are terms within the solution that are resonant to ω , $(\Omega + \omega)$, and 3ω , as expected for a nonlinear Mathieu-Hill type problem, plus there is also a constant DC term, and

terms proportional to t and t^{-3} , respectively, with the penultimate term, Ft , presenting obvious difficulties.

6.2. Solution procedure

In order to get a numerical solution from this analysis we need first to solve equations (6.39) and (6.40), reproduced below for convenience,

$$\begin{aligned} \beta\omega + \frac{B}{4}\sin\Psi - \frac{C}{4}\cos\Psi &= 0 \\ \omega\frac{(\Omega - 2\omega)}{2} - \frac{3}{8}Dp^2 - \frac{B}{4}\cos\Psi - \frac{C}{4}\sin\Psi &= 0 \end{aligned} \tag{6.56}$$

This means that we need data for β, ω, B, C, D , and Ω , and the two unknowns are p and Ψ .

Having determined real valued solutions for p and Ψ we can then solve for equation (6.55), reproduced below for convenience, to get W against time t ,

$$\begin{aligned} W(t) = W_0 + \epsilon W_1 = & p \cos(\omega t + \alpha) + \frac{Bp}{2\Omega(\Omega+2\omega)} \cos[(\Omega + \omega)t + \alpha] + \\ & \frac{Cp}{2\Omega(\Omega+2\omega)} \sin[(\Omega + \omega)t + \alpha] + \frac{Dp}{32\omega^2} \cos[3(\omega t + \alpha)] + E + Ft + Gt^{-3} \end{aligned}$$

For this we also need data for E, F , and G .

There is one other requirement for solution and that is to relate the nonautonomous phase angle α to the autonomous variable Ψ .

The relationship between them is given in equation (6.32) and re-stated below,

$$\Psi = \epsilon\eta T_0 - 2\alpha \quad (6.57)$$

This is at its simplest for those cases where $\epsilon\eta = 0$, hence $\Omega = 2\omega$.

(a) Therefore, for the case of perfectly tuned principal parametric resonance then we have,

$$\alpha = -\frac{\Psi}{2} \quad (6.58)$$

(b) If the principal parametric resonance is not perfectly tuned then we are left with this,

$$\Psi = \epsilon\eta t - 2\alpha = (\Omega - 2\omega)t - 2\alpha \quad (6.59)$$

meaning that,

$$\alpha = -\frac{\Psi}{2} + \frac{(\Omega - 2\omega)t}{2} \quad (6.60)$$

noting that α is explicitly time-variant.

6.3. Numerical example

As discussed at the beginning of this chapter we are concentrating on the panel behaviour described by Eq. (6.4) including the planar forces, as $P_x(t)$ and $P_y(t)$, summarised in Eq.(6.6).

We recall that constraints were introduced for the functions $F_1(t)$ and $F_2(t)$, in the form of $T_1(t) = N_1 + N_2t + M_1t^{-3}$ and $T_0(t) = M_2 - \text{constant}$, at a first approximation. This means that the case we will be considering will be applicable for a variety of mechanical loadings but only for static thermal loading under free heat exchange, as shown in Figure 6.2.

Therefore we consider the case of the 15×10^{-3} m thick panel considered in Chapters 2 and 4 with the geometry stated in Table 4.1 and the mechanical and thermal properties summarised in Tables 3.1 & 3.2.

Following the example in Chapter 4, where results were obtained for the displacement $W(t)$ and compared with experimental results, the panel is undergoing a mechanical loading of $q(t)=10*t$ in a thermal environment of 20°C , under free heat exchange conditions. In this case the model in Eq (6.4) reduces down to

$$\begin{aligned} 0.15t + 0.45T_1(t) + (-119447 + 1092.18T_0(t))w(t) - 1.23 \cdot 10^{11}w^3(t) \\ = 0.02w''(t) \end{aligned} \tag{6.61}$$

Considering the assumptions discussed earlier in this Chapter for $T_0(t)$ and $T_1(t)$, we introduce $T_0(t)=20$ and $T_1(t) = e^{-57.1329t} \approx 100$, obtained from Eq(6.7). Therefore Eq.(6.61) can reduce down to

$$w''(t) - (2209.11)^2w(t) + 6.13 \cdot 10^{12}w^3(t) = 7.74t + 227.37 \tag{6.62}$$

This expression has the form of Eq.(6.11):

$$\ddot{W}(t) + 2\beta\dot{W}(t) + (\omega^2 + B \cos \Omega t + C \sin \Omega t)W(t) + DW(t)^3 = E + Ft + Gt^{-3}$$

with the coefficients set as

$$\omega = 2209.11, B \approx C \approx 0, D = 6.13 \cdot 10^{12}, E = 227.37, F = 7.74, G = 0 \tag{6.63}$$

We can compare the numerical solution available from Eq.(6.63) with the solution obtained using the multiple scales method and given in Eq.(6.55) for which we introduce the following parameters:

$$\begin{aligned}
\Omega = 5500, \quad \omega = 2209.11, \quad \beta = 0.00000001, \quad B = 0.001, \quad C = 0.001, \\
D = 6.13 \cdot 10^{12}, \quad E = 227.37, \quad F = 7.74, \quad G = 0
\end{aligned}
\tag{6.64}$$

In order to obtain a multiple scales solution a negligible level of damping was introduced as well as a relatively high excitation frequency of $\Omega = 5500$ rad/s (equivalent to 875.35 Hz), in order to make sure that real-valued analytical solutions can be determined. This is well over twice the value of the natural frequency which is $\omega = 2209.11$ rad/s (equivalent to 351.59 Hz) so the system is operating beyond principal parametric resonance, with positive detuning. It should be noted that this resonance condition is relatively minor due to the low amplitude of the excitation, at 0.001 m, or 1 mm peak. This is entirely consistent with the sort of level of excitation amplitude that would be encountered in a satellite installation.

Directly obtained numerical results obtained by integrating with the NDSolve function in *Mathematica*TM, and the corresponding closed form solution obtained using the multiple scales method in Eq.(6.55), are both presented in Figs. 6.4 and 6.5, respectively, over 100 seconds.

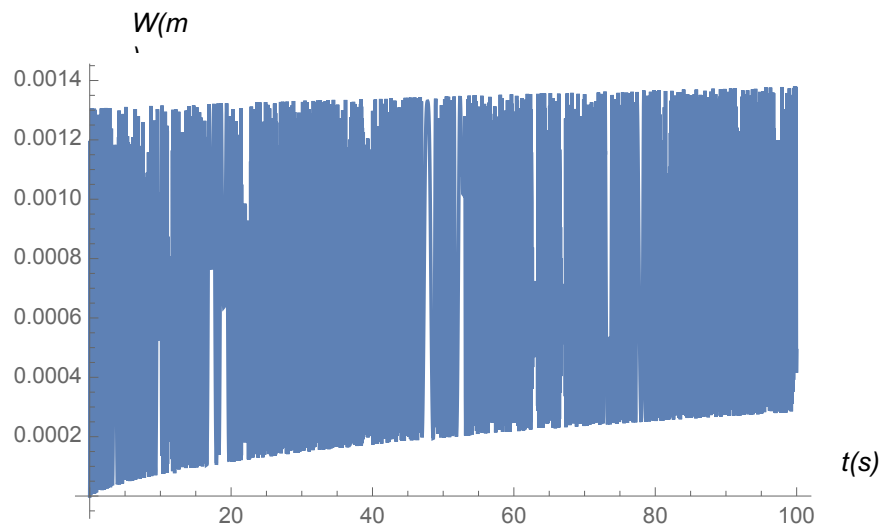


Figure 6.4. Displacement response in the time domain when subjected to increasing mechanical loading 10t within an environmental temperature of $20^{\circ}C$ calculated by direct numerical integration by means of NSDolve in *Mathematica*

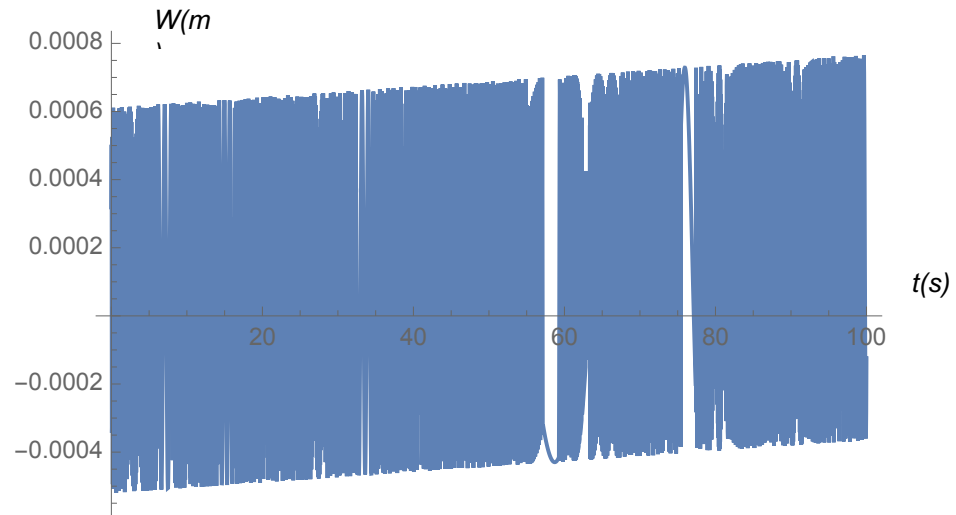


Figure 6.5. Displacement response in the time domain when subjected to increasing mechanical loading $10t$ within an environmental temperature of 20°C based on the approximate analytical solution obtained from the multiple scales procedure as given in Eq.(6.55)

It can be seen that the principal qualitative difference between the two results is the relatively large positive DC offset, and consequent positive drift of this offset with time, in the numerical integration result, showing a peak-to-peak amplitude of ~ 0.00107 m. This compares directly with the approximate analytical solution from the multiple scales expansion which starts from a point of almost no DC offset, but with an almost identical peak-to-peak amplitude of ~ 0.00113 m. It can be clearly seen that in this case a DC offset also starts to grow over time. There are small but potentially significant differences in the conditions under which the two solution forms are obtained, summarised by the fact that the approximate analytical solution requires a very small level of dissipation and a small parametric excitation amplitude at a frequency well above the critical point of principal parametric resonance, in order to generate real valued solutions of commensurate value (peak-to-peak amplitude) and characteristic (a DC offset which grows with time). On that basis it is hard to make an absolutely meaningful comparison between the two solutions, as the operating conditions are different, and so a qualitatively and quantitatively reliable and accurate closed-form solution is not obviously available from the perturbation method of multiple scales for the coupled model developed in Chapter 2 in order to simulate the dynamic behaviour of the panel undergoing a variety of different mechanical and thermal loadings.

6.4 Conclusions

The solution for the model developed and verified in the previous Chapters for the sandwich honeycomb panel was obtained using numerical integration within the *Mathematica* software. Therefore in this chapter an attempt has been made to reduce the main system of partially coupled equations to one governing equation, with the purpose of obtaining a closed form analytical solution which can be used without *Mathematica* software simply by varying parameters in the solution function. The governing equation was obtained successfully by introducing some limitations on applicability, and equation Equation (6.10) appeared to be a particular case of the Mathieu-Hill equation. Thus it was decided to solve it using the perturbation method of multiple scales, notwithstanding the fact that the principal parametric resonance condition will emerge as a consequence of the treatment of secular terms in order to guarantee the uniformity of the expansion for $W(t)$. As a result the solution obtained was capable of demonstrating the general behaviour of the system which showed a qualitatively identical dynamic pattern. However, the accuracy of the amplitude of vibration was characterised by an unacceptable level of error. After close examination of the peculiarities of the method it was concluded that due to the presence of the secular terms, this method would not allow us to obtain an accurate analytical closed form solution which could provide representative results for the system's behaviour. Therefore, the use of the *Mathematica* software and numerical integration is recommended for obtaining the most accurate results for simulating the dynamic behaviour of the panel when it undergoes a variety of different mechanical and thermal loadings.

7. Guidance for use of the code developed for obtaining the deflection results and heat distribution along the thickness of the panel

This chapter is developed as a guide for Airbus DS engineers to be able to obtain the results for deflection of the panel considered in Chapter 2 and heat distribution along the thickness of the panel while being subjected to the mechanical dynamic loading as well as thermal loading. The model, and therefore the code, were both developed for free heat exchange and for heat flux conditions in Chapter 2. This code will allow the engineers to obtain a link missing so far in their practice and to see how the coupling of the thermo-elastic effect can affect the results obtained separately for the mechanical and thermal models. With time this might potentially lead to evidence based conclusions to budget in additional adjustments for the effect of coupling, to guarantee a higher accuracy of the existing model used in Airbus DS practice.

7.1 A guide for the use of the annotated code for obtaining the deflection results and heat distribution along the thickness of the panel under free heat exchange conditions

As an example of the code we are considering the solution for the panel $a \times b$ of thickness $h = 0.015$ mm undergoing dynamic mechanical loading of 10t in the environment of 150°C as discussed in Chapter 2. It should be noted that the figures below are extracts from the code, and those which are highlighted in pink are stages requiring input, and those which are highlighted in blue do not require any input as they are different stages of the calculation.

The first stage of the solution is running the code in the file **Stage 1** and starts with the input of data for the material properties, as well as the reference and absolute temperatures of the environment. All these parameters are identified with symbols, as shown in Fig.7.1. The output parameters and their meanings are identified in this part of code as well (Fig.7.1). In this part of the code nothing needs to be changed. It only provides instructions for the symbols. The actual numerical values are set in the code below, shown in Fig.7.2.

```

(*Input needed for:
    Q11, Q12, Q22, Q66 - elastic stiffness for an orthotropic plate
    lam33-conductivity of the 1st lamina;
lam11, lam12, lam22 - thermal conductivities
    h-plate thickness
    p-mass density of lamina; c-specific heat at constant strain of lamina
For these parameters above M - middle ply, Ex-external ply

    alpha1,
alpha2 - coefficients of thermal expansion in x and y directions respectively
    Tinf=|Absolute temperature of environment-reference temperature|
    Tref - reference temperature
    H-boundary conductance
    delta-damping coefficient

Output:
    T0, T1 - temperature variables the system of eq to be resolved for,
to demonstrate constant,
linear quadratic and cubic behaviour in thermal gradient along z
    u,v,w - displacement variables the system of eq to be resolved for *)

```

Figure 7.1. Annotated part of the code in the Stage 1 file, explaining the definitions of the parameters.

```

a = 0.3
b = 0.1
Tinf = 150 - 0
Tref = 0
H = 1200
h = 0.015 (*h-plate thickness, H-boundary conductance*)
delta = 0
L = 10 * t
q[t] = (2 / a) * Integrate[L * (Sin[(Pi * x) / a]), {x, 0, a}]
px = py = 0

```

Figure 7.2. The input parameters are set to numerical values in the Stage 1 file

It should be pointed out that in this solution the plain loading in the x and y directions (p_x and p_y) was set to zero, as we are interested primarily in the deflection of the panel as the

largest output of deformation, and the normal loading is set in $q[t]$ with the parameter $L=10t$ representing the dynamic part of this transvers loading.

Since we are considering a sandwich panel we need to consider the external layers (subscript Ex) and a middle ply (subscript M) having different properties. All these parameters (Q, lam, p, c, h) with subscripts Ex and M corresponding to the external and middle plies are defined in Fig.7.1.

```

QEx11 = QEx22 = ((73 * (10^9) * 0.33) / ((1 + 0.33) * (1 - 2 * 0.33))) + 2 * 669 * (10^6)
QEx12 = ((73 * (10^9) * 0.33) / ((1 + 0.33) * (1 - 2 * 0.33)))
QEx66 = 2 * 669 * (10^6)
lamEx33 = lamEx11 = lamEx12 = lamEx22 = 149
pEx = 2780
cEx = 875
hEx = 0.00038

QM11 = QM22 = ((669 * (10^6) * 0.33) / ((1 + 0.33) * (1 - 2 * 0.33))) + 2 * 310 * (10^6)
QM12 = (669 * (10^6) * 0.33) / ((1 + 0.33) * (1 - 2 * 0.33))
QM66 = 2 * 310 * (10^6)

lamM33 = lamM11 = lamM12 = lamM22 = 209
pM = 50
cM = 904
hM = 0.01424

```

Figure 7.3. Input parameters are set to numerical values for the skins and the middle ply, in the Stage 1 file

The following part of the code described in Fig.7.4 follows the methodology described in Chapter 2 and sets the procedure for calculation of the parameters needed for the law of temperature distribution (output T) described in Eq.(2.9). No addition the input parameters are needed in this part of this code.

```

alpha1 = ((2 * 25 * hEx + 2.4 * hM) / h) * (10 ^ (-6))
alpha2 = ((2 * 25 * hEx + 2.4 * hM) / h) * (10 ^ (-6))

T = fa[z] * T0[x, y, t] + fb[z] * T1[x, y, t] + fc[z]
fa[z] = r1 + r2 * z + r3 * (z ^ 2) + r4 * (z ^ 3)
fb[z] = r5 + r6 * z + r7 * (z ^ 2) + r8 * (z ^ 3)
fc[z] = r9 + r10 * z + r11 * (z ^ 2) + r12 * (z ^ 3)
T
(*Free heat exchange with environment coefficients*)
p = (2 * pEx * hEx + pM * hM) / h
lam33 = (2 * lamEx33 * hEx + lamM33 * hM) / h
r1 = r6 = 1
r3 = -(4 * H) / (h * (h * H + 4 * lam33))
(*h-plate thickness, H-boundary conductance*)
r8 = -(4 * (h * H + 2 * lam33)) / ((h ^ 2) * (h * H + 6 * lam33))
(*lam33-conductivity of the 1st lamina*)
r11 = (4 * H * Tinf) / (h * (h * H + 4 * lam33))
(*Tinf=|Absolute temperature of environment-reference temperature|*)
r2 = r4 = r5 = r7 = r9 = r10 = r12 = 0
(*Free heat exchange with environment coefficients - end*)
TextCell["Law of temperature distribution"]
T

```

Figure 7.4. Calculation of the law of temperature distribution for the free heat exchange case, in the Stage 1 file

Following the Galerkin method for the displacement representation, all displacement outputs (normal and planar) are set in the harmonic form with the purpose of simplification through integration, which is a standard approach in plate theory. After that the strain parameters, membrane forces and bending moments are defined, following the procedure in Chapter 2, where Eqs.(2.2) – (2.6) are needed for derivation of the mechanical equations of motion. No additional input is required in this part of code (Fig.7.5).

```

(*Galerkin simplification*)
w[x, y, t] = ww[t] * (Sin[(Pi * x) / a]) * (Sin[(Pi * y) / b])
u[x, y, t] = uu[t] * (Sin[(Pi * x) / a]) * (Sin[(Pi * y) / b])
(*In Rega u and v are more complex*)
v[x, y, t] = vv[t] * (Sin[(Pi * x) / a]) * (Sin[(Pi * y) / b])
T1[x, y, t] = TT1[t] * (Sin[(Pi * x) / a]) * (Sin[(Pi * y) / b])
T0[x, y, t] = TT0[t] * (Sin[(Pi * x) / a]) * (Sin[(Pi * y) / b])
(*Galerkin-end*)

(*Strain - 2D , no rotation of the transverse normal around x and y*)
eps11 = D[u[x, y, t], x] + 0.5 * ((D[w[x, y, t], x]) ^ 2)
eps22 = D[v[x, y, t], y] + 0.5 * ((D[w[x, y, t], y]) ^ 2)
eps12 = D[u[x, y, t], y] + D[v[x, y, t], x] +
  (D[w[x, y, t], x] * D[w[x, y, t], y]) + (z ^ 3) * (-2 * c1) * D[w[x, y, t], x, y]
c1 = 4 / (3 * (h ^ 2))
(*No transverse shearing strain - end*)

```

```

(*For orthotropic plate*)
betaM11 = QM11 * alpha1 + QM12 * alpha2
betaM22 = QM12 * alpha1 + QM22 * alpha2 (*beta11,
beta22 - thermoelastic stiffness*)
betaM12 = 0 (*corrected as for External*)
  betaEx11 = QEx11 * alpha1 + QEx12 * alpha2
  betaEx22 = QEx12 * alpha1 + QEx22 * alpha2
(*beta11, beta22 - thermoelastic stiffness*)
  betaEx12 = 0 (*corrected to 0 for orthotropic Eq(40) in Rega paper*)
sigM11[z] = QM11 * eps11 + QM12 * eps22 - betaM11 * T
sigM22[z] = QM12 * eps11 + QM22 * eps22 - betaM22 * T
sigM12[z] = QM66 * eps12
  sigEx11[z] = QEx11 * eps11 + QEx12 * eps22 - betaEx11 * T
  sigEx22[z] = QEx12 * eps11 + QEx22 * eps22 - betaEx22 * T
  sigEx12[z] = QEx66 * eps12

sig11[z] = (2 * sigEx11[z] * hEx + sigM11[z] * hM) / h
sig22[z] = (2 * sigEx22[z] * hEx + sigM22[z] * hM) / h
sig12[z] = (2 * sigEx12[z] * hEx + sigM12[z] * hM) / h

N11 = Integrate[sig11[z], {z, -h / 2, h / 2}]
N12 = Integrate[sig12[z], {z, -h / 2, h / 2}]
N22 = Integrate[sig22[z], {z, -h / 2, h / 2}]

M11 = Integrate[z * sig11[z], {z, -h / 2, h / 2}]
M12 = Integrate[z * sig12[z], {z, -h / 2, h / 2}]
M22 = Integrate[z * sig22[z], {z, -h / 2, h / 2}]

```

Figure 7.5. Calculation of parameters needed for the mechanical equations of motion, in the Stage 1 file

This leads to the derivation of the mechanical equations of motion Eqs.(2.1) (Fig. 7.6). No additional input is required for this part of code.

```
(*Mechanical Equations of Motion*)
TextCell["Mechanical Equations of Motion"]
Integrate[(Integrate[(D[N11, x] + D[N12, y]), {x, 0, a}]), {y, 0, b}] == 0
Integrate[(Integrate[(D[N12, x] + D[N22, y]), {x, 0, a}]), {y, 0, b}] == 0
s1[x, y, t] = (N11 * D[w[x, y, t], x]) + (N12 * D[w[x, y, t], y])
s2[x, y, t] = (N12 * D[w[x, y, t], x]) + (N22 * D[w[x, y, t], y])
Integrate[
  (Integrate[(D[M11, {x, 2}] + 2 * (D[M12, x, y]) + D[M22, {y, 2}] + D[s1[x, y, t], x] +
    D[s2[x, y, t], y] - px * D[w[x, y, t], {x, 2}] - py * D[w[x, y, t], {y, 2}] +
    q[t]) * (Sin[Pi * x] / a) * (Sin[Pi * y] / b)], {x, 0, a}], {y, 0, b}] ==
Integrate[(Integrate[(p * h * (D[w[x, y, t], {t, 2}]) + delta * (D[w[x, y, t], t])) *
  (Sin[Pi * x] / a) * (Sin[Pi * y] / b)], {x, 0, a}], {y, 0, b}]

(*Mechanical Equations of Motion - end*)
```

Figure 7.6. Derivation of the final mechanical equations of motion, in the Stage 1 file

The next stage is to derive the thermal equations of motion Eqs. (2.12). Following the procedure described in Chapter 2, noting Eqs. (2.13)-(2.19), the code calculates all the necessary parameters, as can be seen in Fig.7.7. No any additional input is required in this part of the code.

```
TextCell["Thermal effect parameters"]

(*2D Thermal balance Equations parameters*)
(*lam11, lam12, lam22 - thermal conductivities;

qij- heat flow along the x,y,z directions*)
g1[z] = fa[z] * D[T0[x, y, t], x] + fb[z] * D[T1[x, y, t], x]
(*g1, g2 thermal gradients corresponding to Tx, Ty*)
g2[z] = fa[z] * D[T0[x, y, t], y] + fb[z] * D[T1[x, y, t], y]
lam11 = (2 * lamEx11 * hEx + lamM11 * hM) / h
lam12 = (2 * lamEx12 * hEx + lamM12 * hM) / h
lam22 = (2 * lamEx22 * hEx + lamM22 * hM) / h
(*q0, q1 - bending components of the heat flow*)
q01[x, y, t] = Integrate[lam11 * g1[z] + lam12 * g2[z], {z, -h / 2, h / 2}]
q02[x, y, t] = Integrate[lam12 * g1[z] + lam22 * g2[z], {z, -h / 2, h / 2}]
q11[x, y, t] = Integrate[z * lam11 * g1[z] + z * lam12 * g2[z], {z, -h / 2, h / 2}]
q12[x, y, t] = Integrate[z * lam12 * g1[z] + z * lam22 * g2[z], {z, -h / 2, h / 2}]
```

```

(*Q0, Q1 - energy rates due to heat flow q3 in z direction*)
Q0 =
  2 * (Integrate[lam33, {z, -h/2, h/2}]) * (r3 * T0[x, y, t] + r7 * T1[x, y, t] + r11) +
  6 * (Integrate[lam33 * z, {z, -h/2, h/2}]) *
    (r4 * T0[x, y, t] + r8 * T1[x, y, t] + r12)
Q1 = 2 * (Integrate[lam33 * z, {z, -h/2, h/2}]) *
    (r3 * T0[x, y, t] + r7 * T1[x, y, t] + r11) +
  6 * (Integrate[lam33 * (z^2), {z, -h/2, h/2}]) *
    (r4 * T0[x, y, t] + r8 * T1[x, y, t] + r12)
(*b0, b1 - internal energy; p-mass density of lamina;
c-specific heat at constant strain of lamina*)
c = (2 * cEx * hEx + cM * hM) / h
b0[x, y, t] = Integrate[p * c * T, {z, -h/2, h/2}]
b1[x, y, t] = Integrate[p * c * z * T, {z, -h/2, h/2}]
(*b0, b1 - interaction energy;*)
beta11 = (2 * betaEx11 * hEx + betaM11 * hM) / h
beta22 = (2 * betaEx22 * hEx + betaM22 * hM) / h
a0[x, y, t] = Tref * (Integrate[beta11 * eps11 + beta22 * eps22, {z, -h/2, h/2}])
(*for orthotropic eps21=0*)
a1[x, y, t] =
  Tref * (Integrate[z * beta11 * eps11 + z * beta22 * eps22, {z, -h/2, h/2}])

```

Figure 7.7. Calculation of the parameters needed for the thermal equations of motion, in the Stage 1 file

After that the final thermal equations of motion Eq.(2.12) are calculated by the code shown (Fig.7.8).

```

(*Thermal balance Equations*)
TextCell["Thermal balance Equations "]
Integrate[(Integrate[(D[q01[x, y, t], x] + D[q02[x, y, t], y] -
  D[b0[x, y, t], t] - D[a0[x, y, t], t] + Q0), {x, 0, a}]), {y, 0, b}] == 0
Integrate[(Integrate[(D[q11[x, y, t], x] + D[q12[x, y, t], y] -
  D[b1[x, y, t], t] - D[a1[x, y, t], t] + Q1), {x, 0, a}]), {y, 0, b}] == 0

Quit[]

```

Figure 7.8. The final thermal equations of motion, in the Stage 1 file

All these steps of code result in the numerical output of the law of temperature distribution, the Mechanical equation of motion and the thermal equations of motion, presented in Fig.7.9.

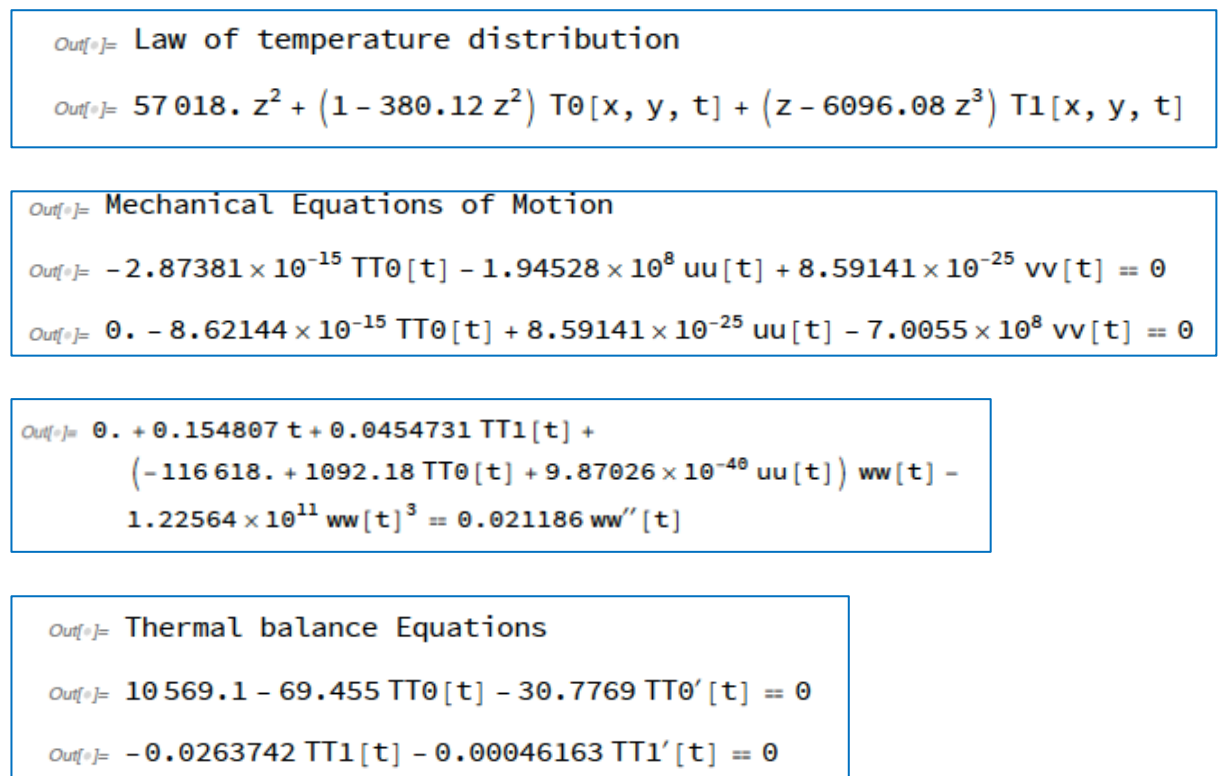


Figure 7.9. Numerical Output after running the code for the law of temperature distribution, the mechanical equation of motion and the thermal equations of motion, in the Stage 1 file

Now that we have derived all the necessary equations of motion, they need to be solved to obtain the displacement and temperature distribution along the thickness. Therefore the second stage of the process, the solution of the equations of motion, is performed in the file **Stage 2**.

Since we are ignoring the planar loading and concentrating on the deflection as an output, the third equation of motion from the mechanical equations of motion is copied into the code in the Stage 2 file, together with the thermal equations of motion, as presented in Figure 7.10. At this stage the initial conditions for the environmental temperature 150°C and the displacement at the moment of time 0 are set here as well. The code is set to perform a numerical solution of the system of equations using the NDSolve function with the set initial conditions.


```

In[ ]:=
s = NDSolve[{0. + 0.154807 t + 0.0454731 TT1[t] +
(-117706. + 1092.18 TT0[t]) ww[t] - 1.22564 x 1011 ww[t]3 == 0.021186 ww''[t],
7046.05 - 69.455 TT0[t] - 30.7769 TT0'[t] == 0,
-0.0263742 TT1[t] - 0.00046163 TT1'[t] == 0, TT1[0] == 150, ww[0] == 0,
ww'[0] == 0, TT0[0] == 0}, {TT1[t], ww[t], TT0[t]}, {t, 0, 500}]

```

Figure 7.10. Code to perform solution of the system of mechanical and thermal equations of motion in the Stage 2 file

The code in Fig.7.11 following the section in Fig.7.10 instructs the programme to produce numerical and graphical representations of the solution obtained for the displacement $w(t)$ for different intervals of time ($[0..20]$, $[0..100]$, $[0..500]$), and thermal components $T1(t)$, $T0(t)$ for the law of thermal distribution T (as set in Fig.7.9). While setting the moment of time to $t=0.1$ and $t=100$, we are also able to obtain the final graphical representations for the temperature distribution along the thickness of the plate (z coordinate). Considering that the total thickness of the plate is $h=0.015$, the z variable spans from -0.0075 to 0.0075 .

```

TextCell["displacement w(t)"]
Plot[Evaluate[{ww[t]} /. s], {t, 0, 20}, PlotStyle -> Automatic]
Plot[Evaluate[{ww[t]} /. s], {t, 0, 100}, PlotStyle -> Automatic]
Plot[Evaluate[{ww[t]} /. s], {t, 0, 500}, PlotStyle -> Automatic]
TextCell["Thermal component T1(t)"]
Plot[Evaluate[{TT1[t]} /. s], {t, 0, 10}, PlotStyle -> Automatic]
TextCell["Thermal component T0(t)"]
Plot[Evaluate[{TT0[t]} /. s], {t, 0, 10}, PlotStyle -> Automatic]

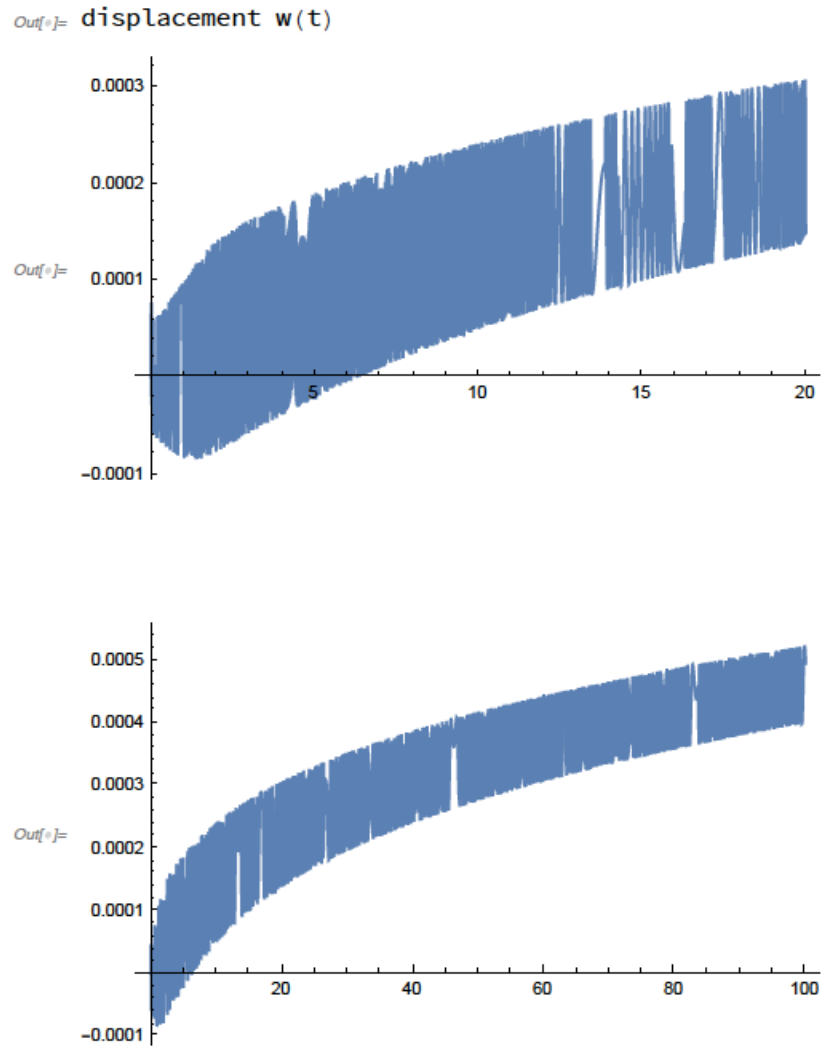
t = 0.1
Plot[Evaluate[57018. z2 + (1 - 380.12 z2) TT0[t] + (z - 6096.08 z3) TT1[t] /. s],
{z, -0.0075, 0.0075}, PlotStyle -> Automatic]

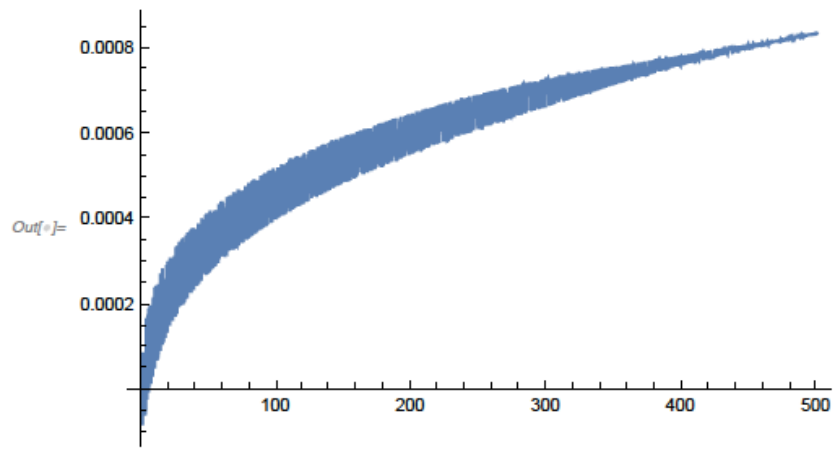
t = 100
Plot[Evaluate[57018. z2 + (1 - 380.12 z2) TT0[t] + (z - 6096.08 z3) TT1[t] /. s],
{z, -0.0075, 0.0075}, PlotStyle -> Automatic]
Quit[]

```

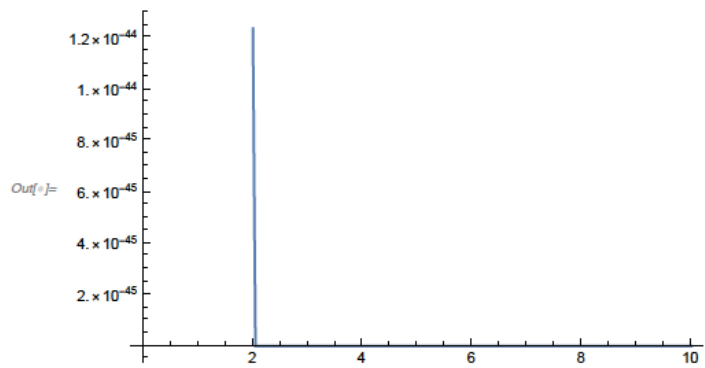
Figure 7.11. Code to performing the numerical and graphical representations of the solution in the Stage 2 file

The output of the code in Fig.7.11 results in the graphical representations for displacement $w(t)$, and the thermal components $T_0(t)$ and $T_1(t)$, as well as the final temperature distribution T along the thickness of the plate for selected moments of time, as shown in Figure 7.12.

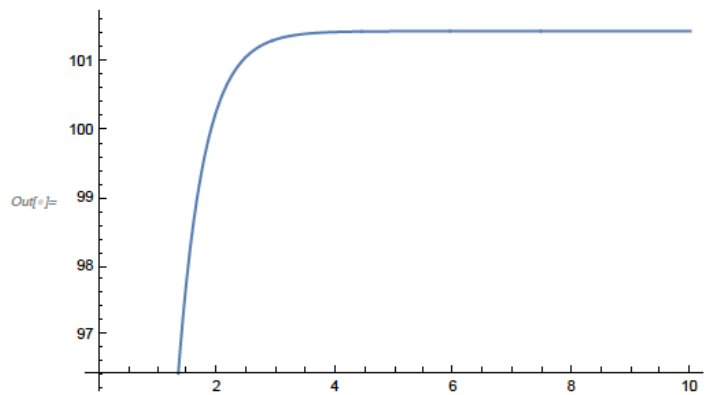




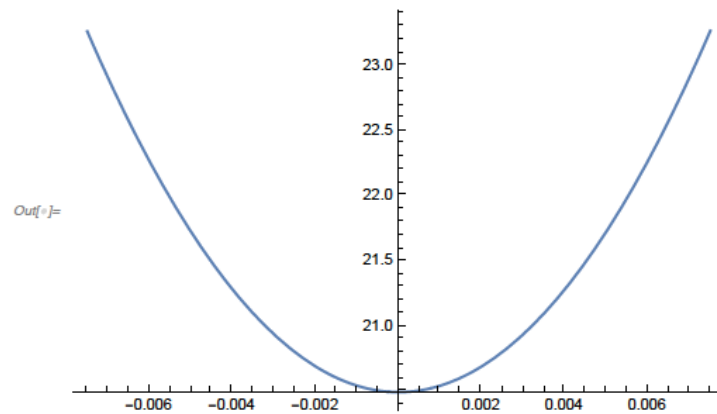
$Out[] =$ Thermal component T1(t)



$Out[] =$ Thermal component T0(t)



$Out[] = 0.1$



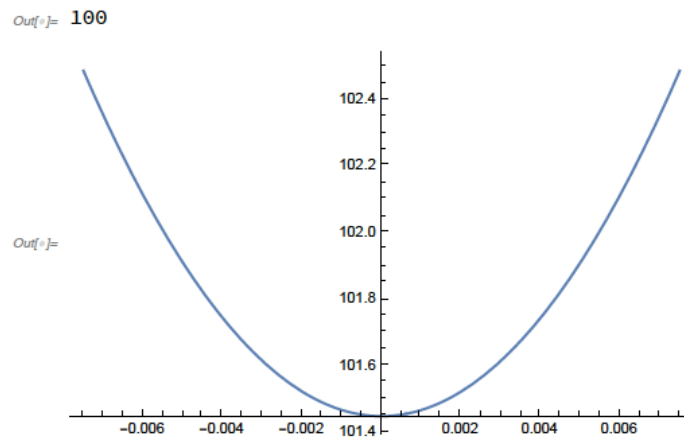


Figure 7.12. Graphical output of the solution in the Stage 2 file

7.2 Guid for use of the annotated code for obtaining the deflection results and the heat distribution along the thickness of the panel under heat flux conditions

As an example of the code we are still considering the solution for the panel $a \times b$ of thickness $h = 0.015$ mm undergoing dynamic mechanical loading of $10t$ with heat flux of $q_3^*(x, y, t) = 150t \sin \frac{\pi x}{a} \sin \frac{\pi y}{b}$, as discussed in Chapter 2.

The code in the Stage 1 file developed for this thermal loading condition was based on the same methodology as in the previous section, however as mentioned in Chapter 2, when introducing heat flux instead of free heat exchange conditions, the model has to be adjusted through the change of thermal coefficients r_i in Eqs (2.10) corresponding to Eq.(2.8) which would affect Eq. (2.9) and thus all the equations representing the thermal part of the model discussed in Section 2.2. Additionally the heat flux law has to be introduced in the Input section (Fig.7.2).

Therefore the Stage 1 file will consist of the code identical to the case discussed in section 7.1, except for the part of the code responsible for the input of data (Fig.7.2) which will now have the heat flux law set as well (Fig. 7.13) and calculation of the law of temperature distribution (Fig. 7.4) will be replaced with the part of code shown in Fig.7.14.

```

a = 0.3
b = 0.1
Tinf = 150 - 0
Tref = 0
qq[x, y, t] = -150 * t * Sin[(Pi * x) / a] * Sin[(Pi * y) / b]
(*heat flow*)
H = 1200
h = 0.015 (*h-plate thickness, H-boundary conductance*)
delta = 0
L = 10 * t
q[t] = (2 / a) * Integrate[L * (Sin[(Pi * x) / a]), {x, 0, a}]
px = py = 0

```

Figure 7.13. Input parameters are set to numerical values in the Stage 1 file

```

alpha1 = ((2 * 25 * hEx + 2.4 * hM) / h) * (10 ^ (-6))
alpha2 = ((2 * 25 * hEx + 2.4 * hM) / h) * (10 ^ (-6))

T = fa[z] * T0[x, y, t] + fb[z] * T1[x, y, t] + fc[z]
fa[z] = r1 + r2 * z + r3 * (z ^ 2) + r4 * (z ^ 3)
fb[z] = r5 + r6 * z + r7 * (z ^ 2) + r8 * (z ^ 3)
fc[z] = r9 + r10 * z + r11 * (z ^ 2) + r12 * (z ^ 3)
T

(*Free heat exchange with environment coefficients*)
p = (2 * pEx * hEx + pM * hM) / h
lam33 = (2 * lamEx33 * hEx + lamM33 * hM) / h
r1 = r6 = 1
r3 = -(12 * H) / (h * (5 * h * H + 24 * lam33))
(*h-plate thickness, H-boundary conductance*)
r4 = -(16 * H) / ((h ^ 2) * (5 * h * H + 24 * lam33))
r7 = -(4 * H) / (5 * h * H + 24 * lam33)
r8 = -(4 * (3 * h * H + 8 * lam33)) / ((h ^ 2) * (5 * h * H + 24 * lam33))
(*lam33-conductivity of the 1st lamina*)
r11 = -2 * (H * h * qq[x, y, t] + 6 * lam33 * (qq[x, y, t] - H * Tinf)) /
(h * lam33 * (5 * h * H + 24 * lam33))
r12 = (4 * H * h * qq[x, y, t] + 4 * lam33 * (qq[x, y, t] - H * Tinf)) /
((h ^ 2) * lam33 * (5 * h * H + 24 * lam33))
(*Tinf=|Absolute temperature of environment-refrence temperature|*)
r2 = r5 = r9 = r10 = 0
(*Free heat exchange with environment coefficients - end*)
TextCell["Law of temperature distribution"]
T

```

Figure 7.14. Calculation of the law of temperature distribution for the free heat exchange case, in the Stage 1 file

The rest of the code responsible for the derivation of the mechanical and thermal equations of motion and their parameters described in Chapter 2 and in Figures 7.1, 7.3, 7.5-7.8 remain the same, in line with the model described in Chapter 2.

Therefore the output from running the code will still give us the numerical output of the law of temperature distribution, Mechanical equation of motion and the thermal equations of motion as was presented in Fig.7.9 for free heat exchange case but for the heat flux condition it will be as shown in Fig.7.15.

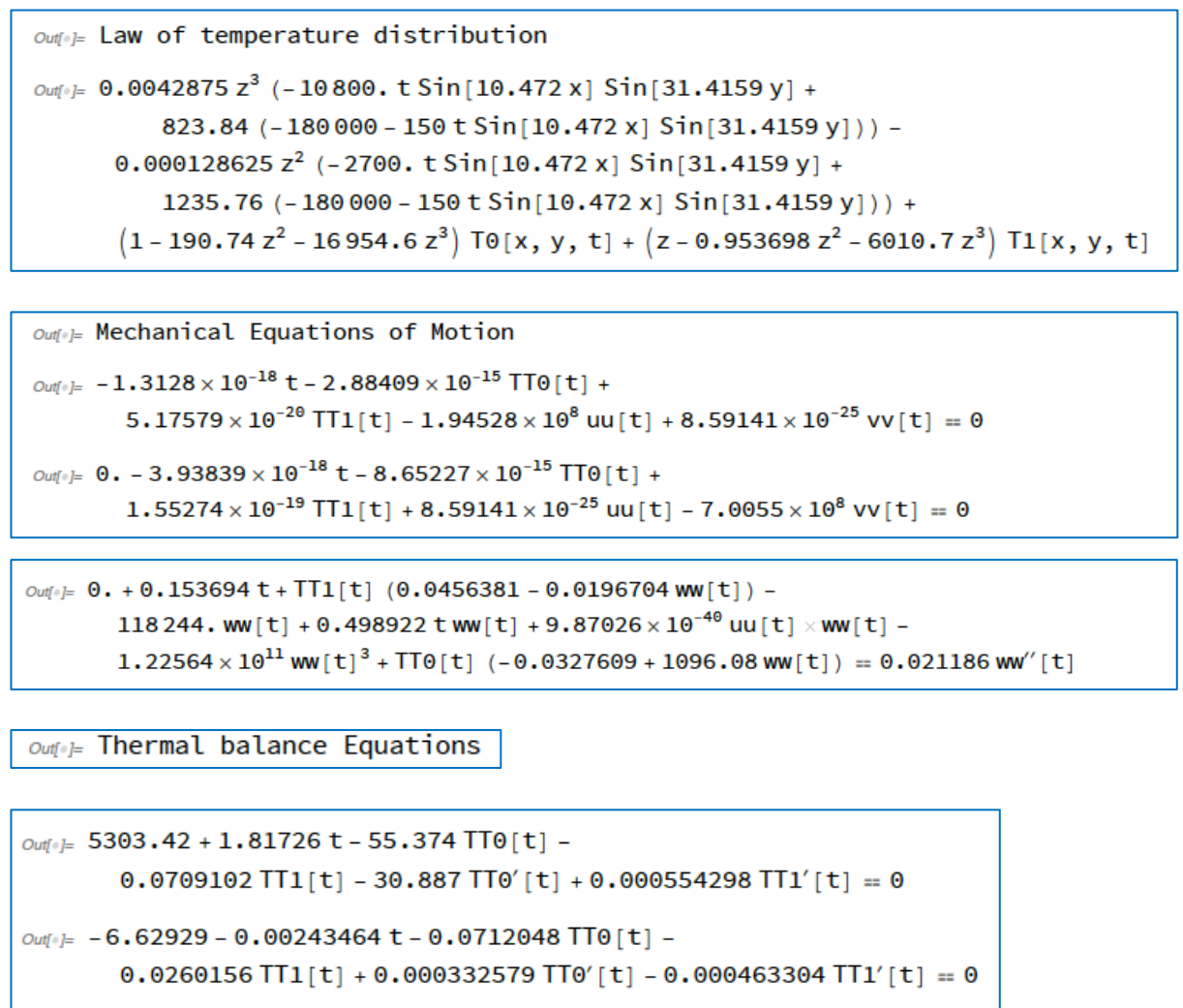


Figure 7.15. Numerical Output after running the code for the law of temperature distribution, the mechanical equation of motion and the thermal equations of motion, given in the Stage 1 file

As can be seen from Fig.7.15 the equations obtained are more complex than in the case of free heat exchange, and therefore potentially more approximation in the numerical solution process might take place.

Now that we have derived all the necessary equations of motion they need to be solved to obtain the displacement and temperature distribution along the thickness, just like for the case of free heat exchange. Therefore the second stage of the process, the solution of the equations of motion, is performed in the file **Stage 2** which consists of code (Fig.7.16) identical to that described in Figs.7.10 and 7.11, but with a different law of temperature distribution, mechanical equation of motion and the thermal equations of motion inserted from Fig.7.15.

```

In[ ]:=
s = NDSolve[{0.153694 t + TT1[t] (0.0456381 - 0.0196704 ww[t]) - 118244. ww[t] +
0.498922 t ww[t] - 1.22564 x 1011 ww[t]3 + TT0[t] (-0.0327609 + 1096.08 ww[t]) =
0.021186 ww''[t], 5303.42 + 1.81726 t - 55.374 TT0[t] -
0.0709102 TT1[t] - 30.887 TT0'[t] + 0.000554298 TT1'[t] = 0,
-6.62929 - 0.00243464 t - 0.0712048 TT0[t] - 0.0260156 TT1[t] +
0.000332579 TT0'[t] - 0.000463304 TT1'[t] = 0, TT1[0] = 150,
ww[0] = 0, ww'[0] = 0, TT0[0] = 0}, {TT1[t], ww[t], TT0[t]}, {t, 0, 500}]

```

```

TextCell["displacement w(t)"]
Plot[Evaluate[{ww[t]} /. s], {t, 0, 20}, PlotStyle -> Automatic]
Plot[Evaluate[{ww[t]} /. s], {t, 0, 500}, PlotStyle -> Automatic]
TextCell["Thermal component T1(t)"]
Plot[Evaluate[{TT1[t]} /. s], {t, 0, 10}, PlotStyle -> Automatic]
TextCell["Thermal component T0(t)"]
Plot[Evaluate[{TT0[t]} /. s], {t, 0, 100}, PlotStyle -> Automatic]
TextCell["Thermal distribution T(t,z)"]

x = 0.15
y = 0.05
ThL = 0.0042875 z3 (-10 800. t Sin[10.472 x] Sin[31.4159 y] +
      823.84 (-180 000 - 150 t Sin[10.472 x] Sin[31.4159 y])) -
      0.000128625 z2 (-2700. t Sin[10.472 x] Sin[31.4159 y] +
      1235.76 (-180 000 - 150 t Sin[10.472 x] Sin[31.4159 y])) +
      (1 - 190.74 z2 - 16 954.6 z3) TT0[t] + (z - 0.953698 z2 - 6010.7 z3) TT1[t]

t = 0.1
Plot[Evaluate[ThL /. s], {z, -0.0075, 0.0075}, PlotStyle -> Automatic ]

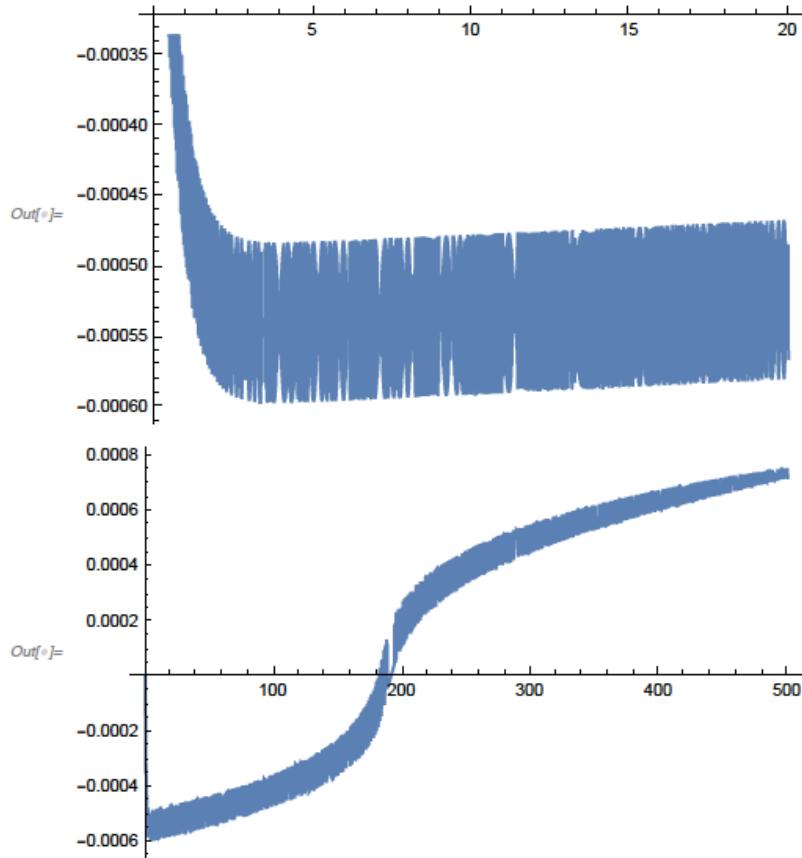
t = 100
Plot[Evaluate[ThL /. s], {z, -0.0075, 0.0075}, PlotStyle -> Automatic ]
Quit[]

```

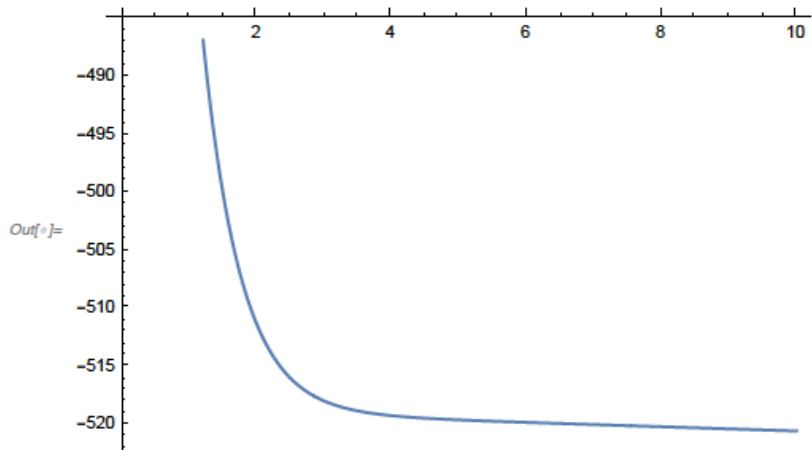
Figure 7.16. Code to perform solution of the system of mechanical and thermal equations of motion and its graphical representation of the solution in the Stage 2 file

The output of the code in Fig.7.16 results in graphical representations for displacement $w(t)$, thermal components $T_0(t)$ and $T_1(t)$, as well as the final temperature distribution T along the thickness of the plate for selected moments of time, as shown in Figure 7.17.

Out[10]= displacement $w(t)$



Out[11]= Thermal component $T1(t)$



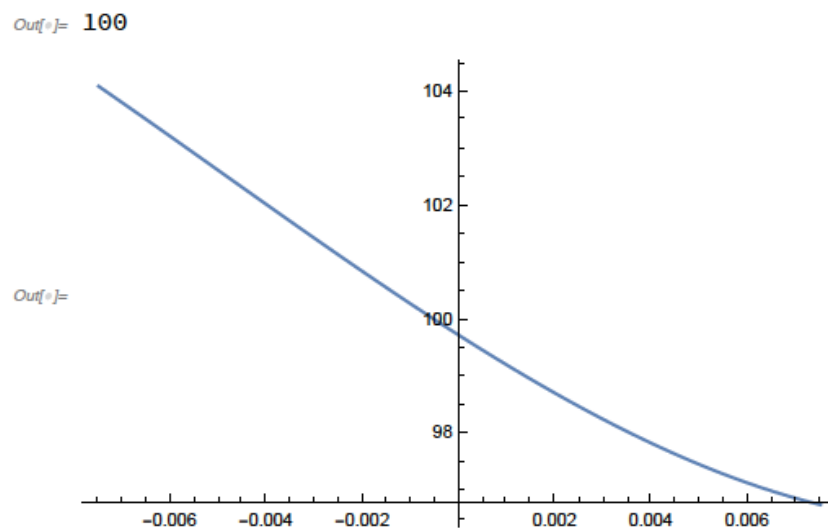
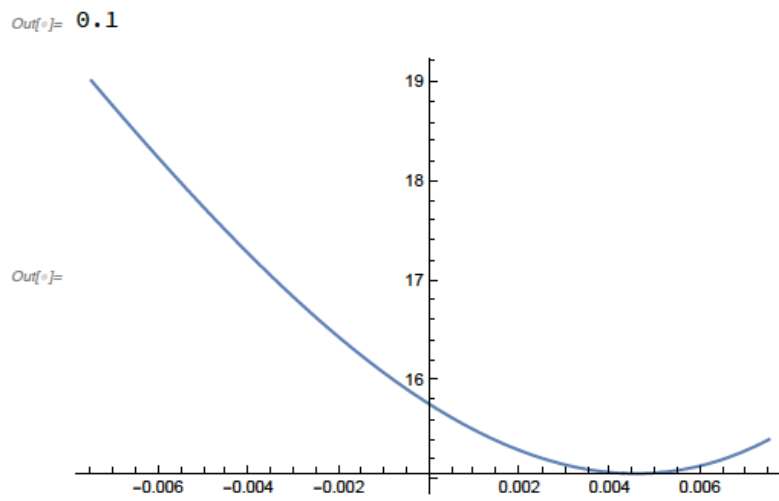
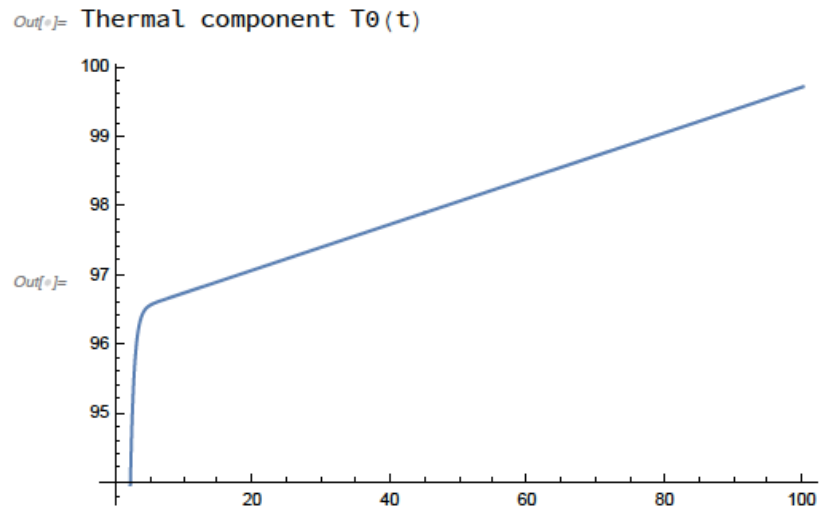


Figure 7.17. Graphical output of the solution in the Stage 2 file

Please note that detailed analysis of the numerical results obtained are performed in Chapter 2

7.3. Conclusions

As intended, an annotated code has been developed in this thesis for automation of the model derivation and its solution. Thus this chapter represents a step-by-step description of the code to produce a comprehensive guide for use by Airbus DS engineers. An attempt was made to reduce the system of equations of motion, consisting of the mechanical and thermal equations of motion, down to a known type of equation, the solution of which could be found analytically. This was performed through the method of multiple scales with the intention to find a closed form solution which would mean that we would not need the Stage 2 file for numerical solution of the system of equations derived in the Stage 1 file. However, even though this was done for a simpler system of equations, for the case of free heat exchange, the complexity of the equations did not allow the determination of an accurate enough closed form solution (Chapter 6). Therefore both stages of the process, Stage 1 – derivation of the governing equations based on the model in Chapter 2 and Stage 2 – numerical solution and graphical representation of the solution, still must be integral parts of the process. Both files (Stage 1 and Stage 2) are fully annotated, as described in this chapter, and therefore allow easy use for engineers at Airbus DS. If the *Mathematica* software is not available the code can easily be transferred to a different syntax software, following the instructions and explanations of what each part of the code represents, all described in this chapter. However it must be pointed out that the *Mathematica* software was chosen due to its powerful capability for solving numerically quite complex systems of equations similar to the ones obtained for both free heat exchange and heat flux conditions. Therefore, if in the future Airbus DS decides to transfer the code to a different software for future use, it should be checked that the software is capable of solving boundary value problems similar to those described in Figs. 7.10 and 7.16.

Conclusions

Airbus DS had identified a problem of parasitic deformation in their spacecraft structures and payloads due to the temperature gradient variations in materials characterised by different properties. This was therefore seen to affect the pointing vectors or the line-of-sight of critical payloads. However, because the mission pointing needs that are demanded of payloads can vary from several arc-seconds down to sub-arc second angular shifts in their pointing vectors, such anomalies of distortion have to be taken into account, and therefore accommodated within the system design.

Therefore the work reported in this thesis has been based on the consideration of a large selection of confidential reports and project proposals investigating the uncertainties in dynamic and thermal analyses, as well current engineering design practices in Airbus DS and a strong need was identified for further research into methods to improve the prediction accuracy in existing multistage techniques, or to propose an alternative modelling approach to the existing mapping approach hitherto adopted by Airbus DS. It was already known that the modelling of spacecraft structures depends on the ability of the model to predict or take into account the temperature gradients through the thickness of the structure, and that this capability might provide a solution to the problem of de-pointing. On that basis it was decided that an alternative approach should include not only a resolution of the mapping approach but also an inclusion of the influence of the thermal distribution through the thickness of the structural material.

Since the problem had been initiated by Airbus DS and had started with an in-depth analysis of confidential documentation provided by the Company the treatment of the thermo-elastic problem was first analysed and discussed. It was evident that the Company has a marked preference for the Nastran FEM package and the Systema TMM tool in order to obtain results separately for the elasto-mechanical and thermal parts of the problem, and that these results later had to be merged through data export and interpolation techniques. It was concluded that although this multistage process was part of a well-developed practice undertaken with the full involvement of expert engineers, this process in general has clearly had the potential to result in significantly reduced

accuracy of the predicted thermo-elastic dynamics due to unmodelled, but fundamentally important, coupling effects between the thermal and mechanical models.

Since the FEM approach as traditionally preferred by Airbus DS was well developed for the Company's users it was also known not to be capable of delivering the levels of accuracy necessary, so it was decided to perform research into other software packages, not necessarily based on numerical analysis through FEM but on the use of automated tools founded on the exact analytical solutions, since they potentially should provide more accurate results whereas FEM was known somewhat to underestimate the prediction. While considering this form of analytical approach it was proposed that a physics based coupling process of the two physical effects of temperature and mechanical deformation could be the only real way forward to achieve the required increase in the accuracy of the results.

In order to make progress a detailed review of the phenomenon of thermo-elasticity was undertaken, and this concluded that a mechanical deformation of a body is connected to a change of heat inside it and therefore with a change of the temperature distribution within the body. At the same time a deformation of the body can be generated by certain temperature changes. So, the internal energy of the body depends on both the temperature and the deformation. It became clear that in an **isothermal** case, which had been considered by Airbus DS in their experimental programmes, there are processes which are elastically and thermally **reversible**. However if the temperature varies in time we deal with two coupled processes, the *reversible elastic process* and the *irreversible thermodynamic process* (due to a spontaneous and hence irreversible process of heat transfer by means of heat conduction).

Therefore a variety of fully coupled and partially coupled models was considered and that investigative work concluded that although application of a partially coupled approach means that we could face a partial division of the models into the thermal part (defining the temperature or solving the HC equation) and the mechanical part (predicting the displacement based on the set or identified temperature) such an approach can still provide results as accurate as a fully coupled model, but at a well reduced level of

computational cost and complexity. In order to reduce the computational cost it was decided to develop the model following the well-developed and generalised TTC approach which was described in Chapter 2. This approach is a third order theory with thermomechanical coupling and can provide results as accurate as those obtained by using fully coupled models using a fourth order expansion of the configuration variables. It is also flexible enough to accommodate the necessary simplifications of some of the key parameters, to accommodation of appropriate boundary and initial conditions, as well as a variety of different dynamic thermal and mechanical loadings within a multilayered plate.

Since the intention has been to provide a more accurate modelling tool for the resolution of the problem encountered by Airbus DS in their design practice, it was suggested that the newly developed coupled model must ideally be automated and expressed in an annotated code for universality, accessibility, and further development. The output data could be presented graphically but the main output should be annotated and accompanied by a user guide in order to make the data representation easily accessible and usable for practicing engineers at Airbus DS Ltd.

In order to develop a full understanding of the conditions and the levels of loading which needed to be modelled, the literature review covered the relevant confidential material provided by Airbus DS as well as the open literature. This review was undertaken with the purpose of identifying the conditions that the satellite panel would normally experience, including the thermal environmental conditions in LEO, as well as vibration of the system due to installed equipment, where this form of excitation is commonly responsible for the mechanical loading on the satellite panels. The review excluded impacts due to collisions with debris, as this was deemed to be out of scope of the work. As a way of gaining an understanding of the structure of the sandwich honeycomb panels typically used in aerospace practice and specifically for the satellite panel samples provided by Airbus DS, the literature review also included an investigation of the structure and the manufacturing techniques, as well as the behavioural features of similar honeycomb panels.

After the completion of the literature review a new modelling strategy for aluminium honeycomb composite panels was developed to account for the physics of dynamic thermal and mechanical loadings, and this was achieved through an implementation of the partially-coupled modelling procedure coded in the *Mathematica*TM language, whereby different boundary conditions and dynamically varying thermal properties could be easily accommodated. Contrary to the numerical examples presented for verification of the generalised analytical model, the full nonlinear structure of the dynamic thermomechanical model was maintained as far as possible. The model comprised three coupled nonlinear ordinary differential equations for which previous work has shown that an analytical closed-form solution could only be obtained for linearised forms of the differential equations and also only for static thermal and mechanical loads. A comparison of the nonlinear and linearised solutions was performed and it was found that the linearised equations could be useful for predicting the temperature profile through the thickness of panels with no appreciable loss of accuracy. However, for simulation of the displacement of the structure it was found that the full system of nonlinear coupled equations should be solved, and this has been done numerically within this thesis.

In Chapter 2 a full set of numerical results was obtained for a simply supported aluminium honeycomb composite panel, as commonly used within the aerospace industry, and undergoing thermal, mechanical, and thermo-mechanical loading conditions. The thermal load mechanism was underpinned by free heat exchange and the mechanical loading in all cases comprised a normal constant force exerted centrally on the top surface of the panel. The configuration could readily be altered in terms of panel aspect ratio, boundary conditions, and load location. When the panel was subjected solely to a thermal load the nonlinear numerical solution for the displacement of the panel showed a transient oscillation over time at a commensurately small amplitude. The temperature distribution along the thickness of the panel was also calculated demonstrating thermal stabilisation over time, as one would expect. For a linearly increasing thermal load temperature, due to a significant increase of the environmental temperature and its transfer to the panel, it was found that the panel showed signs of accumulated thermal stresses characterised by the transient response and subsequent buckling displacement. The temperature distribution along the thickness of the panel reflected the trend in the rising environmental temperature. Core thickness was seen to affect the results with the thinner panels displaying a more pronounced thermo-mechanical response than thicker components,

through a higher level of displacement and a faster heating-up process along the thickness of the panel. It was also found that for a dynamically increasing thermal loading the core temperature in a thicker panel was always ‘catching-up’ with the surface temperature and would never reach a level of being warmer than the panel surface. In the case of constant mechanical loading at constant environmental temperature a noticeable dc offset in the displacement was observed, as would be expected. The temperature profile in this case showed a thermal stabilisation around the environmental temperature. The effect of the core thickness was also investigated for the case of dynamic mechanical loading at the constant environmental temperature, confirming the conclusions drawn before for the purely thermal loading. In the case of both dynamically increasing mechanical and thermal loading a transient response was observed for around 5s until the mechanical loading dominated the response of the panel and introduced a clearer dynamically-increasing displacement. In this case there was clear evidence of increased displacement due to the combined effects of the time-variant mechanical and thermal loading.

A more realistic case of heat flow for a space application was also considered. In this case the model had to be adjusted to introduce appropriate thermal coefficients, prescribed heat flow and thermal boundary conditions. Results were obtained for simulations of a number of dynamically increasing heat flows. The results of the simulations for the panel exposed to the heat flux were discussed, in comparison with the free heat exchange conditions, and the main differences in displacement outputs as well as heat distribution along the thickness of the panel were discussed. It was evident that the high level of heat introduced by the heat flux on one of the surfaces of the panel was initiating thermal stresses in the panel resulting in the buckling effect. This behaviour resulted in a stiffer deflection response for positive values of heat flux. Negative values of heat flux resulted in increased deflection of the panel. The profile of the temperature distribution along the thickness of the panel for the case of heat flux confirmed the increased temperature on the top surface of the panel, with reducing temperature values towards the bottom surface of the panel.

In both cases the procedure for obtaining the governing equations and their solutions was coded in *Mathematica* representing a fully automated process. The code developed in Chapter 2 is fully annotated to allow open access for any modifications including when

passed on to an industrial analyst. The code has been generalised and is not restricted by the values supplied which means that the parameters described in the input section can be easily varied, and simulation can be performed for different type of materials.

In Chapter 3 a programme of experimental work was performed and, from analysis of the data generated, it was found that there is strong evidence of the thermo-mechanical coupling effect when the panel is immersed in an environment at an extreme temperature, and is loaded mechanically. Evidence was also found that thermal loading caused by the extreme environment affects the deflection value and the level of residual stresses, and conversely the mechanical loading affects the heat accumulation and distribution within the panel. The extreme temperature environment did not cause an accumulation of any residual heat after unloading. However, during the processes of loading and unloading there was evidence of thermo-mechanical coupling which resulted in the presence of extra heat internally within the structure compared to the heat available from the environment, and it was found that this could result in a temperature swing of up to 3 °C. If the environmental temperature is close to the ambient temperature there is an accumulation of residual heat within the panel which is still present to a large extent even at the point of complete unloading of the deformed sample, indicating thermodynamic irreversibility for an environmental temperature close to the nominal ambient. It was found that the environmental temperature effect is significant and that it changes the trend of the deflection - temperature behaviour of the panel. The deflection of the panel affected the distribution of the heat within the panel resulting in a localised temperature swing in the material of around 2.5 °C if deformed in a cool environment and up to 1.2 °C in warmer environments. There was no evidence of residual stress accumulation only in the case of the panel operating in the ambient temperature environment. For negative environmental temperatures and the higher positive temperatures the deflection values for a panel which had already undergone some deformation did not come back to the initial values after the removal of the loading, and were characterised by the presence of some residual stress, and thermodynamic irreversibility. The extent of this residual stress was seen to be dependent on the environmental temperature within which the panel was immersed. For the sample considered in Chapter 3 the deflection during unloading in a very cold environment could reach up 0.1mm lower than the corresponding value during loading. This confirmed the damaging effect of thermal loading on the mechanical properties of the panel.

Although there was no significant thermal swing initiated by deflection within the panel geometry at a certain fixed environmental temperature, there was a dramatic difference in the way the thermal changes occurred in the panel due to the deformation for different hot or cold environments. This demonstrates the connection between the thermal properties of the panel and deformation, and how they affect each other as the deformation progresses - constituting the thermo-mechanical coupling within the panel. There was hysteresis found in the thermal response to the deformation, which was seen to get more significant for the colder environments, and the thermal properties of the panel demonstrated this through a swing in the temperature of the panel of 2.5°C during the unloading process.

Therefore, in order to produce an accurate prediction of the deformation progression and regression during the loading and unloading processes, as well as the heat distribution along the panel geometry, it is recommended to introduce corresponding correction factors to account for:

- the effect of the environmental temperature on the magnitudes of the deformation of the panel;
- the initial thermal conditions of a panel which has undergone a mechanical deformation, even if the loading has been completely removed. The thermal properties for such a panel cannot necessarily be assumed to be fully controlled by the value of the environmental temperature if the panel also undergoes mechanical loading.

In Chapter 3 it was also found that the panel tended to cool down in a relatively uniform way in all three dimensions. However, the heating up process was not uniform and there was some localised heating resulting in certain hot-spot areas accumulating more heat than others. This was the case if the panel was in an environmental temperature between ambient and +80 °C. In the more extreme thermal environment the sample heated up more evenly and reflected the temperature of the environment linearly, even while being mechanically loaded. From the data obtained during this experimental work it is evident that in the environment with the temperature close to the ambient the skins do heat up faster than the honeycomb core, however this trend was found to disappear as the environmental temperature moved to higher or lower extremes. An interesting

observation was that when going into the more extreme hot or cold environments the pattern of temperature feedback from the panel, with respect to the deflection, bifurcates, demonstrating how significant the thermal changes of the environment can be for the pattern of the coupling between the thermal properties and the mechanical deformation of the panel.

In Chapter 4 the panel tested in the experimental set up in Chapter 3 was considered for verification of the analytical model through comparison of the maximum displacement of the panel, as well as for checking the influence of the environmental temperature on the magnitude of displacement induced by a dynamic mechanical loading. The same trend of the higher displacement response in hotter environments and lower displacement response in cooler environments was found, confirming the associated predictions of the analytical model developed in Chapter 2. It was also found that the displacement response was characterised by the transient behaviour, dependent on the environmental temperature, confirming the coupled effects of thermal and mechanical loading. The model was also used to predict the dynamic thermal response of the material within the thickness of the panel, demonstrating a nonlinear temperature distribution profile within the thickness of the panel, something which is very difficult to perform experimentally. It was also found that during the heating up process the core remained at a lower temperature than the skins were at the beginning of the heating up process. However, there was also evidence of heating up of the core beyond the skin temperature by a very small amount. Although the difference between the temperature of the core and the skins at the end of the transformation was very small, it still gave an indication of some nonlinear transformational phenomena occurring within the thickness of the panel when undergoing mechanical loading within the harsher environments. This of course might be more significant for larger or thicker panels and could be particularly significant for large aerospace structures exposed to harsh thermal cycles. These internal transformations due to the heating-up or cooling-down processes could be the key to the explanation of the transient response demonstrated in the displacement response as driven by the environmental temperature. It is also hypothesised that the frequency of the transient response might be higher due to amplitude ‘suppression’ in cooler environments due to the material stiffening effect, which could potentially introduce a parasitic resonance contributing to the problem of de-point of the parent satellite structure. This is still to be investigated in future research. It also should be concluded that inclusion of the coupling

effect between the mechanical and thermal phenomena is essential in the process of modelling since there is strong evidence of their influence on the final dynamic behaviour of the system and this can also potentially be significant due to the effect of resonance.

Since Airbus DS use FEM extensively for their thermo-elastic analysis, the work in Chapter 5 was performed under the supervision of the author of this thesis and resulted in a journal paper being prepared for publication. In this work three different FE models were developed to attempt to simulate a simplified thermo-mechanical FE model. The three models were analysed in terms of validity, accuracy, and computational cost. It was demonstrated that all three models were able to show a significant deviation of panel response at the low load range that is typically associated with satellites, making them suitable for such analysis. The models also demonstrated clearly the effect of the thermal loading and interaction between mechanical and thermal loading in the form of larger deflection at higher thermal loading and stiffer response at lower temperatures, which was in line with the experimental results presented in Chapter 3. It was concluded that the 2D continuum model was the simplest model and that this delivered considerable computational savings at the cost of a lack of response under low-strain conditions, while the 3D continuum model offered higher accuracy and generally with a saving of computational time of around 60% comparing to the 3D Geometrically Accurate Model. The 3D models also demonstrated the effect of buckling with subsequent snap-through due to the initial high thermal loading from the applied heat flux, which was consistent with results obtained for the analytical model in Section 2.4, Chapter 2. These are valuable results since the experimental work performed in Chapter 3 presented results for free heat exchange thermal loading only. In this way the analytical and FE models offer further, more detailed, predictions for the thermo-mechanical behaviour of the sandwich honeycomb panel. However it should be emphasised that the analytical model developed in Chapter 2 is still characterised by the additional capability of accurate prediction of nonlinear temperature distribution along the thickness of the panel, as well as prediction of the deflection response of the panel due to the two coupled phenomena while undergoing simultaneous mechanical and thermal loading.

The solution for the model developed and verified in the previous Chapters for the sandwich honeycomb panel was obtained using numerical integration within the *Mathematica*TM software. Therefore in Chapter 6 an attempt was made to reduce the main system of partially coupled equations to one governing equation, with the purpose of

obtaining a closed form analytical solution which could be used without *Mathematica*TM software simply by varying parameters in the solution function. The governing equation was reduced down to a particular case of the Mathieu-Hill equation and solved using the perturbation method of multiple scales, notwithstanding the fact that the principal parametric resonance condition was shown to emerge naturally as a consequence of the treatment of secular terms in order to guarantee the uniformity of the expansion for deflection. The solution obtained was capable of demonstrating the general behaviour of the system which showed a qualitatively identical dynamic pattern. However, the accuracy of the amplitude of vibration was characterised by an unacceptable level of error and therefore it was concluded that due to issues with the secular terms this method would not allow us to obtain an accurate analytical closed form solution which could provide representative results for the system's behaviour. Therefore, the use of the *Mathematica*TM software and numerical integration is recommended for obtaining the most accurate results for simulating the dynamic behaviour of the panel when it undergoes a variety of different mechanical and thermal loadings.

As was the aim, an annotated code was developed in this thesis for automation of the model derivation and its solution, and in Chapter 7 a step-by-step comprehensive guidance through the code was produced. This guidance is intended specifically for the use of Airbus DS engineers. The code requires implementation within the *Mathematica*TM software due to the complexity of the nonlinear governing equations, and consists of two stages described in detail in Chapter 7. It should be pointed out that the *Mathematica*TM software was chosen here due to its uniquely powerful capability for solving quite numerically complex systems of equations similar to those obtained for both free heat exchange and heat flux conditions.

Therefore the intended aim of this thesis, which was to consider a variety of thermoelastic modelling approaches and to develop a more accurate methodology has been achieved, and provides an additional tool for the engineers at Airbus DS Ltd to estimate the heat propagation along the thickness of the panels, as well as to predict the deformation of the panel due to both heat exposure and vibration from neighbouring sub-systems and installations.

As mentioned above and in Chapter 4 the displacement response was found to be characterised by the transient behaviour, dependent on the environmental temperature or thermal disturbance, confirming the coupled effects of thermal and mechanical loading. In this respect it is recommended the use of active damping should be considered, based on the careful introduction of smart materials into satellite structures, similar to technology suggested in [235]. A combination of piezoelectric sensors and actuators was successfully applied in an aluminium structure to suppress thermally induced vibration caused by an applied heat flux.

Through the development of further expertise in the area of vibration and investigation of the related phenomena, it should be emphasised that in [236] evidence was given from the vibrational mechanics point of view which also accommodated a nonlinear approach to complex systems, that an effect of self-excitation takes place which was originally discovered for pendulums. Blekhman showed that this effect can be extended to the self-synchronisation of mechanical vibratory systems, and non-balanced rotors, which were rotationally excited by asynchronous drives. The research in this thesis has demonstrated both theoretical and experimental observations supporting this phenomenon.

The work discussed in [236] studied the displacement and de-pointing effects due to the vibrational influences from the transportation of solids along a conveyor, the separation of materials of different properties, the micro-displacement and wear of parts, the de-pointing of the read-out needles of measuring devices and gyroscopic axes, and many other instances, having both intentional and parasitic effects. It should be noted that the direction of displacement can be vibration dependent and potentially could be controlled by changes in the frequency of vibration.

Studies of the effect of de-pointing from a stable equilibrium position due to vibration have demonstrated that a key position in a system could be attracted to the direction of the acting vibration. In this case the vibrational de-pointing effects would principally be caused by vibrational forces and moments [237-240]. However this effect can also work in reverse and it is possible to achieve a stable equilibrium position of under vibration which did not exist in the rest position.

It was also shown that material strength can be undermined by vibration. In particular applied vibration may change the elastic moduli of a material, as well as its dissipative properties. One example of this particular effect is the well-known Indian rope trick.

Based on wider perspective it is fair to hypothesise that the predicted effect of de-pointing in a satellite could be emphasised or mis-represented by inaccuracies in the model, and that this problem could potentially be rectified by using the model developed in this thesis. However, there could also be the presence of sources of vibration from neighbouring sub-systems which could attract critical parts of the equipment such as antenna arrays, and that effects such as this could contribute to the de-point effect. Unintended and unmodelled changes in important material properties, again for example in critical antenna arrays or supporting parts, could also contribute to the de-point issue. Therefore it is highly recommended that further research is undertaken that includes the additional phenomena mentioned here, in parallel with the coupled thermal and mechanical responses considered in the modelling process in this thesis.

References

[1] M. Boscolo, J. R. Banerjee, “Dynamic stiffness formulation for composite Mindlin plates for exact modal analysis of structures”, *Part I: Theory. Computers & Structures*, vol. 96-97, pp. 61-73, 2012, doi: 10.1016/j.compstruc.2012.01.002.

Disc 1 with confidential reports and documents:

[2-4] ‘01_Climatic_chamber_test&photogrammetry’ (3 reports containing details on experimental set-up and outputs.)

[5-8] ‘02_Process’ (4 reports containing information about Airbus DS approach to thermoelastic modelling)

[9-16] ‘03_programms’ (contains 8 reports dedicated to thermoelastic analysis performed for specific programmes)

[17] ‘04_FEM_requirements_spec’ (1 report describing FEM analysis procedure in NASTRAN software)

[18-21] ‘05_solar_orb’ (4 reports describing test results and specifications for the Solar Orbiter)

Disc 2 with confidential reports and documents:

[22] ‘01_NASTRAN_static_user_guide’ (contains a NASTRAN user guide)

[23-28] ‘02_honeycomb_HEXCEL_data’ (contains 6 reports from HEXECEL describing properties of the panels and an ESA Handbook on honeycombs)

[29-37] ‘03_Various refs1’ (contains 8 papers describing research outputs with respect to the properties of honeycomb panels)

[38-49] ‘03_Various refs2’ (contains 11 papers describing research outputs with respect to the variety of properties and geometry of honeycomb panels)

[50-57] ‘03_Various ref3’ (contains 7 papers describing research outputs with respect to the variety of properties and structure of honeycomb panels)

[58-60] '03_Various_refs4' (contains 1 thesis and 2 papers on structural performance and thermal response of honeycomb panels)

[61-63] '04_BAE_TN' (contains 3 files with technical reports and notes on some analytical calculations for honeycomb panels)

Disc 3 with confidential reports and documents:

[64-88] '01-STM FEM and Nastran Files' (containing 24 files including Nastran run files, bulk data files and results files.

[89-93] '02-TED Analysis Documents' (contains 4 Guides to the FEM analysis procedure for thermoelastic analysis).

[94] '03-Pre-Test Documents' (contains a report on a Solar Orbiter test specifications)

[95-108] '04-Test Data and Reports' (containing 2 ESA test report of thermoelastic tests and Airbus' thermoelastic sensitivity assessment report; 11 test results files containing unprocessed test data from ESA).

[109] A.Bouchery. "Thermoelastic prediction and verification methodology". MTF.R&D.TN.5665. *Airbus Defence and Space*. 16/12/2015.

[110] "Improvement of methodologies for thermo-elastic predictions and verification". Technical Proposal. Part 1. AO/1-8619/16/NL/KML. *Airbus Defence and Space SAS-2016*.

[111] "Statement of Work & Requirements: Thermal Imaging & Photogrammetry. STM Thermo-Elastic Verification Test". 211 000. *Airbus Defence and Space Ltd*, 2023.

[112] "Photogrammetry trial summary report". Aicon DPA vs. Leica TM6100A. *Airbus Defence and Space*, 15/08/18.

- [113] “PLATO TED Joint {ESA/Airbus DS} Workshop”. [PLATO-ADSS-SYS-RP-1000153481]. *Airbus Defence and Space*.
- [114] S. Iugovich, A. Bouchery. “Thermoelastic methodology and thermo V2 associated tool user’s manual”, 26/09/2012.
- [115] P. Hopkins. “Generic Mechanical FEM specification”. ADS.E.0787. *Astrium*.
- [116] S. Sablerolle. “Test Report. Thermal Imaging & Photogrammetry on SOLO STM. Thermo-Elastic Verification Test”. ESA-TEC-MX-MTL-TR-01315.
- [117] “PLATO-TED verification strategy. B1X Final presentation”. PLATO-ADSS-SYS-PS-1000128627. *Airbus Defence and Space*.
- [118] R. Geddes. “Solar orbiter STM thermo elastic distortion test specification SOL.S.ASTR.TS.00091”. *Airbus Defence and Space*.
- [119] P. Malik, R. Kadoli, “Thermo-elastic response of SUS316-Al₂O₃ functionally graded beams under various heat loads”. *International Journal of Mechanical Sciences*, vol. 128–129, pp. 206–223, 2017.
- [120] W. H. Wittrick, “A unified approach to initial buckling of stiffened panels in compression”, *International Journal of Numerical Methods in Engineering*, vol. 11, pp. 1067–1081, 1968.
- [121] W. Wittrick, F. Williams, “Buckling and vibration of anisotropic or isotropic plate assemblies under combined loadings”, *International Journal of Mechanical Sciences*, vol. 16, no. 4, pp. 209–239, 1974.

[122] M. Anderson, F. Williams, C. Wright, “Buckling and vibration of any prismatic assembly of shear and compression loaded anisotropic plates with an arbitrary supporting structure”, *International Journal of Mechanical Sciences*, vol. 25, no. 8, pp. 585–596, 1983.

[123] W. Anderson, J. Stroud, B. J. Durling, K. W. “Hennessy, Structural panel analysis and sizing code”, *Tech. Rep. TM-80182*, NASA, Lagley, Virginia, Nov. 1981.

[124] J. Stroud, W. H. Greene, W. Anderson, “Buckling loads for stiffened panels subjected to combined longitudinal compression and shear loading”, *Tech. Rep. TM-83194*, NASA, Lagley, Virginia, Oct. 1981.

[125] F. W. Williams, W. H. Wittrick, “An automatic computational procedure for calculating natural frequencies of skeletal structures”, *International Journal of Mechanical Sciences*, vol. 12, no. 9, pp. 781–791, 1970.

[126] F. W. Williams, D. Kennedy, R. Butler, M. S. Anderson, “VICONOPT: Program for exact vibration and buckling analysis or design of prismatic plate assemblies”, *AIAA Journal*, vol. 29, pp. 1927–1928, 1991.

[127] J. Reddy, *Mechanics of laminated composite plates and shells: theory and analysis. Classical and first-order theories of laminated composite plates*. CRC Press, 1997.

[128] W. H. Wittrick, F. W. Williams, “A general algorithm for computing natural frequencies of elastic structures”, *Quarterly Journal of mechanics and applied sciences*, vol. 24, no. 3, pp. 263–284, 1970.

[129] M. Boscolo, J.R. Banerjee, “Dynamic stiffness formulation for composite Mindlin plates for exact modal analysis of structures. Part II: Results and applications”, *Computers*

[130] O. Civalek, “Free vibration analysis of symmetrically laminated composite plates with first-order shear deformation theory (FSDT) by discrete singular convolution method”, *Finite Elements in Analysis and Design*, vol. 44, pp. 725–731, 2008.

[131] A. A. Khdeir, L. Librescu, “Analysis of symmetric cross-ply laminated elastic plates using higher-order theory: Part II - buckling and free vibration”, *Composite Structures*, vol. 9, pp. 259–277, 1988.

[132] M. Kabir, B.T. Tehrani, “Closed-form solution for thermal, mechanical, and thermo-mechanical buckling and post-buckling of SMA composite plates”, *Composite Structures*, vol. 168, pp. 535–548, 2017.

[133] J. N. Reddy, N. D. Phan, “Stability and vibration of isotropic, orthotropic and laminated plates according to a higher-order shear deformation theory”, *Journal of Sound and Vibration*, vol. 98, no. 2, pp. 157–170, 1985.

[134] W. Nowacki, *Thermoelasticity*. 2nd edition. Pergamon press, 1986.

[135] S. Brischetto, E. Carrera. “Coupled thermo-mechanical analysis of one-layered and multilayered plates”, *Composite Structures*, vol. 92, pp. 1793–1812, 2010.

[136] B.A. Boley, J.H. Weiner. *Theory of thermal stresses*. John Wiley & Sons, 2013.

[137] M. Cetkovic. “Thermo-mechanical bending of laminated composite and sandwich plates using layerwise displacement model”, *Composite Structures*, vol. 125, pp. 388–399, 2015.

- [138] M.F. Caliri Jr., A.J.M. Ferreira, V. Tita, “A review on plate and shell theories for laminated and sandwich structures highlighting the Finite Element Method”, *Composite Structures*, vol. 156, pp. 63–77, 2016.
- [139] M. Cho, J. Oh, “Higher order zig-zag theory for fully coupled thermo-electric-mechanical smart composite plates”, *Int J Solids Struct*, vol. 41, no. 5-6, pp. 1331–56, 2004.
- [140] E. Carrera, “Historical review of zig-zag theories for multilayered plates and shells”, *Appl Mech Rev*, vol. 56, no. 3, pp. 287–308, 2003.
- [141] R.J. Adams, “Analysis and control of thermoelastic vibrations in plate structures” PhD thesis. University of Oklahoma, 2001.
- [142] D. Trajkoviski, R. Cukic, “A coupled problem of thermoelastic vibrations of a circular plate with exact boundary conditions”, *Mech Res Commun*, vol. 26, no. 2, pp. 217–24, 1999.
- [143] L. Adam, J.P. Ponthot, “Thermomechanical modeling of metals at finite strains: first and mixed order finite elements”, *Int J Solids Struct*, vol. 42, no. 21-22, pp. 5615–55, 2005.
- [144] K. Swaminathan, D.M. Sangeetha, “Thermal analysis of FGM plates – A critical review of various modeling techniques and solution methods”, *Composite Structures*, vol. 160, pp. 43–60, 2017.
- [145] S. Chakraverty, K.K. Pradhan. “Free vibration of exponential functionally graded rectangular plates in thermal environment with general boundary conditions”, *Aerospace*

Science and Technology, vol. 36, pp. 132–156, 2014.

[146] N.D. Duc, *et al.*, “Mechanical and thermal stability of eccentrically stiffened functionally graded conical shell panels resting on elastic foundations and in thermal environment”, *Composite Structures*, vol. 132, pp. 597–609, 2015.

[147] Z.X. Lei, K.M. Liew, J.L. Yu. “Free vibration analysis of functionally graded carbon nanotube-reinforced composite plates using the element-free kp-Ritz method in thermal environment”, *Composite Structures*, vol. 106, pp. 128–138, 2013.

[148] B.S. Aragh, *et al.*, “3-D thermo-elastic solution for continuously graded isotropic and fiber-reinforced cylindrical shells resting on two-parameter elastic foundations”, *Applied Mathematical Modelling*, vol. 37, pp. 6556–6576, 2013.

[149] J. Han, *et al.*, “Modal density and mode counts of sandwich panels in thermal environments”, *Composite Structures*, vol. 153, pp. 69–80, 2016.

[150] M. Adineh, M. Kadkhodayan. “Three-dimensional thermo-elastic analysis and dynamic response of a multi-directional functionally graded skew plate on elastic foundation”, *Composites Part B*, vol. 125, pp. 227-240, 2017.

[151] M. Tanaka, T. Matsumoto, M. Moradi, “Application of boundary element method to 3-D problems of coupled thermoelasticity”, *Eng Anal Bound Elem*, vol. 16, no. 4, pp. 297–303, 1995.

[152] Y.S. Joshana, N. Grovera, B.N. Singh, “Analytical modelling for thermo-mechanical analysis of cross-ply and angle-ply laminated composite plates”, *Aerospace Science and Technology*, vol. 70, pp. 137–151, 2017.

- [153] Y. X. Hao, Z. Cao, W. Zhang, J. Chen. “A new displacement field for the stability analysis of FGM sandwich shallow shell under parametric excitation in thermal environment”, *Journal of Sound and Vibration*, to be published.
- [154] X. Xia, H. Shen, “Vibration of postbuckled FGM hybrid laminated plates in thermal environment”, *Engineering Structures*, vol. 30, pp. 2420–2435, 2008.
- [155] V. Ungbhakorn, N. Wattanasakulpong, “Thermo-elastic vibration analysis of third-order shear deformable functionally graded plates with distributed patch mass under thermal environment”, *Applied Acoustics*, vol. 74, pp. 1045–1059, 2013.
- [156] V.N. Pilipchuk, V.L. Berdichevsky, R.A. Ibrahim, “Thermo-mechanical coupling in cylindrical bending of sandwich plates”, *Composite Structures*, vol. 92, pp. 2632–2640, 2010.
- [157] Sh. Pandey, S. Pradyumna, “Free vibration of functionally graded sandwich plates in thermal environment using a layerwise theory”, *European Journal of Mechanics A/Solids*, vol. 51, pp. 55-66, 2015.
- [158] M. Dehghan, M.Z. Nejad, A. Moosaie, “Thermo-electro-elastic analysis of functionally graded piezoelectric shells of revolution: Governing equations and solutions for some simple cases”, *International Journal of Engineering Science*, vol. 104, pp. 34–61, 2016.
- [159] K. Gao, W. Gao, D. Wu, Ch. Song, “Nonlinear dynamic characteristics and stability of composite orthotropic plate on elastic foundation under thermal environment”, *Composite Structures*, vol. 168, pp. 619–632, 2017.
- [160] M. Kabir, B.T. Tehrani, “Closed-form solution for thermal, mechanical, and

thermo-mechanical buckling and post-buckling of SMA composite plates”, *Composite Structures*, vol. 168, pp. 535–548, 2017.

[161] J. Han, J. Kim, M. Cho, “Improved thermo-mechanical stress prediction of laminated composite and sandwich plates using enhanced LCW theory”, *European Journal of Mechanics A/Solids*, vol. 66, pp. 143-157, 2017.

[162] Sh. Li, Sh. Chen, X. Xu. “Thermoelastic Damping in the Free Vibrating Functionally Graded Material Micro-Plate Resonators”, *Journal of Sound and Vibration*, to be published.

[163] W. Soedel. *Vibrations of shells and Plates*, New York: Marcel Dekker, 2004.

[164] P. Ponnusamy, “Dispersion analysis of generalized thermo elastic plate of polygonal cross-sections”, *Applied Mathematical Modelling*, vol. 36, pp. 3343–3358, 2012.

[165] K. Zhoua, X. Huang, Zh. Zhanga and H. Hua. “Aero-thermo-elastic Flutter Analysis of Supersonic Moderately Thick Orthotropic Coupled Plate Structures with General Boundary Conditions”, *Journal of Sound and Vibration*, to be published.

[166] K.M. Liew, C.M. Wang, Y. Xiang, S. Kitipornchai, *Vibration of Mindlin plates: programming the p-version Ritz method*, Oxford: Elsevier, 1998.

[167] S. Chakraverty, K.K. Pradhan, “Free vibration of exponential functionally graded rectangular plates in thermal environment with general boundary conditions”, *Aerosp Sci Technol*, vol. 36, pp. 132-156, 2014.

- [168] K.M. Liew, C.M. Wang, Y. Xiang, S. Kitipornchai. *Vibration of Mindlin Plates. Programming the p-Version Ritz Method*, Elsevier, 1998.
- [169] H. Shen, Zh. Wang, “Nonlinear vibration of hybrid laminated plates resting on elastic foundations in thermal environments”, *Applied Mathematical Modelling*, vol. 36, pp. 6275–6290, 2012.
- [170] E. Carrera, “A class of two-dimensional theories for multilayered plates analysis”, *Accademia delle Scienze Torino, Memorie Scienze Fisiche*, vol. 1–39, 1995.
- [171] E. Carrera, “Theories and finite elements for multilayered plates and shells: a unified compact formulation with numerical assessments and benchmarking”, *Arch Comput Methods Eng*, vol. 10, no. 3, pp. 215–96, 2003.
- [172] J.N. Reddy, *Mechanics of laminated composite plates and shells. Theory and analysis*. New York (USA): CRC Press, 2004.
- [173] E. Carrera, M. Boscolo, A. Robaldo, “Hierarchic multilayered plate elements for coupled multifield problems of piezoelectric adaptive structures: formulation and numerical assessment”, *Arch Comput Methods Eng*, vol. 14, no. 4, pp. 383–430, 2007.
- [174] E. Saetta, G. Rega. “Third order thermomechanically coupled laminated plate: 2D nonlinear modeling, minimal reduction, and transient/post-buckled dynamics under different thermal excitations”, *Composite Structures*, vol. 174, pp. 420–441, 2017.
- [175] J.N. Reddy, *Mechanics of laminated composite plates and shells*. Boca Raton FL: CRC Press, 2004.

[176] W. Nowacki, *Dynamic problems of thermoelasticity*. Warszawa: PWN-Polish Scientific Publishers, 1975.

[177] E. Saetta, G. Rega, “Unified 2D continuous and reduced order modeling of thermomechanically coupled laminated plate for nonlinear vibrations”, *Meccanica*, vol. 49, pp. 1723–49, 2014.

[178] E. Saetta, G. Rega, “Modeling, dimension reduction, and nonlinear vibrations of thermomechanically coupled laminated plates”. *Procedia Eng*, vol. 144, pp. 875–82, 2016.

[179] “A Researcher’s guide to space environmental effects”. *International Space Station*. NASA. NP-2015-03-015-JSC.

[180] J.F. Clawson, G.T. Tsuyuki, B.J. Anderson, C.G. Justus, W. Batts, D. Ferguson, and D.G. Gilmore. Spacecraft thermal Environments. [Online]. Available:

http://matthewturner.com/uah/IPT2008_summer/baselines/LOW%20Files/Thermal/Spacecraft%20Thermal%20Control%20Handbook/02.pdf

[181] J.B. Bai, R.A. Shenoi, J.J. Xiong, “Thermal analysis of thin-walled deployable composite boom in simulated space environment”, *Composite Structures*, vol. 173, pp. 210–218, 2017.

[182] M.M. Finckenor, K.K. De Groh, “A Researcher’s guide to space environmental effects. International Space Station”. NASA. NP-2015-03-015-JSC. 2016 [Online]. Available at: https://www.nasa.gov/connect/ebooks/researchers_guide_space_environment_detail.html

- [183] A.C. Santos Silva, C.M. Sebastian, J. Lambros, E.A. Patterson, “High temperature modal analysis of a non-uniformly heated rectangular plate: Experiments and simulations”, *Journal of Sound and Vibration*, vol. 443, pp. 397-410, 2019.
- [184] X. Zhao, T. Chen, S. Wang, “Effect of NiTi content and test temperature on mechanical behaviours of NiTi-PU composites”, *International Journal of Lightweight Materials and Manufacture*, vol. 1, pp. 215-218, 2018.
- [185] P. Lv, *et al.*, “Microstructure Evolution of 2024 and 7A09 Aluminium Alloys Subjected to Thermal Cycling in Simulated LEO Space Environment”, *Materials Research Innovations*, vol. 18, no. 3, pp. 169-175, 2013.
- [186] K. Shin, *et al.*, “Prediction of Failure Thermal Cycles in Graphite/Epoxy Composite Materials under Simulated Low Earth Orbit Environments”, *Composites Part B: Engineering*, vol. 31, no. 3, pp. 223-235, 2000.
- [187] S. Park, *et al.*, “Effect of Vacuum Thermal Cyclic Exposures on Unidirectional Carbon Fiber/Epoxy Composites for Low Earth Orbit Space Applications”, *Composites Part B: Engineering*, vol. 43, no. 2, pp. 726-738, 2012.
- [188] Airbus Defence and Space. *Confidential communication*, 2019.
- [189] J.J. Wijker. *Spacecraft Structures*. Berlin Heidelberg: Springer, 2010.
- [190] G. F. Abdelal, N. Abuelfoutouh, A. H. Gad, *Finite Element Analysis for Satellite Structures*, Springer, 2012.

- [191] V. Tahmasbi, S. Noori, "Thermal Analysis of Honeycomb Sandwich Panels as Substrate of Ablative Heat Shield", *Journal of Thermophysics and Heat Transfer*, vol. 32, pp. 1-12, 2017.
- [192] B. Pan, L. Yu, D. Wu, "Thermo-mechanical response of superalloy honeycomb sandwich panels subjected to non-steady thermal loading", *Materials & Design*, vol. 88, pp. 528-536, 2015.
- [193] K.K. Rao, K.J. Rao, "Thermostructural analysis of honeycomb sandwich panels". *International Journal of Engineering Science & Advanced Technology*. vol. 2, no. 5, pp. 1402-1409.
- [194] T. Bitzer, *Honeycomb Technology*, Dordrecht: Springer, 1997.
- [195] A. Abbadi, Y. Koutsawa, A. Carmasol, S. Belouettar and Z. Azari, "Experimental and Numerical Characterization of Honeycomb Sandwich Composite Panels," *Simulation Modelling Practice and Theory*, vol. 17, no. 10, pp. 1533-1547, 2009.
- [196] V. Crupi, G. Epasto and E. Guglielmino, "Collapse Modes in Aluminium Honeycomb Sandwich Panels under Bending and Impact Loading," *International Journal of Impact Engineering*, vol. 43, pp. 6-15, 2012.
- [197] J. Paik, A. Thayamballi and G. Kim, "The Strength Characteristics of Aluminium Honeycomb Sandwich Panels," *Thin-Walled Structures*, vol. 35, no. 3, pp. 205-231, 1999.
- [198] G. Belingardi, P. Martella and L. Peroni, "Fatigue Analysis of Honeycomb-Composite Sandwich Beams," *Composites Part A: Applied Science and Manufacturing*, vol. 38, no. 4, pp. 1183-1191, 2006.

- [199] A. Boudjemai, M. Bouanane, A. Mankour, H. Salem, R. Hocine and R. Amri, “Thermo-Mechanical Design of Honeycomb Panel with Fully-Potted Inserts used for Aircraft Design,” *6th Int Conference on Recent Advances in Space Technologies*, pp. 39-46, 2013.
- [200] Y. Jen and L. Chang, “Evaluating Bending Fatigue Strength of Aluminium Honeycomb Sandwich Beams using Local Parameters,” *International Journal of Fatigue*, vol. 30, no. 6, pp. 1103-1114, 2008.
- [201] S. Pan, L. Wu and Y. Sun, “Transverse Shear Modulus and Strength of Honeycomb Cores,” *Composite Structures*, vol. 84, no. 4, pp. 369-374, 2008.
- [202] M. Grediac, “A finite element study of the transverse shear in honeycomb cores,” *International Journal of Solids and Structures*, vol. 30, no. 13, pp. 1777-1788, 1993.
- [203] A. Petras, M.P.F. Sutcliffe. “Failure mode maps for honeycomb sandwich panels”. *Composite structures*, vol. 44, no. 4, pp. 237-252.
- [204] M.F. Caliri, A.J.M. Ferreira, Tita V. “A review on plate and shell theories for laminated and sandwich structures highlighting the Finite Element Method”, *Composite Structures*, vol. 156, pp. 63–77, 2016.
- [205] E. Carrera, “Historical review of zig-zag theories for multilayered plates and shells”. *Appl Mech Rev*, vol. 56, no. 3, pp. 287–308, 2003.
- [206] Geometric nonlinearity. 2017 [Online]. Available: https://abaqus-docs.mit.edu/2017/English/SIMACAEGSARefMap/simagsa-c-nlgeomnonlin.htm#simagsa-c-nlgeomnonlin__simagsa-c-gss-deflection.

- [207] G. Belingardi, P. Martella, L. Peroni, “Fatigue Analysis of Honeycomb-Composite Sandwich Beams”, *Composites Part A: Applied Science and Manufacturing*, vol. 38, no. 4, pp. 1183-1191, 2006.
- [208] S. Brischetto, E. Carrera, “Thermomechanical effect in vibration analysis of one-layered and two-layered plates”, *Int J Appl Mech*, vol. 3, no. 01, pp. 161–85, 2011.
- [209] Y. Yeh. “Chaotic and bifurcation dynamic behavior of a simply supported rectangular orthotropic plate with thermo-mechanical coupling”. *Chaos Solutions & Fractals*, vol. 24, pp. 1243-1255, 2015.
- [210] E. Saetta, G. Rega, Supplementary Data, *Composite Structures* 2017, doi: <http://dx.doi.org/10.1016/j.compstruct.2017.03.048>.
- [211] V. Crupi, G. Epasto, E. Guglielmino, “Collapse Modes in Aluminium Honeycomb Sandwich Panels under Bending and Impact Loading”, *International Journal of Impact Engineering*, vol. 43, pp. 6-15, 2012.
- [212] A. Boudjemai, *et al.*, “Thermo-Mechanical Design of Honeycomb Panel with Fully-Potted Inserts used for Aircraft Design”. *Proceedings of the 16th International conference on recent advances in space technologies*, Istanbul, Turkey, 12-14 June 2013, doi: 10.1109/RAST.2013.6581238.
- [213] O.A. Ganilova, M.P. Cartmell, and A. Kiley, Open Data for the paper ‘Experimental investigation of the thermoelastic performance of an aerospace aluminium honeycomb composite panel’, University of Strathclyde, 2019, <https://doi.org/10.15129/28a67ac3-0daf-4c8d-81c7-3af6a847c211>

[214] G. De Matteis, G. Brando, F.M. Mazzolani, “Hysteretic behaviour of bracing-type pure aluminium shear panels by experimental tests”. *Earthquake Engineering and Structural Dynamics*, vol. 40, pp. 1143-1162, 2010.

[215] A. Krasnobrizha, *et al.*, “Modelling the hysteresis composite behaviour using an elasto-plasto-damage model with fractional derivatives”. *HAL archives-ouvertes*, 2015 [Online]. Available at: <https://hal.archives-ouvertes.fr/hal-01240728>.

[216] M. Lambert, F.K. Schafer, T. Geyer, “Impact damage on sandwich panels and multi-layer insulation”, *International Journal of Impact Engineering*, vol. 26, no. 1-10, pp. 369-380, 2001.

[217] J.J. Wijker. *Spacecraft Structures*. Berlin Heidelberg: Springer, 2008.

[218] K.K. Rao, K. Jayathirtha, R.A.G. Sarwade, B. Madhava. “Bending Behaviour of Aluminium Honey Comb Sandwich Panels”, *International Journal of Engineering and Advanced Technology (IJEAT)*, vol. 1, no. 4, 2012.

[219] K.K. Rao, K. Jayathirtha, R.A.G. Sarwade, M.S.Ch. “Strength Analysis on Honeycomb Sandwich Panels of different Materials”. *International Journal of Engineering Research and Applications (IJERA)*, 2(3), 2012, pp. 365-374

[220] J.K. Shang *et al.* “Role of silicon carbide particles in fatigue crack growth in SiC-particulate-reinforced aluminium alloy composites”. *Mater Sci Eng A.*, 1988.

[221] HBK Company Data. 2018 [Online]. Available: <https://www.hbm.com/en/3067/series-c-the-specialist-strain-gages-for-extreme-temperatures/>

[222] RS Components Ltd Type T thermocouples specifications. 2018 [Online]. Available: <https://uk.rs-online.com/web/p/thermocouples/6212209/>

- [223] G. Sun, J. Zhang, Sh. Li, J. Fang, E. Wang, Q. Li, "Dynamic response of sandwich panel with hierarchical honeycomb cores subject to blast loading", *Thin-Walled Structures*, vol. 142, Sep. 2019, pp. 499-515.
- [224] O.A. Ganilova, M.P. Cartmell, A. Kiley, "The development of a dynamic coupled model for aluminium composite sandwich plates under thermo-elastic loading", *Proceedings of the Second International Nonlinear Dynamics Conference, NODYCON2021*, Rome, Italy, 16 - 19 February 2021.
- [225] O.A. Ganilova, M.P. Cartmell, A. Kiley, "Experimental investigation of the thermoelastic performance of an aerospace aluminium honeycomb composite panel", *Composite Structures* vol. 275, pp. 113-159, 2021.
- [226] G. F. Abdelal, *Finite element analysis for satellite structures : applications to their design, manufacture & testing*, 1st ed. London: Springer, 2012.
- [227] İ. Aydinçak and A. Kayran, "An Approach for the Evaluation of Effective Elastic Properties of Honeycomb Cores by Finite Element Analysis of Sandwich Panels", *Journal of Sandwich Structures & Materials*, vol. 11, no. 5, pp. 385-408, 2009.
- [228] M. Giglio, A. Gilioli, A. Manes, "Numerical investigation of a three point bending test on sandwich panels with aluminum skins and Nomex™ honeycomb core", *Computational Materials Science*, vol. 56, pp. 69-78, 2012.
- [229] H. Luo, G. Liu, S. Ma, and W. Liu, "Dynamic analysis of the spacecraft structure on orbit made up of honeycomb sandwich plates", vol. 1, *IEEE*, pp. 83-87, 2011.
- [230] M.P. Arunkumar *et al.*, "Numerical and experimental study on dynamic characteristics of honeycomb core sandwich panel from equivalent 2D model", *Sādhanā*, vol. 45, 2020.

- [231] J. Fatemi and M. H. J. Lemmen, "Effective Thermal/Mechanical Properties of Honeycomb Core Panels for Hot Structure Applications", *Journal of spacecraft and rockets*, vol. 46, no. 3, pp. 514-525, 2009.
- [232] G. Sun, X. Huo, D. Chen, and Q. Li, "Experimental and numerical study on honeycomb sandwich panels under bending and in-panel compression", *Materials & Design*, vol. 133, pp. 154-168, 2017.
- [233] A.H. Nayfeh. *Perturbation methods*. Wiley, 2008.
- [234] O.R. Asfar, A.H. Nayfeh, "The application of the method of multiple scales to wave propagation in periodic structures", *SIAM Review*, vol. 25, no. 4, pp. 455-480.
- [235] M.I. Friswell, D.J. Inman, R.W. Rietz, "Active damping of thermally induced vibrations", *Journal of intelligent material systems and structures*, vol. 8, pp. 678-685, 1997.
- [236] I.I. Blekhman, *Theory of Vibratory Processes and Machines. Vibration Mechanics and Vibration Technology*. Ruda and Metals, 2013 (in Russian).
- [237] K. Magnus, *Vibration: Introduction into investigation of vibratory systems*. Translation from German. Mir. 1982 (in Russian).
- [238] A.U. Ishlinskiy, *Mechanics of Gyroscopic systems*. AN USSR. 1963 (in Russian).
- [239] L.K. Ragulskis, K.M. Ragulskis, *Vibratory systems with dynamically pointing excitor. Machinostroyeniye*. Leningrad. 1987 (in Russian).
- [240] I.K. Shubin, *Vibration influence on duo-mode pointer. Applied Mathematics*. Leningrad. 1979 (in Russian).

Appendix

Appendix A

Mathematica code for derivation of the Mechanical and Thermal equations for the coupled system

```
(*Input needed for:
    Q11, Q12, Q22, Q66 - elastic stiffness for an orthotropic plate
    lam33-conductivity of the 1st lamina;
lam11, lam12, lam22 - thermal conductivities
    h-plate thickness
    p-mass density of lamina; c-specific heat at constant strain of lamina
For these parameters above M - middle ply, Ex-external ply

    alpha1,
alpha2 - coefficients of thermal expansion in x and y directions respectively
    Tinf=|Absolute temperature of environment-reference temperature|
    Tref - reference temperature
    H-boundary conductance
    delta-damping coefficient

Output:
    T0, T1 - temperature variables the system of eq to be resolved for,
to demonstrate constant,
linear quadratic and cubic behaviour in thermal gradient along z
    u,v,w - displacement variables the system of eq to be resolved for *)

a = 0.3
b = 0.1
Tinf = 150 - 0
Tref = 0
H = 1200
h = 0.015 (*h-plate thickness, H-boundary conductance*)
delta = 0
L = 10 * t
q[t] = (2 / a) * Integrate[L * (Sin[(Pi * x) / a]), {x, 0, a}]
px = py = 0
```

```

QEx11 = QEx22 = ((73 * (10^9) * 0.33) / ((1 + 0.33) * (1 - 2 * 0.33))) + 2 * 669 * (10^6)
QEx12 = ((73 * (10^9) * 0.33) / ((1 + 0.33) * (1 - 2 * 0.33)))
QEx66 = 2 * 669 * (10^6)
lamEx33 = lamEx11 = lamEx12 = lamEx22 = 149
pEx = 2780
cEx = 875
hEx = 0.00038

QM11 = QM22 = ((669 * (10^6) * 0.33) / ((1 + 0.33) * (1 - 2 * 0.33))) + 2 * 310 * (10^6)
QM12 = (669 * (10^6) * 0.33) / ((1 + 0.33) * (1 - 2 * 0.33))
QM66 = 2 * 310 * (10^6)

lamM33 = lamM11 = lamM12 = lamM22 = 209
pM = 50
cM = 904
hM = 0.01424

alpha1 = ((2 * 25 * hEx + 2.4 * hM) / h) * (10^(-6))
alpha2 = ((2 * 25 * hEx + 2.4 * hM) / h) * (10^(-6))

T = fa[z] * T0[x, y, t] + fb[z] * T1[x, y, t] + fc[z]
fa[z] = r1 + r2 * z + r3 * (z^2) + r4 * (z^3)
fb[z] = r5 + r6 * z + r7 * (z^2) + r8 * (z^3)
fc[z] = r9 + r10 * z + r11 * (z^2) + r12 * (z^3)
T
(*Free heat exchange with environment coefficients*)
p = (2 * pEx * hEx + pM * hM) / h
lam33 = (2 * lamEx33 * hEx + lamM33 * hM) / h
r1 = r6 = 1
r3 = -(4 * H) / (h * (h * H + 4 * lam33))
(*h-plate thickness, H-boundary conductance*)
r8 = -(4 * (h * H + 2 * lam33)) / ((h^2) * (h * H + 6 * lam33))
(*lam33-conductivity of the 1st lamina*)
r11 = (4 * H * Tinf) / (h * (h * H + 4 * lam33))
(*Tinf=|Absolute temperature of environment-reference temperature|*)
r2 = r4 = r5 = r7 = r9 = r10 = r12 = 0
(*Free heat exchange with environment coefficients - end*)
TextCell["Law of temperature distribution"]
T

```

```

(*Galerkin simplification*)
w[x, y, t] = ww[t] * (Sin[(Pi * x) / a]) * (Sin[(Pi * y) / b])
u[x, y, t] = uu[t] * (Sin[(Pi * x) / a]) * (Sin[(Pi * y) / b])
(*In Rega u and v are more complex*)
v[x, y, t] = vv[t] * (Sin[(Pi * x) / a]) * (Sin[(Pi * y) / b])
T1[x, y, t] = TT1[t] * (Sin[(Pi * x) / a]) * (Sin[(Pi * y) / b])
T0[x, y, t] = TT0[t] * (Sin[(Pi * x) / a]) * (Sin[(Pi * y) / b])
(*Galerkin-end*)

(*Strain - 2D , no rotation of the transverse normal around x and y*)
eps11 = D[u[x, y, t], x] + 0.5 * ((D[w[x, y, t], x]) ^ 2)
eps22 = D[v[x, y, t], y] + 0.5 * ((D[w[x, y, t], y]) ^ 2)
eps12 = D[u[x, y, t], y] + D[v[x, y, t], x] +
  (D[w[x, y, t], x] * D[w[x, y, t], y]) + (z^3) * (-2 * c1) * D[w[x, y, t], x, y]
c1 = 4 / (3 * (h^2))
(*No transverse shearing strain - end*)

(*For orthotropic plate*)
betaM11 = QM11 * alpha1 + QM12 * alpha2
betaM22 = QM12 * alpha1 + QM22 * alpha2 (*beta11,
beta22 - thermoelastic stiffness*)
betaM12 = 0 (*corrected as for External*)
  betaEx11 = QEx11 * alpha1 + QEx12 * alpha2
  betaEx22 = QEx12 * alpha1 + QEx22 * alpha2
(*beta11, beta22 - thermoelastic stiffness*)
  betaEx12 = 0 (*corrected to 0 for orthotropic Eq(40) in Rega paper*)
sigM11[z] = QM11 * eps11 + QM12 * eps22 - betaM11 * T
sigM22[z] = QM12 * eps11 + QM22 * eps22 - betaM22 * T
sigM12[z] = QM66 * eps12
  sigEx11[z] = QEx11 * eps11 + QEx12 * eps22 - betaEx11 * T
  sigEx22[z] = QEx12 * eps11 + QEx22 * eps22 - betaEx22 * T
  sigEx12[z] = QEx66 * eps12

sig11[z] = (2 * sigEx11[z] * hEx + sigM11[z] * hM) / h
sig22[z] = (2 * sigEx22[z] * hEx + sigM22[z] * hM) / h
sig12[z] = (2 * sigEx12[z] * hEx + sigM12[z] * hM) / h

N11 = Integrate[sig11[z], {z, -h / 2, h / 2}]
N12 = Integrate[sig12[z], {z, -h / 2, h / 2}]
N22 = Integrate[sig22[z], {z, -h / 2, h / 2}]

M11 = Integrate[z * sig11[z], {z, -h / 2, h / 2}]
M12 = Integrate[z * sig12[z], {z, -h / 2, h / 2}]
M22 = Integrate[z * sig22[z], {z, -h / 2, h / 2}]

```

```

(*Mechanical Equations of Motion*)
TextCell["Mechanical Equations of Motion"]
Integrate[(Integrate[(D[N11, x] + D[N12, y]), {x, 0, a}]), {y, 0, b}] == 0
Integrate[(Integrate[(D[N12, x] + D[N22, y]), {x, 0, a}]), {y, 0, b}] == 0
s1[x, y, t] = (N11 * D[w[x, y, t], x]) + (N12 * D[w[x, y, t], y])
s2[x, y, t] = (N12 * D[w[x, y, t], x]) + (N22 * D[w[x, y, t], y])
Integrate[
  (Integrate[(D[M11, {x, 2}] + 2 * (D[M12, x, y]) + D[M22, {y, 2}] + D[s1[x, y, t], x] +
    D[s2[x, y, t], y] + -px * D[w[x, y, t], {x, 2}] - py * D[w[x, y, t], {y, 2}] +
    q[t]) * (Sin[Pi * x] / a) * (Sin[Pi * y] / b)], {x, 0, a}), {y, 0, b}] ==
Integrate[(Integrate[(p * h * (D[w[x, y, t], {t, 2}]) + delta * (D[w[x, y, t], t])) *
  (Sin[Pi * x] / a) * (Sin[Pi * y] / b)], {x, 0, a}), {y, 0, b}]

(*Mechanical Equations of Motion - end*)

TextCell["Thermal effect parameters"]

(*2D Thermal balance Equations parameters*)
(*lam11, lam12, lam22 - thermal conductivities;

qij- heat flow along the x,y,z directions*)
g1[z] = fa[z] * D[T0[x, y, t], x] + fb[z] * D[T1[x, y, t], x]
(*g1, g2 thermal gradients corresponing to Tx, Ty*)
g2[z] = fa[z] * D[T0[x, y, t], y] + fb[z] * D[T1[x, y, t], y]
lam11 = (2 * lamEx11 * hEx + lamM11 * hM) / h
lam12 = (2 * lamEx12 * hEx + lamM12 * hM) / h
lam22 = (2 * lamEx22 * hEx + lamM22 * hM) / h
(*q0, q1 - bending components of the heat flow*)
q01[x, y, t] = Integrate[lam11 * g1[z] + lam12 * g2[z], {z, -h/2, h/2}]
q02[x, y, t] = Integrate[lam12 * g1[z] + lam22 * g2[z], {z, -h/2, h/2}]
q11[x, y, t] = Integrate[z * lam11 * g1[z] + z * lam12 * g2[z], {z, -h/2, h/2}]
q12[x, y, t] = Integrate[z * lam12 * g1[z] + z * lam22 * g2[z], {z, -h/2, h/2}]
(*Q0, Q1 - energy rates due to heat flow q3 in z direction*)
Q0 =
  2 * (Integrate[lam33, {z, -h/2, h/2}]) * (r3 * T0[x, y, t] + r7 * T1[x, y, t] + r11) +
  6 * (Integrate[lam33 * z, {z, -h/2, h/2}]) *
  (r4 * T0[x, y, t] + r8 * T1[x, y, t] + r12)
Q1 = 2 * (Integrate[lam33 * z, {z, -h/2, h/2}]) *
  (r3 * T0[x, y, t] + r7 * T1[x, y, t] + r11) +
  6 * (Integrate[lam33 * (z^2), {z, -h/2, h/2}]) *
  (r4 * T0[x, y, t] + r8 * T1[x, y, t] + r12)
(*b0, b1 - internal energy; p-mass density of lamina;
c-specific heat at constant strain of lamina*)
c = (2 * cEx * hEx + cM * hM) / h
b0[x, y, t] = Integrate[p * c * T, {z, -h/2, h/2}]
b1[x, y, t] = Integrate[p * c * z * T, {z, -h/2, h/2}]
(*b0, b1 - interaction energy;*)
beta11 = (2 * betaEx11 * hEx + betaM11 * hM) / h
beta22 = (2 * betaEx22 * hEx + betaM22 * hM) / h
a0[x, y, t] = Tref * (Integrate[beta11 * eps11 + beta22 * eps22, {z, -h/2, h/2}])
(*for orthotropic eps21=0*)
a1[x, y, t] =
  Tref * (Integrate[z * beta11 * eps11 + z * beta22 * eps22, {z, -h/2, h/2}])

```

```

(*Thermal balance Equations*)
TextCell["Thermal balance Equations "]
Integrate[(Integrate[(D[q01[x, y, t], x] + D[q02[x, y, t], y] -
    D[b0[x, y, t], t] - D[a0[x, y, t], t] + Q0), {x, 0, a}], {y, 0, b}] == 0
Integrate[(Integrate[(D[q11[x, y, t], x] + D[q12[x, y, t], y] -
    D[b1[x, y, t], t] - D[a1[x, y, t], t] + Q1), {x, 0, a}], {y, 0, b}] == 0

Quit[]

```

Appendix B

Output from the *Mathematica* coded solution (Appendix B) presented in an annotated format

```
(*Numerical solution for Tinf=300-22, q=1 *)

In[ ]:=
s = NDSolve[{0. + 0.154807 t + 0.0454731 TT1[t] +
  (-117706. + 1092.18 TT0[t]) ww[t] - 1.22564 x 1011 ww[t]3 = 0.021186 ww''[t],
  7046.05 - 69.455 TT0[t] - 30.7769 TT0'[t] = 0,
  -0.0263742 TT1[t] - 0.00046163 TT1'[t] = 0, TT1[0] = 150, ww[0] = 0,
  ww'[0] = 0, TT0[0] = 0}, {TT1[t], ww[t], TT0[t]}, {t, 0, 500}]

TextCell["displacement w(t)"]
Plot[Evaluate[{ww[t]} /. s], {t, 0, 20}, PlotStyle -> Automatic]
Plot[Evaluate[{ww[t]} /. s], {t, 0, 100}, PlotStyle -> Automatic]
Plot[Evaluate[{ww[t]} /. s], {t, 0, 500}, PlotStyle -> Automatic]
TextCell["Thermal component T1(t)"]
Plot[Evaluate[{TT1[t]} /. s], {t, 0, 10}, PlotStyle -> Automatic]
TextCell["Thermal component T0(t)"]
Plot[Evaluate[{TT0[t]} /. s], {t, 0, 10}, PlotStyle -> Automatic]
TextCell["Thermal distribution T(t,z)"]
Plot3D[Evaluate[38012. z2 + (1 - 380.12 z2) TT0[t] + (z - 6096.08 z3) TT1[t] /. s],
  {t, 0, 10}, {z, -0.0075, 0.0075}, PlotRange -> All]

t = 0.1
Plot[Evaluate[57018. z2 + (1 - 380.12 z2) TT0[t] + (z - 6096.08 z3) TT1[t] /. s],
  {z, -0.0075, 0.0075}, PlotStyle -> Automatic ]

t = 1
Plot[Evaluate[57018. z2 + (1 - 380.12 z2) TT0[t] + (z - 6096.08 z3) TT1[t] /. s],
  {z, -0.0075, 0.0075}, PlotStyle -> Automatic ]

t = 5
Plot[Evaluate[57018. z2 + (1 - 380.12 z2) TT0[t] + (z - 6096.08 z3) TT1[t] /. s],
  {z, -0.0075, 0.0075}, PlotStyle -> Automatic ]

t = 10
Plot[Evaluate[57018. z2 + (1 - 380.12 z2) TT0[t] + (z - 6096.08 z3) TT1[t] /. s],
  {z, -0.0075, 0.0075}, PlotStyle -> Automatic ]

t = 100
Plot[Evaluate[57018. z2 + (1 - 380.12 z2) TT0[t] + (z - 6096.08 z3) TT1[t] /. s],
  {z, -0.0075, 0.0075}, PlotStyle -> Automatic ]

Quit[]
```

Appendix C.

Open Data for the paper ‘Experimental investigation of the thermoelastic performance of an aerospace aluminium honeycomb composite panel’ by Olga A. Ganiłova, Matthew P. Cartmell, and Andrew Kiley

This data is presented as an open source data and published as Open Data for the paper ‘Experimental investigation of the thermoelastic performance of an aerospace aluminium honeycomb composite panel’, University of Strathclyde, 2019, <https://doi.org/10.15129/28a67ac3-0daf-4c8d-81c7-3af6a847c211>

It represented as a folder of 7 files and for convenience attached to this submission.

Appendix D

Experimental tests procedure log

- a) A test plate was cut with dimensions 300 x 100 mm and this was fitted with a rosette gauge configuration on the top and bottom surfaces, as shown in Figure 1. The upper skin thickness of the plate was 0.39mm, and the lower skin thickness was 0.34mm. The thickness of the honeycomb core was 9.21mm. The plate was simply supported equidistant from each end, and the centre-to-centre distance between the supports was 257mm.
- b) We performed three incremental load-deflection tests from 0 to 20 N, then to 50 N, and then to 100N, all at ambient laboratory temperature (20 deg C) and the data logger recorded both the displacements of the Instron loading tool and the strains measured by the gauges for these three load ranges.
- c) We checked for hysteresis, and found it clearly evident in all three loading cases. We did the tests again to check the consistency of results (confirmed). The maximum central (load point) deflection for the 100 N load was found to be 0.58 mm (see Figure 2 below). The results data files are available on request.
- d) The 100 N loading test was to be repeated as follows: from ambient (20 deg C) up to +100 deg C, by setting the environmental chamber temperature, and holding it constant during the test. Then to cool back down to ambient temperature (20 deg C) and then go down to 0, -20, -40, -60 deg C, respectively. Each fixed temperature test was intended to take around 5 minutes to complete before the temperature was changed for the next one. **This was delayed due to partial failure of the Instron environmental chamber temperature controller. The decision was made to replace the defective parts so that the test could be performed accurately and correctly.**
- e) The final test in this series was for one long-duration thermal soak test at 100 deg C in which the chamber was to be held at that temperature for three days, and a load-deflection test performed each day up to 100 N, to see if there was an observable thermally-driven creep effect.

Appendix E

Communication on properties for the panels supplied

From: "ROGERS, Samuel [UK]" <samuel.rogers@ardec.com>
 Subject: Panel Samples
 Date: 17 October 2018 14:52:17 GMT-01:00
 To: Matthew Carnell <mattew.carnell@stah.ac.uk>; Olga Gavrilova <olga.gavrilova@stah.ac.uk>
 Cc: "KILEY, Andy [UK]" <andy.kiley@stah.ac.uk>

Hi Matthew/Olga,

I have managed to obtain some honeycomb panel offcuts that I will send up to you today or tomorrow. There are 4 panels, larger than the required samples and all the same composition so there is plenty of material for you to work with.

The panels have aluminium 2024-T81 skins of 0.38 to 0.48 mm thick and the core is 3/15-5056-001 of 14.24-14.44 mm thick. The skins are bonded to the core with Redux 312U/312UL thermosetting epoxy film adhesive (properties can be found online).

Hopefully all of the properties you need can be found or derived from the datasheets we have sent over to you.

Based on datasheets/reports supplied:

Honeycomb properties are extracted from **HEXCEL Honeycomb Sandwich Design Technology.PDF**

Foil thickness is 0.001 inches.

Cell dimensions are 3/16

Density = 50 kg/m³

Youngs = 669 MPa = $669 \cdot 10^6$ Pa (Hexcel), Shear modulus = $310 \cdot 10^6$ Pa

Appendix F.

Temperature distribution along the thickness for other environments

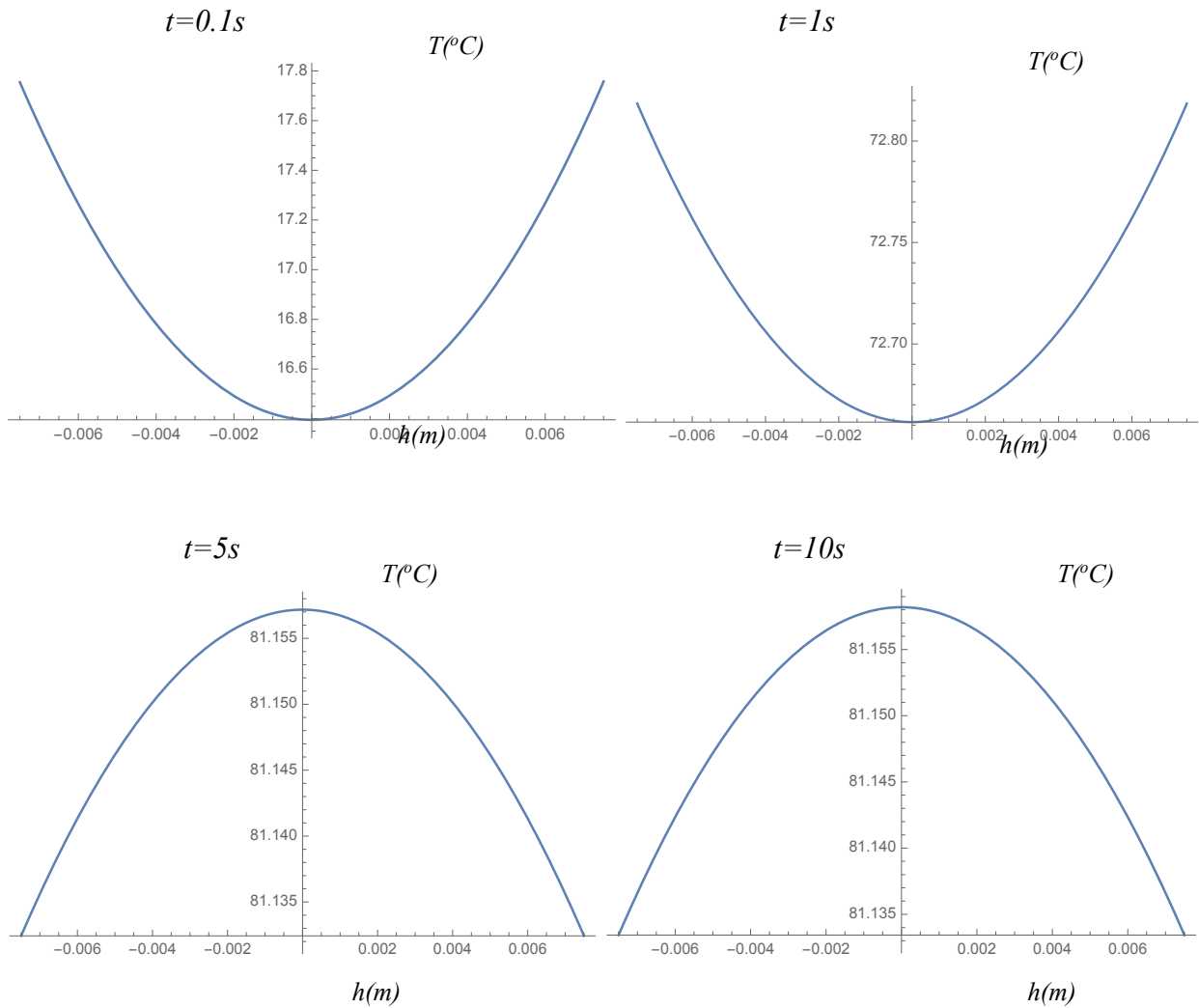
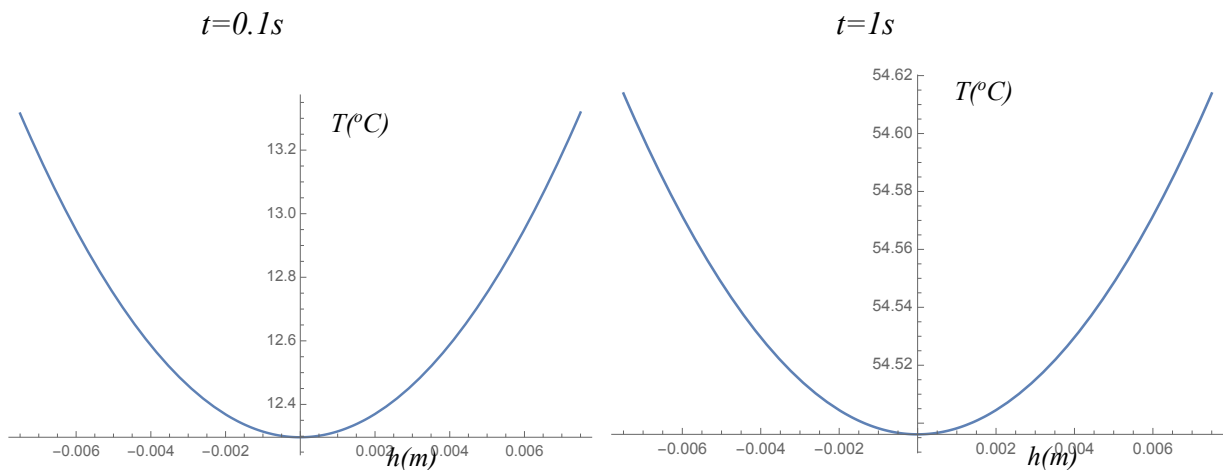


Figure F1. Temperature distribution across the thickness of the panel (x coordinate) when the panel is under dynamic mechanical loading and in an environmental soak temperature of $80^{\circ}C$, presented at different instants in time.



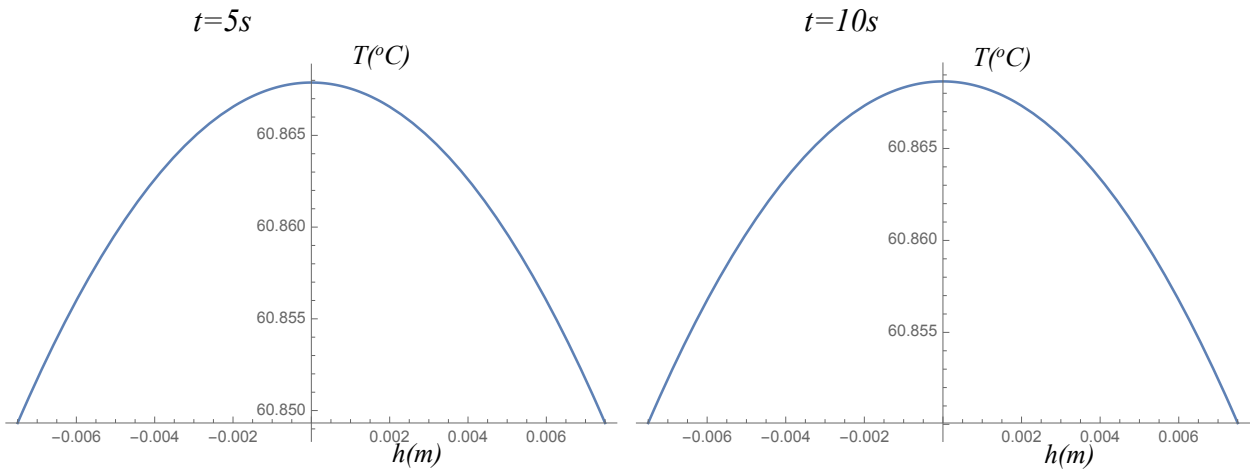


Figure F2. Temperature distribution across the thickness of the panel (x coordinate) when the panel is under dynamic mechanical loading and in an environmental soak temperature of 60° C, presented at different instants in time.

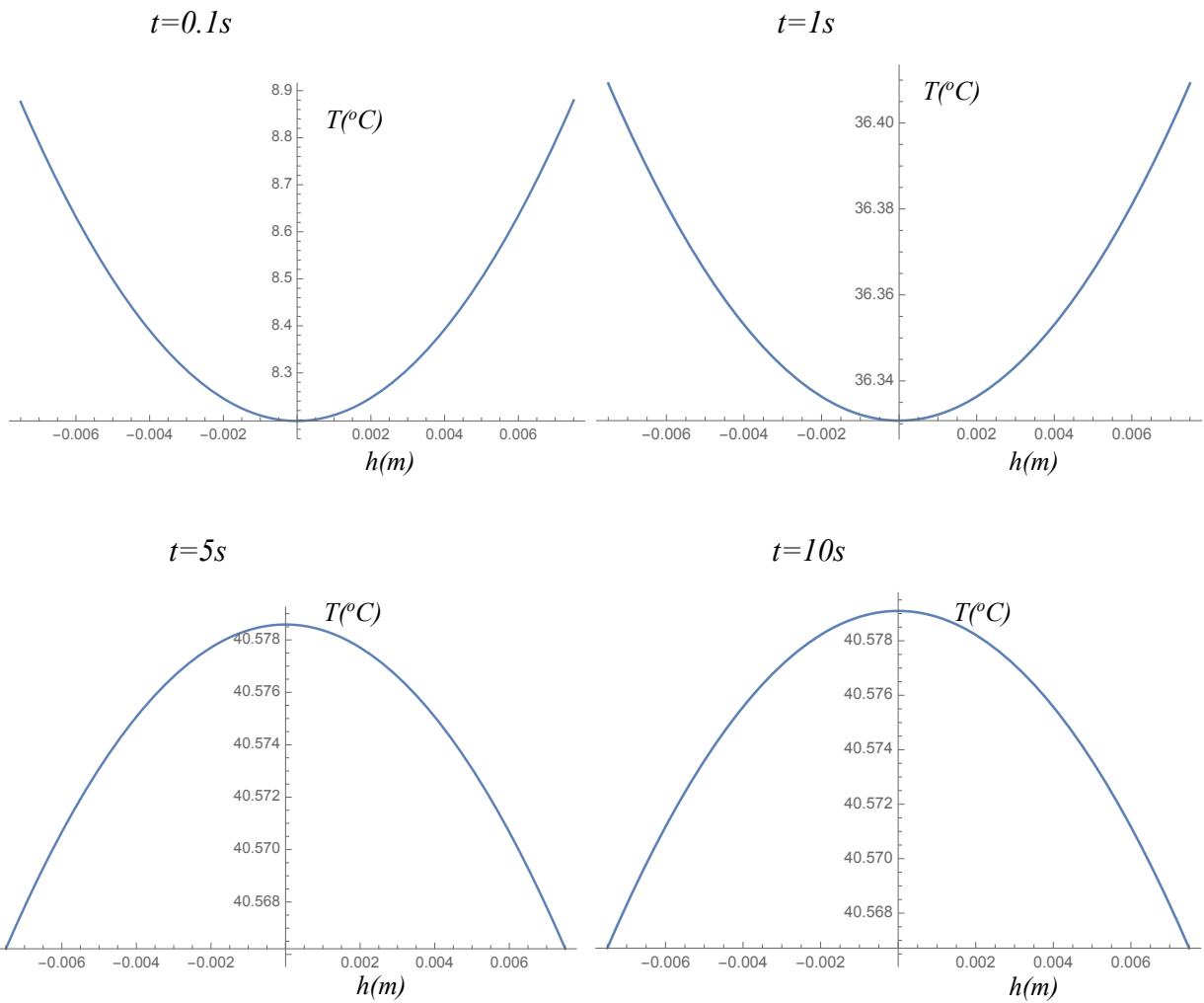


Figure F3. Temperature distribution across the thickness of the panel (x coordinate) when the panel is under dynamic mechanical loading and in an environmental soak temperature of 40° C, presented at different instants in time

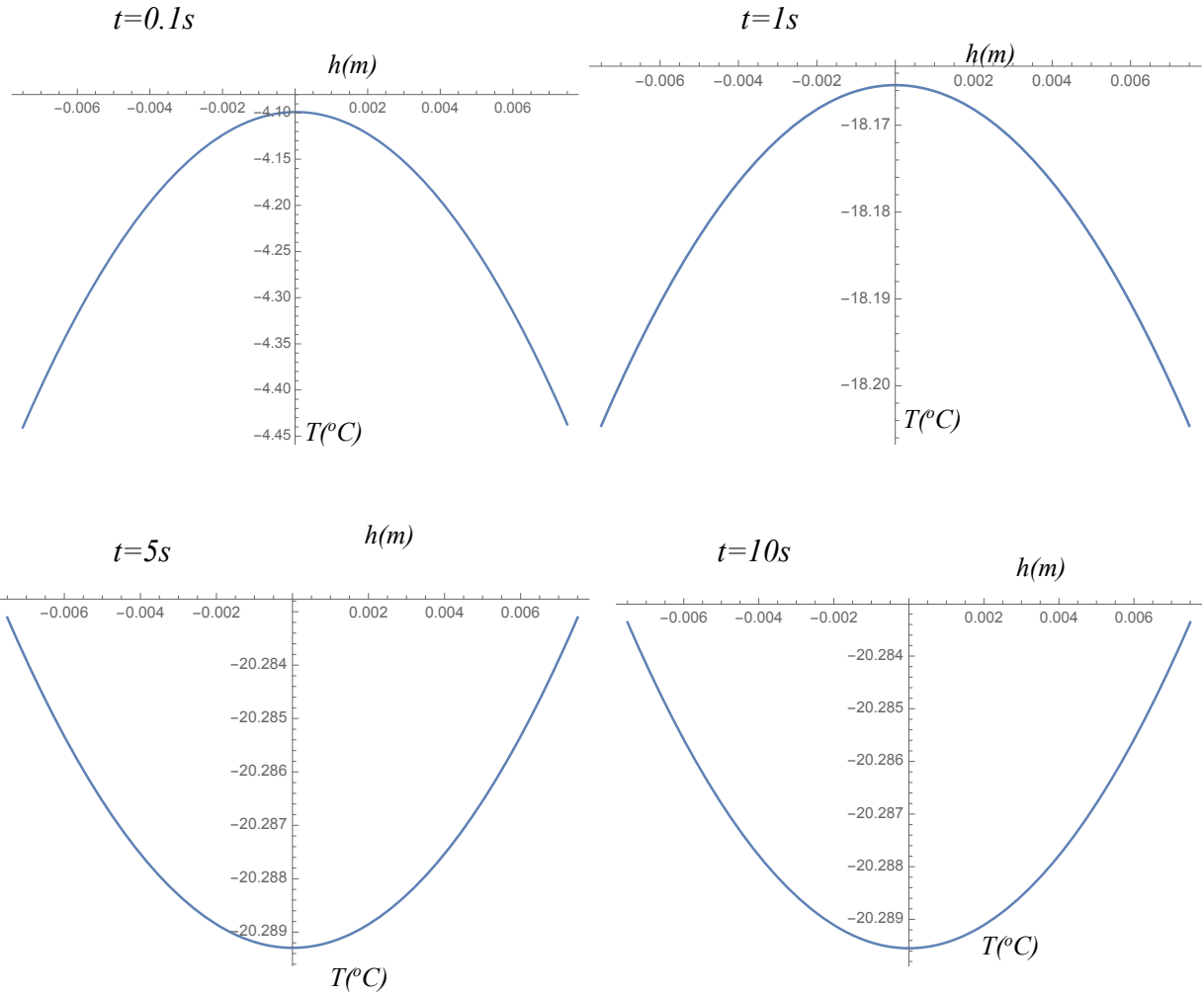
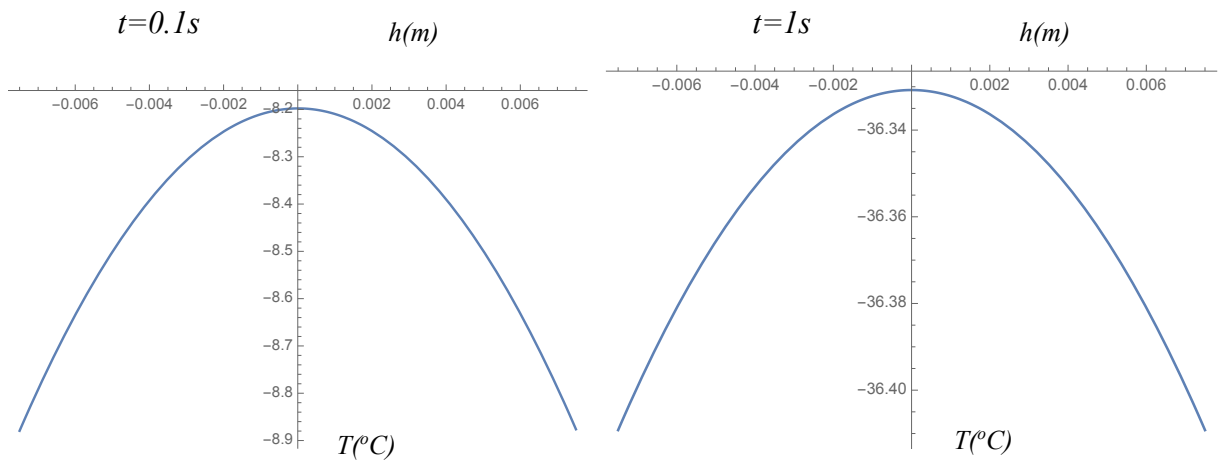


Figure F4. Temperature distribution across the thickness of the panel (x coordinate) when the panel is under dynamic mechanical loading and in an environmental soak temperature of -20°C , presented at different instants in time.



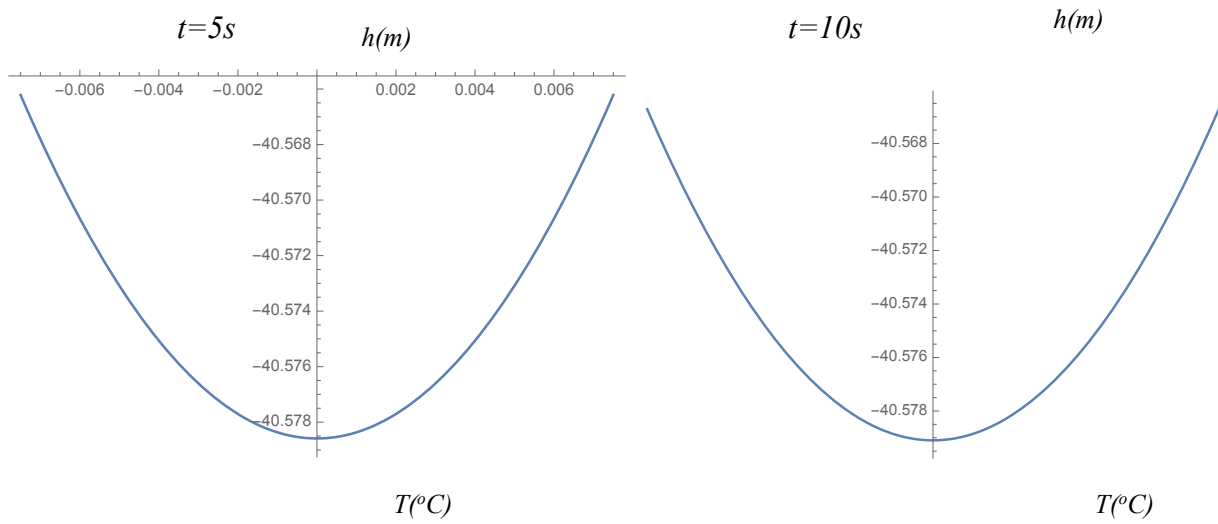


Figure F5. Temperature distribution across the thickness of the panel (x coordinate) when the panel is under dynamic mechanical loading and in an environmental soak temperature of -40°C , presented at different instants in time.

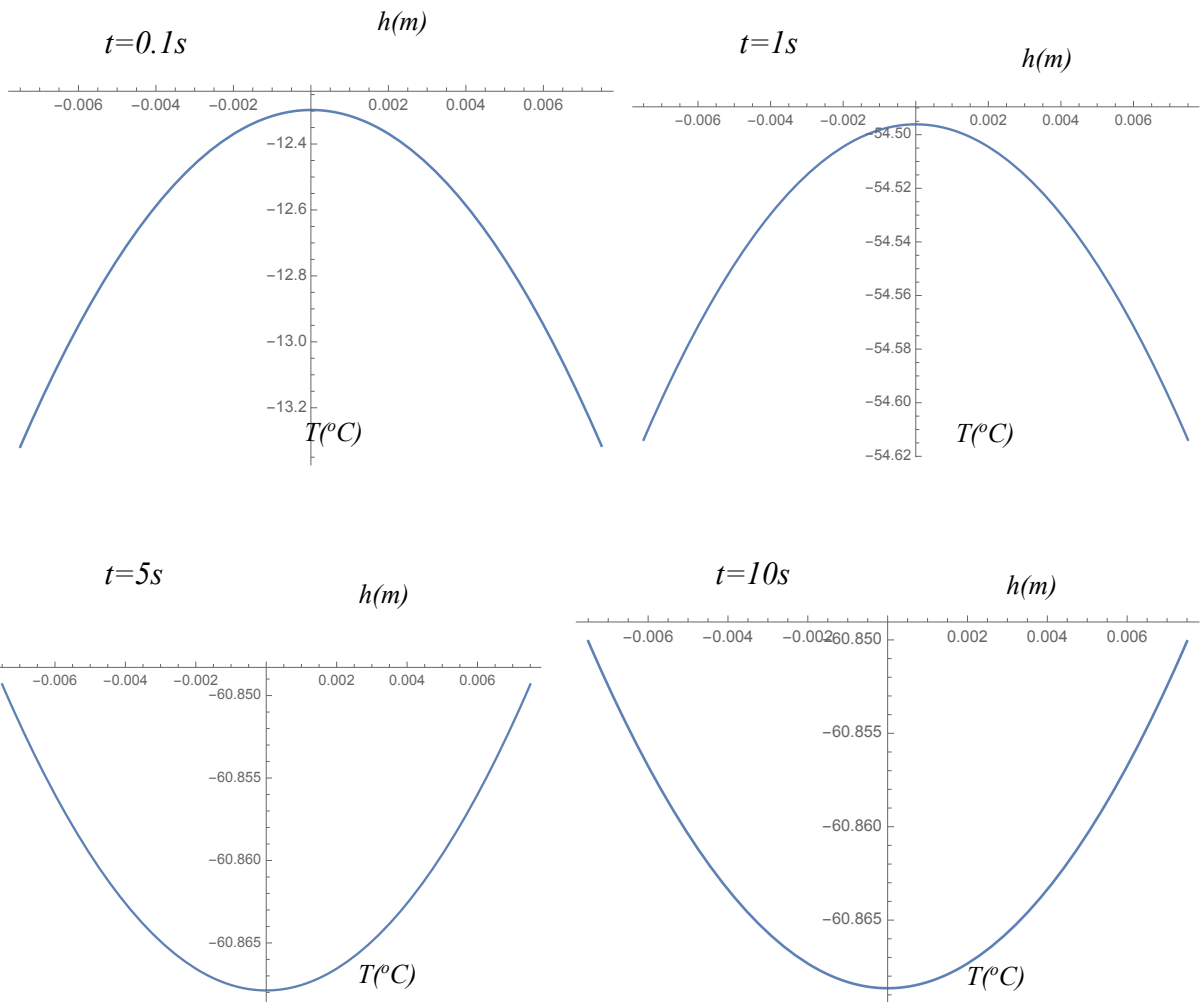


Figure F6. Temperature distribution across the thickness of the panel (x coordinate) when the panel is under dynamic mechanical loading and in an environmental soak temperature of -60°C , presented at different instants in time.

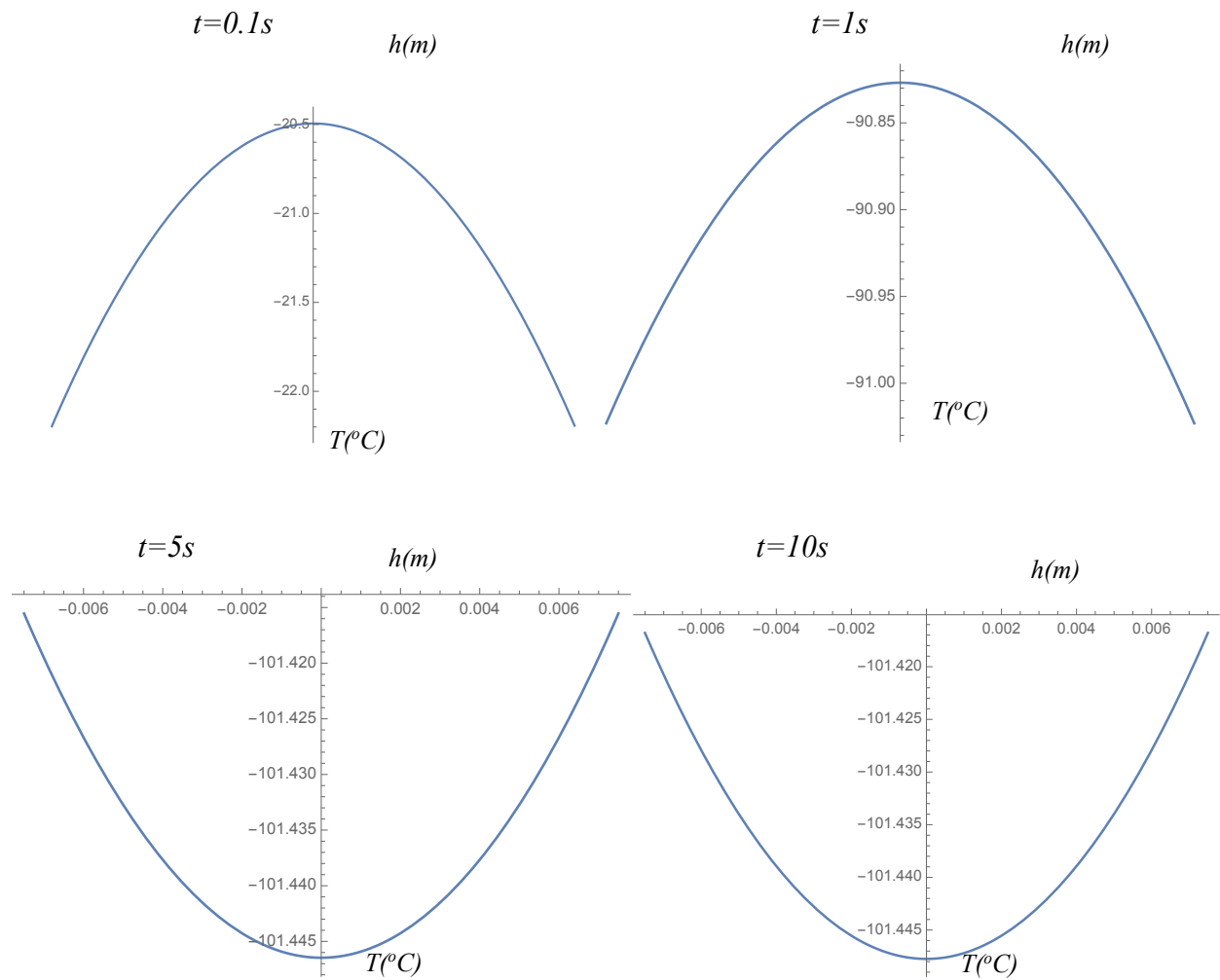


Figure F7. Temperature distribution across the thickness of the panel (x coordinate) when the panel is under dynamic mechanical loading and in an environmental soak temperature of -100°C , presented at different instants in time.

Appendix G

Published papers as a result of work performed for this thesis

Composite Structures

Application of a dynamic thermoelastic coupled model for an aerospace aluminium composite panel –Manuscript Draft–

Manuscript Number:	
Article Type:	Full Length Article
Keywords:	thermoelastic; thermomechanical; coupled model; dynamic; sandwich plate, aluminum
Corresponding Author:	Olga Ganilova University of Strathclyde UNITED KINGDOM
First Author:	Olga Ganilova
Order of Authors:	Olga Ganilova Matthew P. Cartnell, Prof Andrew Kilef
Abstract:	An analytical-numerical coupled model has been derived to predict the effects of dynamic thermo-mechanical loading on aluminium composite panels specifically in the form of metallic skin sandwich structures, for the purposes of enhanced design of spacecraft structures where the environmental conditions comprise combined mechanical and thermal loading. The mechanical loading can arise as a consequence of localised structural dynamics, and the thermal loading is attributable principally to the effects of solar irradiation and eclipse during a satellite's orbit, and together they have the potential to influence de-point adversely, in particular. On this basis a combined physics model is required to deal with the generalised thermoelastic problem and this paper reports on the theoretical work done to achieve that. The research has considered the literature in detail and a refined model has been proposed for an aerospace application which results in an analytical-numerical solution for the thermoelastic problem in aluminium composite panels. The model is explored for a panel under a range of centrally located static mechanical loads, in conjunction with thermal loading provided in the form of various controlled and elevated environmental temperature functions, all for prescribed physical boundary conditions.
Suggested Reviewers:	Inna Gitman i.gitman@sheffield.ac.uk Expert in analytical modelling of materials and their applications Walter Lacarbonara walter.lacarbonara@uniroma1.it Expert in composite multilayered structures and their modelling

Application of a dynamic thermoelastic coupled model for an aerospace aluminium composite panel

Olga A. Ganilova¹, Matthew P. Cartmell¹, and Andrew Kiley²

¹ Aerospace Centre of Excellence, Department of Mechanical & Aerospace Engineering, University of Strathclyde, Glasgow, G1 1XJ, Scotland, UK

² Airbus Defence & Space Ltd., Gunnels Wood Road, Stevenage, Hertfordshire, SG1 2AS, UK

Abstract: An analytical-numerical coupled model has been derived to predict the effects of dynamic thermo-mechanical loading on aluminium composite panels specifically in the form of metallic skin sandwich structures, for the purposes of enhanced design of spacecraft structures where the environmental conditions comprise combined mechanical and thermal loading. The mechanical loading can arise as a consequence of localised structural dynamics, and the thermal loading is attributable principally to the effects of solar irradiation and eclipse during a satellite's orbit, and together they have the potential to influence de-point adversely, in particular. On this basis a combined physics model is required to deal with the generalised thermoelastic problem and this paper reports on the theoretical work done to achieve that. The research has considered the literature in detail and a refined model has been proposed for an aerospace application which results in an analytical-numerical solution for the thermoelastic problem in aluminium composite panels. The model is explored for a panel under a range of centrally located static mechanical loads, in conjunction with thermal loading provided in the form of various controlled and elevated environmental temperature functions, all for prescribed physical boundary conditions. Both forms of loading are shown to influence the displacement of the panel significantly, thereby confirming the importance of a combined physics model for analysing structures in this context.

Keywords: thermoelastic; thermomechanical; coupled model; dynamic; sandwich plate, aluminum.

1. Introduction

The materials used on the exterior of spacecraft are subjected to many environmental threats that can degrade them, including the vacuum of space itself, solar ultraviolet (UV) radiation, ionising charged particle radiation, plasma, surface charging and arcing, temperature extremes, thermal cycling, impacts from micrometeoroids and orbital debris (MMOD), and environment-induced contamination. In terms of material degradation in space, low-Earth orbit (LEO), defined as the region from 200 to 1000 km above the Earth's surface, is a particularly harsh environment because of the presence of atomic oxygen (AO) along with the threats just mentioned [1]. The environmental challenges of space to a spacecraft component vary in their influence mainly due to the component's material properties, its geometry, and the stresses that it undergoes during normal duty. As a spacecraft moves in and out of eclipse during its orbit around Earth, the degree to which its materials experience thermal cycling temperature extremes depends on their thermo-optical properties (solar absorptance and thermal emittance), the view of the sun, the view of Earth, the view of other surfaces of the spacecraft, the durations of time in sunlight and in shadow, their thermal masses and the influences of equipment or components that produce heat [1]. At the extreme end of operation the cyclic temperature variations can be from $-120\text{ }^{\circ}\text{C}$ to $+120\text{ }^{\circ}\text{C}$, and high solar absorptance with low infrared emittance can contribute to such temperature swings in the absence of a spacecraft thermal control system. Sixteen thermal cycles a day, taking the case of the ISS which orbits Earth approximately once every 92 minutes, may lead to cracking, peeling, spalling or the formation of pinholes in the coating, which then allow AO to start to attack the underlying material [1].

The main forms of environmental heating on orbit are sunlight, sunlight reflected from Earth, a planet, or the Moon, and infrared energy emitted from Earth. During launch or in exceptionally low orbits, there is also a free molecular heating effect caused by friction in the rarified upper atmosphere [2]. The main conditions of LEO that are highlighted are the temperature extremes and the thermal cycles

* Corresponding author. E-mail: olga.ganilova@strath.ac.uk.

experienced throughout the orbit, with a spacecraft completing from eleven to sixteen thermal cycles daily, within a possible temperature range of -120°C to $+120^{\circ}\text{C}$. The thermo-optical properties of the spacecraft play a factor in the temperature that it reaches. For instance, a material with high solar absorptance and low thermal emittance will experience greater temperature swings.

In [3] an experiment was performed to investigate the thermal behaviour of a sandwich plate or panel deployable as an integral part of a satellite in a space environment using a ground thermal-vacuum test. It was highlighted that the heat sink, solar radiation, infrared radiation of the Earth, heat conduction, surface radiation and cavity radiation would all influence the temperature field, and the conclusion was that these combined effects would result in a serious challenge for thermal testing in the laboratory of the simulated space environment. The experiment was relatively sophisticated and satisfied the general requirements of the inclusion of three key conditions: ultra-high level of vacuum (lower than 10^{-5} Pa), a heat sink (-180°C) achieved in this case by using black panels with a liquid-nitrogen cooling system, and thermal loading, achieved through infrared lamps. An interesting study carried out by [4] focused on the effect of thermal cycling in a simulated LEO environment on the microhardness of aluminium alloys, and subjected these alloys to thermal cycles ranging from -140°C to $+110^{\circ}\text{C}$. This was in order to induce thermal fatigue and to study the resulting stress state and mechanical properties of the material. The testing resulted in cyclic plastic deformation which was found to lead to crack initiation, identified using a transmission electron microscope (TEM). A total of 400 thermal cycles was imposed on the samples which showed an eventual decrease in hardness that, from 300-400 cycles, then increased with every cycle. Although rapid temperature changes were implied, the exact value of the rate of change of temperature was not stated in the study. The mechanical load was applied at intervals to test the microhardness of the material and was not applied in conjunction with the change in temperature. The study concluded that aluminium alloys exposed to extended thermal cycling (typically of the order of 400 cycles) exhibited obvious softening behaviour, causing phase transformations that, if the cycles were to continue, would lead to crack initiation. The principal finding from this work was that the bulk of aeronautical materials that undergo periodic heating and cooling can be damaged to varying degrees, with thermal fatigue having a great impact on the mechanical properties of the materials used. Although it is difficult to recreate terrestrially the conditions of low Earth orbit, such work has been attempted in the past by [5]. The study focused on subjecting graphite-epoxy composites to the conditions of low Earth orbit. Not only did the materials undergo thermal cycling similar to that experienced in LEO, but the environment was also in a high vacuum state while the effect of ultraviolet radiation was applied during heating but not during cooling. A single thermal cycle was judged to be from -70°C to $+100^{\circ}\text{C}$ and back to -70°C again. This was with a temperature change rate of $3\text{-}5^{\circ}\text{C}$ per minute and a dwell-time at the temperature extremes of 15 minutes, giving an average cycle time of 100 minutes, typical of a low Earth orbital period. The results examined were for composites subjected to this environment for 8, 16, 40 and 80 thermal cycles in which the transverse flexural strength and transverse tensile strength showed the most severe reduction with thermal cycling, with losses of 34% and 21% respectively, after 80 thermal cycles. It was considered that the matrix-dominated mechanical properties suffered the greatest loss because of the loss of the matrix due to high vacuum and thermal cycling. Overall, the strength and stiffness of the graphite epoxy composites was shown to decrease exponentially with increasing thermal cycles. Further work into the synergistic effects of high vacuum and thermal cycling was implemented by [6], this time on carbon fibre epoxy composites. The experiment took place in a high vacuum state of 10^{-5} Torr where a single thermal cycle was judged to be from $+120^{\circ}\text{C}$ to -175°C and back to $+120^{\circ}\text{C}$, over a duration of approximately 43 minutes. The experiment ran for 500, 1000, 1500 and 2000 cycles. Panels were then subjected to mechanical tests at an ambient temperature of 23°C to observe the mechanical properties of the samples. The results confirmed gradual damage with the progression of thermal cycles. This was coupled with the degradation of the fibre-matrix interface due to a weakened fibre-matrix bond which led to interfacial sliding.

Some industrial experiments involving the thermal loading of aluminium composite panels, but not using temperatures as extreme as those experienced in low Earth orbit, measured thermo-elastic deformation under thermal load with temperature steps from -20°C to $+40^{\circ}\text{C}$ with static loads imposed on

the panel between 0 and 78 N – in steps of 19.6 N. The experiment was carried out in a climatic chamber with the measurements being corroborated by a finite element model. Measurements for the deflection and sample temperature of the structural model were taken at set temperatures using photogrammetry and infrared cameras to map a thermal cartographic image of the structural model, where temperatures were assumed as for black body conditions (emissivity, $\epsilon = 1$). Looking at the problem of a spacecraft panel undergoing *cyclic loading* from the perspective of modelling it is possible to find that the structure must combine the effects of thermal loading as well as mechanical disturbance. This is because from a physical point of view the deformation of a body is connected to a change of heat inside it, and therefore to a change in the temperature distribution in the body. So, *a deformation of the body leads to temperature changes, and conversely*. The internal energy of the body depends on both the temperature and the deformation and so, in the case of a practical body, such as a spacecraft panel, this necessarily undergoes processes that are intrinsically coupled, defined collectively as thermoelasticity [7]. In order to summarise, the theory of thermal stresses (TTS) commonly applies a simplifying assumption that the influence of the deformation on the temperature field may be neglected [7]. In TTS the classical heat conduction (HC) equation is usually used but this does not routinely contain the term representing the deformation of the body. Knowing the temperature distribution from the solution of the HC equation, the displacement equations of the theory of elasticity can be solved. At the same time classical dynamic elasticity has been developed under the assumption that the heat exchange between different parts of the body due to the heat conduction occurs very slowly, and therefore the thermal motion may be regarded as *adiabatic*.

However, thermoelasticity deals with a wide class of phenomena. It covers the general theory of heat conduction as well as the general theory of thermal stresses, and it describes the temperature distribution produced by deformation. Thermoelasticity also describes the phenomenon of thermoelastic dissipation. As mentioned above many modelling approaches tend to separate the mechanical and thermal effects, but thermoelastic processes are not generally reversible because although the elastic part may be reversed - the deformations may be recoverable through cooling - the thermal part may not be reversed due to the dissipation of energy during heat transfer [8].

Apart from that, thermal changes in the body cause mechanical deformation in the body, which in return affects these thermal changes, representing the process as two-way feedback, and this mechanism is at the heart of the current work presented in this paper. To do this properly requires that the modelling techniques and representations really do have to couple the mechanical and thermal aspects of the problem to achieve results of meaningful accuracy. A literature review of commonly used techniques for thermoelastic problems is presented in [8]. It was pointed out there that some works have looked at the problem of displacements and stresses in laminated structures under thermal bending. These have assumed a linear temperature profile through the thickness direction for both laminated plates and multilayered composite shells, as well as for circular plates and cylindrical shells. In these models the assumption has been that the temperature profile through the thickness is of linear and constant nature. This assumption could not be valid for anisotropic structures where the thickness temperature profile is never linear. Therefore, even if the structural model is accurate, the final solution could be in error due to the incorrectly assumed profile of the temperature distribution along the thickness. In [9,10] it has been shown that dependent on how the displacement and/or stress field are presented in the normal direction, mathematical models for thermal analysis of composite laminates can be derived using the three-dimensional theory of elasticity, Equivalent Single Layer theories (ESL), Layer Wise theories (LW) or zig-zag theories, and more recently by means of Carrera's Unified Formulation (CUF). To reduce the computational cost of three-dimensional theories and also maintain acceptable accuracy, several solutions for the thermal problems in composites have been proposed using the ESLs. These are the Classical Laminated Plate Theory (CLPT), First-order Shear Deformation Theory (FSDT) and Higher-order Shear Deformation Theory (HSDT). It has been highlighted in [8] that the literature so far only contains a relatively small amount of work devoted to the coupled thermo-mechanical analysis of structures, in the form of both thermoelastic and thermoplastic analyses. There also have been some works comparing coupled and uncoupled analysis, the accuracy and efficiency of the coupled theory [11], and the extension

of a higher-order zig-zag plate theory [12] for prediction of the fully coupled mechanical, thermal, and electric behaviour. Partially coupled models are commonly derived that neglect the interactions between temperature effects and mechanical deformations, and instead assume *a priori* the distribution of temperature along the thickness, or obtain it from the heat conduction equation and then they solve the mechanical equations with known temperature gradient terms. In contrast, fully coupled thermoelastic models take into account explicitly the interaction between temperature effects and mechanical deformations, because of the presence of coupling displacement and temperature terms in the thermal and mechanical equations, respectively. Furthermore, if the temperature varies in time we deal with two coupled processes, the *reversible elastic process* and the *irreversible thermodynamic process*, due to a spontaneous and hence irreversible process of heat transfer by means of heat conduction). This means that fully coupled approaches are the most appropriate for model development to investigate the influence of the thermal loading on the global thermomechanical behaviour of the structure.

From the foregoing discussion it can be seen that in order to consider thermoelasticity reasonably properly it is necessary to accept that deformation of a body leads to temperature changes, and conversely, and the internal energy of the body depends on both the temperature and the deformation. Therefore, for increased accuracy the problem has to be treated as a *coupled* process.

In this paper, to try to reduce the computational cost, it was decided to implement the Third order theory with Thermomechanical Coupling (TTC) approach described in [13]. This approach is a third order theory with thermomechanical coupling and demonstrated in [13] as giving results as accurate as those obtained from using CUF, which is a fully coupled approach using a fourth order expansion of the configuration variables. The underlying theory is extensive and covers a wide range of approaches and cases, which means that we are able to introduce the necessary simplifications to incorporate appropriate boundary and initial conditions.

It should also be mentioned that in recent years honeycomb panels have become more and more widely used within the aerospace industry [4,14,15,16] due to their structural efficiency, and because they demonstrate a generally high strength to weight ratio. This type of design consists of two thin parallel face sheets separated typically by a cellular foil core that transmits transverse shear and via skin separation has a naturally high cross-sectional second moment of area. The core can be composed of different types of material, but the most frequently used one is a hexagonal honeycomb made from sheets of aluminium foil (Fig.1). Despite their many benefits sandwich panels do have a number of structural limitations. They are known to have poor resistance to impact loads, particularly when combined with thermal loading, due to the risk of debonding between the sandwich core and the outer faces under these conditions.

In this paper we consider a typical aerospace aluminium honeycomb sandwich panel, this being a generally common form of structural material encountered across the aerospace industry (Fig.1).

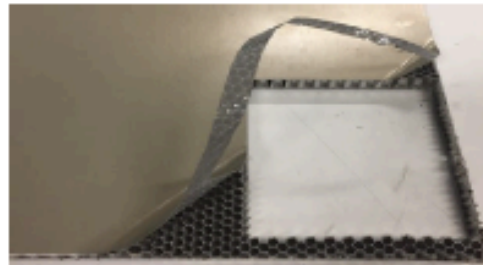


Figure 1: Honeycomb sandwich panel typically used in the aerospace industry

2. Aluminium alloy composite panel

The type of sandwich panel considered here is composed of two grades of aluminium alloy. For the outer faces of thickness 0.38×10^{-3} m, an Al-2024 alloy is used, whilst an Al-5056 alloy foil is used to form the hexagonal honeycomb core. This core is of depth 14.24×10^{-3} m and comprises a foil of thickness 0.0254×10^{-3} m. The mechanical and thermal properties of these materials, excluding the adhesive, are summarised in Tables 1 & 2, noting that the data in Table 1 does not contain explicit information on the thin film adhesive bonding of the core to the skin. It should be noted that the density of the Al-5056 core is much lower than that of the Al-2024 skins because it is an average figure covering the material itself and the volumetrically large voids within the honeycomb.

Table 1: Mechanical properties of sandwich panel

	Al-2024	Al-5056 3/16 Honeycomb
Density, ρ (kg/m ³)	2780	50
Young's Modulus, E (Pa)	73.1×10^9	669×10^6
Shear Modulus, G (Pa)	27.5×10^9	310×10^6
Poisson's Ratio, ν	0.33	0.3
Foil thickness (m [in])		0.0254×10^{-3} [0.001]

Table 2: Thermal properties of sandwich panel skin and honeycomb materials

	Al-2024	Al-5056
Coefficient of Thermal Expansion ($^{\circ}$ C)	2.47×10^{-5}	2.41×10^{-5}
Coefficient of Thermal Expansion for 3/16 honeycomb ($^{\circ}$ C)		2.4×10^{-6}
Thermal Conductivity @ 25 $^{\circ}$ C (W/mK)	149	209
Specific Heat (J/kg $^{\circ}$ C)	875	904

Despite the fact that finite element analysis is widely used for thermo-mechanical analysis, there is a significant industrial need for modelling that can avoid major re-definitions of statically and dynamically correlated spacecraft system level models. Ideal modelling should be capable of 'communication' between the mechanical and thermal aspects of the problem in order to predict the behaviour of the panel accurately in time. Such a facility would provide further insight into areas such as the structural reliability of the system, the dynamic changes in the structural properties due to thermo-mechanical loadings, and potential resonances arising from thermal loading and structural changes within the panel.

It is also desirable that this model remains conceptually straightforward in use and is able to accommodate different mechanical and thermal boundary conditions as well as dynamic mechanical and thermal loading, in order to simulate properly the behaviour of different structural elements. Clearly, the middle core will generally behave differently from the top and bottom plies, both mechanically and thermally. It is hypothesised that the middle core will experience nonlinear non-uniform deformation due

to the long-lasting heating effects that it experiences from the top and bottom layers. This means that the model needs to accommodate dynamically varying thermal properties.

To keep the model tractable it has been decided to implement a partially coupled TTC model. Although TTC in [13,18] is partially coupled it still demonstrates very high accuracy when compared with the fully coupled CUF model [8,17]. The TTC model consists of well-developed mechanical and thermal parts connected through additional coupling terms, these being temperature and time dependent in the mechanical part, and displacement and time dependent in the thermal part, respectively.

3. A model for the mechanical behaviour of the panel

The mechanical equations of motion are based on the Reddy plate theory [13] and [19], and an adaptation of this follows on directly, noting that it is assumed that deflection due to shear is negligible with respect to flexure between the layers, and so the basis for the model has been reduced to the interpretation given by [19],

$$N_{11,x} + N_{12,y} = 0$$

$$N_{12,x} + N_{22,y} = 0$$

$$M_{11,xx} + 2M_{12,xy} + M_{22,yy} + N_{11}w_{,xx} + 2N_{12}w_{,xy} + N_{22}w_{,yy} + q(x, y, t) - p_x w_{,xx} - p_y w_{,yy} = \rho h w_{,tt} + \delta w_{,t}$$

(1a,b,c)

where

$$\begin{Bmatrix} N_{11} \\ N_{22} \\ N_{12} \end{Bmatrix} = \int_{-h/2}^{h/2} \begin{Bmatrix} \sigma_{11} \\ \sigma_{22} \\ \sigma_{12} \end{Bmatrix} dz; \quad \begin{Bmatrix} M_{11} \\ M_{22} \\ M_{12} \end{Bmatrix} = \int_{-h/2}^{h/2} z \begin{Bmatrix} \sigma_{11} \\ \sigma_{22} \\ \sigma_{12} \end{Bmatrix} dz;$$

(2a,b)

and where N_{ij} are membrane forces, M_{ij} are bending moments, p_x and p_y are forces applied along the x and y coordinate directions respectively, δ is a damping coefficient, $q(x,y,t)$ is a transversely distributed loading, and ρ and h are the density and thickness of the panel.

For a laminated plate with arbitrarily oriented plies, the thermoelastic linear constitutive relations for the k th orthotropic lamina in the principal material coordinates of the lamina are,

$$\begin{Bmatrix} \sigma_{11} \\ \sigma_{22} \\ \sigma_{12} \end{Bmatrix} = \begin{bmatrix} \bar{Q}_{11} & \bar{Q}_{12} & 0 \\ \bar{Q}_{12} & \bar{Q}_{22} & 0 \\ 0 & 0 & \bar{Q}_{66} \end{bmatrix}^{(k)} \begin{Bmatrix} \epsilon_{11} \\ \epsilon_{22} \\ \epsilon_{12} \end{Bmatrix} - \begin{Bmatrix} \beta_{11} \\ \beta_{22} \\ 0 \end{Bmatrix}^{(k)} T$$

(3)

where $\bar{Q}_{ij}^{(k)}$ are the plane stress-reduced elastic stiffnesses, and $\bar{\beta}_{11}^{(k)} = \bar{Q}_{11}^{(k)} \alpha_1 + \bar{Q}_{12}^{(k)} \alpha_2$ and $\bar{\beta}_{22}^{(k)} = \bar{Q}_{12}^{(k)} \alpha_1 + \bar{Q}_{22}^{(k)} \alpha_2$ are the thermoelastic stiffnesses, with α_1 and α_2 being the coefficients of thermal expansion in the x and y directions.

The relationships between strains and displacements are given by the following [13],

$$\begin{aligned}\varepsilon_{11}^{(0)} &= u_{,x} + \frac{1}{2}w_{,x}^2; & \varepsilon_{22}^{(0)} &= v_{,y} + \frac{1}{2}w_{,y}^2 \\ \varepsilon_{12}^{(0)} &= u_{,y} + v_{,x} + w_{,x}w_{,y}\end{aligned}\quad (4)$$

$$\varepsilon_{12}^{(3)} = -C_1(2w_{,xy}), \quad \text{where } C_1 = 4/(3h^2) \quad (5)$$

and $u(x,y,t)$, $v(x,y,t)$, $w(x,y,t)$ are the displacements of a point located on the mid-plane, where the comma is used in the conventional way to denote the derivative compactly with respect to the associated independent variables.

The strains in Eq.(4) are related to the three dimensional strains in Eq.(6), as in [13], neglecting the rotations of the transverse normal around the x - and y - axes,

$$\varepsilon_{11} = \varepsilon_{11}^{(0)}; \quad \varepsilon_{22} = \varepsilon_{22}^{(0)}; \quad \varepsilon_{12} = \varepsilon_{12}^{(0)} + z^3\varepsilon_{12}^{(3)} \quad (6)$$

In Eqs.(4)-(6), $\varepsilon_{ij}^{(0)}$ are the von Karman nonlinear membrane strains, $\varepsilon_{ij}^{(3)}$ are the Reddy higher order bending strains. The transverse shearing strains are neglected.

Following [13] we also assume that the temperature varies according to a cubic law,

$$T = T_0 + zT_1 + z^2T_2 + z^3T_3 \quad (7)$$

where $T(x,y,z,t)$ is the three dimensional temperature variable, while $T_0(x,y,t)$, $T_1(x,y,t)$, $T_2(x,y,t)$, $T_3(x,y,t)$ are the hitherto unknown components of the temperature of the two dimensional model, and cover the full profile up to a cubic distribution.

The components T_2 and T_3 can be expressed in terms of T_0 and T_1 by imposing a variable combination of the following thermal boundary condition, in this case a \pm distribution of the free heat exchange on the upper and lower surfaces of the plate [17,20],

$$q_3|_{z=\pm h/2} = \pm H[T_\infty - (T)_{\pm h/2}] \quad (\text{for free heat exchange}) \quad (8)$$

where q_3 is the heat flow in the z direction, H is the boundary conductance, and T_∞ is a constant difference between the absolute temperature of the surrounding medium and the reference temperature,

$$T = f_a(z)T_0 + f_b(z)T_1 + f_c(z) \quad (9)$$

where

$$\begin{aligned}f_a(z) &= (r_1 + r_2z + r_3z^2 + r_4z^3) \\ f_b(z) &= (r_5 + r_6z + r_7z^2 + r_8z^3) \\ f_c(z) &= (r_9 + r_{10}z + r_{11}z^2 + r_{12}z^3)\end{aligned}\quad (10)$$

and where the r_i are defined by the imposed boundary conditions. For a free heat exchange thermal boundary condition the r_i are introduced as given in [13,20],

$$r_1 = r_6 = 1; \quad r_3 = -\frac{4H}{h(hH + 4\lambda_{33}^{(1)})}; \quad r_8 = -\frac{4(hH + 2\lambda_{33}^{(1)})}{h^2(hH + 6\lambda_{33}^{(1)})}$$

$$r_{11} = \frac{4HT_{\infty}}{h(hH + 4\lambda_{33}^{(1)})}; \quad r_2 = r_4 = r_5 = r_7 = r_9 = r_{10} = r_{12} = 0$$

where the $\lambda_{ij}^{(k)}$ are the thermal conductivities of the k th laminate.

4. A model for the thermal behaviour of the panel

The thermal balance equations are introduced for the case of non-stationary conduction and thermoelastic coupling, as in [13],

$$q_{1,x} + q_{2,y} + q_{3,z} - b_x - a_x + E = 0 \quad (11)$$

where the $q_i(x,y,z,t)$ represents the three dimensional heat flow along the x,y,z directions, $b(x,y,z,t)$ is the three dimensional internal energy due to non-stationary conduction, $a(x,y,z,t)$ is the three dimensional interaction energy due to the thermoelastic coupling, and $E(x,y,z,t)$ is the three dimensional source energy. The two-dimensional balance consists of two equations obtained from Eq. (11), [13,18],

$$\begin{aligned} q_{1,x}^{(0)} + q_{2,y}^{(0)} - b_x^{(0)} - a_x^{(0)} + Q^{(0)} &= 0 \\ q_{1,x}^{(1)} + q_{2,y}^{(1)} - b_x^{(1)} - a_x^{(1)} + Q^{(1)} &= 0 \end{aligned} \quad (12)$$

where the following two dimensional quantities are defined as

$$\begin{aligned} \begin{Bmatrix} q_1^{(0)} \\ q_2^{(0)} \end{Bmatrix} &= \int_{-h/2}^{h/2} \begin{Bmatrix} q_1 \\ q_2 \end{Bmatrix} dz; \quad b^{(0)} = \int_{-h/2}^{h/2} b dz; \quad a^{(0)} = \int_{-h/2}^{h/2} a dz \\ \begin{Bmatrix} q_1^{(1)} \\ q_2^{(1)} \end{Bmatrix} &= \int_{-h/2}^{h/2} z \begin{Bmatrix} q_1 \\ q_2 \end{Bmatrix} dz; \quad b^{(1)} = \int_{-h/2}^{h/2} bz dz; \quad a^{(1)} = \int_{-h/2}^{h/2} az dz \\ Q^{(0)} &= \int_{-h/2}^{h/2} q_{3,x} dz; \quad Q^{(1)} = \int_{-h/2}^{h/2} q_{3,x} z dz \end{aligned} \quad (13)$$

The source energy $E(x,y,z,t)$ is neglected due to the absence of chemical reactions, nuclear fission effects or inputs due to electric currents. The heat flow definition is based on the Fourier law for the k th orthotropic lamina and expressed in the principal material coordinates of a lamina as follows,

$$\begin{aligned} \begin{Bmatrix} q_1^{(0)} \\ q_2^{(0)} \end{Bmatrix} &= \sum_{k=1}^N \int_{z_k}^{z_{k+1}} \begin{bmatrix} \lambda_{11}^{(k)} & \lambda_{12}^{(k)} \\ \lambda_{12}^{(k)} & \lambda_{22}^{(k)} \end{bmatrix} \left(\begin{bmatrix} f_a(z) & 0 \\ 0 & f_a(z) \end{bmatrix} \begin{Bmatrix} g_1^{(0)} \\ g_2^{(0)} \end{Bmatrix} + \right. \\ &\quad \left. + \begin{bmatrix} f_b(z) & 0 \\ 0 & f_b(z) \end{bmatrix} \begin{Bmatrix} g_1^{(1)} \\ g_2^{(1)} \end{Bmatrix} \right) dz \end{aligned}$$

$$\begin{aligned} \begin{Bmatrix} q_1^{(1)} \\ q_2^{(1)} \end{Bmatrix} &= \sum_{k=1}^N \int_{z_k}^{z_{k+1}} \begin{bmatrix} \lambda_{11}^{(k)} & \lambda_{12}^{(k)} \\ \lambda_{12}^{(k)} & \lambda_{22}^{(k)} \end{bmatrix} \left(\begin{bmatrix} f_a(z) & 0 \\ 0 & f_a(z) \end{bmatrix} \begin{Bmatrix} g_1^{(0)} \\ g_2^{(0)} \end{Bmatrix} + \right. \end{aligned}$$

$$+ \begin{bmatrix} f_b(z) & 0 \\ 0 & f_b(z) \end{bmatrix} \begin{Bmatrix} g_1^{(1)} \\ g_2^{(1)} \end{Bmatrix} z dz \quad (14)$$

where the $\lambda_{ij}^{(k)}$ are the thermal conductivities of the k th laminate, and thermal gradients $g_1^{(0)} = T_{0,x}$, $g_1^{(1)} = T_{1,x}$, $g_2^{(0)} = T_{0,y}$, $g_2^{(1)} = T_{1,y}$ as defined in [13].

The internal energy for the k th lamina is defined in terms of temperature,

$$b^{(k)} = C^{(k)}T = \rho^{(k)}c_v^{(k)} \quad (15)$$

where $C^{(k)}$ is the thermal capacity of the k th lamina, the function of mass density is $\rho^{(k)}$ and the specific heat at constant strain is given by $c_v^{(k)}$.

The components of internal energy can then be re-written, taking into account Eqs. (9)-(10), (15), as,

$$b^{(0)} = \int_{-h/2}^{h/2} b dz = \sum_{k=1}^N \int_{z_k}^{z_{k+1}} b^{(k)} dz = \sum_{k=1}^N \int_{z_k}^{z_{k+1}} C^{(k)} [f_a(z)T_0 + f_b(z)T_1 + f_c(z)] dz \quad (16)$$

$$b^{(1)} = \int_{-h/2}^{h/2} b dz = \sum_{k=1}^N \int_{z_k}^{z_{k+1}} b^{(k)} dz = \sum_{k=1}^N \int_{z_k}^{z_{k+1}} C^{(k)} [f_a(z)T_0 + f_b(z)T_1 + f_c(z)] z dz \quad (17)$$

The interaction energy for the k th orthotropic lamina is expressed in terms of strain within the three dimensional thermoelastic theory, with the assumption that $\epsilon_{zz} = \epsilon_{33} = 0$,

$$\begin{aligned} a^{(0)} &= \int_{-h/2}^{h/2} a dz = \sum_{k=1}^N \int_{z_k}^{z_{k+1}} a^{(k)} dz = \\ &= T_{ref} \sum_{k=1}^N \int_{z_k}^{z_{k+1}} \left[\beta_{11}^{(k)} (\epsilon_{11}^{(0)} + z\epsilon_{11}^{(1)} + z^3\epsilon_{11}^{(3)}) + \beta_{22}^{(k)} (\epsilon_{22}^{(0)} + z\epsilon_{22}^{(1)} + z^3\epsilon_{22}^{(3)}) + \right. \\ &\quad \left. + \beta_{12}^{(k)} (\epsilon_{12}^{(0)} + z\epsilon_{12}^{(1)} + z^3\epsilon_{12}^{(3)}) \right] dz \\ a^{(1)} &= \int_{-h/2}^{h/2} a z dz = \sum_{k=1}^N \int_{z_k}^{z_{k+1}} a^{(k)} z dz = \\ &= T_{ref} \sum_{k=1}^N \int_{z_k}^{z_{k+1}} \left[\beta_{11}^{(k)} (\epsilon_{11}^{(0)} + z\epsilon_{11}^{(1)} + z^3\epsilon_{11}^{(3)}) + \beta_{22}^{(k)} (\epsilon_{22}^{(0)} + z\epsilon_{22}^{(1)} + z^3\epsilon_{22}^{(3)}) + \right. \\ &\quad \left. + \beta_{12}^{(k)} (\epsilon_{12}^{(0)} + z\epsilon_{12}^{(1)} + z^3\epsilon_{12}^{(3)}) \right] z dz \end{aligned} \quad (18)$$

The energy exchange rates of the out-of-plane heat flow $Q^{(0)}$ and $Q^{(1)}$ due to the heat flow q_3 in the z direction are,

$$\begin{aligned}
Q^{(0)} &= \int_{-h/2}^{h/2} q_{3,x} dz = \sum_{k=1}^N \int_{z_k}^{z_{k+1}} \lambda_{33}^{(k)} g_{3,x} dz = \sum_{k=1}^N \int_{z_k}^{z_{k+1}} \lambda_{33}^{(k)} [(f_a(z)T_0 + f_b(z)T_1 + f_c(z))_{,xx}] dz \\
Q^{(1)} &= \int_{-h/2}^{h/2} q_{3,x} z dz = \sum_{k=1}^N \int_{z_k}^{z_{k+1}} \lambda_{33}^{(k)} g_{3,x} z dz = \sum_{k=1}^N \int_{z_k}^{z_{k+1}} \lambda_{33}^{(k)} [(f_a(z)T_0 + f_b(z)T_1 + f_c(z))_{,xx}] z dz
\end{aligned}
\tag{19}$$

A procedure specifically for computing the solutions to the principal equations (1) and (12), and invoking all the parameters that follow, defined with respect to specified boundary and initial conditions, has been coded in the *Mathematica*TM programming language.

Having derived the necessary components of the thermal and mechanical equations it is then possible to obtain the system of equations. Since we are interested in the temperature and displacement distribution in the z -direction for the structure when it is subjected to combined mechanical and thermal loading, the system can be reduced to the following three equations to find the displacement $W(t)$, membrane temperature $T_0(t)$ and bending temperature $T_1(t)$ as defined in [18,21], and then to identify $T(t)$ in Eq.(9):

$$\begin{aligned}
C_1 \ddot{W}(t) + C_2 \dot{W}(t) + [C_3 + C_4 p_x(t) + C_5 p_y(t) + C_6 T_0(t) + C_7 T_{\infty}(t)] W(t) + C_8 W^3(t) \\
+ C_9 T_1(t) + q(t) = 0 \\
C_{10} \dot{T}_0(t) + C_{11} T_0(t) + C_{12} T_{\infty}(t) + C_{13} \dot{W}(t) W(t) = 0 \\
C_{16} \dot{T}_1(t) + C_{17} T_1(t) + C_{18} T_{\infty}(t) + C_{19} \dot{W}(t) = 0
\end{aligned}
\tag{20}$$

It has to be pointed out that in reference [13] this form of system of equations was solved analytically obtaining a general solution using features within a *Mathematica*TM code. However, this was done by eliminating the nonlinear terms and for static values of the mechanical and thermal loading, thus,

$$\begin{aligned}
C_1 \ddot{W}(t) + C_3 W(t) + C_9 T_1(t) = 0 \\
C_{10} \dot{T}_0(t) + C_{11} T_0(t) = 0 \\
C_{16} \dot{T}_1(t) + C_{17} T_1(t) + C_{19} \dot{W}(t) = 0
\end{aligned}
\tag{21}$$

Here our overall aim has been to look for a solution for the system in its generalised form, as stated in full in Eq. (20). The implications of the simplification in Eq. (21) were discussed in [22].

5. Numerical experiment

A numerical study is presented for the solutions obtained for the system (20) with full nonlinear coupling terms, and by exploiting the powerful numerical functions within NDSolve. The loading is considered as a combined thermo-mechanical load consisting of a constant thermal component and a dynamic mechanical component.

The plate-like panel under consideration is of the dimensions provided in Table 3. These properties, as well as loading conditions and boundary and initial conditions, are considered for verification of the performance of the model against the experimental results presented in [23].

Table 3: Dimensions of Sandwich Panel Sample

Length, a ($\times 10^{-3}$ m)	Width, b ($\times 10^{-3}$ m)	Face Thickness ($\times 10^{-3}$ m)	Honeycomb layer thickness ($\times 10^{-3}$ m)	Honeycomb Cell size (m)	Foil Thickness (m)
300	100	0.38	14.24	0.0048 (3/16 in)	2.54×10^{-5} m (0.001 in)

The panel was considered to be simply supported and was analysed under dynamic mechanical loading increasing up to 160 N while being positioned within an environmental chamber exhibiting thermal loading in the form of a variety of thermal environments. Within the analytical model thermal loading was applied by means of imposing different environmental temperatures in order to represent free heat exchange conditions similar to those of the experiment in [23], and mechanical loading was taken as a dynamically increasing normal force governed by $q(t)=10*t$ to simulate a ramped increase up to 160N after 16s has elapsed, and this is applied centrally to the top-face sheet.

It should be pointed out that in the experiment [23] an initial displacement was introduced to more clearly portray the gradual displacement that emerged naturally within the experiment, therefore in order to calculate the actual displacement from the graphs presented in [24] the initial displacement has to be deducted.

Based on the results presented graphically in [24] the maximum value of the actual displacement is summarised in Table 4. These outputs from the experiment will be used for verification of the model discussed in this paper.

Table 4: Maximum actual displacement presented in [24] at maximum mechanical loading of 160N

Temperature of environment ($^{\circ}$ C)	100	80	60	40	20	-20	-40	-60	-100	-150
Maximum displacement ($\times 10^{-3}$ m)	0.7	0.5	0.45	0.45	0.4	0.3	0.3	0.25	0.25	0.2

5.1 Displacement distribution in response to the dynamic mechanical loading and variable environmental temperature

When elevated temperature conditions apply at the outer faces of the sandwich panel, representing the free heat exchange condition, these faces will heat up first of all, with the heat then distributing from the outer faces inwards towards the centre of the core. To understand the process of the displacement due to the heating-up process, as well as the characteristics of the thermal gradient along the thickness, a constant environmental surround temperature of 100 $^{\circ}$ C, 80 $^{\circ}$ C, 60 $^{\circ}$ C, 40 $^{\circ}$ C and ambient as 20 $^{\circ}$ C were applied with the ambient reference temperature set to 20 $^{\circ}$ C, and a solution for the system of Eq. (20) was obtained using the NDSolve function in *Mathematica*TM and presented in Fig 2-6 corresponding to the temperature of the environment.

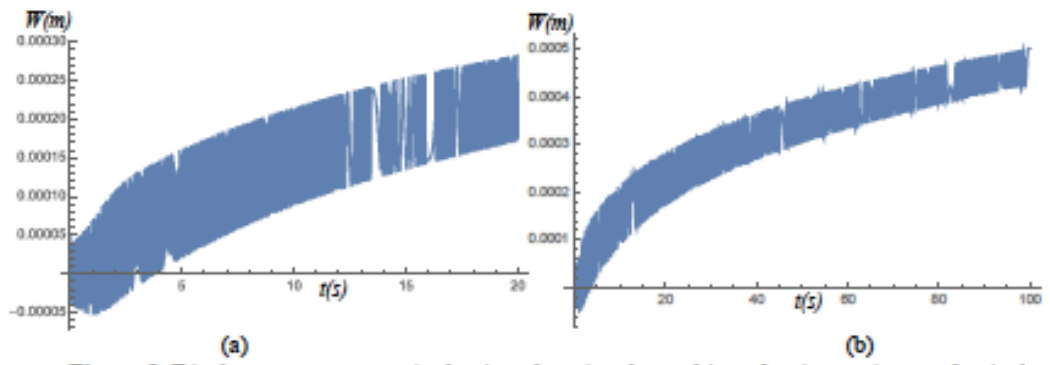


Figure 2. Displacement response in the time domain when subjected to increasing mechanical loading (a) up to 160 N at 16s and (b) – further loading in time, within an environmental temperature of 100°C .

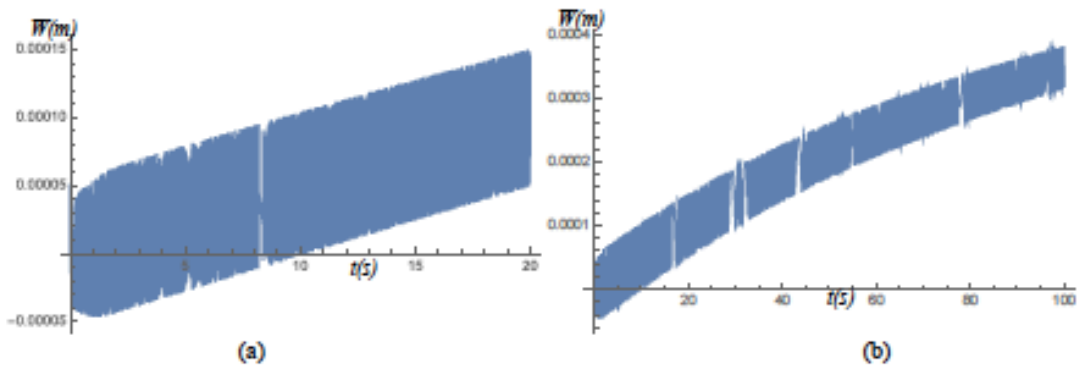


Figure 3. Displacement response in the time domain when subjected to increasing mechanical loading (a) up to 160 N at 16s and (b) – further loading in time, within an environmental temperature of 80°C .

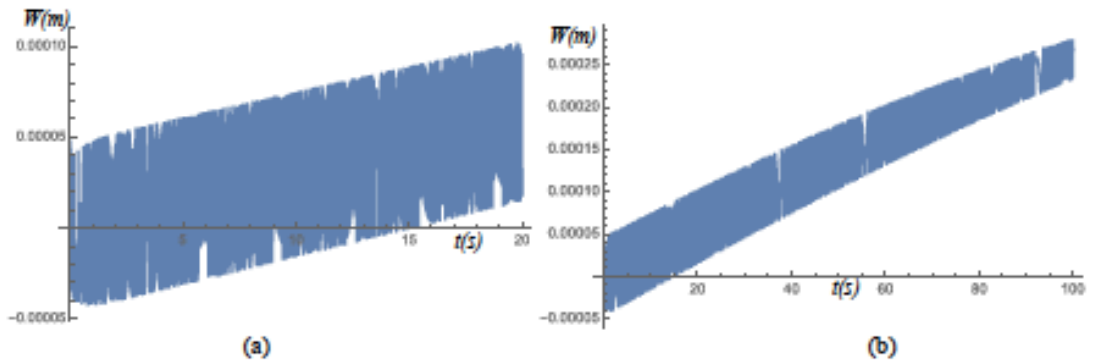


Figure 4. Displacement response in the time domain when subjected to increasing mechanical loading (a) up to 160 N at 16s and (b) – further loading in time, within an environmental temperature of 60°C .

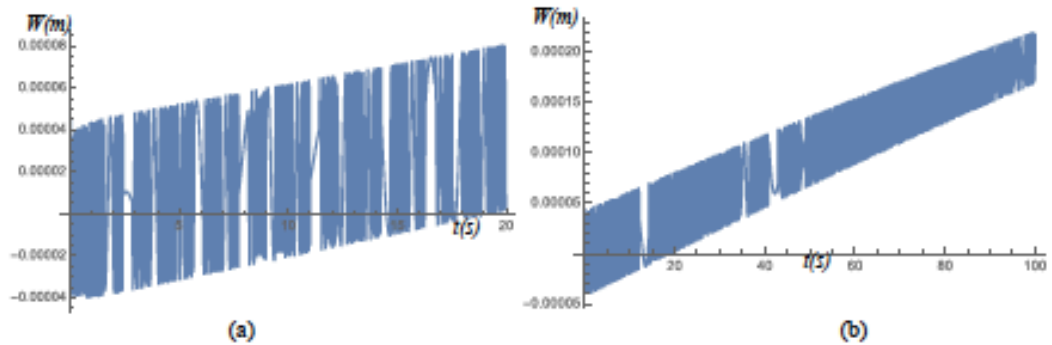


Figure 5. Displacement response in the time domain when subjected to increasing mechanical loading (a) up to 160 N at 16s and (b) – further loading in time, within an environmental temperature of 40°C .

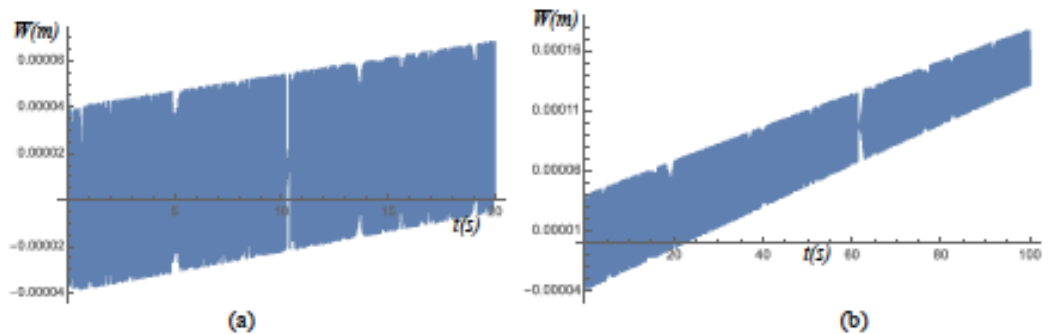


Figure 6. Displacement response in the time domain when subjected to increasing mechanical loading (a) up to 160 N at 16s and (b) – further loading in time, within an environment of ambient temperature.

Figures 2-6 (a) demonstrate the maximum value of the displacement after 16s when it has reached 160N according to the loading being represented by $q(t)=10*t$, as corresponding with the experimental study in [23]. As can be seen in Figs 2-6 (a) there is evidence of an increasing trend in the maximum displacement value, where it is seen to be increasing with the elevating temperature of the environment. This confirms the pattern of behaviour demonstrated in [23] and is summarised in Table 4 . It can be justified by the presence of a softening effect of the material within hot environments. This trend becomes even more evident with time, as can be observed in Figs 2-6 (b).

In Figs. 2-6 we can also see clearly the reflection of the dynamically increasing mechanical loading in an almost linear increasing behaviour of the displacement response. This accords with practical expectations for a plate under this form of loading, as well as with the results for loading up 160 N from the experiment [23].

The principal features of the displacement responses are the transient over time and the largely symmetrical peak to peak amplitudes. It is also important to note that the peak-to-peak transient disturbance increases with the harshness of the environmental temperature, and this confirms the coupling between the environmental heat and the mechanical deformation, and the fact that harsh environments bring in a destabilising effect into the panel's response when undergoing mechanical loading.

To understand the process of the displacement distribution due to the cooler or even extreme environmental conditions a constant environmental surround temperature of -20°C , -40°C , -60°C , -100°C

and -150°C was applied. A solution for the system of Eq. (20) was again obtained using the NDSolve function in *Mathematica*TM and presented in Fig 7-11 corresponding to the environmental temperature.

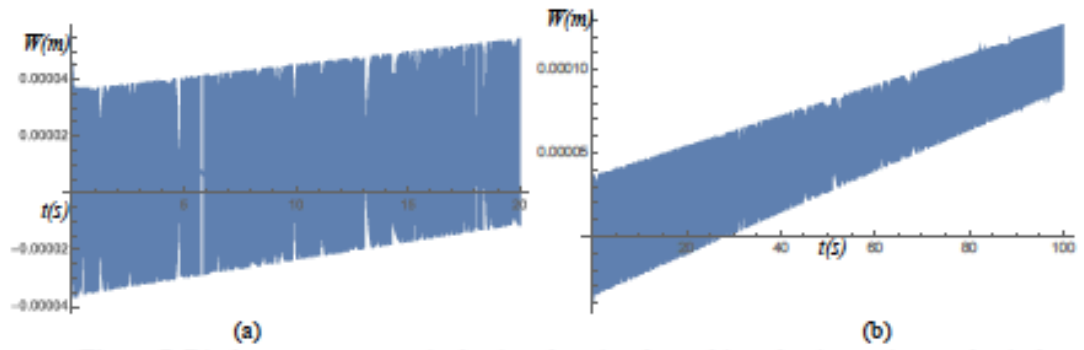


Figure 7. Displacement response in the time domain when subjected to increasing mechanical loading (a) up to 160 N at 16s and (b) – further loading in time, within an environmental temperature of -20°C .

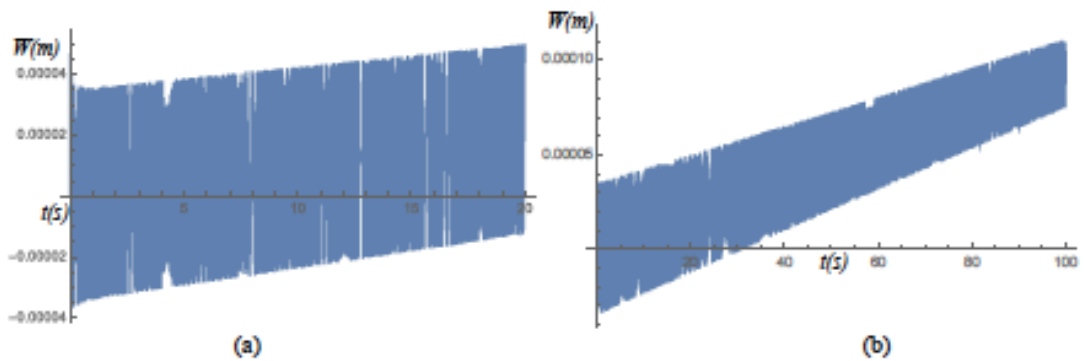


Figure 8. Displacement response in the time domain when subjected to increasing mechanical loading (a) up to 160 N at 16s and (b) – further loading in time, within an environmental temperature of -40°C .

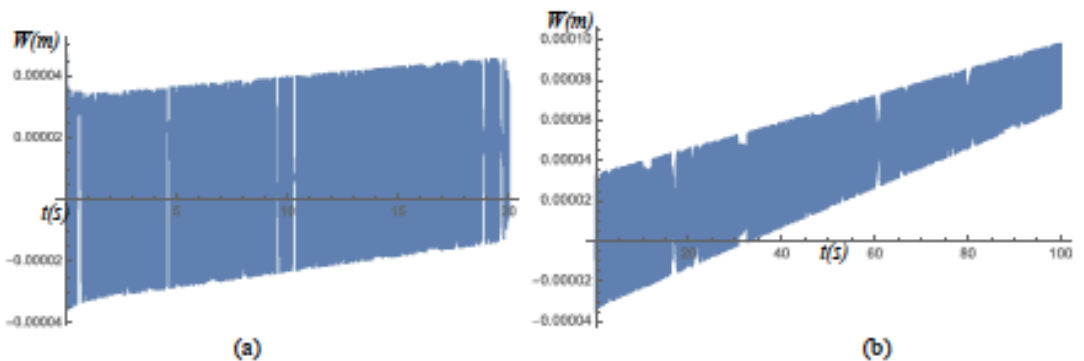


Figure 9. Displacement response in the time domain when subjected to increasing mechanical loading (a) up to 160 N at 16s and (b) – further loading in time, within an environmental temperature of -60°C .

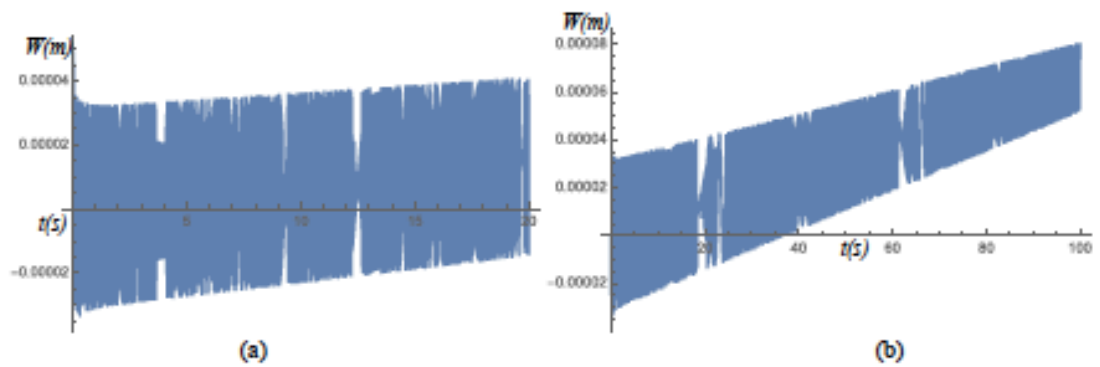


Figure 10. Displacement response in the time domain when subjected to increasing mechanical loading (a) up to 160 N at 16s and (b) – further loading in time, within an environmental temperature of -100°C .

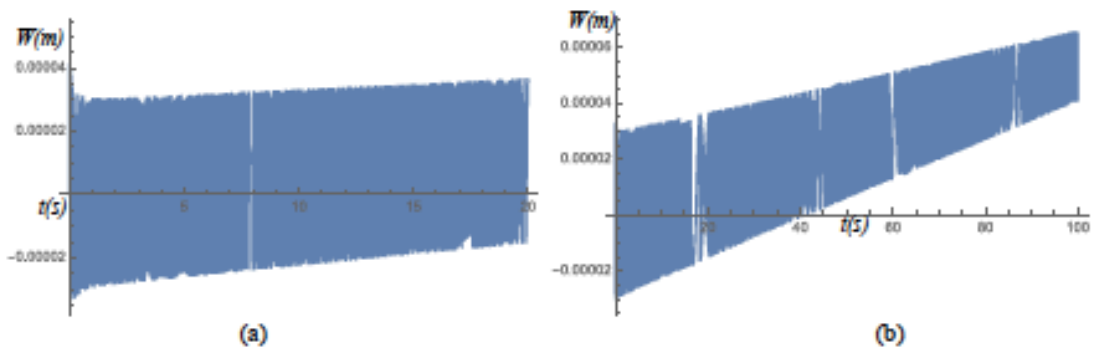


Figure 11. Displacement response in the time domain when subjected to increasing mechanical loading (a) up to 160 N at 16s and (b) – further loading in time, within an environmental temperature of -150°C .

An analysis of the response of the panel to the same increasing mechanical loading $q(t)=10*t$ but for a colder environment going down to the harsh extreme of -150°C (Figs 7-11), confirms the trend demonstrated in [23] which is summarised in Table 4 (Table 5). The maximum value of the displacement is reached at 16s and corresponds to 160N and is decreasing with decreasing environmental temperature (Figs 7-11 (a)) and this can again be justified by a hardening effect of the material within the colder environment. This trend becomes even more evident at times beyond 16s, as can be observed in Figs 7-11 (b). This hardening effect in a colder, harsher, environment also impacts on the transient response. The symmetrical peak to peak amplitude response of displacement clearly decreases, demonstrating stiffer structural properties. However, this 'suppression' of the amplitude might be characterised by a higher frequency response. This confirms the coupling between environmental temperature and mechanical deformation, and the fact that a colder environment is still characterised by a destabilising effect into the panel's response when undergoing mechanical loading.

In Figs. 7-11 we can clearly see again the reflection of the dynamically increasing mechanical loading in an almost linearly increasing behaviour of the displacement response.

Table 5: Maximum actual displacement presented in [24] and obtained from analytical model at a maximum mechanical loading of 160 N

Temperature of environment (°C)	100	80	60	40	20	-20	-40	-60	-100	-150
Maximum displacement Experimental ($\times 10^{-3}$ m)	0.7	0.5	0.45	0.45	0.4	0.3	0.3	0.25	0.25	0.2
Maximum displacement Analytical ($\times 10^{-3}$ m)	0.3	0.15	0.1	0.08	0.06	0.053	0.05	0.045	0.04	0.03

It has to be pointed out that the disparity in the results in Table 5 occurs due to the possible inconsistency in material properties. Some properties required for the analytical model were not available for the sample tested in [23] therefore typical properties for Al-2024 and Al-5056 were assumed for some of the required material parameters.

For verification of the response of the model the case of a larger plate of dimensions 0.8 x 0.8 m, otherwise with the same properties and under the same mechanical loading in an environment of 100°C, was considered in Fig. 12.

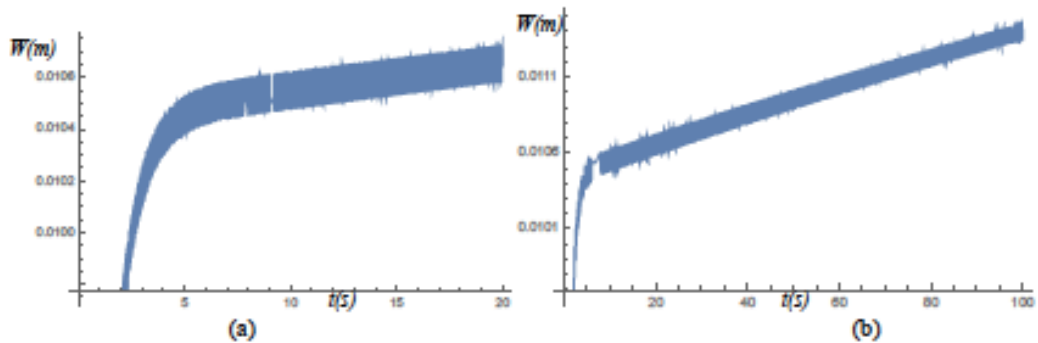


Figure 12. Displacement response for a larger panel 0.8x0.8 m when subjected to increasing mechanical loading up to 160 N within an environment of 100°C.

Comparing the response in Fig. 12 with the results presented in Fig. 2, the panel under consideration with the same thickness but larger length and width dimensions, responds with a larger displacement as expected for a large thin plate.

5.2 Temperature distribution along the thickness of the panel in response to the dynamic mechanical loading and variable environmental temperature

When elevated temperature conditions apply at the outer faces of the sandwich panel, representing the free heat exchange condition, these faces will heat up first of all, with the heat then distributing from the outer faces inwards towards the centre of the core. However, because of differences in the material of the skins and the honeycomb core, it is reasonable to predict a nonlinear temperature distribution along the thickness of the panel. This effect is very difficult to explore experimentally, especially if the panel is relatively thin. But the model applied in this paper allows us to predict the dynamic distribution of the heat along the thickness of the panel.

To understand the process of heating up or cooling down of the panel in response to the high or low environmental temperature, the following values for the constant environmental surround temperature were taken, 100°C, 80°C, 60°C, 40°C, ambient at 20°C and then down to -20°C, -40°C, -60°C, -100°C and -150°C in line with the investigation of the displacement response considered in 5.1. A solution for the

system of Eq. (20) and Eq. (7) was obtained using the NDSolve function in *Mathematica*TM and presented in Fig 14-16 for environmental temperatures of 100°C, 20°C, -150°C and in Appendix A for 80°C, 60°C, 40°C and then -20°C, -40°C, -60°C, -100°C.

It should be noted that the thickness of the panel in Figs 14-16 is along the *X* coordinate and the temperature readings are along the *Y* coordinate, as shown schematically in Fig 13.



Figure 13. Representation of the panel for interpretation of temperature distribution across the thickness in Figs 14-16

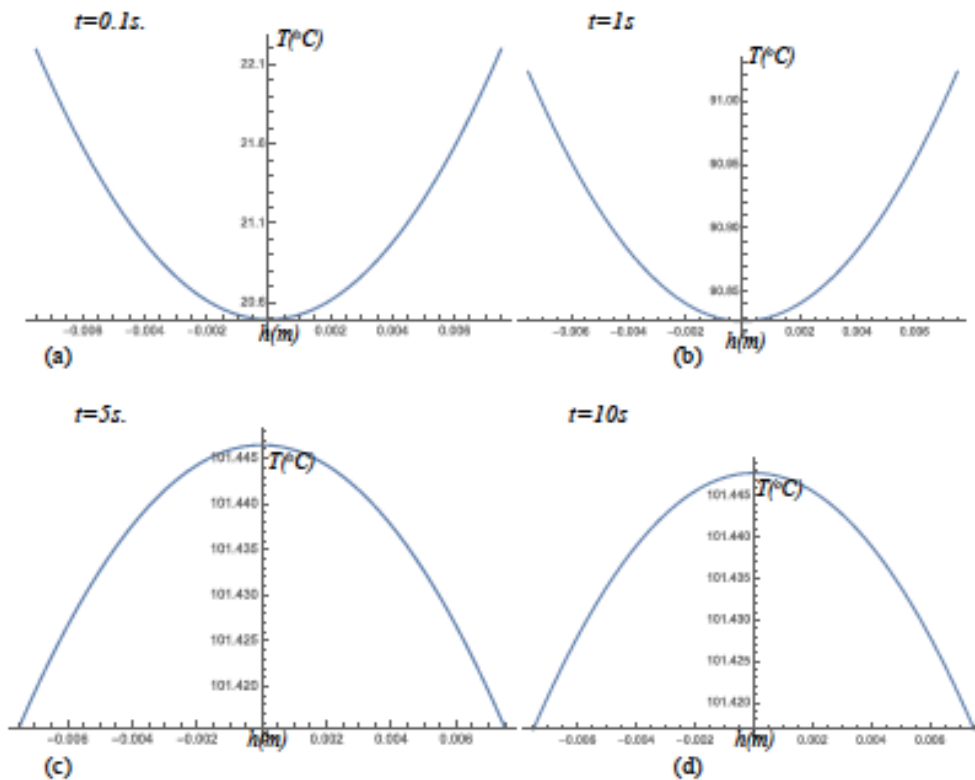


Figure 14. Temperature distribution across the thickness of the panel (*x* coordinate) when the panel is under dynamic mechanical loading and in an environmental soak temperature of 100° C, presented for different instants in time.

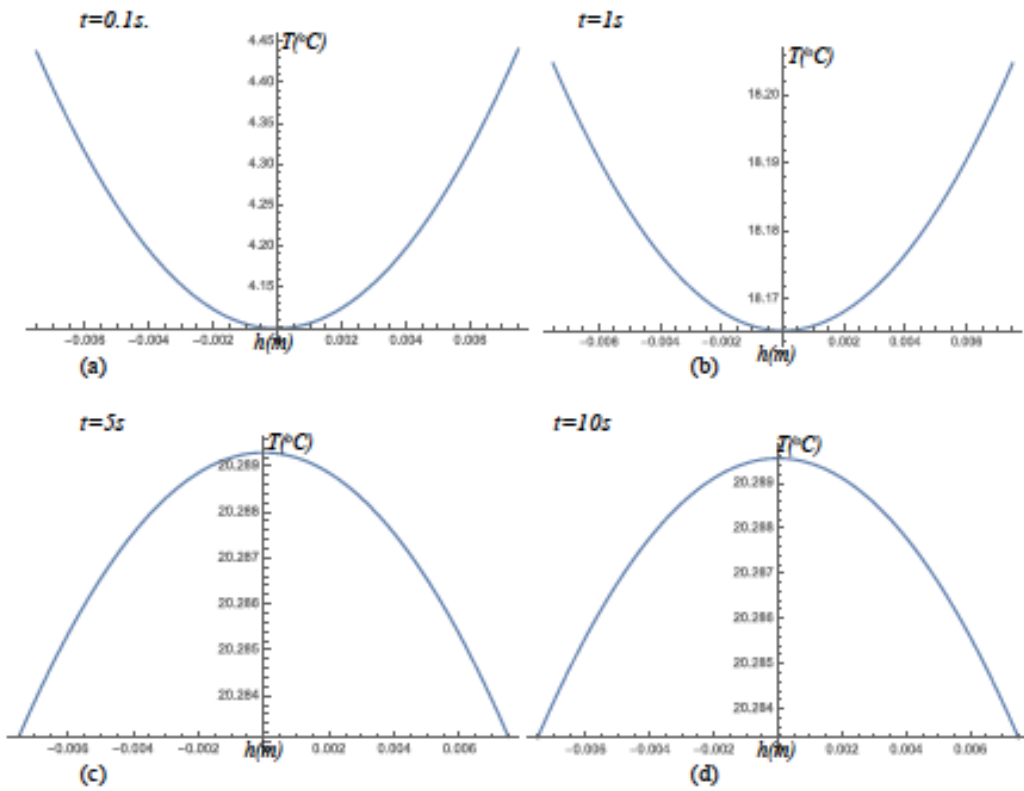
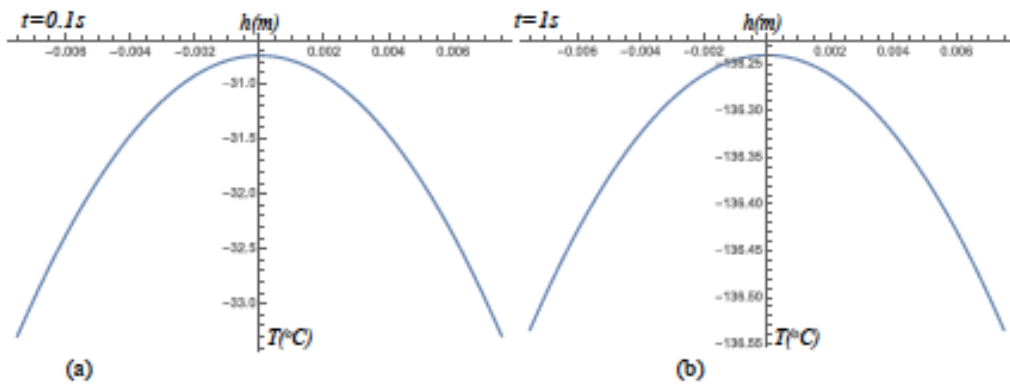


Figure 15. Temperature distribution across the thickness of the panel (x coordinate) when the panel is under dynamic mechanical loading and in an environmental soak temperature of 20^o C, presented for different instants in time.



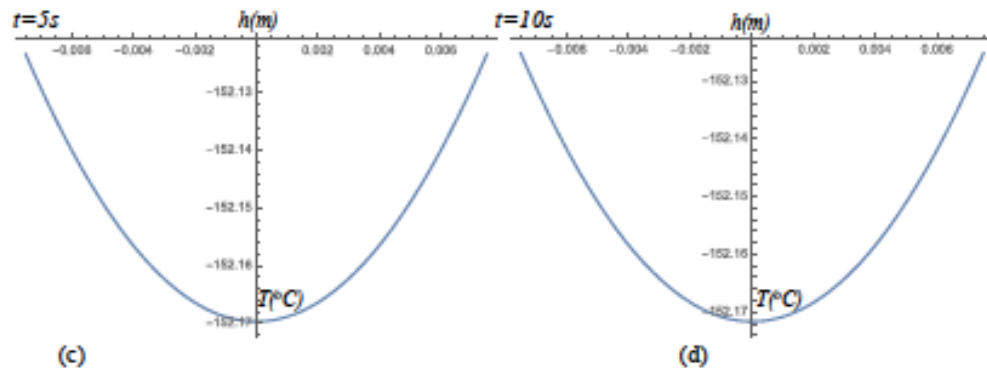


Figure 16. Temperature distribution across the thickness of the panel (x coordinate) when the panel is under dynamic mechanical loading and in an environmental soak temperature of -150°C , presented for different instants in time.

By fixing the time steps and observing the progression of the temperature distribution through the plate we see the main stages of the temperature stabilisation process that are also described in [13]. In brief, this amounts to the following. By applying heat to the plate through an elevated environmental soak temperature the temperature distribution through the thickness is as shown in Fig. 14(a), with the temperature of the honeycomb core being close to the top skin temperature but slightly cooler by 1.8°C , and after $1s$ (Fig. 14(b)) this stabilises and settles within a small difference of 0.2°C between that of the skin temperature and the honeycomb core. The process of equilibrating temperature due to the plate heating-up progresses further with time and after $5s$ an equilibrium temperature is reached and the profile thereafter remains constant in time exhibiting a small difference in temperature between the core and the skins of about 0.03°C (Fig. 14(c-d)).

On analysing the history of the thermal outputs over time for other environments in Figs. 15, 16 and in Appendix A, it is evident that the plate is undergoing a similar process of stabilisation, and reaches the equilibrium state with a small residual disparity in temperature between the skins and core.

From the parabolic output in Figs. 14 it is also obvious that at the start of the heating-up process (time step $t = 0.1s$), when the heat is only just starting to distribute through the thickness of the panel, the temperature in the middle is lower than in the skins. However, as the heating-up process progresses, the core, made of thinner honeycomb aluminium, tends to heat up slightly further demonstrating a higher temperature reading around 0.03°C than that of the skins. A similar flip in the behaviour can be observed for the cooling process shown in Figs. 16, with around 0.04°C difference between the skins and the core temperature. These internal transformations due to the heating-up or cooling-down process could be the key to an explanation for the transient response demonstrated in the displacement response which is clearly driven by the environmental temperature.

6. Conclusions

1. A new modelling strategy for aluminium honeycomb composite panels widely applied in aerospace structures, has been considered in this paper. The physics of dynamic thermal and mechanical loadings have been integrated into a conceptually straightforward and partially coupled modelling procedure coded in the *Mathematica*TM language which can accommodate different boundary conditions, dynamically varying thermal properties, and dynamic forms of mechanical loading.

2. The panel presented in the experimental set up in [23] has been considered to verify the analytical model through comparison of the maximum displacement of the panel, as well as the influence of the environmental temperature on the magnitude of displacement induced by a dynamic mechanical loading. The same trend of the higher displacement response in hotter environments and lower displacement response in cooler environments was found, confirming the associated predictions of the analytical model. It was also found that the displacement response was characterised by the transient behaviour, dependent on the environmental temperature, confirming the coupled effects of thermal and mechanical loading.

3. The model was also used to predict the dynamic thermal response of the material within the thickness of the panel, demonstrating a nonlinear temperature distribution profile within the thickness of the panel. It was also found that during the heating up process the core remains at a lower temperature than the skins were at the beginning of the heating up process. However, there was also evidence of heating up of the core beyond the skin temperature by a very small amount. Although the difference between the temperature of the core and the skins at the end of the transformation was very small, it still gave an indication of some nonlinear transformational phenomena occurring within the thickness of the panel when undergoing mechanical loading within the harsher environments. This of course might be more significant for larger or thicker panels and could be particularly significant for large aerospace structures exposed to harsh thermal cycles.

4. These internal transformations due to the heating-up or cooling-down processes could be the key to the explanation of the transient response demonstrated in the displacement response as driven by the environmental temperature. It is also hypothesised that the frequency of the transient response might be higher due to the amplitude 'suppression' in cooler environments due to the material stiffening effect, which could potentially introduce a parasitic resonance contributing to the problem of de-point of the parent satellite structure. This is still to be investigated in future research.

Funding Acknowledgement

The first two authors would like to acknowledge the financial support made available by Airbus Defence & Space Ltd and also the award of funding from the Strathclyde Centre for Doctoral Training. The authors would also like to thank Airbus Defence & Space Ltd for confidential access to data, noting that no disclosure of any such data whatsoever has been made within this paper.

Data Availability Statement

The raw/processed data required to reproduce these findings cannot be shared at this time due to legal or ethical reasons.

Acknowledgments: The first two authors would like to acknowledge the financial support made available by Airbus Defence & Space Ltd and also the award of funding from the Strathclyde Centre for Doctoral Training. The authors would also like to thank Airbus Defence & Space Ltd for confidential access to data, noting that no disclosure of any such data whatsoever has been made within this paper.

References

[1] Finckenor MM, De Groh KK (2016) A Researcher's guide to space environmental effects. International Space Station. NASA. NP-2015-03-015-JSC. Available at: https://www.nasa.gov/connect/ebooks/researchers_guide_space_environment_detail.html (accessed 13 August 2020)

- [2] Clawson JF, Tsuyuki GT, Anderson BJ, Justus CG, Batts W, Ferguson D and Gilmore DG. *Spacecraft thermal Environments. Spacecraft Thermal Control Handbook, Volume I: Fundamentals Technologies*, 2nd edn., El Segundo, California 90245- 4691: Aerospace Press, 2003.
- [3] Bai JB, Sheno RA, Xiong JJ. Thermal analysis of thin-walled deployable composite boom in simulated space environment. *Composite Structures* 2017;173:210–218.
- [4] Lv P, Zhang Z, Ji L, et al. Microstructure Evolution of 2024 and 7A09 Aluminium Alloys Subjected to Thermal Cycling in Simulated LEO Space Environment. *Materials Research Innovations* 2013;18 (3):169-175.
- [5] Shin K, Kim C, Hong C, et al. Prediction of Failure Thermal Cycles in Graphite/Epoxy Composite Materials under Simulated Low Earth Orbit Environments. *Composites Part B: Engineering* 2000;31(3):223-235.
- [6] Park S, Choi H, Choi W, et al. Effect of Vacuum Thermal Cyclic Exposures on Unidirectional Carbon Fiber/Epoxy Composites for Low Earth Orbit Space Applications. *Composites Part B: Engineering* 2012;43(2):726-738.
- [7] Nowacki W. *Thermoelasticity*. Pergamon press, 1986.
- [8] Brischetto S, Carrera E. Coupled thermo-mechanical analysis of one-layered and multilayered plates. *Composite Structures* 2010;92:1793–1812.
- [9] Cetkovic M. Thermo-mechanical bending of laminated composite and sandwich plates using layerwise displacement model. *Composite Structures* 2015;125:388–399.
- [10] Caliri MF, Ferreira AJM, Tita V. A review on plate and shell theories for laminated and sandwich structures highlighting the Finite Element Method. *Composite Structures* 2016;156:63–77.
- [11] Cho M, Oh J. Higher order zig-zag theory for fully coupled thermo-electric-mechanical smart composite plates. *Int J Solids Struct* 2004;41(5-6):1331–56.
- [12] Carrera E. Historical review of zig-zag theories for multilayered plates and shells. *Appl Mech Rev* 2003;56(3):287–308.
- [13] Saetta E, Rega G. Third order thermomechanically coupled laminated plate: 2D nonlinear modeling, minimal reduction, and transient/post-buckled dynamics under different thermal excitations. *Composite Structures* 2017;174:420–441.
- [14] Paik J, Thayamballi A, Kim G. The Strength Characteristics of Aluminium Honeycomb Sandwich Panels. *Thin-Walled Structures* 1999;35(3): 205-231.
- [15] Abbadi A, Koutsawa Y, Carmasol A, Belouettar S, Azari Z. Experimental and Numerical Characterization of Honeycomb Sandwich Composite Panels. *Simulation Modelling Practice and Theory* 2019;17(10):1533-1547.
- [16] Belingardi G, Martella P, Peroni L. Fatigue Analysis of Honeycomb-Composite Sandwich Beams. *Composites Part A: Applied Science and Manufacturing* 2006;38(4):1183-1191.
- [17] Brischetto S, Carrera E. Thermomechanical effect in vibration analysis of one-layered and two-

layered plates. *Int J Appl Mech* 2011;3(01):161–85.

[18] Saetta E, Rega G. Unified 2D continuous and reduced order modeling of thermomechanically coupled laminated plate for nonlinear vibrations *Meccanica* 2014;49:1723–49.

[19] Yen-Liang Yeh. Chaotic and bifurcation dynamic behavior of a simply supported rectangular orthotropic plate with thermo-mechanical coupling. *Chaos Solutions & Fractals* 2015;24:1243-1255.

[20] Saetta E, Rega G. Supplementary Data. *Composite Structures* 2017
<http://dx.doi.org/10.1016/j.compstruct.2017.03.048>.

[21] Saetta E, Rega G. Modeling, dimension reduction, and nonlinear vibrations of thermomechanically coupled laminated plates. *Procedia Eng* 2016;144:875–82.

[22] Ganiłova OA, Cartmell MP, Kiley A. The development of a dynamic coupled model for aluminium composite sandwich plates under thermo-elastic loading. *Proceedings of the Second International Nonlinear Dynamics Conference, NODYCON2021, Rome, Italy, 16 - 19 February 2021, Publication Date September 2021.*

[23] Ganiłova OA, Cartmell MP, Kiley A. Experimental investigation of the thermoelastic performance of an aerospace aluminium honeycomb composite panel. *Composite Structures* 2021;275:113159.

[24] Ganiłova OA, Cartmell M.P, Kiley A. Open Data for the paper 'Experimental investigation of the thermoelastic performance of an aerospace aluminium honeycomb composite panel', University of Strathclyde, 2019, <https://doi.org/10.15129/28a67ac3-0daf-4c8d-81c7-3af6a847c211>



Experimental investigation of the thermoelastic performance of an aerospace aluminium honeycomb composite panel

Olga A. Ganilova^{a,*}, Matthew P. Cartmell^a, Andrew Kiley^b

^a Aerospace Centre of Excellence, Department of Mechanical & Aerospace Engineering, University of Strathclyde, Glasgow G1 1XJ, Scotland, UK

^b Airbus Defence & Space Ltd., Gunpowder Wood Road, Stevenage, Hertfordshire SG1 2AS, UK

ABSTRACT

Aluminium composite sandwich panels are widely used to enhance the design of structures subjected to dynamic mechanical loading in thermally harsh environments. Spacecraft structures fall into this category because typical environmental conditions include combined and variable mechanical and thermal loading. Usually mechanical loadings arise as a consequence of localised structural dynamics and the thermal loadings are attributable principally to the effects of solar irradiation and eclipse during the vehicle's orbit. Together these have the potential to influence satellite de-point in particular. Therefore, building a combined physics model which is representative of the thermal and mechanical loadings has emerged as an interesting and useful aim, which can be thought of as defining an important thermoelastic deformation problem in this application. The performance of such a structure loaded in this way could obviously be considered in the context of separate thermodynamic and mechanical interpretations. However, multiphysics modelling is currently in hand based on the premise that the pseudo-static thermal loadings and the mechanical loadings encountered in various operating environments are not necessarily decoupled processes, and this will be the subject of a separate publication. The analytical modelling fully represents both static and dynamic mechanical and thermal loading conditions. It has become clear that predictive accuracy may be compromised by separation of the phenomena, at least without the introduction of a judicious correction factor. Therefore, in this paper an attempt has been made to identify experimentally the presence, and then to understand the attendant effects, of the coupling between the thermal and mechanical effects in an aluminium composite sandwich panel under test. The authors have performed a series of experiments on an aluminium honeycomb composite panel under three-point mechanical bending and controlled environmental temperature. The panel was subjected to a controllable, centrally located, very slowly increasing mechanical load in conjunction with thermal loading in the form of precisely controlled lowered and elevated environmental temperature. The tests were performed on a computer controlled Instron 8901 100 kN test machine for which the rate of change of applied mechanical load was automatically linked through feedback control to the rate of change of displacement. This ensured that the exact load-deflection profile can be obtained, even for materials with highly nonlinear characteristics. Both forms of loading have been shown to influence the displacement of the panel in significant ways, thereby confirming the importance of a combined physics approach.

1. Introduction

The materials used on the exterior of spacecraft are subjected to many environmental threats that can degrade them quite quickly, including the vacuum of space itself, solar ultraviolet (UV) radiation, ionising charged particle radiation, plasma, surface charging and arcing, temperature extremes, thermal cycling, impacts from micrometeoroids and orbital debris (MMOD), and environment-induced contamination. In terms of material degradation in space, low-Earth orbit (LEO), defined as the region from 200 to 1000 km above the Earth's surface, is a particularly harsh environment because of the presence of atomic oxygen (AO)

along with the other detrimental environmental components and effects [1]. The environmental threats of space to spacecraft components vary in their influence mainly due to the specific material properties of the component and its structural interconnections, its geometry, and the stresses that it undergoes during normal duty. All orbiting spacecraft move in and out of sunlight during their progress around Earth and the degree to which a material experiences thermal cycling temperature extremes depends on its thermo-optical properties (specifically solar absorptance and thermal emittance), its exposure to the sun, its view of Earth and other surfaces of the spacecraft, the duration of time in direct sunlight and shadow, its thermal mass, and the influence of equipment

or components that produce heat [1]. As a rule, the cyclic temperature variation is from $-120\text{ }^{\circ}\text{C}$ to $+120\text{ }^{\circ}\text{C}$ but high solar absorptance with low infrared emittance can contribute to even greater temperature swings [1]. The ISS orbits Earth approximately once every 92 min and therefore experiences sixteen thermal cycles a day, and this can lead directly to cracking, peeling, spalling or the formation of pinholes in the coating, which then allows AO to attack the underlying material [1].

The main forms of environmental heating on orbit are sunlight, sunlight reflected from Earth, a planet, or the Moon, and infrared energy emitted directly from Earth. During launch or in exceptionally low orbits, there is also a free molecular heating effect caused by friction in the rarified upper atmosphere [2]. Therefore, the main conditions of LEO that may be highlighted are the severe temperature extremes and the thermal cycling experienced throughout the orbit, with an orbiting spacecraft typically completing from eleven to sixteen thermal cycles daily, all within a temperature range of approximately $-120\text{ }^{\circ}\text{C}$ to $+120\text{ }^{\circ}\text{C}$. The thermo-optical properties of the spacecraft itself can also play a part in the temperature that it reaches. For instance, a material with high solar absorptance and low thermal emittance will experience greater temperature swings.

In [3] an experiment was performed to investigate the thermal behaviour of a sandwich panel which was to be deployed as an integral part of a satellite in the space environment, by means of a ground thermal-vacuum test. It was highlighted that the heat sink, solar radiation, infrared radiation of the Earth, heat conduction, surface radiation and cavity radiation would all influence the temperature field, and the conclusion was that these combined effects would present a serious challenge for realistic thermal testing in the laboratory of the simulated space environment. The experiment was relatively sophisticated and satisfied the general requirements for the inclusion of three key conditions: ultra-high level of vacuum (lower than 10^{-5} Pa), a heat sink (down to $-180\text{ }^{\circ}\text{C}$) achieved in this case by using black panels with a liquid-nitrogen cooling system, and thermal loading achieved through infrared lamps. An interesting study carried out by [4] focused on the effect of thermal cycling in a simulated LEO environment on the microhardness of aluminium alloys, and subjected these alloys to cycles ranging from $-140\text{ }^{\circ}\text{C}$ to $+110\text{ }^{\circ}\text{C}$. This was in order to induce thermal fatigue and to study the resulting stress state and mechanical properties of the material. The testing resulted in cyclic plastic deformation which was found to lead to crack initiation, identified using a transmission electron microscope (TEM). A test totalling 400 thermal cycles was carried out on the samples and these showed an eventual decrease in hardness, and then from 300 to 400 cycles the hardness started to increase with every cycle. Although rapid temperature changes were implied, the exact value of the rate of change of temperature was never stated in the study. The mechanical load was applied at intervals to test the microhardness of the material and was not applied simultaneously with the change in temperature. The study concluded that the bulk of aerospace materials that undergo periodic heating and cooling are damaged to varying degrees, with thermal fatigue having a significant impact on the mechanical properties of the materials used. Although it is difficult to recreate truly the conditions of LEO on Earth, such work has been attempted in the past by [5]. The study focused on subjecting graphite-epoxy composites to the conditions of LEO. Not only did the materials undergo thermal cycling similar to that experienced in LEO, but the environment was also in a high vacuum state while the effect of ultraviolet radiation was applied during heating but not during cooling. A single thermal cycle was judged to be from $-70\text{ }^{\circ}\text{C}$ to $+100\text{ }^{\circ}\text{C}$ and back to $-70\text{ }^{\circ}\text{C}$ again. This was with a rate of change of temperature of $3\text{--}5\text{ }^{\circ}\text{C}$ per minute and a dwell-time at the temperature extremes of 15 min, giving an average cycle time of 100 min, typical of a low Earth orbital period. The results examined were for composites subjected to this environment for 8, 16, 40 and 80 thermal cycles, in which the transverse flexural strength and transverse tensile strength showed the most severe reduction with ther-

mal cycling, after 80 thermal cycles, with losses of 34% and 21% in each property respectively. It was considered that the matrix-dominated mechanical properties suffered the greatest loss, due to high vacuum and thermal cycling. Overall, the strength and stiffness of graphite epoxy composites was shown to decrease exponentially with increasing thermal cycles. Further work into the synergistic effects of high vacuum and thermal cycling was implemented by [6], this time on carbon fibre epoxy composites. The experiment took place in a high vacuum state of 133×10^{-5} Pa, and a single thermal cycle was judged to be from $+120\text{ }^{\circ}\text{C}$ to $-175\text{ }^{\circ}\text{C}$ and back to $+120\text{ }^{\circ}\text{C}$, with a duration of approximately 43 min. The experiment was run for 500, 1000, 1500 and 2000 cycles. Panels were then subjected to mechanical tests at an ambient temperature of $23\text{ }^{\circ}\text{C}$ to observe the mechanical properties of the samples. The results confirmed the onset of gradual damage with increasing thermal cycles. This was coupled with the degradation of the fibre-matrix interface due to a weakened fibre-matrix bond, which led to interfacial sliding.

Some industrial experiments [7] involving the thermal loading of aluminium composite panels, but not using temperatures as extreme as those experienced in LEO, measured thermo-elastic deformation under thermal load with temperature steps from $-20\text{ }^{\circ}\text{C}$ to $+40\text{ }^{\circ}\text{C}$ and with static loads imposed on the panel between 0 and 78 N – in steps of 19.6 N. The experiment was carried out in a climatic chamber with the measurements being corroborated by a finite element model. Measurements for the deflection and sample temperature of the structural model were taken at set temperatures using photogrammetry and infrared cameras to map a thermal cartographic image of the structural model, where temperatures were assumed as for black body conditions. Looking at the problem of a spacecraft panel undergoing cyclic loading from the perspective of modelling it is possible to find that the structure must combine the effects of thermal loading as well as mechanical disturbance. This is because from a physical point of view the deformation of a body is connected to a change of heat inside it, and therefore to a change of the temperature distribution in the body. So, a deformation of the body leads to temperature changes, and conversely. The internal energy of the body depends on both the temperature and the deformation and so, in the case of a practical body, such as a spacecraft panel, this necessarily undergoes processes that are intrinsically coupled, defined collectively as thermoelasticity [8].

However, thermoelasticity deals with a wide class of phenomena. It covers the general theory of heat transfer as well as the general theory of thermal stresses, and it describes the temperature distribution produced by deformation. Thermoelasticity also describes the phenomenon of thermoelastic dissipation. As mentioned above many modelling approaches tend to separate the mechanical and thermal effects, but thermoelastic processes are not generally reversible because although the elastic part may be reversed – the deformations may be recoverable through cooling – the thermal part may not be reversible due to the dissipation of energy during heat transfer [9].

Apart from that, thermal changes in the body cause mechanical deformation in the body, which in return affects these thermal changes, involving a two-way feedback. This means that the modelling techniques and representations really do have to couple the mechanical and thermal aspects of the problem to achieve results of adequate accuracy that describe the problem properly.

It should also be mentioned that in recent years, honeycomb panels have become more and more widely used within the aerospace industry [4,10–12] due to their structural efficiency, and because they demonstrate a generally high strength to weight ratio. This type of design consists of two thin parallel face sheets – usually coated – attached to a core material that separates them. The core can be composed of different types of material, but the most frequently used one is a hexagonal honeycomb made from sheets of aluminium foil, as shown in Fig. 1.

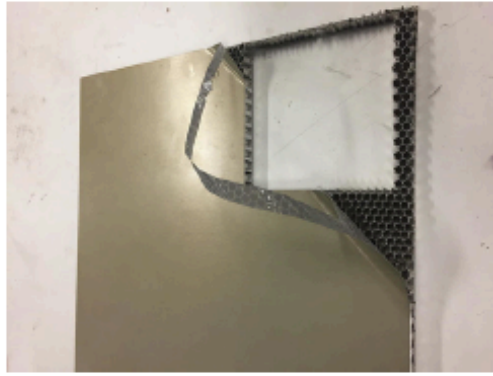


Fig. 1. A honeycomb sandwich panel as typically used in the aerospace industry.

Despite their many benefits sandwich panels do have a number of structural limitations. They are known to have poor resistance to impact loads, particularly when combined with thermal loading, due to the risk of debonding between the sandwich core and the outer faces under these conditions.

It has been found in the literature that honeycombs with thicker core are characterised by higher strength [10] and an increase in the core density leads to an increased stiffness of the sandwich structure [11]. It was also shown experimentally in [13] that a change in honeycomb cell size, as well as in the distance between the supports, has an impact on the collapse mode of the samples.

In [14] a thermal effect of the inserts in the honeycomb core was demonstrated. It was concluded that any electronic equipment (including batteries) that might be attached to the honeycomb would cause dissipation of possibly excessive heat through the inserts causing additional thermal loading within the panel.

Therefore, to the best of the authors' knowledge, there has not yet been an experimental investigation on the behaviour of an aluminium sandwich panel undergoing simultaneous thermal and dynamic mechanical loading to investigate coupling between the two of them and the response of the panel to harsh thermal environments of up to +100 °C and down to -150 °C. Most authors consider the heat distribution within the material for mechanical testing performed after the thermal cycling has been completed. Thus, in this paper we consider, for the first time, the thermoelastic response of a typical aluminium honeycomb sandwich panel when tested for load deflection characteristics within an environmentally controlled enclosure. It should be noted that this type of structural panel is routinely used within spacecraft structures.

2. Experimental set-up

In order to plan an appropriate experiment a literature review was undertaken in order to study the basic thermal properties of the space environment that would necessarily have to be emulated. It became evident that the International Space Station (ISS) environment would include exposure to extreme thermal cycling, ultra-vacuum, atomic oxygen, and high energy radiation [1]. As discussed previously when an orbiter such as the ISS moves in and out of sunlight during its orbit around Earth the degree to which the outer structural materials experience thermal cycling temperature extremes depends on their thermo-optical properties (solar absorptance and thermal emittance), exposure to the sun, their view of Earth and the other surfaces of the spacecraft, the duration of time spent in sunlight and shadow, the important thermal masses and the influences of nearby onboard equipment and components that produce heat [1]. As a rule, the cyclical temperature variation was taken to be -120 °C to +120 °C, acknowledging that high solar absorptance

with low infrared emittance will contribute to greater temperature swings.

Therefore, the test was designed to simulate the extreme thermal environments experienced by the sandwich panel of the spacecraft due to the solar radiation. Based on the information in the open literature summarised in Section 1, it was assumed that only solar radiation causes an extreme thermal impact on the spacecraft panel. Thus, the solar radiation was considered to vary, resulting in thermal loading from -150 °C up to 100 °C.

The test sandwich panel of $300 \cdot 10^{-3} \times 100 \cdot 10^{-3} \times 15 \cdot 10^{-3}$ m was composed of two types of aluminium alloy. For the outer skins of thickness $0.38 \cdot 10^{-3}$ m an Al-2024 alloy was used, whilst an Al-5056 alloy foil was used to form the hexagonal honeycomb core. This core was of cross-sectional thickness $14.24 \cdot 10^{-3}$ m and was made up from a foil of thickness $0.0254 \cdot 10^{-3}$ m. The mechanical and thermal properties of these materials are summarised in Tables 1 and 2, noting that the structural coefficient of thermal expansion stated in Table 2 was extrapolated from the data made available for AL-5056.

It was shown in [7] that typical models of the honeycomb panels do not take into account the fact that the temperature profiles within the thickness of the panel may vary, as in Fig. 2.

This was considered to be a very important point so it was decided to take thermal measurements not only on the top and bottom skins but from within the honeycomb layer as well, to record any disparity in the temperature within the honeycomb and the skins.

Table 1
Mechanical properties of the sandwich panel.

	Al-2024	Al-5056
3/16 Honeycomb		
Density, ρ (kg/m ³)	2780	50
Young's Modulus, E (Pa)	73.1×10^9	669×10^6
Shear Modulus, G (Pa)	27.5×10^9	310×10^6
Poisson's Ratio, ν Foil thickness (m)	0.33	$0.3 \cdot 0.0254 \times 10^{-3}$
[Ref]		[0.001]

Table 2
Thermal properties of the sandwich panel materials.

	Al-2024	Al-5056
Coefficient of Thermal Expansion (°C)	2.47×10^{-5}	2.41×10^{-5}
Coefficient of Thermal Expansion for 3/16 honeycomb (°C)		2.4×10^{-6}
Thermal Conductivity @ 25 °C (W/mK)	149	149
Specific Heat (J/kg°C)	875	904
Reference Temperature (°C)	22	22

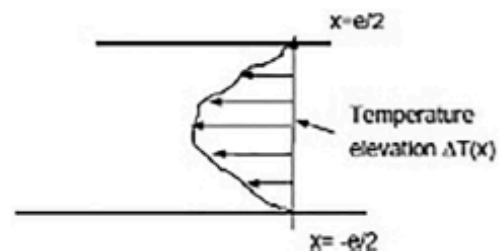


Fig. 2. Temperature profile of a honeycomb panel [7].

The experiment was performed in an environmental testing chamber fitted to a computer driven Instron 8801 100 kN tensile and compressive testing machine in the University of Strathclyde's Advanced Materials Research Lab (AMRL), shown in Fig. 3.

The environmental test chamber offers a temperature range of $-150\text{ }^{\circ}\text{C}$ to $+350\text{ }^{\circ}\text{C}$ and uses a liquid nitrogen cooling system. When the chamber is sealed there is no internal visible access, therefore the use of imaging equipment wasn't possible so strain gauges were used to register the displacement of the panel. High performance C series strain gauges from HBM UK were used, with an operating temperature range from -269 to $+250\text{ }^{\circ}\text{C}$, and a nominal terminal resistance of 120 Ohms.

To extract as much information as possible from the experiment a rosette configuration was used on the top and bottom faces, adjacent in each case to the centralised load point, with uni-axial gauges elsewhere, as shown in Figs. 4 and 5.

In order to record the temperature data on the panel sample within the chamber, as well as to validate the distribution of the heat flux within the panel, thermocouples of type T from RS Components Ltd were selected, with an operating range of $-200\text{ }^{\circ}\text{C}$ to $+350\text{ }^{\circ}\text{C}$. Six thermocouples were positioned on the top, bottom and middle layers of the

panel to record the pattern of the temperature distribution in three dimensions, as shown in Fig. 5.

The experiment comprised a three point bending test, shown in Fig. 6, with the sample honeycomb panel simply supported in the thermal chamber, undergoing an incremental mechanical loading profile with line contact established between a 6 mm diameter circular loading bar and the upper surface of the plate, orientated such that the loading line was across the width of the plate, and centrally located along the length. The loading and unloading procedure was automated using the built-in control options embedded in the software of the Instron testing machine. The loading starting from zero and gradually increasing up to 150 N, and then back to zero, and this was repeated at specific temperatures over the full range of environmental temperatures required, as follows: $-150\text{ }^{\circ}\text{C}$, $-100\text{ }^{\circ}\text{C}$, $-60\text{ }^{\circ}\text{C}$, $-40\text{ }^{\circ}\text{C}$, $-20\text{ }^{\circ}\text{C}$, $20\text{ }^{\circ}\text{C}$ (ambient), $40\text{ }^{\circ}\text{C}$, $60\text{ }^{\circ}\text{C}$, $80\text{ }^{\circ}\text{C}$, and $100\text{ }^{\circ}\text{C}$. It should be re-confirmed here that the process of cyclical loading and unloading, in the form of a dynamic mechanical load imposed over a range of different thermal environments has not been reported in the literature to date, to the authors' knowledge.

The overall aim of the experiment, and fundamental novelty of this work, has been to evaluate the nature and significance of the coupling

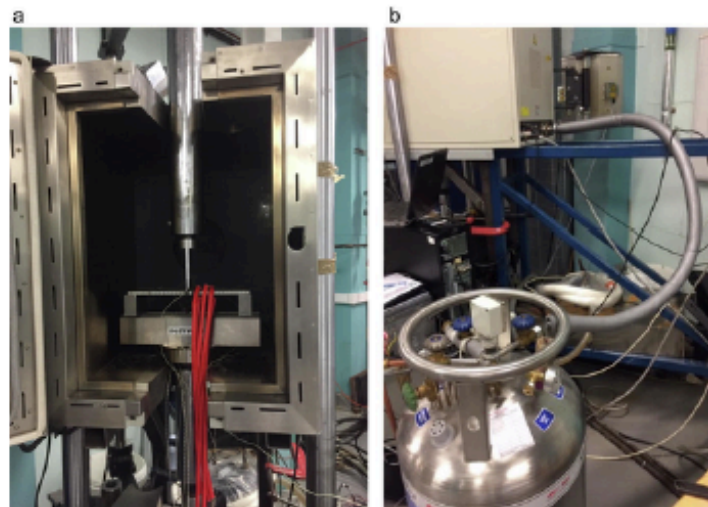


Fig. 3. Panel sample fitted within the Instron test machine's environmental chamber, also showing the liquid nitrogen dewar, and the nitrogen gas flow regulator system.

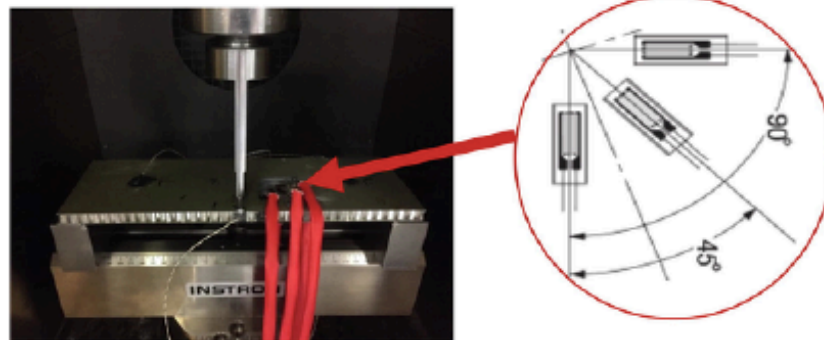


Fig. 4. Strain gauges rosette configuration shown on the upper face of the sample, and thermocouples T_1 , T_2 , and T_3 .

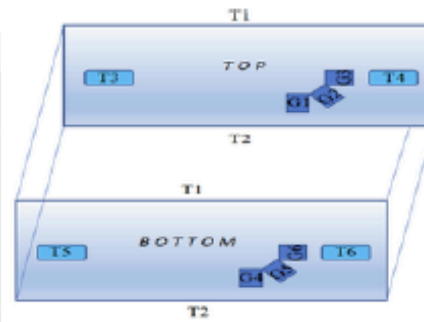
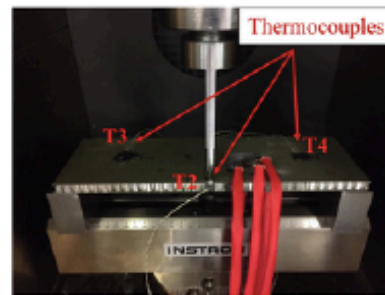


Fig. 5. Thermocouple distribution on the test panel (a) on the top surface of the sample and (b) on the top and bottom surfaces, as a schematic. Note that gauges T1 and T2 are located halfway down the edge thickness of the panel.

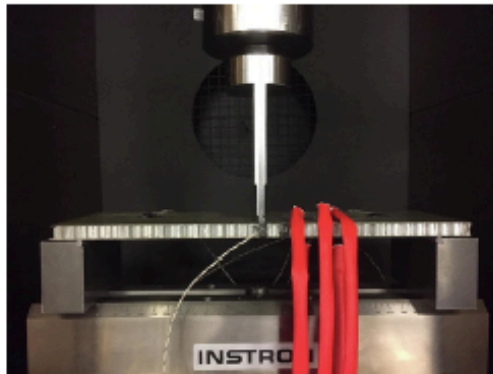


Fig. 6. Three point bending test arrangement, looking end-on at the circular loading bar orientated across the width of the plate.

between the mechanical and the thermal effects within an aluminium composite plate. In order to accomplish this successfully, given prior expectations from the literature, and insights gained from the authors' own modelling work that has been carried out as a parallel study, the following research hypotheses were formulated, as a general basis for observation and interpretation:

H1. Due to the different structural properties of the top, bottom, and middle plies of the sandwich panel, there may be a different distribution of temperature in the middle ply from that in the top and bottom layers.

H2. Within the environmental chamber the environmental temperature is stabilised, but there may still be a significant disparity between the temperature recorded on the top and bottom skins.

H3. The environmental temperature may have a significant quantitative effect on the bending performance as well as a generally qualitative effect on the deformation of the panel, and this may be due to possible thermoelastic coupling between the thermal and mechanical loading effects.

H4. The qualitative deformation characteristics of the panel at extreme environment temperatures may differ significantly from those observed at environmental temperatures that are closer to moderate ambient temperatures.

In order to address these research questions systematically data was logged continuously for the applied load and the corresponding deflection at the load point, at the stabilised environmental temperature points, as well as local temperature data from the thermocouples located on the top and bottom skins and inside the honeycomb surface on the sides of the panel. This data set was then composed into suitable graphs for subsequent analysis. It should be noted that each set of deflection

data was subject to a nonzero offset of magnitude 52.2707 mm, (stated here to four decimal places to maintain the setup accuracy for the Instron 8801 machine, running under Bluehill™ control software) although the effects to be described are all based on relative displacements, so this offset only needs to be subtracted if absolute displacements are also required.

The remaining sections of the paper present the analysis and the findings that were deduced from this, leading to conclusions formulated in the context of the defining research questions.

3. Results analysis and discussion

3.1. The effect of retention or loss of heat due to dynamic mechanical loading in extreme thermal environments, and the implications of this for modelling

The full data set was initially considered from all the thermocouples (T_1 – T_6) and with respect to the mechanical loading. This first investigation of the data was undertaken in order to start to understand the effect of any possible cooperation between the mechanical loading and the thermal conditions of the environment, and also to ascertain the nature of the temperature distribution along the panel in different areas of the panel. Thus, the data was represented graphically as the temperature recorded by each thermocouple within the environmental temperatures (T_{env}) of -150 °C, -100 °C, -60 °C, -40 °C, -20 °C, 20 °C, 40 °C, 60 °C, 80 °C, 100 °C against the mechanical load from 0 N up to 150 N.

Due to the constraints of space we present results from the 6 thermocouples only for two environmental temperatures of -20 °C and -150 °C, shown in Figs. 7 and 8, together with summative findings from all data for all the environmental conditions considered. Graphical data for other environmental conditions are openly available from [15].

As a result of analysis of data obtained it can be seen that the same qualitative form of hysteresis is evident in the temperature readings from all the thermocouples T_1 – T_6 for a specified environmental temperature T_{env} . An initial but very important conclusion from this is that all the thermocouples performed consistently and responded in the same manner to the local conditions in the material of the panel. It was also found that the hysteresis is represented by an open loop at the following environmental temperatures: -20 °C, -40 °C, ambient, and $+40$ °C, see Fig. 7 for the specific case of $T_{env} = -20$ °C. It is also seen that when operating closer to the ambient temperature, and if the panel then undergoes a cycle of loading and unloading, shown counter-clockwise on the Figure, then after unloading it does not return to its initial thermal state. Instead it retains some heat after unloading, resulting in a gain of 1–2 °C over the initial state, which is indicative of an irreversible process, as mentioned in [9].

The hysteresis is represented by a closed loop at the following environmental temperatures: -150 °C, -100 °C, $+60$ °C, $+80$ °C, $+100$ °C, and refer to Fig. 8 for the specific case of $T_{env} = -150$ °C. This means

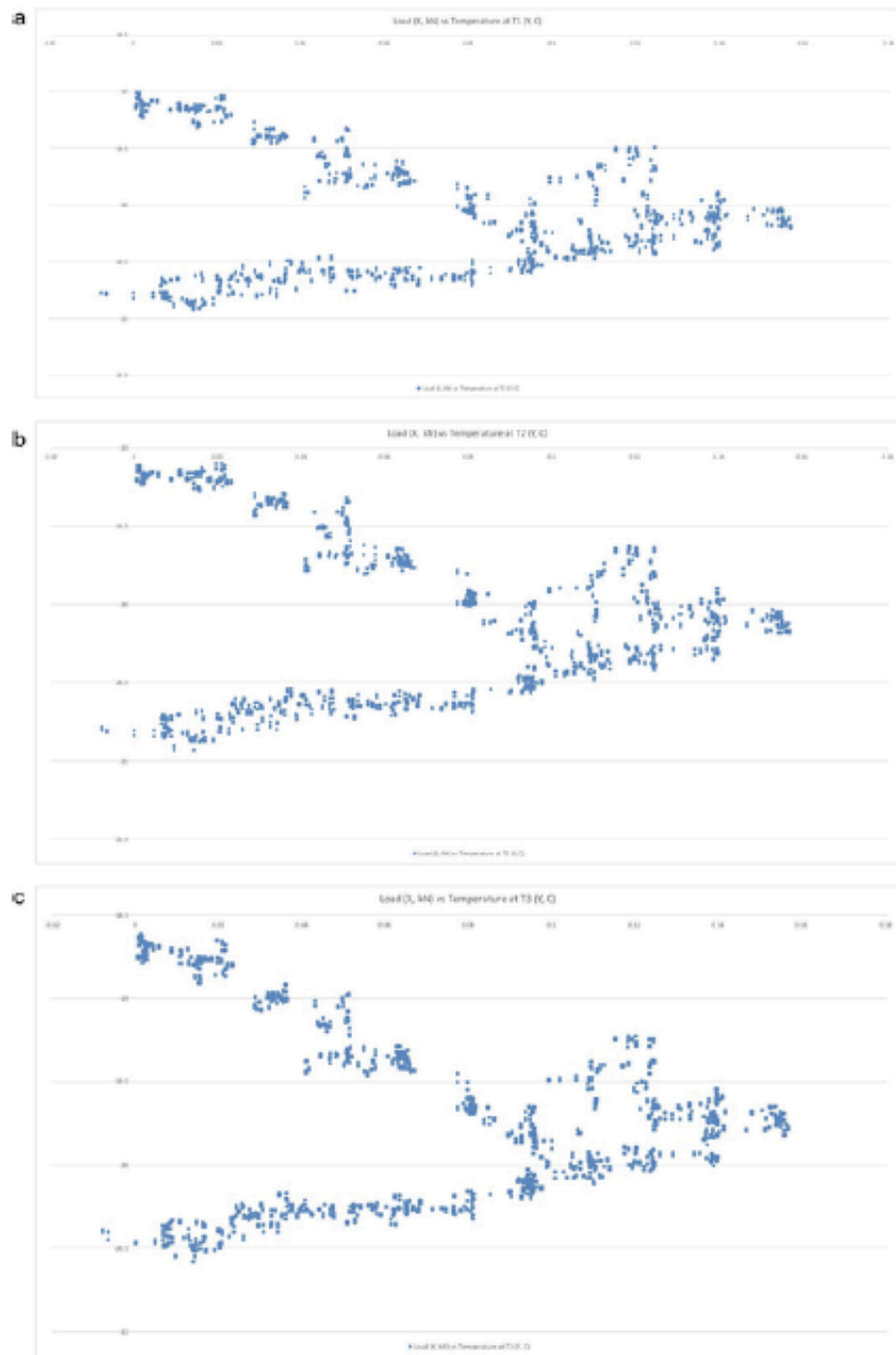


Fig. 7. Temperature distribution from thermocouples $T_1 - T_3$ as a function of loading [0 N, 150 N] at the environmental temperature of $T_{env} = -20$ °C.



Fig. 7. Continued

that the panel appears not to retain residual heat when operating at the more extreme levels of environmental temperature, irrespective of whether or not this is positive or negative, and so after unloading at

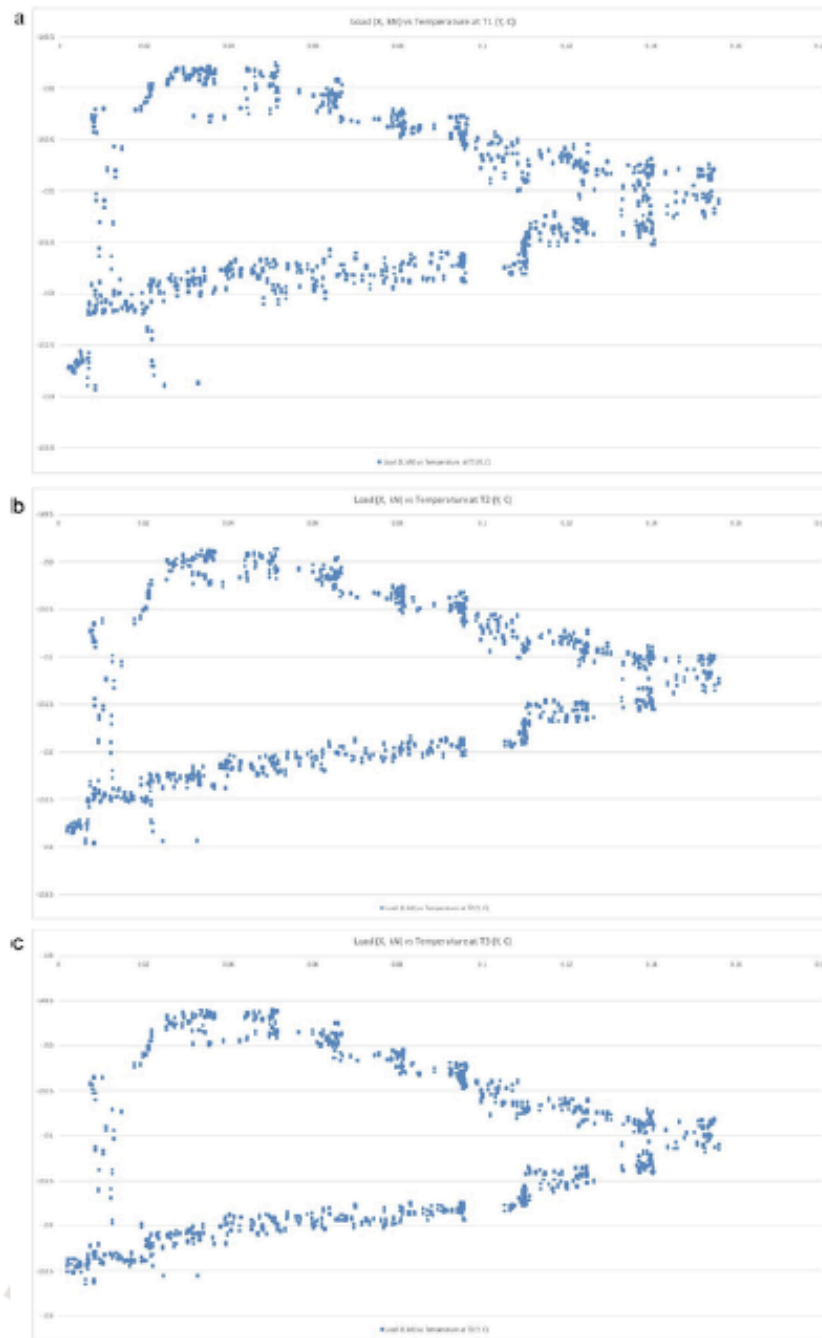


Fig. 8. Temperature distribution from thermocouple T_1 – T_3 as a function of loading [0 N, 150 N] at the environmental temperature of $T_{amb} = -150$ °C.



Fig. 8. Continued

those temperatures it returns, reversibly, to the thermal condition from which it started. This is a novel finding detected only because of the cyclical dynamic loading and unloading regime that was specifically undertaken at extreme temperatures.

It must be mentioned that there is a distinctly unstructured response within the loop at the specific case of $T_{env} = -60$ °C, noting that this phenomenon occurred only at this particular environmental temperature and is probably an artefact of the specific material we have been considering. It is also evident that this unstructured behaviour occurs as a transition from the open loop hysteretic behaviour, which is found closer to the ambient environmental temperature, to the closed loop response which occurred at the more extreme environmental temperatures. The fact that we do not see a clear hysteretic loop for the loading process at this environmental temperature means we do not see a clear temperature difference for the loading and unloading processes. This means that the thermal response of the panel changes during loading and unloading, and so there might be a retention of heat within the panel, but we cannot predict from this data how much hotter the sample would be during the unloading process. Therefore, we cannot predict in this specific case the extent of the thermo-mechanical coupling, i.e. how the deformation that occurred resulted in a change of the thermal properties of the panel, and some further research around this phenomenon should be undertaken in the near future.

At the environmental temperature of -100 °C the behaviour is characterised by a bow-like double loop which becomes a more clearly defined single loop when the environment becomes colder still at -150 °C. It seems obvious that the environmental temperatures of -60 °C and -100 °C are defining points at which there is a transition from an open hysteretic loop to one that is closed, and from an irreversible thermodynamic process to one that is reversible.

At the maximum load of 150 N it can be seen from Fig. 8 that the loop ends at a single valued temperature for all the six thermocouples, and it was also noted that this is independent of the environmental temperature. This confirms the correctness of readings taken across the profile of thermocouples, and that the unloading phase starts from the point at which the maximum loading was reached.

Therefore the experimental results offer strong evidence of progress from an open hysteresis loop (at -40 °C, -20 °C, and ambient temperature) towards a closed loop, and this progresses either in the positive or negative temperature directions starting from the ambient environmental temperature, up to the extreme values of -150 °C and $+100$ °C. There is evidence that the hysteresis loop is structurally closed at the extreme environmental temperatures (very hot [$+100$ °C] and very cold [-150 °C]), showing thermodynamic reversibility, and clearly open, and therefore thermodynamically irreversible, when the environmental temperature gets closer to 0 °C. This means we can conclude that the loading of the panel in the extreme temperature environment does not cause an accumulation of any residual heat after unloading. However, during the processes of loading and unloading there is evidence of thermo-mechanical coupling, which results in the presence of extra heat internally compared with the heat available from the environment. However, at an environmental temperature close to the ambient temperature (noticed specifically at -40 °C, -20 °C, and at ambient itself) the open hysteretic loop confirms an accumulation of residual heat within the panel which is still present to a large extent even at the point of complete unloading of the deformed sample. This means that a correction factor has to be introduced for the thermal initial condition of a panel when it is close to

ambient environmental temperature and when it has undergone a mechanical deformation, even if the loading has been completely removed, due to the tendency to irreversible thermodynamics at those environmental temperatures. Further research into the identification of this correction factor should be undertaken in the near future, as a priority.

It also has to be emphasised that the width of the hysteretic loop demonstrates the difference in the temperature of the sample at the position of loading and unloading, thus the extent of the heat that accumulates within the sample is due to the deformation, apart from that portion of heat that comes from the environment during the process of loading-unloading.

From Table 3 it is evident that the width of the temperature loop is the highest at an environmental temperature below 0 °C. This means that the loading and unloading process of a panel placed in an environment at a temperature below 0 °C will be accompanied by a temperature swing of up to 3 °C due to the thermo-mechanical coupling. Therefore, the thermal properties for such a panel cannot be assumed to be governed just by the temperature of the environment if a panel of this sort undergoes a form of dynamic mechanical loading, but would need to have a correction factor applied to cater for the thermo-mechanical coupling, thus guaranteeing a higher level of accuracy of load-deflection prediction.

3.2. Effect of the dynamic loading and extreme environmental temperature on the temperature distribution along the surfaces and through the thickness of the panel

In order to analyse the temperature distribution at various locations of the panel it was decided to investigate how it differs from the temperature of the environment. Specific differences between the environmental temperature and the temperature feedback data from the individual thermocouples were evaluated. The intention was to see whether certain areas of the panel would heat up faster in response to the environmental temperature. This difference was considered graphically with respect to the mechanical loading of up to 150 N and then unloading from there back to 0 N, for thermal environmental temperatures (T_{env}) of -150 °C, -100 °C, -60 °C, -40 °C, -20 °C, 20 °C, 40 °C, 60 °C, 80 °C, and 100 °C.

In Fig. 9 the results for $T_{env} - T_i$ are presented for all 6 thermocouples, taken for the environmental temperature of -20 °C as an example, and this was calculated together with summative findings from all the data for all the environmental conditions mentioned. Graphical data for other environmental conditions are openly available from [15].

Referring again to Fig. 5 we recall that thermocouples T_3 , T_4 are placed on the top skin surface, T_5 and T_6 are placed on the lower surface of the bottom skin, and T_1 and T_2 are fitted on both sides, directly onto the honeycomb material. Now from Fig. 9 it is evident that when the environmental temperature is negative all the thermocouple data demonstrates the same hysteretic loop behaviour. From this we can conclude that the cooling of the sample at all six locations occurs in the same manner, at the same rate, and with the same level of thermo-mechanical effect during the loading and unloading processes. Conversely when the environmental temperature is positive the thermocouple data shows a difference in the feedback from all the thermocouples, especially when the environmental temperature is between $+20$ °C and $+80$ °C. This confirms that the sample plate's heating-up process, during loading and unloading, can be faster at certain locations, especially when the environmental temperature is closer to ambient. Some

Table 3

Peak-to-peak (p-t-p) temperature range denoted by the width of the hysteresis loop.

T_{env}	-20 °C	-40 °C	-60 °C	-100 °C	-150 °C	amb	$+40$ °C	$+60$ °C	$+80$ °C	$+100$ °C
p-t-p	2-3 °C	2-3 °C	1 °C	2-3 °C	2-3 °C	1 °C	1-2 °C	1 °C	1 °C	0.5 °C

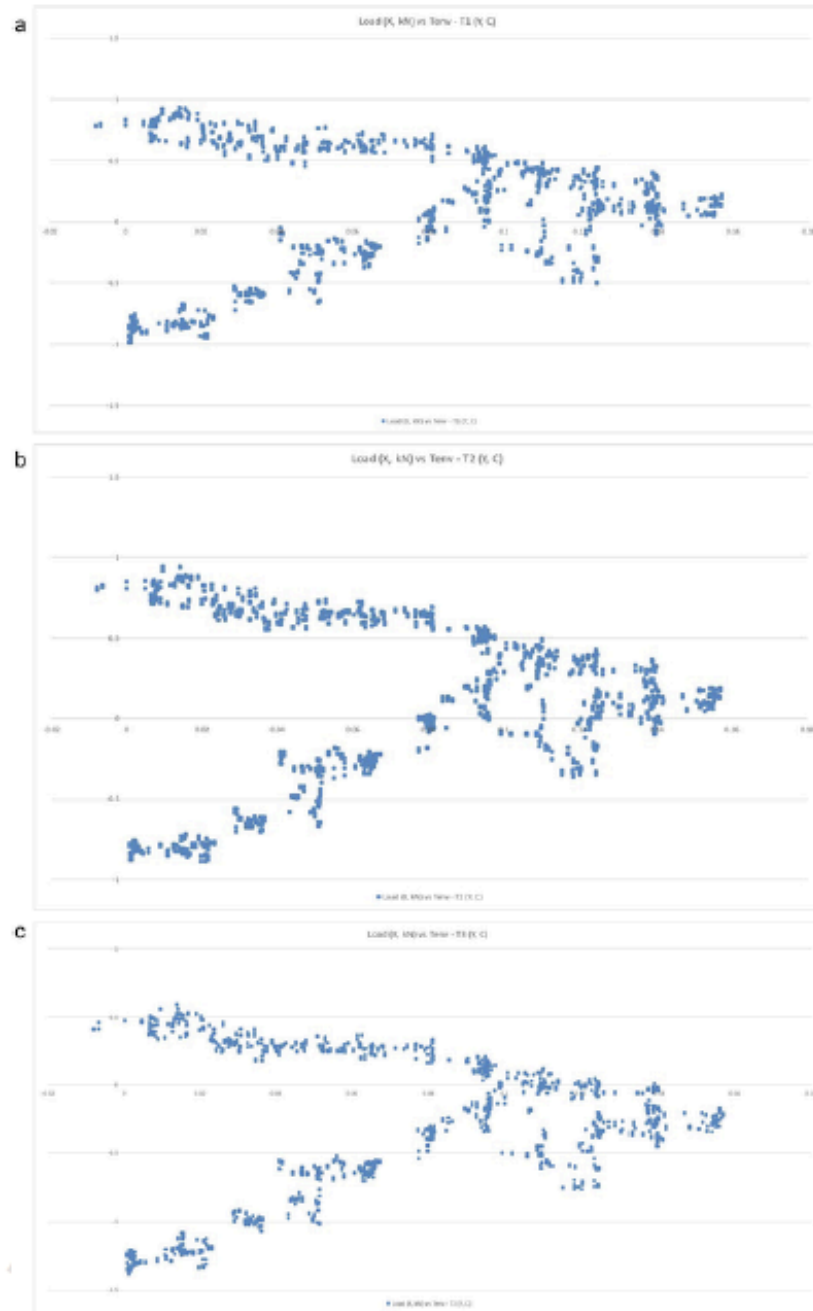


Fig. 9. Distribution of the difference in temperature between the environmental temperature and the temperature recorded from the thermocouples ($T_{env} - T$) versus mechanical loading.



Fig. 9. Continued

distortion in the feedback from T_4 and T_5 is also evident, possibly because the strain gauges were attached to the skins very close to T_4 and T_5 which possibly resulted in a slight increase in the width of the hys-

teretic loop. When the environmental temperature is going up to extreme, between + 80 °C and + 100 °C all the thermocouples show results that demonstrate a generally flatter behaviour in the temperature

loop output, with a peak-to-peak of around 0.5 °C. This means that the difference between the environmental temperature and the thermocouple readings is smaller, implying that the temperature of the panel is closer to the environmental temperature, and has minimal thermal distortion due to the imposed mechanical loading and thus characterises a weaker thermo-mechanical coupling.

3.3. Effect of extreme environmental temperature on the panel deflection response under the imposed dynamic mechanical loading

This investigation shows how the extreme environmental temperature affects the panel deformation in response to gradual mechanical loading ramping up to 150 N and back down to 0 N. Data has been considered for the panel deflection versus loading over the range of environmental temperatures, as follows, -150 °C, -100 °C, -60 °C, -40 °C, -20 °C, 20 °C, 40 °C, 60 °C, 80 °C, and 100 °C.

In this part of the study results are presented for an environmental temperature of -20 °C and also for the ambient temperature, as examples given in Fig. 10, together with summative findings made available from the data for all the environmental temperatures under consideration. Graphical data for other environmental conditions are openly available from [15].

It can be seen in Fig. 10 that the load - deflection characteristics are consistent for both positive and negative environmental temperatures, meaning that the progressive changes in the panel deformation, this being the deflection at the load line, in response to the external loading on the panel has the same general trend for both hot and cool environmental conditions. There is no hysteretic behaviour in the load-deflection curve at the ambient temperature, but this characteristic then progresses into a clearer open hysteretic loop form as the environment gets colder or hotter, and it can be noted that in the case of the colder environments the width (i.e. the peak-to-peak) of the loop is wider. The peak-to-peak of the hysteretic loading and unloading loop is generally bigger for nega-

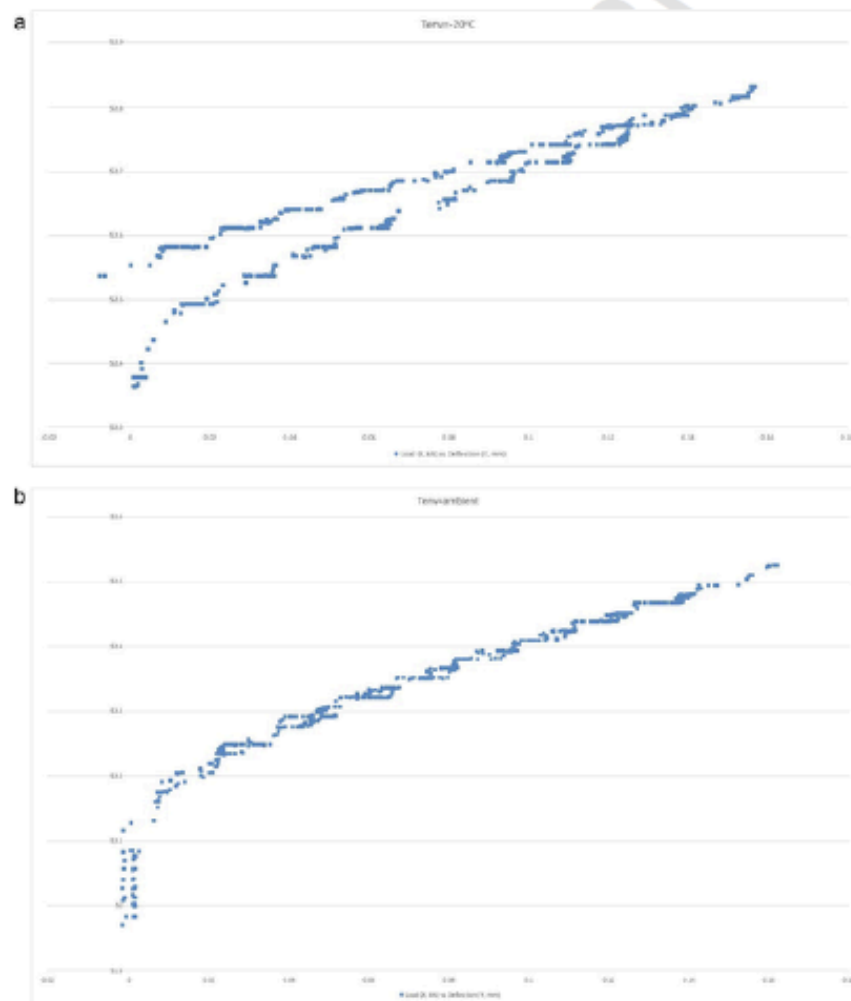


Fig. 10. Deflection versus mechanical loading for two different thermal environments.

tive environmental temperatures, at around 0.1 mm, than for the positive cases, but does build up again to approximately 0.1 mm at an environmental temperature of + 100 °C. The fact that there is no hysteresis effect apparent at the ambient temperature environment means that the loading and unloading progression there is characterised by the same values of deflection. This is in line with findings from [3] where either an additional deflection took place, or a shift in vibration frequency [16] was evident, in response to the thermal changes, especially as the temperature was increased up to extreme values. This means that the deflection values for panels which have undergone some deformation do not come back to the initial values after removal of loading for hotter and especially for colder environments, and are characterised by some residual stress, and characterised thermodynamically by irreversibility. The extent of this residual stress is dependent on the environmental temperature to which the panel is exposed. Thus, another correction factor has to be introduced to account for the effect of the environmental temperature on the magnitude of the deformation of the panel. This further confirms the presence of thermo-mechanical coupling, especially for the colder environments. Therefore, in order to produce an accurate prediction of the deformation progression and regression during the loading and unloading processes, the environmental temperature should be the basis for introducing another correction factor for the deflection responses.

3.4. Effect of deflection on the temperature distribution along the surface and through the thickness of the panel in extreme environmental temperatures

This penultimate analysis was undertaken to find out if the environmental temperature affects not only the deflection of the panel but also if the deflection affects the temperature distribution along the panel. This potentially provides a novel perspective into the general problem, since the combination of dynamic mechanic loading within extreme thermal environments has not been investigated before, to the authors' knowledge. To investigate this it was decided to consider how the temperature distribution in certain locations of the panel is affected by the induced deflection. Thus, the temperature feedback from thermocouples T_1 - T_8 at different locations of the panel has been considered against deflection within the discrete fixed thermal environmental temperatures of -150 °C, -100 °C, -60 °C, -40 °C, -20 °C, 20 °C, 40 °C, 60 °C, 80 °C, and 100 °C.

Results are shown in Fig. 11 for all 6 thermocouples at the environmental temperature of -20 °C as an example, again together with the summative findings made available from the data taken for all the environmental conditions. Graphical data for other environmental conditions are openly available from [15].

As it can be noted from Fig. 11, the readings from all the thermocouples show the same trend with respect to the deflection within a certain environmental temperature T_{env} , except for the case of the ambient temperature for which T_8 shows a flatter hysteretic loop, and T_6 shows a wider loop for this thermocouple. This means that the deflection response from the surface of the panel appears to be the same, independent of the location of the thermocouples, except for the case of ambient environmental temperature. Although the thermal feedback is consistent for all thermocouples within a certain environment, there is an evidence that the temperature of the environment T_{env} is significant and changes the trend of the deflection-temperature behaviour of the panel. For the environment characterised by a negative temperature the peak-to-peak temperature variation, with respect to the deflection is around 2.5 °C, and for the positive temperature environment the peak-to-peak decreases from 1.2 °C down to 0.5 °C at the hottest environment of + 100 °C. There is also a dramatic difference in the way the thermal changes occur in the panel due to the deformation for different extreme environmental temperatures. This means the connection between the thermal properties of the panel and its deformation, and how they affect

each other as the deformation progresses, and essentially what defines the thermo-mechanical coupling, is affected by the environmental temperature within which the panel is immersed. There is hysteresis to be found in the thermal response to the deformation, and this gets more significant in the colder environments which was observed earlier on as well. The thermal properties of the panel demonstrate this through a swing in the temperature of the panel of 2.5 °C during the unloading process. The patterns of open and closed hysteresis loops are the same as for the loading-temperature feedback from the thermocouples in section 3.1, closing for the environmental temperatures above + 60 °C and below -100 °C. As in section 3.1 the hysteresis loop is closed to a single value at the maximum value of deflection. This confirms that there is a direct connection between loading and deflection, and the readings are consistent with the data presented for loading versus temperature of the panel. This is a good control point for verifying that the results are consistent for deflection and loading.

It is interesting to note that when going into the extremely cold or hot environments the pattern of temperature feedback from the panel, with respect to the deflection, bifurcates as shown in Fig. 12. This demonstrates how significant the thermal changes in the environment can change the qualitative aspects of the coupling between the thermal properties and the mechanical deformation of the panel.

3.5. Effect of simultaneous mechanical loading and extreme environmental temperatures on the heating-up and cooling-down processes within the panel

Thermocouple data at fixed loading and unloading points can be used to understand in a clearer way how the temperature is distributed along the whole panel, and how thermal conditions of certain areas of the panel are affected by the mechanical loading as well as the extreme environmental temperature. For this part of the study the following specific loading values were taken, noting that a small amount of approximation was inevitable in extracting this particular data: 0 N, 50 N, 100 N, 150 N, 100 N [unloading], 50 N [unloading] within the environmental temperatures of -150 °C, -100 °C, -60 °C, -40 °C, -20 °C, 20 °C, 40 °C, 60 °C, 80 °C, and 100 °C.

Results are shown in Fig. 13 for the environmental temperatures of -20 °C and -150 °C as examples, noting that summative findings are openly available for all the environmental conditions mentioned from [15].

From Fig. 13(b) it can be noted that thermocouples T_3 and T_5 record the highest temperature readings for most cases, and for a variety of environmental temperatures, and T_4 and T_8 sense the lowest temperature readings. The exception to this seems to be at the environmental temperatures closest to 0 °C, i.e. + 20 °C and -20 °C, for which T_1 and T_2 detect the lowest temperature and at + 40 °C when the highest temperature is demonstrated by T_4 and the lowest by T_5 . From this data it is evident that in the environment where the temperature is close to the ambient the skins do heat up faster than the honeycomb core, however this trend disappears as the temperature moves to higher or lower extremes. As mentioned in Section 3.2, the proximity of the strain gauges to the T_4 and T_8 thermocouples seems to influence the response, and, as a result, those thermocouples sensed a lower panel skin temperature than thermocouples T_3 and T_5 . It is possible to speculate from this that any reasonably significant geometrical imperfections, or extrusions, probably have to be accounted for when attempting to assimilate the thermal properties of the panel into the thermoelastic performance with full accuracy.

4. Conclusions

As a result of the analyses subsequently conducted on the data generated by this experiment it has been found that there is a strong evidence of the thermo-mechanical coupling effect when the panel is immersed in an environment with extreme temperature, and is loaded mechanically.

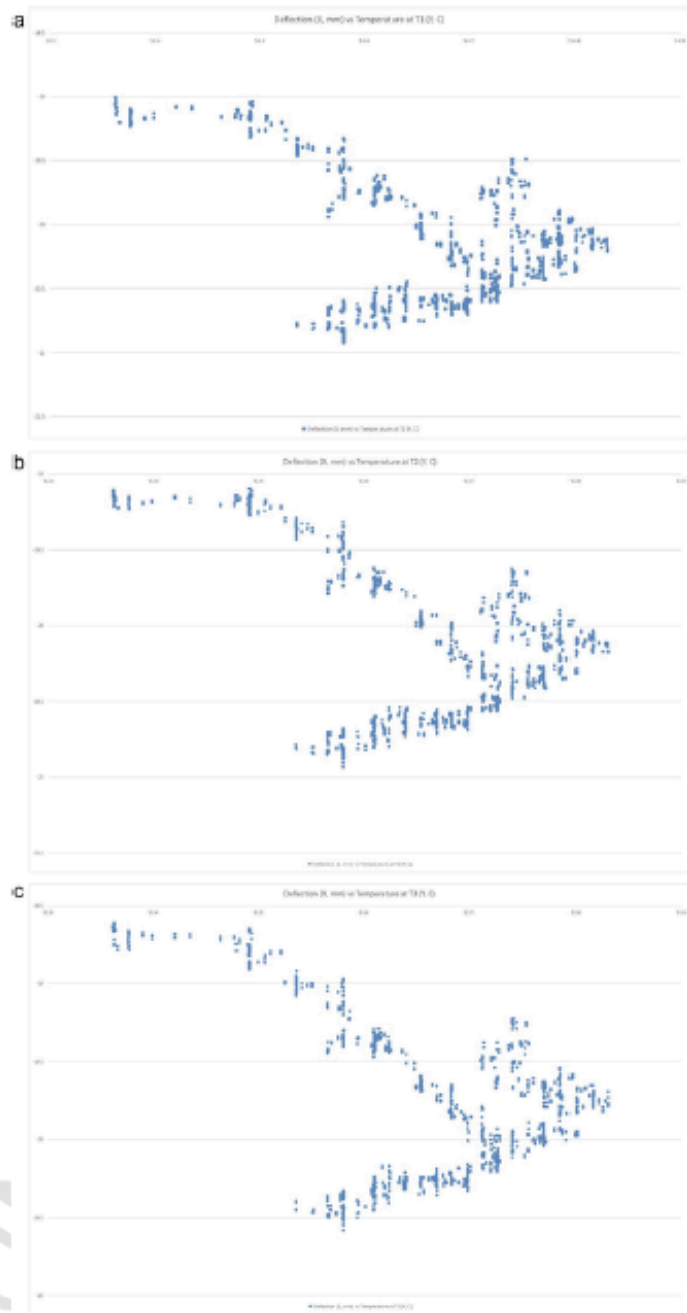


Fig. 11. Fluctuation of the temperature feedback data from the thermocouples T_1 – T_6 with respect to the increasing deflection due to a loading ramped up to 150 N and then back to 0 N, subjected to an environmental temperature of -20 °C.

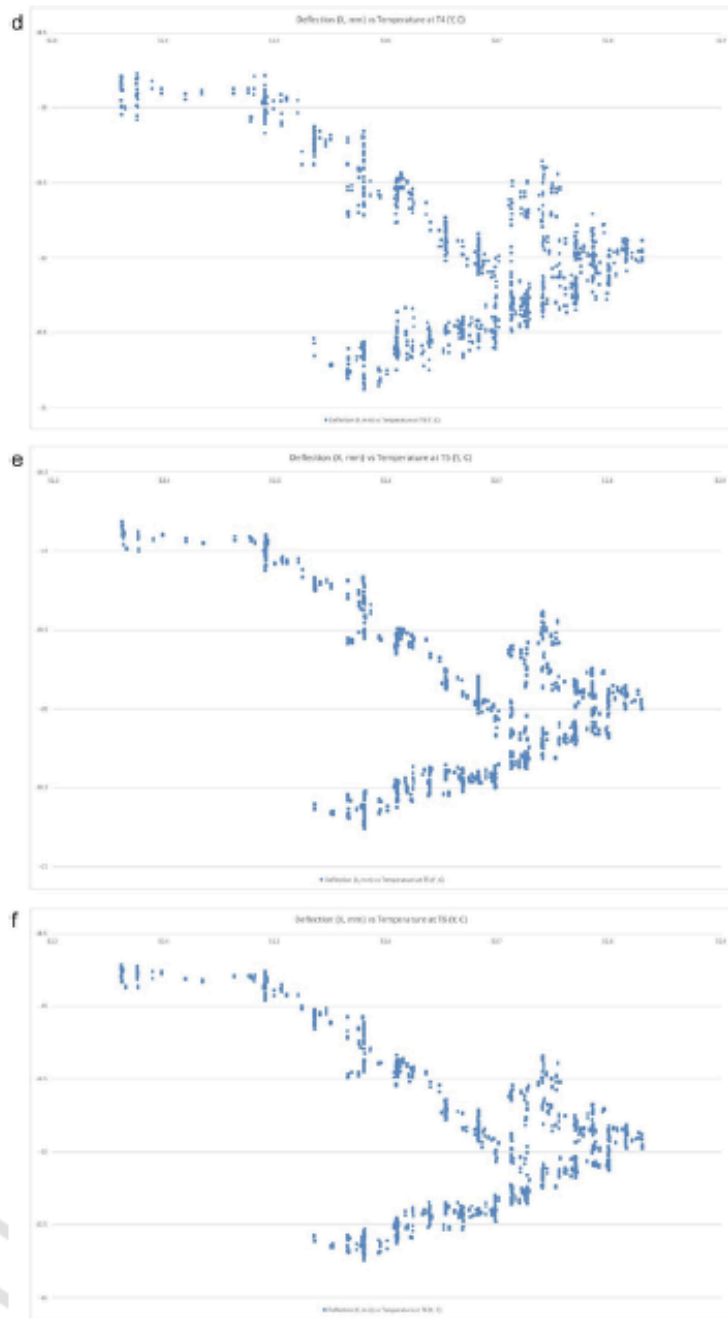


Fig. 11. Continued

There are experimental precedents for the coupling of mechanical and thermal loading in certain structures, notably in NiTi-PU composites [17], and also for complex internal dissipation effects within aluminium

structural elements constructed into the form of braced shear panels [17]. In addition, it is shown in [19] that hysteretic responses to mechanical loading are typically encountered in many different types of

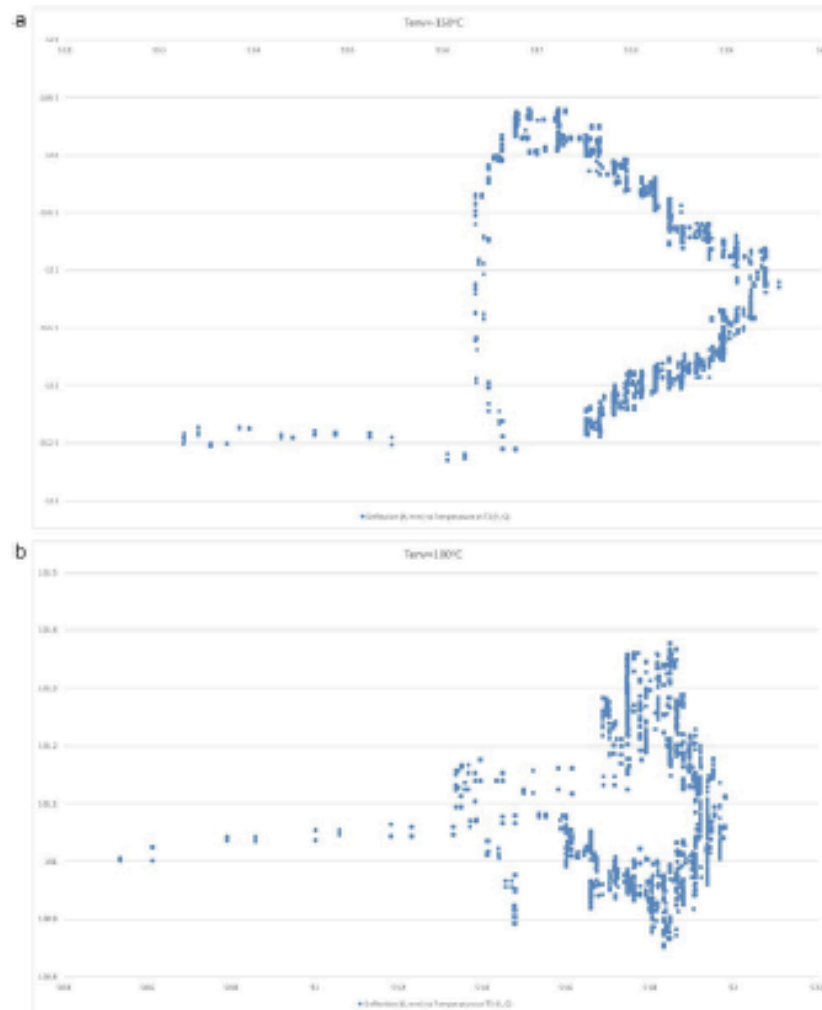


Fig. 12. Fluctuation of the temperature feedback from the thermocouple T_3 with respect to the increasing deflection due to loading up to 150 N and back to 0 N, within the environment of (a) 150 °C and (b) 100 °C.

composite, in addition to plasticity effects due to isotropic strain hardening where post-yield hardening is observed. It is also pointed out in the conclusions to [19] that a mathematical model that properly represents the inherent hysteresis in a composite can potentially be used as a basis for thermo-mechanical simulations. It is interesting to note that the experimental results obtained in [17] explicitly confirm that for a given composition of the NiTi-PU composite the bending modulus and the area of the load–deflection hysteresis loops both decrease with increasing test temperature over the investigated range of 0–50 °C. It is the case that the phenomenology discussed in [17–19] is specific to those particular material compositions, and different in each study, and therefore not exactly the same as reported here. But it is important to note that there are parallels in terms of the stated thermo-mechanical dependencies with some of the key observations made in this paper.

On the basis of the experimental work reported in this paper, there is evidence that thermal loading caused by the extreme environment affects the deflection value and the level of residual stresses, and conversely the mechanical loading affects the heat accumulation and distribution within the panel. The following points may be made to elaborate a little further on this general finding.

- The extreme temperature environment does not cause an accumulation of any residual heat after unloading. However, during the processes of loading and unloading there is evidence of thermo-mechanical coupling which results in the presence of extra heat internally within the structure comparing to the heat available from the environment, and this can result in a temperature swing of up to 3 °C. If the environmental temperature is close to the ambient temperature (specifically noted

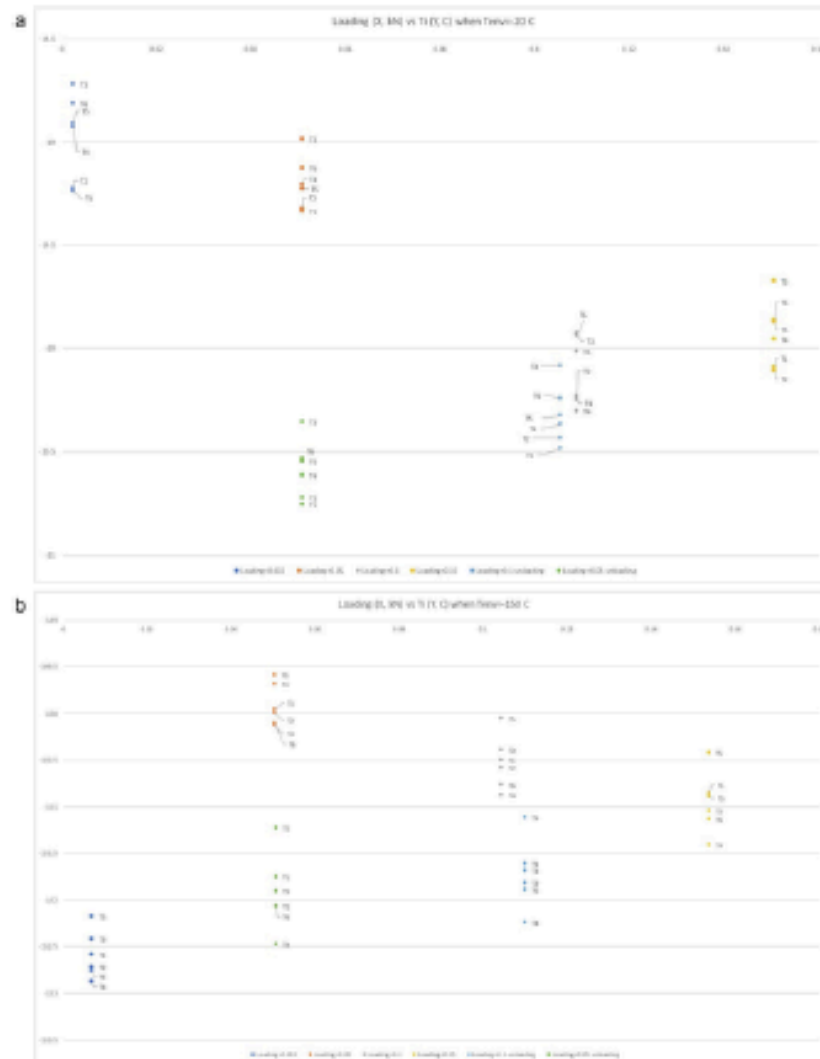


Fig. 13. Temperature feedback from the thermocouples T_1 – T_6 with respect to the loading ramping up to 150 N and back to 0 N within the environments of (a) -20 °C and (b) -150 °C.

for the cases at -40 °C, -20 °C, and ambient) then there is an accumulation of residual heat within the panel which is still present to a large extent even at the point of complete unloading of the deformed sample, indicating thermodynamic irreversibility for an environmental temperature close to the nominal ambient.

- It was found that the environmental temperature effect is significant and that it changes the trend of the deflection – temperature behaviour of the panel. The deflection of the panel affects the distribution of the heat within the panel resulting in a localised temperature swing in the material of around 2.5 °C if deformed in a cool environment and up to 1.2 °C in warmer environments;

- There was no evidence of residual stress accumulation only in the case of the panel operating in the ambient temperature environment. For negative environmental temperatures and the higher positive temperatures the deflection values for a panel which has already undergone some deformation did not come back to the initial values after the removal of the loading, and were characterised by the presence of some residual stress, and thermodynamic irreversibility. The extent of this residual stress is dependent on the environmental temperature within which the panel is immersed. For the sample considered here the deflection during unloading in a very cold environment could reach up to 0.1 mm lower than the corresponding value during loading. This con-

firm the damaging effect of thermal loading on mechanical properties described in [4–6].

- Although there was no significant thermal swing initiated by deflection within the panel geometry at a certain fixed environmental temperature, there is a dramatic difference in the way the thermal changes occur in the panel due to the deformation for different hot or cold environments. This means that the connection between the thermal properties of the panel and deformation, and how they affect each other as the deformation progresses - constituting the thermo-mechanical coupling within the panel, is defined by the temperature of the environment in which the panel is immersed. There is hysteresis to be found in the thermal response to the deformation, which gets more significant for the colder environments, and the thermal properties of the panel demonstrate this through a swing in the temperature of the panel of 2.5 °C during the unloading process.

Therefore, in order to produce an accurate prediction of the deformation progression and regression during the loading and unloading processes, as well as the heat distribution along the panel geometry, it is recommended to introduce corresponding correction factors to account for:

- the effect of the environmental temperature on the magnitudes of the deformation of the panel;
- the initial thermal conditions of a panel which has undergone a mechanical deformation, even if the loading has been completely removed. The thermal properties for such a panel cannot necessarily be assumed to be fully controlled by the value of the environmental temperature if the panel also undergoes mechanical loading.

This study has shown that the panel tends to cool down in a relatively uniform way in all three dimensions. However, the heating up process is not uniform and there is some localised heating resulting in certain hot-spot areas accumulating more heat than others. This is the case if the panel is in an environmental temperature between ambient and + 80 °C. In the more extreme thermal environment the sample heats up more evenly and reflects the temperature of the environment linearly, even while being mechanically loaded. It can be noted that in [13] where an attached battery resulted in higher heat, there was also evidence of increased heat around the attached strain gauges, noting that these are passive devices that are conducting small currents due to their connection to the conditioning bridge electronics.

From the data obtained during this experimental work it is evident that in the environment with the temperature close to the ambient the skins do heat up faster than the honeycomb core, however this trend disappears as the environmental temperature moves to higher or lower extremes.

An interesting observation is that when going into the more extreme hot or cold environments the pattern of temperature feedback from the panel, with respect to the deflection, bifurcates, as shown in Fig. 12, demonstrating how significant the thermal changes of the environment can be for the pattern of the coupling between the thermal properties and the mechanical deformation of the panel.

5. Funding acknowledgements

The first two authors would like to acknowledge the financial support made available by Airbus Defence & Space Ltd and also the award of funding from the Strathclyde Centre for Doctoral Training. The authors would also like to thank Airbus Defence & Space Ltd for confident

tial access to data, noting that no disclosure of any such data whatsoever has been made within this paper.

6. Data availability

All data underpinning this publication are openly available from the University of Strathclyde at: <https://doi.org/10.15129/28a67ac3-0daf-4c8d-81c7-3affa847c211>.

Declaration of Competing Interest

The authors declare that they have no known competing financial interests or personal relationships that could have appeared to influence the work reported in this paper.

References

- [1] Findebor MM, De Grib EK (2016) A Researcher's guide to space environmental effects. International Space Station. NASA. NP-2015-03-015-39C. Available at: https://www.nasa.gov/connect/whoola/researcher_guide_space_environment_detail.html (accessed 13 August 2020)
- [2] D.G. Gilmore Spacecraft thermal control handbook. Fundamentals Technologies The Aerospace Corporation; 2002.
- [3] J.B. Bai, R.A. Shenoi, J.J. Xiong Thermal analysis of thin-walled deployable composite boom in simulated space environment. *Compos Struct* 2017;173:210–219. doi:10.1016/j.compstruct.2017.04.022.
- [4] F. Lu, Z. Zhang, X. Wang, L. Ji, X. Hsu, Q. Guan Microstructure evolution of 2024 and 7A09 aluminum alloys subjected to thermal cycling in simulated LEO space environment. *Mater Res Innovations* 2014;18(3):169–175. doi:10.1179/1433075313Y.0000000182.
- [5] K.-B. Shin, C.-G. Kim, C.-S. Hong, H.-H. Lee Prediction of failure thermal cycle in graphite/epoxy composite materials under simulated low earth orbit environment. *Compos B Eng* 2000;31(3):223–235. doi:10.1016/S1359-8368(99)00073-5.
- [6] S.Y. Park, H.S. Choi, W.J. Choi, H. Ewon Effect of vacuum thermal cyclic exposure on unidirectional carbon fiber/epoxy composite for low earth orbit space applications. *Compos B Eng* 2012;43(2):726–738. doi:10.1016/j.compositesb.2011.03.007.
- [7] Airbus Defence and Space. Confidential communication 2019.
- [8] Nowicki W. Thermoelasticity. Pergamon press, 1966.
- [9] S. Brischetto, R. Carrera Coupled thermo-mechanical analysis of one-layered and multilayered plates. *Compos Struct* 2010;92(8):1769–1812. doi:10.1016/j.compstruct.2010.01.020.
- [10] J. Park, A. Theysenballi, G. Kim The strength characteristics of aluminum honeycomb sandwich panels. *Thin-Walled Struct* 1999;35(3):205–231.
- [11] A. Abbadi, Y. Koutasova, A. Corrao, S. Belostec, Z. Anzi Experimental and numerical characterization of honeycomb sandwich composite panels. *Sinul Model Pract Theory* 2009;17(10):1533–1547. doi:10.1016/j.smap.2009.05.008.
- [12] G. Bellaguidi, P. Marrella, L. Ferri Fatigue analysis of honeycomb-composite sandwich beams. *Compos A Appl Sci Manuf* 2007;38(4):1180–1191. doi:10.1016/j.compositesa.2006.06.007.
- [13] V. Crupi, G. Epasto, E. Guglielmino Collapse modes in aluminum honeycomb sandwich panels under bending and impact loading. *Int J Impact Eng* 2012;43:5–15. doi:10.1016/j.ijimpeng.2011.12.002.
- [14] A. Bradjend, M. Bouzane, A. Mankour, et al. Thermo-Mechanical Design of Honeycomb Panel with Fully-Formed Inners used for Aircraft Design. Proceedings of the 16th International conference on recent advances in space technologies; 2013. doi:10.1109/RAST.2013.6501290.
- [15] O.A. Gaidova, M.P. Carmel, A. Elley Open Data for the paper 'Experimental investigation of the thermoelastic performance of an aerospace aluminum honeycomb composite panel'. *Thin Strathclyde* 2019.
- [16] A.C. Santos Silva, C.M. Sebastian, J. Lambros, R.A. Farnham High temperature modal analysis of a non-uniformly heated rectangular plate: Experiments and simulation. *J Sound Vib* 2019;443:397–410. doi:10.1016/j.jsv.2018.11.041.
- [17] X. Zhao, T. Chen, S. Wang Effect of NITi-coater and test temperature on mechanical behaviours of NITi-PU composite. *Int J Lightweight Mater Manuf* 2018;1:215–218.
- [18] G. De Martis, G. Brando, F.M. Mazzolani Hysteretic behaviour of bracing-type pure aluminum shear panels by experimental tests. *Earthquake Eng Struct Dyn* 2011;40(10):1143–1162. doi:10.1002/eqe.1079.
- [19] Kramobritza A, Roychild P, Coonan P, et al. Modelling the hysteresis composite behaviour using an elasto-plastic-damage model with fractional derivatives. *HAL archivée-curves*, 2015. Available at: <https://hal.archivée-curves.fr/hal-01240728> (accessed 13 August 2020).

The development of a dynamic coupled model for aluminium composite sandwich plates under thermo-elastic loading

Olga A. Ganiłova¹[0000-0003-0203-9825], Matthew P. Cartmell¹[0000-0002-3982-6315], and Andrew Kiley²

¹Aerospace Centre of Excellence, Department of Mechanical & Aerospace Engineering, University of Strathclyde, Glasgow, G1 1XJ, Scotland, UK

²Airbus Defence & Space Ltd., Gunnels Wood Road, Stevenage, Hertfordshire, SG1 2AS, UK
olga.ganiłova@strath.ac.uk

Abstract. An analytical-numerical coupled model has been developed to predict the effects of dynamic thermomechanical loading on aluminium composite panels in the form of metallic skin sandwich structures, for the enhanced design of spacecraft structures where the environmental conditions comprise combined mechanical and thermal loading. The model is explored for a centrally located static mechanical load in conjunction with thermal loading in the form of controlled environmental temperatures, for prescribed physical boundary conditions. The physics of dynamic thermal and mechanical loadings have been integrated into a partially coupled modelling procedure which can easily accommodate different boundary conditions and dynamically varying thermal properties.

Keywords: Sandwich Panel, Honeycomb, Thermoelastic, Thermomechanical.

1 Introduction

The materials used on the exterior of spacecraft are subjected to many degrading environmental threats. In terms of material degradation in space, low-Earth orbit (LEO), is a particularly harsh environment because of the presence of atomic oxygen (AO) along with all other environmental components [1]. As a spacecraft moves in and out of sunlight during its orbit around Earth, the degree to which a material experiences thermal cycling temperature extremes depends on its thermo-optical properties (solar absorptance and thermal emittance), its view of the sun, the Earth, and other surfaces of the spacecraft, time in sunlight and eclipse, thermal mass and equipment or components that produce heat [1]. The cyclic temperature variations can range from -120 °C to +120 °C, due to high solar absorptance with low infrared emittance, in the absence of spacecraft system thermal control. Sixteen thermal cycles a day, taking the case of the ISS which orbits Earth approximately every 92 minutes, may lead to cracking, peeling, spalling, or pinholes in the coating, allowing AO to attack the underlying material [1].

In [2] an experiment was performed to investigate the thermal behaviour of a sandwich panel deployable as an integral part of a satellite using a ground thermal-vacuum test. An interesting study carried out by [3] focused on the effect of thermal cycling in a simulated LEO environment on the microhardness of aluminium alloys, and subjected these alloys to cycles ranging from -140°C to +110°C, to study thermal fatigue and resulting stress state. The study concluded that aluminium alloys exposed to extended thermal cycling exhibited obvious softening behaviour, causing phase transformations leading to crack initiation. The principal finding was that aeronautical materials that undergo periodic heating and cooling can be damaged to varying degrees, with thermal

fatigue having a great impact on the mechanical properties of the materials used.

For a spacecraft panel undergoing cyclic loading under the perspective of modelling it is logical to propose that the structure must combine the effects of thermal loading as well as mechanical disturbance. This is because from a physical point of view the deformation of a body is connected to a change of heat inside it, so to a change of the temperature distribution in the body. So, a deformation of the body leads to temperature changes, and conversely. The internal energy of the body depends on both the temperature and the deformation and so, in the case of a spacecraft panel, it necessarily undergoes processes that are intrinsically coupled, defined collectively as thermoelasticity [4]. Many modelling approaches tend to separate the mechanical and thermal effects, but thermoelastic processes are not generally reversible because although the elastic part may be reversed - the deformations may be recoverable through cooling - the thermal part may not be reversible due to the dissipation of energy during heat transfer [5]. So, there is a strong need to couple the mechanical and thermal aspects of the problem to achieve results of meaningful accuracy. In order to reduce the computational cost, it was decided to adopt the TTC approach described in [6] to an industrial application of an aluminium honeycomb sandwich panel. Such panels are routinely used within spacecraft structures, but this is also a common form of structural material encountered right across the aerospace industry. We consider an industrial case of thermodynamic loading with room temperature initial thermal conditions, and gradual mechanical loading, both combined together for the first time. Working at the micro-vibration level tackles an important spacecraft phenomenon because even moderate thermo-mechanical loading conditions generate micro-vibration, which contribute to the all-important satellite de-point problem, which industry is very keen to minimise as far as possible.

2 Problem under consideration

The sandwich panel to be considered is composed of two types of aluminium alloy. For the outer faces of thickness 0.4 mm, an Al-2024 alloy is used, whilst an Al-5056 alloy foil is used to form the hexagonal honeycomb core. This core is of depth 14.24×10^{-3} m and comprises a foil of thickness 0.0254×10^{-3} m. It has been decided to develop a partially coupled model, and although TTC in [6,8] is a partially coupled model it still demonstrates very high accuracy when compared with the fully coupled model [5,7].

3 A model for mechanical and thermal behaviour of the panel

The mechanical equations of motion are based on the Reddy plate theory development [6] noting that it is assumed that deflection due to shear is negligible with respect to flexure between the layers, and so the basis for the model has been reduced to the interpretation given by [9],

$$\begin{aligned}
 N_{11,x} + N_{12,y} &= 0 \\
 N_{12,x} + N_{22,y} &= 0 \\
 M_{11,xx} + 2M_{12,xy} + M_{22,yy} + N_{11}w_{,xx} + 2N_{12}w_{,xy} + N_{22}w_{,yy} + q(x,y,t) - p_x w_{,xx} - p_y w_{,yy} \\
 &= \rho h w_{,tt} + \delta w_{,t}
 \end{aligned} \tag{1}$$

and where N_{ij} are membrane forces, M_{ij} are bending moments, p_x and p_y are forces applied along the x and y coordinate directions respectively, δ is a damping coefficient, $q(x,y,t)$ is a transversely distributed loading, and ρ and h are the density and thickness of the panel.

For a laminated plate with arbitrarily oriented plies, the thermoelastic linear constitutive relations for the k th orthotropic lamina in the principal material coordinates of the lamina are,

$$\begin{Bmatrix} \sigma_{11} \\ \sigma_{22} \\ \sigma_{12} \end{Bmatrix} = \begin{bmatrix} Q_{11} & Q_{12} & 0 \\ Q_{12} & Q_{22} & 0 \\ 0 & 0 & Q_{66} \end{bmatrix}^{(k)} \begin{Bmatrix} \varepsilon_{11} \\ \varepsilon_{22} \\ \varepsilon_{12} \end{Bmatrix} - \begin{Bmatrix} \beta_{11} \\ \beta_{22} \\ 0 \end{Bmatrix}^{(k)} T \quad (2)$$

where $\bar{Q}_{ij}^{(k)}$ are the plane stress-reduced elastic stiffnesses, and $\bar{\beta}_{11}^{(k)} = \bar{Q}_{11}^{(k)} \alpha_1 + \bar{Q}_{12}^{(k)} \alpha_2$ and $\bar{\beta}_{22}^{(k)} = \bar{Q}_{12}^{(k)} \alpha_1 + \bar{Q}_{22}^{(k)} \alpha_2$ are the thermoelastic stiffnesses, with α_1 and α_2 being the coefficients of thermal expansion in the x and y directions. The relationships between strains and displacements are derived in detail in [6].

Following [6] we also assume that the temperature varies according to a cubic law, consistent with assumptions:

$$T = T_0 + zT_1 + z^2T_2 + z^3T_3 \quad (3)$$

where $T(x,y,z,t)$ is the three dimensional temperature variable, while $T_0(x,y,t)$, $T_1(x,y,t)$, $T_2(x,y,t)$, $T_3(x,y,t)$ are the hitherto unknown components of the temperature of the two dimensional model, and cover the full profile up to a cubic distribution.

The thermal balance equations are introduced for the case of non-stationary conduction and thermoelastic coupling, as in [6,8],

$$\begin{aligned} q_{1,x}^{(0)} + q_{2,y}^{(0)} - b_{,t}^{(0)} - a_{,t}^{(0)} + Q^{(0)} &= 0 \\ q_{1,x}^{(1)} + q_{2,y}^{(1)} - b_{,t}^{(1)} - a_{,t}^{(1)} + Q^{(1)} &= 0 \end{aligned} \quad (4)$$

where the $q_i(x,y,z,t)$ represents the three dimensional heat flow along the x,y,z directions, $b(x,y,z,t)$ is the internal energy due to non-stationary conduction, $a(x,y,z,t)$ is the interaction energy due to the thermoelastic coupling, all defined in detail in [6,8].

A procedure for computing the solutions to the principal equations (1) and (2), and invoking all the parameters that follow, defined with respect to specified boundary and initial conditions, has been coded in MathematicaTM.

Since we are interested in the temperature and displacement distribution in the z -direction for the structure when subjected to combined mechanical and thermal loading, the system can be reduced to the following equations to find the membrane temperature $T_0(t)$ and bending temperature $T_1(t)$ as defined in [8,10]:

$$\begin{aligned} C_1 \ddot{W}(t) + C_2 \dot{W}(t) + [C_3 + C_4 P_x(t) + C_5 P_y(t) + C_6 T_0(t) + C_7 T_\infty(t)] W(t) + C_8 W^3(t) + C_9 T_1(t) \\ + Q(t) &= 0 \\ C_{10} \dot{T}_0(t) + C_{11} T_0(t) + C_{12} T_\infty(t) + C_{13} \dot{W}(t) W(t) &= 0 \\ C_{16} \dot{T}_1(t) + C_{17} T_1(t) + C_{18} T_\infty(t) + C_{19} \dot{W}(t) &= 0 \end{aligned} \quad (5)$$

In reference [6] this form of system of equations was solved analytically obtaining a general solution using features within the Mathematica™ code. However, this was done by eliminating the nonlinear terms and for static values of the mechanical and thermal loading, thus,

$$\begin{aligned} C_1 \ddot{W}(t) + C_3 W(t) + C_9 T_1(t) &= 0 \\ C_{10} \dot{T}_0(t) + C_{11} T_0(t) &= 0 \\ C_{16} \dot{T}_1(t) + C_{17} T_1(t) + C_{19} \dot{W}(t) &= 0 \end{aligned} \quad (6)$$

Here our overall aim has been to look for a solution for the system in its generalised form, as stated in full in Eq. (5).

Before starting to look for an analytical solution it was decided to investigate whether the presence of the nonlinear terms eliminated in [6] would have a pronounced effect on the behaviour of the panel under consideration. Therefore, an analytical closed form solution (using the DSolve function in Mathematica™) was found for the simplified system (6), as well as a comparable numerical solution (using NDSolve in Mathematica™) for the full system with nonlinear terms in Eq. (5). As an initial test example we assumed that the panel should be subjected to a small constant mechanical load, arbitrarily set to 1N, and a thermal load in the form of an environmental soak temperature of 70°C, and no mechanical damping.

The purely numerical solution to Eq. (5) for $W(t)$ and the closed form analytical solution for $W(t)$ obtained for the reduced system of Eq. (6) are both plotted in the time domain in Fig. 1.

The two time domain plots of Fig. 1 suggest that for the data considered retaining the nonlinear and coupling terms provides a solution offering more detailed information about the behaviour of the panel, including an important internal energy transfer phenomenon arising from the interaction between the mechanical and thermal aspects of the problem, demonstrated in Fig. 1(a) as a transient decay in the displacement response. However, the numerical solution found for the full nonlinear system obviously doesn't offer any generic insight into the phenomenology of the problem and is restricted in use to specific data cases such as the one just discussed.

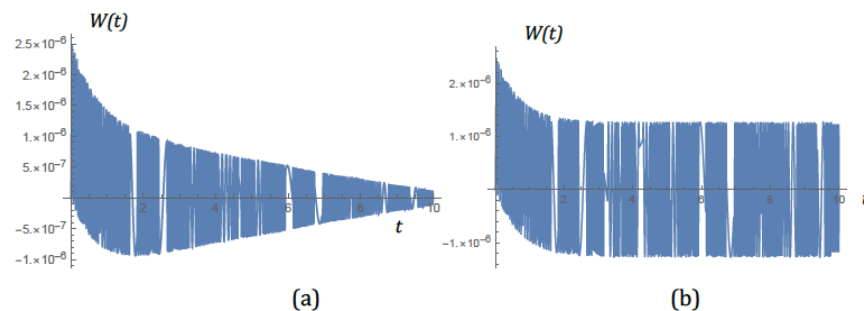


Fig. 1. Deflection $W(t)$ in metres for the panel under $Q=1\text{N}$, $T=70^\circ\text{C}$ based on the following solutions: (a) – numerical solution of Eqs (5), (b)-closed form solution for Eqs (6)

Given that this particular numerical solution, and others too, confirm the transient nature of the displacement response with time, as one would fully expect, the next logical step in the investigation would be to obtain a proper closed form solution for the full nonlinear system. An immediate benefit of this would be the calculation of accurate and generalised responses, and greatly reduced calculation times for different geometries, loading conditions and different material properties for the panel. Nevertheless, despite the

limitations of Eq. (6), it should be mentioned that the predicted profile of the temperature distribution along the thickness was found to be phenomenologically accurate for this solution and can be used without any loss of accuracy.

4 Numerical experiment

For the numerical study of the system (5) with full nonlinear coupling terms, different forms of loading are considered: a constant thermal load only, a dynamic thermal load only, a constant mechanical load only, and a combined thermo-mechanical load consisting of a dynamic thermal component and a constant mechanical component. In this paper results are presented for a constant and dynamic thermal loads and a combined thermo-mechanical load. The plate-like sandwich panel under consideration is of the dimensions $(100 \times 100) \times 10^{-3}$ m with variable thickness honeycomb and was considered to be simply supported. The thermal loading was applied by means of imposing a difference between the reference temperature and the environmental temperature, in order to represent free heat exchange conditions. The mechanical loading was taken as a normal constant force applied centrally to the top-face sheet.

4.1 The case of thermal loading

When elevated temperature conditions apply at the outer faces of the sandwich panel, to represent the free heat exchange condition, these faces will heat up first of all, with the heat then distributing from the outer faces inwards towards the centre of the core. To understand the process of the displacement emerging due to this changing thermal equilibrium, as well as the characteristics of the thermal gradient along the thickness, a constant environmental surround temperature of 100°C was initially applied with the ambient reference (start) temperature set to 22°C , and a solution for the system of Eq. (5) was obtained using the NDSolve function in Mathematica™.

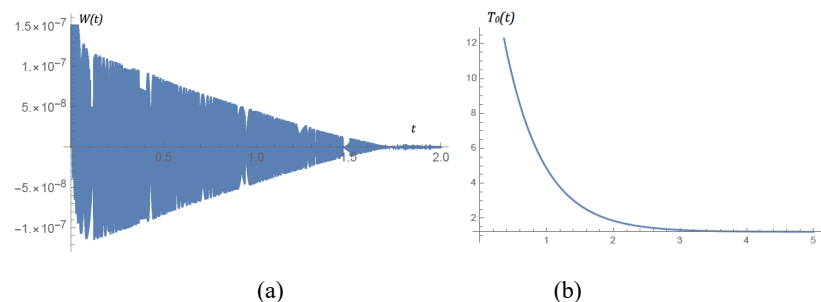


Fig. 2. (a) Displacement response (in metres) in the time domain and (b) time history of the distribution of the thermal component $T_0(t)$ (in $^\circ\text{C}$) when subjected solely to a thermal load defined by an environmental temperature of 100°C and with a core thickness of 0.01424m and total plate thickness of 0.015m.

The principal features of the displacement response are the transient over time and the largely symmetrical peak to peak amplitude over the time of the transient's decay. This accords with practical expectations for a plate under this form of loading. In Fig. 3 discrete snapshots between 0.001 s through to 5 s are given for the time history of the thermal gradient across the thickness of the panel, in order to understand the thermal changes that the panel undergoes, and the conditions under which it stabilises.

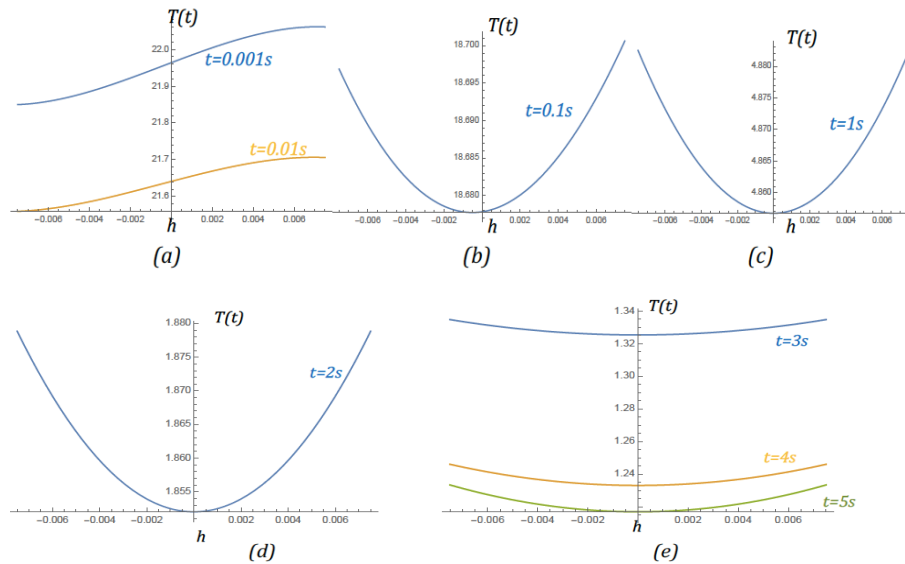
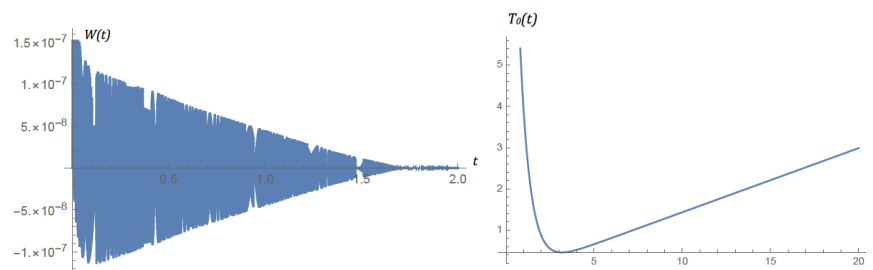


Fig. 3. Plots of the temperature (in °C) distribution through the thickness h (in metres) of the panel under a thermal load due to an environmental soak temperature of 100° C.

By fixing the time steps and observing the progression of the temperature distribution through the plate we see the main stages of the temperature stabilising process described in [6]. By applying heat to the plate through an elevated environmental soak temperature the temperature distributes through the thickness as shown in Fig. 3(a) with the intermediate temperature of the honeycomb core being very close to the top skin temperature (Fig. 3(b)) and after 1s this stabilises and settles within the range of 1.1°C, with a small difference between that of the skin temperature and the honeycomb core. The process of equilibrating temperature is reflected in the behaviour of $T_o(t)$ in Fig. 2(b) where we clearly see that after 5s the equilibrium temperature is reached and the profile thereafter remains constant in time. The process of obtaining the solution for $T_o(t)$ can in itself be a useful tool for finding out if the temperature stabilises at a certain equilibrium, and what the temperature of that equilibrium might be, as well as to determine how long it takes for the panel to reach an equilibrium state. To investigate the behaviour of the panel when the environmental temperature varies under the prescribed dynamic condition Eq. (5) are solved for $T(t) = 20 + 10t$ with the reference temperature set to 22°C, as in the previous case.



(a)

(b)

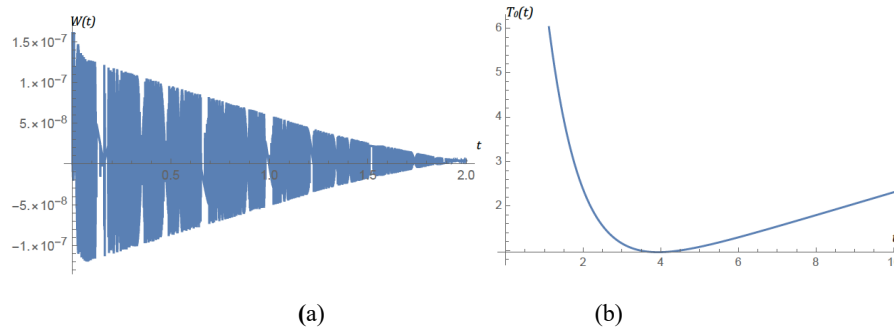
Fig. 4. (a) Displacement response (in metres) in the time domain (in seconds); (b) Time history of the thermal component $T_0(t)$ (in °C) for the panel under a thermal load of $(20 + 10t)$ °C with a core thickness of 0.01424m, and for a total plate thickness of 0.015m. Time is in seconds.

The same qualitative conditions prevail for the response to this form of load, and the transient dies out after about 1.75s. Analysing the history of the thermal gradient over time shows that the sample underwent the same process of stabilisation and reached equilibrium after 3s, however due to the linearly increasing thermal load $(20 + 10t)$ °C, the temperature in the sample rapidly increased after equilibrium. This is clear from the distribution of the middle plane thermal component $T_0(t)$ in Figure 4(b).

4.2 The case of thermo-mechanical loading

For the case of thermo-mechanical loading the physics of the separate thermal and mechanical loading scenarios are combined, using the model discussed previously.

An initial check on the combined effect of a constant mechanical load of 1N and a dynamic thermal load initiated by the environmental temperature which obeys the linear law given by $(20 + 10t)$ °C was carried out. This showed that the deformation under these conditions is virtually the same as when undergoing purely the linear thermal load law, but the structure experiences a generally greater level of principal stress than for the case of the isolated mechanical load. This is due to the additional compressive stress caused by the thermal expansion of the panel. The deformation response, thermal gradient, and general correspondence to the cases of purely dynamic thermal loading can all be observed for very thin and thick panels, with the results given in Figs. 5.



(a)

(b)

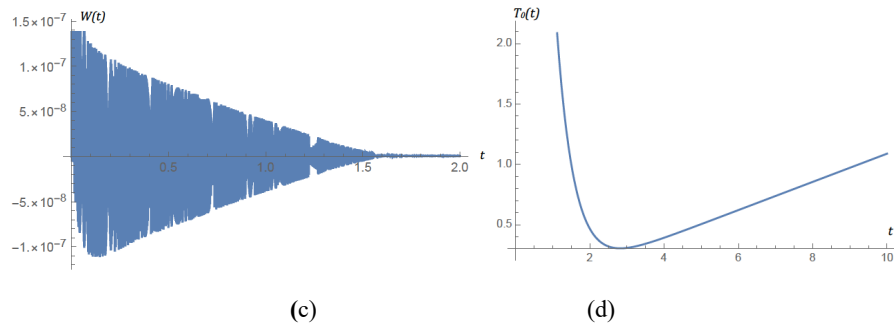


Fig. 5. (a),(c) Displacement response (in meters) in the time domain and (b),(d) time history of the distribution of the thermal component $T_0(t)$ (in $^{\circ}\text{C}$): (a),(b) - for core thickness of 0.00824m and total plate thickness of 0.009m and (c),(d) - for core thickness of 0.01924m and total plate thickness of 0.02m when subjected to a thermal load of $(20 + 10t)$ $^{\circ}\text{C}$ and a constant mechanical loading of 1N.

A more pronounced dc offset occurs in the displacement response when the constant mechanical load is increased up to more realistic values, such as 10N or 100N and this phenomenon is shown very clearly in Figs. 6.

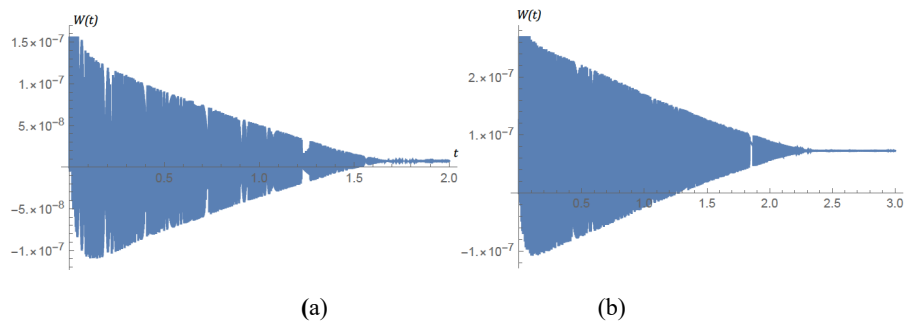


Fig. 6. Displacement response (in metres) in the time domain when subjected to a thermal load of $(20 + 10t)$ $^{\circ}\text{C}$ and a constant mechanical load of (a) 10N and (b) 100N, with core thickness of 0.01924m and total plate thickness of 0.02m.

5 Conclusions

A new modelling strategy for aluminium honeycomb composite panels has been suggested, in which the physics of dynamic thermal and mechanical loadings are integrated into a partially coupled modelling procedure which can easily accommodate different boundary conditions and dynamically varying thermal properties. The nonlinear thermomechanical model comprises three coupled nonlinear ordinary differential equations for which an analytical closed-form solution can only be obtained for the linearised equations and for static thermal and mechanical loads, and so a comparison has been undertaken between this solution and a corresponding numerical solution for the full nonlinear model. The simplified analytical solution obtained in [6] has been found to be useful for predicting the temperature profile through the thickness of panels with no appreciable loss of accuracy. However, for simulation of displacement the system of coupled equations can be solved numerically, results for this are discussed here. An approximate closed-form analytical solution for this equation could be sought using an asymptotic method, such as the perturbation method of multiple scales. A full set of numerical results have been obtained for a simply supported aluminium honeycomb composite panel commonly used within industry, undergoing thermal, mechanical, and thermo-mechanical

loading conditions. The thermal load mechanism involves free heat exchange and the mechanical loading in all cases comprises a normal constant force exerted centrally on the top surface of the panel. When the panel is subjected solely to a thermal load, applied by means of a fixed environmental temperature, then the solution for the displacement of the panel shows a transient oscillation over time at a commensurately small amplitude. The thermal gradient through the thickness of the panel is also calculated based on the coupled system (5) using the numerical solution derived, and thermal stabilisation emerges over time, as one would expect. Broadly the same qualitative responses are observed for a linearly increasing thermal load temperature, but with the stabilisation showing close coupling to the rising environmental temperature. Core thickness affects the results, with the thinner panels displaying a more pronounced thermo-mechanical response than thicker ones. In the case of pure mechanical loading, at a constant but arbitrary low level initially, the panel behaves as normal theory would predict, with a small dc offset in the displacement once the very small transient has decayed. The temperature profile shows a thermal response which reduces to zero in time, indicating that the internal and environmental temperatures are equal. This is a persistent effect for different geometry and mechanical load magnitude. Finally, in the case of combined dynamic thermo-mechanical loading the panel is subjected to a linearly increasing thermal load temperature and a constant arbitrary mechanical load. The increasing thermal equilibrium over time and the dc offset in the displacement amplitude are strongly persistent features of the results despite different core thicknesses, with the level of the dc offset increasing significantly with applied mechanical load.

Acknowledgments: The first two authors would like to acknowledge the financial support made available by Airbus Defence & Space Ltd and also the award of funding from the Strathclyde Centre for Doctoral Training. The authors would also like to thank Airbus Defence & Space Ltd for confidential access to data, noting that no disclosure of any such data whatsoever has been made within this paper.

References

1. Finckenor, M.M., Groh, K.K.: A Researcher's guide to space environmental effects. International Space Station. NASA. NP-2015-03-015-JSC.
2. Bai, J.B., Sheno, R.A., Xiong J.J.: Thermal analysis of thin-walled deployable composite boom in simulated space environment. *Composite Structures* 173, 210–218 (2017).
3. Lv, P., Zhang, Z., Ji, L., Hou, X., Guan, Q.: Microstructure Evolution of 2024 and 7A09 Aluminium Alloys Subjected to Thermal Cycling in Simulated LEO Space Environment. *Materials Research Innovations* 18(3), 169–175 (2013).
4. Nowacki, W.: *Thermoelasticity*. 2nd edition. Pergamon press (1986).
5. Brischetto, S., Carrera E.: Coupled thermo-mechanical analysis of one-layered and multilayered plates. *Composite Structures* 92, 1793–1812 (2010).
6. Saetta, E., Rega, G.: Third order thermomechanically coupled laminated plate: 2D nonlinear modeling, minimal reduction, and transient/post-buckled dynamics under different thermal excitations. *Composite Structures* 174, 420–441 (2017).
7. Brischetto, S., Carrera, E.: Thermomechanical effect in vibration analysis of one-layered and two-layered plates. *Int J Appl mech* 3(01), 161–85 (2011).
8. Saetta, E., Rega G.: Unified 2D continuous and reduced order modeling of thermomechanically coupled laminated plate for nonlinear vibrations. *Meccanica* 49, 1723–49 (2014).

9. Yen-Liang Yeh.: Chaotic and bifurcation dynamic behavior of a simply supported rectangular orthotropic plate with thermo-mechanical coupling. *Chaos Solutions & Fractals* 24, 1243-1255 (2015).
10. Saetta, E, Rega, G.: Modeling, dimension reduction, and nonlinear vibrations of thermomechanically coupled laminated plates. *Procedia Eng* 144, 875–82 (2016).

Appendix H

Draft of the paper for publication ‘Development of a Simplified Thermomechanical Finite Element Model of a Honeycomb Sandwich Panel for Satellites in Orbit’, Eoin Reilly, Aaron Weidmann, Jon Richardson, Matthew Dougan, Neil Gordon, Olga Ganilova

Development of a Simplified Thermomechanical Finite Element Model of a Honeycomb Sandwich Panel for Satellites in Orbit

Eoin Reilly, Aaron Weidmann, Jon Richardson, Matthew Dougan, Neil Gordon, Dr. Olga Ganilova

University of Strathclyde, Department of Mechanical and Aerospace Engineering, 75 Montrose Street, Glasgow, G1 1XJ

Abstract

Satellites require a body that is light, and cost efficient enough to send into space, while also being strong and stiff enough to stand up to constant use without any practical repair or maintenance for the entire service life. As such, honeycomb sandwich panels are an obvious choice for satellites thanks to their high specific stiffness and strength. However, modern modelling approaches fail to properly model thermo-mechanical responses of these panels, leading to misleading results, and selection criteria for composites often rely on practical testing. This is an issue, as satellites experience significant temperature fluctuations. This report examines the limitations of mechanical-only or separated thermo-mechanical modelling and proposes effective methods to develop accurate simplified models which capture panels’ thermo-mechanical responses with small amounts of computational effort. A mechanical geometrically accurate model was validated using previous experimental data of Honeycomb Sandwich Panels under Three Point Bending. Then two thermo-mechanical models were developed which were able to distinguish panel response for varying temperature at low load cases typical of satellite loading. Subsequently 3D and 2D Simplified models were developed based on an equivalent orthotropic homogenous core which significantly reduces computational time while maintaining acceptable accuracy. It was determined that the best-case methods presented in this report can reduce computational time and demonstrate distinct behaviours which cannot be captured solely by thermal or mechanical models.

1 Introduction

Structures in space face several extreme conditions. Maintenance is rarely possible, as it is prohibitively difficult and expensive to send up any practical means of repairing a space structure. They must endure extreme temperature fluctuations, especially for satellites in low Earth orbit experiencing conditions such as: direct solar radiation without an atmosphere which means very high irradiance; and while in the shadow of the Earth, the heat of a structure will quickly radiate away. While precise temperatures are dependent on the precise design of a satellite and would have to be determined by a finite element model assessing the geometry, materials, orientation, internal components, and exposure time of the satellite, variations between -150°C and $+150^{\circ}\text{C}$ would not be unreasonable, with significant variations of temperature within an orbiting body at a given point in time [1]. Collisions with space debris can degrade a structure over time, but impacts are hard to foresee and will cause highly variable forms of damage to a structure. On top of this, it is necessary for space structures to be as light as possible, as rocket launches are limited by mass. As such, low-weight materials are crucial, making honeycomb sandwich panels (HSPs) a popular choice. These are constructions with thin metal faces and a lightweight core of rows of hexagons. HSPs are often vacuum-packed, so internal convection is minimal [2]. Heat dominates one side of the panel either due to internal components or external solar flux. This alongside the insulating properties of the epoxy present in these panels and conditions of internal heat transfer (driven by conduction) makes modelling heat flux through these panels a difficult task.

During space operation, mechanical loading on the panels is typically small and is restricted to vibrational loads from either the operation of machinery on the structure (such as adjustable solar panels) or impacts with space debris, including micrometeoroids.

The simplest means of modelling a HSP is to recreate the geometry in FEA software. This was dismissed as unrealistic due to computational demands as recently as 2006 [3] but is now much more feasible [4].

Alternatively, a continuum model can be developed. This assumes that portions of the panel can be modelled as a homogenous solid with orthotropic material properties. The validity of the continuum approach is well documented and has been used extensively for many years since it offered a significant simplification. Limitations of this approach are evident as detail of localised effects cannot be represented and the core does not provide even support across the surface of the face sheet. [5]

Additionally, 2D models have been explored by several researchers. Both [6] and [5] considered a range of methods of interpreting the honeycomb core as a 2D model.

Both papers recommended anisotropic core theory, which has three components: each face of the plate along with the anisotropic core.

Investigations into thermal behaviour was conducted in [2], where a 1D analysis of heat transfer within a honeycomb sandwich panel was carried out. They identified two key conclusions: firstly, that the maximum temperature of a heated HSP can be altered by changing its geometry: in general, a taller core leads to a hotter front/top face, as there will be less radiation heat transfer from the front to back plate, while thicker honeycomb walls allow for more conductive heat transfer. Secondly, they found that radiation contributes a minority but non-negligible portion of heat transfer.

The development of a simplified honeycomb model which accounts for radiation is taken further in work [7], who built off from work by Swann and Pittman from 1961. This paper discusses a method of incorporating the effects of radiation as an additional conductive term for the purposes of developing a less computationally demanding thermal model for honeycomb sandwich panels. The method makes various simplifying assumptions, such as neglecting quadratic terms in the radiation heat transfer equation and deriving the various view factors of surfaces within a unit cell of the core by assuming the cell is circular rather than hexagonal. However, the associated errors reported in the paper are reasonable and the computational savings of the method are impressive.

With further development of technology for space and aircraft applications involving honeycomb based complex structures a need for a higher precision modelling tools is becoming more acute. Previously modelling of both effects of heat and vibration has been separated in FE models to minimise the computational cost. However, there is more and more evidence of interconnection and mutual interaction between these two phenomena. Therefore, considering the advancement in modern FE techniques an attempt to develop a more accurate model which accounts for both effects is presented in this paper.

2 Model description

1.1 To investigate the possibility of development of a coupled model using FE required by industry [9], mechanical and thermo-mechanical loading of HSPs under three-point bending was considered. The methodology for the model was separated into mechanical loading (the mechanical model) and a combination of thermal and mechanical effects (the thermo-mechanical model).

The HSP geometry, F1.5-T0.07-H15-L4 was chosen following the work done in [8]. To investigate the aspects of accuracy and computational cost, the panel was discretised through 3 different FE approaches: the 3D Geometrically Accurate Model, the 3D Continuum Model, and the 2D Continuum Model. Each

model was firstly subjected to mechanical loading only, through Three Point Bending (TPB) and the results were compared to the physical test data from [8]. Then thermal conditions were applied through two different methods: through uniform environmental temperature change in the mechanical simulation, and temperature gradient through the panel in a coupled thermo-mechanical simulation.

Initial models were set up with a simple beam, defined by reference to the ASTM C-393 standard, representing the sandwich panel (Fig. 1), with results presented in Table 1.

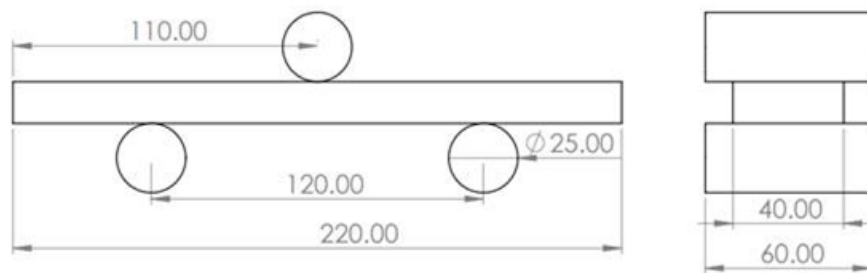


Figure 1: Three Point Bending Geometry

FEA Results	EQV, von Mises	Max Principle (MPa)	Deflection (mm)	Force Reaction
Numerical evaluation:		124.6	0.3	6233
1-1 Model cylinder displacement	112	120	0.3	6233.2
Face split supports and applied force	124	125	0.3	6369.9
Face split shell beam	124	125	0.3	6369

Table 1: Simple Beam Comparison

For the simulations which model the contact between supports and panels, displacement constraints were found to be more reliable than applied forces.

Both face split constraint models match the numerical estimation very closely and behave as expected, which validates the method of assessment. The face split and shell beam models have one fixed and one frictionless support, which is one of the fundamental assumptions in the derivation of the flexural stress equations.

The 1:1 model beam shows the typical behaviour indicative of true bending, however, significantly differs from the numerical estimation. This difference in maximum stress is due to utilising two frictionless supports and constraining the panels lateral movement with the centre face split, which allowed for slight inward movement of the beam as it is deformed by the puncher. This suggests that the 1:1 model more accurately predicts the result of the TPB since it accounts for these differences. As stated in in [8] the models can be further optimised through adjusting friction coefficients of the contact regions. Additionally, the cylinder

displacement model is a more accurate representation for the GA model thanks to the inclusion of puncher indentation failure modes.

2.0 2.1 Data used for 3D Geometrically Accurate Model

A high-fidelity model of the panel described in [8] and in Figure 1 was simulated to replicate the results and verify the developed model. The 3D geometrically accurate (GA) model uses a solid geometry and mesh discretisation.

The material properties from [8] were used to define the geometry in ANSYS. The paper provides the Young's modulus, the Poisson ratio, and the density for the AA5052 skin alloy and the AA3003 foil used for the honeycomb core. However, no plasticity data was given in [8]. Given that both are aluminium alloys, a 1% bilinear hardening model was assumed. No ultimate stress values were given, and to simplify the model, damage models were ignored. Nevertheless, this should not be detrimental to the verification since the simulations are conducted with satellite use in mind, and, as such, modelling the failure behaviour of the panels is not necessary.

Material properties of skin panel (AA5052) and honeycomb core (AA3003).

Material	AA5052	AA3003
Young's modulus (GPa)	69	69
Yield strength (MPa)	138	94
Poisson's ratio	0.3	0.3
Density (kg/m ³)	2680	2680

Table 2: Reference Material Properties from [8]

The geometry was modelled in Autodesk Inventor 2020 according to Table 3.

Panel (I)	Reference ID	Skin thickness (mm)	Foil thickness (mm)	Core height (mm)	cell edge (mm)	Panel length (mm)	Panel width (mm)
2	F1.5-T0.07-H15-L4	1.5	0.07	15	4	220	40

Table 3: Reference Geometry for GA Validation [8]

In the Static Structural analysis, the core was assigned as AA3003, the skin-plates as AA5052, and the supports were assigned as structural steel. Bonded contacts were used between the honeycomb and the skin, omitting the presence of a layer of adhesive as can be seen in Figure 2.

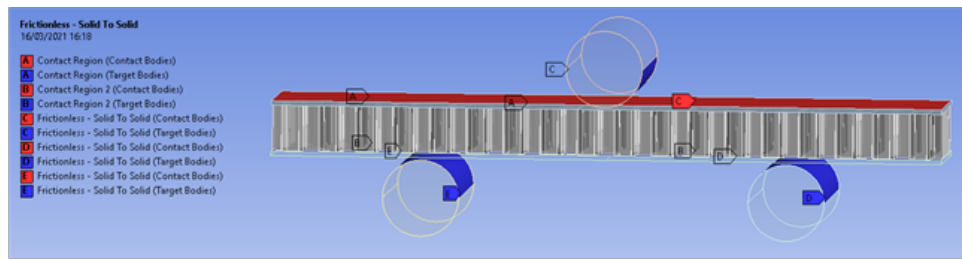


Figure 2: Geometrically Accurate Contact Modelling

Frictionless contacts were used between the rods and the panel skins with the interface treatment set to “adjust to touch”. This allows the panel to slide against the supports during bending, simulating real world conditions.

The mesh size was controlled with body sizing, where both skin plates (hex elements) and core (tetrahedral elements) were sized at 2mm. The tetrahedral mesh (Figure 3) was a trade-off to minimise the computational cost and was kept the same for all analyses to ensure consistent behaviour.

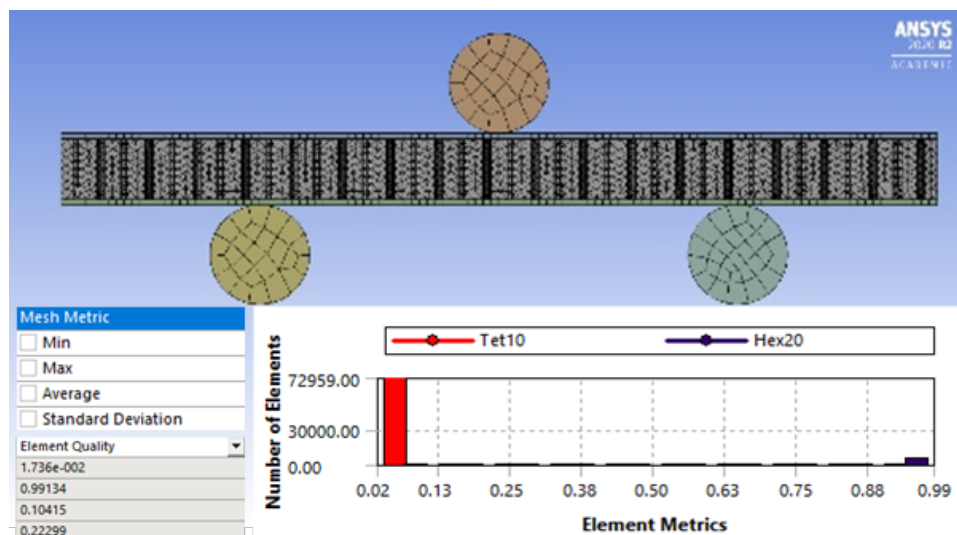


Figure 3: GA Tetrahedron Mesh Quality

The two bottom rods were fixed in place, while the top rod was displaced in the negative y-direction by 1mm to create bending (Figure 4).

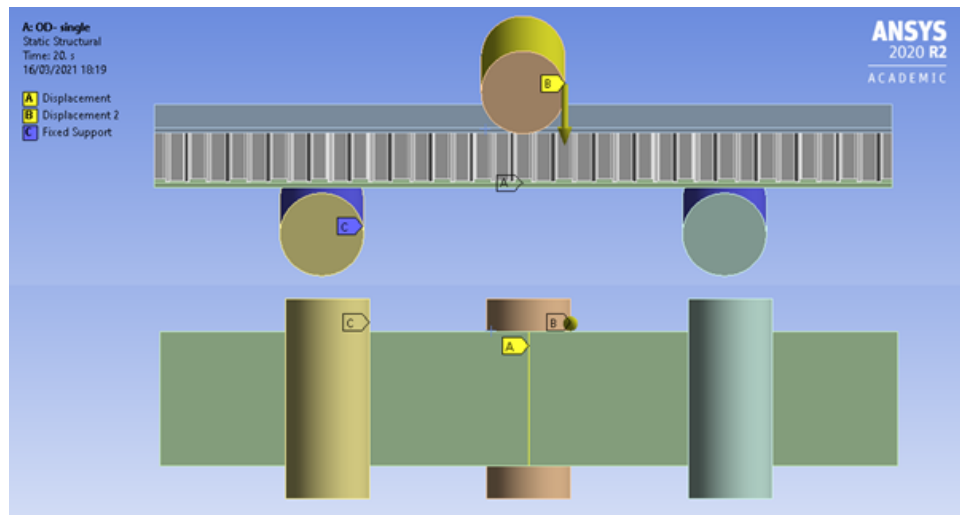


Figure 4: GA - Boundary Constraints

The motion of the panel was constrained by creating a face split on the bottom face of the panel and applying a displacement constraint to that split. This constrains the centreline of the panel to move only in the y-direction. A force reaction probe was applied to the displaced rod to measure the load against the displacement, so that the model could be validated by the test data.

For the main body analysis, the displacement was split into two steps from 0 to 0.3mm and from 0.3 to 1mm with 25 datapoints each to ensure sufficient resolution in the 200N range. The solution method was program controlled and large deflections were turned ON. The primary analysis from FEA to test data was through the force displacement behaviour of the panels.

2.2 Mechanical Model Validation

The mechanical behaviour and force reaction response of the panel was initially analysed through variation of panel geometry and GA, Mixed Shell and Quarter models. The different FEMs were described above, and the panel geometries and designations are represented in Table 3. For further work, a single panel from Table 3 was chosen, as geometric comparison was not a goal of this paper. Their effective stiffnesses and buckling strengths were compared to the test data. The stiffness was estimated through the gradient of the trendline of the linear behaviour section of the force reaction curve. Whereas the buckling strength compared the reaction force at 1mm deflection to the maximum load of the test data. For the purposes of comparison, both gradient and buckling strength are presented as percentage changes of gradient and stress, Δm and $\Delta \sigma_f$. When the test data buckling strength occurred before the 1mm deflection, the reaction force of the FEA was taken at the equivalent deflection. While buckling strength was not used as the main means of verifying models (the assumptions made earlier meant that these results were not fully reliable), they were used to discriminate between otherwise comparable models.

2.3 Data for Thermo–Mechanical Modelling

The primary goal of thermal integration is to showcase how temperature dependant behaviour can be implemented in FEMs in ANSYS. The most important component of the proposed FEM, which allows for temperature dependant analysis, is the integration of a temperature dependant material model. For this analysis, suitable data was sourced through the GRANTA Edupack material database because no temperature dependant data was available for either material of the mechanical model. The material selection approach was based on:

- A material with broadly the same chemical composition, AA3000/5000 series
- The mechanical properties (i.e., any data of the 3000 and 5000 series which has temperature dependant properties, which are as close as possible to the mechanical properties of the original material)

Edupack Material Data				
Material Properties	Paper AA5052	A5052H32	Paper AA3003	A3105 O
E (GPa)	69	70-73.6	69	69-72
Temperature dependant data?		yes		yes
Yield (MPa)	138	152-172	94	86-95
Temperature dependant data?	no	yes	no	no
Thermal Conductivity W/m°C	no	140-152	no	169-175
Specific Heat Capacity J/kg°C	no	963-1000	no	879-915
CTE (microstrains/°C)	no	23.7-24.9	no	23.4-24.6
Temperature dependant data?	no	Yes	no	yes

Table 4: Material Selection, Temperature Dependent Data

The chosen materials are detailed in (Table 4). The core material, A3105 O did not contain temperature dependent yield data. These were approximated by scaling the temperature dependent data of a 3000-series aluminium alloy. ANSYS estimates intermediate points in the bilinear hardening model through linear interpolation. (The bilinear hardening model is limited to 6 datapoints)

The material data has temperature dependent Young’s modulus, yield strength and coefficient of thermal expansion.

2.1.1 2.4 Methodology for Mechanical Model with Environmental Temperature

The first way to analyse the effect of temperature is through varying the environmental temperature of a static structural analysis. This homogenous temperature distribution throughout the panel is a significant simplification of the “actual” temperature distribution, especially considering an application to space structures. For the purposes of this analysis, this is valid because the objective was to show general trends in mechanical response. Many experiments simulating extreme temperatures are done in homogenous environments (Ganilova et al [9] showed that with increasing temperature the panel is more likely to show uniform temperature distributions). An additional benefit of homogeneous environments is that they eliminate the need to couple thermal and mechanical simulations, which will save computational time.

The variation of environmental temperature within the static structural environment of ANSYS was used to create the base data sets for both GA and continuum models (CMs). As discussed above, the environmental temperatures of the static structural three-point bending simulation were varied from -150°C to 150°C .

2.1.2 2.5 Methodology for Thermo-mechanical Model with Heat Flux

In the combined thermo-mechanical models, the results of a steady state thermal analysis were imported into a static structural analysis. The coupling of thermal effects to mechanical could be applied to uniform temperature distributions, to show the effects of thermal expansion and transient simulations. However, in this analysis, a more complex, varying temperature distribution was applied to the panel, in order to more closely emulate the conditions of a satellite in orbit.

In the steady state thermal analysis (Figure 5), the top or bottom skin surface was subject to opposing temperature and convection. The desired temperature was set, and the convection at the opposing surface was adjusted such that the required temperature gradient was created within the panel. The supports were excluded from the static thermal analysis through the ‘element birth and death’ feature. Additionally, the thermal strain effects had to be disabled for the 3 supports in the static structural analysis. The initial temperature was set as room temperature, 22°C .

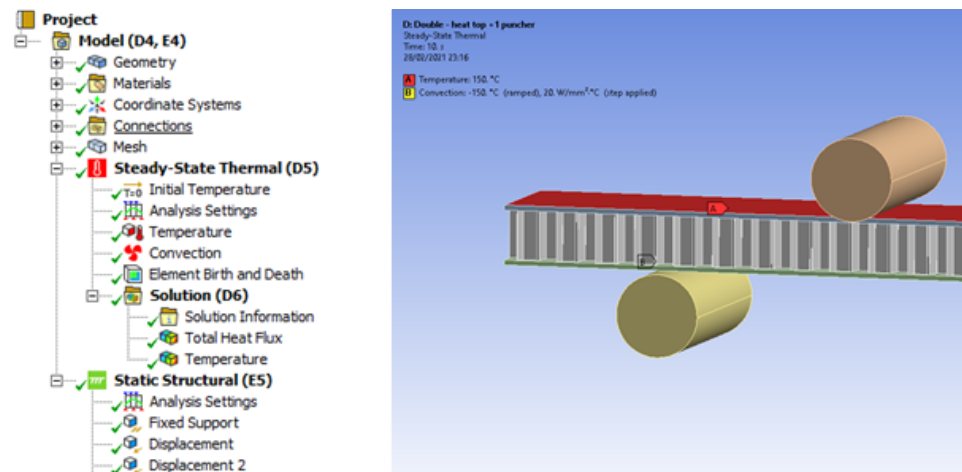


Figure 5: Steady State Thermal Boundary Conditions and Project Tree

Multiple load case scenarios were created under extreme temperature gradients (22°C to 150°C as well as -150°C to 22°C). To understand the effect of the temperature flux, the panel was analysed with and without mechanical loading.

3. Simulation Results for three FE models

Results below are presented for 3 different models with the panel undergoing mechanical or thermo-mechanical loading within each of them.

2.2 3.1 Simulation results for the Geometrically Accurate Model

To represent loading conditions in application to space structures, the main focus of the analysis will be within the range of 200N, which typically occurs within the first 0.1mm of deflection. However, the deflection of the individual analyses was chosen to be 1mm to encompass the full linear region of the panel’s force-deflection response, which is useful for validation and may provide a broader context to the development of the FEM.

The panel response is presented in Figure 6 and compared with experimental results from [8] (denoted “test data”), with a purpose of validation. Figure 6 shows the mechanical response of the chosen panel, for both original material data, and the proposed material model with temperature dependant properties. The material properties listed, which are described in table 2, are referred to as “original data”. The proposed temperature dependant material model in Table 4 is referred to as “edupack”.

Different manufacturing techniques of honeycomb cores, result in shared cell walls of either uniform or doubled thickness (in legends denoted as “single” or “double”). However, for aluminium cores, the most common procedures result in double wall thickness through the expansion method. Since there was no mention of this in [8], it was assumed that the honeycomb core was oriented such that the

double thickness sections were aligned for maximum stiffness, in parallel with the axis of bending of the panel.

2.2.1 3.1.1 Results for GA model for Mechanical loading only

Figure 6 clearly shows that proposed material model is in very good agreement with the original data and represents the behaviour of the honeycomb panel under TPB in a way which is sufficient for the purpose of this analysis.

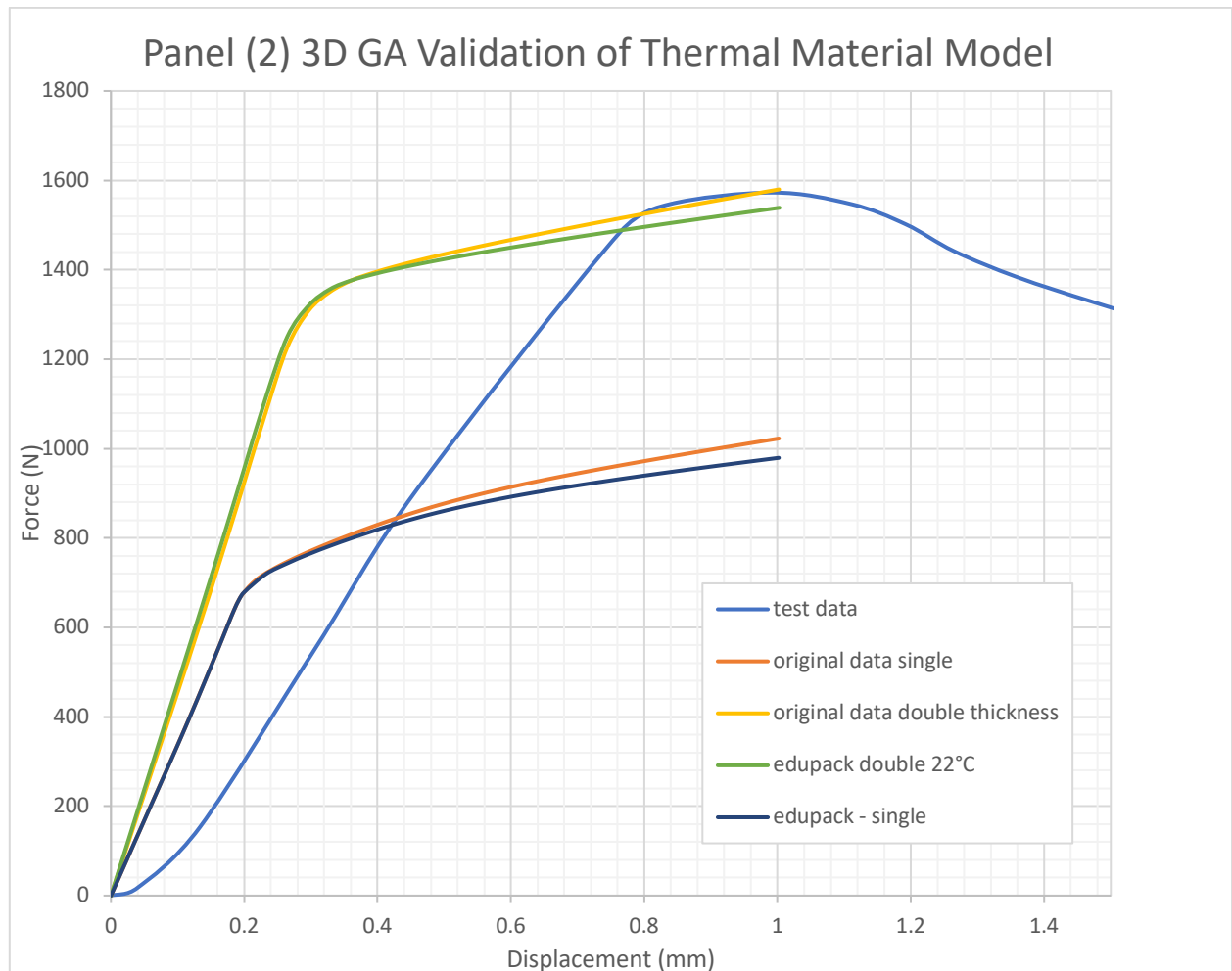


Figure 6: Validation of Mechanical Response of Thermal Material Model

It can be observed that the single thickness simulations match the gradient more closely than the double thickness simulations, however, the double thickness simulations closer predict the buckling strength of the sandwich panels. This is a good indication that the panels in fact are using expanded aluminium core, which means that the double thickness models more accurately predict the panels behaviour. In further analysis, the double thickness will be considered for use in the finite element models.

The early panel response of the double thickness model was identified as a primary concern for the analysis in the application to space structures. Hence, an accurate finite element panel response in terms of gradient could be desirable. However, the overall accuracy of the panel response is poor, which may be primarily due to lack of information and control about the details and parameters of the test setup (e.g., material properties, manufacturing techniques, processing techniques, pre-existing imperfections, and limitations of the bilinear hardening model).

2.2.2 3.1.2 Results for GA model for Thermo-Mechanical loading

introduced with Environmental Temperature

The first model for consideration of thermal effects was created by changing the environmental temperature within the static structural analysis. Figure 7 shows the variation in panel mechanical response for varying temperature.

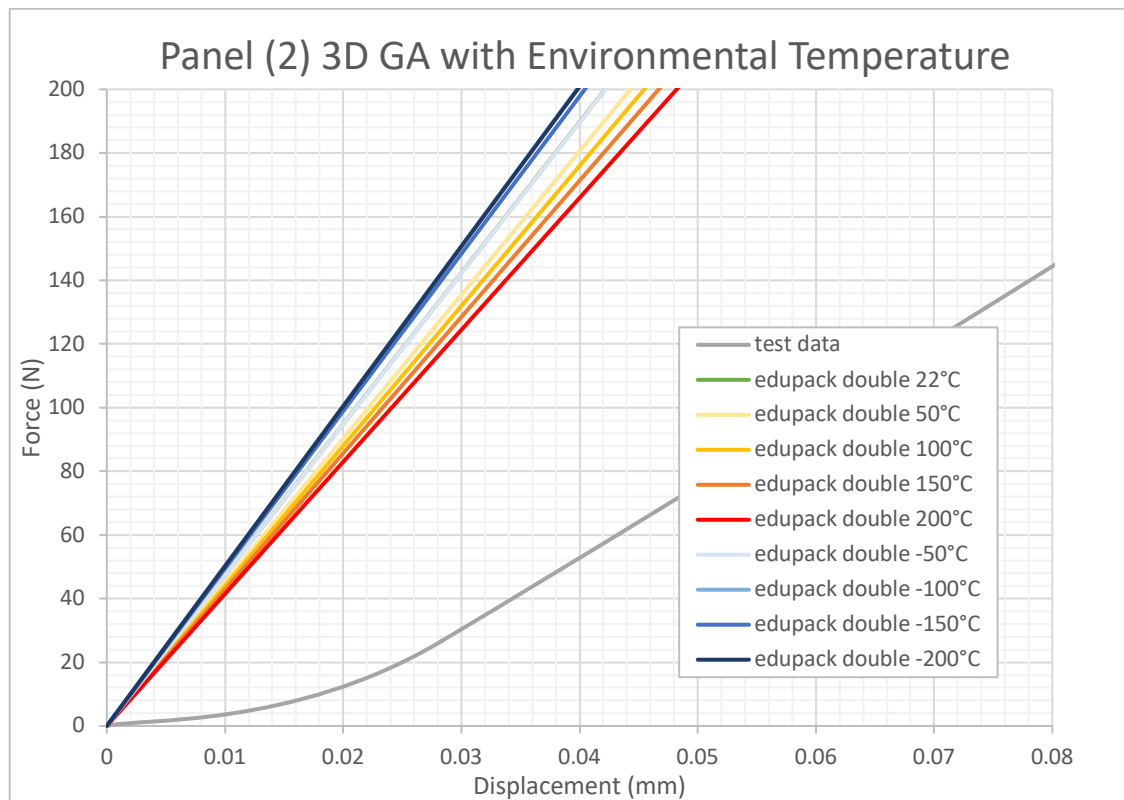


Figure 7: Thermomechanical Response of Varying Environmental Temperature (Up to 200N)

As can be seen in Fig.7, a high temperature environment causes a decrease in the panel bending stiffness, whereas low temperatures increase the panel bending stiffness. The change in panel response at high temperatures is less varied than at lower temperatures (a 10°C difference in temperature will create a larger deviation in panel response at high temperatures than at a low temperature). From 22 to -50°C there is hardly any change in behaviour, then a large jump from -50 to -100°C, and again very little change from -

100 to -200°C. It is apparent that the impact of temperature is notable even at these low load and displacement conditions. This observation is directly related to the material model and has been similarly observed in the experimental TPB of aluminium HSPs under extreme temperature conditions [9]. Overall, smaller deflections occur in cold conditions and larger deflections occur in hotter conditions, and the extent of the deviation of deflection from room temperature increases at temperature extremes.

The model is a very simple implementation of temperature dependent behaviour and predicts certain variation in panel behaviour.

The effect of temperature becomes much greater at higher loads and deflections, where the difference in predicted strength is up to 700N from 200°C to -200°C at 1mm (Figure 8). The panel behaviour is a direct result of the material model. As the temperature increases, the Young's modulus and yield strength decrease.

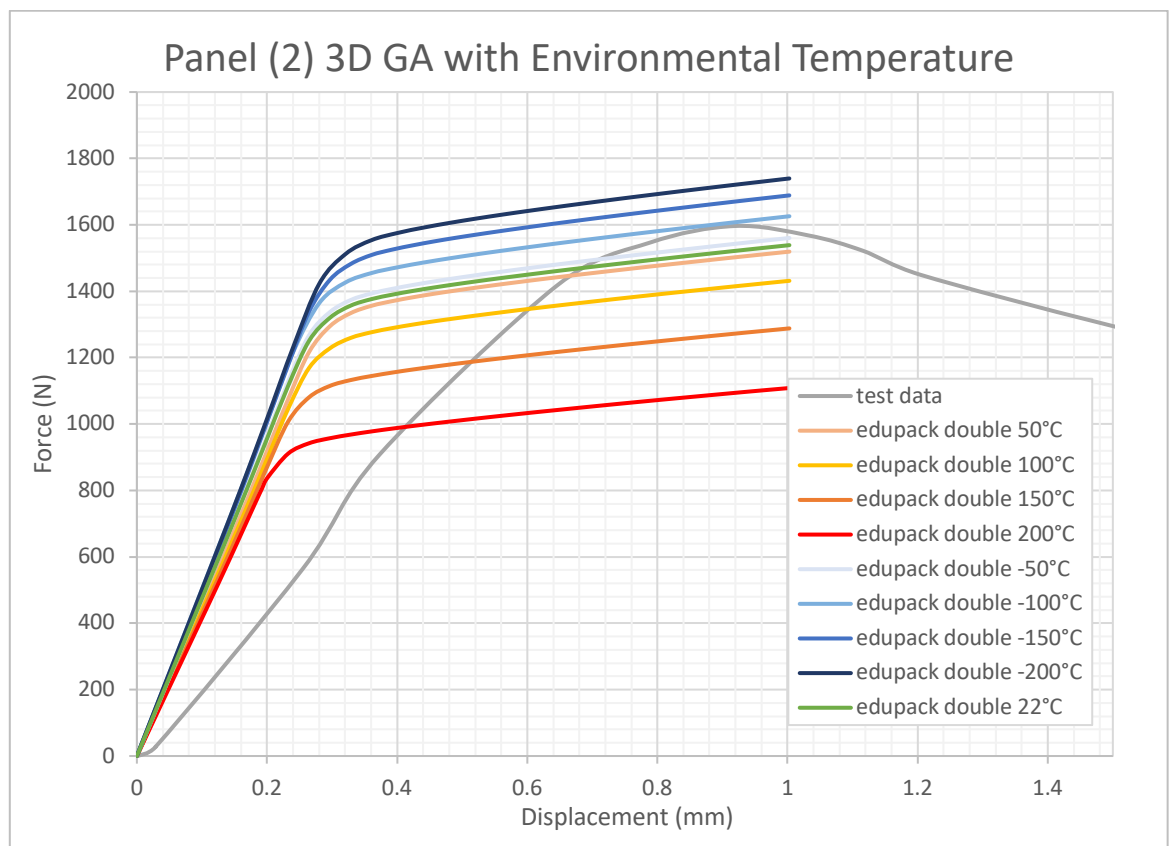


Figure 8: Thermomechanical Response of Varying Environmental Temperature

At normalised stress, the intensity of the stress distribution in the core increases with decreasing temperature. This is expected behaviour as the Young's modulus of the material also increases with decreasing temperatures.

Deformation (mm) at which plastic deformation first occurs				
22°C	±50°C	±100°C	±150°C	±200°C

0.12028	0.11226	0.11226	0.10425	0.0882 1
0.12028	0.11226	0.12028	0.12028	0.1202 8

Table 5: FEA of GA onset of plastic strain at varying temperature

Another measurable metric is the deformation at which plastic strain first occurs. This generally decreases as the temperature increases, while staying constant at decreasing temperatures. The observed behaviour shows the sensitivity of plastic deformation with changing temperature. This is particularly interesting in reference to the hysteretic behaviour, where the residual stress state resulting in the open loop behaviour was linked to a change in temperature distribution. The key distinction, however, is that the change in temperature resulted from mechanical loading in a uniform temperature environment.

The environmental temperature implementation only partially fulfils the goal of developing a combined thermo-mechanical model as it can only identify steady state behaviour, which is broadly similar to the separation of thermo-mechanical response, which was identified as inadequate for the purposes of this work. The model cannot show varying temperature conditions within the panel, account for thermal expansion effects (which would be required to model the effect of thermal cycling on fatigue), nor capture the dynamic thermal response seen in the research of Ganiłova et al. [9].

2.2.3 3.1.2 Results for GA model for Thermo-Mechanical loading introduced with Heat Flux

The purpose of the thermo-mechanical model with heat flux is to create a more detailed FEM, capable of showing the mechanical response to thermal loading and combined thermo-mechanical loading. This is achieved by coupling a thermal analysis to a mechanical analysis in ANSYS and the details of the setup are described above. Considering the environmental conditions of the above section, heat would cause slight expansion of the panel, which may change the panel response (the degree of which was assumed to be negligible). An uneven heat distribution through the panel is considered in the analysis of this section. Figure 10 shows the force reaction behaviour of the heat flux models during TPB. The Environmental temperature data is grey. The Legend shows the extent of the heat flux applied between the top surface “top” and bottom surface “bot”, where the temperature is in °C.

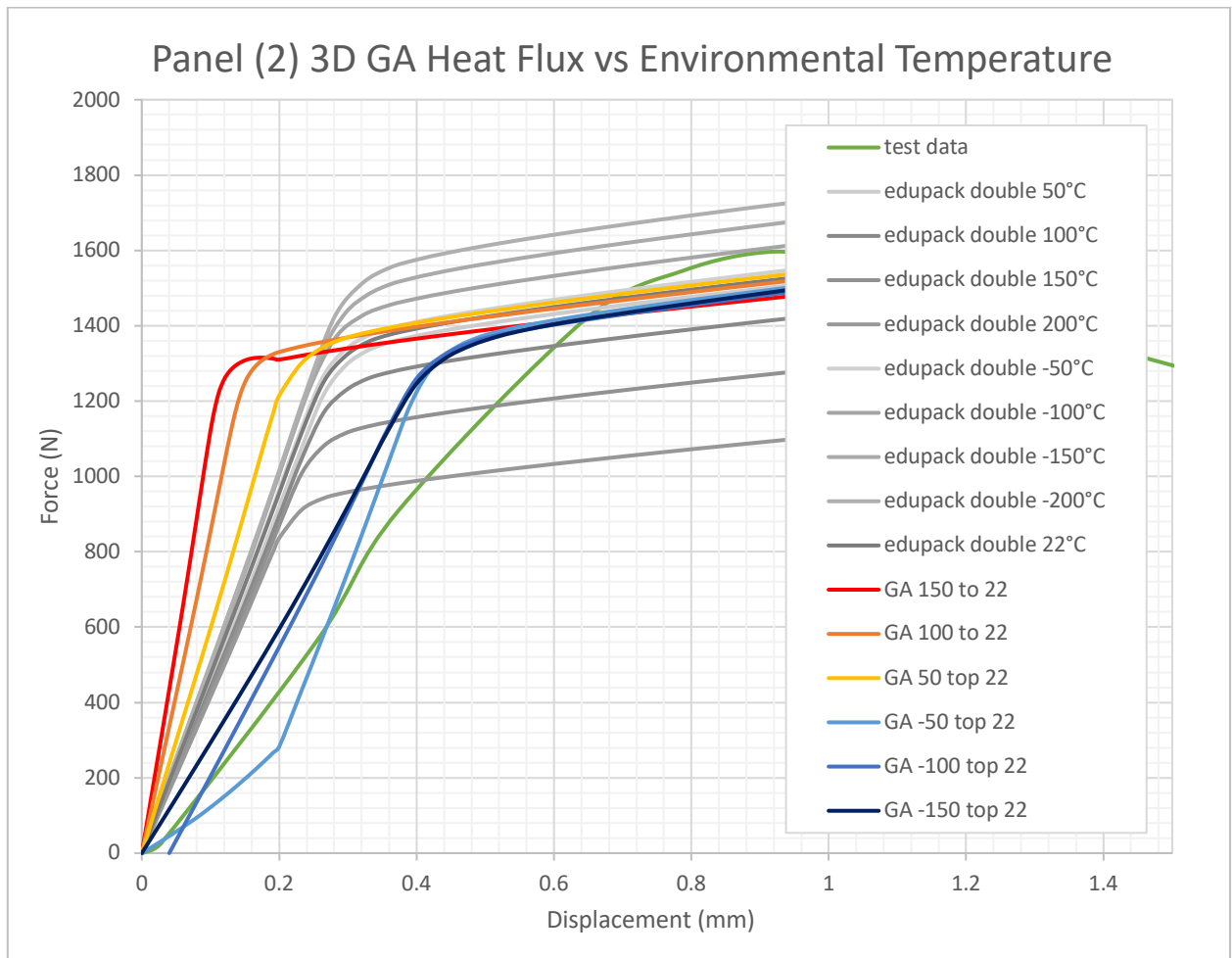


Figure 9: Force Displacement Response of GA Heat Flux Models

As can be observed in Fig.9, both positive and negative temperature flux appear to behave differently, additionally the negative temperature flux appears to be inconsistent in the initial displacement. This could be due to the panel deforming from thermal strain in the same direction as the puncher is displacing the panel, which makes the current model setup invalid for analysis in the low displacement range.

The positive heat flux results in a stiffer panel response, which is due to the preloading of the panel due to thermal strain opposing the puncher. The increase of ΔT results in distinct and distinguishable responses in the 200N range which means that the FEM satisfies the goal of the analysis. Interestingly, the 150°C panel has a sudden drop in force after an initial peak which could be explained through the geometric nonlinearity described in [10].

The heat flux coupled model improves the environmental temperature model in that it can show the effect of uniformly changing temperature (not shown in the analysis) as well as temperature gradients, as shown above. It can show the mechanical response to any predetermined thermal condition. It may not show dynamic coupling behaviour where the mechanical loading is linked to a thermal response. However, the presented model(s) show the fundamental

thermomechanical responses of aluminium HSPs under TPB. Furthermore, they indicate significant deviation in panel response in the 200N range, subject to investigation for space structures.

To represent the mechanical effect on thermal loading, a mechanical-to-thermal coupling, or a three-way coupling of thermal-to-mechanical-to-thermal, is required, which may not ultimately be practically possible.

2.3 3.2 Simulation results for the 3D Continuum Model

The Continuum Modelling approach simplifies the GA Model by replacing the honeycomb core with an equivalent, homogenous, orthotropic material. The same panel from [8] was chosen for validation of this model and simulation under thermo-mechanical loading. With the development of this model an attempt is made to derive a model which is as accurate as the GA model but with a much lower computational cost.

The development of equivalent material properties is the most important part of the development of the continuum model and is therefore discussed in detail. The mechanical properties required for an orthotropic material are the Young's moduli, the shear moduli and the Poisson's ratios which vary along the three principal axes.

The Material Designer tool within ANSYS 2020 R1 was used to create both the Mechanical and the Thermomechanical equivalent orthotropic material properties (Figure 10).

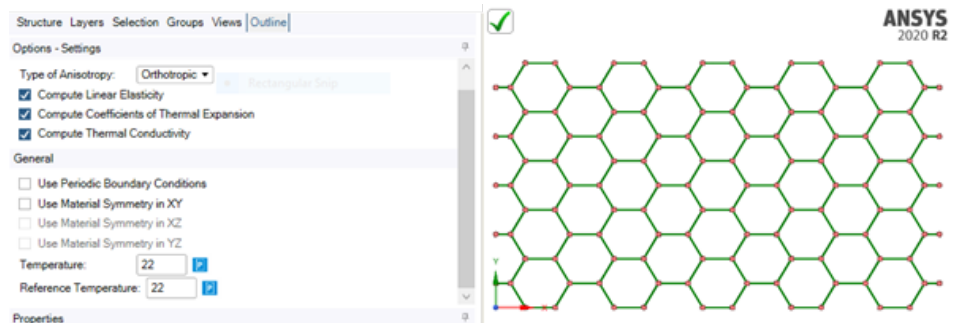


Figure 10: Material Designer Settings

Firstly, the material of the structure was defined as the temperature dependent A3105 from above. The honeycomb type was selected as “expanded” and the material geometry of a unit cell was defined according to the specification of the chosen panel (panel 2). The repeat count for cells in the unit volume was set to 5 and the mesh was discretized through cell sizing of 2mm. These settings allowed the inclusion of both mechanical and thermal properties (Figure 10). The analysis was performed with variable material evaluation, where the orthotropic properties were calculated repeatedly for a changing variable (temperature). Due to the temperature-dependent

aluminium material properties, the resultant orthotropic material also shows temperature dependent behaviour.

Engineering Constants	25°C	Units		
E1	1.26E+06	Pa		
E2	1.31E+06	Pa		
E3 (out of plane)	1.85E+09	Pa		
G12	7.46E+05	Pa		
G23 (out of plane width)	2.67E+08	Pa		
G31 (out of plane length)	3.92E+08	Pa		
nu12	0.97905			
nu13	0.000225			
nu23	0.000234			
Density	71.305	kg m ⁻³		
			Thermal Expansion Coefficients	
			Units	
			aX	1.96E-05 °C ⁻¹
			aY	1.96E-05 °C ⁻¹
			aZ	1.96E-05 °C ⁻¹
			Thermal Conductivity	
			K1	2.5963 W m ⁻¹ °C ⁻¹
			K2	1.7773 W m ⁻¹ °C ⁻¹
			K3	4.5424 W m ⁻¹ °C ⁻¹
			Specific Heat Capacity	
			cp	896.8 J kg ⁻¹ °C ⁻¹

Table 6: Equivalent Orthotropic Material Properties of Honeycomb Core

A relevant observation is that both the in-plane Young's moduli are similar in magnitude, but E2 with reference to panel length is larger. Similarly, both the out-of-plane shear moduli are of the same order of magnitude and again the lengthwise value, G31, is greater. This difference originates from the slight asymmetry of the core structure and is increased by the double wall thickness. While the Material Designer predicts a uniform thermal expansion along all axes, the thermal conductivity is largest in the out-of-plane direction, which is logical given the core geometry.

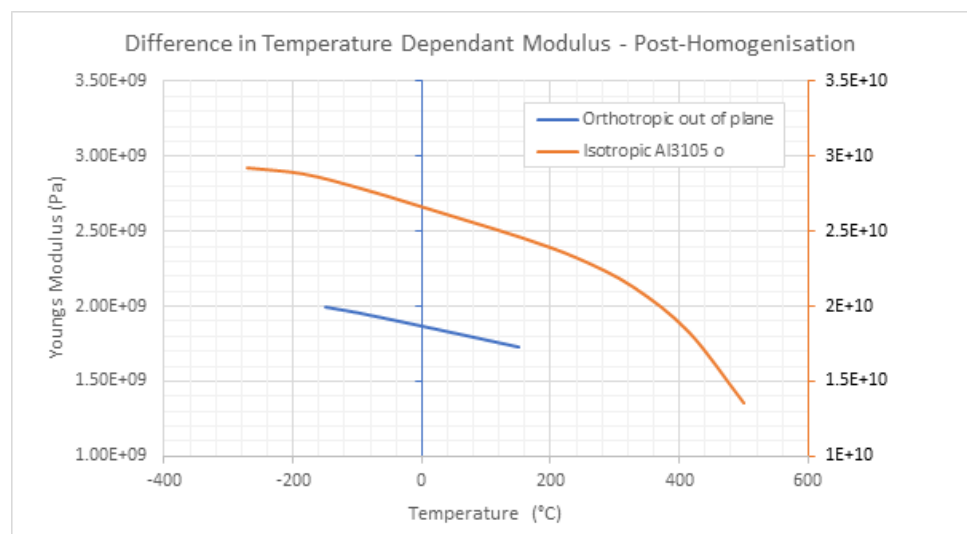


Figure 11: Comparison of Continuum and Isotropic Temperature Dependant Material Data

With a normalised stress range (in Pascals) it is apparent that the behaviour of the homogenised core is very similar to the isotropic material data in the out-of-plane direction (Figure 11). The continuum material model is fundamentally limited because it does not include a plasticity model and is much harder to implement. Anisotropic plasticity may be implemented into ANSYS through the addition of a generalised Hill yield criterion.

2.3.1 3.2.1 Results for 3D Continuum Model for Mechanical loading only

The fundamental difference in the FEM for 3D Continuum Model is the geometry of the core, which is replaced by a solid 3D element, and the material model for the core (Figure 12). The contacts, boundary constraints, mesh method and analysis settings are all kept the same to provide consistency between analyses.

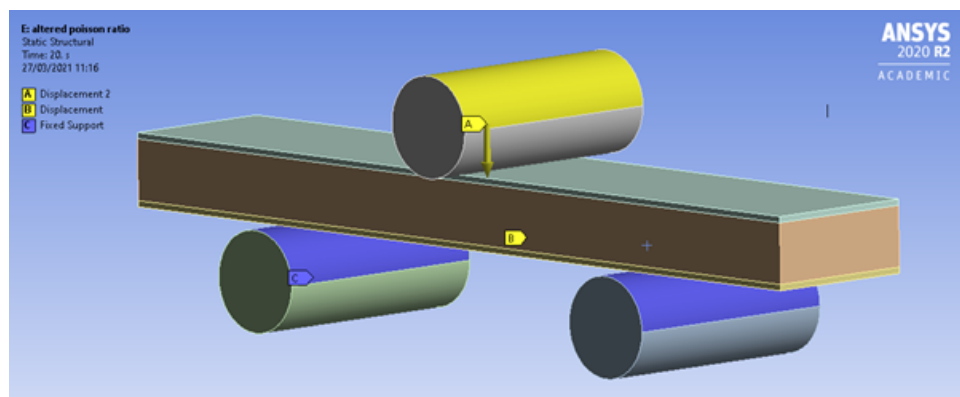


Figure 12: 3D Continuum Model Setup

The mechanical model's validity was primarily assessed by considering the force reaction response to the GA model and the test data. Furthermore, FEA was considered to identify the key differences between the two FEM approaches. Since the CM does not provide limitations to mesh quality due to geometric complexity, a mesh convergence study was performed with the goal set to identify the most optimal mesh parameters which would not affect the accuracy of the solution. Here, both tetrahedral and hexagonal elements were considered at varying mesh sizes.

The mechanical response of the 3D continuum model is used to validate the model behaviour in comparison to both the previous model and the test data. Additionally, the FEA of the panel is presented to explain the panel behaviour.

With the core replaced by a homogenous material the sandwich panel behaves more like a beam under bending than in the GA model. This is evident because the deformation or curved shape of the panel extends beyond the supports at the plate ends.

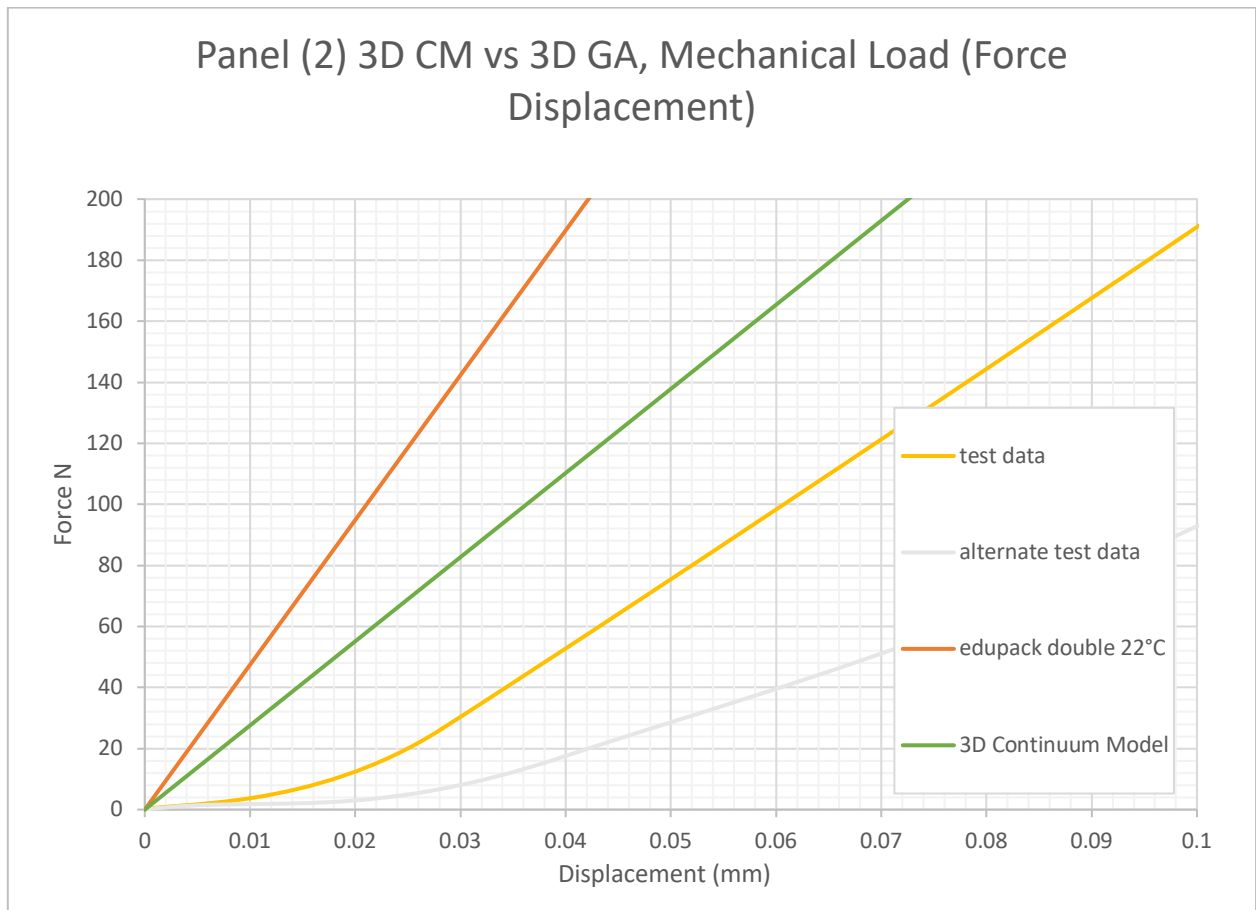


Figure 13: Force Reaction of CM Panel Response and Validation

The continuum model shows a significant deviation from the GA model and, despite the continuum material being developed using a double thickness unit cell, shows closer resemblance to the single thickness model (Figure 13). Surprisingly, this means that, overall, it matches the test result better than the GA result. Due to the lack of a plasticity model for the material, the system response is linear and cannot accurately predict the buckling strength of the panel. The continuum response deviates from the GA model and could be described through two separate linear gradients: initially a shallower gradient, then secondly a gradient which more closely matches the GA model.

2.3.2 3.2.2 Mesh Convergence

The aim of this section was to simplify the continuum model, in order to achieve faster solving times. Initially, the continuum model offered limited time savings compared to the full geometrically accurate (GA) model. However, the continuum model's geometry is much simpler compared to that of the GA model, suggesting that larger elements could be introduced. A mesh convergence study was conducted to identify the most efficient mesh. A maximum acceptable error compared to the original continuum mesh of $\pm 5\%$ was selected, regardless of time savings, to minimise cumulative error. Both hex-dominant and tet-dominant mesh methods were considered, after significant time savings when using the

hex-dominant method were noted by one group member. However, that result was not replicated during this study, implying that these savings are hardware dependent.

A variety of meshing approaches were used. Element size biasing around stress concentrations was considered but failed to provide sufficient accuracy as the element count was decreased. At low element counts, it was difficult to generate a mesh with elements properly aligned between bodies: this unsurprisingly led to less reliable results.

As the element count decreased and accuracy declined, there were some models which offered relatively stable (but large) errors. These were not considered for the following analysis, but it is reasonable to consider these if either a larger error, or a result adjusted by a corrective factor would be acceptable.

A selection of meshes considered are presented below.

Mesh Name	Number of Elements	Simulation Time	Average Error (%)
Original	22760	33m 10s	N/A
Tet 1	13960	25m 43s	-2.24
Tet 2	5940	10m 43s	17.9
Tet 8	8012	12m 03s	16.6
Hex 0Q	22615	31m 35s	0.494
Hex 1Q	22814	34m 04s	0.415
Hex 3	12220	16m 47s	12.1
Hex 5	12528	26m 02s	4.80

Table 7: CM - Mesh Convergence study

In Table 7, the average error is in comparison with the original mesh, a tetrahedral element mesh with 22760 elements which took 33m 10s to solve. 0Q and 1Q denote that the mesh followed the same instructions as the equivalent tetrahedral element mesh but used hex-dominant meshing instead.

Following this study, the mesh Tet 1 was taken forward for environmental temperature analysis.

2.4 3.2.3 Results for 3D Continuum Model for Thermo-Mechanical loading introduced with Environmental Temperature

Firstly, the panel was subject to changing environmental temperature within the static structural analysis, ranging from -150°C to 150°C . Then the thermo-mechanical model was created through coupling of thermal and mechanical analyses in ANSYS. The same methodology as in Section 3.1 was used to create the variable temperature distribution across the CM models. Subsequently, the same variable temperature gradients were considered in the range of $\pm 150\text{--}22^{\circ}\text{C}$ within this analysis.

The 3D continuum, mechanical model from Section 3.2.1 is subjected to changes in environmental temperature in order to assess the panel behaviour under thermal loading (Figure 14). Additionally, the generated results in this section are compared to the results of the GA model of the same loading (Section 3.1.2). FEA was not explicitly included as results were found to be in good agreement with the discussion of Section 3.1.2.

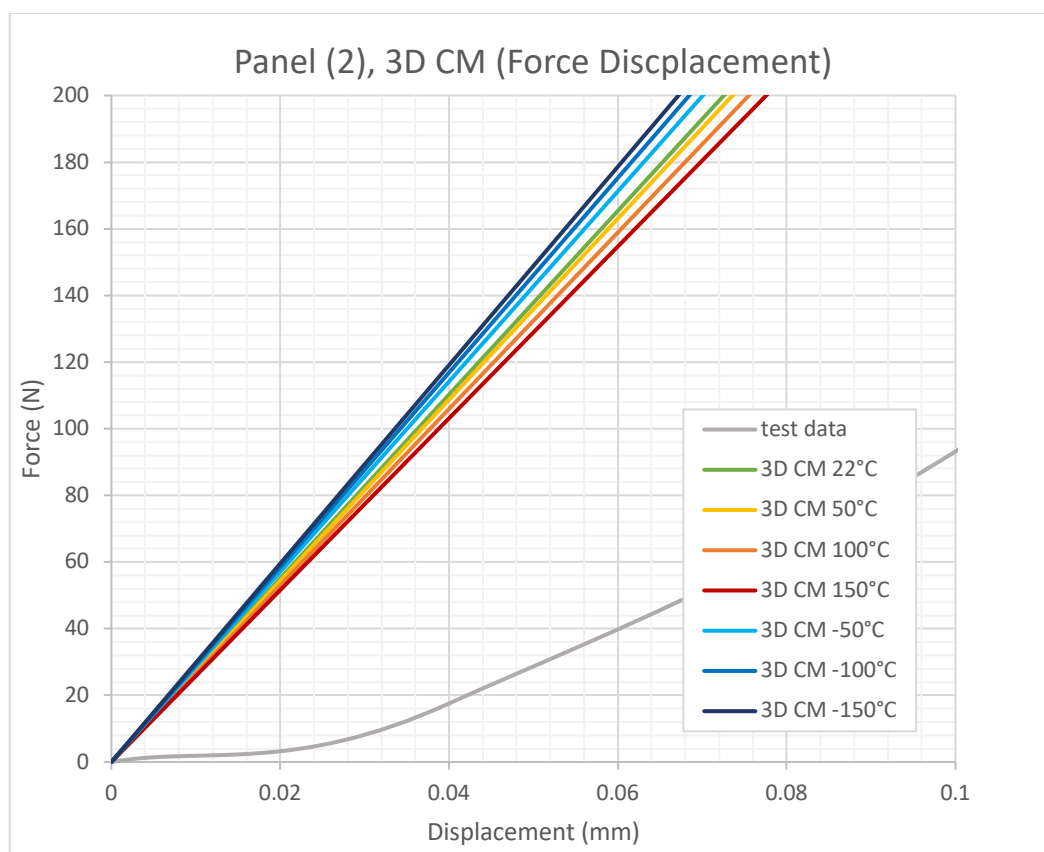


Figure 14: Force Displacement of CM at Varying Environmental Temperature 200N Range

As can be seen in Fig.14 the temperature-dependent continuum model shows the same trends as the GA model: higher temperature equals lower stiffness; lower temperature equals higher stiffness. More importantly, it shows a clear

separation of panel behaviour for changes in environmental temperature in the 200N range. Therefore, the continuum model would be just as suitable to distinguish thermomechanical behaviour as the GA model.

Compared to the GA model, the continuum model is less stiff and shows the ramp up behaviour as discussed above (Figure 15).

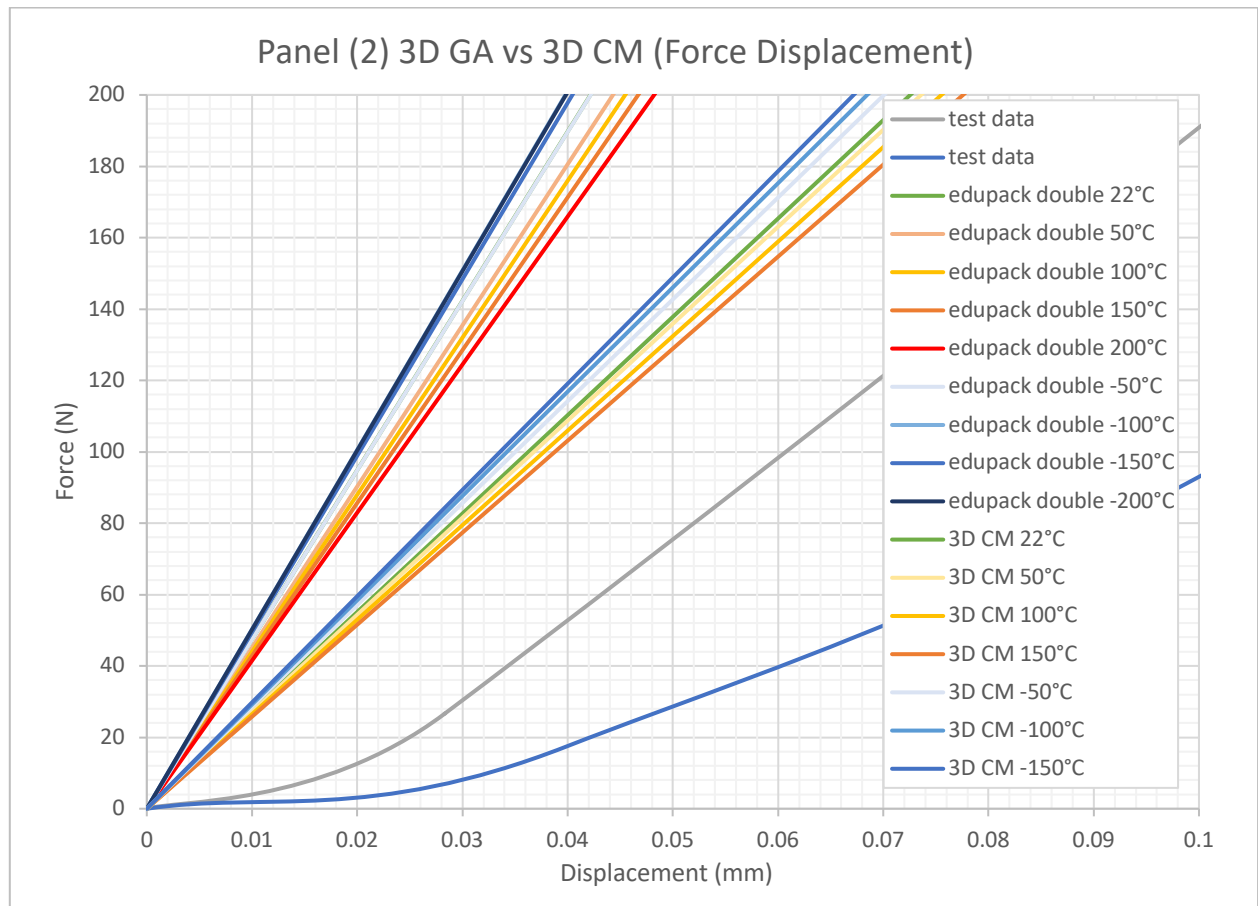


Figure 15: GA vs 3D CM, Force Displacement 200N Range

As can be observed in Fig.15 the panel stiffness decreases at high temperature and increases at low temperatures, as observed in the GA model. Both the GA and the 3D CM's high-temperature responses' incremental stiffness decrease are uniform, however the difference between room temperature and 50°C is much larger in the GA model. At incrementally decreasing temperature, the GA model's response is staggered (previously discussed above) whereas, the CM shows a uniform incremental response. The key observation is the lack of plasticity model which limits the significance on the analysis at this range.

2.4.1 3.2.4 Results for 3D Continuum Model for Thermo-Mechanical loading introduced with Heat flux

Results of the simulation for the thermal effect introduced with heat flux, similar to the case in Section 3.1.3, are presented in Figure 16.

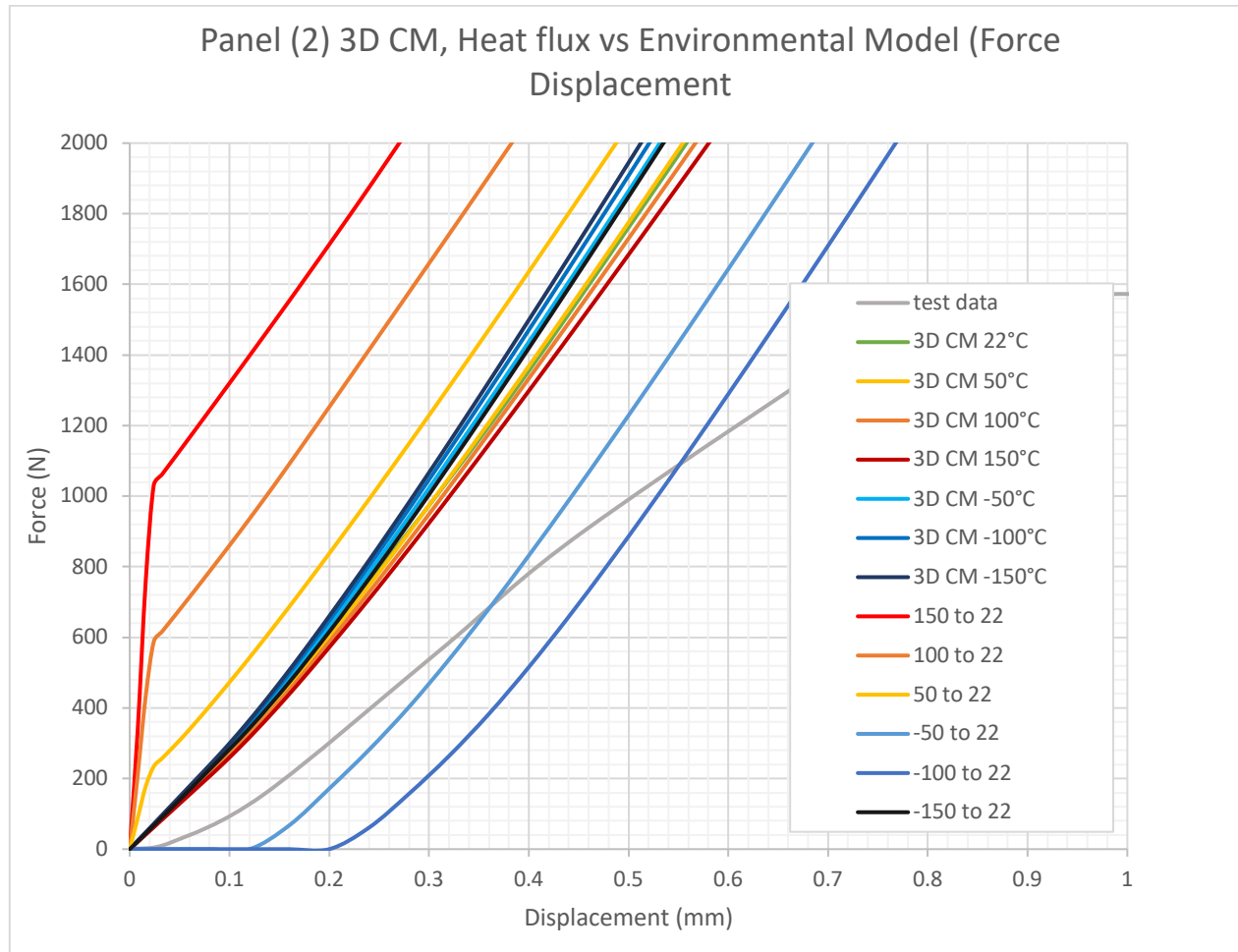


Figure 16: Force Displacement Response of the CM Panel at Varying Heat Flux

As can be seen in Fig.16 for the positive heat flux, due to the thermally induced residual stress and bending opposing the direction of deformation, the overall panel response is stiffer. The behaviour of the 3D continuum model is consistent with the GA thermo-mechanical model with heat flux. For the negative temperature distributions, the early response is inconsistent, as also evident in the GA model. Interestingly, in both models, the -150-22°C condition is significantly different to the other two negative temperature flux conditions.

The positive heat flux models again show the snapping behaviour seen in the GA model, however here the behaviour is seen for all three positive heat flux scenarios, whereas the GA only showed this for the highest heat flux. This could be explained by the increased deformation along the length of the panel of the continuum models during TPB, whereas the GA model tends to show more localised deformations between the supports, under purely mechanical loads.

For both implementations of the thermo-mechanical effects, the continuum model is a valid simplification in terms of behaviour, but slightly inaccurate in terms of numerical comparison.

3.3 Simulation results for the 2D Continuum Model

To introduce further simplifications to the model and investigate its validity at even lower computational cost, the 2D surfaces are used for the 2D continuum model in the ANSYS Design Modeller. From the 3D continuum models a 2D surface was created at the centre of each of the bodies using the “mid-surface” tool. The dimension of these surfaces was then set to 2D in the geometry section of a Static Structural Analysis. For the three-point bending simulation the 2D behaviour was set to “Plane Stress” for all the bodies. “Plane Stress” and “Plane Strain” behaviour are approximations to allow 3D problems to be reduced into 2D problems. “Plane Stress” assumes that the normal stress in the Z axis is zero, which is a valid assumption for the three-point bending simulation as the sides of the panels are not constrained by anything. However, depending on the component being simulated, “Plane Strain” may be a more valid assumption. “Plane Strain” assumes that the normal strain in the Z axis is zero, which usually happens when the dimension in the Z direction is substantially larger than either the X or Y direction, meaning that the material is constrained on both sides. Following this the model was meshed using the same elements and resolution as the previous 3D simulations and the same contacts were applied in order to allow for a fair comparison.

The same constraints and analysis settings were applied, and the force reaction measured to be compared to the 3D continuum model.

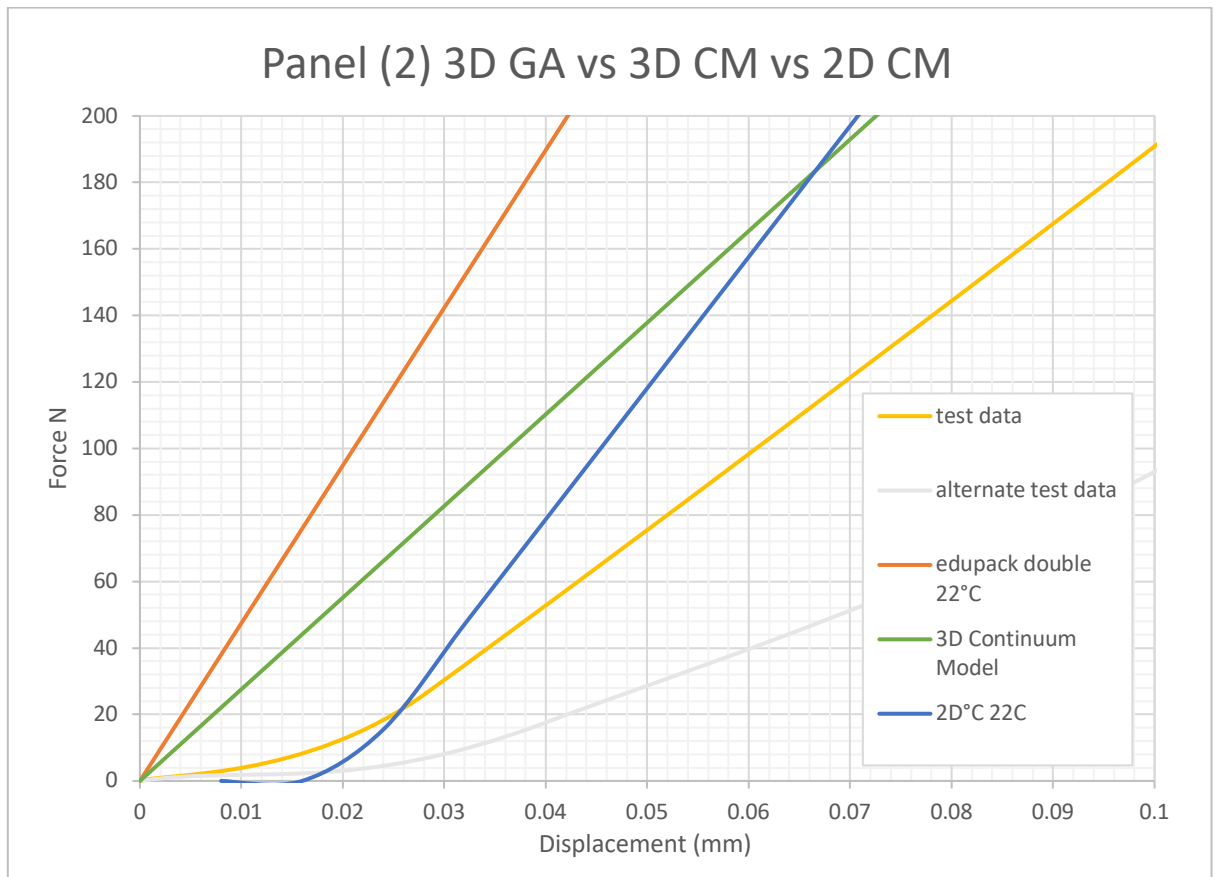


Figure 17: Force Displacement Response of 2D CM vs 3D CM vs 3D GA Model (Mechanical only)

As can be seen in Figure 17 the 2D model shows excellent agreement with the 3D Continuum model but solves in only a small fraction of the time. The same general behaviour was observed as with the 3D continuum models, with the panel becoming less stiff as the ambient temperature increases, which would be expected in reality. The same thermal behaviour occurs as in the 3D GA and 3D C models in that the difference between the load deflection curves is larger for the same ΔT at higher temperatures than at lower temperatures. The trend displayed here is different to both the 3D GA or 3D C models, in that the force required to cause further deflection increases until roughly 0.62mm when it suddenly decreases.

4 Conclusion

In this paper an attempt to develop a simplified thermo-mechanical FE model was described. Three different models were analysed in terms of validity, accuracy and computational cost. It has been demonstrated that all three models were able to show significant deviation of panel response at the low load range typically associated with satellites, making them suitable for such analysis. The models also demonstrated clearly the effect of the thermal loading

and interaction between mechanical and thermal loading in the form of larger deflection at higher thermal loading and stiffer response at lower temperatures. The 2D continuum model was the simplest model and delivered considerable computational savings at the cost of a lack of response under low-strain conditions. The 3D continuum models offer good accuracy in these regions with around 60% less computational time compared to geometrically accurate models. Therefore, it is recommended to implement the 2D continuum method in the case of iterative design or for geometries which allow it, due to only small differences in behaviour but the large time saving. In the cases where a 2D method is not applicable – such as for cases with very small deflections - a 3D continuum model would be suitable for most purposes. These recommendations based on the results presented for 3 models offer modellers the ability to be more confident that their designs can more accurately represent realistic loading conditions, while allowing rapid prototyping of designs at lower computational cost.

References

- [1] G. F. Abdelal, *"Finite element analysis for satellite structures : applications to their design, manufacture & testing"*, 1st ed. 2013.. ed. London: London : Springer, 2012.
- [2] V. Tahmasbi and S. Noori, *"Thermal Analysis of Honeycomb Sandwich Panels as Substrate of Ablative Heat Shield"*, *Journal of Thermophysics and Heat Transfer*, vol. 32, pp. 1-12, 06/22 2017.
- [3] İ. Aydinçak and A. Kayran, *"An Approach for the Evaluation of Effective Elastic Properties of Honeycomb Cores by Finite Element Analysis of Sandwich Panels"*, *Journal of Sandwich Structures & Materials*, vol. 11, no. 5, pp. 385-408, 2009/09/01 2009.
- [4] M. Giglio, A. Gilioli, A. Manes , *"Numerical investigation of a three point bending test on sandwich panels with aluminum skins and Nomex™ honeycomb core"*, *Computational Materials Science*, vol.56, pp.69-78, April 2012
- [5] H. Luo, G. Liu, S. Ma, and W. Liu, *"Dynamic analysis of the spacecraft structure on orbit made up of honeycomb sandwich plates"*, vol. 1, ed: IEEE, 2011, pp. 83-87.
- [6] A. M P, J. Pitchaimani, G. K V, and C. Reddy, *"Numerical and experimental study on dynamic characteristics of honeycomb core sandwich panel from equivalent 2D model"*, *Sādhanā*, vol. 45, 12/01 2020.
- [7] J. Fatemi and M. H. J. Lemmen, *"Effective Thermal/Mechanical Properties of Honeycomb Core Panels for Hot Structure Applications"*, *Journal of spacecraft and rockets*, vol. 46, no. 3, pp. 514- 525, 2009.

- [8] G. Sun, X. Huo, D. Chen, and Q. Li, "Experimental and numerical study on honeycomb sandwich panels under bending and in-panel compression", *Materials & Design*, vol. 133, pp. 154-168, 2017/11/05/ 2017.
- [9] O. A. Ganilova, M. P. Cartmell, and A. Kiley, "Experimental investigation of the thermoelastic performance of an aerospace aluminium honeycomb composite panel" *Composite Structures*, vol. 257, p. 113159, 02/01/2021.
- [10] *Geometric nonlinearity*. Available: https://abaqus-docs.mit.edu/2017/English/SIMACAEGSARefMap/simagsa-c-nlgeomnonlin.htm#simagsa-c-nlgeomnonlin_simagsa-c-gss-deflection , Abaqus. (2017, 13/03/2021).